



# Targeted Use of Forming-induced Residual Stresses in Metal Components

Final Report of the DFG Priority Program 2013

Funding period 2017 to 2023

Editor: Wolfram Volk

# **Targeted Use of Forming-Induced Residual Stresses in Metal Components**

Editor:

Prof. Dr.-Ing. Wolfram Volk  
Chair of Metal Forming and Casting

Technical University of Munich  
Germany



## **Fachbuch**

All projects on which the book is based were funded by the  
Deutsche Forschungsgemeinschaft DFG, Project No. 313778369

Coverdesign: Fa-Ro Marketing GmbH, Munich

Layout: Typohandwerker, Leipzig

Bibliografische Information der Deutschen  
Nationalbibliothek: Die Deutsche  
Nationalbibliothek verzeichnet diese Publikation  
in der Deutschen Nationalbibliografie; detaillierte  
bibliografische Daten sind im Internet über  
<http://dnb.d-nb.de> abrufbar.

Das Werk ist urheberrechtlich geschützt.  
Sämtliche, auch auszugsweise Verwertungen  
bleiben vorbehalten.

Copyright © 2024, 1st edition, the copyright of  
the individual chapters lies with the respective  
authors

ISBN 978-3-8316-5048-4 (gebundenes Buch)  
ISBN 978-3-8316-7781-8 (E-Book)

Printed in EU  
utzverlag GmbH, München  
089-277791-00 · [www.utzverlag.de](http://www.utzverlag.de)

## Preface

The current book is a final report of the Priority Program 2013, “Targeted Use of Forming-Induced Residual Stresses in Metal Components,” funded by the German Research Foundation (DFG) in the years 2017–2023.

Residual stresses are defined as stresses within a stationary system or component which exist despite the absence of external mechanical or thermal loads. The residual stress state of a component is essentially determined by the sequence of manufacturing steps within production. Referring to forming processes, they typically induce forces that lead to a plastic deformation of the produced components. After the unloading, the workpiece deforms until it reaches its final geometry with a resulting residual stress state. The component is in a static equilibrium. This means that tensile and compressive residual stresses always occur simultaneously. This residual stress state has a decisive influence on the properties of the parts produced by forming processes. It is well known that tensile residual stresses considerably reduce the fatigue strength in most applications. In contrast, compressive residual stresses in areas close to the surface improve the fatigue strength.

In many forming process chains, the state of tensile residual stress is therefore significantly reduced by heat treatment in industrial applications. Since the yield strength of metals decreases considerably with increasing temperature, the residual stresses during heat treatment lead to plastic deformations and, after subsequent cooling, to a significantly reduced residual stress state. For both sheet metal and bulk forming processes, the deliberate induction of compressive residual stresses by the actual forming

process has not yet been realized. One important reason is a lack of knowledge about the relationship between production parameters and the induced residual stresses. In addition, the established methods for determining residual stresses can only be used to a limited extent in most applications.

The present book is organized in three general parts: First, we give an overview of the basics of forming induced residual stresses from different viewpoints. Secondly, the results of the 12 individually funded projects are explained in detail, followed by the third part summarizing the acquired knowledge and discussing open topics and need for further research.

The results presented here could only be achieved through the generous financial support of the DFG. Many thanks go here to the whole DFG and its responsible staff. I also extend special thanks to my colleagues Peter Groche, Jens Gibmeier, Markus Kästner, A. Erman Tekkaya, Jörg Schröder and Markus Bambach for their willingness to lead the crossproject expert groups. Furthermore, such excellent results can only be achieved with highly motivated and committed researchers. I would therefore like to thank everyone who has contributed to the success of this priority program over the past six years. Last but not least, I would also like to thank my own team, which has mastered the extensive tasks behind the coordination of such a priority program with flying colors.

Munich, November 2023

Wolfram Volk



# Contents

<b>I Basic Principles</b>	<b>13</b>
<b>1 Residual Stresses in Modern Production Engineering</b>	<b>13</b>
1.1 Introduction . . . . .	13
1.2 Definition of Residual Stresses . . . . .	13
1.3 Residual Stress Engineering . . . . .	14
1.4 Classification of Residual Stresses by Length Scale . . . . .	15
1.5 Origins of Residual Stresses . . . . .	17
1.5.1 Type I Residual Stress . . . . .	17
1.5.2 Type II Residual Stress . . . . .	19
1.5.3 Type III Residual Stress . . . . .	19
1.6 Residual Stress Measurement Methods . . . . .	19
1.6.1 Destructive and Semi-destructive Measurement Methods . . . . .	20
1.6.2 Nondestructive Measurement Methods . . . . .	21
<b>II Results of Cross-cutting Issues</b>	<b>24</b>
<b>2 Thin-walled Product Forming</b>	<b>24</b>
2.1 Introduction . . . . .	24
2.2 Residual Stress Prediction . . . . .	24
2.3 Young's Modulus . . . . .	25
2.4 Material Hardening . . . . .	26
2.4.1 Isotropic hardening . . . . .	26
2.4.2 Kinematic hardening . . . . .	26
2.5 Benchmark Material Characterization . . . . .	27
2.5.1 Test Setup and Basic Material Data . . . . .	27
2.5.2 Results . . . . .	29
2.5.3 Conclusion . . . . .	29
2.6 Benchmark Numerical Analysis . . . . .	29
2.6.1 Incremental Sheet Forming . . . . .	30
2.6.2 Combined Deep Drawing and Embossing . . . . .	31
2.6.3 Embossing . . . . .	34
2.6.4 Conclusion . . . . .	34
<b>3 Residual Stresses in Bulk Forming</b>	<b>36</b>
3.1 Classification in Bulk Forming . . . . .	36
3.2 Potential Benefit of Forming-induced Residual Stresses . . . . .	38
3.3 Reproducibility of the Initial State . . . . .	38
3.4 Strategies for the Manipulation of Residual Stresses . . . . .	40
3.5 Thermal Stability of Forming-induced Residual Stresses . . . . .	45

3.6	Property Improvement Due to Residual Stresses . . . . .	49
3.7	Conclusion and Summary . . . . .	52
<b>4</b>	<b>Simulation and Modeling</b>	<b>57</b>
4.1	Residual Stresses in the Simulation of Forming Processes . . . . .	57
4.2	Mathematical Formulation . . . . .	58
4.2.1	Thermodynamic Framework for Finite Strain Plasticity . . . . .	58
4.2.2	Contact Mechanics . . . . .	59
4.3	Discretization . . . . .	60
4.3.1	Temporal . . . . .	60
4.3.2	Spatial . . . . .	60
4.3.3	Contact . . . . .	61
4.4	Typical Problems Arising During Process Modeling . . . . .	62
4.5	Macroscopic Modeling of Residual Stresses . . . . .	62
4.5.1	Cyclic Loading . . . . .	64
4.5.2	Models for Cyclic Plasticity . . . . .	65
4.6	Multiscale Modeling of Residual Stresses . . . . .	66
4.6.1	Micromechanical Modeling of Residual Stresses . . . . .	66
4.6.2	Modeling of Residual Stresses Based on Crystallographic Texture . . . . .	68
4.7	Fundamentals of Fatigue Life Estimation . . . . .	68
4.8	Residual Stresses as Benchmark: 4 Point Bending Beam . . . . .	70
4.8.1	Setup and Aim . . . . .	71
4.8.2	Resulting Residual Stresses and Simulation . . . . .	71
<b>5</b>	<b>Residual Stress Analysis on Metal Components Manufactured by Forming</b>	<b>80</b>
5.1	Basic Problems and Possible Solutions . . . . .	80
5.2	Special Challenges with Formed Sheet Metal Components . . . . .	86
5.3	Procedure for Analyzing Multi-phase Material States . . . . .	87
5.4	Real-time Insights into Metal Forming Processes Using Diffraction Methods . . . . .	88
5.5	Benchmarks . . . . .	90
<b>III</b>	<b>Results of Research Projects</b>	<b>95</b>
<b>6</b>	<b>Targeted Induction and Stabilization of Residual Stresses in Austenitic Disc Springs by Incremental Forming and Integrated Surface Layer Treatment</b>	<b>95</b>
6.1	Summary . . . . .	95
6.2	Keywords . . . . .	96
6.3	Introduction . . . . .	96
6.4	Experimental Methods . . . . .	97
6.4.1	Production of Various Batches with Rolling . . . . .	97
6.4.2	Robot Based Incremental Forming . . . . .	97
6.4.3	Multisensor Test Setup . . . . .	98
6.4.4	Microstructural Analyses and Residual Stress Measurements . . . . .	98
6.4.5	Developing a Micromagnetic Method for Residual Stress Measurements . . . . .	99
6.5	Numerical Models . . . . .	99
6.5.1	Microscale Simulation Model (CPFEM) . . . . .	99
6.5.2	Macroscale Simulation Model . . . . .	100
6.5.3	Machine Learning . . . . .	101

6.6	Results and Discussion . . . . .	101
6.6.1	Experimental Results of the Rolling Process . . . . .	101
6.6.2	Micromechanical Simulations of Material Properties . . . . .	102
6.6.3	Macromechanical Simulations of the Rolling Process . . . . .	103
6.6.4	Finite Element Based Temperature Control in High-speed Incremental Forming	103
6.6.5	Simulation of the Residual Stresses and Properties of the Disc Springs . . . . .	105
6.6.6	Mechanical Testing of the Disc Springs . . . . .	106
6.6.7	Developing a Micromagnetic Method for Residual Stress Measurements . . . . .	107
6.6.8	Machine Learning Prediction of the Process Chain . . . . .	107
6.7	Conclusion . . . . .	108
<b>7</b>	<b>Experimental and Numerical Modeling and Analysis of Microstructural Residual Stresses in Hot Bulk Forming Parts under Specific Cooling</b>	<b>111</b>
7.1	Introduction . . . . .	III
7.2	Materials and Methods . . . . .	II3
7.2.1	Setup of Hot Forging Process Chain . . . . .	II3
7.2.2	Numerical Process Design . . . . .	II3
7.2.3	Single-scale Model . . . . .	II4
7.2.4	Two-scale Model . . . . .	II5
7.3	Results . . . . .	II6
7.3.1	Influence of Forming and Disturbance Parameters . . . . .	II7
7.3.2	Comparative Study of Different Cooling Media . . . . .	II7
7.3.3	Experimental Realization . . . . .	II8
7.3.4	Investigation on Microscopic Residual Stresses . . . . .	II9
7.3.5	Properties improved by residual stresses . . . . .	II23
7.4	Conclusion . . . . .	II23
<b>8</b>	<b>Forming Generation of Residual Compressive Stresses During Wire Drawing for the Production of Heavy-duty Springs</b>	<b>127</b>
8.1	Introduction . . . . .	127
8.2	Work and Results . . . . .	128
8.2.1	Presentation of the Results and Discussion . . . . .	128
8.2.2	Statement on the Economic Usability of the Results . . . . .	144
8.2.3	Cooperation Partners at Home and Abroad . . . . .	144
8.2.4	Qualification of Young Scientists in Connection with the Project . . . . .	144
8.3	Summary . . . . .	144
<b>9</b>	<b>Targeted Introduction of Residual Stresses via Local Embossing of Structures in Sheet Normal Direction to Improve Component Properties</b>	<b>147</b>
9.1	Introduction . . . . .	147
9.2	Studies of the Design of the Combined Forming and Embossing Process . . . . .	148
9.3	Numerical Design of the Tool Concept . . . . .	149
9.4	Tool Concept Design . . . . .	150
9.5	Experimental Analysis of Residual Stresses on Textured, Multi-phase Sheet Metal Materials . . . . .	151
9.6	Theoretical Framework for the Simulation of Phase-specific Residual Stresses . . . . .	157
9.7	Validation of the Simulation Strategy . . . . .	159
9.8	Summary and Conclusions . . . . .	160

<b>10 Experimental Characterization and Numerical Analysis of Increasing Fatigue Strength by Residual Stresses for Cross-rolled Parts</b>	<b>164</b>
10.1 Motivation and Objective . . . . .	164
10.2 The Cross-rolling Process . . . . .	164
10.2.1 Process Kinematic and Parameters . . . . .	164
10.2.2 Material Selection . . . . .	165
10.3 Joining Mechanism and Achievable Joint Strength . . . . .	166
10.4 Process Simulation . . . . .	166
10.4.1 Material Characterization and Model . . . . .	166
10.4.2 Simplified FE-model . . . . .	167
10.5 Residual Stress Analysis . . . . .	168
10.6 Experimental Validation . . . . .	168
10.6.1 Residual Stress Measurements . . . . .	168
10.6.2 Experimental Fatigue Life Tests . . . . .	170
10.6.3 Thermal and Mechanical Stability of Residual Stresses . . . . .	171
10.6.4 Joint Quality Testing . . . . .	171
10.7 Fatigue Life Calculations Considering Residual Stresses . . . . .	172
10.7.1 Extension of Local Strain Approach . . . . .	172
10.7.2 Phase-field Model for Fatigue Fracture . . . . .	175
10.8 Conclusion . . . . .	178
<b>11 Requirement-specific Adjustment of Residual Stresses During Cold Extrusion</b>	<b>180</b>
11.1 Introduction . . . . .	180
11.2 Formation of Residual Stresses During Conventional Extrusion . . . . .	181
11.3 Material Characterisation . . . . .	182
11.4 Methodology for Reducing Residual Stresses Due to a Counter Punch . . . . .	183
11.5 Methodology for Reducing Residual Stresses through an Active Die . . . . .	188
11.6 Validation of Improvement of Material Properties . . . . .	193
11.7 Modeling the TaReS Strategy . . . . .	196
11.8 Conclusion . . . . .	198
<b>12 Increased Efficiency of Electrical Steel by Targeted Residual Stress</b>	<b>201</b>
12.1 Introduction . . . . .	201
12.2 Embossing Process . . . . .	202
12.3 Mechanical Material Behavior of Embossed Flux Barriers . . . . .	203
12.3.1 Embossed Flux Barriers under Tensile Load . . . . .	203
12.3.2 Embossing Induced Residual Stresses . . . . .	204
12.4 Advances in the Characterization and Simulation of Magneto-mechanical Coupling .	205
12.5 Analysis of the Local Magnetic Properties in the Bulk of the Material . . . . .	206
12.5.1 Upgrade of the Neutron Grating Interferometer . . . . .	207
12.5.2 Influence of Residual Stresses on DFI . . . . .	208
12.5.3 Determination of Optimal Embossing Punch Shape . . . . .	208
12.5.4 Validation of Mechanical Simulations . . . . .	209
12.6 Results . . . . .	210
12.6.1 Repeatable Results . . . . .	210
12.6.2 Magnetic Flux Guidance . . . . .	211
12.6.3 Embossing Patterns and Embossing Force . . . . .	211
12.6.4 Residual Stress Distribution and Magnetic Behavior under Tensile Load . . . . .	212
12.7 Summary . . . . .	213

<b>13 Targeted Introduction of Residual Stresses through Suitable Forming Processes to Produce Bistable, Metallic, Fully Closed Tube Profiles</b>	<b>216</b>
13.1 Introduction . . . . .	216
13.2 Bistability in Thin Metal Sheets . . . . .	217
13.3 Materials . . . . .	218
13.4 Considered Production Process Strategies . . . . .	218
13.4.1 Two-step Incremental Bending PR <sub>1</sub> . . . . .	219
13.4.2 Incremental Bending Followed by Roll Forming PR <sub>2</sub> . . . . .	223
13.4.3 Validation of the Models . . . . .	224
13.4.4 Experimental Determination of Residual Stress Distribution . . . . .	225
13.5 12-stand Roll Forming Process . . . . .	225
13.6 Properties of the Bistable Profiles . . . . .	226
13.6.1 Stiffness of the Deployed Structure . . . . .	226
13.6.2 Thermal Stability of Forming-induced Residual Stresses . . . . .	228
13.6.3 Stability of Residual Stresses at Room Temperature under Cyclic State Changes	228
13.7 Conclusion . . . . .	229
<b>14 Control of Component Properties in the Rotary Swaging Process</b>	<b>231</b>
14.1 Introduction . . . . .	231
14.2 Rotary Swaging Process . . . . .	231
14.3 Residual Stress Analysis . . . . .	233
14.3.1 X-Ray Diffraction . . . . .	233
14.3.2 Neutron Diffraction . . . . .	234
14.3.3 Micromagnetic Method . . . . .	235
14.3.4 In-Situ Synchrotron XRD . . . . .	236
14.4 Insight into Residual Stress Generation . . . . .	237
14.4.1 2D-Simulation Results . . . . .	238
14.4.2 In-Situ Recess Swaging of Rings . . . . .	238
14.5 Experimental Studies of Process Influence on Residual Stress Generation . . . . .	239
14.5.1 Process Variations Influencing the Residual Stress Depth Profile . . . . .	239
14.5.2 Surface Residual Stress Distribution and Fluctuations . . . . .	241
14.5.3 Residual Stresses in Multi-stage Rotary Swaging . . . . .	242
14.5.4 Residual Stresses Generation in Austenitic Steel . . . . .	243
14.6 Further Material and Parts Properties . . . . .	243
14.6.1 Hardness . . . . .	244
14.6.2 Fatigue Properties . . . . .	244
14.6.3 Mechanical Stability of Residual Stresses . . . . .	246
14.7 Summary . . . . .	247
<b>15 Investigation of Residual Stress-related Elementary Processes for Cold Forged Components in the Manufacturing and Operating Phase</b>	<b>249</b>
15.1 Introduction . . . . .	249
15.2 Objectives and Methodology . . . . .	250
15.3 Residual Stress Generation during Forming . . . . .	252
15.4 Adjustment of Residual Stresses . . . . .	255
15.5 Residual Stress Stability . . . . .	256
15.6 Operating Behavior . . . . .	257
15.7 Implications for Component and Process Design . . . . .	260
15.8 Summary and Outlook . . . . .	261

<b>16 Improvement of Product Properties by Selective Induction of Residual Stresses in Incremental Sheet Metal Forming</b>	<b>265</b>
16.1 Introduction . . . . .	265
16.2 Incremental Sheet Metal Forming . . . . .	265
16.2.1 Forming Mechanisms . . . . .	266
16.2.2 Residual Stress Analysis in Incremental Sheet Forming . . . . .	267
16.3 Analysis of the Single Point Incremental Forming Process . . . . .	267
16.3.1 Forming Mechanisms . . . . .	268
16.3.2 Process Forces, Geometry, and Material Hardness . . . . .	269
16.3.3 Residual Stresses . . . . .	271
16.4 Analysis of the Process Enhancements . . . . .	272
16.4.1 Incremental Sheet Metal Forming with Counter Pressure . . . . .	273
16.4.2 Process Forces, Geometry and Material Hardness . . . . .	273
16.4.3 Residual Stresses . . . . .	274
16.4.4 Tensile Stress-superposed Incremental Forming . . . . .	275
16.4.5 Geometry and Material Hardness . . . . .	275
16.5 Analysis of Fatigue Strength . . . . .	277
16.5.1 Numerical Fatigue Strength Model . . . . .	277
16.5.2 Influence of Corrosion . . . . .	278
16.6 Transferability of the Results and Application . . . . .	278
16.7 Conclusion . . . . .	279
<b>17 Characterization and Utilization of Process-induced Residual Stresses for the Manufacture of Functional Surfaces by Near-net-shape Blanking Processes</b>	<b>282</b>
17.1 Introduction . . . . .	282
17.2 State of the Art . . . . .	282
17.3 Funding Period I - Choice of NNSB Process . . . . .	284
17.3.1 Experimental Setup and Test Equipment I . . . . .	284
17.3.2 Results I . . . . .	285
17.4 Funding Period II – Fineblanking with Targeted Process-induced Residual Stresses . . . . .	288
17.4.1 Experimental Setup and Test Equipment II . . . . .	288
17.4.2 Results II . . . . .	288
17.5 Funding Period III — Application Oriented Pinion/Wheel Pair . . . . .	290
17.5.1 Experimental Setup and Test Equipment III . . . . .	290
17.5.2 Results III . . . . .	291
17.6 Conclusion and Outlook . . . . .	294
<b>IV Conclusion</b>	<b>298</b>
<b>18 Summary and Outlook</b>	<b>298</b>
18.1 Summary . . . . .	298
18.2 Outlook . . . . .	300
<b>List of Authors</b>	<b>302</b>

# 1 Residual Stresses in Modern Production Engineering

Reberger, E.; Volk, W.

## 1.1 Introduction

The existence of residual stresses was recognized over 150 years ago. In 1841, Neumann [1] related “internal stresses” to the birefringence of light in transparent solids. Over time, researchers from various interdisciplinary fields agreed on basic taxonomies and developed an increasing understanding about the nature of residual stresses.

Manufacturing processes typically cause residual stresses. They can significantly impact a material’s properties, such as its strength and ductility. Thus, they affect the performance of a component or structure, leading to a potential decrease in durability or reliability. As such, it is essential to understand the nature of residual stresses and how they can be managed to ensure optimal performance.

One example where residual stresses played a role in failure is the collapse of the Silver Bridge in 1967. The bridge, which crossed the Ohio River between West Virginia and Ohio, had been constructed in 1928. Over time, tensile residual stresses originating from the manufacturing process – combined with a corrosive environment – favored stress corrosion. This led to the growth of a small crack within a bar link and the eventual failure of the bridge. This example expresses the importance of understanding and managing the residual stresses of manufactured products. [2]

## 1.2 Definition of Residual Stresses

Residual stresses are mechanical stresses within a stationary body that acts as a closed system. Two conclusions result from this definition. First, residual stresses can exist despite the absence of external

mechanical or non-mechanical influences since the body represents a closed system. These external influences include external forces, moments, or temperature gradients. Second, these residual stresses are self-equilibrating – otherwise, force or moment resultants would deform the body, which impedes the assumed prerequisite of a stationary state. Within this work, residual stresses are denoted by  $\sigma_{\text{res}}$ . [3]

Residual stresses obey first principles such as Newton’s second law, which states in differential form:

$$\operatorname{div} \boldsymbol{\sigma} + \mathbf{f}_{\text{vol}} = \rho \ddot{\mathbf{x}}. \quad (\text{Equation 1.1})$$

By imposing formerly introduced boundary conditions, *Equation 1.1* transforms into:

$$\operatorname{div} \boldsymbol{\sigma}_{\text{res}} = 0. \quad (\text{Equation 1.2})$$

Here, volumetric forces  $\mathbf{f}_{\text{vol}}$  of arbitrary nature, as well as the acceleration  $\ddot{\mathbf{x}}$ , are set to zero. *Equation 1.2* underlines the self-equilibrating nature of residual stresses. Consequently, tensile and compressive residual stresses always occur simultaneously within a body. [4]

Nearly all modern production technologies induce residual stresses within a manufactured component [5, 6]. In a more detailed view, every processing step within manufacturing and possible postprocessing changes a component’s residual stress state.

Figure 1.1 illustrates the evolution of the residual stress state within manufacturing. Accordingly, semi-finished materials – the starting point of manufacture – inherit residual stresses since they have been subjected to a history of processing steps, too. During manufacture, this chain of processing steps leads to intermediate residual stress states of a component. Finally, the residual stresses of a component can be further manipulated by postprocessing techniques to obtain a desired final residual stress state. [7]

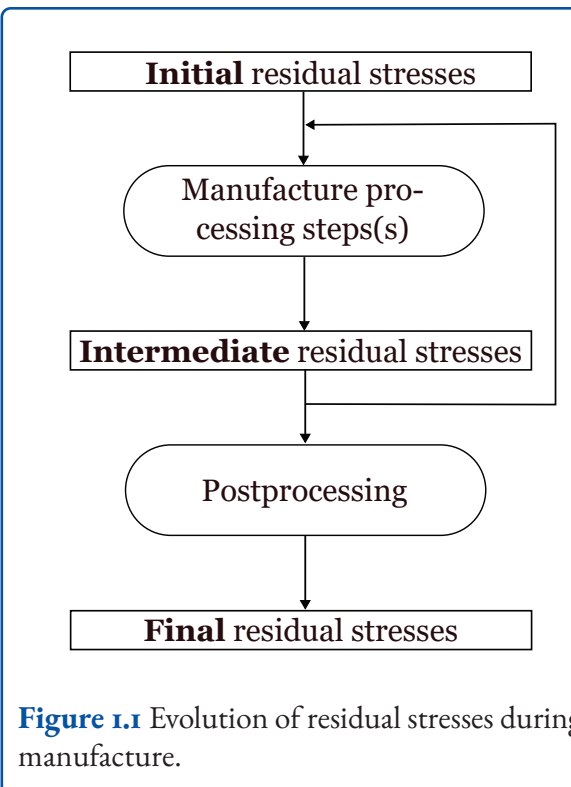


**Figure 1.1** Evolution of residual stresses during manufacture.

### 1.3 Residual Stress Engineering

During the manufacture and the subsequent service life of a mechanical component, these pre-existing residual stresses add up to the applied load stresses. Up to now, the conservative goal has been to avoid the creation of residual stresses during manufacturing or at least to reduce them through post-processing [6]. Regarding service life, components were designed for defined load cases as if they were free of residual stress. However, such an approach that disregards pre-existing residual stresses must be countered by design – for example, by higher safety factors. Naturally, this contradicts a lean design approach.

Consequently, unavoidable residual stresses influence the yield strength, fracture strength, and fatigue behavior of the component [5]. Thus, residual stresses affect the component behavior either positively or negatively. This is true for the manufacturing process and the subsequent service life [6]. The component behavior depends on the local distribution of the residual stresses and the applied load stresses. Following this argumentation,

unavoidable residual stresses must be considered during a component's design stage. Regarding service life, residual stresses are most favorable when they oppose load stresses, which shifts yielding or fracture toward greater values. Furthermore, compressive residual stresses near the surface increase fatigue life, whereas tensile residual stresses reduce fatigue life and favor corrosion tendency [6]. [8]

With the help of novel models, it is possible to create targeted residual stress states during and after manufacturing. These target states are optimized for following manufacturing steps as well as adapted to the component requirements and defined load cases within service life. There are two ways to achieve this goal. As figure 1.1 demonstrated, postprocessing techniques can achieve the desired final residual stress state. But this is an additional process step that is incorporated into the environmental footprint and pricing of the component. Here, residual stresses that interact negatively with defined load cases can be relieved by heat treatment and successive straightening, for example [6]. Similarly, beneficial residual stresses can be introduced in a postprocessing step to improve component properties. For example, shot peening is used to induce compressive residual stresses near the surface, which is advantageous for fatigue life [9]. Here, the component surface is plastically deformed and compressed by shooting small metal balls at the surface. This increases surface hardness and improves fatigue strength by introducing compressive residual stresses near the surface [6]. [4]

The more elegant approach would be to shape the evolution of residual stress during manufacture within early processing steps [8]. This allows for innovative tooling concepts within the process design and optimized geometries within the mechanical design which already introduce beneficial residual stress states during manufacture [6]. Downstream postprocessing steps can thus be eliminated or reduced to a minimum. This can only be achieved with the help of novel models and simulation techniques for residual stress estimation. Volk et al. [4] distinguish between white and black models, which either are based on mathematical and physical principles or have phenomenological approaches, re-

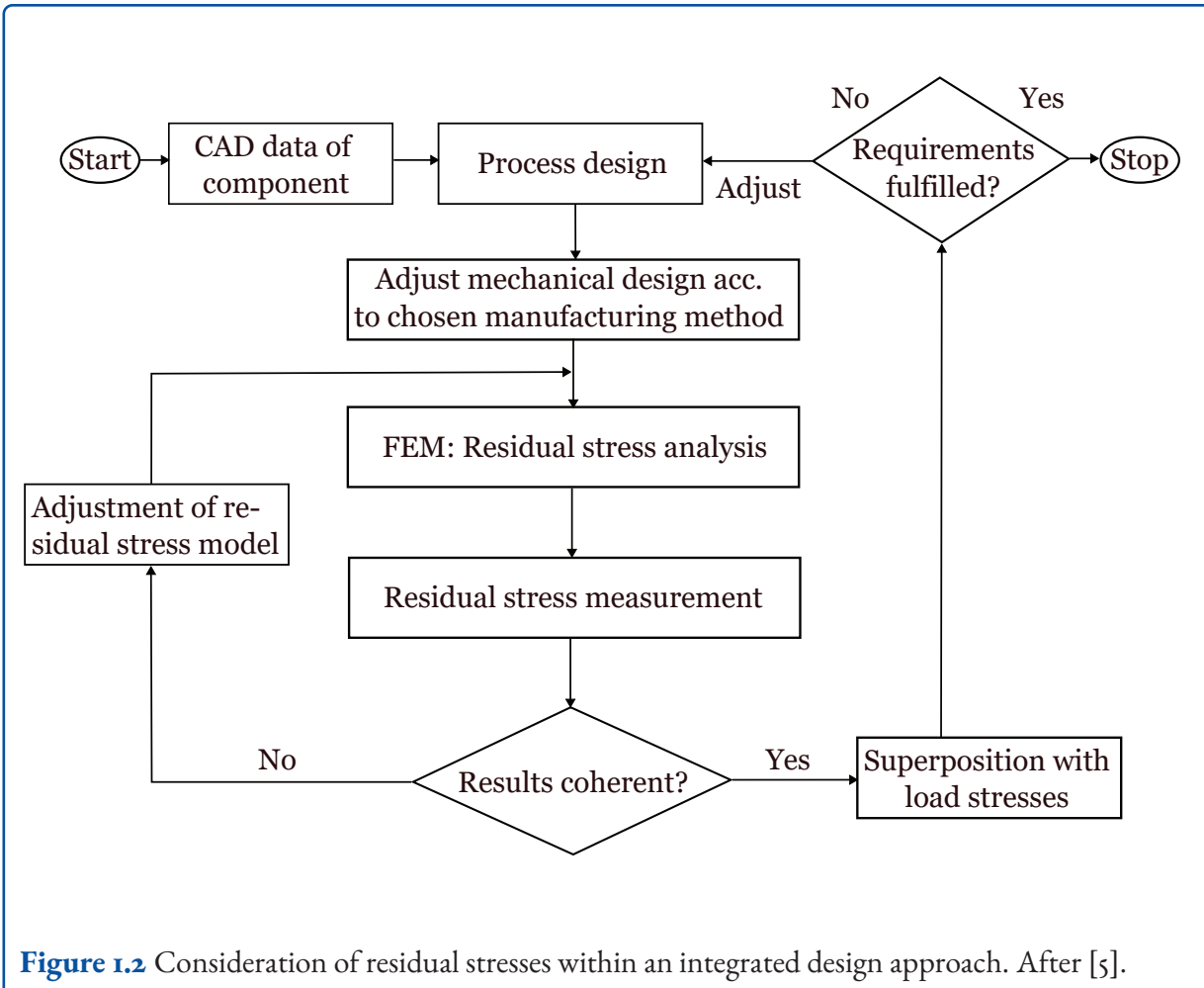


**Figure 1.2** Consideration of residual stresses within an integrated design approach. After [5].

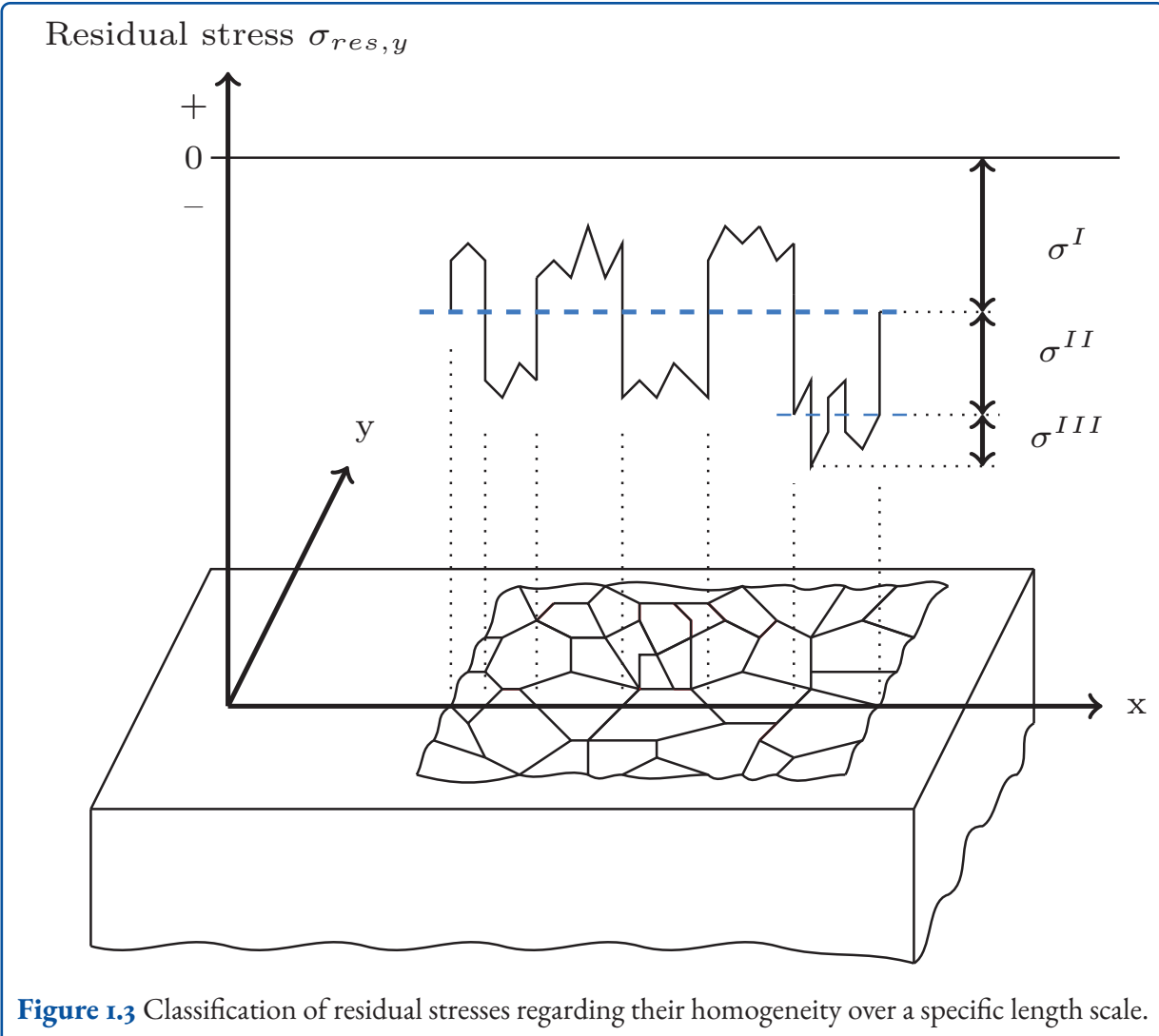
spectively. In addition, there are gray mixed forms of both types of models.

Figure 1.2 shows an integrated design approach where residual stresses are utilized as a design criterion. Here, a suitable manufacturing method is chosen within a first process design step, depending on the initial geometrical CAD data of the component. The geometry is then optimized for the chosen manufacturing method. Residual stresses form due to manufacture processing steps. These residual stresses must be modeled adequately. Inherent model parameters, which include elastic-plastic material behavior and production parameters are identified. These model parameters need to be accessible in order to correlate the process design and induced residual stresses [6]. Model and FEM simulation results must match residual stress measurements. Hereby, the residual stress model is calibrated. If the results are not coherent,

the residual stress model needs adjustments. After successful calibration, residual stresses are superposed with defined load cases. Here, requirements regarding loading limits must be met – otherwise, the design circle is restarted by readjusting the process and mechanical design. This way, a beneficial and loading-appropriate distribution of residual stresses can be achieved. [4]

## 1.4 Classification of Residual Stresses by Length Scale

Commonly, residual stresses are classified regarding their homogeneity over a specific length scale [3]. This approach averages residual stresses over characteristic path lengths and directions. Here, homogeneity means that the residual stresses tend to be constant along the characteristic path length and direction [10]. Figure 1.3 presents these different



**Figure 1.3** Classification of residual stresses regarding their homogeneity over a specific length scale.

scales for type I to type III residual stresses. It depicts an arbitrary body that inherits compressive residual stresses at its surface. The curve shows the residual stresses in the y-direction along the intersecting x-axis.

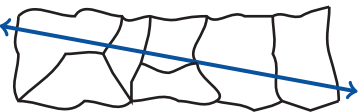
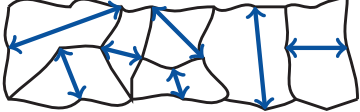
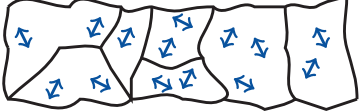
Following a top-down approach, type I residual stress is homogeneous over millimeters. Within figure 1.3, this homogenous level is implied by the bold dashed line and denoted by  $\sigma^I$ . Internal forces which result from residual stresses of type I equilibrate with respect to any arbitrary section plane through the whole body. Thus, type I residual stresses are often referred to as macroscopic residual stresses. Likewise, associated internal moments disappear with respect to each axis. Disturbances of the stress equilibrium, such as material removal,

always lead to macroscopic dimensional changes. [3]

Type II residual stresses ( $\sigma^{II}$ ) are homogenous over one grain or one partial grain, which is represented by the thin dashed line in figure 1.3. The associated internal forces and moments are in equilibrium over a sufficient number of grains. Consequently, they are also called mesoscopic residual stresses. When this equilibrium is interfered with, macroscopic dimensional changes can occur. [3]

In contrast, type III residual stresses ( $\sigma^{III}$ ) are inhomogeneous over the smallest material ranges – that is to say, within lattice dimensions. Associated internal forces and moments equilibrate over grain size dimensions. Thus, they are called microscopic residual stresses. When this equilibrium is

**Table 1.1** Taxonomy of residual stresses.

Type I	Type II	Type III
Homogenous <u>macroscopic</u> residual stresses over millimeters	Homogenous <u>mesoscopic</u> residual stresses over one (partial) grain	Inhomogeneous <u>microscopic</u> residual stresses over atomic lattice spacing
		
Macroscopic dimensional change due to equilibrium disturbance		
Yes	Potentially	No

disturbed, macroscopic dimensional changes do not occur. Hence, their sphere of influence is limited to the typical lattice spacing. Table 1.1 summarizes the aforementioned taxonomy of residual stresses. [3]

At the moment, type I residual stresses are of main interest within production engineering. They are considered for practical evaluation regarding superposition with stresses due to external load forces. According to the previous definition, they are macroscopic stresses and therefore may be included within the framework of a continuum mechanics approach. In contrast, meso- and microscopic residual stresses are more significant for explaining certain phenomena from materials science and solid-state physics. However, the effects of forming on microscopic residual stresses are the focus of current studies and still need to be fully understood [4]. [8]

## 1.5 Origins of Residual Stresses

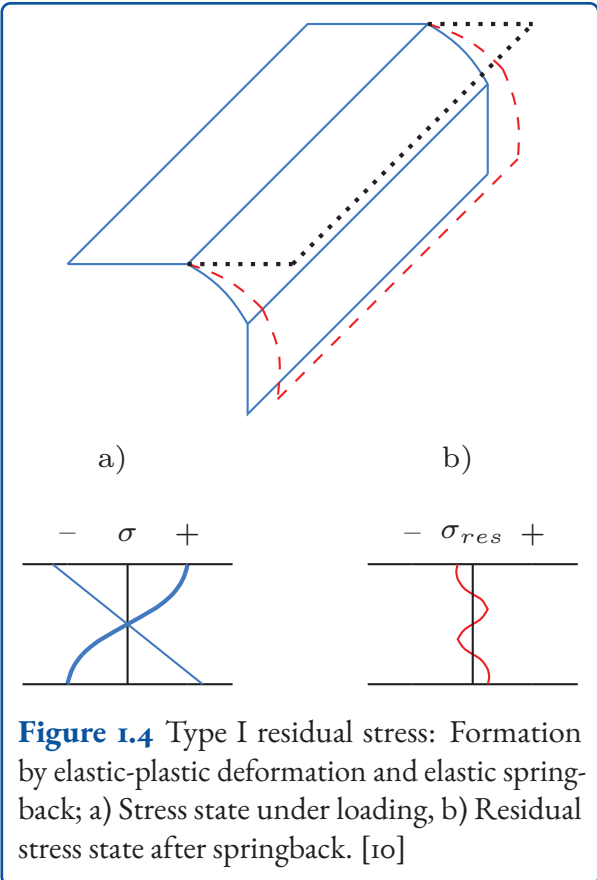
Generally, residual stresses result from geometrical misfits within different regions of a mechanical part [11]. These misfits result from inhomogeneous elastoplastic deformations of varying nature [8]. Whenever regions of a material try to change their dimensions but are hindered in doing so, residual stresses form [10]. The following sub-

sections present different formation mechanisms of residual stresses of different types. They will be detailed within the framework of characteristic length scales.

### 1.5.1 Type I Residual Stress

One cause for type I residual stress is inhomogeneous plastic deformation due to external forces, which is illustrated within a bending use case in figure 1.4. It shows a plastically deformed metal sheet after springback as a dashed red line. Also, associated stress states over the thickness of the metal sheet are depicted. Here, part a) represents the stress state during loading as well as the fictitious elastic stresses during unloading. Part b) shows the resulting residual stress distribution after elastic springback. It results from the superposition of the load stresses and the fictitious elastic stresses due to unloading. The maximum absolute values of the fictitious elastic stresses are higher than the initial load stresses due to the strain hardening of the sheet metal surface. [10]

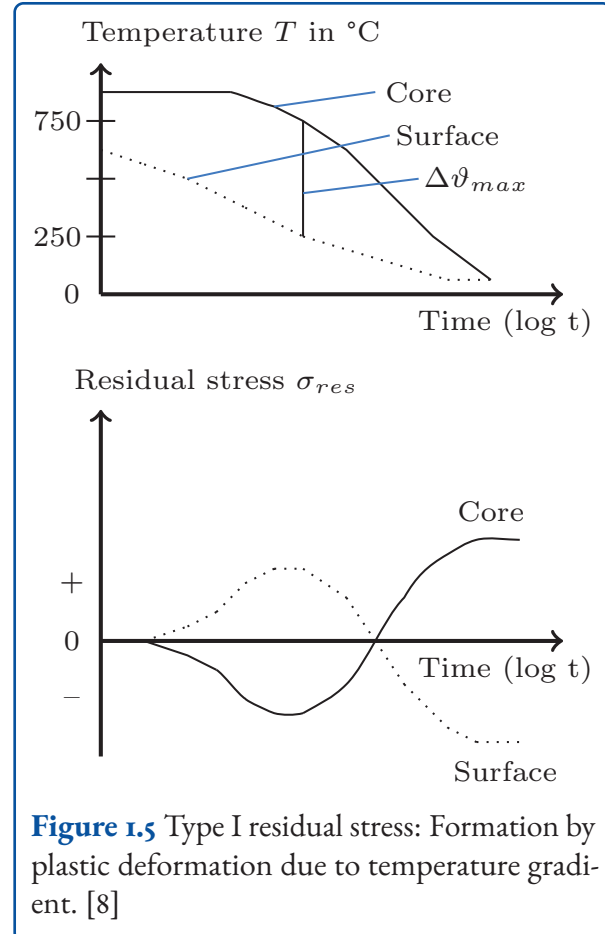
During forming, plastic tensile strains occur in the upper edge region, whereas compressive strains dominate in the lower edge region of the metal sheet. Between both regions, mostly elastic strains occur. After elastic relieve, the metal sheet springs back into the end position. Since the upper edge fibers were elongated during forming, the upper



edge region inherits compressive residual stresses during springback. Analogously, the lower edge fibers were shortened, which results in tensile residual stresses within the lower edge region. [8]

Thermally induced residual stresses are another form of type I residual stresses. When a metallic body cools sufficiently quickly, these residual stresses occur due to inhomogeneous plastic deformations caused by a temperature gradient between its edge and core regions. Furthermore, these inhomogeneous plastic deformations can be caused by varying thermal expansion coefficients in different cross-sectional areas. Residual stresses due to possible microstructure transformations are disregarded here.

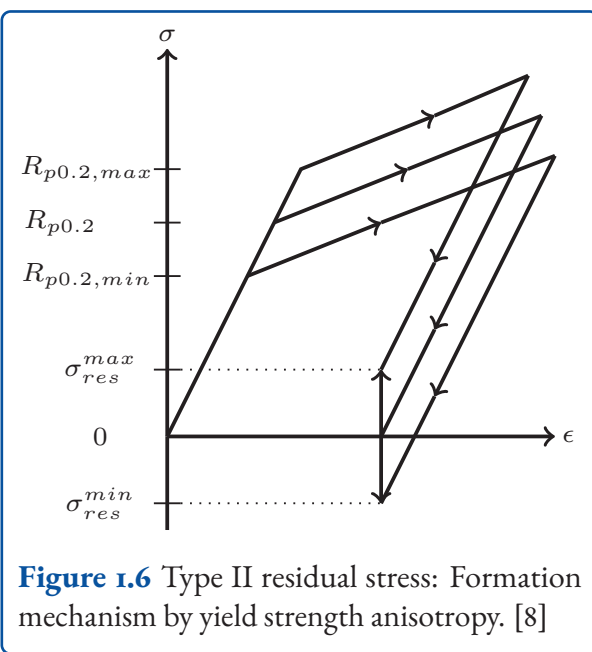
Figure 1.5 shows the temperature gradient during cooling for an isotropic, conversion-free cylinder and resulting residual stresses due to inhomogeneous plastic deformation. [3, 8] Here, the surface initially cools faster than the core, so tensile stresses develop at the surface and compressive stresses in



the core. This is due to the shrinkage of the faster cooling surface layer onto the core [12]. The stresses increase steadily during cooling and reach a maximum at the largest temperature difference  $\Delta\vartheta_{max}$  between the edge and the core. If the hot yield strength of the material is exceeded, inhomogeneous plastic deformation occurs due to the growing stresses induced by the varying temperature gradient. With increasing temperature equalization of the core and edge, the tensile stresses in the edge and the compressive stresses in the core decrease until a stress reversal occurs. At the end of cooling, compressive residual stresses are present at the edge region, and tensile residual stresses in the core. It should be emphasized again that inhomogeneous plastic deformation or constrained shrinkage must occur in the process of cooling for residual stresses to form. Otherwise, thermally induced stresses decrease to zero after cooling is completed. [3, 8]

### 1.5.2 Type II Residual Stress

Residual stresses of type II are caused by the present grain structure of metallic components. Respective elastically isotropic grains are randomly oriented in the material under consideration. The yield strength of the individual grains lies between  $R_{p0.2,min}$  and  $R_{p0.2,max}$ , which leads to an average yield strength  $R_{p0.2}$  of the entire crystal structure. When a load is applied, the grains with lower yield strength start to yield first. Only when the load is increased do the grains with higher yield strength start to yield. As a result, the grains with a lower yield strength undergo higher plastic deformations. After elastic unloading, grains with low yield strength are under compressive residual stress, while grains with high yield strength are under tensile residual stress. Type II residual stresses thus compensate for these deformation incompatibilities during unloading. [8]



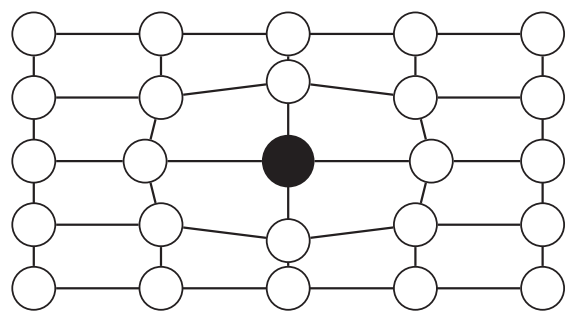
**Figure 1.6** Type II residual stress: Formation mechanism by yield strength anisotropy. [8]

Figure 1.6 shows the stress-strain relations after elastic unloading. Following the curves for grains with different yield strengths, the explained effect for residual stresses becomes apparent. Consequently, type II residual stresses ensure that the material remains in a continuum state as long as no damage occurs. In practice, grains are not elastically isotropic, which amplifies the described effect. Analogous considerations regarding heterogeneous tempera-

ture expansion coefficients at grain level are possible. Again, plastic deformation during cooling or heating is a prerequisite for residual stresses to form. [8]

### 1.5.3 Type III Residual Stress

Residual stresses of type III are microscopic stresses caused by lattice distortions on an atomic level. Lattice distortions are deviations from the ideal crystal lattice structure. Dissolved foreign atoms, vacancies, or dislocations cause these distortions. An example is shown in figure 1.7 where a foreign atom substitutes a regular lattice atom. Here, the reason for the lattice distortion is to find within the varying atom radii of the substitution atom and the regular lattice atoms. [3]



**Figure 1.7** Type III residual stress: Formation mechanism by lattice defect: Dissolved foreign atom. [8]

## 1.6 Residual Stress Measurement Methods

The measurement of residual stresses plays a major role in the calibration as well as the validation of models. All measurement methods have in common that the stresses are measured only indirectly via occurring strains at various scales. The stresses are then backcalculated with suitable material models [13]. Existing measurement methods can be categorized by the degree of sample destruction, the volume characteristics, and the measurable type of residual stresses [11]. In the following, the structure follows the classification by destruction. Volume

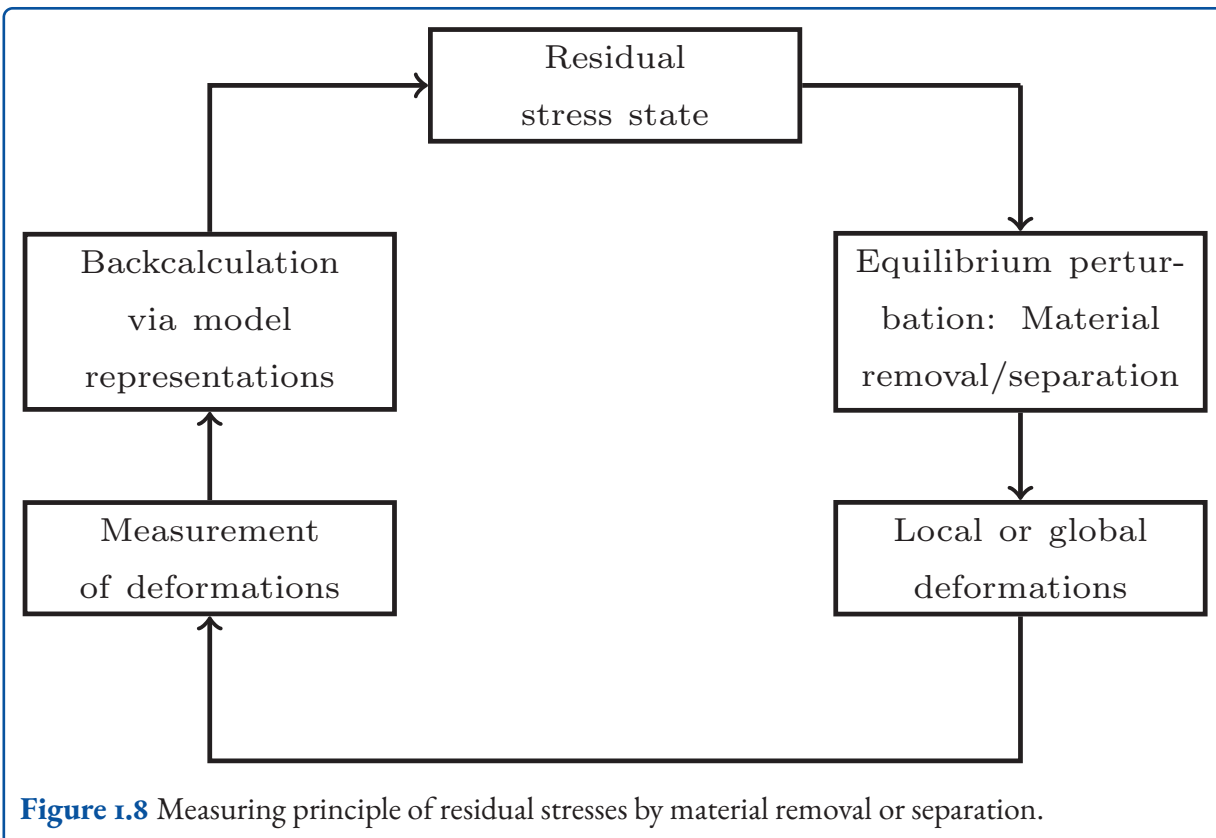


**Figure 1.8** Measuring principle of residual stresses by material removal or separation.

characteristics and the measurable residual stress types are detailed within the chosen taxonomy. Due to the introductory nature of this chapter, only a selection of the commonly used methods is shown. Table 1.2 summarizes the presented methods within this chapter.

### 1.6.1 Destructive and Semi-destructive Measurement Methods

Destructive and semi-destructive measurement methods include the contour method and hole drilling method, respectively. With semi-destructive testing, specimens can possibly still be used in field, whereas destructive testing produces scrap. Both methods follow the scheme within figure 1.8. The static equilibrium of the residual stress state is perturbed by a material separation or material removal. This causes the residual stresses to redistribute in order to maintain the equilibrium state [14]. This redistribution leads to local or global deformations, depending on the severity of material removal. Furthermore, the methods of material removal or separation

must not introduce high new residual stresses into the component – otherwise, the measurement results will be strongly influenced [8]. Occurring deformations are retrieved by suitable measuring devices and inferred within a model which backcalculates the original residual stress state. In the following, both methods already mentioned will be discussed in more detail. [15]

The contour method is a destructive measurement method which gives an areal residual stress state. Figure 1.9 presents the measuring procedure where a specimen is cut into two pieces in a first step. Consequently, residual stresses at the intersection plane relax, leading to global deformations of the cut pieces. These deformations are measured optically and serve as input for a finite element simulation. Based on defined material behavior the stresses needed to reproduce a flat intersection surface are calculated. These calculated stresses represent the residual stress state of the intersection plane. Thus, a global two-dimensional residual stress state is retrieved at the cost of destroying the specimen. [14]

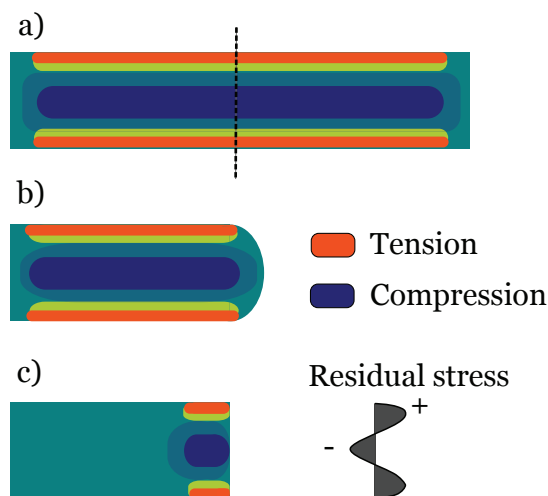


**Figure 1.9** Contour method. a) Original stresses b) Global deformation after material separation c) Calculated stresses to restore flat surface [14].

Another widely used measuring method for residual stresses is the hole drilling method, which is a semi-destructive method. Figure 1.10 presents the procedure schematically. Here, a blindhole is drilled incrementally into the specimen. If macroscopic residual stresses are relaxed, dimensional changes of the borehole geometry result. This deformation is recorded with the aid of strain gauge. It serves as input for the chosen backcalculation model. Here, models often assume a planar residual stress state. This way, residual stresses in the proximity of the blindhole can be deduced up to a depth of 1 mm. The hole drilling method is standardized by ASTM International [16]. [14]

### 1.6.2 Nondestructive Measurement Methods

Diffraction methods, for example X-ray diffraction, allow for measuring residual stresses in a non-destructive way. X-rays enable measurement the distance between atomic planes within crystal structures. This method is based on Bragg's law which states:

$$k\lambda_b = 2d \sin \theta. \quad (\text{Equation 1.3})$$

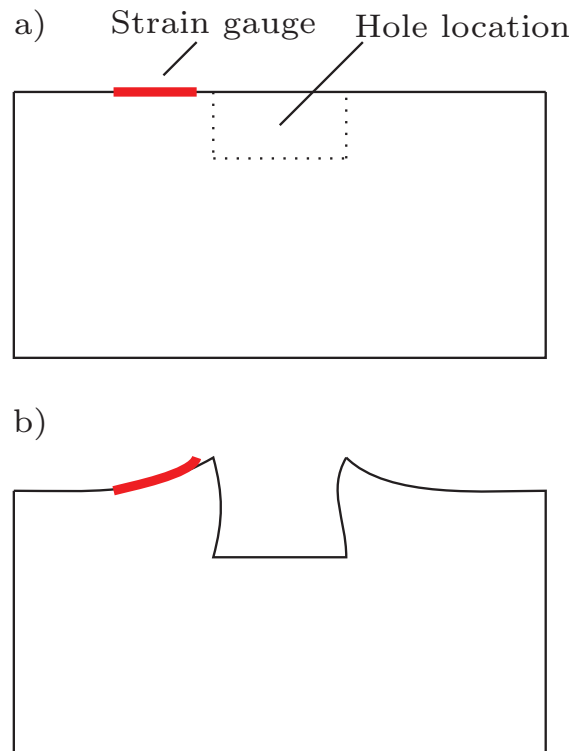


**Figure 1.10** Hole drilling method. a) Before drilling, b) After drilling [14].

Here,  $k$  is an integer,  $\lambda_b$  is the X-ray wavelength,  $d$  corresponds to the interatomic lattice spacing and  $\theta$  is the Bragg angle. [14]

The measurement principle is shown in figure 1.11. Here, the angle  $\theta$  is varied within a defined range. Diffracted X-rays are shown as red dashed lines. The angle at which the most intense radiation is diffracted corresponds to the Bragg angle. With the help of *Equation 1.3* it is possible to calculate the interatomic lattice spacing. Since there exists a linear relationship between stresses and lattice strains, residual stresses of type II and III can be deduced by this procedure. [14]

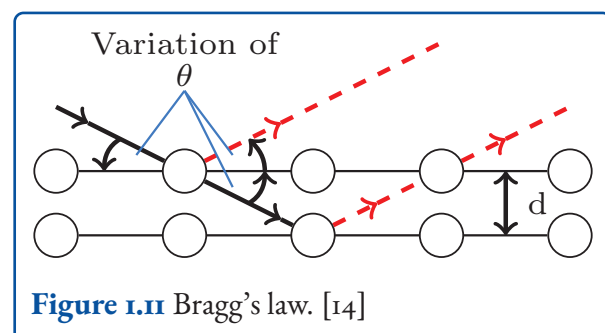
Furthermore, there are nondestructive measurement methods that do not depend on the measurement of strains. Their underlying physical principle distinguishes them. For example, a magnetic method is the measurement of Barkhausen noise which is a phenomenon that occurs in ferromagnetic materials such as iron and steel. Here, a fer-

**Table 1.2** Excerpt of measurement methods for residual stresses based on strains. [10]

Method	Character	Residual stress type	Measured quantities
Contour method	Destructive	Type I	Macroscopic surface strains
Hole drilling method	Semi-destructive	Type I	Macroscopic surface strains
X-ray diffraction	Nondestructive	Type II & III	Microscopic lattice strains

romagnetic component is subjected to a changing magnetic field which causes the material to be magnetized. Thus, the magnetic domains within the material align with the applied magnetic field. As the magnetic field changes, the component's magnetic domains snap into new positions, producing a series of small, discrete jumps within the hysteresis curve – known as Barkhausen noise. Barkhausen noise can be detected and analyzed to provide information about the residual stress state of the component. [14]

Also, acoustic measurement methods are non-destructive techniques used to measure residual stresses in materials. These methods are based on the principle that the elastic properties of a material, such as its speed of sound, are affected by residual stresses. One standard method is the ultrasonic pulse-echo technique. It involves sending an ultrasonic pulse into the material and measuring the time it takes for the pulse to travel through the material and return to the surface. The speed of sound in the material is calculated from the time of travel, and the residual stress can be determined from the change in the speed of sound. However, there exist uncertainties within this measurement principle as the speed of sound is also affected by other microstructural characteristics – for example, grain size or texture. [14]

**Figure 1.11** Bragg's law. [14]

## References

- [1] T. E. Neumann. "Die Gesetze der Doppelbrechung des Lichts in comprimirten oder ungleichförmig erwärmten unkristallinischen Körpern". In: *Abhandlungen der Königlichen Akademie der Wissenschaften zu Berlin aus dem Jahre 1841, Zweiter Theil* (1843).
- [2] Silver Bridge. URL: [https://transportation.wv.gov/highways/bridge\\_facts/Modern-Bridges/Pages/Silver.aspx](https://transportation.wv.gov/highways/bridge_facts/Modern-Bridges/Pages/Silver.aspx) (visited on 12/17/2022).
- [3] E. Macherauch, H. Wohlfahrt, and U. Wolfstieg. "Zur zweckmäßigen Definition von Eigenspannungen". In: *TM Journal of Heat Treatment and Materials* 28.3 (1973), pp. 201–211. DOI: 10.1515/htm-1973-280305.
- [4] W. Volk et al. "Models and modelling for process limits in metal forming". In: *CIRP Annals* 68.2 (2019), pp. 775–798. DOI: 10.1016/j.cirp.2019.05.007.

- [5] J. Lu. "Prestress Engineering of Structural Material: A Global Design Approach to the Residual Stress Problem". In: *Handbook of Residual Stress and Deformation of Steel*. Ed. by G. Totten. ASM International, 2002, pp. ii–26.
- [6] W. Volk et al. "Introduction to residual stresses in production technology". In: *Production Engineering* 13.2 (2019), pp. 119–121. DOI: 10.1007/s11740-019-00881-8.
- [7] C. Casavola et al. "Introductory Chapter: New Challenges in Residual Stress Measurements and Evaluation". In: *New Challenges in Residual Stress Measurements and Evaluation*. Rijeka: IntechOpen, 2020. DOI: 10.5772/intechopen.92620.
- [8] H.-D. Tietz. *Grundlagen der Eigenspannungen*. Dt. Verl. für Grundstoffindustrie, 1982.
- [9] T. Klotz et al. "Surface characteristics and fatigue behavior of shot peened Inconel 718". In: *International Journal of Fatigue* 110 (2018), pp. 10–21. DOI: 10.1016/j.ijfatigue.2018.01.005.
- [10] E. Macherauch. "Residual Stresses". In: *Application of Fracture Mechanics to Materials and Structures*. Ed. by G. C. Sih, E. Sommer, and W. Dahl. Dordrecht: Springer Netherlands, 1984, pp. 157–192. ISBN: 978-94-009-6146-3.
- [11] P. J. Withers and H. K. D. H. Bhadeshia. "Residual stress. Part 1 – Measurement techniques". In: *Materials Science and Technology* 17.4 (2001), pp. 355–365. DOI: 10.1179/026708301101509980.
- [12] M. Habschied et al. "Fertigung und Eigenspannungen". In: *HTM - Journal of Heat Treatment and Materials* 70.3 (2015), pp. 111–121. DOI: 10.3139/105.110261.
- [13] F. A. Kandil, J. D. Lord, and P. V. Grant. "A Review of Residual Stress Measurement Methods - A Guide to Technique Selection". In: *NPL Report MATC(A)04* (2001).
- [14] G. S. Schajer and C. O. Ruud. *Practical Residual Stress Measurement Methods*. Chichester, UK: John Wiley & Sons, Ltd., 2013. DOI: 10.1002/9781118402832.
- [15] T. Schwarz. *Beitrag zur Eigenspannungsermittlung an isotropen, anisotropen sowie inhomogenen, schichtweise aufgebauten Werkstoffen mittels Bohrlochmethode und Ringkernverfahren*. Staatliche Materialprüfungsanst. (MPA) Univ. Stuttgart, 1996.
- [16] ASTM E 837:2020. "Standard Test Method for Determining Residual Stresses by the Hole-Drilling Strain-Gage Method". In: *Book of Standards Volume: 03.01* (2020). DOI: 10.1520/E0837-20.

## 2 Thin-walled Product Forming

Erman Tekkaya, A.; Maasß, F.; Hahn, M.; Volk, W.; Plötz, M.; Gilch, I.; Buhl, J.; Liewald, M.; Heinzelmann, P.; Lampke, T.; Winter, L.; Hirt, G.; Pavliuchenko, P.

### 2.1 Introduction

Sheet metal forming processes induce residual stresses in formed parts that affect fatigue strength, component failure, and even corrosion resistance of the final part during operation. Residual stresses are a major factor in the geometrical distortion of particularly thin-walled formed parts and thus have an enormous impact on the production of complex, thin-walled parts. The SPP 2013 includes several projects dealing with thin-walled sheet metal forming, such as incremental sheet metal forming processes, roll forming, combined deep drawing, embossing, and embossing of electrical sheets (figure 2.1). The expert group Thin-walled Product Forming coordinates joint work of the sub-projects of the SPP 2013 for the targeted generation and use of residual stresses focusing on sheet metal forming processes of thin-walled components.

### 2.2 Residual Stress Prediction

The key to planning tailored component properties in an early stage of part design is an accurate prediction of the residual stresses in the component after the forming. An accurate estimation requires suitable models. In Chapter 1, it was shown that the prediction of the springback behavior is essential for the accurate prediction of the residual stresses by numerical analysis. Especially for conventional forming processes, with axisymmetric product geometries, for instance bulk forming processes such as cold extrusion, there are suitable numerical models for an accurate residual stress prediction [1]. Sheet metal forming processes with com-

#### Forming processes - Thin-Walled Product Forming

Incremental forming



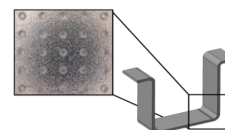
TPIF

SPIF

Roll forming and incremental bending



Embossing



Deep drawing and embossing

**Figure 2.1** “Thin-walled Product Forming” processes.

plex three-dimensional part geometries and multi-level or incremental sheet forming operations are challenging due to stress superposition, complex stress gradients over the sheet thickness, or texture influences. Accurate springback prediction in numerical analysis to evaluate residual stresses makes demands on material modeling. Material modeling depicts the elastoplastic material behavior in the forming process and includes many parameters, e.g., Young's modulus and hardening behavior, which determine the final geometry, and the quality of the residual stress prediction. Determining the yield strength and Young's modulus is a key factor in predicting springback. The change in the apparent Young's modulus and the Bauschinger effect as a function of plastic strain are of crucial relevance for the prediction of springback and residual stresses.[2]

## 2.3 Young's Modulus

- Residual stress
- Preload history and
- Dimensions.

The value of Young's modulus  $E$  is a material property in Hooke's law, where under a uniaxial load the strain is proportional to the applied force.

$$E = \frac{\sigma}{\varepsilon} \quad (\text{Equation 2.1})$$

The Young's modulus of a material is, according to the laws of physics, unique for a given material composition. However, the apparent Young's modulus or more generally the elastic stiffness of the material that is measured macroscopically might change with processing. Hereforth, the term "Young's modulus" will be used for simplicity for the apparent value. The stress-strain response of a material is different under load and unloading. Young's modulus at unloading, referred to as the Chord modulus, is the linear relationship between the onset of unloading and the stress-free point at full unloading (figure 2.2) [3]. The strain difference after unloading indicates the elastic springback.

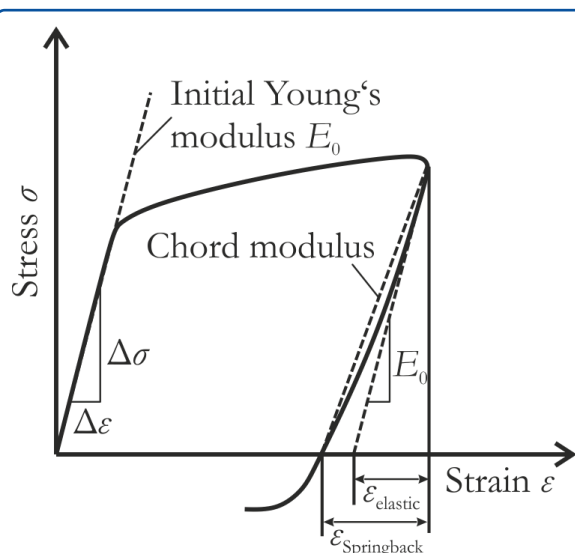


**Figure 2.2** Stress-strain curve indicating elastic springback behavior, after [4].

Young's modulus is influenced by the properties of the specimen [5]:

- Orientation of the grains relative to the direction of stress
- Grain size

The effect of preload on Young's modulus was described in [5]. The  $E_0$ -strain path of pre-strained mild steel material (SPCC) under axial load is highly nonlinear (figure 2.3). Average apparent Young's moduli  $E_{av}$  decreases rapidly with increasing pre-strain and they gradually approach asymptotic values. The difference between the initial Young's modulus of the first cycle and the last cycle is up to 30% less. The effect of pre-strain on the average Young's modulus  $E_{av}$  can be calculated by:

$$E_{av} = (E_0 - E_a)1 - \exp[-\xi\varepsilon_0^p] \quad (\text{Equation 2.2})$$

where  $E_0$  and  $E_a$  stand for the Young's modulus of annealed and infinitely large pre-strained materials, respectively,  $\xi$  is a material constant.

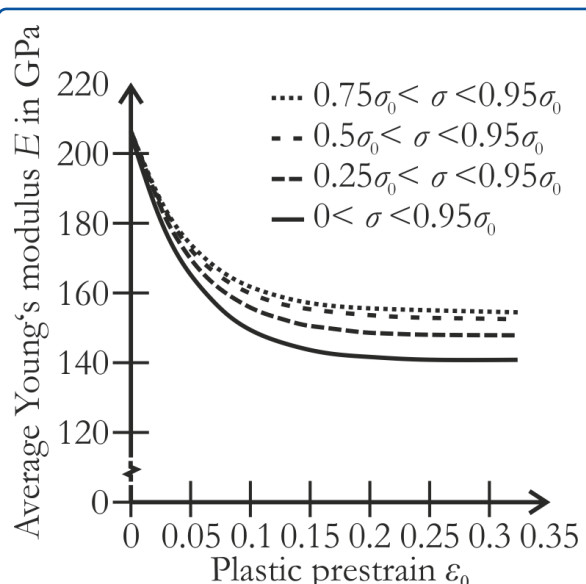


**Figure 2.3** Average Young's moduli and reverse plastic strain for mild steel sheet (SPCC) [6].

For the experimental determination of Young's modulus, physical methods such as ultrasonic and mechanical methods such as the tensile tests can be used. To determine the Young's modulus, the elastic behavior of the material's experimental stress-strain curve must be clearly defined [7]. There are several methods described in literature to determine

the material's elasticity. A description of how to determine Young's modulus in uniaxial tensile test is given by DIN EN ISO 6892 [8] and ASTM E III [5]. The method is based on a numerical determination of the best fit line for the elastic range (least squares method) including the visual assessment of the agreement between this best fit line and the curve with the actual measured values, followed by a recalculation with modified parameters, if necessary. In cases where the material does not show a linear elastic behavior, e.g., cast iron, or the regression data are not of sufficient quality Young's modulus, a tangent modulus or secant modulus can be determined as described in DIN EN ISO 6892-2.

## 2.4 Material Hardening

Material hardening and its modeling influence residual stress prediction. Anisotropic hardening behavior characterizes the transition of the initial isotropic yield locus of a material to an anisotropic one in the case of a linear strain path [9]. The Bauschinger effect describes that the yield stress of a plastically deformed material under compression is less than the yield stress before unloading in tension [10]. If this phenomenon is not considered in the material modeling, errors will inevitably occur in the prediction of residual stresses. Two models for modeling hardening effects are discussed below.

### 2.4.1 Isotropic hardening

A plastic deformation leads to an isotropic expansion of the yield surface according to:

$$\sigma_f = \sigma_f(\bar{\varepsilon}, \dots) \quad (\text{Equation 2.3})$$

The current flow stress  $\sigma_f$ , which according to that equation corresponds to the radius of the yield cylinder in the deviatoric stress plane, depends on the accumulated or equivalent plastic strain  $\bar{\varepsilon}$  (figure 2.4a). Hardening evolves equally in all directions.

### 2.4.2 Kinematic hardening

Plastic deformations lead to a translation of the yield surface without altering its size and shape (figure 2.14b). The translation is symbolized by the relation

$$f = \bar{\sigma}(\boldsymbol{\sigma} - \boldsymbol{\alpha}), \quad (\text{Equation 2.4})$$

where the back stress tensors  $\boldsymbol{\sigma}$  and  $\boldsymbol{\alpha}$  corresponds to the current position of the yield surface center in the stress space. Most metals exhibit a combination of isotropic and kinematic hardening according to:

$$f = \bar{\sigma}(\boldsymbol{\sigma} - \boldsymbol{\alpha}) - \sigma_f(\bar{\varepsilon}, \dots) \leq 0 \quad (\text{Equation 2.5})$$

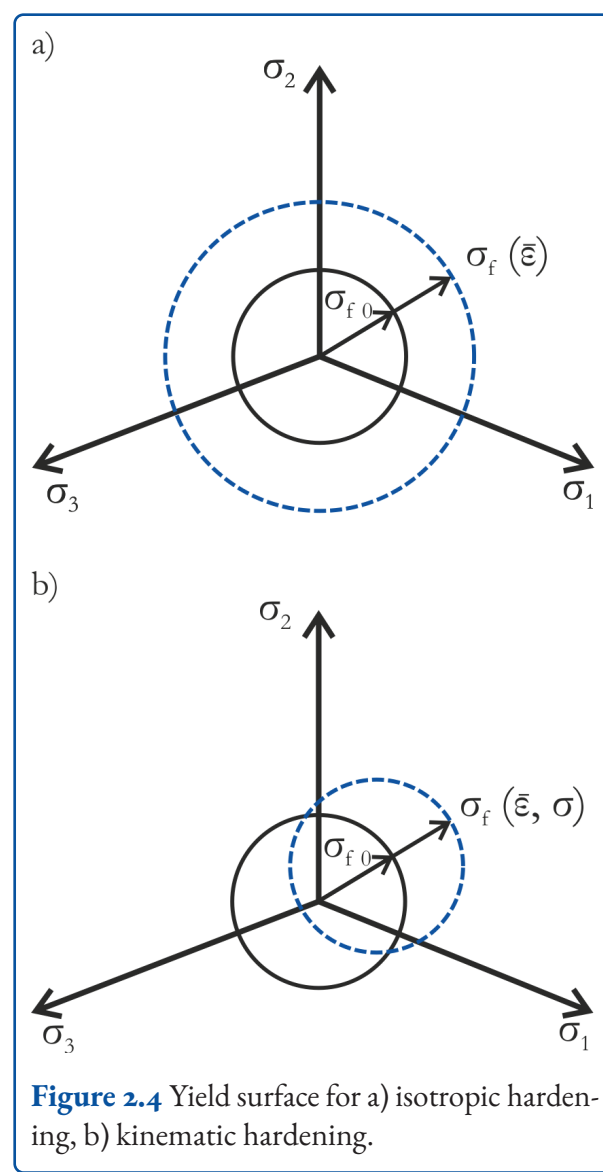


**Figure 2.4** Yield surface for a) isotropic hardening, b) kinematic hardening.

This type of hardening is most frequently referred to as mixed or combined hardening. The exact hardening behavior is defined by the evolution equations of the back stress tensor  $\alpha$  (kinematic hardening part) and the current flow stress  $\sigma_f$  (isotropic hardening part).

## 2.5 Benchmark Material Characterization

Within the expert group “Thin-walled Product Forming” benchmark tests are performed to compare the influence of material characterization and material model on the residual stress prediction for different forming processes.

### 2.5.1 Test Setup and Basic Material Data

The benchmark material is HC46oLA (1.0574), a cold-rolled micro-alloyed steel with an initial sheet thickness of  $s_0 = 1.5$  mm. The material is characterized using standard tensile tests, cyclic tensile tests, and monoton/cyclic in-plane torsion tests to determine Young’s modulus change with increasing strain and the material’s hardening behavior. The tensile tests were performed on a Zwick Roell Z250 universal testing machine at room temperature according to DIN EN ISO 6892-1 [8]. Using standard tensile tests, with a tactile measuring device, the initial yield strength was determined  $\sigma_{f0} = 495$  MPa and the ultimate tensile strength  $\sigma_{UTS} = 582$  MPa (figure 2.5).

Young’s modulus is evaluated at three angles relative to the rolling direction (figure 2.6). The given values are mean values of three repetitions. The highest Young’s modulus is measured  $90^\circ$  to the rolling direction  $E_{90^\circ} = 232$  GPa, and the lowest Young’s modulus is measured  $45^\circ$  to the rolling direction,  $E_{45^\circ} = 207$  GPa. This can be assumed as an initial average Young’s modulus of  $E_0 = 219$  MPa.

Cyclic tests were performed with different material characterization methods, measuring equipment, and evaluation methods to determine the change

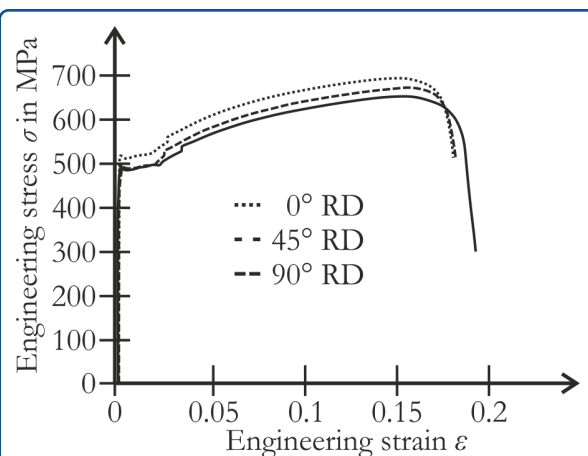


**Figure 2.5** Uniaxial tensile test evaluation of HC46oLA.

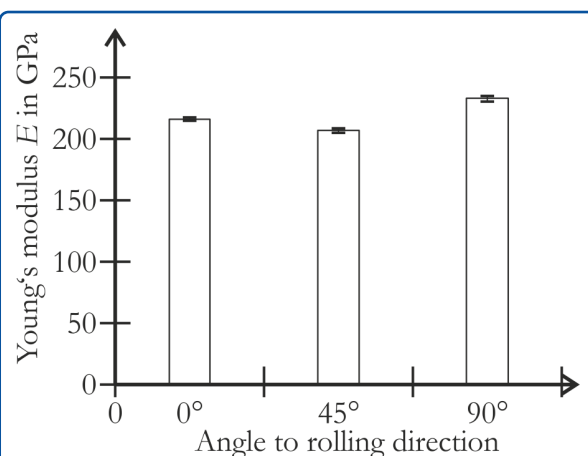


**Figure 2.6** Young's modulus evaluation of HC46oLA.

of Young’s modulus with increasing strain. The setups used is:

- Uniaxial tensile test with strain gauge measurement.
- Uniaxial tensile test with thermocouple temperature measurement (class A and class B).
- In-plane torsion test with optical DIC strain measurement.

For the strain gauge measurements, strain gauges were applied to the middle of the measuring length on the surface of the pre-stretched samples in order to record the strains during the cyclic test in three strain areas (figure 2.7). The recorded stress-strain

development shows a decreasing Young's modulus with increasing pre-strain.

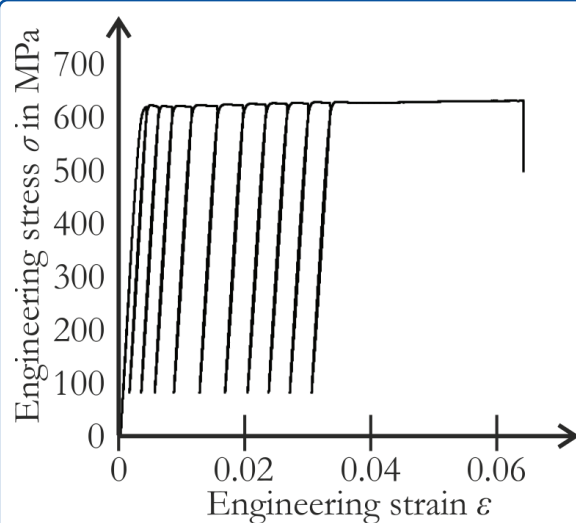


**Figure 2.7** Cyclic uniaxial tensile test of HC460LA using strain gauge measurement set-up.

The cyclic uniaxial tension tests with thermal Young's modulus measurement use an approach described in [11] to determine the onset of yielding. This temperature-dependent minimization method uses the relation between the onset of plastic yielding and the thermo-elastic effect on a micro level.

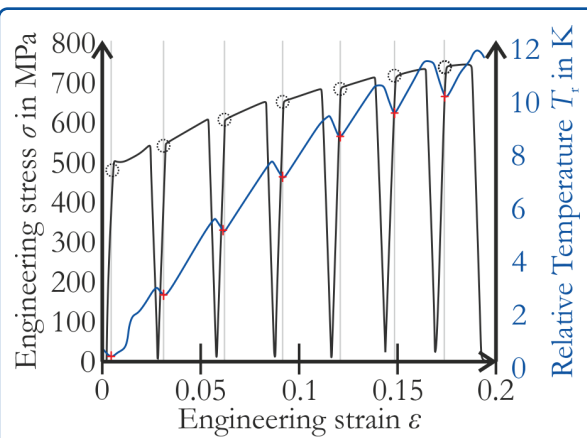


**Figure 2.8** Cyclic uniaxial tensile test of HC460LA using thermocouple temperature measurement (class A).

The determination of the elastic part of the stress-strain curve is thereby physical based and repeatable accurate by determine the local thermal minima

during the tensile test. The specimen's temperature change during uniaxial tensile tests is measured by a clip-on temperature couple during the experiment. Two different setups were used for stress-strain measurement:

- An optical 3D measurement system GOM Aramis-4M combined with a clip-on temperature couple (class A) (figure 2.8).
- An optical laser measurement system Zwick laserXtens Array HP combined with a clip-on temperature couple (class B) (figure 2.9).

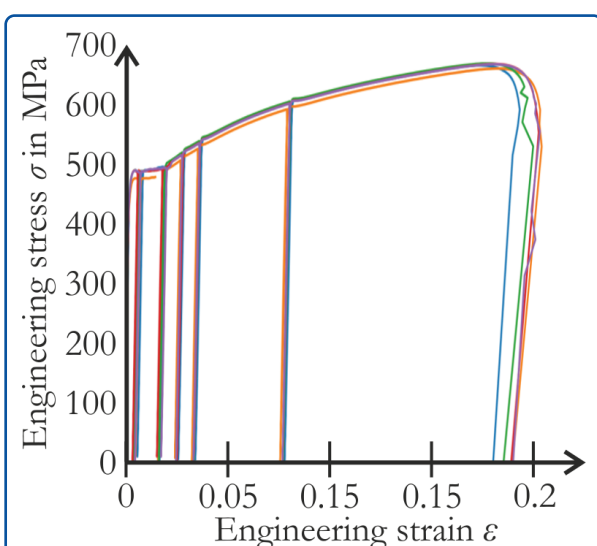


**Figure 2.9** Cyclic uniaxial tensile test of HC460LA using thermocouple temperature measurement (class B).

Additionally, cyclic tests were performed using an in-plane torsion test according to [12]. Where the specimen is a circular sheet sample. It is clamped concentrically on the outer rim and in the central area back-and-forth. By planar rotation the outer fixture is rotated against the inner ones. The strain development is measured by DIC. The HC460LA material with an initial sheet thickness of  $s_0 = 1.5$  mm is led in 25 cycles while the stress-strain response is measured (figure 2.10). Young's modulus can be calculated using the in-plane torsion test through the relationship of shear modulus  $G$  and Youngs' modulus  $E$ , taking Poisson's ratio  $\nu$  into account:

$$G = \frac{E}{2 \cdot (1 + \nu)} \quad (\text{Equation 2.6})$$

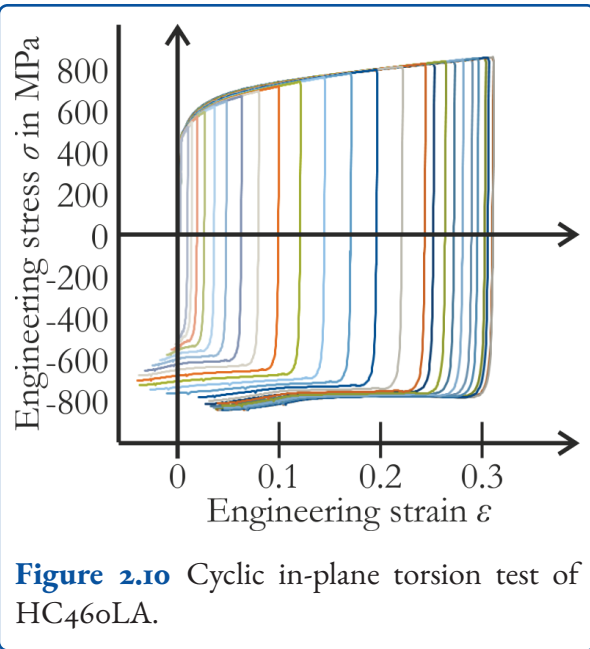


**Figure 2.10** Cyclic in-plane torsion test of HC46oLA.

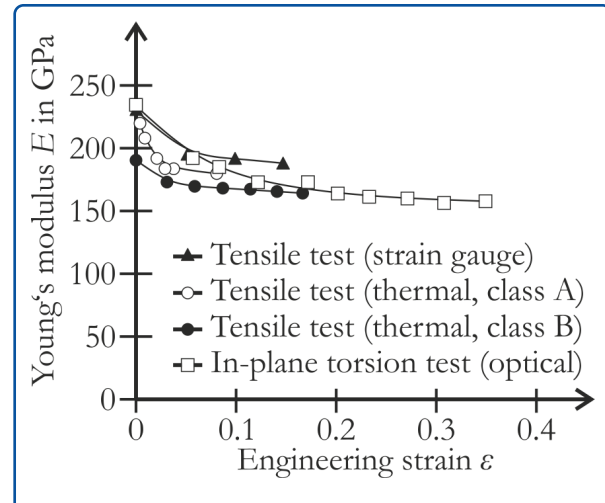


**Figure 2.11** Evolution of Young's modulus with increasing pre-strain for HC46oLA.

## 2.5.2 Results

Based on the cyclic test, the evolution of Young's modulus with increasing prestrain is evaluated for the benchmark material (figure 2.11). The number of cycles and the accumulated strain values are different for the specific test. The strain increments evaluated differ from four cycles for the strain gauge measurement to 10 cycles and evaluation points for the in-plane torsion test. The benchmark material used is from the same batch. According to the quasi-static uniaxial tensile test with tactile strain measurement, the initial Young's modulus for the first cycle varies between  $E_0 = 192$  GPa for the temperature-based onset of necking method to  $E_0 = 233$  GPa for the in-plane torsion test results. The average initial Young's modulus for all analyzed methods is  $E_0 = 214$  GPa. As described in [10], Young's modulus is decreased drastically within the first few cycles up to a strain value of  $\varepsilon = 0.08$  and on the average up to 21 %. After that point, the decrease in Young's modulus is saturated for the analyzed material. The test with the highest accumulated strain is the in-plane torsion test. The evaluated Young's modulus  $E_{10}$  for the final cycle is 31 % reduced compared to the initial Young's modulus.

## 2.5.3 Conclusion

The state of the art and the benchmark test indicate the importance of Young's modulus on residual stress prediction. In benchmark material characterization tests for the material HC46oLA (1.0574), the influence of the material testing method has been quantified. Depending on the testing method, the difference in the initial Young's modulus value is up to 21 %. The strain sensitivity for the material HC46oLA on Young's modulus was shown for all testing methods. The Young's modulus is decreased up to 31 % within the range of the pre-strain investigated.

## 2.6 Benchmark Numerical Analysis

The benchmark material characterization indicated a wide range of variation of 21 % in relation to the value of the initial Young's modulus and the importance of its change with an increasing strain induced during the forming process. A numerical process analysis is set up to quantify the influence of Young's modulus on the numerical residual stress prediction. The processes and process models are extracted from the sub-projects as described in Chapter 2. The numerical benchmark test includes the single point incremental sheet forming process (SPIF), embossing and combined

deep drawing and embossing. The benchmark material is the characterized cold-rolled micro-alloyed steel HC46oLA with an initial sheet thickness of  $s_0 = 1.5$  mm. Based on the same material data obtained from a uniaxial tensile test with tactile strain measurement, the stress-strain curve, initial modulus of elasticity and Poisson's ratio are used for all numerical models to ensure comparability of results. The influence of Young's modulus is analyzed numerically by changing the initial value in a range of 10 % to 20 % of the experimentally measured average value of 218 GPa. The estimated value of 80 % of  $E_0$  is  $E_{0.8} = 174$  GPa and 90 %  $E_0$ , which is equal to  $E_{0.9} = 196$  GPa. In addition to the variation of Young's modulus, the influence of the material hardening is investigated. A process model with isotropic hardening behavior and constant Young's modulus is compared to a process model using combined isotropic-kinematic hardening. Evaluated is the influence of the hardening rule on the resulting residual stress of the formed part. The values for the HC46oLA material description in Abaqus are the following. The density is estimated to  $\varrho = 7.85e^{-9}$  t/mm<sup>3</sup> and the initial yield strength is  $\sigma_{f0} = 495$  MPa. The initial Young's modulus is  $E_0 = 218$  GPa. The combined isotropic-kinematic hardening model, by Lemaitre and Chaboche [10] is used. The material parameters are determined inversely using cyclic loading to  $Q_\infty = 98$  MPa and  $b = 10.11$ . Where  $Q_\infty$  is the yield surface change in dependency of the material parameter  $b$ :

$$\sigma_f = \sigma_{f0} + Q_\infty(1 - e^{-b\bar{\varepsilon}}) \quad (\text{Equation 2.7})$$

## 2.6.1 Incremental Sheet Forming

As described in figure 8 truncated cone geometries are manufactured by the process of single point incremental sheet forming (SPIF). The target geometry of the cones with an initial diameter  $D = 65$  mm and a height  $h = 15$  mm is formed in quadratic sheets with an edge length  $l = 130$  mm in a one-step process. The residual stresses are evaluated in the middle on the inside (tool side) and on the outside (non-tool side) of the cone. The residual stresses are evaluated in two directions at the same evaluation point, in the circumferential direction  $\sigma_t$  and in radial direction,  $\sigma_r$  (figure 2.12).

The two-step numerical model consists of the manufacturing step followed by an unclamping step to evaluate the final residual stress in the load-free state. The final part geometry is kept constant for all different setups.

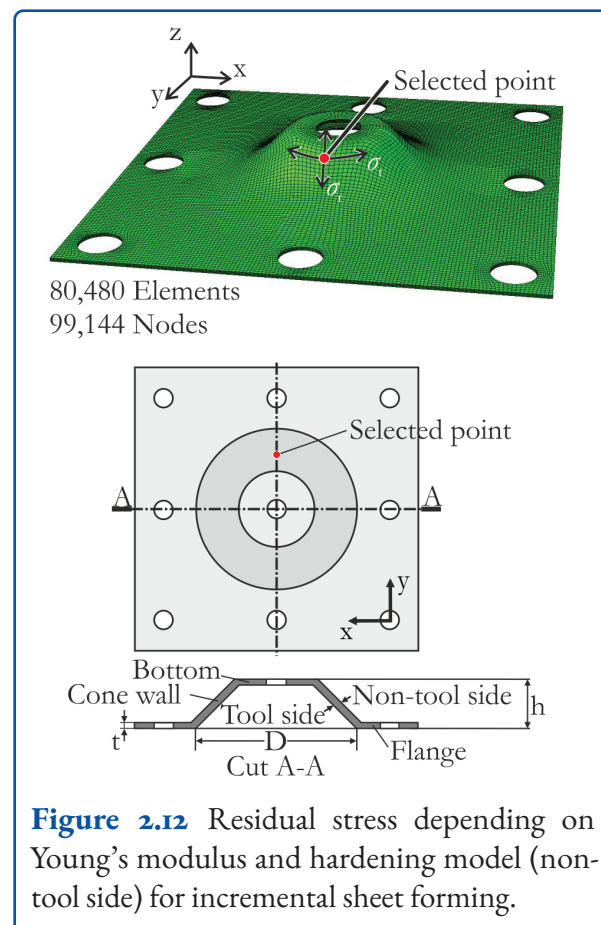


**Figure 2.12** Residual stress depending on Young's modulus and hardening model (non-tool side) for incremental sheet forming.

On the outside of the truncated cone produced by SPIF, there are compressive stresses for all stress components and material models used (figure 2.12). First, the results with combined isotropic kinematic hardening are evaluated. For the initial Young's modulus  $E_0 = 218$  GPa, there are compressive residual stresses of  $\sigma_t = 279$  MPa in the circumferential direction and  $\sigma_r = 343$  MPa in the radial direction (figure 2.13). These compressive residual stresses are monotonously decreasing with decreasing estimated Young's modulus. For the lowest estimated value  $E_{0.8} = 174$  GPa with a 20 % reduced Young's modulus, the residual stresses are evaluated in the same geometric point as  $\sigma_t = 217$  MPa in the circumferential direction and  $\sigma_r = 301$  MPa in the radial direction. Regarding the change in residual stresses depend-

ing of Young's modulus, the adjustment of 10 % decreased initial Young's modulus leading to a decrease of 11 % in residual stress on the non-tool side of the component.

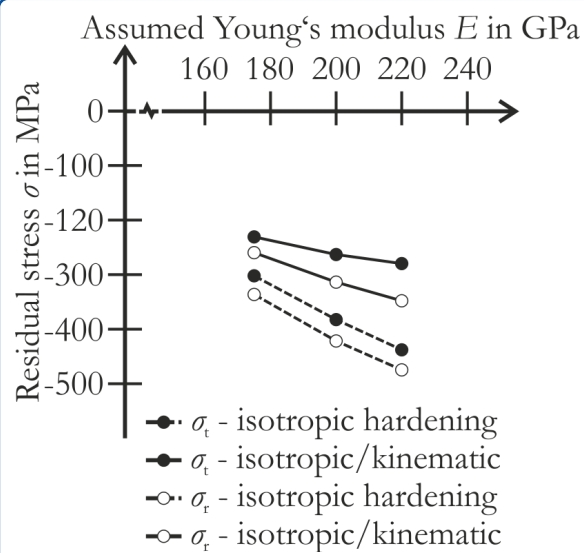


**Figure 2.13** Truncated cone geometry produced by Single Point Incremental sheet forming (SPIF).

A further decrease in Young's modulus totaling 20 % generates reduced residual stresses in both directions of about 23 %. For the investigated material model and boundary conditions, there is an equal trend of residual stress reduction caused by the decreasing Young's modulus on the non-tool side of the component. If the material hardening model is considered, additionally it can be seen, that the residual stress prognosis using isotropic hardening, without the Bauschinger effect, leads to higher residual stresses compared to the combined isotropic-kinematic hardening model (figure 2.13). The residual stresses for the initial Young's modulus  $E_0 = 218$  GPa are compressive,  $\sigma_t = 482$  MPa in the circumferential direction and  $\sigma_r = 429$  MPa in the radial direction. According to the results using the combined isotropic-kinematic hardening model, the residual stress prediction is decreased simultaneously with decreasing estimated Young's modulus.

The residual stresses on the inside of the truncated cones (tool-side) are tensile residual stresses for all stress components and material models used

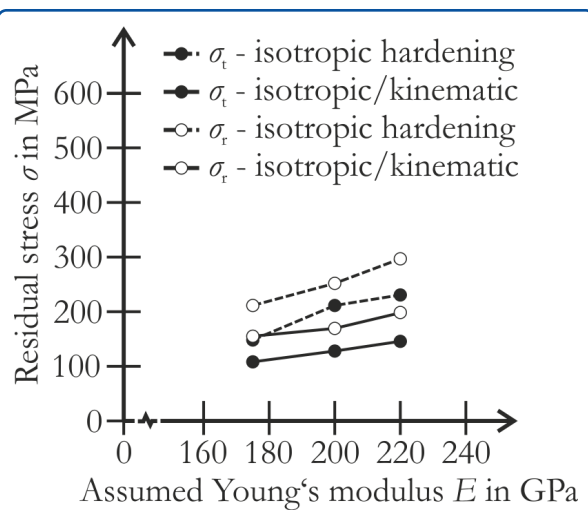


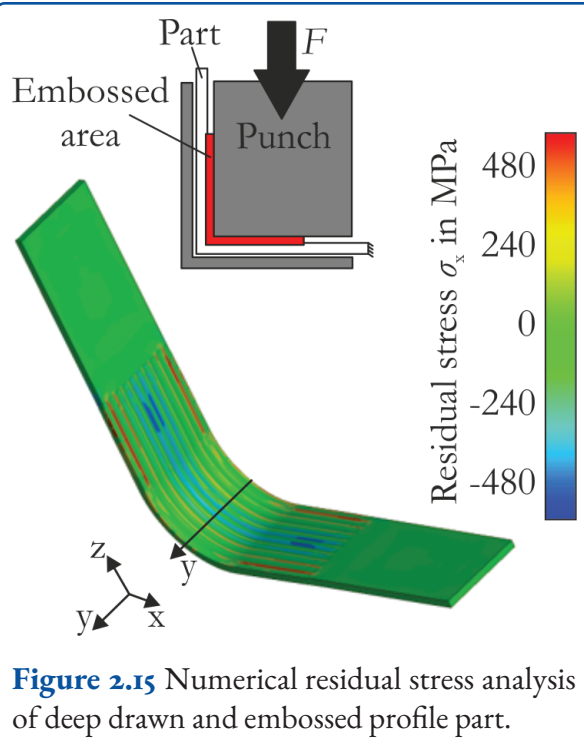
**Figure 2.14** Residual stress depending on Young's modulus and hardening model (tool side) for incremental sheet forming.

(figure 2.14). Concerning the material hardening model used, the combined isotropic-kinematic hardening model leads to lower residual stress values than does the isotropic hardening model. The difference is equal to the values on the non-tool side of the component. The average difference is about 32 %. According to the trend on the non-tool side, the tensile residual stress amplitudes on the non-tool side are monotonously decreasing, if the initial Young's modulus is reduced. If the Bauschinger effect is taken into account, the residual stresses are reduced by an average by 15 % for 90 %  $E_0$  and 27 %, if 80 % of Young's modulus are assumed.

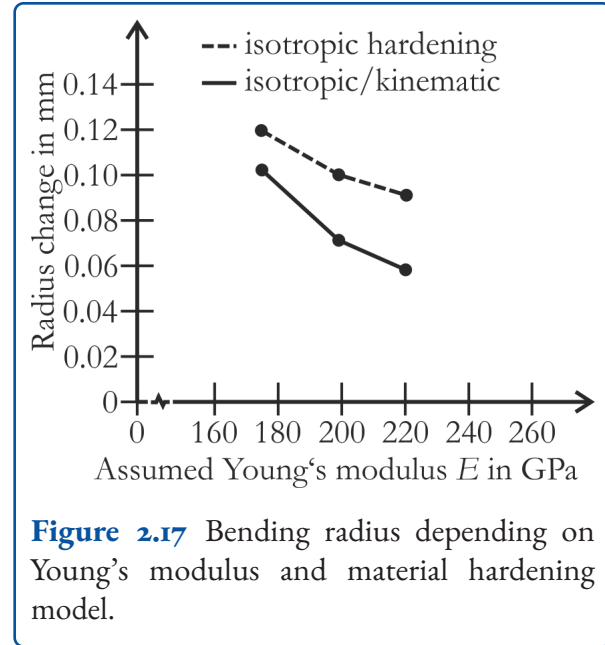
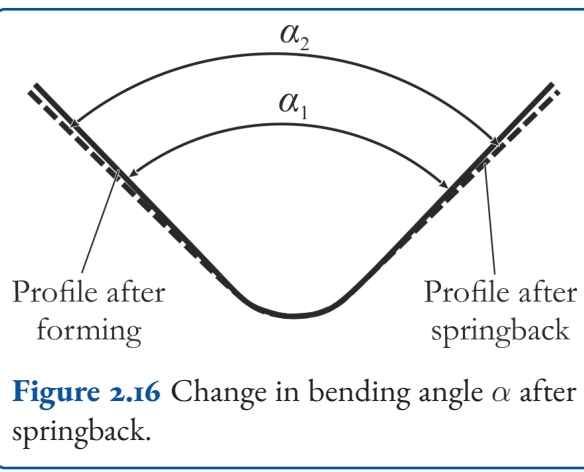
## 2.6.2 Combined Deep Drawing and Embossing

In a combined deep drawing and embossing process, a metal strip of HC46oLA material is formed. The process and the final shape are shown in figure 2.15.

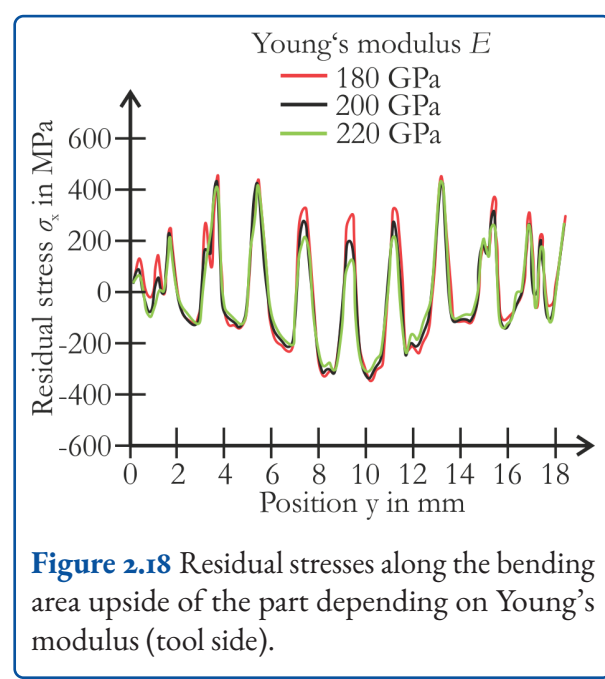
In the numerical analysis, based on the benchmark material data, the influence of Young's modulus and the material hardening model used is analyzed. Six different numerical models are built up. The resulting residual stresses in the bend and embossed area are evaluated in the x-direction on both sides (upside and downside) of the part in the indicated



cross-section (figure 2.15). The residual stresses of the formed component directly influences its geometry and vice versa. The key criterion for the part shown in (figure 2.16) is the resulting bending radius. A numerical analysis of the bending radius after the forming process is made (figure 2.15). Regarding the change in Young's modulus, there is an increase in bending radius with decreasing Young's modulus. The change is higher for the isotropic hardening model used, without considering the Bauschinger effect (figure 2.17).



An initial Young's modulus of  $E_0 = 218$  GPa leads to a changed bending radius of  $\Delta R = 0.06$  mm. Taking kinematic hardening into account, a 20 % decrease of the initial Young's modulus  $E_{0.8} = 174$  GPa leads to an increase in the bending radius of about 40 %. If the initial Young's modulus is higher,  $E_{0.9} = 198$  GPa, this 10 % decrease in Young's modulus cause a change of 29 % in the bending radius.



If the residual stresses are evaluated in the bending area in the  $y$ -direction (figure 2.15), there are maximum tensile stresses on the upside (figure 2.18) of the bent part and maximum compressive residual stresses on the downside of the part (figure 2.19).

Regarding the range of Young's modulus change of 10 % to 20 % of  $E_0 = 218 \text{ GPa}$ , residual stresses increase with a higher Young's modulus for this process on both sides of the part. The lowest residual stress amplitudes are measured in the middle of the path. Here the largest increase in residual stresses depending on Young's modulus can be seen. A change in the initial Young's modulus by 20 % leads to an increase in residual stresses of about 30 %, especially on the tool side.

The residual stresses at the bottom of the deep-drawn and embossed profile shown in figure 2.19 demonstrate how the tensile stresses induced by the forming process counteract the compressive stresses induced by the forming process so that fewer compressive stresses are induced in the center of the specimen than would be expected. The opposite effect can be seen in the edge regions. In these areas, where the embossing cannot be reproduced as distinctly as in the central area due to the manufacturing process, the compressive stresses are much higher.

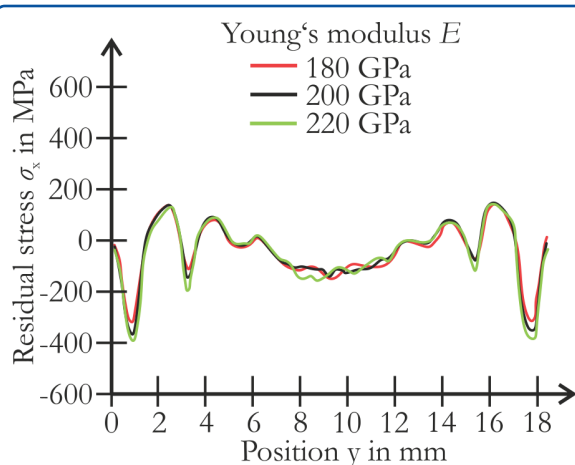


**Figure 2.19** Residual stresses along the bending area downside of the part depending on the Young's modulus (non-tool side).

For a better understanding, figure 2.20 and figure 2.21 show the maxima of the results from the

variation of the elastic moduli. The influence of the change in material properties, in terms of strain hardening, on the residual stresses introduced by the embossing can be seen here, particularly in the middle.

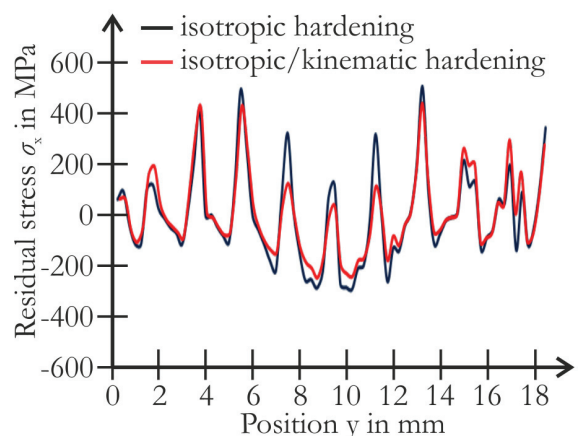


**Figure 2.20** Maximum residual stresses of the simulations along the bending area upside of the part depending on the material hardening model (tool side).

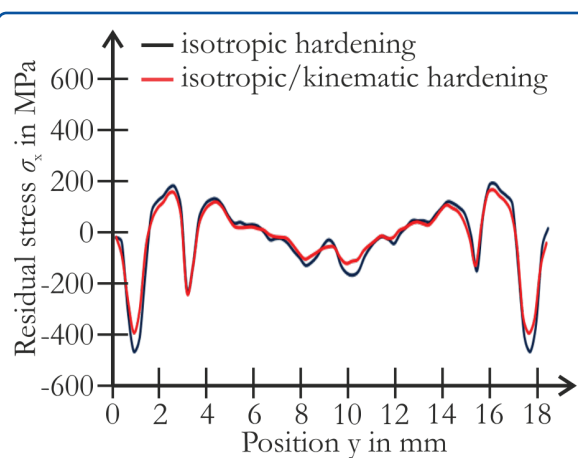


**Figure 2.21** Maximum residual stresses of the simulations along the bending area downside of the part depending on the material hardening model (non-tool side).

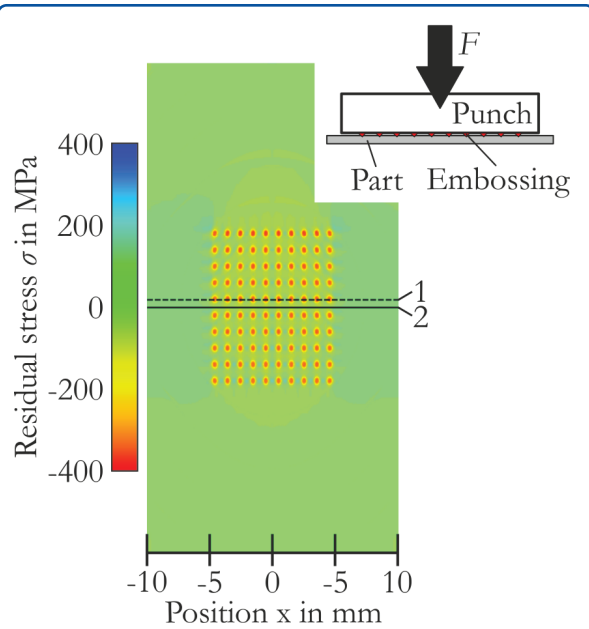


**Figure 2.22** Numerical residual stress analysis of embossed part.

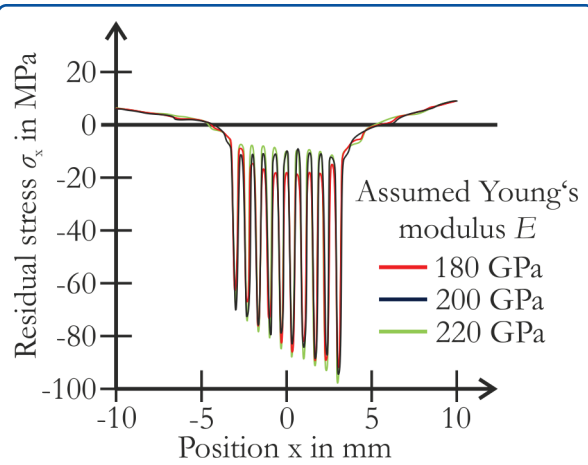


**Figure 2.23** Residual stresses along path 1 of the embossed area depending on Young's modulus.

### 2.6.3 Embossing

The effect of Young's modulus for an embossing process is analyzed numerically by embossing multiple points into the material (figure 2.22). A four-sided pyramidal geometry with a tip angle of  $136.5^\circ$  and a flat die were used as embossing tool. 100 embossing points were fabricated with equal distance in a squared areas. The residual stress distribution along the x-axis (figure 2.22, path 1) of the embossed areas averaged over the sheet thickness is plotted. The maximum absolute principal stress is split into tensile and compressive stress. The maxima of compressive stress in x-direction appear next to the embossing points. With an increasing assumed Young's modulus the amount of compressive residual stresses is increased, too.

For the residual stress distribution along the x-axis (figure 2.22, path 2) of the unembossed areas, the value averaged over the sheet thickness is plotted. The maximum absolute principal stress is split into tensile and compressive stress. The maximum tensile stress in the x-direction occurs near an embossing point. As already shown for the embossed areas, with increasing assumed Young's modulus the

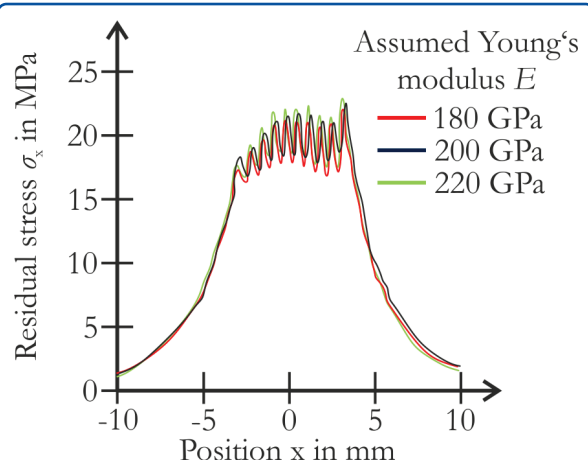


**Figure 2.24** Residual stresses along path 2 of the unembossed area depending on Young's modulus.

tensile residual stresses are increased in the unembossed area.

### 2.6.4 Conclusion

In a benchmark comparison, the material HC460LA (1.0574) was characterized cyclically and monotonically. With increasing pre-strain the Young's modulus of the material decreased up to 31 %. Depending on the characterization method, there are differences of up to 21 % for the measured initial Young's modulus. Material characterization is essential for an accurate numerical residual

stress prediction. To determine the influence of the initial modulus of elasticity on the residual stress prediction, a representative variation of the modulus of elasticity on the residual stresses was analyzed in a benchmark test. A process of incremental sheet metal forming, embossing and combined deep drawing and embossing was analyzed. A reduction of Young's modulus by 20 % results in a monotonous decrease in the residual stresses near the surface by up to 23 %. If the Bauschinger effect is taken into account in the material modeling, the predicted residual stresses are reduced by up to 27 %.

## References

- [1] A. Erman Tekkaya. *Ermittlung von Eigenspannungen in der Kaltmassivumformung*. Vol. 83. Berichte aus dem Institut für Umformtechnik der Universität Stuttgart. Berlin, Heidelberg: Springer Berlin Heidelberg, 1986. ISBN: 978-3-642-82799-0.
- [2] Fabrice Morestin and Maurice Boivin. "On the necessity of taking into account the variation in the Young modulus with plastic strain in elastic-plastic software". In: *Nuclear Engineering and Design* 162.1 (1996), pp. 107–116. ISSN: 00295493. DOI: 10.1016/0029-5493(95)01123-4.
- [3] Robert H. Wagoner, Hojun Lim, and Myoung-Gyu Lee. "Advanced Issues in spring-back". In: *International Journal of Plasticity* 45 (2013), pp. 3–20. ISSN: 07496419. DOI: 10.1016/j.ijplas.2012.08.006.
- [4] Simon Vitzthum et al. "In-situ analysis of the elastic-plastic characteristics of high strength dual-phase steel". In: *Materials Science and Engineering: A* 857 (2022), p. 144097. ISSN: 09215093. DOI: 10.1016/j.msea.2022.144097.
- [5] E28 Committee. *Test Method for Youngs Modulus, Tangent Modulus, and Chord Modulus*. West Conshohocken, PA. DOI: 10.1520/E0111-04R10.
- [6] Fusahito Yoshida, Takeshi Uemori, and Kenji Fujiwara. "Elastic–plastic behavior of steel sheets under in-plane cyclic tension–compression at large strain". In: *International Journal of Plasticity* 18.5-6 (2002), pp. 633–659. ISSN: 07496419. DOI: 10.1016/S0749-6419(01)00049-3.
- [7] H.-M. SONNE. "Bestimmung des Elastizitätsmoduls im Zugversuch". In: *Vortrags- und Diskussionstagung Werkstoffprüfung 1999* (1999).
- [8] DIN EN ISO 6892-1, *Metallische Werkstoffe – Zugversuch. Teil 1, Prüfverfahren bei Raumtemperatur (ISO 6892-1:2019)*: Metallic materials – tensile testing. Part 1, Method of test at room temperature (ISO 6892-1:2019). Deutsche Fassung EN ISO 6892-1:2019. Deutsche Norm. Berlin: Beuth Verlag GmbH, 2020.
- [9] A. Baltov and A. Sawczuk. "A rule of anisotropic hardening". In: *Acta Mechanica* 1.2 (1965), pp. 81–92. ISSN: 0001-5970. DOI: 10.1007/BF01174305.
- [10] Johann Bauschinger. *Über die Veränderung der Elastizitätsgrenze und der Festigkeit des Eisens und Stahls durch Strecken, Quetschen, Erwärmern, Abkühlen und durch oftmals wiederholte Belastung*. Vol. 13. Mitteilungen des mechanischen technischen Labors der Technischen Hochschule München. München: Ackermann, 1886.
- [11] Simon Vitzthum et al. "Temperature-based determination of the onset of yielding using a new clip-on device for tensile tests". In: *Procedia Manufacturing* 29 (2019), pp. 490–497. ISSN: 23519789. DOI: 10.1016/j.promfg.2019.02.166.
- [12] Qing Yin, A. Erman Tekkaya, and Heinrich Traphöner. "Determining cyclic flow curves using the in-plane torsion test". In: *CIRP Annals* 64.1 (2015), pp. 261–264. ISSN: 00078506. DOI: 10.1016/j.cirp.2015.04.087.

### 3 Residual Stresses in Bulk Forming

Groche, P.; Franceschi, A.; Siedbürger, C.

The generation and development of residual stresses in a mechanical component manufactured by hot and cold forming processes are closely related to the process chain of its manufacture. Residual stresses influence both the static and the dynamic lifetime and the behavior of the components. Although basic knowledge about the development of residual stresses exists, there are currently still numerous gaps in our knowledge about the possible targeted influence of the stress distribution. Due to the non-uniform plastic strain distribution of components manufactured by means of bulk forming processes, a prediction of residual stresses in this context is only possible to a limited extent. In addition, the effects of the types of residual stresses on the performance of components subjected to complex stresses have not yet been fully clarified. The Working Group Thick-Wall comprises the seven projects of the SPP2013 program mentioned below, see table 3.1. The focus of these projects is on the investigation of bulk forming processes in which residual stresses are generated during the production of components due to a three-dimensional stress and strain state.

#### 3.1 Classification in Bulk Forming

The bulk forming family includes a variety of different manufacturing processes. An initial distinction is made on the basis of the process temperature: Cold, semi-hot and hot forming. In hot forming, forming temperatures above the recrystallization temperature are commonly used for steels, i.e., in the ranges from 900 °C to 1,200 °C [1]. At this temperature level, the forming forces are reduced due to lower material strength and dynamic recrystallization, i.e., there is an immediate compensation of strain hardening. The additional increase in elongation at break allows higher degrees of forming and the production of more complex geometries.

**Table 3.1** Overview of Working Group „thick wall“

Forming process	Authors/Institution
Cold extrusion	<b>LFT:</b> Jobst, A.; Merklein, M.
Hot forming	<b>IFUM:</b> Kock, C.; Behrens, B.-A.
Cross rolling	<b>FF:</b> Guilleaume, C.; Brosius, A.
Rotary swaging	<b>bime:</b> Ortmann-Ishkina, S.; Kuhfuß, B.
Wire drawing	<b>IWU:</b> Selbmann, R.; Bergmann, M.
Cold extrusion and Bending	<b>PtU:</b> Franceschi, A.; Groche, P.
Near-Net-Shape-Blanking	<b>utg:</b> Nürnberger, A.; Volk, W.

Furthermore, a very fine-grained micro-structure based on dynamic recrystallization effects is possible by adjusting process parameters such as forming temperature and forming speed. These effects are used to increase the strength of the components. Typical representatives of bulk forming are open-die forging or closed-die forging [2]. In contrast, cold forging is characterized by a better surface finish, smaller achievable tolerances and work hardening, but higher process forces and tribological stresses are present due to the lower processing temperatures [3]. A second distinction is made between tool-bound and incremental forming. Tool-bound forming processes are processes in which the part geometry is generated in a continuous process and this depends exclusively on the geometric shape of the die. Examples of the die-bonded forming processes are wire drawing, extrusion or closed-die forging. In contrast, in incremental bulk forming, the final shape of a component is determined mainly

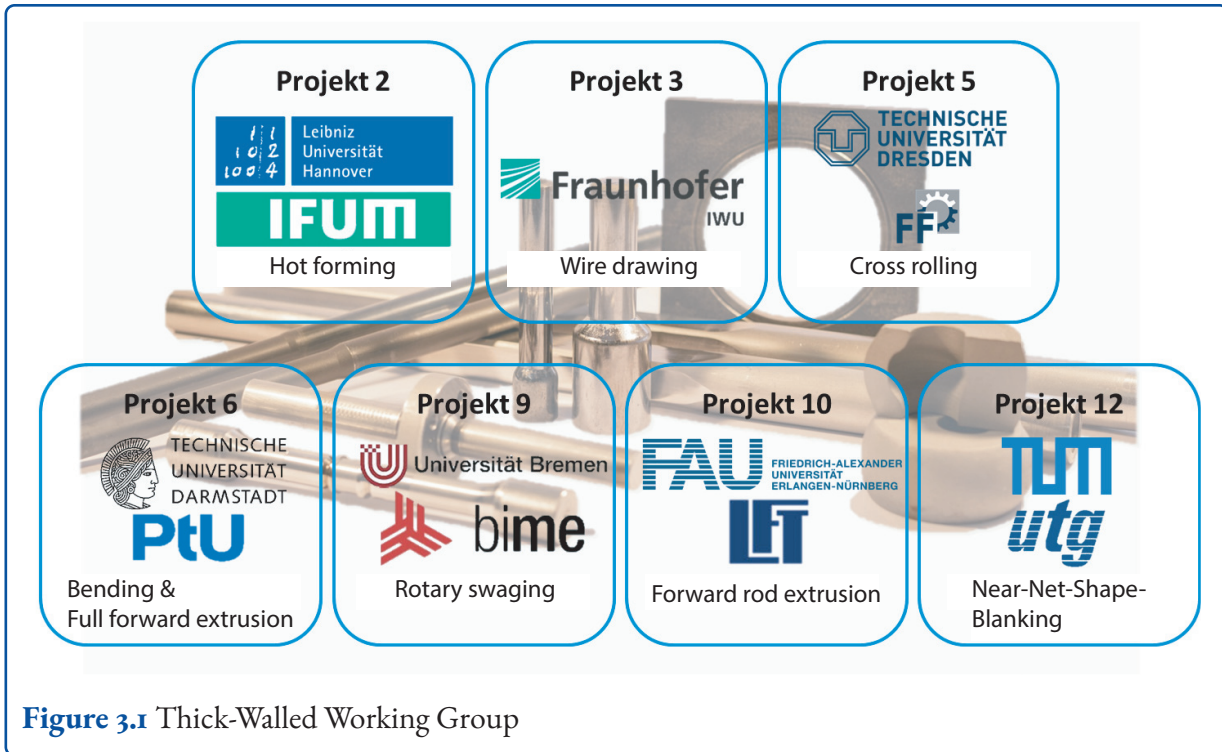


**Figure 3.1** Thick-Walled Working Group

by the die kinematics. In these processes, deformation is limited to areas of the workpiece at any given time, and the formed area undergoes more than one loading and unloading cycle during the forming process. Incremental plastic deformation affects not only the geometry, but also the static and dynamic strengths through work hardening as well as the generation of residual stresses [4]. Examples of incremental bulk forming include rotary swaging and thread rolling, which are industrially established incremental forming processes. Last, some bulk forming processes use not only rotationally symmetric bars and dies, but also sheet metal [5]. A typical example is sheet extrusion, which uses a punch and die to deform a material [6]. This process is closely related to the stamping process, with the difference that in the latter the sheet is separated. Breakage in a stamping process can be minimized by fine blanking. Here, high compressive stresses are generated to achieve cut edges without a broken surface. In contrast to conventional stamping, completely smooth surfaces are achieved [7]. Consequently, a clear differentiation between bulk forming and sheet metal forming based on the geometry of the component is not clear. A better classification is given by the definition through the stress and strain state of the components: While in

sheet metal forming the stress condition is mainly a plane stress state, bulk forming processes are characterized by a three-dimensional stress and strain state [8].

Compared to other manufacturing technologies, the processes of bulk forming are characterized by clear advantages for industrial application: low unit costs, high production rates and favorable product properties [9]. From an environmental point of view, bulk forming also exhibits significantly higher resource and energy efficiency compared to subtractive and additive processes [10]. The high material input in forming processes leads to low production costs for raw materials per cost of manufactured parts compared to machining processes [3]. On the other hand, bulk forming is characterized by comparatively high process forces, which lead to high investment costs for machines and tools. In addition, these processes are generally characterized by lower flexibility.

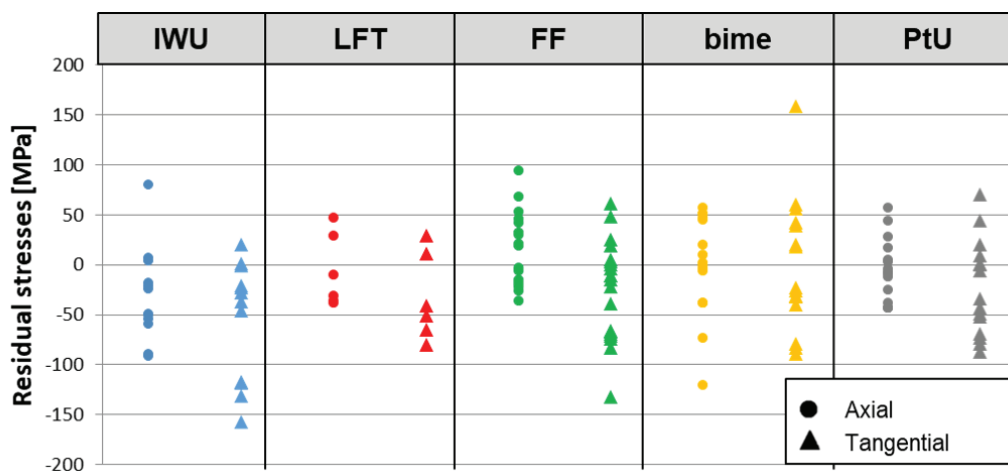


**Figure 3.2** Overview of the specimens in the initial state

### 3.2 Potential Benefit of Forming-induced Residual Stresses

In addition to the shape and material properties, residual stresses are also influenced in bulk forming processes. The residual stresses resulting in the process have a considerable influence on the material properties, which are discussed in chapter 3.6. In particular, residual stresses close to the surface improve the fatigue life, the development of corrosion as well as workpiece distortion. [1, 2, 11] Since residual stresses can be significantly affected by controlling the forming and material parameters, knowledge and deeper understanding of the underlying mechanisms are essential to ensure optimized and reliable process and manufacturing design. However, this aspect is not yet consciously used in many industrial process chains. Instead, additional machining steps are usually carried out to reduce the effects of unfavorable residual stress conditions and their negative consequences on component properties. Heat treatment steps such as stress relieving are used to reduce tensile residual stresses at the surface. To introduce residual compressive stresses on the surface, the manufactured components are shot-peened or hard-rolled in a subsequent processing step. For example, the maximum load cycle of an aircraft rim until reaching a critical length was quintupled by hard rolling and the occurrence of corro-

sion of a shot-peened pipeline was prevented. [12, 13, 14] However, both options lead to an extension of the process chain, thus affecting the economics of the process and reducing overall resource efficiency. Within the expert group, various bulk forming processes were examined with regard to their potential for unused residual stresses. These include the forming strategies that can be used to specifically influence the residual stresses already in the process, the component property improvements due to the forming-induced residual stresses, and the residual stress stability.

### 3.3 Reproducibility of the Initial State

The following questions are related with the forming-induced residual stresses and the influence of the residual stresses in the initial state: Is it possible to produce a reproducible initial state in the workpiece? What influence does a changed residual stress distribution in the initial state have on the result after the forming process? To analyze this issue, investigations were carried out on the initial state of the various forming processes as illustrated in the overview in table 3.1. For this purpose, samples of one batch each were produced, the individual samples were subsequently stress-relief annealed at the IFUM Institute, and at the end the residual stress state was checked by X-ray diffraction.

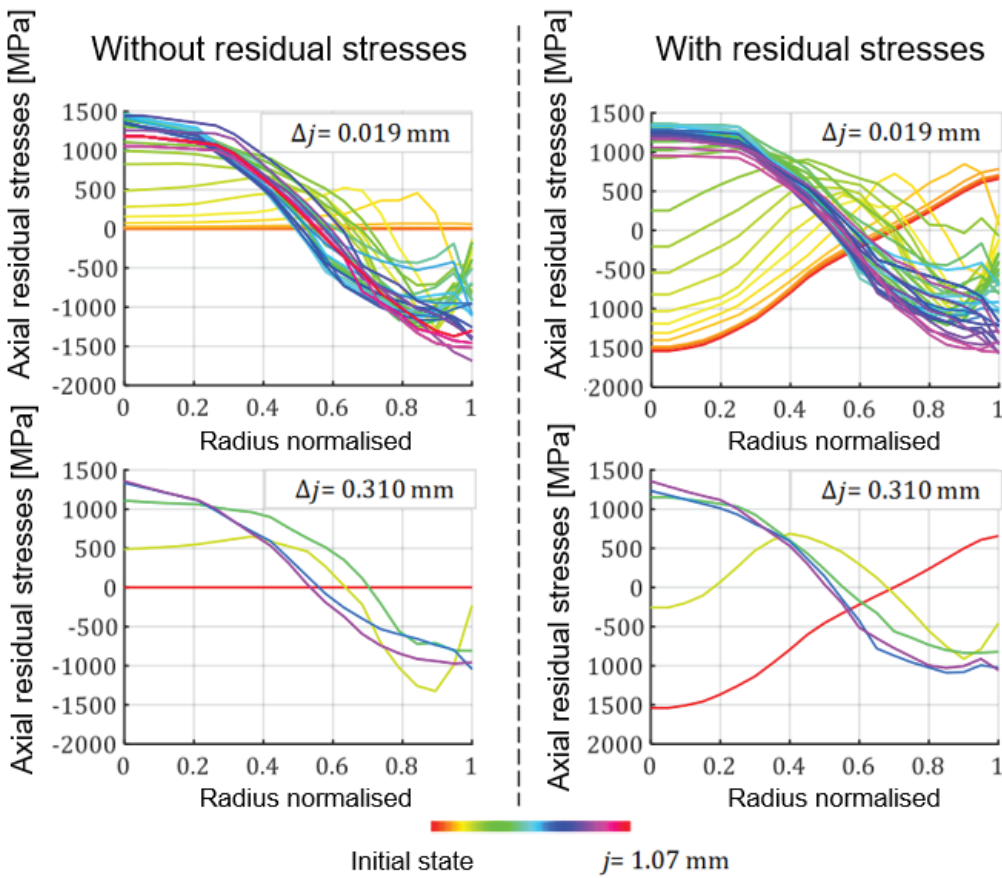


**Figure 3.3** Simulation of the influence of residual stresses for the combination of forward extrusion and rotary swagging from [15].

The result of this study is shown in the figure 3.2. From the analysis of the individual samples, non-negligible variations in the initial state can be seen, with the individual residual stress states fluctuating around the value of 0 MPa. In particular, for the material specimens from IWU and bime, absolute scattering of up to 150 MPa results in both the tensile and the compressive directions. The fluctuations in the residual stress state can be attributed to inhomogeneities in the microstructure as well as to the manufacturing process, so that no complete relaxation of the residual stresses occurs due to the subsequent heat treatment process. On the other hand, the deviation can also be attributed to the measurement error caused by the X-ray diffraction itself. [16] Based on the data, it can first be concluded that the residual stresses in the initial state are not reproducible, since unavoidable fluctuations occur. Of particular interest, however, are

the effects of the different residual stress states on the result after the forming process. Numerical studies have been carried out to investigate this aspect in order to clarify the sensitivity of a varying residual stress state to the result after the forming process. Numerical FE investigations by Franceschi [15] are plotted in figure 3.3, where a specimen was reworked in each case with and once without residual stress profile by an additional rotary swaging operation. The introduced residual stress profile in the initial state was generated here by cold extrusion, see figure 3.3 on the right. The individual colors show the curves of the current residual stress profile as a function of the normalized radius and the respective radial infeed  $\Delta j$ . Since no feed rate is set in the axial direction, an ever-increasing plastic deformation and penetration depth are achieved over the machining cycles at the specimen location to be examined. Consequently, by superposition,

compressive stresses increase in the area near the surface, while tensile residual stresses are induced in the core. What is striking is the range above a certain number of machining operations at which the residual stress profile no longer changes significantly. If the results are compared with and without residual stresses, the curves are similar. Two basic definitions are essentially derived from this fact: Above a slight plastic deformation, a superposition of the stress values is achieved. This range is defined as partial plastic deformation. Above a certain level of deformation, a constant range is reached where no significant change occurs even after the increase in deformation  $\Delta j$ . This range, on the other hand, is defined as fully plastic deformation. As applied to the problem, there is thus only a reproducible initial state in the blank when a fully plastic forming takes place. Accordingly, the original residual stress state is completely erased and the final residual stress state is only influenced depending on the process parameters. For this reason, the final residual stress states are similar to the figures 3.3 left and right. For partially plastic deformation, on the other hand, only a superposition of the deformation-induced residual stresses with the initial state takes place. [15]

The application of the theory of fully plastic forming was also verified by profile rolling and cold extrusion. Here, in the first process, a specimen was cold extruded and then the specimen was notched by profile rolling. From the results on the notch, it was shown that the residual stress condition introduced by cold extrusion was eliminated via the fully plastic deformation during profile rolling. This was deduced because, even by varying the residual stress state after cold extrusion, there were no significant differences in the final profile after profile rolling.

### 3.4 Strategies for the Manipulation of Residual Stresses

In today's processes, the possibility of specifically influencing residual stresses in solid forming is not yet used in a targeted manner. The modification of the residual stress state is strongly dependent on the respective process itself and it is not pos-

sible to derive a uniform guideline for the design of residual stress-compatible process control from the literature. On the one hand, this situation is due to the large number of process parameters, material properties and process control as well as their complex interrelationship. On the other hand, it is due to the measurement uncertainties and the statistical nature of the residual stresses themselves [17]. From the cooperation of the individual projects, diverse knowledge of the individual forming processes for manipulating the residual stress state was collected and compiled. The aim of the cooperation was to identify correlations between the individual process parameters and the residual stresses. For this purpose, the respective forming strategies were systematically subdivided into a total of five categories, which are shown schematically in figure 3.4. The individual forming strategies are subject to the three mechanisms for generating residual stresses: Inhomogeneous deformation, temperature gradients and phase changes. These have already been explained in chapter Basic Principles. For cold forging, inhomogeneous plastic deformation is the most common mechanism, so material flow plays a crucial role in influencing the residual stress state. Depending on the strain rate, forming-related phase changes also occur (e.g., forming martensite) and influence the forming-induced residual stresses. Due to the low process temperatures, effects caused by temperature gradients play a minor role in cold forging, which is why they are disregarded in numerical simulations [18]. In contrast, hot forging is based on

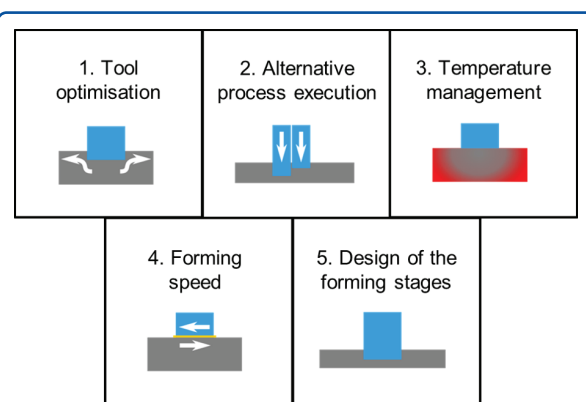


**Figure 3.4** Strategies to control residual stresses in bulk metal forming

the effects due to temperature gradients as well as the associated phase changes in the microstructure. Consequently, the crucial process factor is temperature control, while the study of material deformation reflects only a secondary aspect. At this point, it should be emphasized that the subsequent forming strategies are strongly dependent on the material configuration. Thus, it cannot be ruled out that the transferability of the findings will lead to contradictions.

## Tool Optimization

In certain cold forming processes, it is possible to control the material flow by modifying the die geometry and thus to adjust residual stress states by influencing the deformation speed of the material. In particular, it is conceivable to reduce tensile stresses that occur by controlling the material flow by reducing inhomogeneities in the plastic deformation. For impact extrusion, this is possible by adjusting the geometry of the die. Here, a small opening angle leads to a more homogeneous velocity field in the forming zone, resulting in a reduction of the final residual stress state and in a reduction of tensile stresses at the surface [22]. The same phenomenon is observed for radial cold forging, where optimization of residual stresses is achieved by reducing the angle of entry [23]. An extension of the studies for the opening angle was carried out for extrusion, where for an identical degree of deformation the inlet angle was designed concave and convex, respectively. In addition to the influence of residual stresses, a forming-induced phase transformation also occurs, which is determined by the design of the die opening [19, 24, 25]. Among other things, the influence of the proportion of martensite and austenite formed is determined. The influence of tool geometry on flow behavior is also transferable for fine blanking [20]. By using different cutting edge preparations, the material flow can be controlled, whereby a redistribution of residual stresses occurs for the blank as well as for the fine-cut sheet strip. Preferably, higher compressive stresses are generated in the sheet strip by a round punch edge, whereas this effect is reversed for the blank. Investigations into the formation of residual stresses during rotary swaging showed instead a dependence

of the stress state on the process parameters. In this technology, the formation of intrinsic material properties is closely correlated with the extremely complex material flow that characterizes this process [26]. Incremental plastic forming affects not only the geometry, but also the static and dynamic strengths through strain hardening and the introduction of residual stresses [27]. In this context, inhomogeneous conditions can affect the different areas of the surface of the workpiece. It was shown that not only the shape of the tool but also the tool kinematics have an influence on the residual stresses. As an example, it was shown that when the rotary swaging tool and the workpiece rotate at the same angular velocity, a more homogeneous residual stress profile is achieved in the z-direction. [28]

## Alternative Process Execution

With alternative process control as the second strategy, extensions within the conventional process are to be understood. The extensions include, on the one hand, the use of active elements and, on the other hand, the exploitation of the phenomenon of stress superposition. Thus, alternative process control is to be understood as a temporal, path-bound or force-bound process extension. The addition and subtraction of residual stress states are subject to the theory of full forming and partial forming, which have already been explained in chapter 3.3. Two examples of this approach with respect to cold extrusion are presented in this section. Franceschi et al. have shown that an active counter punch can significantly reduce axial and tangential residual stresses in extruded components and avoid subsequent heat treatment [29]. Here, the ejector, which is normally activated only after the first forming process is completed, is actively controlled to apply an axial counterforce to the workpiece during extrusion. Similar to changing the opening angle, the difference in material flow between the center and surface of the workpiece is affected. By controlling the material flow, stress control is achieved, reducing stress gradients in the calibration zone in particular. In [30], a second alternative process control for cold extrusion was investigated. In contrast to the previous process control, in this case

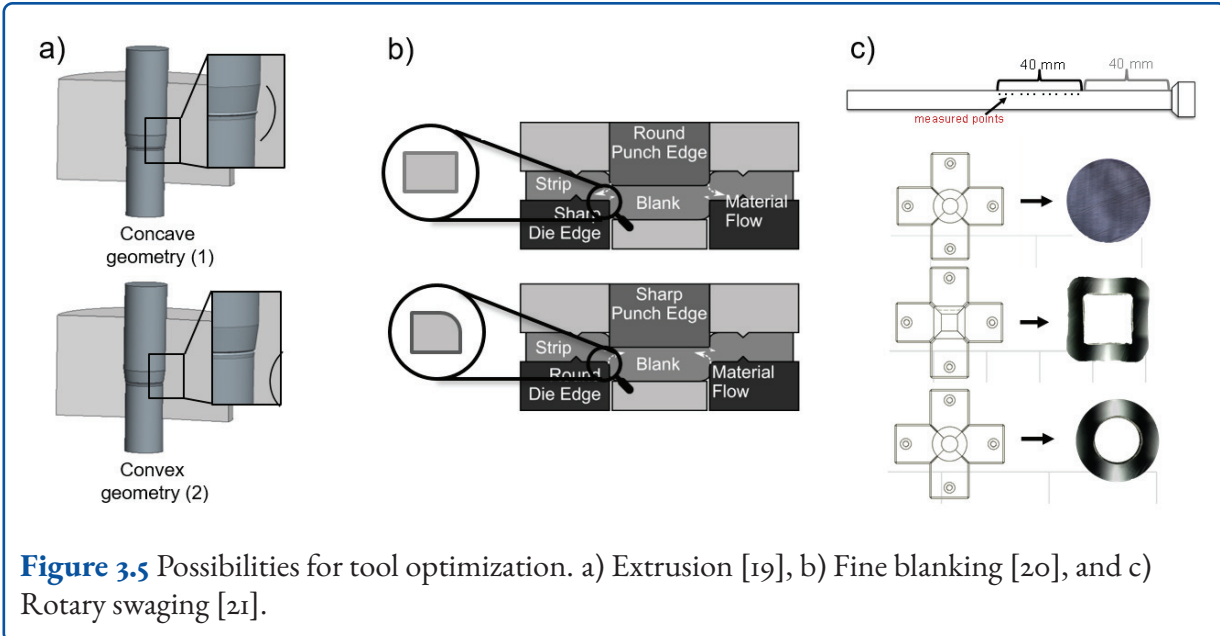
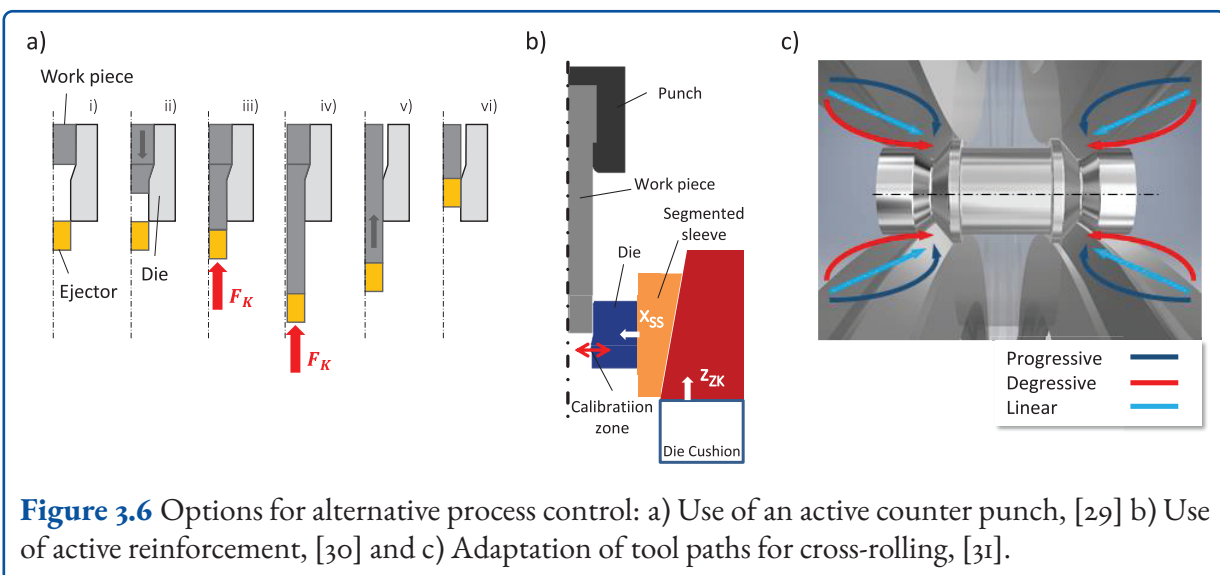


**Figure 3.5** Possibilities for tool optimization. a) Extrusion [19], b) Fine blanking [20], and c) Rotary swaging [21].



the residual stress state is not set directly during the forming process, but during the subsequent ejection of the workpiece. It is known from the literature that the extruded part, which is pushed through the calibration zone a second time during ejection, undergoes a second plastic deformation. After this step, the tensile residual stresses on the surface of the specimen in the axial and tangential directions are usually significantly reduced [32]. This is especially true after ejection. The reason for this is the lower degree of deformation experienced by the specimen in the ejection phase, and was explained by Tekkaya in terms of the “extreme layer”

theory [32]. By adjusting the tooling system, it is possible to adjust the preload during ejection and, based on this principle, to adjust the degree of deformation during ejection. The active die system for this alternative process control is shown in figure 3.6 b), where an inner conical reinforcement can be displaced via an outer conical sleeve by means of an internal drive system in the press. In this way, the radial infeed of the internal die is adjusted, thus enabling precise adjustment of the forming degree in the ejection phase and finally an adjustment of the superimposed residual stress state. In summary, it is shown that by controlling both active elements,

the final residual stress state in the manufactured part is adjusted. For incremental forming, the alternative process control is introduced by selectively changing the tool path. By adjusting the radial and axial infeed during cross rolling over time, a change in work hardening as well as plastic deformation is possible. Consequently, the different deformation speeds during cross rolling control the final residual stress state [31].

## Temperature Management

Temperature management represents the primary forming strategy for hot forming in order to set the final residual stress state. In [17], in addition to the process temperature and cooling rate, different materials and component geometries, which represent the process parameters of temperature management were investigated for this purpose. The comprehensive material characterization by the authors in [33] has shown that the plastic behavior, the transformation-induced and the transformation-plastic parameters of the two materials are different. The investigations show that at the same process temperature, the influence of the component geometry as well as the material used affect the final residual stress state. With regard to residual stresses, hot forming as a thermo-mechanically coupled process basically offers the potential for several control parameters. However, a targeted adjustment of residual stresses to improve component properties by combining defined forming parameters with an adapted cooling strategy has not yet been explored. From an engineering point of view, heating the workpiece prior to the forming process offers an important advantage: All stresses previously prevailing in the material are largely relieved by recrystallization and a new residual stress profile can be generated in the process. In addition to process parameters such as forming speed and degree of forming, the forming temperature and the cooling path also have an influence on the induced residual stresses [17]. Higher residual stresses are due to the change in austenite grain size caused by the forming temperature. The higher austenitizing temperature results in increased grain growth in the material, leading to larger austenite grains [34]. The increased grain size in turn leads to several effects. The

enlarged grains cause an increase in the martensite start temperature and the martensite end temperature [35]. Due to the coarser structure of austenite grains, the diffusion of interstitial atoms at the long grain boundaries of the austenitic crystal lattice is hindered and the diffusion-free martensitic phase transformation is facilitated. Since the martensitic transformation is adjusted with the setting of the forming temperature, the proportion of retained austenite can be influenced [36]. The resulting volume shift adjusts the strain gradients as well as the final residual stress profile. In addition, since the maximum possible residual stresses are limited by the yield strength, increasing the proportion of the harder martensitic phase and reducing the softer austenitic phase can lead to an increase in residual stresses. These effects obviously conceal the fundamental reduction in yield stress that occurs as a result of grain enlargement according to the Hall-Petch [37] and [38] laws. In another study, the influences of the two different cooling media, water and air, for cooling after hot forming at 1,000 °C on the resulting residual stresses [17] were investigated. Here it is shown that the diffusion-controlled phase transformation is influenced by the different cooling media. At fast cooling rates, such as with water, the formation of martensitic tetragonal lattice microstructures is favored, while at slow cooling rates the formation of body-centered cubic lattices with bainitic microstructures is favored. Depending on the cooling rate, the entire material microstructure is adjusted, thus controlling the volumetric expansion and the strain gradients within the component, which ultimately results in a new residual stress state.

## Forming Speed

For cold forming processes such as extrusion, there is no clear evidence in the literature of the possibility of influencing the residual stresses of the final products by adjusting the forming speed. In [39], it was shown that the forming and ejection speed affects the temperature of the cold extrusion parts. However, no correlation was found between the forming speed and the residual stresses close to the surface, since the deviations are in the range of measurement uncertainty. In addition to temperature,

the change in forming speed also affects the conditions in the contact area between the workpiece and the die. In particular, the sliding speed between two surfaces affects the coefficient of friction  $\mu$ . It has been shown for most materials that the coefficient of friction decreases with increasing speed [40]. Studies by Franceschi et al. showed that with an increase in forming speed there is a reduction in near-surface tensile stresses. This effect is due to the reduction of the frictional shear stresses at the die opening, so that at the near-surface region the material flow is affected less. For this reason, analogous to die optimization, there is a greater homogenization of the material flow, which results in a reduction of the residual stresses. Therefore, as a general rule for cold forming, extremely low forming speeds should be avoided. In this context, investigations with different lubricants and friction coefficients  $m$  for cold extrusion were carried out in [39]. For this purpose, it was shown that with the change of the coefficient of friction at the same forming speed, the material flow can be controlled very tightly. With lubricants such as soaps, which have significantly lower friction than conventional lubricant systems, it was even possible to induce compressive stresses in the surface. In hot forming, on the other hand, the forming rate influences the final stress state through various phenomena and can lead to significant variations in residual stresses in the specimens [41]. However, no general tendencies can be derived from the investigations based on the relationship between the forming speed and the resulting residual stresses measured by X-ray diffraction. Rather, it is necessary to consider each parameter combination individually, since dynamic recrystallization occurs in different forms in each case study. Dynamic recrystallization means that above a certain level the dislocations and lattice defects caused by deformation are absorbed via the resulting grain formation and growth. This leads to a reduction in yield stress, reducing the required process forces and increasing the maximum plasticity of the material [2]. Depending on the relationship between the temperature-dependent diffusion rate and the forming rate, an austenitic microstructure is formed, resulting in varying levels of residual stress. The influence of the forming rate and the theory behind it can also be applied to incremental solid forming. In [21], curved rotary swaging

dies and increased the forming speed reduce compressive stresses, while flat-formed dies relieve near-surface tensile stresses at higher forming speeds. In the depth direction (300  $\mu\text{m}$ ), however, the process variation was largely independent of the forming speed or the influence of the tool shape.

## Design of the Forming Speed

The last forming strategy is based on the design of the process in several forming steps. Analogous to the modeling presented in chapter 3.3, the final stress state results from the stress superposition from the individual forming steps. Therefore, it is possible to investigate different strategies to design a residual stress compliant process chain by combining the individual process steps. In particular, it is possible to exploit the different stress development by varying the degree of forming in order to optimize the stress state after the final forming step. However, the response of residual stresses to an increase in the degree of forming in cold and hot forming processes is very different. For cold forming, the forming and unloading sections are important in this respect, and the restrictions to influence springback during unloading are also crucial. Consequently, the two sections are closely related to inhomogeneous plastic deformation, so that these process steps must be studied separately. To demonstrate the point, the conventional two-stage process for full forward extrusion is considered, with the second forming stage describing ejection. Typically, the final stress state is improved after the part is ejected. Tekkaya, in [32], describes the effects of this second deformation step on residual stresses using a conceptual experiment. The extruded specimen during ejection can be modeled as a tensile test, as shown in figure 3.7. The core of the part consists of a solid body with residual compressive stresses, while the surface is a hollow body with residual tensile stresses. The shape of the stress-strain curve during the different steps of the tensile test is shown in figure 15b. Due to the initial stress state, the surface reaches the plastic region (from point A) much earlier than does the core of the specimen, which is plastically deformed only from point B onward. The deformation continues until point C, where the specimen is then relieved. At

this point, the strain range of the core is less than that of the surface, which should be compensated for when the external force is removed. However, the constraints in this system force the core and surface to be the same length at the end of the unloading phase. As can be seen in the diagram, this results in a significant reduction in residual stresses, which is often desirable for later use of the part. The resulting residual stress state in a conventionally extruded part is thus the result of the interaction of the two different deformation characteristics, the forming with large cross-sectional reduction and the ejection process with small cross-sectional reduction.

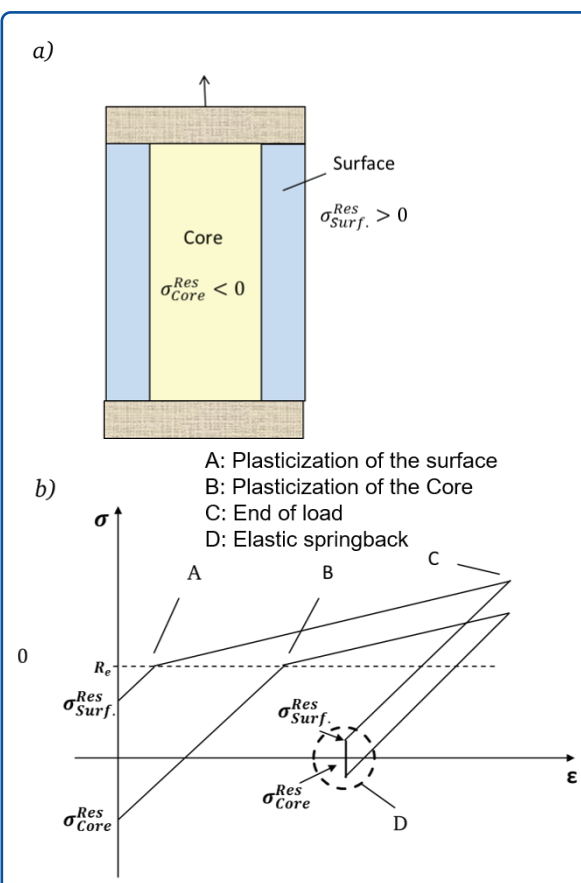


**Figure 3.7** Conceptual experiment to represent the mechanisms during the ejection phase of full-forward extrusion from [32]: Setup of the experiment (a) and stress-strain diagram (b).

The example of extrusion shows how the superposition of successive forming stages can be a successful strategy for influencing residual stresses in cold forming processes. In particular, it could be

advantageous to perform smaller degrees of deformation in the final forming operation. This could be of particular interest in incremental forming processes, in which a higher degree of compression deformation is achieved by stringing together several loading and unloading steps. In these processes, it would be more target-oriented to adjust the forming degree of the last process step in order to calibrate the residual stresses without negative effects on the production times. However, such a strategy has not yet been described in the literature for these processes. The effects of the degree of deformation are also important for hot forming. The influence of this parameter on residual stresses in hot forming processes was investigated in [41]. The specimens were upset to two different final heights. Increasing the upset distance resulted in a decrease in residual stresses. As the final height of the specimen decreases, the degree of deformation of the material increases and so does the number of dislocations. As mentioned in the section on temperature management, dynamic recrystallization occurs at a critical degree of deformation. Nucleation forms in the deformed areas, leading to the growth of new austenite grains. The higher the deformation, the higher the number of dislocations and the finer the newly formed grains. Accordingly, depending on the resulting grain size, the same effects were found with a reduction in the forming parameter “degree of deformation” as with the increase in forming temperature described above.

### 3.5 Thermal Stability of Forming-induced Residual Stresses

In chapter 3.4, an overview of possible forming strategies in bulk forming for different processes was already discussed, which have a significant influence on the residual stress distribution in the manufactured component. However, in order to utilize the residual stresses introduced into the process and thus influence component properties, two conditions must be ensured. On the one hand, the forming process must introduce a residual stress state that improves the component properties in a targeted manner. On the other hand, the residual

stress state must be sufficiently stable under typical operating loads over the product lifetime to verify an improvement in properties. These operating conditions include both mechanical and thermal loads. Thus, there is a need to assess the two aspects: Whether the forming-induced residual stresses remain unchanged and to what extent the residual stresses evolve over time to validate their effectiveness during service. In the literature, this issue is also defined as residual stress stability. Numerous studies already exist for residual stress stability under mechanical cyclic loads, and the methodology is discussed as an example in chapter 4 within the mechanics section. For thermal residual stress stability, existing research on stress relief annealing has already identified temperature ranges at which residual stresses can be specifically relieved. In contrast, the focus of the following investigations relates to residual stress stability at low temperatures from 80 °C to 240 °C. Although the temperature range to be investigated is well above the recrystallization temperature, the literature does not provide a clear answer for the phenomena in this temperature range that are encountered in real service conditions. Thus, the following investigations are intended to identify whether the subject matter is a problem, whether characteristic temperatures exist, and how the process and material parameters affect the underlying phenomena. In the following, the issue was investigated using the processes as well as selected materials which are included in the following figure 3.8. The experimental analysis includes the following steps:

1. **Forming:** The production of the benchmark components was carried out with reproducible and constant process parameters.
2. **Measurements after forming:** For each benchmark component, characteristic measurement points were selected for residual stress measurement on the specimens, representing residual stress stability. The selected measurement points are listed in the figures below. In the as-formed state, residual stress measurements are performed at the measurement points by X-ray diffraction.

3. **Heat treatment:** Specimens are placed in pre-heated ovens at selected temperatures for a duration of 100 h.
4. **Measurements after heat treatment:** After subsequent heat treatment, the samples are measured again with respect to residual stresses using the measurement points from step 2. In this way, the relaxation of the residual stress can be assessed.

Processing steps 3 and 4 were then repeated at defined temperature points: 80 °C, 120 °C, 180 °C, 240 °C. The results are listed in figure 3.8, where for the different manufacturing processes of each institute are merged in the seven figures. The respective temperature range at which the residual stresses were recorded at the respective listed measuring point is indicated in the individual colors.

## LFT: Full Forward Extrusion

In the full forward extrusion sample in figure 3.8 a), there is a clear trend for the near-surface residual stresses to be affected with the through-heating time of 100 h. For the stainless steel X6Cr17 (1.4016), axial tensile residual stresses are reduced with increasing temperature and soak times, while compressive residual stresses increase slightly in the tangential direction. This effect results in the relaxation of the tensile stress maxima, which are below the surface, leading to an equalization of the residual stresses along the component.

## PtU: Bending

Three-point bending of 16MnCr5 sections results in pronounced axial compressive stresses and low tangential compressive stresses in the specimen exterior. During annealing at 80 °C, the axial stresses are only slightly reduced, but higher process temperatures lead to significantly higher relaxations. In the tangential direction, an increase in compressive stresses is observed at temperatures up to 180 °C, followed by relaxation at 240 °C. Similar to the other processes, relaxation of the stress maxima and rearrangement of the residual stress state is also present.

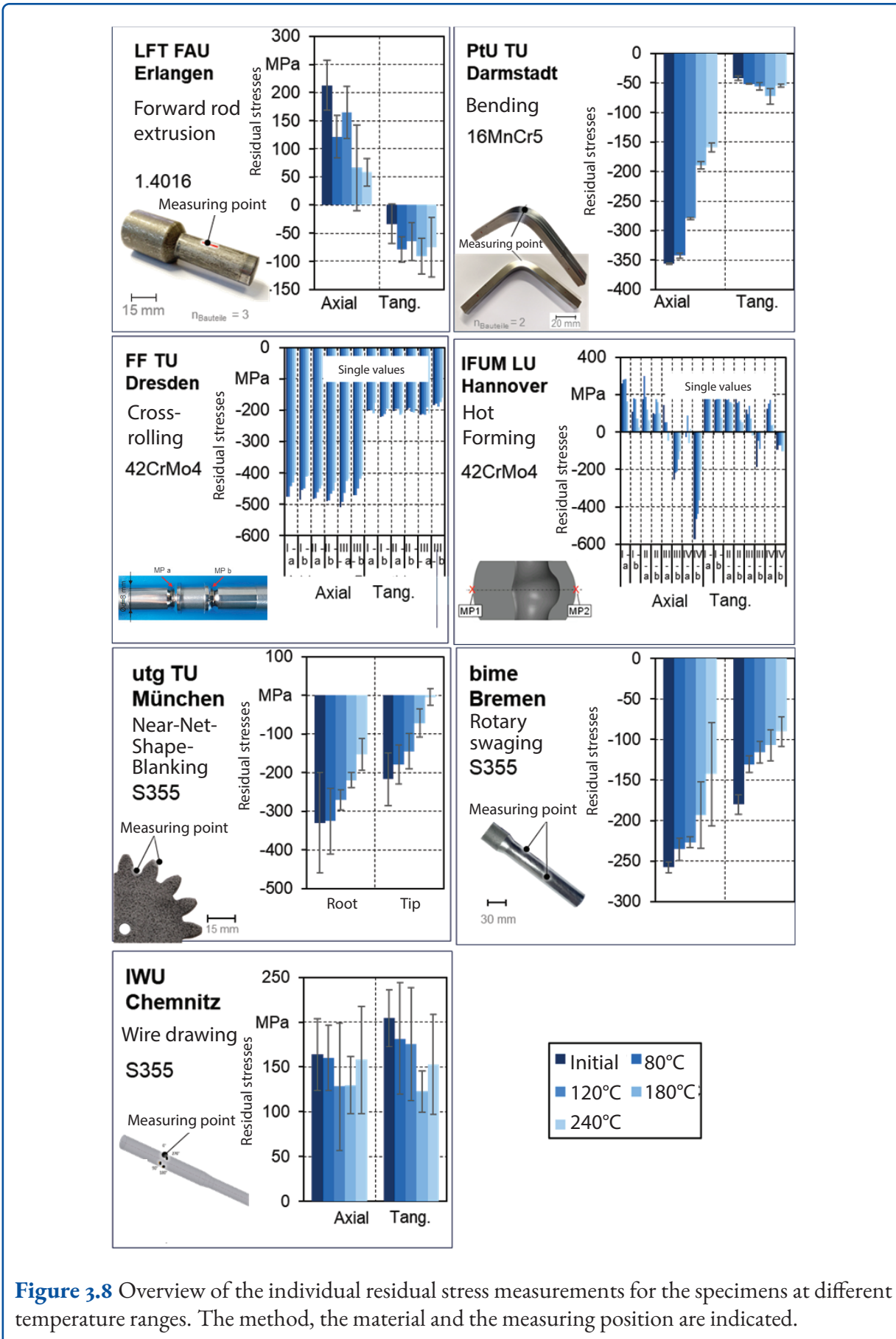


**Figure 3.8** Overview of the individual residual stress measurements for the specimens at different temperature ranges. The method, the material and the measuring position are indicated.

## FF: Cross-rolling

The typical residual stress profile of cross-rolled specimens made of 42CrMo4 is characterized by high compressive residual stresses in the axial and tangential directions, see figure 3.8. For all specimens, a reduction of residual stresses by 10 % to 20 % is observed with increasing holding time and temperature. The compressive residual stresses induced by cold section rolling exhibit high stability under thermal load up to 240 °C. While some relaxation of about 16 % is observed for the high axial residual stresses during the heat treatment, the lower tangential residual stresses remain almost unchanged. The reason for this high residual stress stability is the high degrees of deformation locally achieved in the notch area of the specimen during the rolling process, which lead to high local yield stresses due to strain hardening. These decrease slightly due to the influence of temperature, so that residual stresses can be relieved to a small extent by microplastic strains in the material. This corresponds to results documented in the literature, according to which high-strength materials exhibit higher residual stress stability under the influence of temperature than those with lower flow stress.

## IFUM: Hot Forming with Upsetting

Different behaviors are observed in the hot-formed specimens (IFUM). In specimens made of 42CrMo4, tensile residual stresses have been measured directly after forming. After subsequent heat treatment, these tensile residual stresses initially increase up to a temperature of 120 °C, but are relieved at higher temperature ranges. This effect at a critical temperature of 120 °C occurs for the axial as well as tangential residual stresses. For the material 16MnCr5, compressive residual stresses are measured in the axial direction, and are relieved with higher temperature, especially at MP1, i.e., at the thick-walled measuring point. The compressive residual stresses occurring at MP2 vein only slightly at the surface; for the tangential stresses the reversal point is again visible at a critical temperature 120 °C. For the material 42CrMo4, this effect can be explained by the relaxation of the stress max-

imum below the surface: Due to the fact that the tensile stress maximum below the surface is relieved first, a redistribution of the residual stresses in this region occurs first, which leads to an increase of the tensile residual stresses directly at the surface [17]. Only at temperature 120 °C and above does relaxation also occur in the near-surface region. The earlier reduction of residual stresses in 16MnCr5 compared to 42CrMo4 can be justified by the lower yield strength. At a low residual stress level, as is the case for 16MnCr5 in the tangential direction, the effects of heat treatment cannot be clearly identified due to the measurement uncertainties.

## utg: Near-Net-Shape-Blanking

Compressive residual stresses occur in the tooth roots and flanks on fine-blanked gears made of the material S355 MC (1.0976). During heat treatment, the expected degradation is also observed here. While the flank is stress-free after 240 °C, some residual stresses remain in the tooth root. In addition to creep and relaxation processes, this behavior was attributed to dislocation core diffusion.

## bime: Rotary Swaging

In rotary swaged components made of E355 (1.0580), residual compressive stresses occur due to the process. While the axial stresses undergo little reduction during annealing up to 120 °C, they are significantly reduced at 180 °C and 240 °C. In the tangential direction, a significant stress reduction is observed in the first cycle at 80 °C, followed by a constant slight relaxation at higher temperatures.

## IWU: Wire Drawing

Wire drawing from S355JR is characterized by tensile stresses at the surface. Compared to the other processes, no residual stress reduction with increasing temperature is observed here. While there is no significant stress relaxation in the axial direction, a trend toward a slight reduction in tangential stresses can be observed. This behavior is attributed

to the creep and relaxation processes in the material.

From the results of the various specimens at temperatures ranging from 80 °C to 240 °C, three typical behaviors can be identified. In most cases, a reduction in residual stresses is observed. Here, a partially pronounced degradation as well as a complete relaxation occurred. In the case where the residual stress maximum is located directly at the surface, a stress reduction is observed over all temperatures. In other cases, an increase in the measured residual stresses, followed by a decrease, was observed. This is due to the fact that the residual stress maximum is located below the surface. As the temperature increases, a redistribution occurs due to the reduction of the residual stress maximum, resulting in the initial increase in residual stresses. With further temperature increase, the residual stress reduction also extends to the region near the surface, which subsequently explains the reduced residual stresses in the measurements. Only one process investigated was found to have a minor influence. Overall, several physical mechanisms act within the heat treatment. The first physical mechanism is the reduction of the yield stress of the material at higher temperatures [42]. This leads to microplasticization in stressed areas and thus to a reduction of the residual stress to the current yield stress. Creep mechanisms are additionally influenced by the process temperature, taking into account the load and the exposure time. Here, residual stresses also favor induction from the creep phenomenon. A final mechanism relates to the atomic level, where temperature-induced dislocations lead to a reduction in the local dislocation density and thus to a relaxation of residual stresses. In practice, a combination of mechanisms occurs within the annealing process, which results in different changes depending on the component and the residual stress state present.

### 3.6 Property Improvement Due to Residual Stresses

As already explained in chapter 3.2, the potential for utilizing residual stresses is only exploited by additional finishing steps such as deep rolling and

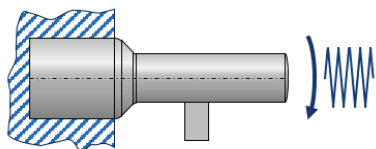
shot peening [14, 13]. Depending on the final residual stress profile, certain component properties are affected negatively as well as positively, with certain properties depending in particular on the direction of the stress. To demonstrate the potential of forming-induced residual stresses, examples of possible component property improvements are presented below. In total, four known component properties which are modified depending on the residual stress state are addressed: fatigue life, distortion, hardening and corrosion.

#### Fatigue Life

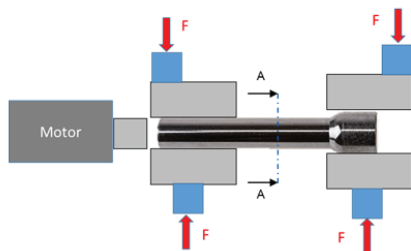
The first component property affected by residual stresses is fatigue life. This refers to the time period after which the component fails under a cyclic mechanical load. Essentially, this property results from the stress superposition of an external load and the residual stress state present in the component. A typical material test for determining fatigue life is the Wöhler test commonly used in practice, in which the component is loaded cyclically, usually in a sinusoidal function, under a given load [43]. Fatigue is subdivided into two types in terms of load cycles: Low load cycle fatigue (LCF) and high load cycle fatigue (HCF). LCF describes fatigue at stresses above the yield strength and usually involves fewer than 10.000 cycles to failure. Analogous to the static load case, residual stresses often have little effect on LCF life because they are extinguished within the first cycle by the large amplitudes of oscillating plastic strains [44]. Thus, there is no mechanical residual stress stability in the LCF region, which is why the HCF region is of particular interest for the forming-induced residual stresses. In particular, high near-surface compressive residual stresses are of interest, since they restrain crack growth compared to tensile stresses and thus avoid early failure due to initial surface cracking.

Possible experimental tests are demonstrated in the following figure 3.9 for a cold extruded specimen as well as gear manufactured by fine blanking. Via the 3-point bending test (a), a superposition of residual stresses with axial residual stresses is achieved by the modified setup, and this test is primarily used to investigate the mechanical residual stress stability.

a) Three-point bending test



b) Circular bending test



c) Tooth root fatigue strength

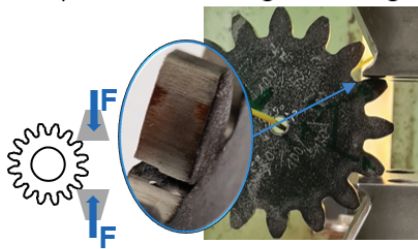


**Figure 3.9** Experimental setup for fatigue life investigation in cold forming [39, 45, 15].

From the results of [46] it was shown that at low mechanical loads the residual stresses are stable and only at higher loads a redistribution of the residual stresses takes place. To mimic real loading conditions of a gear shaft, the rotating bending test in (b) is used. From the investigations of [47], a similar result was obtained for the residual stress stability, where instability in the residual stress state occurs only at higher loads. With respect to fatigue life, it was shown that the use of a counter punch increases the maximum load cycle that can be sustained by 78 % at an average load (250 MPa). The improvement in fatigue life is due to the reduced residual stress gradients due to the counter punch, so with the superposition with the bending load, the equivalent stress is reduced. Consequently, the counter punch also creates a larger buffer to the yield stress, which delays an occurrence of the possible plastic deformation within the cyclic loads. The same positive effects have been verified for fine blanking with

a matched cutting edge. In this case, the generation of higher compressive stresses at the surface also leads to an increase of the fatigue strength within the Wöhler diagram [45]. The results are also transferable to incremental forming such as cross wedge rolling. This forming process can be used to join hybrid components in a form-fit and force-fit manner to create a shaft-hub connection [48]. A characteristic notch is created by the joining process through radial rolling, and when an external load is applied, there is an excess stress in the notch base. Accordingly, the notch is the critical location where early failure due to cracking occurs under load. By indexing increased compressive stresses through a progressiv tool path (alternative process execution), higher tolerable load cycles are also achieved here in cyclic tensile tests, which has been validated numerically and experimentally [31].

## Component Distortion

The cause of distortion is usually due to residual stresses remaining in the component. If high residual stress gradients are present in the component, i.e., high absolute differences between the surface and the core, slight disturbances of this equilibrium can lead to undesirable plastic deformations. When the yield strength is exceeded, the residual stresses are converted into plastic strains and deformations and a change in shape occurs [49]. For this reason, components must be low in residual stress, which in turn is made possible by stress relieving after forming [50]. To check the distortion potential of formed components, separation tests are usually used in practice [3]. In investigations by [29], it was shown that cold extruded specimens with a counter punch exhibit significantly lower deformation compared to conventionally produced specimens in the separation test, see figure 3.10. This effect results from the reduced stress gradients due to the use of a counter punch during cold extrusion, so that a significantly lower deformation results from the stress compensation after the separation process.

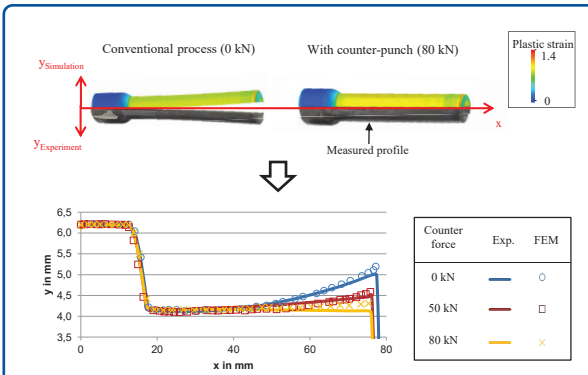


**Figure 3.10** Investigation of distortion on cold extruded components by separation tests [29]

## Solidification

Tekkaya points out that more strengthening materials should maintain higher residual stresses because the difference in forming between the core and the surface is larger [32]. Existing studies by Jobst et al. confirm this fact, as the different induced residual stresses also influence the strain hardening distribution by varying the die opening angle during cold extrusion [39]. Similarly, for incremental forming such as cross wedge rolling, an increase in strain hardening is achieved by the matched die paths, again due to the increased residual compressive stresses at the surface. In fine blanking, on the other hand, it is shown that cutting edge preparation hardly influences the hardness distribution. The residual compressive stresses correlate with the increased tooth root bearing capacity due to hardness and residual compressive stresses [51].

## Corrosion

A final listed component property that correlates with residual stress is corrosion. Stress corrosion cracking is a time-dependent cracking phenomenon that occurs in a metal when certain metallurgical, mechanical, and environmental conditions exist simultaneously [52]. Stress corrosion cracking is a dangerous type of degradation because it occurs even at stress levels within the design range. The residual stresses present in the material play an important role in evaluating the susceptibility of

the material to stress corrosion cracking, in addition to the external stresses that act on the components during operation. The literature clearly shows how tensile residual stresses at the surface promote corrosion [53].

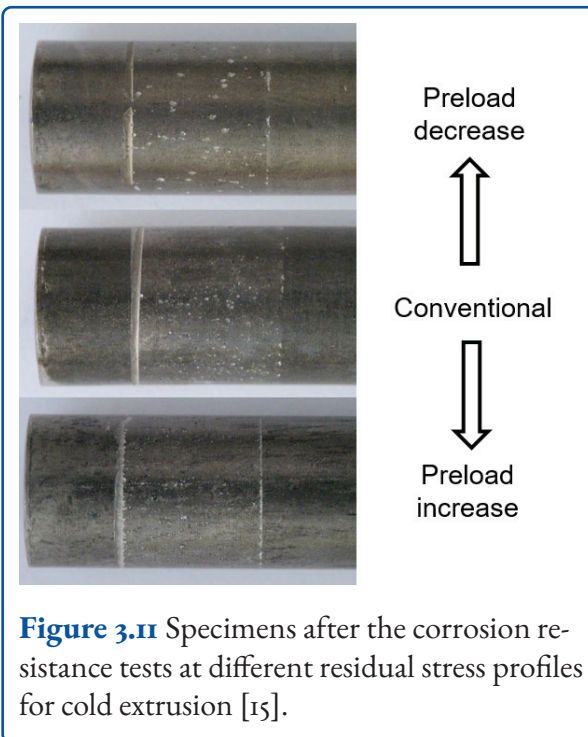


**Figure 3.11** Specimens after the corrosion resistance tests at different residual stress profiles for cold extrusion [15].

In contrast, the introduction of compressive residual stresses facilitates the production of a passivation film regardless of the surface condition, as this film can be produced and maintained at low current density. One reason for this is believed to be the reduction in interatomic distances due to compressive residual stresses, which facilitates the growth and maintenance of the passivation film [54]. Figure 3.11 plots each of three full forward extruded specimens with different residual stress states on which a corrosion resistance test was performed using the material 1.4307. Here, the specimens were used for alternative process control by using the active die from subsection 3.4 to adjust the residual stress profile from tension to compression by increasing and decreasing the die stress. From the recordings it can be seen that a clear trend toward reduction of pitting corrosion: When compressive residual stresses are applied to the surface specimen, fewer and smaller corrosion pits are observed [15].

### 3.7 Conclusion and Summary

In the present paper, different aspects of residual stresses in bulk metal forming were investigated within the collaboration of the Thick-Walled Working Group. It is known from the literature that residual stresses are only specifically controlled by post-processing steps, while the residual stresses occurring within the respective forming process are largely ignored. Consequently, this paper deals on the one hand with the possibility of controlling residual stresses during the forming process. On the other hand, the component properties resulting from the forming-induced residual stresses and their stability under mechanical and thermal load were investigated. The challenge for the industrial establishment of forming strategies for the targeted adjustment of residual stresses and the associated advantages is to understand the complex interrelationships. In particular, residual stresses are dependent not only on the process parameters and the process control of the respective forming method, but also on material properties and the geometric shape of the component as well as the tool.

The forming strategies investigated were grouped into five categories in terms of a systematic approach: Tooling Optimization, Alternative Process Execution, Temperature Management, Forming Speed, and Forming Stage Design. From the summary, it is clear that the topic of deliberate stress induction has not yet been studied in depth for many bulk forming processes, resulting in the complexity of residual stress generation. Despite this knowledge deficit, interesting strategies have been developed for some technologies and these have been classified by a systematic description. Thus, for the future investigation of further forming strategies, a classification in terms of the mechanism to influence the residual stress state is possible. The question of the influence of residual stresses in the initial state is closely related to the mechanism for stress superposition. By examining combinations of various bulk forming processes within the expert group, two definitions were derived: Fully plastic forming above a critical degree of forming, in which an initial residual stress state is completely extinguished

so that the final state depends only on the last forming step and semi-plastic forming below a critical degree of forming, in which an expected stress superposition takes place. Thus, the influence of variations in the initial state is contained only below a critical degree of forming. In terms of the challenge regarding material and process complexity, it is of interest for future investigations at which critical degrees of deformation the occurrence of a fully plastic deformation takes place. Analyses of residual stress stability under mechanical loading showed that residual stresses are stable only up to a critical load. The forming-induced residual stresses are thus only stable with knowledge of the respective process, the component properties and the external load, which requires further investigations due to the process. Analogously, the desired stability for all investigated processes is only present at low operating temperatures below 100 °C, in the temperature ranges from 120 °C upwards some results indicate a relaxation of the residual stresses, which however strongly depends on the respective process and material. Necessary mechanisms in thermal relaxation at low operating temperatures were identified for this purpose. The extent to which the potential of forming-induced residual stresses should be exploited is evident from the improvement in component properties: studies confirm that an increase in product service life, a reduction in distortion, a hardening behavior that can be adjusted and an improvement with stress corrosion cracking can be achieved by deliberate adjustment through residual stresses.

Although clearly different processes were discussed in this chapter, a large number of similarities and analogies were identified despite the complex interrelationships. Thus, there is motivation for further research in order to fully exploit the potential of forming-induced residual stresses and thus exploit the associated benefits for industrial applications. For the future, further investigations should aim at establishing application and design guidelines for a deliberate use of residual stresses in bulk forming.

## Abbreviations

bime	Bremen Institute for Mechanical Engineering
FF	Chair of Forming and Machining Processes
IFUM	Institute of Forming Technology and Machines
IWU	IWU Fraunhofer-Institute for Machine Tools and Forming Technology
LFT	Institute of Manufacturing Technology
PtU	Institut Produktionstechnik und Umformtechnik
utg	Chair of Metal Forming and Casting

## References

- [1] E. Paul DeGarmo, J. T. Black, and Ronald A. Kohser. *DeGarmo's Materials and Processes in Manufacturing*. 10., Aufl. New York, NY: Wiley, J, 2007. ISBN: 9780470055120.
- [2] R. J. Shipley. "Precision Forging. ASM Metals Handbook". In: *ASM International* (1988), pp. 337–384.
- [3] Eckart Doege and Bernd-Arno Behrens. *Handbuch Umformtechnik: Grundlagen, Technologien, Maschinen*. 3., überarbeitete Auflage. VDI-Buch. Berlin and Heidelberg: Springer Vieweg, 2016. ISBN: 9783662438909. DOI: 10.1007/978-3-662-43891-6.
- [4] Radim Kocich et al. "Improvement of mechanical and electrical properties of rotary swaged Al-Cu clad composites". In: *Materials & Design* 123 (2017), pp. 137–146. ISSN: 02641275. DOI: 10.1016/j.matdes.2017.03.048.
- [5] M. Merklein et al. "Fundamental investigations on the material flow at combined sheet and bulk metal forming processes". In: *CIRP Annals* 60.1 (2011), pp. 283–286. ISSN: 00078506. DOI: 10.1016/j.cirp.2011.03.146.
- [6] P. F. Zheng, L. C. Chan, and T. C. Lee. "Numerical analysis of the sheet metal extrusion process". In: *Finite Elements in Analysis and Design* 42.3 (2005), pp. 189–207. ISSN: 0168874X. DOI: 10.1016/j.finel.2005.06.002.
- [7] Serope Kalpakjian and Steven R. Schmid, eds. *Manufacturing engineering and technology*. 7. ed. in SI units. Always learning. Singapore: Pearson Education South Asia, 2014. ISBN: 9789810694067.
- [8] George E. Totten, Kiyoshi Funatani, and Lin Xie. *Handbook of metallurgical process design*. New York and Basel: Marcel Dekker, 2004. ISBN: 0-8247-4106-4.
- [9] Kurt Lange. "Modern metal forming technology for industrial production". In: *Journal of Materials Processing Technology* 71.1 (1997), pp. 2–13. ISSN: 09240136. DOI: 10.1016/S0924-0136(97)00113-1.
- [10] Hae-Sung Yoon et al. "A comparison of energy consumption in bulk forming, subtractive, and additive processes: Review and case study". In: *International Journal of Precision Engineering and Manufacturing-Green Technology* 1.3 (2014), pp. 261–279. ISSN: 2288-6206. DOI: 10.1007/s40684-014-0033-0.
- [11] P. Groche et al. "Incremental Bulk Metal Forming". In: *CIRP Annals* 56.2 (2007), pp. 635–656. ISSN: 00078506. DOI: 10.1016/j.cirp.2007.10.006.
- [12] G. Totten. *Handbook of Residual Stress and Deformation of Steel*. Materials Park: A S M International, 2002. ISBN: 9781615032273. URL: <https://ebookcentral.proquest.com/lib/kxp/detail.action?docID=3002377>.
- [13] Wolfram Volk et al. "Introduction to residual stresses in production technology". In: *Production Engineering* 13.2 (2019), pp. 119–121. ISSN: 0944-6524. DOI: 10.1007/s11740-019-00881-8.
- [14] ECOROLL. *Festwalzen zweier Bereiche an einer Flugzeugfelge*. URL: <https://www.ecoroll.de/anwendungen/luft-raumfahrt--energie/flugzeugfelge.html> (visited on 06/20/2022).
- [15] A. Franceschi. "Anforderungsspezifische Einstellung des Eigenspannungszustands in der Kaltmassivumformung". Dissertation. TU Darmstadt, 2022.

- [16] Fabian Jaeger et al. "Statistical analysis of the reproducibility of residual stress measurements in cold extruded parts". In: *Archive of Applied Mechanics* 91.8 (2021), pp. 3665–3677. ISSN: 0939-1533. DOI: 10.1007/s00419-021-01953-x.
- [17] Bernd-Arno Behrens et al. "Investigations on Residual Stresses within Hot-Bulk-Formed Components Using Process Simulation and the Contour Method". In: *Metals* 11.4 (2021), p. 566. DOI: 10.3390/met11040566.
- [18] Philipp Landkammer et al. "Investigations on residual stress generation in full-forward-extrusion". In: *Production Engineering* (2019). ISSN: 0944-6524. DOI: 10.1007/s11740-019-00892-5.
- [19] R. Neugebauer et al. "Gradation extrusion - Severe plastic deformation with defined gradient". In: *Materialwissenschaft und Werkstofftechnik* 43.7 (2012), pp. 582–588. ISSN: 09335137. DOI: 10.1002/mawe.201200004.
- [20] Stahl, J., Müller, D., Tobie, T., Golle, R., Volk, W., Stahl, K. "Residual Stresses in Parts Manufactured by Near-Net-Shape-Blanking". In: *Production Engineering – Research and Development* (2018).
- [21] Svetlana Ishkina et al. "Influence of Process Fluctuations on Residual Stress Evolution in Rotary Swaging of Steel Tubes". In: *Materials (Basel, Switzerland)* 12.6 (2019). ISSN: 1996-1944. DOI: 10.3390/ma12060855.
- [22] Miura, S., Saeki, Y., Matushita, T. "Metals and Materials". In: (1973), pp. 441–447.
- [23] J. H. Liou and D. Y. Jang. "Forging parameter optimization considering stress distributions in products through FEM analysis and robust design methodology". In: *International Journal of Machine Tools and Manufacture* 37.6 (1997), pp. 775–782. ISSN: 08906955. DOI: 10.1016/S0890-6955(96)00043-0.
- [24] Philipp Frint et al. "Microstructural Evolution during Severe Plastic Deformation by Gradation Extrusion". In: *Metals* 8.2 (2018), p. 96. DOI: 10.3390/met8020096.
- [25] M. Baumann, Graf, A., Selbmann, R., and Brömmelhoff, K., Kräusel, V., Landgrebe, D. and Bergmann, M. "Influence of a modified drawing process on the resulting residual stress state of cold drawn wire. MATEC web of Conferences 190". In: (2018).
- [26] Qi Zhang et al. "Rotary Swaging Forming Process of Tube Workpieces". In: *Procedia Engineering* 81 (2014), pp. 2336–2341. ISSN: 18777058. DOI: 10.1016/j.proeng.2014.10.330.
- [27] Seong-Joo Lim, Ho-Joon Choi, and Chi-Hwan Lee. "Forming characteristics of tubular product through the rotary swaging process". In: *Journal of Materials Processing Technology* 209.1 (2009), pp. 283–288. ISSN: 09240136. DOI: 10.1016/j.jmatprotec.2007.08.086.
- [28] A. Ghaei, A. Karimi Taheri, and M. R. Movahhedy. "A new upper bound solution for analysis of the radial forging process". In: *International Journal of Mechanical Sciences* 48.11 (2006), pp. 1264–1272. ISSN: 00207403. DOI: 10.1016/j.ijmecsci.2006.06.002.
- [29] A. Franceschi et al. "Effects of a counter-punch system for cold full-forward extrusion. NUMIFORM 2019: The 13th International Conference on Numerical Methods in Industrial Forming Processes". In: (2019).
- [30] Alessandro Franceschi et al. "Calibration of the residual stresses with an active die during the ejection phase of cold extrusion". In: *International Journal of Material Forming* 14.2 (2021), pp. 223–233. ISSN: 1960-6206. DOI: 10.1007/s12289-020-01572-x.
- [31] Christina Guilleaume et al. "Eigenspannungsorientiertes Fügen von hybriden Bauteilen mittels Radial-Walzen". In: *Forschung im Ingenieurwesen* 85.3 (2021), pp. 745–755. ISSN: 0015-7899. DOI: 10.1007/s10010-021-00486-7.
- [32] A. Erman Tekkaya. "Eigenspannungen in Kaltumgeformten Massivteilen". In: *Ermittlung von Eigenspannungen in der Kaltmassivumformung*. Ed. by Kurt Lange and A. Erman Tekkaya. Vol. 83. Berichte aus dem Institut für Umformtechnik der Universität Stuttgart. Berlin, Heidelberg: Springer Berlin Heidelberg, 1986, pp. 67–103. ISBN: 978-3-540-16498-2. DOI: 10.1007/978-3-642-82799-0{\textunderscore}5.

- [33] B.-A. Behrens, A. Chugreev, and C. Kock. "Experimental-numerical approach to efficient TTT-generation for simulation of phase transformations in thermomechanical forming processes". In: *IOP Conference Series: Materials Science and Engineering* 461 (2018), p. 012040. DOI: 10.1088/1757-899X/461/1/012040.
- [34] H. YANG and H. BHADESHIA. "Austenite grain size and the martensite-start temperature". In: *Scripta Materialia* 60.7 (2009), pp. 493–495. ISSN: 13596462. DOI: 10.1016/j.scriptamat.2008.11.043.
- [35] Payares-Asprino, M.C., Katsumoto, H., Liu, S. "Effect of Martensite Start and Finish Temperature on Residual Stress Development in Structural Steel Welds." In: *WELDING JOURNAL*, Nr. 12 (), pp. 279–289.
- [36] Carola Celada-Casero, Jilt Sietsma, and Maria Jesus Santofimia. "The role of the austenite grain size in the martensitic transformation in low carbon steels". In: *Materials & Design* 167 (2019), p. 107625. ISSN: 02641275. DOI: 10.1016/j.matdes.2019.107625.
- [37] E. O. Hall. "The Deformation and Ageing of Mild Steel: III Discussion of Results". In: *Proceedings of the Physical Society. Section B* 64.9 (1951), pp. 747–753. ISSN: 0370-1301. DOI: 10.1088/0370-1301/64/9/303.
- [38] N. J. Petch. "The Cleavage Strength of Polycrystals". In: *The Journal of the Iron and Steel Institute* 17 (1953), pp. 25–28.
- [39] A. Jobst et al. "Component residual stress control in forward rod extrusion by material flow and tribology—experiments and modeling". In: *Forschung im Ingenieurwesen* 85.3 (2021), pp. 733–744. ISSN: 0015-7899. DOI: 10.1007/s10010-021-00509-3.
- [40] M. Stembalski, P. Preś, and W. Skoczyński. "Determination of the friction coefficient as a function of sliding speed and normal pressure for steel C45 and steel 40HM". In: *Archives of Civil and Mechanical Engineering* 13.4 (2013), pp. 444–448. ISSN: 16449665. DOI: 10.1016/j.acme.2013.04.010.
- [41] Bernd-Arno Behrens et al. "Experimental investigations on the interactions between the process parameters of hot forming and the resulting residual stresses in the component". In: *Procedia Manufacturing* 50 (2020), pp. 706–712. ISSN: 23519789. DOI: 10.1016/j.promfg.2020.08.127.
- [42] Huchtelmann B. Brandis H. "Technologie der Wärmebehandlung warm- und hochwarmfester Stähle". In: *Thyssen Delstahl Tech Berichte* 11986 (), pp. 27–40.
- [43] Georg Jacobs, ed. *Maschinengestaltung*. Ausgabe 10/2016. Aachen: Mainz, 2016. ISBN: 3861307480.
- [44] I. Nikitin and M. Besel. "Correlation between residual stress and plastic strain amplitude during low cycle fatigue of mechanically surface treated austenitic stainless steel AISI 304 and ferritic–pearlitic steel SAE 1045". In: *Materials Science and Engineering: A* 491.1-2 (2008), pp. 297–303. ISSN: 09215093. DOI: 10.1016/j.msea.2008.03.034.
- [45] Anian Nürnberg et al. "Advantages in the production of power transmitting gears by fineblanking". In: *The International Journal of Advanced Manufacturing Technology* 128.9-10 (Aug. 2023), pp. 4413–4425. DOI: 10.1007/s00170-023-12160-z. URL: <https://doi.org/10.1007/s00170-023-12160-z>.
- [46] Andreas Jobst and Marion Merklein. "Stability of forming induced residual stresses in stainless steel components under mechanical load". In: *Manufacturing Letters* 35 (Aug. 2023), pp. 49–54. DOI: 10.1016/j.mfglet.2023.07.022. URL: <https://doi.org/10.1016/j.mfglet.2023.07.022>.
- [47] Alessandro Franceschi. "Anforderungsspezifische Einstellung des Eigenspannungszustands in der Kaltmassivumformung". In: (2023). DOI: 10.26083/TUPRINTS-00023286. URL: <https://tuprints.ulb.tu-darmstadt.de/id/eprint/23286>.
- [48] Alexander Brosius and Christina Guilleaume. "New cross-rolling process for joining of hybrid components". In: *CIRP Annals* 69.1 (2020), pp. 245–248. ISSN: 00078506. DOI: 10.1016/j.cirp.2020.04.034.

- [49] H. Surm et al. "Manufacturing Residual Stress States in Heat Treatment Simulation of Bearing Rings". In: *Materialwissenschaft und Werkstofftechnik* 37.1 (2006), pp. 52–57. ISSN: 09335137. DOI: 10.1002/mawe.200500973.
- [50] D. Mackenzie. "Metallurgical Aspects of Distortion and Residual Stresses in Heat Treated Parts". PhD thesis. 2016.
- [51] A. Rose. "Eigenspannungen als Ergebnis von Wärmebehandlung und Umwandlungsverhalten". HtM. 1965.
- [52] A. S.M. International. *Corrosion: Fundamentals, testing and prevention*. 4. pr. Vol. Vol. 13A. ASM handbook / prepared under the direction of the ASM International Handbook Committee. Materials Park, Ohio: ASM International, 2008. ISBN: 978-0-87170-705-5.
- [53] Volodymyr Okorokov et al. "Corrosion Fatigue of Low Carbon Steel under Compressive Residual Stress Field". In: *Procedia Engineering* 213 (2018), pp. 674–681. ISSN: 18777058. DOI: 10.1016/j.proeng.2018.02.063.
- [54] Osamu Takakuwa and Hitoshi Soyama. "Effect of Residual Stress on the Corrosion Behavior of Austenitic Stainless Steel". In: *Advances in Chemical Engineering and Science* 05.01 (2015), pp. 62–71. ISSN: 2160-0392. DOI: 10.4236/aces.2015.51007.

## 4 Simulation and Modeling

Kästner, M.; Schneider, T.; Kalina, M.; Böhllke, T.; Erdle, H.; Krause, M.; Steinmann, P.; Lara, J.

In the following, a mechanics-oriented view of the characteristics and properties of residual stresses is established. First, principal aspects of process simulation in order to predict residual stresses after forming are discussed. Furthermore, the formation of residual stresses in metallic materials is presented in a very basic way with special emphasis on classical macroscopic material modeling. Additionally, an introduction to possibilities of multiscale modeling in the context of residual stresses and the incorporation of the crystallographic texture is given. In order to evaluate the influence of residual stresses on the performance of engineering parts, their effects on fatigue life and methods for estimating fatigue life under the influence of residual stress are described. Lastly, as an example, the simulation of residual stresses is illustrated using a 4-point bending beam. Fundamental aspects from experimental and simulative observations of residual stresses can be clarified on this example.

### 4.1 Residual Stresses in the Simulation of Forming Processes

In order to investigate how residual stresses develop during forming processes, the field of computational mechanics provides a valuable resource that complements and deepens the results of experimental study. An experimentally validated numerical implementation of a mathematical model describing the forming process is able to determine – in a nondestructive manner – the residual stress field at the surface and in the bulk of the workpiece during the whole forming process. Furthermore, it enables the cost- and time-efficient realization of an extensive study of the factors that determine the resulting residual stress field.

Nonetheless, a reliable numerical reproduction of a forming process that is also not too computationally expensive is not trivial. On one hand, the material behavior of the workpiece, which will be elaborated upon in chapter 4.5, is quite complex and the interaction between all the machine parts involved in the forming process have to be taken into account. On the other hand, the numerical treatment can be done through different methods, each with advantages and disadvantages, such that careful consideration is required to ensure the solvability and accuracy within an acceptable computation time.

The simulation of the forming process has to be followed by a controlled unloading of all external loads in order to determine the actual residual stresses of the workpiece. The numerical results have to be validated by comparing them with experimental data, as indicated in the integrated design approach outlined in figure 1.2. In case of any discrepancies, an adjustment of the numerical implementation has to be done. This is not trivial given that, although to different degrees, all the aspects of the simulation, which are briefly described in this section, have an effect on the resulting residual stress field as it can be seen among the results presented by the projects within the Priority Program 2013.

The current section is organized based on two of the main components required to simulate a forming process: A continuous and a discrete problem describing the process at hand. The former is posed following a mathematical framework and the latter derives from the continuous problem by means of discretization strategies. A short overview of the mathematical framework and the discretization strategies are respectively the focus of the first and second half of this section.

## 4.2 Mathematical Formulation

The mathematical formulation is composed by the conservation of mass,

$$\dot{\rho} + \rho \operatorname{div} \mathbf{v} = 0 \quad (\text{Equation 4.1})$$

the linear equation *Equation 1.1* and angular momentum balance

$$\rho \mathbf{x} \times \ddot{\mathbf{x}} = \operatorname{div}(\mathbf{x} \times \boldsymbol{\sigma}) + \rho \mathbf{x} \times \mathbf{f}_{\text{vol}} \quad (\text{Equation 4.2})$$

as well as by the first and second law of thermodynamics, which lead to

$$\begin{aligned} \rho \dot{u} &= -\operatorname{div} \mathbf{q} + \rho r + \boldsymbol{\sigma} : \operatorname{grad} \dot{\mathbf{x}} \\ \rho [\dot{\psi} + \dot{\vartheta} \eta] &\leq \boldsymbol{\sigma} : \operatorname{grad} \dot{\mathbf{x}} - \frac{\mathbf{q} \cdot \operatorname{grad} \vartheta}{\vartheta} \end{aligned} \quad (\text{Equation 4.3})$$

Here  $u$  is the specific internal energy,  $\mathbf{q}$  the heat flux,  $r$  the heat sources,  $\psi$  the specific free energy,  $\vartheta$  the temperature and  $\eta$  the specific entropy. Furthermore, the equations of balance have to be complemented by constitutive laws that are admitted in the established thermodynamic framework and a strain measure has to be chosen. In forming processes the contact between components and the forces that occurs because of it plays an important role, which need to be included in the formulation. In the following, these points will be expanded upon to give the reader an idea of what to consider while formulating the continuous problem.

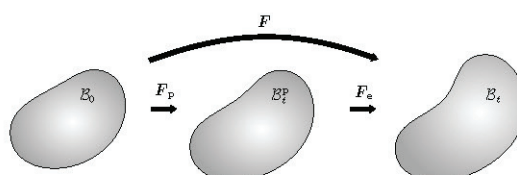


**Figure 4.1** The multiplicative decomposition of the deformation gradient into an elastic and a plastic part

### 4.2.1 Thermodynamic Framework for Finite Strain Plasticity

During forming processes the material undergoes large deformations which lead to an irreversible change of the workpiece's geometry. As a result, finite plasticity has to be taken into account. Although the key ideas behind infinitesimal and finite plasticity are the same – the former will be discussed in chapter 4.5 – there is much debate over the proper mathematical representation of the latter, especially regarding its kinematic description. Most theories are based the concept of an intermediate configuration between the initial and current configuration (see figure 4.1) and the formulation of a multiplicative decomposition of the deformation gradient into an elastic and plastic parts, i.e.,  $\mathbf{F} = \mathbf{F}_e \cdot \mathbf{F}_p$  [1]. Alternatively, there are also theories based on an additive decomposition of the strain measure, i.e.,  $\mathbf{E} = \mathbf{E}_e + \mathbf{E}_p$  [2]<sup>1</sup>. Both the multiplicative and the additive decompositions have their shortcomings [4, 5], but theories derived from these principles, i.e., the CHABOCHE model [6] or the model proposed by Vladimirov, Pietryga, and Reese [7] to name a few, can be extensively found applied in the literature and in this book.

As the workpiece undergoes the forming process, energy is dissipated inside the material. Further dissipation occurs at the contact surfaces as a consequence of the friction between the components. This dissipated energy can lead to temperature changes that can not be considered as negligible and must be incorporated in the framework. Furthermore, material parameters can be susceptible to temperature. As such, they are no longer constants but functions of the temperature, which leads to a stronger coupling between the mechanical and the thermodynamic problems. A few examples of finite thermoplasticity formulations are those of Canadiga and Mosler [8], Aldakheel, Hudobivnik, and Wriggers [9], and Seitz, Wall, and Popp [10].

<sup>1</sup> The difference between the total and the plastic strain, which is introduced as a primitive variable, leads to an *elastic-like* strain [3]. Therefore, this is not additive decomposition into an elastic and plastic part in the strict sense

Once a measure for the irreversibility in a deformation process has been chosen and the relevance of the increase in temperature has been determined, the restrictions on the constitutive laws can be obtained from the second law of thermodynamics.

## 4.2.2 Contact Mechanics

As a pair of material bodies comes in physical contact they interact with each other through a contact force density  $t$ . A pointwise consideration of the contact surfaces makes it possible to decompose these forces with respect to the surface's normal into a normal and a tangential force and it also allows definition of the distance between a pair of points in potential contact as the gap  $g$ . The aforementioned decomposition motivates the notation  $(\cdot)_n$  and  $(\cdot)_t$  used in this section to denote normal and tangential quantities or components, respectively.

Frictional contact – the contact relevant for forming processes – is characterized by a contact force with  $t_n \neq 0$  and  $t_t \neq 0$ . It exhibits two behaviors or stages. The sticking stage occurs when the  $t_t$  is not enough to cause a relative tangential displacement of the contact point pair, i.e.,  $\dot{g}_t = 0$ . Once  $t_t$  reaches a threshold value, the slipping stage occurs and relative motion is allowed, i.e.,  $\dot{g}_t \neq 0$ .

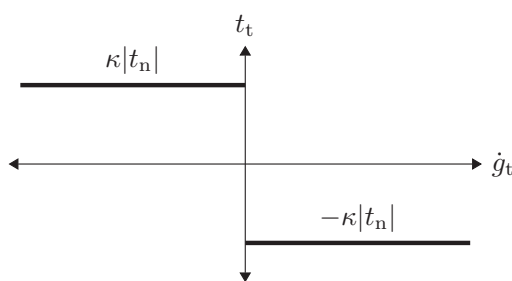


**Figure 4.2** COULOMB's law with  $\kappa$  denoting the friction coefficient

A simple model describing both scenarios is given by COULOMB's friction law, which is graphically presented in figure 4.2.

This form of COULOMB's friction law is not suitable for forming processes as the tangential force becomes too large when the contact pressure is too high. As a solution a threshold value can be defined as the maximum allowed tangential force, e.g., COULOMB-OROWAN model. Alternatively, one can employ a non-linear law where the tangential reaction increases asymptotically toward the threshold value, e.g., the model used by Stupkiewicz [11].

In order to incorporate these concepts into the formulation the model has to be enhanced at the energetic level by contact energy  $\Psi_c$ . For brevity, only two of the most-known methods will be presented but there are several approaches in the literature. Refer to the textbook [12] for an overview.

The LAGRANGE multiplier method

$$\Psi_c = \int_{\Gamma_c} [\lambda_n g_n + \boldsymbol{\lambda}_t \cdot \mathbf{g}_t] da \quad (\text{Equation 4.4})$$

formally ensures that no penetration occurs between the contact bodies and that the materials stick to each other by enforcing the inequality constraints through the LAGRANGE multipliers  $\lambda_n$  and  $\boldsymbol{\lambda}_t$ , which are identified as reaction forces. This formulation leads to a saddle point problem. Numerically this translates into a change in the structure of the system matrix and an increase in the degrees of freedom. As a result, the computation time also increases.

The penalty method

$$\Psi_c = \frac{1}{2} \int_{\Gamma_c} [\epsilon_n g_n^2 + \epsilon_t \mathbf{g}_t \cdot \mathbf{g}_t] da \quad (\text{Equation 4.5})$$

introduces quadratic energies for both the normal and tangential contact. This can be visualized as the replacement of the contact surface by a layer of a linear elastic material. The thinness, i.e., the stiffness of the layer is then controlled by the penalty factors  $\epsilon_n$  and  $\epsilon_t$ . Hence, some penetration is intrinsically allowed in the method. As the penalty factors tend to infinity, the solution converges to the values obtained from the LAGRANGE multiplier method.

Nonetheless, if their values are too large, the numerical problem can become ill-conditioned.

*Equation 4.4* and *Equation 4.5* are valid only during sticking. Once the threshold to slipping has been surpassed,  $\lambda_t$  and  $\epsilon_t g_t$  have to be replaced by the constitutive law for  $t_t$ .

## 4.3 Discretization

Forming processes are mathematically described by a boundary value problem. Due to the complex nature of the poised problem, its solution can only be obtained numerically. To this end, the continuous problem has to be transferred to a discrete setting, both temporally and spatially. Mathematically this translates into going from the local balance equations to the discrete weak form of the balance equations. In the case of the local linear momentum balance (*Equation 1.1*) one obtains the weak form

$$\int_{\mathcal{B}} \rho \boldsymbol{\nu} \cdot \ddot{\boldsymbol{x}} \, dv = \int_{\mathcal{B}} [\boldsymbol{\nu} \cdot \mathbf{f}_{\text{vol}} - \text{grad } \boldsymbol{\nu} \cdot \boldsymbol{\sigma}] \, dv \quad (\text{Equation 4.6})$$

$$+ \int_{\partial\mathcal{B}} \boldsymbol{\nu} \cdot \mathbf{t} \, da$$

where  $\boldsymbol{\nu}$  is the test function and  $\mathbf{t}$  the traction vector. *Equation 4.6* has to then be temporally and spatially discretized. Furthermore, the contact between bodies has to be also defined in the discrete setting. The numerical problem has to resolve the temporal and spatial scales of the continuous problem and the contact discretization has to properly reproduce the force distribution at the contact surfaces. Otherwise the numerical solution will not correspond to the continuous one. While a globally fine discretization complies with the aforementioned requirements, this is not feasible in a computationally reasonable time. In the following subsections some strategies toward an efficient temporal and spatial discretization will be presented and some examples of contact discretization will be shown.

### 4.3.1 Temporal

The discrete time consists of a series of snapshots  $t_i$ , where the time step is defined as the jump between discrete values, i.e.,  $\Delta t_i = t_i - t_{i-1}$ . In this discrete setting the time derivatives can be defined by explicit methods, e.g., a central difference time integration scheme; implicit methods, e.g., the generalized  $\alpha$ -method; or a combination of both, e.g., the family of implicit-explicit methods compared by Ascher, Ruuth, and Wetton [13] or the implicit-explicit RUNGE-KUTTA methods proposed by Ascher, Ruuth, and Spiteri [14] to name a few. Even if inertia can be ignored, a pseudo time variable has to still be introduced in order to apply the load in a controlled manner, as the material response during forming processes is non-linear. Nonetheless, there may be time intervals at which the material behavior is approximately linear, in which a certain time step size can be used with no loss in accuracy. On the other hand, the same time step size will not be appropriate at intervals where the response rapidly changes, e.g., at the plastic flow onset. Clearly a strategy to resolve both scales without having to waste computational time is advantageous. This can be achieved by quantifying the rate of change of the material response, e.g., the scheme proposed by Lee and Hsieh [15] for transient problems; or by introducing an error measurement, e.g., the adaptive scheme formulated by Bartels and Keck [16] for elastoplasticity. Based on the chosen measurement the time step size can be adjusted during the simulation.

### 4.3.2 Spatial

In the finite element method the continuous domain is approximated by a mesh, in which each element is enriched by a function space of local shape functions and a set of local nodal variables. This framework allows the approximate description of the continuous fields, e.g., the displacement field as

$$\boldsymbol{u} \approx \boldsymbol{u}_h = \sum_{i=1}^{n_{\text{dof}}} U_i \boldsymbol{\varphi}_i \quad (\text{Equation 4.7})$$

where  $n_{\text{dof}}$  is the total number of degrees of freedom,  $U_i$  are nodal values and  $\boldsymbol{\varphi}_i$  the corresponding

shape functions. The size of the linear system to solve is proportional to the number of elements in the mesh. Hence, an inhomogeneous element density, which sufficiently resolves the different local spatial scales in the domain, is needed in order to reduce computational cost. This translates into a high element density in regions where the gradient of one or more field variables is high and a low element density where the gradients are low. In cases where the evolution of the gradient field can be estimated *a priori*, e.g., during a forming process, the tailoring of a mesh to fit the aforementioned requirements can greatly reduce the computational cost. Another alternative is to include an adaptive mesh refinement strategy in the numerical implementation. The idea is an element-wise estimation of the error (see for example the overview of Ainsworth and Oden [17]), which determines if a refinement and coarsening respectively must or can be performed. After the new mesh is created the discrete fields are transferred to it.

The tailored approach has the advantage of a constant discrete domain throughout the simulation. However, this can become disadvantageous if a high gradient occurs at different regions at different load steps. The adaptive approach is not constrained by this as the refinement and coarsening occur both where and when needed, thus, providing a very versatile option, especially when the gradient fields are not known *a priori*. Nonetheless, an appropriate error estimation method has to be chosen for it to work properly. The transfer operation also introduces an inherent error due to the interpolation or projection schemes used. Furthermore, the element-wise computation of the error and the transfer of the field across meshes adds to the computational cost of the numerical implementation.

Both approaches have to control for element distortion. In forming processes the material undergoes large deformations, which have to be described by the discrete element. It can occur that such large deformations lead to the collapse of element, which can produce an ill-conditioned numerical problem.

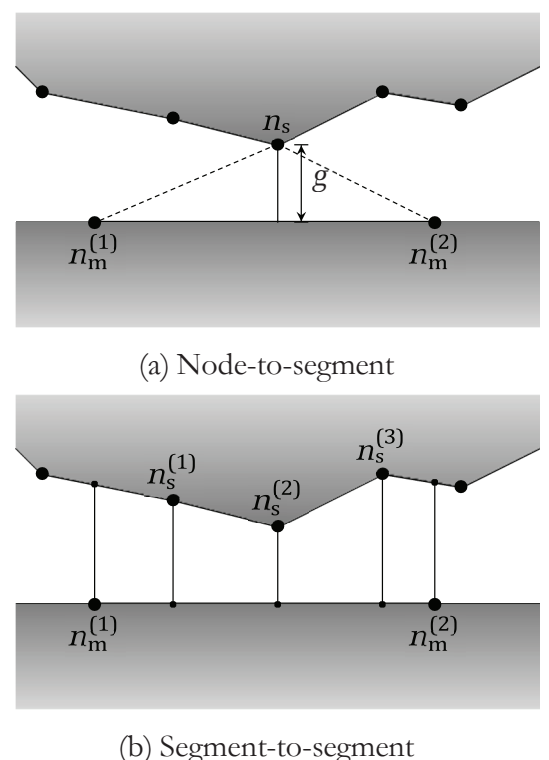


**Figure 4.3** The contact inequality is enforced between a segment of the master surface delimited by the nodes  $n_m^{(1)}$  and  $n_m^{(2)}$  and (a) a single slave node  $n_s$  (node-to-segment discretization) or (b) all the slave nodes inside the projection of the master segment into the slave surface (segment-to-segment discretization) [18].

### 4.3.3 Contact

The description of contact in the discrete setting for the case of large deformations is commonly done through node-to-segmented discretization, in which the contact inequalities are enforced only between a node on the slave surface and a segment of the master surface, as depicted in figure 4.3 (a). This asymmetric approach requires some care during the selection of master and slave surfaces. If they are not chosen properly it can lead to nonphysical results. The method can be made more robust against this problem by a two-way treatment, in which the inequality constraints are enforced twice by exchanging the master and slave roles between the surfaces. Nonetheless, the accuracy improvement comes at a higher computational cost.

One alternative is provided by the segment-to-segment discretization. It projects the facet segments of the slave surface onto the master facet, see figure 4.3 (b), and enforces the inequalities at the limits of the resulting subintervals. This approach avoids penetration to a greater extent and produces a better load distribution at the contact surface than does node-to-segment discretization but its implementation is more complex and has a higher computational cost.

In general it is not known *a priori* which parts of the domain's boundary are in contact with another body in a given load step. Therefore, an algorithm needs to be implemented in order to determine which discrete contact pairs interact with each other at a given time. The general scheme is composed of an spatial search, where surfaces that may interact with each other are located and marked, and a contact detection phase, where the elements at the marked surfaces are controlled for penetration.

The discrete approximation of the domain is generally done by a first order mapping of the reference finite element; thus, the normal vector at the discrete boundary is given by a discontinuous field. As a slave node slides from one master surface to another, the jump of the normal vector may lead to computational instability. To obtain a continuous normal vector field one can smooth the contact surface using a Hermite, BÉZIER, spline or NURBS interpolation. For an overview refer to Neto, Oliveira, and Menezes [19].

## 4.4 Typical Problems Arising During Process Modeling

The most common problems during simulation of such complexity are the divergence of the solution of the linear system or of the nonlinear scheme and obtaining nonphysical or incorrect results. Determining their cause is not trivial as it can be caused by one or more of the factors addressed above. The temporal discretization may be too coarse and too much information could be lost between time steps or, in the case of non-globally convergent non-

linear schemes, the initial solution based on previous ones may also prove to be outside of the convergence locus, leading to convergence to a false solution or to divergence. A too coarse spatial discretization may lead to nonphysical or incorrect results, as the different local length scales may not be sufficiently resolved. If noticeable penetration or nonphysical behavior of the fields at the contact surfaces occurs, the chosen contact discretization will be most likely at fault. Numerical parameters, e.g., the penalty coefficients may prove to be to high, leading to an ill-conditioned linear system. Certain combinations of values of material parameters – alone or in combination with one of the above – may also lead to an ill-conditioned numerical problem.

## 4.5 Macroscopic Modeling of Residual Stresses

Concepts of modeling metallic materials are widely known. A huge literature base dealing with elasto-plastic material models exists for a wide range of applications.

Key aspects of classical continuum modeling are summarized in figure 4.4. Assuming a completely pristine and undeformed material at time  $t = 0$ , the loading path of a fictive one dimensional bar starts with a purely elastic section. The purely elastic loading ends with the actual stress reaching the initial yield stress  $\sigma_{y0}$ . Afterwards, the process continues under combined elastic-plastic deformation and successive hardening of the metallic material, see figure 4.4. In order to describe this deformation process and to account for the irreversibility of plastic deformation, usually the constitutive assumption of additive decomposition of the total infinitesimal strain tensor

$$\boldsymbol{\varepsilon} = \boldsymbol{\varepsilon}^e + \boldsymbol{\varepsilon}^p \quad (\text{Equation 4.8})$$

into elastic  $\boldsymbol{\varepsilon}^e$  and plastic  $\boldsymbol{\varepsilon}^p$  parts is made. The elastic response of the metallic material can be described using HOOKE's law

$$\boldsymbol{\sigma} = 2\mu \boldsymbol{\varepsilon}^e + \lambda \operatorname{tr}(\boldsymbol{\varepsilon}^e) \boldsymbol{I} \quad (\text{Equation 4.9})$$

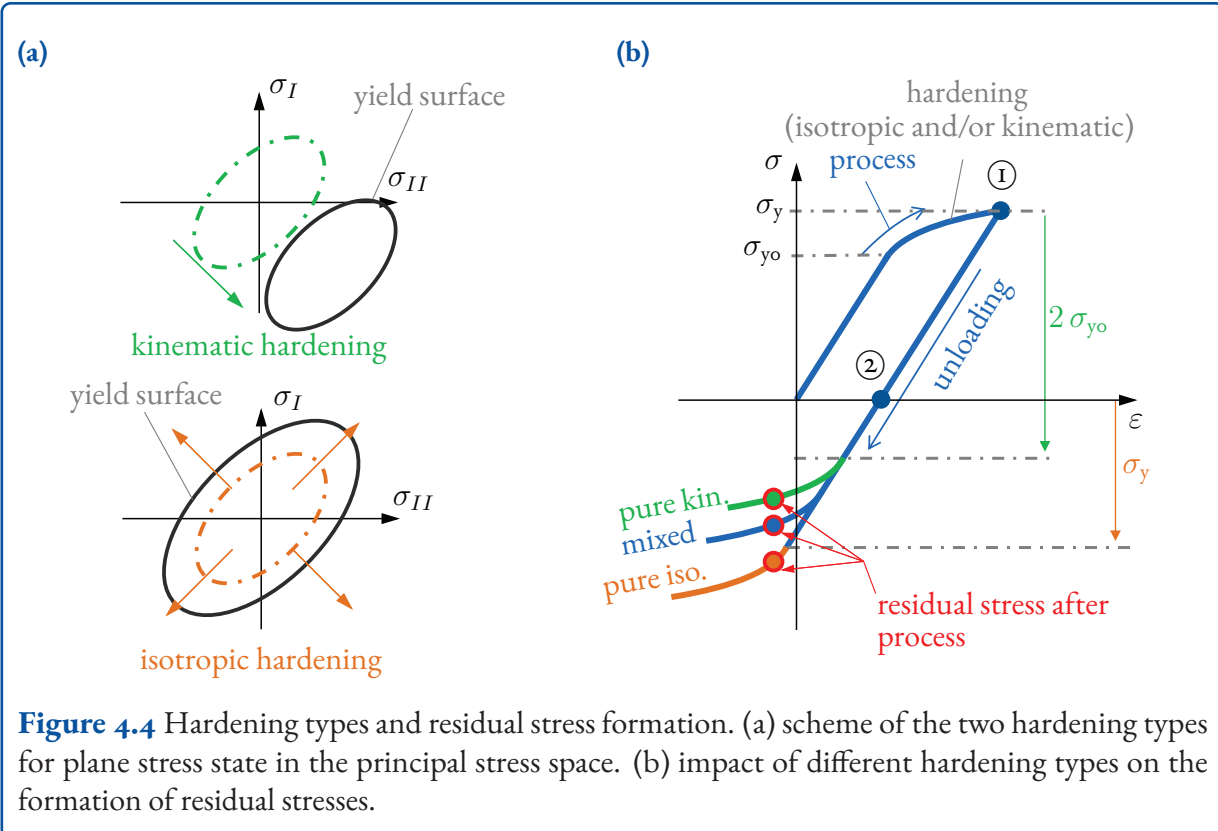


**Figure 4.4** Hardening types and residual stress formation. (a) scheme of the two hardening types for plane stress state in the principal stress space. (b) impact of different hardening types on the formation of residual stresses.

written in the three dimensional form.  $\boldsymbol{\sigma}$  is the Cauchy stress tensor,  $\mu = E / (2 + 2\nu)$  and  $\lambda = E \nu / ((1 + \nu)(1 - 2\nu))$  are the two Lamé parameters, respectively, and  $\mathbf{I}$  is the second order identity tensor. The distinction between elastic and elastic-plastic loading is made using the yield criterion, which can be written as

$$f(\boldsymbol{\sigma}, \mathbf{q}) \leq 0 \quad (\text{Equation 4.10})$$

in an arbitrary, three dimensional formulation using the yield function  $f$ . Internal variables of arbitrary tensorial order describing the hardening process and dissipative behavior of the material are denoted by  $\mathbf{q}$ . The yield function can be interpreted as yield surface in space of principal stresses, see figure 4.4 (a).

The phenomenological hardening of an engineering material can be modeled by changing the position, shape and size of the yield surface during plastification. Typically, two types of hardening named *isotropic* and *kinematic* hardening are distinguished. Mathematically, isotropic hardening influences the actual yield stress  $\sigma_y$  depending on

the accumulated plastic equivalent strain  $p$ , which can be defined by its rate  $\dot{p} = \sqrt{\frac{2}{3}\dot{\epsilon}^p : \dot{\epsilon}^p}$ . The change in yield stress is associated with isotropic hardening, denoted by  $R(p)$ . Kinematic hardening is formulated as a stress offset in the calculation of an equivalent stress which is used in the definition of  $f$ . One common way is to introduce the backstress tensor  $\mathbf{X}$  in order to describe kinematic hardening. An example for a typical definition of a yield function using a VON MISES type equivalent tensile stress with the stress deviator being  $\mathbf{s} = \boldsymbol{\sigma} - \frac{1}{3}\text{tr}(\boldsymbol{\sigma}) \mathbf{I}$  can be written as

$$f(\mathbf{s}, R, \mathbf{X}) = \sqrt{\underbrace{\frac{3}{2}(\mathbf{s} - \mathbf{X}) : (\mathbf{s} - \mathbf{X})}_{\text{kinematic}}} \dots - \left( \overbrace{\sigma_{yo}}^{\sigma_y} + \underbrace{R}_{\text{isotropic}} \right) . \quad (\text{Equation 4.11})$$

The initial yield stress of the material is introduced as  $\sigma_{yo}$  and the arbitrary hardening tensor quantities from Equation 4.10 are now defined by

$$\mathbf{q} := \{R, \mathbf{X}\} . \quad (\text{Equation 4.12})$$

Both hardening types influence the actual size and the position of the yield surface, defined by *Equation 4.11*, respectively. As depicted in figure 4.4, isotropic hardening leads to an increase or decrease in size of the yield surface  $f$  while the center of  $f$  remains fixed in the space of principal stresses. Kinematic hardening in turn marks the translation of  $f$  by means of displacement of its midpoint. The model is to be completed by hardening laws, which prescribe the evolution of the internal variables  $q$  depending on the actual loading state. It is primarily the choice of particular hardening laws that makes the difference between the many plasticity models available in literature.

The effect of different hardening types on the one-dimensional loading behavior of a fictive uniaxial rod is also shown in figure 4.4. If it is ensured that the different hardening types describe the same flow curve, no difference is visible in monotonic loading paths with maximum point ①. Only if the monotonic load is followed by reverse loading, do the changes in model behavior become visible. Due to the increase in yield surface's size and a fixed midpoint of  $f$  in case of pure isotropic hardening, the yield criterion is fulfilled again at  $-\sigma_y$  during reverse loading. In case of pure kinematic hardening, the re-plastification in reverse direction starts at  $-\sigma_{y0}$ , since the yield surface is only shifted and has not changed its size. The combination of both hardening types yields an intermediate result in which the plastification in the reverse loading direction starts in between both cases described, which is also known as the Bauschinger effect. The level of local unloading determines the actual the final residual stress. Figure 4.4 (b) clearly underlines that the choice of hardening types significantly influences this emerging residual stress.

### 4.5.1 Cyclic Loading

Besides the formation of residual stresses, their cyclic evolution in the final structure is often of interest. Especially their impact on the fatigue life of the later structure makes the understanding of changes in residual stresses necessary for a successful usage in industrial design processes, see

chapter 4.7. For this purpose, material models are needed which are capable of modeling the changes in material behavior during cyclic load. Usually, fatigue behavior is characterized using standard test methods. In constant amplitude tests the basic behavior of the material can be evaluated without influences of the loading sequence [20]. The typical material response to such simple tests is discussed below to provide a comprehensive overview of cyclic phenomena in metallic materials.

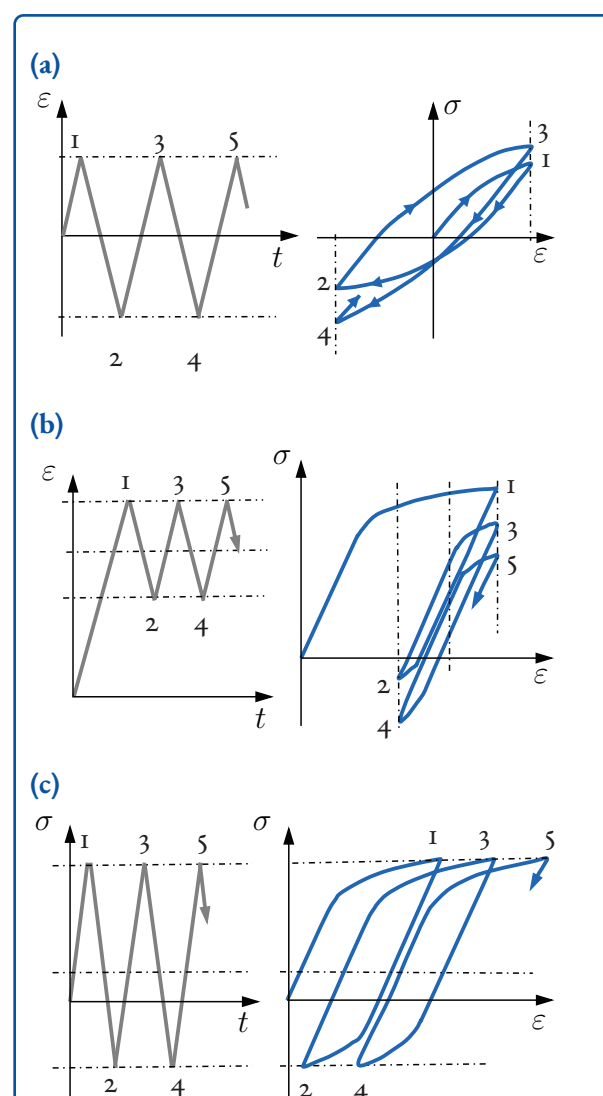


**Figure 4.5** Typical cyclic behavior of metals. (a) cyclic hardening under prescribed strain path with  $\varepsilon_a = \text{const.}$  (b) mean stress relaxation under prescribed strain path with  $\varepsilon_a = \text{const.}$  (c) cyclic ratcheting under prescribed stress path with  $\sigma_a = \text{const.}$

First, loading with constant uniaxial strain amplitude is considered. The typical stress response for this strain path is depicted in figure 4.5 (a). Starting with the first load cycle, the material undergoes plastic deformation. During further cycling, the material experiences reversed loading and plasticification. Thereby, the stress-strain hysteresis size changes with accumulating load cycles. In the example in figure 4.5 (a), the hysteresis grows due to *cyclic hardening* of the material. The opposite behavior of shrinking hysteresis during fatigue life of the specimen is also possible and is termed *cyclic softening*. Whether cyclic hardening or softening occurs depends on the used material. This change in hysteresis size has been modeled by isotropic hardening [6].

Another important phenomenon caused by cyclic plasticity is *mean stress relaxation* in the strain controlled test, see figure 4.5 (b). Due to redistribution of dislocations in the metallic microstructure during repetitive cycling, the hysteresis in the stress-strain plot slowly shifts toward a lower mean stress state. Even a totally mean stress free state is possible. Hence, a change of residual stresses is likely to occur.

Lastly, *cyclic ratcheting* has to be named as an important cyclic plasticity effect. It is depicted in figure 4.5 (c). Main characteristic in the stress controlled test with non-zero mean stress is the accumulation of plastic strain with accumulating load cycles. Depending on the material and load level this process may lead to a shakedown state where ratcheting stabilizes and the increase in plastic strain is stopped. Otherwise, if no steady shakedown state can be reached it is possible that ratcheting directly leads to failure of the structure. Due to the subsequent plastification of the material, initial residual stresses are likely to change. This makes the understanding of the material's response to this type of loading necessary.

## 4.5.2 Models for Cyclic Plasticity

A basic requirement for successful modeling of occurring stresses and strains in cyclically loaded structures and hence the phenomena outlined above is a

material model suitable for cyclic plasticity. For this purpose, many models are available in the literature. The basic one is Chaboche's plasticity model [21, 22] with its non-linear kinematic hardening rule

$$\begin{aligned} \dot{\mathbf{X}} &= \sum_{i=1}^M \dot{\mathbf{X}}^{(i)} \dots \\ \dots &= \sum_{i=1}^M \underbrace{\frac{2}{3} C^{(i)} \dot{p} \overbrace{\frac{\partial f}{\partial \sigma}}^{\dot{\epsilon}^p}}_{\text{linear hardening term}} - \underbrace{\gamma^{(i)} \dot{p} \mathbf{X}^{(i)}}_{\text{recall term}} \end{aligned} \quad (\text{Equation 4.13})$$

for the sum of  $M$  backstress tensors using the idea of Armstrong & Frederick [23].  $C^{(i)}$ ,  $\gamma^{(i)}$  are material parameters for each backstress. This non-linear kinematic hardening is usually combined with a proper isotropic hardening part, e.g., with the isotropic hardening part used in Chaboche et al. [21]

$$\dot{R} = b(Q - R) \dot{p} \quad (\text{Equation 4.14})$$

wherein  $b$ ,  $Q$  are material constants. The model is able to capture effects of cyclic plasticity at least qualitatively. Unfortunately, it overpredicts ratcheting since the evolution law predicts full recovery of backstress with increasing plastic loading [24, 25] which is caused by the recall term in *Equation 4.13*.

Improved and more complicated model formulations for cyclic plasticity are widely available in the literature. Their aim is to account for more complex material behavior such as non-proportional hardening, transient material behavior and complicated ratcheting phenomena. To name some of them, the models presented by Ohno and Wang [24], Abdel-Karim and Ohno [25], Döring et al. [26] and even a model for large strain application by Yoshida and Uemori [27] are available. For brevity, the reader is referred to the literature [20, 25] for further information on useful models for cyclic plasticity.

## 4.6 Multiscale Modeling of Residual Stresses

### 4.6.1 Micromechanical Modeling of Residual Stresses

Phenomenological macroscopic material models predict residual stresses as a function of the deformation history, taking into account internal variables. In these models, the microstructure of the material, e.g., the presence of multiple phases with individual phase-specific material behavior or the orientation of individual grains is not taken into account. The macroscopic stresses only represent the ensemble average of heterogeneous stresses on the microscale

$$\bar{\sigma} = \langle \sigma \rangle = \int_V \sigma \, dV. \quad (\text{Equation 4.15})$$

In order to predict residual stresses on various scales of the material and to allow a direct validation with experimental results, micromechanical models can be used for the prediction of residual stresses. Micromechanical homogenization techniques estimate the effective material behavior based on the material microstructure and the material properties of the individual material components.

Homogenization methods can be classified as follows: a) asymptotic homogenization [28], b) mean-field approaches [29], c) transformation field analysis [30, 31]. Moreover, homogenization can be performed using full-field simulations (d) with the aid of the finite element (FE) method [32], or voxel-based with Fourier methods [33]. For an overview of the different methods, the reader is referred to the review article of Kanouté et al. [34].

Full-field methods achieve a high resolution of the microscopic fields, but global FE calculations, which calculate the stress-strain relationship at the integration point by resorting to local FE solutions (FE<sup>2</sup> method [35, 36]), are currently still too time-consuming for component-level modeling with nonlinear material behavior.

Approaches exist to reduce the computational cost of full-field simulations. One approach is the use of

statistically similar representative volume elements [37–39]. These are constructed on the basis of image data of the real microstructure, under the restriction that important effective properties coincide with the statistically similar structure. Another possibility is an order-reduced FEM-based method [40, 41]. Here, the potential structure of generalized standard materials is exploited using an incremental variational approach. Field quantities are determined by a superposition of modes calculated in advance, thus increasing efficiency. An alternative approach to FEM-based methods is the use of Fast Fourier Transformation (FFT) for the solution of the boundary value problem of the microstructure. For an overview of FFT methods the reader is referred to the review article of Schneider [42]. A possible coupling of microstructure and macroscopic material behavior is offered by two-scale FE-FFT simulation [43, 44] or by sequential homogenization (SH) methods [45] for materials with more than two scales.

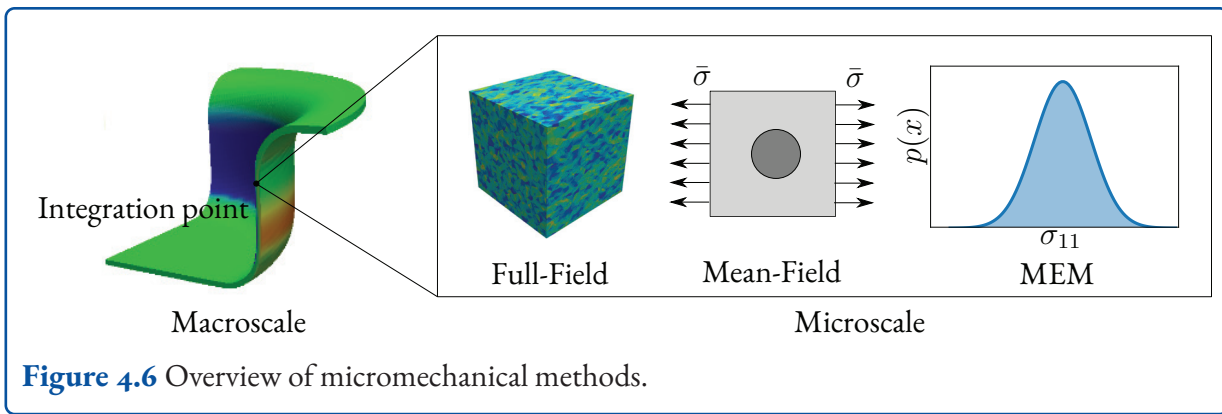
In contrast to full-field methods, the numerical efficiency of mean-field approaches allows for a simulation on the component level.

For a multi-phase material bounds for the effective elastic stiffness can be constructed based on the assumption of a homogeneous deformation (Voigt [46]) or a homogeneous stress distribution (Reuss [47]).

These bounds, however, only take the volume fraction and the elastic properties of the individual phases into account.

Based on the homogenization of ellipsoidal inclusions embedded in an elastic matrix material (Eshelby [48]) more sophisticated solutions can be obtained by including more information about the microstructure into the elastic homogenization approach, see the self-consistent method (Kröner [49]), Mori-Tanaka method [50] or Liebhafsky method [51]. Using a variational principle, tighter bounds on the elastic stiffness are recovered (Hashin and Shtrikman [52]).

For small deformations, an elastic constitutive law can be formulated with a location-dependent stress-



free strain. This strain may include thermal, plastic, and transformation strains, the latter depending on the local thermomechanical process.

In Böhlke et al. [53], an extension of the Hashin-Shtrikman homogenization method for nonlinear problems with internal variables was proposed. It can be used to estimate the evolution of dislocation densities during the austenite-martensite phase transformation in a dual-phase steel. In this context, the plastic strain fields are treated analogously to thermal strains.

In Rieger and Böhlke [54], the residual stresses induced by phase transformations in a dual-phase steel were simulated based on the Hashin-Shtrikman method. The effective strain hardening behavior of the dual-phase steel could be accurately modeled when the microstructure (grain size and martensite volume fraction) was taken into account. The method was applied in Neumann and Böhlke [55] to complex phase transformation processes, such as those occurring during press hardening.

For the application of mean-field approaches to the modeling of residual stresses the following results are of particular importance.

For heterogeneous elastic stiffnesses and constant heterogeneous eigenstrains, the local stresses  $\sigma(\mathbf{x})$  and strains  $\varepsilon(\mathbf{x})$  can be given as a linear function of the associated effective values  $\bar{\sigma}$  and  $\bar{\varepsilon}$ . The localization relations  $\varepsilon(\mathbf{x}) = \mathbb{A}(\mathbf{x})[\bar{\varepsilon}] + \mathbf{a}(\mathbf{x})$  and  $\sigma(\mathbf{x}) = \mathbb{B}(\mathbf{x})[\bar{\sigma}] + \mathbf{b}(\mathbf{x})$  apply, see [56, 57]. The localization tensors  $\mathbb{A}(\mathbf{x})$  and  $\mathbb{B}(\mathbf{x})$  depend on

the microstructure and elastic properties of the grains. The fluctuation fields  $\mathbf{a}(\mathbf{x})$  and  $\mathbf{b}(\mathbf{x})$ , each having vanishing mean values, give the strains and stresses induced by the inhomogeneous plastic strain field.

As shown in Hofinger et al. [58], for a two-phase material, explicit expressions of the localization tensors and fluctuation fields can be constructed based on the Mandel-Hill lemma  $\langle \sigma \rangle \cdot \langle \varepsilon \rangle = \langle \sigma \cdot \varepsilon \rangle$ . The mean-field approach is applied in Simon et al. [59] for the prediction of residual stresses using a Ramberg-Osgood relation of the localized strain. In Hofinger et al. [58] the framework is extended to account for large deformations in an objective incremental setting.

In addition to the mean-field model for the prediction of the effective and phase-specific residual stresses, the maximum entropy method (MEM) of Kreher and Pompe [57] can be applied to determine the stresses within individual grains. The MEM is based on the principle of maximization of information-theoretic entropy introduced by Jaynes [60]. The results of the MEM generally represent an approximation for statistical quantities whose exact values are only accessible with numerically complex full-field simulations.

General formulations of the maximum entropy method were developed in Krause and Böhlke [61]. The validity of the maximum entropy estimate was investigated for diverse materials, with good agreement of the method with FFT simulations, especially for polycrystals. In Krause and Böhlke [62], the MEM was used to test whether the multiscale

modeling of duplex steel used in the simulation is valid with respect to the representation of residual stresses on individual grain level.

#### 4.6.2 Modeling of Residual Stresses Based on Crystallographic Texture

The mechanical behavior of polycrystalline materials may be affected by the crystallographic texture in terms of both, the elastic anisotropy and the plastic anisotropy.

In Bertram and Böhlke [63] a model for texture induced elastic anisotropy is constructed and applied to polycrystalline copper.

It is shown in Böhlke [64] that the use of the leading crystallographic texture coefficients alone (fourth-order coefficients in the case of cubic single crystals) allow the prediction of a deformation-induced plastic anisotropy. For example, the Swift effect, i.e., the elongation or contraction of torsion specimens in the presence of large inelastic deformations can be described in good agreement with experiments. In addition to the phenomenological approach introduced in Böhlke et al. [64], an evolution equation of the texture coefficients based on the conservation equation of the orientation distribution function can be used, see Böhlke [65].

If the crystallographic texture is to be taken into account in two-scale models, low-dimensional texture approximations must be determined to reduce the computational cost of texture induced anisotropy models. These approximation can be determined by optimization techniques [66] or by partitioning strategies of the orientation space [67].

Using such reduction techniques, forming processes can be simulated based on experimentally determined texture distributions [68], thereby using the properties of the individual phases in combination with microstructure information.

An application to the modeling of residual stresses in textured multi-phase materials is given in Simon et al. [69].

The phase-specific elastic anisotropy is determined from the experimentally analysed orientation distribution function and single-crystal elastic constants. For plastic anisotropy, the calibration parameters of the crystallographic texture coefficients are obtained by an optimization problem based on the experimentally characterized macroscopic plastic anisotropy.

#### 4.7 Fundamentals of Fatigue Life Estimation

Fatigue life estimation is a crucial part of the design process of formed components. Residual stresses have a paramount influence on fatigue behavior, which is shown in the Wöhler graph in figure 4.7 (a): Compressive residual stresses shift the Wöhler curve higher, allowing for more load cycles until failure  $N$  compared to residual stress-free components, given the same external load amplitude  $\sigma_A$ . Tensile residual stresses, on the other hand, reduce the fatigue life of a component. Thus, their effect is analogous to the one of the *mean stress* which occurs in case of asymmetrical loads with a loading ratio  $R_\sigma = \frac{\text{Maximum load}}{\text{Minimum load}} \neq -1$ . The influence can therefore also be displayed in a Haigh diagram (figure 4.7 (b)). However, this Wöhler curve only allows description of the residual stress's influence for one material point of the component. Since residual stresses are inhomogeneous by definition,

- local stressing – due to the tensorial superimposition of loading stress and residual stress
- and local strength – depending on the material parameters such as tensile strength, fatigue limit or fracture toughness which are also dependent on the material history, e.g., due to forming

have to be evaluated pointwise.

The load amplitude plays an important role for fatigue behavior. In the range of *Low-Cycle Fatigue (LCF)*, stresses are relatively high and can exceed the elastic limit. Plastic processes can lead to redistribution and increase or decrease of residual stresses. The decisive factor for fatigue life is the (elastic and plastic) strain amplitude. On the other

hand, in *High-Cycle Fatigue (HCF)*, loading amplitudes are low and stresses remain macroscopically elastic. Changes in the residual stress state also happen, but these are due to microscopic plastic and damage processes. Fatigue life is mostly stress-controlled.

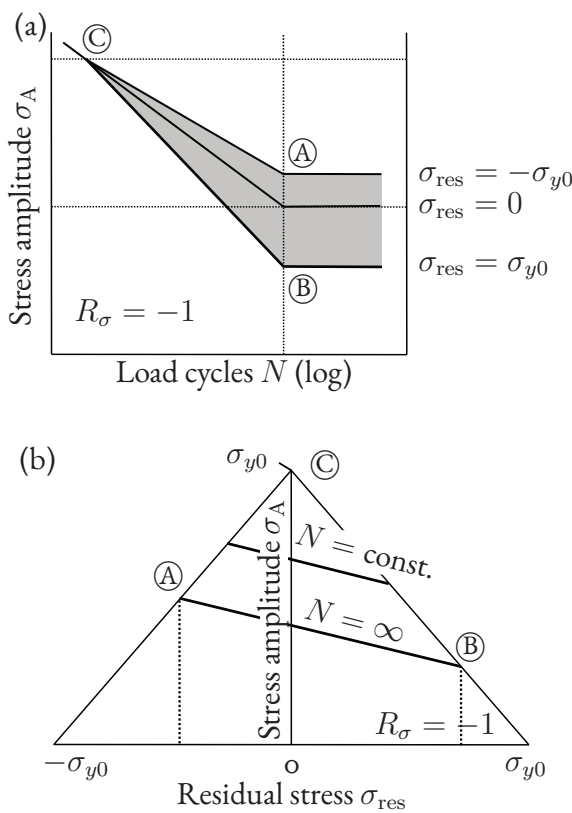


**Figure 4.7** (a) Wöhler curves and (b) Haigh diagram of smooth specimen subjected to alternating tensile-compressive load without mean stress. Grey area marks possible range for varying residual stresses  $\sigma_{\text{res}}$ . Both based on [70].

As shown in figure 4.8, the fatigue life of a component can be divided into the crack initiation stage and the crack propagation stage, leading to failure eventually. Most components are designed with regard to their lifetime until crack initiation. Nonetheless, especially for thin-walled structures, the lifetime of crack propagation is decisive as well. Traditional fracture mechanics concepts can be used to estimate the remaining fatigue life of an already existing crack. However, recently the phase-field method has also gained attention as it covers

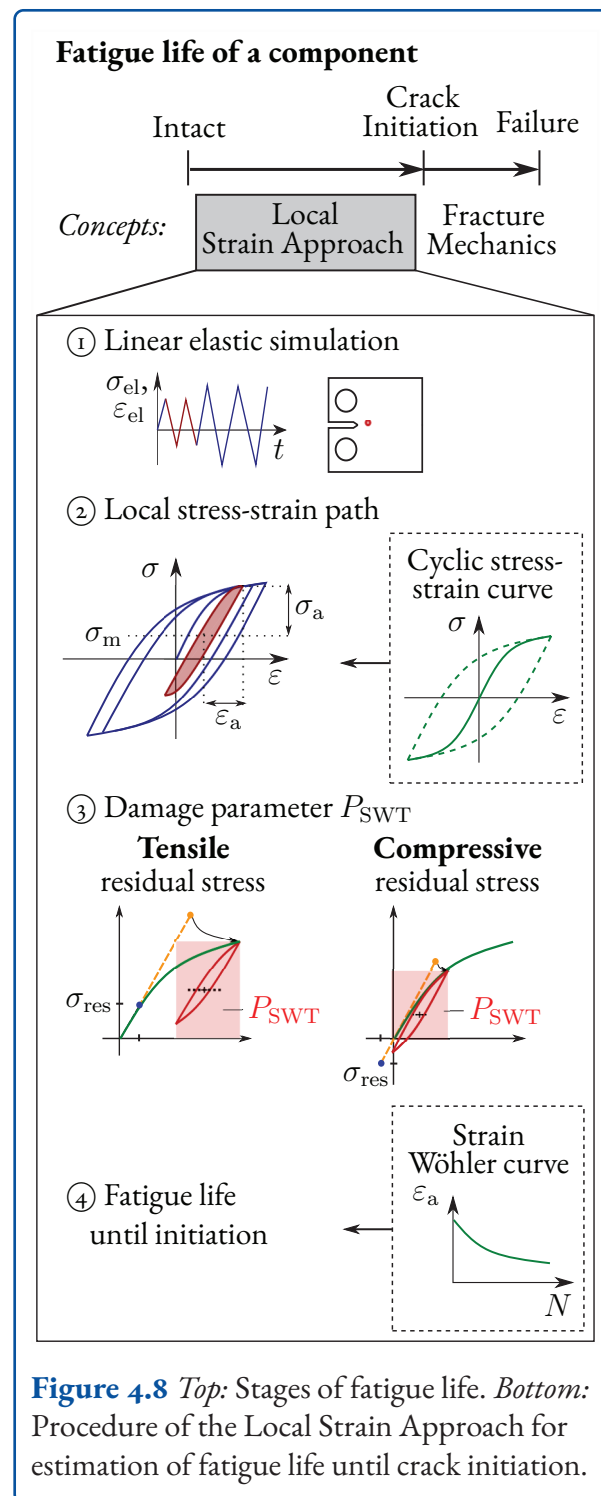


**Figure 4.8** Top: Stages of fatigue life. Bottom: Procedure of the Local Strain Approach for estimation of fatigue life until crack initiation.

both the crack initiation stage and the propagation stage in one framework, see chapter 10.

For the estimation of fatigue life until crack initiation the *Local Strain Approach (LSA)* is the method of choice as it evaluates the stressing and resistance locally at the material point. It is therefore called a material concept. Figure 4.8 gives an overview of its

procedure. A linear elastic simulation of the component ① is the starting point. The subsequent damage evaluation can be carried out at every material point, typically only the most critical one – e.g., a notch – is chosen. The local stress-strain path ② for the given load sequence at this point is approximated with the cyclic stress-strain curve, which is a material-specific curve that has to be provided as an input. This reevaluation of stresses and strains (called Neuber's rule) represents a simplified model for local plastic effects. Thereafter, the local damaging effect of every load cycle is characterized by a damage parameter, e.g.,  $P_{SWT}$  by Smith, Watson and Topper ③.

Residual stresses lead to a shift of the stress-strain hysteresis. Since  $P_{SWT}$  is dependent on the strain amplitude and the positive stress range of the hysteresis (displayed by red rectangle), compressive residual stresses decrease  $P_{SWT}$  while tensile residual stresses increase it. The material's resistance is characterized by strain Wöhler curves. The underlying idea is that the resistance of a material point equals the one of a homogeneous specimen subject to the same strain amplitude. In combination with the damage parameter, they yield the local damage and thereby the fatigue life of the entire component ④. The LSA is part of the FKM guideline "non-linear" [71]. According to the guideline, the stress-strain behavior of the material is assumed to be constant over its whole lifetime. In chapter 10, the concept is extended to non-constant ("transient") material behavior and it is proposed to include the forming history of the component as a first load cycle within the fatigue life estimation.

A popular alternative to the LSA is the *Notch Stress Concept*, governed by the FKM guidelines [72]. It assumes linear elastic material behavior and is therefore mostly suitable for HCF. In contrast to the material concept LSA, it is based on nominal stresses and stress concentration factors and characterizes resistance against fatigue with component-dependent Wöhler curves, requiring different curves for different problem setups.

If ultimately the advantageous effect of compressive residual stresses is to be taken into account in lifetime estimation it is important to ensure the sta-

bility of the residual stress state under cyclic loads. In chapter 4.8, the relevant cyclic evolution of residual stress is discussed for the example of a beam structure.

## 4.8 Residual Stresses as Benchmark: 4 Point Bending Beam

While in the previous sections the fundamentals of modeling residual stresses and the impact on fatigue life were described, in the following a simple test example is discussed. If a force-controlled tension test with homogeneous deformation is considered, no residual stresses will occur at all. Due to the simultaneous loading of neighbored domains, the result is a specimen that has undergone plastic deformation but has no type I residual stresses. The loading path in figure 4.4 thus would end at point ② in a stress free state. As a result, for emergence of residual stresses inhomogeneous stress/strain distributions are a general requirement. The simplest test example which enables inhomogeneous loading states is a bending test. A domain under constant bending moment  $M_b$  is depicted in figure 4.9.

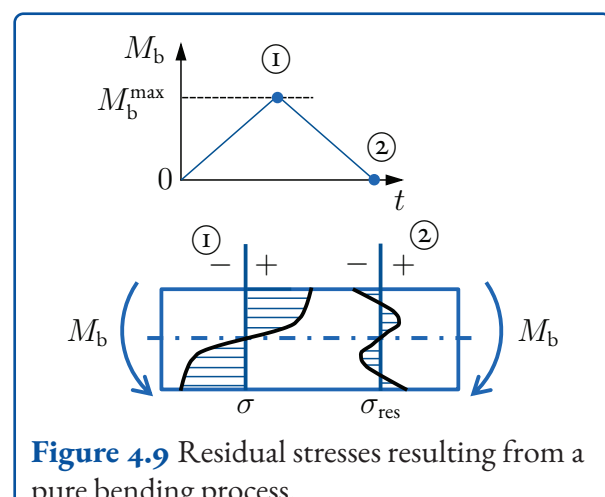


**Figure 4.9** Residual stresses resulting from a pure bending process.

Considering an increasing  $M_b$  over time  $t$ , figure 4.9 shows the typical stress distribution of an elastic-plastic bending state. In maximum load state ①, the cross section shows the elastic domain near the neutral surface, while layers close to the

specimen's surface show the typical stress redistribution due to plastification of the material. Removing the load and ensuring  $M_b = 0$  at the end of unloading ② leads to the profile of residual stresses in typical double s-shape.

#### 4.8.1 Setup and Aim

In order to investigate such a bending process and the resulting residual stresses, a four-point bending setup is chosen, since it leads to a pure bending state between the inner supports. The consideration and conduct of such a bending test enables the construction of a benchmark for different simulation models. A process model, for example, should be able to reproduce the resulting residual stress path depicted in figure 4.9 quantitatively if parametrized correctly for the material used. In addition, this type of investigation allows benchmarking of simulation models that do not exclusively predict Type I residual stresses. Using a multiscale approach and scale transition techniques enables the consideration of textures and the metallic microstructure, see chapter 4.6.1. Such an investigation is carried out in chapter 9 of project P4. Besides the formation of the residual stress, models for simulating their change under cyclic loading as well as models which incorporate the effect of the residual stresses on fatigue life can also be benchmarked against test results obtained using simple bending tests.

For demonstration, four-point bending tests were carried out in order to investigate the level of residual stress in material 42CrMo4+QT (1.7225). The associated test setup is shown in figure 4.10. The cuboid specimens used have the dimension  $8 \times 35 \times 270$  mm.

The parametrization data for the widely used Chaboche plasticity model is presented in figure 4.11 (a) versus the optical measurement data used for calibration via standard optimization procedure. The parameters were determined according to table 4.11 (b).

In the comparison of experiment and simulation, the agreement achieved on the parametrization test is already quite good. Only the initial, manufac-

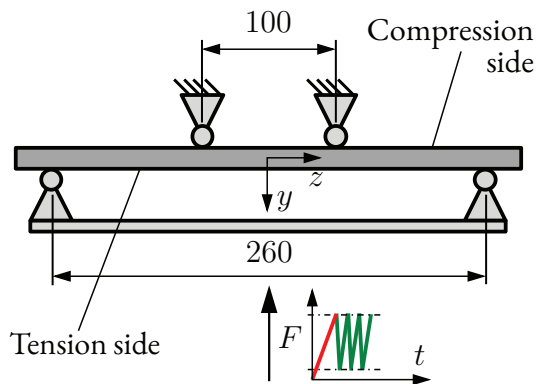


**Figure 4.10** Test setup for the conducted four-point bending tests. It is depicted with the used support structures. The specimen is loaded by an initial load which is followed by cyclic loading of the structure.

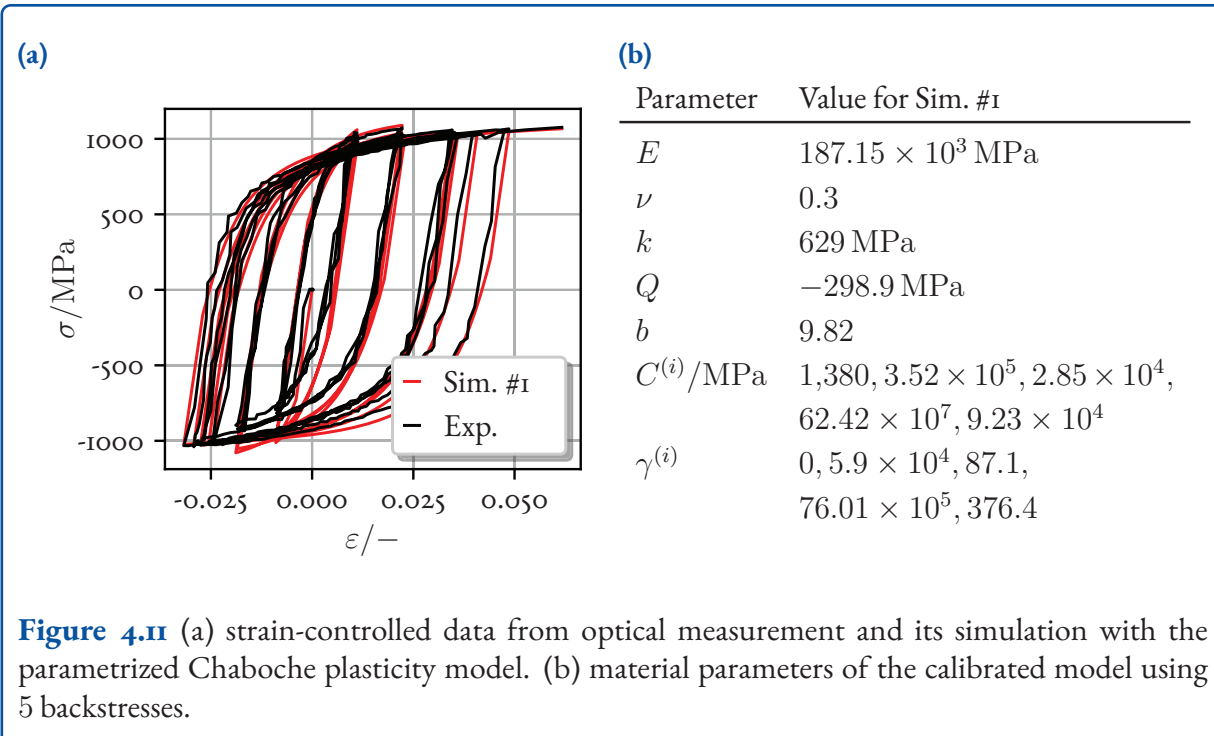
turing induced asymmetry in tension and compression is lacking in the model. However, this effect vanishes with increasing cycles.

#### 4.8.2 Resulting Residual Stresses and Simulation

First, the initial residual stress in figure 4.12 is discussed. It marks the state after initial loading followed by unloading the bending beam, see figure 4.10. The measurements show the residual stress distribution already qualitatively indicated in figure 4.9. On the specimen's tension side compressive residual stresses occur while on the specimen's compression side tensile residual stresses prevail caused by the inhomogeneous loading state.

After initial loading some bending specimens are cyclically loaded with load ratio  $R_\sigma = 0.1$ , as depicted in figure 4.10. Subsequently, the specimen's tests are stopped at various states before fatigue crack initiation. The specimens undergo experimental measurement of residual stress in longitudinal  $z$ -direction.

For the material under investigation, we see from figure 4.12 an increasing tendency in residual stress over accumulating fatigue life of the bending specimen. The relatively short period of increase is fol-



lowed by a stage of stabilization of residual stresses. This behavior can be explained with cyclic softening behavior of the material used. Due to the repetitive loading, the structure experiences cyclic ratcheting in the force controlled experiment. The accumulating plastic strain leads to a cyclic increase in absolute residual stress values. After a phase of stable residual stresses a slight drop in residual stress amount is visible in figure 4.12. This can be explained by emerging fatigue cracks at small length scales. The structure starts failing and macroscopic cracks may emerge afterwards.

For simulating the residual stresses in the bending test the setup is modeled according to figure 4.10. The simulations are then stopped and unloaded after several discrete load cycles in order to investigate the residual stresses at the compression side at  $z = 0$  in longitudinal direction, cf. figure 4.10. The resulting graph of residual stress over load cycles for the four-point bending beam under consideration is depicted in figure 4.13. In addition to Sim. #1, for which the parametrization result is shown in Fig. 4.11 (a), Sim. #2 is included. This simulation was performed with a different set of material parameters, which were determined with slightly different optimization constraints compared to the

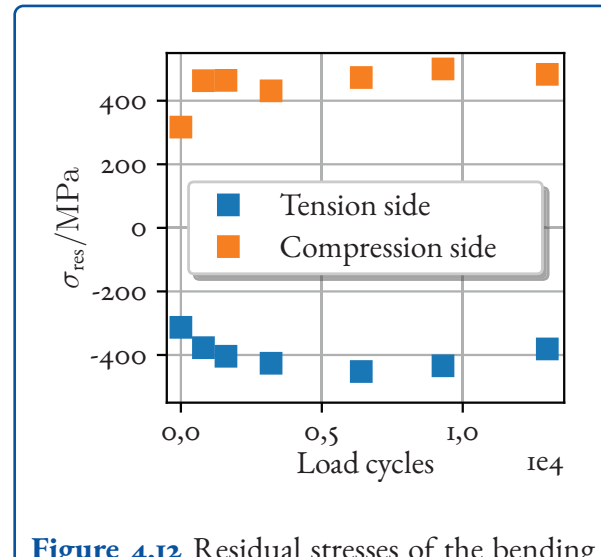


**Figure 4.12** Residual stresses of the bending beam from Fig. 4.10 measured at  $z = 0$  on the tensile and compressive surface, respectively. The x-ray measurement method was used on both beam sides. [Measurements: Gibmeier KIT, 2018].

parameters during parametrization. Sim. #2 also fits well with the parametrization data.

The initial residual stress after bending can be predicted by both simulations. The qualitative in-

crease in residual stress with accumulating load cycles is recognizable in Sim. #1. Sim. #2 in turn does not show any change in residual stress after the initial loading. Compared to the experiments, neither simulation can predict the quantitative evolution of residual stresses to full satisfaction. The reasons for this can be numerous, e.g.:

- The material batches in parametrization and the bending test are not the exactly same. Likely differences may have an impact on performance during residual stress simulation.
- Chaboche's plasticity model overestimates ratcheting. Thus, the shown parametrization was done carefully with just a small amount of ratcheting, i.e.,  $\gamma^{(1)} = 0$ . Using an advanced model for cyclic plasticity could improve the result.
- The choice of constraints on material parameters during optimization affects the parametrization and in particular the prediction of residual stress evolution, see Sim. #2 in figure 4.13. Enhanced parametrization data should be considered.
- Possible sliding of the beam on the cylindrical supports is not modeled in the simulation.

In order to investigate the benchmark more in detail this possible problems have to be addressed in future work. For sake of brevity, this is out of scope of the present chapter.

## Abbreviations and Symbols

HCF	High-Cycle Fatigue	$E_p$	plastic strain tensor (–)
LCF	Low-Cycle Fatigue	$f$	yield function (MPa)
LSA	Local Strain Approach	$F$	force (N)
$a(\vec{x})$	fluctuation field tensor of strain (–)	$F$	deformation gradient (–)
$\mathbb{A}(\vec{x})$	localization tensor (–)	$F_e$	elastic deformation gradient (–)
$b(\vec{x})$	fluctuation field tensor of stress (MPa)	$F_p$	plastic deformation gradient (–)
$\mathbb{B}(\vec{x})$	localization tensor (MPa)	$g$	gap between contact point pair (m)
$\mathbb{C}$	stiffness tensor (MPa)	$g_n$	normal component of the gap (m)
$E$	Young's modulus (MPa)	$g_t$	tangential gap vector (m)
$E$	Strain tensor (–)	$G$	shear modulus (MPa)
$E_e$	elastic-like strain tensor (–)	$M_b$	bending moment (N m)
		$N$	number of load cycles (–)
		$p$	accumulated plastic strain (–)
		$P_{SWT}$	damage parameter of Smith, Watson and Topper (MPa)
		$q$	arbitrary internal variables (–)
		$\mathbf{q}$	heat flux ( $\text{W}/\text{m}^2$ )
		$r$	heat source ( $\text{W}/\text{kg}$ )
		$R$	isotropic hardening variable (MPa)
		$R_\sigma$	load ratio (–)
		$s$	stress deviator (MPa)
		$t$	time (s)

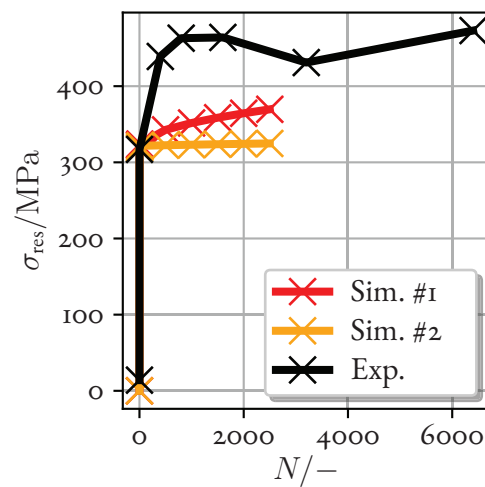


**Figure 4.13** Simulation of residual stresses in bending tests using the parametrized Chaboche model. The evaluation point is  $z = 0$  on the compression side in longitudinal direction according to fig. 4.10. Additionally, Sim. #2 with a different set of material parameters is shown.

$t_n$	normal component of the contact force (MPa)	$\psi$	specific free energy (J/kg s)
$t_t$	tangential component of the contact force (MPa)	$\Psi_c$	total contact energy (J)
$\mathbf{t}$	contact force (MPa)	$\Delta(\cdot)$	increment/change of ( $\cdot$ )
$\mathbf{t}$	traction vector (MPa)		
$u$	specific internal energy (J/kg s)		
$U_i$	$i$ -th nodal value of the displacement (m)		
$\mathbf{u}$	displacement (m)		
$x$	physical coordinate (m)		
$\vec{x}$	osition vector in current configuration (m)		
$\vec{X}$	position vector in reference configuration (m)		
$\mathbf{X}$	backstress tensor (MPa)		
$y$	physical coordinate (m)		
$z$	physical coordinate (m)		
$\epsilon_n$	normal penalty parameter (MPa/m)		
$\epsilon_t$	tangential penalty parameter (MPa/m)		
$\boldsymbol{\varepsilon}^p$	plastic strain tensor (-)		
$\boldsymbol{\varepsilon}^e$	elastic strain tensor (-)		
$\eta$	specific entropy (J/kg K)		
$\vartheta$	temperature (K)		
$\kappa$	friction coefficient (-)		
$\lambda$	1st LAME parameter (MPa)		
$\lambda_n$	normal LAGRANGE multiplier (MPa)		
$\lambda_t$	tangential LAGRANGE multiplier (MPa)		
$\mu$	2nd LAME parameter (MPa)		
$\nu$	Poisson ratio (-)		
$\nu$	test function (-)		
$\rho$	density (kg/m <sup>3</sup> )		
$\sigma$	one-dimensional Cauchy stress (MPa)		
$\sigma_I, \sigma_{II}, \sigma_{III}$	eigenvalues of Cauchy stress tensor/principal stresses (MPa)		
$\boldsymbol{\sigma}$	Cauchy stress tensor (MPa)		
$\boldsymbol{\sigma}_{\text{res}}$	residual Cauchy stress tensor (MPa)		
$\sigma_y$	current yield stress (MPa)		
$\sigma_{y0}$	initial yield stress (MPa)		
$\varphi_i$	$i$ -th shape function (-)		

## References

- [1] E. H. Lee and D. T. Liu. "Finite-Strain Elastic—Plastic Theory with Application to Plane-Wave Analysis". In: *Journal of Applied Physics* 38.1 (Jan. 1967), pp. 19–27. DOI: 10.1063/1.1708953.
- [2] A. E. Green and P. M. Naghdi. "A general theory of an elastic-plastic continuum". In: *Archive for Rational Mechanics and Analysis* 18.4 (Jan. 1965), pp. 251–281. DOI: 10.1007/bf00251666.
- [3] A.E. Green and P.M. Naghdi. "Some remarks on elastic-plastic deformation at finite strain". In: *International Journal of Engineering Science* 9.12 (Dec. 1971), pp. 1219–1229. DOI: 10.1016/0020-7225(71)90086-3.
- [4] Otto T. Bruhns. "The Multiplicative Decomposition of the Deformation Gradient in Plasticity—Origin and Limitations". In: *Advanced Structured Materials*. Springer International Publishing, 2015, pp. 37–66. DOI: 10.1007/978-3-319-19440-0\_3.
- [5] Mikhail Itskov. "On the application of the additive decomposition of generalized strain measures in large strain plasticity". In: *Mechanics Research Communications* 31.5 (Sept. 2004), pp. 507–517. DOI: 10.1016/j.mechrescom.2004.02.006.
- [6] J.L. Chaboche. "Constitutive equations for cyclic plasticity and cyclic viscoplasticity". In: *International Journal of Plasticity* 5.3 (Jan. 1989), pp. 247–302. DOI: 10.1016/0749-6419(89)90015-6.
- [7] Ivaylo N. Vladimirov, Michael P. Pietryga, and Stefanie Reese. "On the modelling of nonlinear kinematic hardening at finite strains with application to springback—Comparison of time integration algorithms". In: *International Journal for Numerical Methods in Engineering* 75.1 (July 2008), pp. 1–28. DOI: 10.1002/nme.2234.

- [8] M. Canadija and J. Mosler. "On the thermo-mechanical coupling in finite strain plasticity theory with non-linear kinematic hardening by means of incremental energy minimization". In: *International Journal of Solids and Structures* 48.7-8 (Apr. 2011), pp. 1120–1129. DOI: 10.1016/j.ijsolstr.2010.12.018.
- [9] Fadi Aldakheel, Blaž Hudobivnik, and Peter Wriggers. "Virtual elements for finite thermo-plasticity problems". In: *Computational Mechanics* 64.5 (May 2019), pp. 1347–1360. DOI: 10.1007/s00466-019-01714-2.
- [10] Alexander Seitz, Wolfgang A. Wall, and Alexander Popp. "A computational approach for thermo-elasto-plastic frictional contact based on a monolithic formulation using non-smooth non-linear complementarity functions". In: *Advanced Modeling and Simulation in Engineering Sciences* 5.1 (Mar. 2018). DOI: 10.1186/s40323-018-0098-3.
- [11] Stanislaw Stupkiewicz. "Extension of the node-to-segment contact element for surface-expansion-dependent contact laws". In: *International Journal for Numerical Methods in Engineering* 50.3 (2001), pp. 739–759. DOI: 10.1002/1097-0207(20010130)50:3<739::aid-nme49>3.0.co;2-g.
- [12] Peter Wriggers. *Computational Contact Mechanics*. Springer-Verlag GmbH, Oct. 6, 2006. 518 pp. ISBN: 9783540326090. URL: [https://www.ebook.de/de/product/8899217/peter\\_wriggers\\_computational\\_contact\\_mechanics.html](https://www.ebook.de/de/product/8899217/peter_wriggers_computational_contact_mechanics.html).
- [13] Uri M. Ascher, Steven J. Ruuth, and Brian T. R. Wetton. "Implicit-Explicit Methods for Time-Dependent Partial Differential Equations". In: *SIAM Journal on Numerical Analysis* 32.3 (June 1995), pp. 797–823. DOI: 10.1137/0732037.
- [14] Uri M. Ascher, Steven J. Ruuth, and Raymond J. Spiteri. "Implicit-explicit Runge-Kutta methods for time-dependent partial differential equations". In: *Applied Numerical Mathematics* 25.2-3 (Nov. 1997), pp. 151–167. DOI: 10.1016/s0168-9274(97)00056-1.
- [15] Sang H. Lee and Steve S. Hsieh. "Expedient implicit integration with adaptive time stepping algorithm for nonlinear transient analysis". In: *Computer Methods in Applied Mechanics and Engineering* 81.2 (Aug. 1990), pp. 151–172. DOI: 10.1016/0045-7825(90)90107-w.
- [16] Sören Bartels and Jakob Keck. "Adaptive time stepping in elastoplasticity". In: *Discrete & Continuous Dynamical Systems - S* 14.1 (2021), pp. 71–88. DOI: 10.3934/dcdss.2020323.
- [17] Mark Ainsworth and J.Tinsley Oden. "A posteriori error estimation in finite element analysis". In: *Computer Methods in Applied Mechanics and Engineering* 142.1-2 (Mar. 1997), pp. 1–88. DOI: 10.1016/s0045-7825(96)01107-3.
- [18] G. Zavarise and P. Wriggers. "A segment-to-segment contact strategy". In: *Mathematical and Computer Modelling* 28.4-8 (Aug. 1998), pp. 497–515. DOI: 10.1016/s0895-7177(98)00138-1.
- [19] D. M. Neto, M. C. Oliveira, and L. F. Menezes. "Surface Smoothing Procedures in Computational Contact Mechanics". In: *Archives of Computational Methods in Engineering* 24.1 (Nov. 2015), pp. 37–87. DOI: 10.1007/s11831-015-9159-7.
- [20] Hamid Jahed and Ali Roostaei, eds. *Cyclic plasticity of metals: modeling fundamentals and applications*. 1st ed. San Diego: Elsevier, 2022. ISBN: 978-0-12-819293-1.
- [21] J.L. Chaboche, K. Dang Van, and G. Cordier. *Modelization of the strain memory effect on the cyclic hardening of 316 stainless steel*. Netherlands: North-Holland Publishing Co, 1979. ISBN: 0444 85367 7. URL: [http://inis.iaea.org/search/search.aspx?orig\\_q=RN:12591218](http://inis.iaea.org/search/search.aspx?orig_q=RN:12591218).
- [22] J.L. Chaboche. "Time-independent constitutive theories for cyclic plasticity". In: *International Journal of Plasticity* 2.2 (Jan. 1986), pp. 149–188. ISSN: 07496419. DOI: 10.1016/0749-6419(86)90010-0. URL: <https://linkinghub.elsevier.com/retrieve/pii/0749641986900100> (visited on 11/26/2021).
- [23] P. J. Armstrong and C. O. Frederick. "A mathematical representation of the multiaxial Bauschinger effect". In: *CEGB Report RD/B/N* 731

- (1966), The Report is reproduced as a Paper: 2007. *Materials at High Temperature*, 24, 1–26.
- [24] N. Ohno and J.-D. Wang. “Kinematic hardening rules with critical state of dynamic recovery, part I: formulation and basic features for ratchetting behavior”. In: *International Journal of Plasticity* 9.3 (Jan. 1993), pp. 375–390. ISSN: 07496419. DOI: 10.1016/0749-6419(93)90042-0. URL: <https://linkinghub.elsevier.com/retrieve/pii/0749641993900420> (visited on 07/20/2022).
- [25] M. Abdel-Karim and N. Ohno. “Kinematic hardening model suitable for ratchetting with steady-state”. In: *International Journal of Plasticity* 16.3 (Jan. 2000), pp. 225–240. ISSN: 07496419. DOI: 10.1016/S0749-6419(99)00052-2. URL: <https://linkinghub.elsevier.com/retrieve/pii/S0749641999000522> (visited on 07/20/2022).
- [26] Ralph Döring et al. “A plasticity model for calculating stress-strain sequences under multiaxial nonproportional cyclic loading”. In: *Computational Materials Science* 28.3 (Nov. 2003), pp. 587–596. ISSN: 09270256. DOI: 10.1016/j.commatsci.2003.08.015. URL: <https://linkinghub.elsevier.com/retrieve/pii/S0927025603001435> (visited on 09/20/2022).
- [27] Fusahito Yoshida and Takeshi Uemori. “A model of large-strain cyclic plasticity describing the Bauschinger effect and workhardening stagnation”. In: *International Journal of Plasticity* 18.5 (Oct. 2002), pp. 661–686. ISSN: 07496419. DOI: 10.1016/S0749-6419(01)00050-X. URL: <https://linkinghub.elsevier.com/retrieve/pii/S074964190100050X> (visited on 05/19/2022).
- [28] A. Bensoussan, J.-L. Lions, and G. Papanicolaou. *Asymptotic Analysis for Periodic Structures*. Vol. 374. Amsterdam: North-Holland, 1978. ISBN: 9780080875262.
- [29] Pedro Ponte Castañeda and Pierre Suquet. “Nonlinear Composites”. In: ed. by Erik van der Giessen and Theodore Y. Wu. Vol. 34. *Advances in Applied Mechanics*. Elsevier, 1997, pp. 171–302. DOI: 10.1016/S0065-2156(08)70321-1.
- [30] George J. Dvorak and Jian Zhang. “Transformation field analysis of damage evolution in composite materials”. In: *Journal of the Mechanics and Physics of Solids* 49.11 (2001). The Jean-Paul Boehler Memorial Volume, pp. 2517–2541. ISSN: 0022-5096. DOI: 10.1016/S0022-5096(01)00066-7.
- [31] Felix Fritzen and Thomas Böhlke. “Reduced basis homogenization of viscoelastic composites”. In: *Composites Science and Technology* 76 (2013), pp. 84–91. ISSN: 0266-3538. DOI: 10.1016/j.compscitech.2012.12.012.
- [32] Christian Miehe, Jan Schotte, and Jörg Schröder. “Computational micro–macro transitions and overall moduli in the analysis of polycrystals at large strains”. In: *Computational Materials Science* 16.1 (1999), pp. 372–382. ISSN: 0927-0256. DOI: 10.1016/S0927-0256(99)00080-4.
- [33] H. Moulinec and P. Suquet. “A numerical method for computing the overall response of nonlinear composites with complex microstructure”. In: *Computer Methods in Applied Mechanics and Engineering* 157.1 (1998), pp. 69–94. ISSN: 0045-7825. DOI: 10.1016/S0045-7825(97)00218-1.
- [34] P. Kanouté et al. “Multiscale Methods for Composites: A Review”. In: *Archives of Computational Methods in Engineering* 16.1 (2009), pp. 31–75. ISSN: 1886-1784. DOI: 10.1007/s11831-008-9028-8.
- [35] Frédéric Feyel. “Multiscale FE2 elastoviscoplastic analysis of composite structures”. In: *Computational Materials Science* 16.1 (1999), pp. 344–354. ISSN: 0927-0256. DOI: 10.1016/S0927-0256(99)00077-4.
- [36] Christian Miehe. “Strain-driven homogenization of inelastic microstructures and composites based on an incremental variational formulation”. In: *International Journal for Numerical Methods in Engineering* 55.11 (2002), pp. 1285–1322. DOI: 10.1002/nme.515.
- [37] Jörg Schröder, Daniel Balzani, and Dominik Brands. “Approximation of random microstructures by periodic statistically similar representative volume elements based on lineal-path functions”. In: *Archive of Applied Mechanics* 81.7 (2011), pp. 975–997. ISSN: 1432-0681. DOI: 10.1007/s00419-010-0462-3.

- [38] M. Ambrozinski et al. "Application of statistically similar representative volume element in numerical simulations of crash box stamping". In: *Archives of Civil and Mechanical Engineering* 12.2 (2012), pp. 126–132. ISSN: 1644-9665. DOI: 10.1016/j.acme.2012.04.011.
- [39] Lisa Scheunemann et al. "Construction of Statistically Similar Representative Volume Elements – Comparative Study Regarding Different Statistical Descriptors". In: *Procedia Engineering* 81 (2014). 11th International Conference on Technology of Plasticity, ICTP 2014, 19-24 October 2014, Nagoya Congress Center, Nagoya, Japan, pp. 1360–1365. ISSN: 1877-7058. DOI: 10.1016/j.proeng.2014.10.157.
- [40] Felix Fritzen and Matthias Leuschner. "Reduced basis hybrid computational homogenization based on a mixed incremental formulation". In: *Computer Methods in Applied Mechanics and Engineering* 260 (2013), pp. 143–154. ISSN: 0045-7825. DOI: 10.1016/j.cma.2013.03.007.
- [41] Felix Fritzen and Max Hodapp. "The finite element square reduced (FE<sub>2</sub>R) method with GPU acceleration: towards three-dimensional two-scale simulations". In: *International Journal for Numerical Methods in Engineering* 107.10 (2016), pp. 853–881. DOI: 10.1002/nme.5188.
- [42] Matti Schneider. "A review of nonlinear FFT-based computational homogenization methods". In: *Acta Mechanica* 232.6 (2021), pp. 2051–2100. ISSN: 1619-6937. DOI: 10.1007/s00707-021-02962-1.
- [43] J. Spahn et al. "A multiscale approach for modeling progressive damage of composite materials using fast Fourier transforms". In: *Computer Methods in Applied Mechanics and Engineering* 268 (2014), pp. 871–883. ISSN: 0045-7825. DOI: 10.1016/j.cma.2013.10.017.
- [44] Julian Kochmann et al. "Two-scale FE-FFT- and phase-field-based computational modeling of bulk microstructural evolution and macroscopic material behavior". In: *Computer Methods in Applied Mechanics and Engineering* 305 (2016), pp. 89–110. ISSN: 0045-7825. DOI: 10.1016/j.cma.2016.03.001.
- [45] M. Agoras and P. Ponte Castañeda. "Homogenization estimates for multi-scale nonlinear composites". In: *European Journal of Mechanics - A/Solids* 30.6 (2011), pp. 828–843. ISSN: 0997-7538. DOI: 10.1016/j.euromechsol.2011.05.007.
- [46] W. Voigt. "Über die Beziehung zwischen den beiden Elasticitätsconstanten isotroper Körper". In: *Annalen der Physik* 274.12 (1889), pp. 573–587. DOI: 10.1002/andp.18892741206.
- [47] A. Reuss. "Berechnung der Fließgrenze von Mischkristallen auf Grund der Plastizitätsbedingung für Einkristalle". In: *Journal of Applied Mathematics and Mechanics* 9.1 (1929), pp. 49–58. DOI: 10.1002/zamm.19290090104.
- [48] John Douglas Eshelby and Rudolf Ernst Peierls. "The determination of the elastic field of an ellipsoidal inclusion, and related problems". In: *Proceedings of the Royal Society of London. Series A. Mathematical and Physical Sciences* 241.1226 (1957), pp. 376–396. DOI: 10.1098/rspa.1957.0133.
- [49] Ekkehart Kröner. "Berechnung der elastischen Konstanten des Vielkristalls aus den Konstanten des Einkristalls". In: *Zeitschrift für Physik* 151.4 (1958), pp. 504–518. ISSN: 0044-3328. DOI: 10.1007/BF01337948.
- [50] T Mori and K Tanaka. "Average stress in matrix and average elastic energy of materials with misfitting inclusions". In: *Acta Metallurgica* 21.5 (1973), pp. 571–574. ISSN: 0001-6160. DOI: 10.1016/0001-6160(73)90064-3.
- [51] G Lielens. "Micro-macro modeling of structured materials". PhD thesis. Belgium: Faculté des Sciences Appliquées, Université catholique de Louvain, 1999.
- [52] Z. Hashin and S. Shtrikman. "A variational approach to the theory of the elastic behaviour of polycrystals". In: *Journal of the Mechanics and Physics of Solids* 10.4 (1962), pp. 343–352. ISSN: 0022-5096. DOI: 10.1016/0022-5096(62)90005-4.
- [53] Thomas Böhlke, Rudolf Neumann, and Florian Rieger. "Two-Scale Modeling of Grain Size and Phase Transformation Effects". In: *steel research international* 85.6 (2014), pp. 1018–1034. DOI: 10.1002/srin.201300200.

- [54] Florian Rieger and Thomas Böhlke. "Microstructure based prediction and homogenization of the strain hardening behavior of dual-phase steel". In: *Archive of Applied Mechanics* 85.9 (2015), pp. 1439–1458. ISSN: 1432-0681. DOI: 10.1007/s0419-014-0974-3.
- [55] Rudolf Neumann and Thomas Böhlke. "Hashin-Shtrikman type mean field model for the two-scale simulation of the thermomechanical processing of steel". In: *International Journal of Plasticity* 77 (2016), pp. 1–29. ISSN: 0749-6419. DOI: 10.1016/j.ijplas.2015.09.003.
- [56] J.R. Willis. "Variational and Related Methods for the Overall Properties of Composites". In: ed. by Chia-Shun Yih. Vol. 21. *Advances in Applied Mechanics*. Elsevier, 1981, pp. 1–78. DOI: 10.1016/S0065-2156(08)70330-2.
- [57] W. Kreher and W. Pompe. *Internal Stresses in Heterogeneous Solids*. Berlin: Akademie Verlag, 1989. ISBN: 3-05-500669-0.
- [58] J Hofinger, H Erdle, and T Böhlke. "Prediction of residual stresses of second kind in deep drawing using an incremental two-scale material model". In: *Philosophical Magazine* (2020), pp. 1–21. DOI: 10.1080/14786435.2020.1798533.
- [59] Nicola Simon et al. "Phase-specific residual stresses induced by deep drawing of lean duplex steel: measurement vs. simulation". In: *Production Engineering* 13.2 (2019), pp. 227–237. DOI: 10.1007/s11740-019-00877-4.
- [60] E. T. Jaynes and R. D. Rosenkrantz. *E.T. Jaynes: Papers on Probability, Statistics and Statistical Physics*. Pallas paperback series. Springer Netherlands, 1983. ISBN: 9789027714480.
- [61] Maximilian Krause and Thomas Böhlke. "Maximum-Entropy Based Estimates of Stress and Strain in Thermoelastic Random Heterogeneous Materials". In: *Journal of Elasticity* 141.2 (2020), pp. 321–348. ISSN: 1573-2681. DOI: 10.1007/s10659-020-09786-5.
- [62] Maximilian Krause and Thomas Böhlke. "Stochastic evaluation of stress and strain distributions in duplex steel". In: *Archive of Applied Mechanics* 91.8 (2021), pp. 3527–3540. ISSN: 1432-0681. DOI: 10.1007/s00419-021-01925-1.
- [63] A. Bertram and T. Böhlke. "Simulation of texture induced elastic anisotropy of polycrystalline copper". In: *Computational Materials Science* 16.1 (1999), pp. 2–9. ISSN: 0927-0256. DOI: 10.1016/S0927-0256(99)00039-7.
- [64] Thomas Böhlke, Albrecht Bertram, and Erhard Krempl. "Modeling of deformation induced anisotropy in free-end torsion". In: *International Journal of Plasticity* 19.11 (2003). Finite Plasticity and Viscoplasticity - Theoretical, Experimental and Computational Aspects, pp. 1867–1884. ISSN: 0749-6419. DOI: 10.1016/S0749-6419(03)0043-3.
- [65] Thomas Böhlke. "Texture simulation based on tensorial Fourier coefficients". In: *Computers & Structures* 84.17 (2006). Formulations and Computational Models for Finite Strains, pp. 1086–1094. ISSN: 0045-7949. DOI: 10.1016/j.compstruc.2006.01.006.
- [66] Thomas Böhlke, Utz-Uwe Haus, and Volker Schulze. "Crystallographic texture approximation by quadratic programming". In: *Acta Materialia* 54.5 (2006), pp. 1359–1368. ISSN: 1359-6454. DOI: 10.1016/j.actamat.2005.11.009.
- [67] Katja Jöchen and Thomas Böhlke. "Representative reduction of crystallographic orientation data". In: *Journal of Applied Crystallography* 46.4 (2013), pp. 960–971. DOI: 10.1107/S0021889813010972.
- [68] Tung Phan Van, Katja Jöchen, and Thomas Böhlke. "Simulation of sheet metal forming incorporating EBSD data". In: *Journal of Materials Processing Technology* 212.12 (2012), pp. 2659–2668. ISSN: 0924-0136. DOI: 10.1016/j.jmatprotec.2012.07.015.
- [69] Nicola Simon et al. "Phase-Specific Strain Hardening and Load Partitioning of Cold Rolled Duplex Stainless Steel X<sub>2</sub>CrNiN<sub>23-4</sub>". In: *Crystals* 10.11 (2020). ISSN: 2073-4352. DOI: 10.3390/crys10110976.
- [70] Dieter Radaj and Michael Vormwald. *Ermüdungsfestigkeit*. de. 3rd ed. Berlin, Heidelberg: Springer Berlin Heidelberg, 2007. ISBN: 978-3-540-71458-3. DOI: 10.1007/978-3-540-71459-0. URL: <http://link.springer.com/10.1007/978-3-540-71459-0> (visited on 03/08/2018).

[71] Melanie Fiedler et al. *Richtlinie Nichtlinear: rechnerischer Festigkeitsnachweis unter expliziter Erfassung nichtlinearen Werkstoffverformungsverhaltens: für Bauteile aus Stahl, Stahlguss und Aluminiumknetlegierungen.* ger. 1. Auflage. FKM-Richtlinie. Frankfurt am Main: VDMA Verlag GmbH, 2019. ISBN: 978-3-8163-0729-7.

[72] Roland Rennert. *Rechnerischer Festigkeitsnachweis für Maschinenbauteile aus Stahl, Eisenguss- und Aluminiumwerkstoffen.* ger. Ed. by Verband Deutscher Maschinen- und Anlagenbau. 6., überarb. Ausg. FKM-Richtlinie. Frankfurt am Main: VDMA-Verl, 2012. ISBN: 978-3-8163-0605-4.

## 5 Residual Stress Analysis on Metal Components Manufactured by Forming

Gibmeier, J.; Simon, N.

In the experimental analysis of residual stresses in components manufactured by forming, it must be taken into account that the sometimes complex component geometries alone can cause problems when even established analyzing methods are applied. In addition, common forming processes can often be associated with high plastic deformations and there are sometimes strong gradients in the residual stresses in the lateral direction and also in depth. Common residual stress analysis methods can very quickly reach their limits here, so that sometimes adapted or new measurement and evaluation strategies have to be tried. Furthermore, the effects of texture, texture gradients and multi-phases that occur in formed components represent major challenges, the influences of which have not yet been satisfactorily taken into account in measurement and evaluation. In the following sections, these fundamental problems are addressed individually and possible solutions are shown. In particular, the problem of thin-walled sheet metal components is dealt with and the multi-phase character is also examined in more detail in a separate section.

### 5.1 Basic Problems and Possible Solutions

In general, methods for analysing residual stress are divided into nondestructive and destructive methods. Nondestructive methods include diffraction methods using (synchrotron) X-rays or neutron radiation, as well as acoustic and magnetic methods [1]. The mechanical methods [2] are assigned to the destructive processes. What all methods have in common is that residual stresses can never be measured directly. For the local analysis of residual stress distributions on components manufac-

tured by forming, the following challenges can be attributed to all established methods:

- Complex component geometries
- Strong gradients of residual stress distributions
- Crystallographic texture
- Thin-walled components
- Multi-phase materials (residual stresses of I. + II. kind).

These problems clearly limit the applicability of the residual stress analysis methods. The points listed are discussed in detail below one after the other. The first point in the list addresses the presence of complex component geometries.

The well-established methods for determining residual stresses (e.g., hole drilling method or X-ray diffraction method) can only be used to a limited extent in most applications with **complex component geometries**, since, e.g., the accessibility to the measuring point is not sufficient or the achievable information depth of the methods is simply too small.

With regard to the destructive or partially destructive mechanical methods (e.g., saw cut method, boring method, turning method, hole drilling method, ring core method), in which the elastic strain relaxations as a result of the disturbance of the residual stresses balance by means of mechanical transducers (strain gauges) or optical methods, it remains to be noted that some of the methods require strictly regular geometries, such as the presence of cylindrical components in the boring or turning methods.

This limits applicability per se immensely. With the ultrasonic methods and the electromagnetic test methods, access to the measuring point is also via the component surface. In the case of complex component states, it must be ensured that the sensor is

suitable for the selected measuring point and that the measuring signals can be properly coupled.

In **diffraction methods**, a distinction is made among diffraction methods using neutron, X-ray and synchrotron X-ray radiation. In all diffraction methods, the relative displacements of the measured interference line positions serve as the measured variable. The elastic distortion of the crystal lattice is then determined from these. The mechanical stresses can be determined on the basis of basic equations of elasticity theory using lattice plane-specific diffraction-elastic constants (DEC), which take into account the elastic anisotropy of a crystallite and the coupling of the crystallites in the multi-crystal compound. The DEC can be determined both experimentally in defined load stress analyses and numerically by means of model assumptions for the coupling of the crystallites (e.g., Voigt [3], Reuss [4], Eshelby/Kröner [5, 6]) in the polycrystal using the single crystal data.

The diffraction methods are generally counted among the nondestructive methods. With regard to the most common laboratory applications, the X-ray residual stress analysis using soft X-rays (photon energies  $<30$  keV), the nondestructive character is not unrestricted if knowledge about the residual stress distribution in the depth of the component is desired. With the help of soft X-rays, it is basically possible to determine residual stress analyses near the surface using the established  $\sin^2 \psi$  method [7]. When examining steel, information depths typically in the range of some micrometer and using shorter wavelength of up to a maximum of about  $20 \mu\text{m}$  are available. The conventional methods deliver averaged amounts of residual stress over this depth of information.

With regard to the application to complex component geometries, the measuring point must be accessible for the actual diffraction analysis as well as for the local electrochemical layer removal. There are hardware limitations to consider here, but also limitations stemming from the primary and secondary beam paths. Here, it must be ensured that the primary and the diffracted X-ray beams are not shadowed by component areas (e.g., by component edges). For recommended measuring and evalua-

tion parameters and procedures it is referred, e.g., to the standard BS EN 15305:2008 Nondestructive testing. Test method for residual stress analysis by X-ray diffraction

Using high-energy X-rays, typically high-energy synchrotron radiation (photon energies  $>50$  keV), or also neutron beams, it is possible to non-destructively analyze volume residual stresses at sample depths of up to a few centimetres. With the use of high-energy synchrotron radiation, the low-index lattice plane types appear at relatively small diffraction angles. This inevitably leads to a loss of spatial resolution in at least one of the spatial directions, since a rod-shaped measurement volume is defined by the primary and secondary beam apertures. In the case of larger component volumes, the absorption of the material can even make it impossible to measure the tri-axial residual stress distribution, so that the workpiece may have to be divided up in view of the accessibility of the measuring point for the residual stress analysis [8, 9].

A major advantage of using neutron beams is the comparatively large penetration depth of the neutrons (about 20 mm for steel), which not only enables measurements far below the surface of samples. With a measurement volume defined by means of the primary and secondary beam apertures in a  $90^\circ$  beam geometry, it is also possible to use a right-angled measurement volume with almost the same resolution in all three spatial directions. The size and shape of the measurement volume can thus be kept constant for all sample orientations required to determine the complete strain tensor. Nowadays, position-sensitive area detectors (PSD) are commonly used to increase the efficiency of neutron diffractometers and to significantly reduce measurement times. When using neutron beams, typically a measurement volume larger than  $1 \times 1 \times 1 \text{ mm}^3$  has to be selected in order to obtain measurement times of an acceptable duration [10]. To calculate the lattice deformation, knowledge of the strain-free or strain-independent lattice parameter  $D_0$  is required. The determination of the reference value  $D_0$  is generally difficult and is to be regarded as problematic, particularly when a multi-phase material is present. Numerous pos-

sibilities for determining  $D_0$  and their limitations (e.g., plane stress state) are summarized in [1]. The main disadvantage of using synchrotron X-rays or neutron radiation for residual stress analysis is undoubtedly the availability of the methods, since this is only given in the context of large-scale research, i.e., using dedicated diffraction instruments at synchrotron sources are neutron reactors or spallation sources.

As already mentioned at the beginning, residual stress distributions induced by forming often have gradients in the lateral direction and also in depth direction. This requires a certain spatial resolution on the part of the analysis methods. In any case, in the majority of cases it is not enough to carry out residual stress analyzes on the immediate surface in order to adequately characterise the process.

Rather, it is important to determine locally resolved residual stress depth distributions over as large a depth range as possible. The laboratory methods most frequently used in technology to determine residual stress depth distributions on complex component geometries are X-ray residual stress analysis using the  $\sin^2 \psi$  method and the incremental hole drilling method. With regard to X-ray methods, special measurement and evaluation strategies have been proposed for pronounced gradients of residual stress distributions near the surface, which allow nondestructive determination of depth distributions of residual stresses via the physically given comparatively low information depth (e.g., [11, 12]).

As a rule, however, there are long-range residual stress depth distributions in components manufactured by forming. For their determination down to great depths of a few millimetres, there is the possibility of repeated application of the  $\sin^2 \psi$  method after a gradual layer removal, usually using electrolytic material removal. With this procedure, repeated residual stress analyses are carried out on the newly created material surfaces. However, this method no longer works non-destructively and is also associated with a great deal of time and effort. In addition, in the case of partial material removal, it must be carefully checked whether corrections are required with regard to the macroscopic resid-

ual stresses that have been triggered. When removing the sub-layer, there is always a risk that significant portions of the residual stress state will be redistributed as a result of the material removal and, as a result, falsified residual stress distributions will be determined.

With the X-ray method and also with the application of the incremental hole drilling method for the analysis of residual stress depth distributions, it must be taken into account that in principle only the plane stress state parallel to the component surface can be imaged, whereas the residual stress component normal to the component surface can usually be imaged with reasonable effort using laboratory methods is not solvable.

With regard to the use of the X-ray method with relatively small layer removal depths of a few  $10 \mu\text{m}$  to a few  $100 \mu\text{m}$ , there is no need to worry about any rearrangement effects. In the case of larger removal depths, however, any redistribution effects of the residual stress distribution as a result of the material removal must be taken into account.

This must be done using suitable correction algorithms, for example according to Moore and Evans [13] or using numerical approaches (e.g., FEM). In this case, the method can also be used for removal depths of a few millimetres.

With the **incremental hole drilling method**, nominal hole diameters of  $\varnothing 0.8 \text{ mm}$  and  $\varnothing 1.6 \text{ mm}$  are usually realized as standard. This allows the determination of the residual stress depth distribution down to depths of approximately  $0.55 \text{ mm}$  or  $1.2 \text{ mm}$  (corresponds to approximately 65 % to 70 % of the hole diameter).

Greater depths can also be mapped here, for example by deviating from the standard and working with larger hole diameters. However, deviation from the standard means also that the established strain gauges for deviating hole diameters are not available and must be designed and manufactured at immensely higher prices. In general, it should be noted that the highest possible number of revolutions ( $100,000 \text{ min}^{-1}$ ) of the drilling tool must be

realized when drilling, so that no additional residual stresses are induced in the measuring point by the drilling procedure itself. At the same time, of course, the use of a larger hole diameter inevitably means a loss of spatial resolution and requires that the calibration curves, which are stored in the commercial evaluation software for the given standard hole diameters, have to be calculated first. Here it must be mentioned that not all commercially available hole drilling evaluation software has a data exchange interface to allow for reading in case-specific calibration data provided from the user. Hence, due to the restrictions mentioned and the fact that the strain gauge measurement technology and the underlying calibration functions for hole diameters that deviate from the standard are not available, this procedure is not recommended at this point.

Another way to increase the depth when using the incremental hole drilling method is to extensively remove this zone near the surface after drilling the first hole (e.g., by milling in combination with subsequent electrochemical material removal) and to reapply the incremental hole drilling method on the newly created surface.

Here, too, it is of course necessary to record the redistribution effects as a result of the local material removal and to correct the residual stress analyses for these effects. Due to the many sources of error in it, this approach is not recommended at this point.

With regard to the presence of lateral residual stress distributions, a spatial resolution that is as high as possible is desirable, i.e., the area integrated over the analysis methods should be kept as small as possible. With the diffraction method, this can be done via the choice of apertures. However, the primary aperture must also be chosen large enough that a sufficient number of crystallites oriented in a favorable diffraction manner can be detected. The choice of the primary aperture and the spatial resolution that can be achieved are thus directly linked to the local microstructure formation. With the incremental hole drilling method, the smallest nominal drill hole diameter in standard use is  $\varnothing 0.8$  mm and thus limits the spatial resolution that can be achieved.

In the application of the incremental hole drilling method on complex shaped components the selection of the measuring position must be in accordance with the geometric boundary conditions that limit the applicability of the method. These conditions are the minimum size of the component, the distance of the hole to component edges, the distance between neighboring holes, the local radius of curvature and the thickness of the component. All these limitations scale with the nominal hole diameter. Recommended values are for instance listed in the descriptive standard ASTM837-20.

The **contour method** has established itself as an alternative method in the area of formed solid components. This process is based on the fact that when a component is separated using a plane cut, the release of residual stresses normal to the cut surface creates a topography. This can be measured using coordinate measuring machines (CMM). These displacements are then applied to an FEM model of the component, so that in the end a 2D distribution of the residual stress component normal to the cut surface can be determined. Figure 5.1 shows an exemplary result that arose as part of a cross-subproject cooperation in the SPP2013 for the case of a hot-bulk-formed component made of steel 100Cr6 (AISI 52100).

Figure 5.1 shows the results of the spatial distribution of tangential RS on the cut surface of AISI 52100 specimens after cooling in water as well as cooling in air, for both, numerical simulation (left) and experimental analysis using the contour method (right). For the water-cooled specimen, the FE simulation calculates a ring-shaped graded distribution of tangential RS for the thick-walled side. The contour method, applied to the correspondingly manufactured specimen, confirms the ring-shaped graded distribution of the tangential RS for the thick walled side. The shape of the surrounding tensile RS distribution and centred compressive RS distribution are qualitatively in very good accordance with the numerical results. A detailed discussion of the results is given in the original paper [14].

What can already be seen from the representation in figure 5.1 is that the contour method is excellently

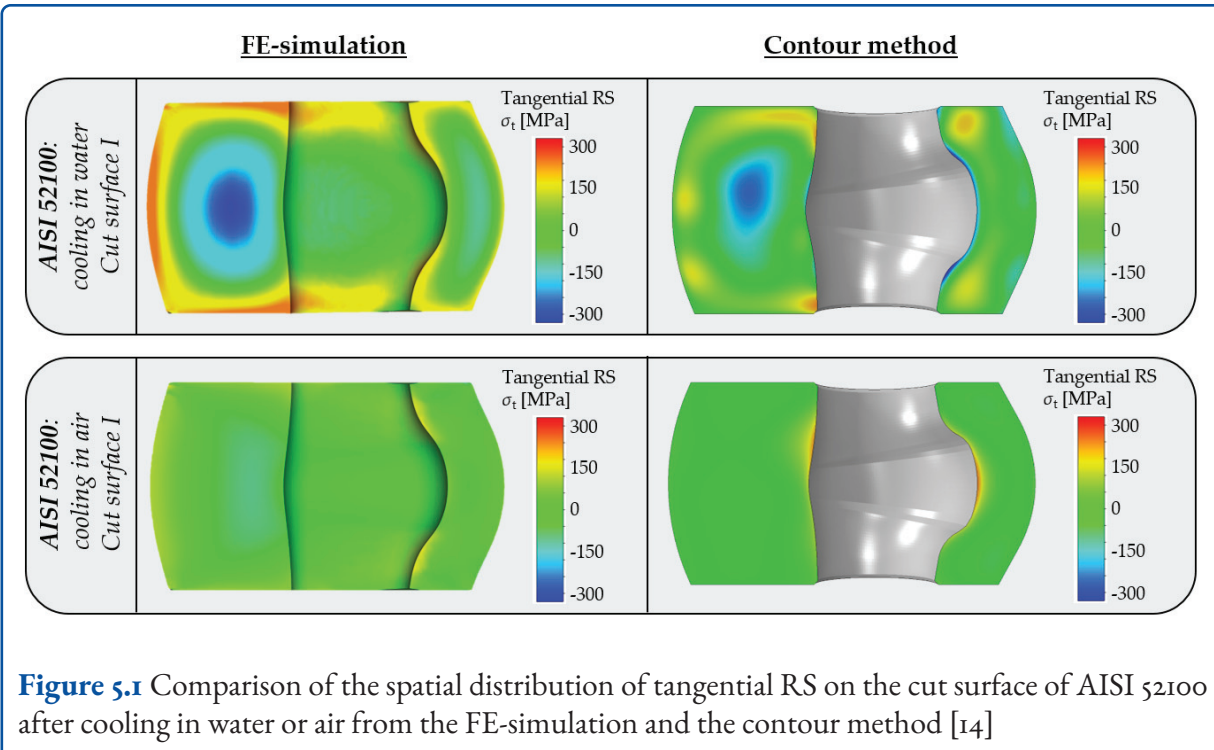


**Figure 5.1** Comparison of the spatial distribution of tangential RS on the cut surface of AISI 52100 after cooling in water or air from the FE-simulation and the contour method [14]

suited to making a direct comparison with FE simulations in terms of its representation of results. However, it should be mentioned that the process requires a minimum component size, so that the method is not suitable for determining residual stress distributions on thin-walled components. Furthermore, the method is also very well suited to determine long-range residual stress distributions on solid components. However, steep gradients of residual stress distributions cannot be mapped as well with this method. The representation of the residual stresses near the component edges is also insufficient. If these are also of particular interest, it is recommended that the residual stress distributions near the surface are determined using complementary methods, such as the incremental hole drilling method or X-ray diffraction.

As already mentioned, the  $\sin^2 \psi$ -method is usually used for X-ray residual stress analysis in laboratory practice, since it is based on the determination of relative line position shifts and the absolute value for the reference state  $D_0$  (strain-free material state) can only be known approximately [7]. However, this method is limited to isotropic material states and therefore cannot be used reliably for materials with a pronounced crystallographic texture.

With regard to forming processes, further problems are associated with the application of experimental methods for residual stress analysis, since these processes are often accompanied by the development of a local crystallographic texture.

In any case, the application of the experimental residual stress analysis methods is associated with problems if there are pronounced preferred crystallographic orientations (local: coarse grain, global: texture) [15]. On the one hand, this can be due to measurement-related aspects, but also to evaluation-related problems. Metrological problems arise when there are preferred crystallographic orientations, mainly in the diffraction method. Here, in special component orientations, due to strong preferred orientations, sometimes no measurement signal can be detected, since crystallites that are oriented too little to favor diffraction simply contribute to the diffraction. Measurement and evaluation strategies described in the literature allow X-ray residual stress analyses to be carried out successfully in the case of pronounced textures (crystallite group method [16], stress factors  $F_{ij}$  [17]). However, the application of these special methods is very complex, as they require sufficient prior knowledge of the local preferred orientation,

for example by determining the orientation distribution function (ODF). When using the  $\sin^2 \psi$  method for materials with a cubic crystal structure, lattice planes of the type {hhh} and {hoo} also provide approximately linear distributions of the line positions over  $\sin^2 \psi$  for textured materials and can be used for the  $\sin^2 \psi$  method [18]. However, nonlinearities also occur for these lattice planes if micro-residual stresses are present. The crystallite group method can only be used with sufficiently sharp textures if the texture can be characterized by a few ideal layers or crystallite groups, respectively. Consequently, for certain measurement directions only one crystallite group contributes to the interference phenomenon of the lattice plane. In the case of multi-phase materials in particular, it can be ruled out that no other crystallite group contributes to the intensity pole [18].

Alternatively, instead of the lattice plane dependent DEC stress factors, which are also dependent on the respective measurement direction, are used for the residual stress analysis [17]. Similar to the DEC, the stress factors can be determined experimentally or analytically. It should be noted here that the stress factors may only be applied if no residual stresses of type II are present. The models for calculating the stress factors are based on a linear-elastic assumption and are therefore inaccurate when ES are caused by plastic deformations [19]. Both methods have in common that the local texture must be known, e.g., in the form of the orientation distribution function (ODF). Even if the material behavior is isotropic, non-linear curves of the lattice spacing  $D^{hkl}$  vs.  $\sin^2 \psi$  occur with increasing plastic deformation. These effects are caused by the plastic anisotropy of the crystallites and cannot be taken into account in the evaluation even if stress factors are used.

The limitations and difficulties of residual stress analysis on highly textured material states described above also apply in principle to the neutronographic method. In [20], for example, the crystallite group method is used to determine residual stresses in a cold-rolled steel sheet using neutron diffraction and the  $\sin^2 \psi$  method. This makes use of the fact that, in comparison to RSA, line positions up to  $\sin^2 \psi = 1$  can be measured with-

out any problems, which is particularly advantageous for textured materials, since intensity poles are often present at  $\sin^2 \psi \geq 0.75$ . The substitution of the DEC by constants dependent on the ODF is also used in neutron diffraction methods [21]. Phase-specific residual stresses in a textured ferritic-pearlitic steel wire were determined in [21]. An elegant alternative to determining the residual stress state is the determination of strain pole figures [22], from which the stress orientation distribution function [23] can be derived, which gives a connection between crystal orientation-dependent residual stresses and the Euler space. In addition to the influence of the texture, the micro-residual stresses are also taken into account. Subsequently, residual stresses can be calculated for specific crystal orientations. However, this method is very time-consuming and expensive.

Also in the field of mechanical methods for residual stress analysis, first approaches were presented to carry out meaningful residual stress analyses in the case of strong crystallographic textures. Here are the first results from the application of the incremental hole drilling method on textured material states [24]

With ultrasonic methods, it is possible to calculate the residual stress state from ultrasonic transit time measurements if the relevant material-specific constants are known and the use of the acousto-elastic effect is used. Electromagnetic test methods are based on the evaluation of electrical and magnetic parameters, which differ in terms of their interaction with structural parameters and stress fields.

In this way, the methods allow a quantitative and qualitative determination of material parameters and stress states.

Acoustic and magnetic methods for the analysis of residual stresses strongly depend on the local microstructure of the material to be examined.

In addition, they integrate, especially in the depth direction, over a relatively large measurement volume with sometimes very complex non-isometric microstructure states and strong local gradients in the lateral and in depth directions, so that these

methods require careful calibration to the local microstructure.

In principle, the use of acoustic and micro-magnetic methods is not recommended when there are preferred crystallographic orientations, since the separation or the separate addressing of the influencing variables with these methods is possible only with great effort or even not at all. Overall, it is recommended that these methods should only be applied accompanying to forming processes if it is guaranteed that the process is characterised by strictly reproducible microstructure since the calibration of the methods is very sensitive to small changes, e.g., in grain size distribution, grain morphologies or crystallographic texture.

## 5.2 Special Challenges with Formed Sheet Metal Components

Sheet metal formed parts, such as those used in the automotive industry, usually have large dimensions (in the cm to m range) but low wall thicknesses of just a few mm. Due to the strong gradients of plastic deformation that typically occur in the forming process, pronounced residual stress gradients are to be expected, both in the direction of the sheet thickness and in the direction of the plane of the sheet.

Only a few methods are suitable for a locally resolved residual stress analysis on thin-walled components.

Among the laboratory methods, the incremental hole drilling method and the X-ray methods can be used here, although certain limitations must also be considered with these methods (see, e.g., standard ASTM837-20 for the hole drilling method). When using the incremental hole drilling method, it should be noted that sheet metal samples have a lower bending stiffness than do solid components.

If the balance of residual stresses is disturbed by the introduction of the blind hole, deviating strain releases occur [25].

If the component thickness is below the minimum required to carry out the standardized procedure, this must be taken into account by selecting special calibration (case-specific calibration) data adapted to the component geometry in the stress evaluation.

Otherwise, the evaluation with standardized calibration data sometimes leads to significant errors. Furthermore, when carrying out the hole drilling experiment, attention must be paid to suitable component support or component fixture, respectively. The support condition should allow free deformation on the top and bottom of the sheet, see figure 5.2. Only if this is considered does the application of numerically calculated calibration data, adjusted to the sheet thickness, finally lead to an improved stress evaluation [26].

When using X-ray diffraction, it must be taken into account that the dimensions of the sheet metal parts often exceed the available sample space in stationary diffractometers. Mobile diffractometers are advantageous here, although their basic limitations, such as the severely limited  $\psi$ -angle range, remain. With regard to an experimental residual stress analysis on sheet metal components, the measuring points that are difficult to access, e.g., beads and radii, are often of interest. In order to avoid shadowing of the X-ray radiation at such measuring points, or to be able to analyse the components in stationary diffractometers, it is therefore essential to section smaller samples from the component. The effects of redistributions of the original residual stress states, which inevitably accompanies the removal of stressed material and caused changes to the residual stress distributions at the chosen measuring position, must be taken into account in this case. With the help of numerical methods, the stress redistribution can be simulated by freeing the measuring point. In addition, strain relaxation can be recorded during the cutting process using strain gauges.

Problems that are connected to crystallographic textures that are often present in sheet metals were already discussed before and must be considered accordingly.

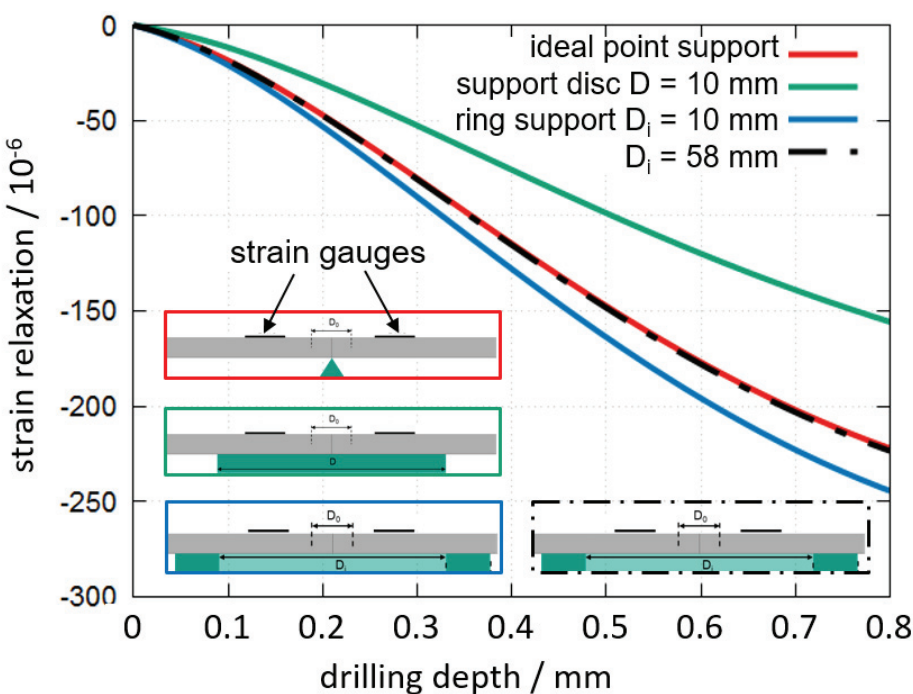


**Figure 5.2** Influence of the sample support or sample fixture on the initiation of strain when performing the incremental hole drilling method on a thin-walled component; ideal point support (red), disc support with  $D_i = 10$  mm (green), ring support with  $D_i = 10$  mm (blue) and ring support with  $D_i = 58$  mm (black) – data modified from [26].

### 5.3 Procedure for Analyzing Multi-phase Material States

The analysis of the phase-specific residual stresses requires the use of diffraction methods such as X-ray, synchrotron X-ray or neutron diffraction methods.

If the microstructure is sufficiently fine-grained, well-established methods have been described for isotropic material states [27, 28].

The basic requirement is that the phase components are sufficiently high to be able to record a diffraction line that can be evaluated at all. For reasons of practical relevance, a minimum volume percentage of approximately 10 % is often given here.

For the displacement of the line positions of the diffraction lines, which are usually evaluated to de-

termine the residual stresses, the sum of the residual stresses of the kind I (macro-residual stresses) and the mean values of the homogeneous (directed) components of the micro-residual stresses (kinds II and III) causal.

The macro-residual stresses, which are important for the engineer, can be determined from the phase-specific residual stresses using a simple rule of mixtures if the existing phase components are known.

The basic requirement here is that the phase-specific residual stresses are also determined in all phases. Conversely, it is also possible to separate the macro-residual stresses from the homogeneous components of the micro-residual stresses, provided that measurements are carried out in all material phases present and the volume proportions of the phases in the total volume of the material are reliably determined [29].

Furthermore, the mean values of the inhomogeneous (non-directional) micro-residual stresses can also be determined on the basis of the widths of the interference lines (half-value width, integral width).

Methods are described in the literature, such as how the degree of strain hardening of a material or the dislocation density can be determined [30, 31].

In the case of multi-phase materials, the crystallographic texture of each phase must be determined for components produced by forming. In addition, the stress-free lattice plane distances  $D_0$  must be known for all phases in order to calculate the residual stresses.

In the presence of gradients (chemical gradients) or a rough multi-phase character, this reference value is difficult to determine. In particular, it is unclear what influence a crystallographic texture has on the determination of the lattice parameters of the strain-free state and thus on the analysis of the local residual stresses in multi-phase material states.

## 5.4 Real-time Insights into Metal Forming Processes Using Diffraction Methods

Diffraction methods as well as ultrasonic and magnetic methods are fundamentally suitable for mapping the development of residual stresses over time during the course of technical manufacturing processes (in-situ analyses). However, the application of the acoustic and magnetic methods appears to be problematic, since the quantities recorded by measurement are sensitive to the existing residual stresses, but also to the locally present microstructures.

In the case of time-varying formations of the local microstructures, a suitable calibration is extremely problematic or even impossible. The greatest potential can be attributed to the diffraction methods using high-energy synchrotron radiation (angle- and energy-dispersive), especially in the case of fast processes. Depending on the beam source used,

there is usually a sufficient photon flow here, which, in combination with fast detector technology, even allows real-time insights into fast-moving heat treatment processes, for example.

In this way, the temporal development of the mechanical stresses and the transformation kinetics in relatively fast technical heat treatment processes such as arc welding [32–34], laser beam hardening [35, 36] or case hardening with low-pressure carburization [37, 38]. In the field of forming processes, for example, in situ diffraction analyses during the rotary swaging process or the deep rolling of steel [39] should be mentioned. With the use of fast measuring techniques, a deeper understanding of the process can be gained via in situ stress analyses and the optimization of the process can be advanced. In addition, the in situ diffraction analyses allow the determination of extensive databases for the time-resolved validation and ultimately also the improvement of the prediction accuracy of process simulations.

As a result of the different interactions between the neutron radiation and the material volume and the associated lower flux at the sample, neutron radiation could be used to carry out processes that take place more slowly, such as, e.g., cooling from the melt in casting experiments [40, 41].

Furthermore, in situ stress analyses are also suitable for studying the load distribution behavior in the elastic and in the elastic-plastic material regime in multi-phase material states in defined load stress tests. While laboratory tests on load distribution are usually limited to a few families of lattice planes  $hkl$ , a large number of different lattice planes of all material phases contributing to diffraction can be studied using high-energy synchrotron X-ray radiation in large-scale research, see figure 5.3.

In this way, detailed knowledge about the direction-dependent, phase-specific hardening behavior and, if crystallographic textures are present, the development of these with increasing plastic deformation can be analysed. In particular, these test data then offer the possibility of applying the complex approach for calculating harmonic strain and stress functions, which also enables a reliable residual

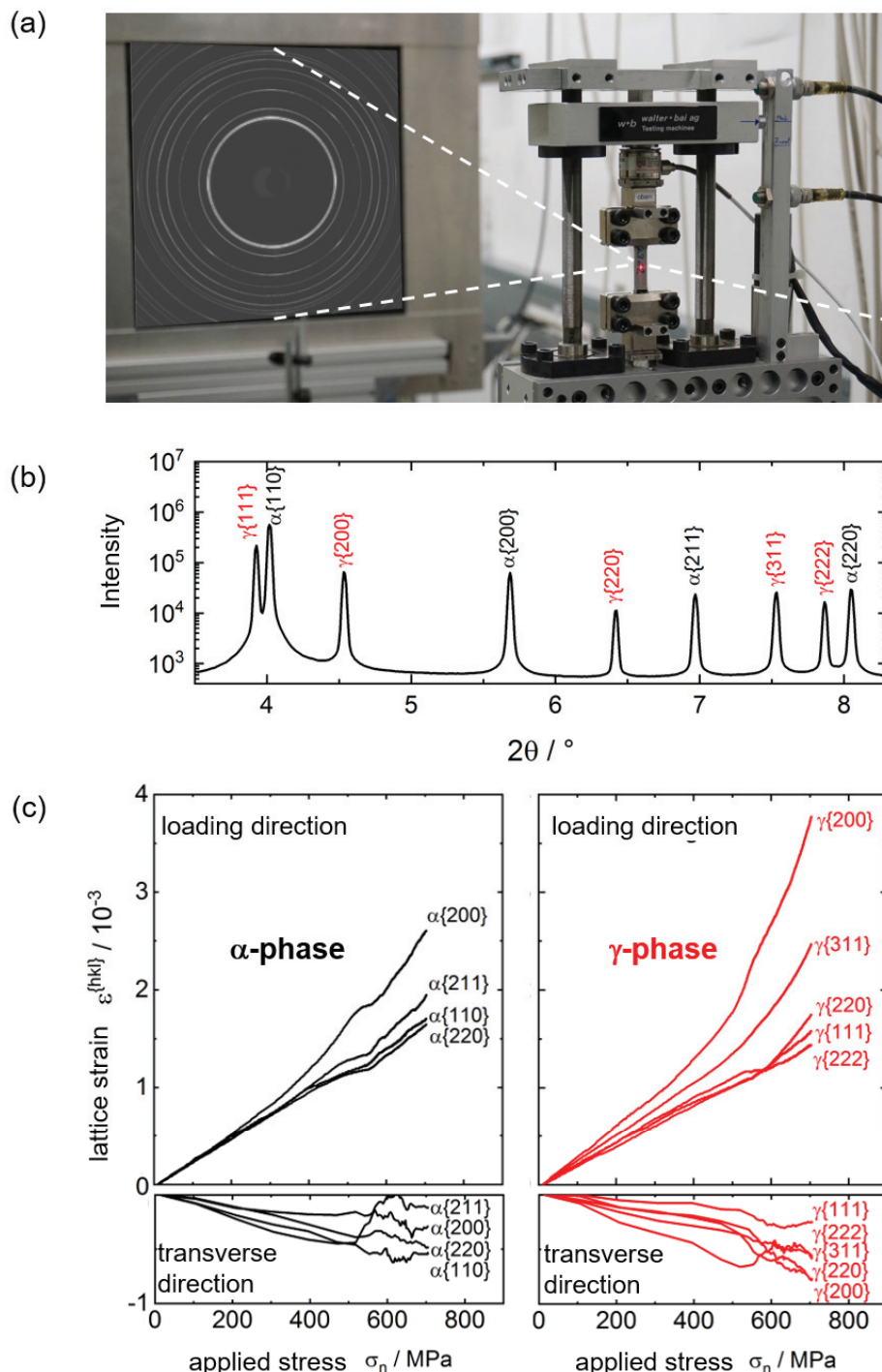


**Figure 5.3** In situ tensile tests on austenitic-ferritic stainless steel EN 1.4362 at the Deutsches Elektronen Synchrotron DESY (Peta III, Po7): a) Experimental setup; b) diffractogram of an angular segment of the diffraction rings; c) Lattice strain development for ferrite ( $\alpha$ ) and austenite ( $\gamma$ ).

stress analysis for heavily plastically deformed, textured material states [42]. Figure 5.3 shows the first exemplary results of such in-situ investigations under uniaxial tensile stress (for the case of the lean du-

plex stainless steel X<sub>2</sub>CrNiN<sub>23-4</sub>, with the phases ferrite ( $\alpha$ ) and austenite ( $\gamma$ ) in a ratio of approximately 50: 50.

## 5.5 Benchmarks

The task of the expert group within the framework of the SPP2013 is to discuss and ultimately provide suitable measurement and evaluation strategies for sometimes complex issues through intensive cooperation between the participating institutions. In addition, the joint work in the expert group focuses on upgrading the different measurement methods for the respective application. In addition, the calibration of the less well-established methods was aimed at in cross-sub-project bilateral/trilateral cooperation by comparing different measurement techniques. The insights gained in this cooperation are reflected back to the group of participants in the regular specialist group meetings so that a valuable transfer of knowledge takes place in this way.

In the course of the work of the expert group, various benchmarks and interlaboratory comparisons were initiated with the aim of bringing the experimental groups together and discussing and finally defining the measurement and evaluation strategies suitable for special measurement tasks.

For this purpose, an interlaboratory test was initially carried out in which the residual stress distribution induced by shot peening was to be determined in a defined – initially single-phase – material condition using different measurement methods. In another round robin test, the depth distributions of the residual stresses on bars that were subjected to a defined elastic-plastic torsional loading were determined.

### Benchmark on Shot-peened Steel 42CrMo4 Samples

The benchmark on the shot-peened sample of the heat-treated steel 42CrMo4, which is considered to be single-phase, was initially initiated in order to determine the extent to which comparable depth distributions of the residual stresses can be mapped using different methods and different measurement and evaluation strategies. On the process side, residual stress depth distributions were determined us-

ing X-ray residual stress analysis, incremental hole drilling methods, micro-magnetic methods and nanoindentation. The results showed that, after adjusting the measurement and evaluation conditions using the X-ray method and the incremental hole drilling method, the participating institutions were ultimately able to determine comparable residual stress depth distributions.

### Benchmark on Torsionally Loaded Cylindrical Specimens

In a further round robin test, which was much more extensive, three different materials, which were all materials that were applied in various sub-projects were examined. The materials applied for this benchmark are 1.4404 (austenitic steel X2CrNiMo17-12-2, fcc), heat-treated steel 1.7225 (42CrMo4, in the heat-treated state, bcc) and duplex stainless steel 1.4462 (X2CrNiMoN22-5-3, fcc/bcc in a 50: 50 ratio). In figure 5.4 the work hardening curves measured using a standard tensile test for the three materials in the as delivered state are compared.

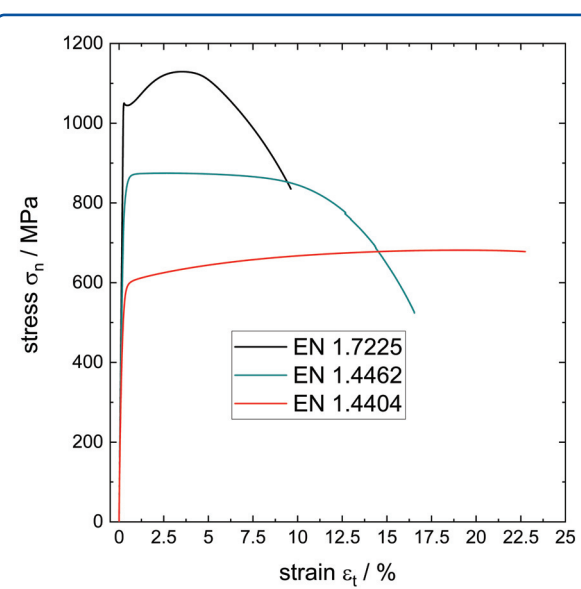


**Figure 5.4** Tensile test results of the three materials investigated (mean values of three samples each).

An elastic-plastic torsion stress (free-end torsion test) up to a maximum machine angle of 80° was

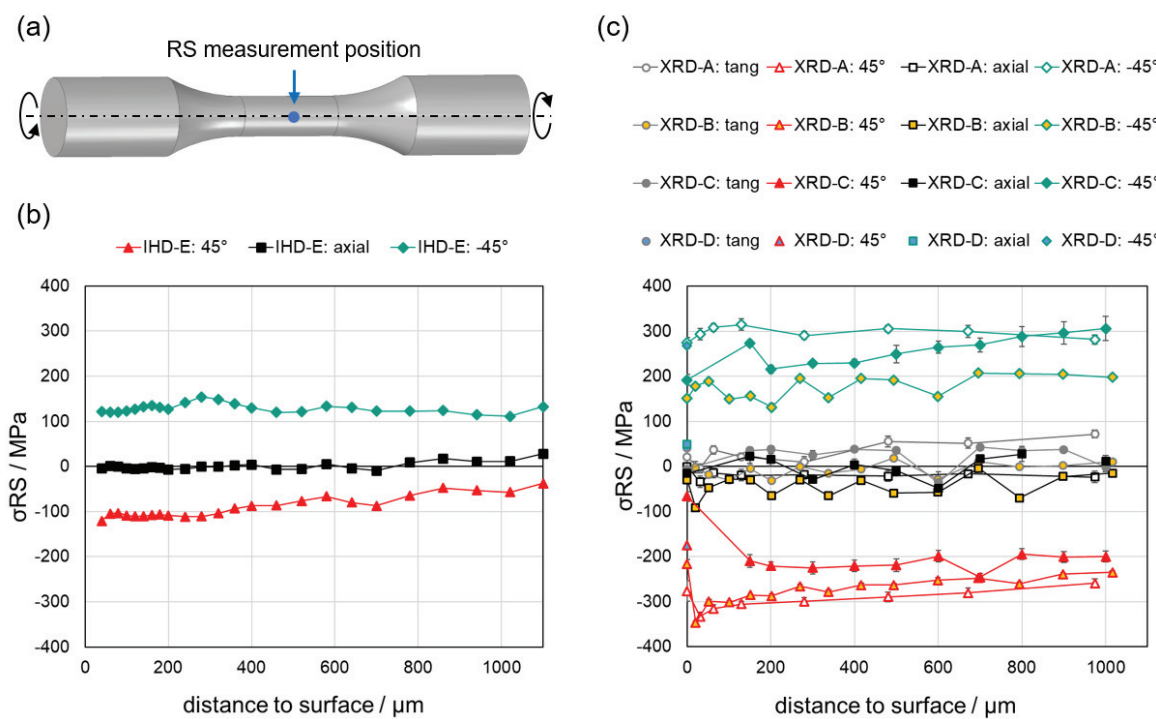


**Figure 5.5** Benchmark on torsionally deformed cylindrical specimens of quenched and tempered steel 1.7225 (42CrMo4): (a) residual stress measurement position; (b) residual stress state according to the incremental hole drilling method (IHD) performed by institute E; (c) residual stress depth gradient according to XRD measurements combined with stepwise layer removal performed by institutes A-D.

applied to cylindrical specimens with a diameter of  $\varnothing$  10 mm in the measuring length cross-section. Figure 5.6 shows the mean curves of the instrumented torsion test with realized machine angles of  $80^\circ$  (torsional moment is plotted vs. the machine angle). Since the benchmark is designed to be interdisciplinary these curves for the tensile tests and from the instrumented torsional tests are used in the working group "mechanics" (Fachkreis Mechanik) as input data for the numerical simulations of the torsional tests. Also information about the microstructure and about the phase-specific crystallographic texture as ODF (orientation distribution functions).

The samples therefore showed characteristic depth distributions of the residual shear stresses, which should be resolved using different analysis methods. What is special about the choice of material is that the austenitic steel 1.4404 and the duplex

stainless steel 1.4462 already have manufacturing related crystallographic (phase-specific) textures in the as-delivered states. In addition to the texture problem, the duplex stainless steel also addresses the problem of multi-phase materials. In the further course of the benchmark, the experimentally determined results were compared with results from numerical simulations of the torsion tests as stated before. The target values in both, the experimental work and the numerical simulations, are the depth distributions of the residual stresses. A joint consideration of the results of the numerical and experimental part of the torsion benchmark test can then be found in the presentation of the "mechanics" working group (Fachkreis Mechanik).

Figure 5.5 shows an example of the experimental results for this torsion benchmark for the material 1.7225. In the partial figure (c) only the results of the X-ray analyses from 4 different institutions (A, B, C

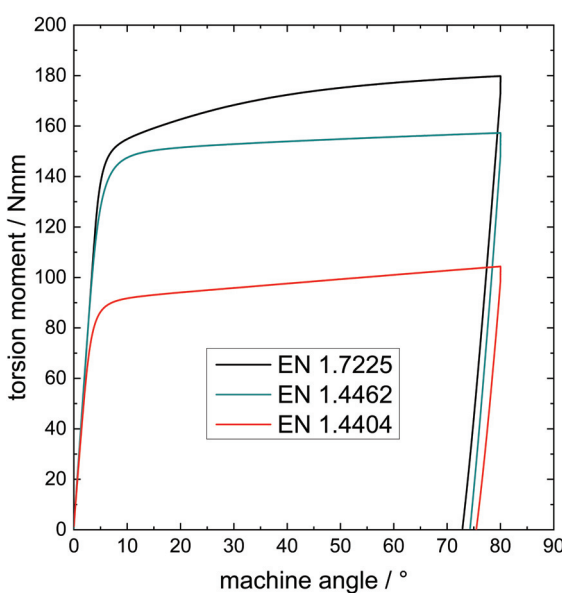


**Figure 5.6** Torsional moment for “free-end torsion” tests up to a machine angle of 80° (including relaxation and unloading) of the three materials investigated (mean values of 8 samples each).

and D) are shown in this exemplary representation of parts of the results for the components in the axial direction, in the tangential direction and for the residual shear stress components  $-45^\circ$  and  $45^\circ$ . In partial figure (b) the corresponding results of the incremental hole drilling method (institute E) are shown. The results indicate that in all cases the shear stress state was well determined, while hole drilling as well as XRD in axial direction proved an almost a stress-free state. The different measurement and evaluation strategies result in a deviation of slightly more than 100 MPa at maximum for the values determined with the X-ray stress analysis. Moreover, there is a tendency to determine slightly lower shear residual stress components using the incremental hole drilling method.

## References

- [1] Viktor Hauk. *Structural and residual stress analysis by nondestructive methods: evaluation, application, assessment*. Elsevier Science, 1997. ISBN: 978-0-08-054195-2.

[2] G. S. Schajer. “Relaxation Methods for Measuring Residual Stresses: Techniques and Opportunities”. In: *Experimental Mechanics* 50 (8 2010), pp. III7–III27. ISSN: 00144851. DOI: 10.1007/s11340-010-9386-7.

[3] W. Voigt. “Ueber die Beziehung zwischen den beiden Elasticitätsconstanten isotroper Körper”. In: *Annalen der Physik* 274 (12 1889), pp. 573–587. DOI: 10.1002/andp.18892741206.

[4] A. Reuss. “Berechnung der Fließgrenze von Mischkristallen auf Grund der Plastizitätsbedingung für Einkristalle.” In: *ZAMM - Journal of Applied Mathematics and Mechanics / Zeitschrift für Angewandte Mathematik und Mechanik* 9 (1 Jan. 1929), pp. 49–58. ISSN: 1521-4001. DOI: 10.1002/ZAMM.19290090104.

[5] J. D. Eshelby. “The determination of the elastic field of an ellipsoidal inclusion, and related problems”. In: *Proceedings of the Royal Society of London. Series A. Mathematical and Physical Sciences* 241 (1226 Aug. 1957), pp. 376–396. ISSN: 0080-4630. DOI: 10.1098/RSPA.1957.0133.

[6] E. Kröner. “Berechnung der elastischen Konstanten des Vielkristalls aus den Konstanten des Einkristalls”. In: *Zeitschrift für Physik* 151 (4 Aug. 1958), pp. 504–518. ISSN: 14346001. DOI: 10.1007/BF01337948.

[7] Eckard Macherauch and Paul Müller. “Das  $\sin^2\psi$ -Verfahren der röntgenographischen Spannungsmessung”. In: *Zeitschrift für angewandte Physik* 13 (7 1961), pp. 305–312.

[8] A Kienzler et al. “Analysis of Residual Stresses of micro milled and micro abrasive peened moulds”. In: *HASYLAB Annual Report* (2006), pp. 445–446.

[9] P. Pagliaro et al. “Measuring Inaccessible Residual Stresses Using Multiple Methods and Superposition”. In: *Experimental Mechanics* 51 (7 2011), pp. II23–II34. ISSN: 00144851. DOI: 10.1007/s11340-010-9424-5.

[10] M.T. Hutchings et al. *Introduction to the Characterization of Residual Stress by Neutron Diffraction*. 1st ed. Taylor & Francis Ltd, Feb. 2005. ISBN: 9780429220791. DOI: 10.1201/9780203402818.

- [ii] K. Tanaka H. Fujiwara T. Abe, ed. *An Improved Technique for X-Ray Residual Stress Determinations on Ceramics with Steep Subsurface Stress Gradients*. 1st ed. Elsevier Applied Science, 1992. ISBN: 9781851668571.
- [12] H. Ruppertsberg and I. Detemple. "Evaluation of the stress field in a ground steel plate from energy-dispersive X-ray diffraction experiments". In: *Materials Science and Engineering: A* 161.1 (1993), pp. 41–44. ISSN: 0921-5093. DOI: 10.1016/0921-5093(93)90473-R.
- [13] M G Moore and W P Evans. "Mathematical Correction for Stress in Removed Layers in X-Ray Diffraction Residual Stress Analysis". In: *SAE Transactions* 66 (1958), pp. 340–345.
- [14] Bernd Arno Behrens et al. "Investigations on Residual Stresses within Hot-Bulk-Formed Components Using Process Simulation and the Contour Method". In: *Metals* 11 (4 Mar. 2021), p. 566. ISSN: 2075-4701. DOI: 10.3390/MET11040566.
- [15] Viktor Hauk and Horst Sesemann. "Abweichungen von linearen Gitterebenenabstandsverteilungen in kubischen Metallen und ihre Berücksichtigung bei der röntgenographischen Spannungsermittlung". In: *International Journal of Materials Research* 67.9 (1976), pp. 646–650.
- [16] Viktor Hauk and Guillaume Vaessen. "Eigenspannungen in Kristallitgruppen texturierter Stähle". In: *Zeitschrift fuer Metallkunde/Materials Research and Advanced Techniques* 76 (2 Feb. 1985), pp. 102–107. ISSN: 00443093. DOI: 10.1515/IJMR-1985-760205/HTML.
- [17] Herfried Behnken and Viktor Hauk. "Berechnung der röntgenographischen Spannungsfaktoren texturierter Werkstoffe - Vergleich mit experimentellen Ergebnissen". In: *Zeitschrift für Metallkunde* 82 (2 1991), pp. 151–158.
- [18] Paul Dieter Evenschor and Viktor Hauk. "Röntgenographische Elastizitätskonstanten und Netzebenenabstandsverteilungen von Werkstoffen mit Textur". In: *Zeitschrift fuer Metallkunde/Materials Research and Advanced Techniques* 66 (3 1975), pp. 164–166. ISSN: 00443093. DOI: 10.1515/IJMR-1975-660308/HTML.
- [19] P. Van Houtte and L. De Buyser. "The influence of crystallographic texture on diffraction measurements of residual stress". In: *Acta Metallurgica et Materialia* 41.2 (1993), pp. 323–336. ISSN: 0956-7151. DOI: 10.1016/0956-7151(93)90063-X.
- [20] L Pintschovius, V Hauk, and W K Krug. "Neutron Diffraction Study of the Residual Stress State of a Cold-rolled Steel Strip". In: *Materials Science and Engineering* 92 (1987), pp. 1–12.
- [21] K. Van Acker et al. "Neutron diffraction measurement of the residual stress in the cementite and ferrite phases of cold-drawn steel wires". In: *Acta Materialia* 44 (10 Oct. 1996), pp. 4039–4049. ISSN: 1359-6454. DOI: 10.1016/S1359-6454(96)00051-1.
- [22] J. Hoffmann et al. "Flächenpolfiguren und Gitterdeformationspolfiguren von texturierten Werkstoffzuständen". In: *HTM Journal of Heat Treatment and Materials* 38 (4 July 1983), pp. 180–183. ISSN: 1867-2493. DOI: 10.1515/HTM-1983-380404/PDF.
- [23] Y. D. Wang et al. "Stress-orientation distribution function (SODF) - description, symmetry and determination". In: *Materials Science Forum* 347 (2000), pp. 66–71. ISSN: 02555476. DOI: 10.4028/www.scientific.net/msf.347-349.66.
- [24] Simone Schuster and Jens Gibmeier. "Residual stress analysis of strongly textured materials by means of the incremental hole-drilling method - Survey on the application limits". In: *Materialprüfung/Materials Testing* 56 (11-12 2014), pp. 915–922. ISSN: 00255300. DOI: 10.3139/120.110651.
- [25] G. S. Schajer and C. Abraham. "Residual Stress Measurements in Finite-Thickness Materials by Hole-Drilling". In: *Experimental Mechanics* 54 (9 2014), pp. 1515–1522. ISSN: 17412765. DOI: 10.1007/s11340-014-9935-6.
- [26] Nicola Simon, Tobias Mrotzek, and Jens Gibmeier. "Reliable Residual Stress Analysis for Thin Metal Sheets by Incremental Hole Drilling". In: *Materials Performance and Characterization* 7 (4 2018). ISSN: 21653992. DOI: 10.1520/MPC20170111.

- [27] Lothar Spieß et al. *Moderne Röntgenbeugung*. 3. Auflage. Springer Fachmedien Wiesbaden, 2019. DOI: 10.1007/978-3-8348-8232-5.
- [28] Ismail C. Noyan and Jerome B. Cohen. *Residual Stress*. Springer New York, 1987. ISBN: 978-1-4613-9571-3. DOI: 10.1007/978-1-4613-9570-6.
- [29] Herfried Behnken. "Mikrospannungen in vielkristallinen und heterogenen Werkstoffen". habilitation. Rheinisch Westfälische Technische Hochschule (RWTH) Aachen, 2003. ISBN: 3-8322-1384-8.
- [30] B. E. Warren and B. L. Averbach. "The effect of cold-work distortion on x-ray patterns". In: *Journal of Applied Physics* 21 (6 1950), pp. 595–599. ISSN: 00218979. DOI: 10.1063/1.1699713.
- [31] G. K. Williamson and W. H. Hall. "X-ray line broadening from filed aluminium and wolfram". In: *Acta Metallurgica* 1 (1 Jan. 1953), pp. 22–31. ISSN: 0001-6160. DOI: 10.1016/0001-6160(53)9006-6.
- [32] J Altenkirch et al. "Time-and temperature-resolved synchrotron X-ray diffraction: observation of phase transformation and strain evolution in novel low temperature transformation weld filler materials". In: *The journal of Strain Analysis for engineering Design* 46.7 (2011), pp. 563–579. DOI: 10.1177/0309324711413190.
- [33] S. S. Babu et al. "Time-resolved X-ray diffraction investigation of primary weld solidification in Fe-C-Al-Mn steel welds". In: *Acta Materialia* 50.19 (2002), pp. 4763–4781. ISSN: 1359-6454. DOI: 10.1016/S1359-6454(02)00317-8.
- [34] J. W. Elmer and T. A. Palmer. "In-situ phase mapping and direct observations of phase tranformations during arc welding of 1045 steel". In: *Metallurgical and Materials Transactions A* 37 (7 July 2006), pp. 2171–2182. ISSN: 10735623. DOI: 10.1007/BF02586137.
- [35] V. Kostov, J. Gibmeier, and A. Wanner. "Spatially resolved temporal stress evolution during laser surface spot hardening of steel". In: *Journal of Materials Processing Technology* 239 (Jan. 2017), pp. 326–335. ISSN: 0924-0136. DOI: 10.1016/J.JMATPROTEC.2016.08.035.
- [36] D. Kiefer et al. "Real-time stress evolution during laser surface line hardening at varying maximum surface temperatures using synchrotron X-ray diffraction". In: *Optics & Laser Technology* 140 (Aug. 2021), p. 106964. ISSN: 0030-3992. DOI: 10.1016/J.OPTLASTEC.2021.106964.
- [37] O. B. Tapar et al. "In-Situ Synchrotron X-ray Diffraction Investigation of Microstructural Evolutions During Low-Pressure Carburizing". In: *Metallurgical and Materials Transactions A: Physical Metallurgy and Materials Science* 52 (4 Apr. 2021), pp. 1427–1442. ISSN: 10735623. DOI: 10.1007/S11661-021-06171-2/FIGURES/15.
- [38] O. B. Tapar et al. "In situ Investigation during Low Pressure Carburizing by Means of Synchrotron X-ray Diffraction". In: *HTM - Journal of Heat Treatment and Materials* 76 (6 Dec. 2021), pp. 417–431. ISSN: 21941831. DOI: 10.1515/HTM-2021-0018/MACHINEREADABLECITATION/RIS.
- [39] Heiner Meyer and Jérémie Epp. "In Situ X-ray Diffraction Analysis of Stresses during Deep Rolling of Steel". In: *Quantum Beam Science 2018, Vol. 2, Page 20* (4 Sept. 2018), p. 20. ISSN: 2412-382X. DOI: 10.3390/QUBS2040020.
- [40] Josef Reissner, ed. *Umformtechnik multimedial: Werkstoffverhalten, Werkstückversagen, Werkzeuge, Maschinen*. Carl Hanser Verlag, 2009. ISBN: 978-3-446-42098-4.
- [41] U. Wasmuth et al. "Optimisation of composite castings by means of neutron measurements". In: *CIRP Annals* 57.1 (2008), pp. 579–582. ISSN: 0007-8506. DOI: /10.1016/j.cirp.2008.03.079.
- [42] V Schulze. *Modern mechanical surface treatment: states, stability, effects*. John Wiley & Sons, 2006.

## 6 Targeted Induction and Stabilization of Residual Stresses in Austenitic Disc Springs by Incremental Forming and Integrated Surface Layer Treatment

Hajavifard, R.; Baak, N.; Walther, F.; Afzal, M. J.; Besong, L. I.; Buhl, J.

### 6.1 Summary

According to DIN 2092, disc springs are conical ring-shaped discs that provide high spring force with minimum spring deflection and optimum spatial efficiency. They must demonstrate considerable stability in their spring characteristics and fatigue strength during operation. Tensile stresses, which limit the application range of disc springs, are observed near the support point on the underside when the operational load is applied. Shot peening can create compressive stresses in these strained areas, extending the operating limits for specific yield and fatigue strength. However, the geometry and characteristics of the spring change during shot peening.

The project aimed to develop incremental forming processes that allow precise control of residual stresses in disc springs, resulting in improved spring characteristics and superior cyclic strength. The approach incorporates residual stress generation into the forming process, thereby avoiding costly post-treatment such as shot peening, the use of more expensive materials, manufacture of special springs, or an increase in the installation space.

The project's initial phase demonstrated that incremental forming allows an integrated process adjustment of desired compressive residual stresses, where the tangential compressive residual stresses exceed the radial stresses in the area of the spring with tensile stresses (see figure 6.1). These residual stresses balance the spring load. In metastable austenitic steels, localized contact also triggers martensite formation near the surface, resulting in high compres-

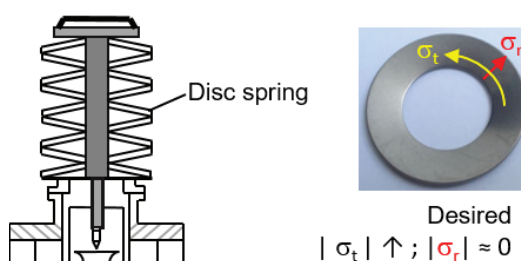


**Figure 6.1** Application of disc springs and desired tangential residual stresses.

sive residual stresses. This phase transformation affects fatigue properties and allows the spring characteristic to shift to higher forces, increasing the capacity for elastic energy storage.

In line with the objectives of the priority program, the aim was to gain a quantitative understanding of the residual stress evolution in austenitic stainless steel during incremental forming with integrated rolling. Here it is important to consider key disturbance variables and material inconsistencies that affect spring properties such as energy storage capacity, fatigue strength, and stability of spring characteristics. The aim is also to quantify the improvements in spring properties achieved by incremental forming and to validate the developed residual stress generation models and the rapid residual stress measurement method using micromagnetic measurements.

At the end of the project, the technological objective is to use temperature-controlled, rapid incremental forming processes to specifically compensate for material variations and to set desired spring characteristics with optimum stability under oscillating loads. In terms of the programmed objectives, the third application phase, therefore, aims to make the ISF process isothermal (minimizing the

disturbance “temperature”) despite high forming speeds, to design the associated tooling technology, and to use a predictive model to optimally adapt the forming parameters based on process force and martensite content to material variations. Another objective is to develop a multisensor system equipped with micromagnetic, thermal, and X-ray diffraction sensors and to use it for condition monitoring of the disc spring characteristics under specific operating conditions. Finally, neural network models are developed to improve or predict spring properties through the selective introduction of residual stresses in spring hard austenitic materials for disc spring operation at low and elevated temperatures.

## 6.2 Keywords

Disc spring; residual stress stability; incremental sheet forming; micromagnetic measurement, metastable austenitic stainless steel; martensite formation.

## 6.3 Introduction

The performance of disc springs can be improved by inducing compressive residual stresses in areas subjected to tensile loading, which delays the initiation and growth of fatigue cracks [1, 2]. The stability of these induced stresses, under continuous or repeated loading, is a critical feature. Shot peening, a traditional process for inducing compressive stresses, involves shooting tiny spherical hard metal or ceramic balls at high speed onto the sample surface, causing local plastic deformation and altering surface properties such as its topography, residual stresses, and work hardening [3, 4]. However, this technique can increase production time and cost and potentially degrade spring properties, including peened components’ surface geometry and texture. In addition, the random nature of the process makes it difficult to control the residual stress content in the treated components consistently [1, 5].

Metastable austenitic stainless steels (MASS), which are flexible, robust, and resistant to stress relaxation and corrosion, show promising potential for manufacturing disc springs. They can withstand plastic deformation during forming and operation. They can undergo a strain-induced phase transformation from  $\gamma$ -austenite to  $\alpha'$ -martensite, which increases the ductility and strength of the material [6, 7, 8].

In this research, the team used incremental sheet forming (ISF) as an alternative technique for inducing targeted compressive residual stresses in disc springs to optimize their properties. In the ISF process, a forming tool follows a toolpath defined by computer-aided manufacturing (CAM) program to form the sheet material to the desired final shape incrementally. The local deformation mechanisms of the ISF process can exceed the standard forming limit curves for similarly shaped components, which inherently increases residual stresses and is often associated with large geometric deviations [9, 10, 11]. Researchers have sought to utilize these forming-induced stresses to enhance the properties of the springs rather than relieving them, as is typically done in post-forming methods to improve the geometric accuracy of formed components [12].

According to a study by Katajärinne et al. [13], martensite transformation can be controlled by incremental sheet forming to modify the ductility and strength of the material. Previous research has investigated the evolution of near-surface compressive stresses on AISI 304L (1.4307) produced by different surface treatments, the relationship between deformation-induced martensite content and compressive residual stress level in AISI 304L components, the effect of a single laser beam on residual stress properties in AISI 304 (1.4301) components, and the comparison of fatigue behavior of annealed and cold-rolled AISI 301LN (1.4318) components after shot peening.

The present study aims to tailor the microstructure and residual stress characteristics of austenitic disc springs using incremental sheet metal forming to improve their properties. A primary objective is to assess the influence of deformation-induced martensite formation on the magnitude and stabil-

ity of induced stresses and to follow the austenite-martensite phase transformation using the finite element method. Artificial neural networks (ANN) are constructed to predict the outcomes of rolling, incremental forming and the spring performance in different conditions.

## 6.4 Experimental Methods

### 6.4.1 Production of Various Batches with Rolling

The most significant disturbance in the production of disc springs with defined properties are fluctuations in the material. Batch fluctuations may occur in the cold rolling process. At the start of the rolling process, the roll and plate are at room temperature and both may heat up to 300 °C due to energy dissipated from forming and friction. The investigations were conducted on the austenitic steels EN 1.4310 and EN 1.4401. In order to eliminate the effects of the processing history, the blanks were heated to 1,060 °C and 1,090 °C, respectively, and cooled in the furnace. This results in dissolution of the initial martensite content. The dimensions of the blank were: Length ( $l$ ) = 155 mm, width ( $w$ ) = 155 mm and thickness ( $t$ ) = 3 mm. The final plate thickness was obtained by rolling. The rolling process was carried out at room temperature, 80 °C and 300 °C (figure 6.2). Table 6.1 shows the desired thickness of the blanks and the number of rolling passes required to obtain the blank thicknesses. The temperable rolling mill of Carl Wezel GmbH with a maximum force of 1,600 kN was used to form the blanks. The roll diameter was 330 mm, the roll width was 800 mm and a rolling speed of 30 m/min was used in the tests. In addition to the blank batches produced in-house, other batches were obtained from industry and used directly in incremental sheet forming.

### 6.4.2 Robot Based Incremental Forming

An ABB industrial robot IRB 6700-300 with 6 axes and a maximum force capacity of 3,000 N in z-direction was used for the incremental forming (see

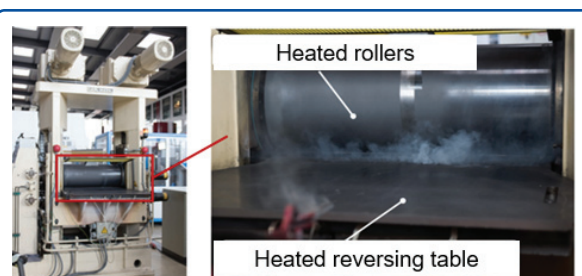


**Figure 6.2** Rolling at elevated temperatures.

figure 6.3 a). Different tooling systems were developed during the project phases. The die used in the third phase had cooling channels through which compressed air or fluids can flow (figure 6.3 b). The die was designed based on the results of numerical simulations. Some details of the die design are presented in the section with numerical models. Various hardening methods were tested to improve the tool hardness due to high abrasion in the forming of spring steel EN1.4310. The highest hardness was measured in the tool made of 1.4571 with a HARD-INOX®-S-treatment. A continuous lubricant supply was used to ensure lubrication even at high temperatures (figure 6.3 c).

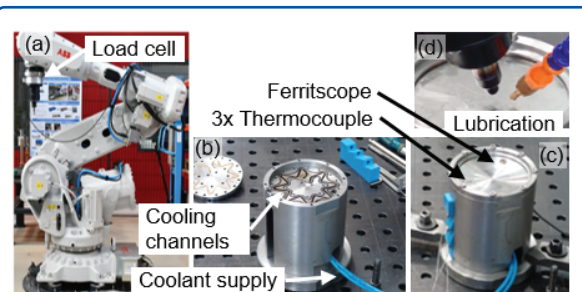


**Figure 6.3** a) Industrial robot b) Die with cooling channels c) Formed disk spring.

The forces in experiments were measured in three spatial directions by the tool holder (load cell sensor 2500). The measured maximum force depends on the robot position. The tool holder can travel at a maximum speed of 180 °/s and switches off in the event of an overload. If the sheet starts to wrinkle during processing or the forming force rapidly increases, the final spring geometry cannot be achieved.

**Table 6.1** Rolling parameters for blank creation

AISI 301 Temp.(°C)	Rolling deformation $\phi$	No. of passes	Rolling force (kN)
RT		5, 4, 3	1,550
	0.4, 0.3, 0.2	4, 3, 2	1,375
		2, 1, 1	1,000
AISI 301 Temp.(°C)	Rolling deformation $\phi$	No. of passes	Rolling force (kN)
	RT	4, 3, 2	1,345
		3, 2, 2	1,150
	300	1, 1, 1	850

In addition to force measurement, the blank temperatures were recorded by welded thermocouples of type K and by means of a thermal camera (InfraTec Variocam 600HD). The Fischer FMP30 feritscope was integrated into the die to measure the formed martensite content (figure 6.3 c). Hence, the forming process is appropriately monitored which permits the implementation of control loops in the forming process.

#### 6.4.3 Multisensor Test Setup

The evaluation of the mechanical properties of disc springs was carried out using a servohydraulic testing system ( $F = \pm 10$  kN) equipped with an inhouse-developed multisensory (figure 6.4).

As mentioned earlier, this multisensor setup contains micromagnetic, thermal, and X-ray diffraction sensors, which are used to monitor the changes in the properties of disc springs under service conditions.

The force-displacement diagrams for disc springs formed incrementally and traditionally from 1.4310, and 1.4401 steels were obtained by flattening at a strain rate of  $\dot{\varepsilon} = 0.0025$ /s. The disc springs had dimensions of 112/57/1 mm ( $D_e/D_i/t$ ).

The same setup was used to evaluate the fatigue behavior of disc springs and analyze residual stresses stability.

A sinusoidal load-time function with a frequency of  $f = 10$  Hz and a force ratio of  $R = 10$  to an ultimate load cycle number of  $N = 2.5 \times 10^{16}$  was used for these tests.

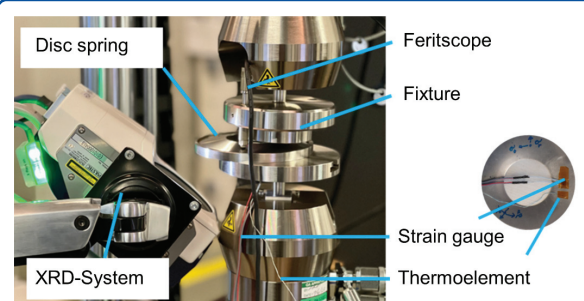


**Figure 6.4** Inhouse-developed multisensor test setup for the disc springs.

#### 6.4.4 Microstructural Analyses and Residual Stress Measurements

The initial microstructures of the plates, which were rolled at various temperatures, were studied using scanning electron microscopy. Residual stresses within the disc springs were measured using two different X-ray diffractometers (XRD) setups. A portable instrument called  $\mu$ -X360 was used for in-situ measurements (figure 6.4). This instrument uses CrK $\alpha$ -radiation and operates according to the cos  $\alpha$  method [14]. An X-ray incidence angle of  $\psi_0 = 35^\circ$  was selected to measure the residual stress content of the disc springs. Retained austenite content was measured at an X-ray incidence angle of  $\psi_0 = 18^\circ$ . The Bruker D8 Discover XRD

was used for intermittent measurements in the tangential direction based on the  $\sin^2 \theta$  method. For these analyses, five measurement angles [0; 11.25; 22.5; 37.75; 45°] were considered for both 90° and 270° azimuth positions using Cu radiation with a current of 40 mA and a voltage of 40 kV. The 2θ range was from 112° to 123° with a peak at 118.194°. The plane of diffraction was, therefore, the [400] plane. A step size of 0.1° was used, with each measurement point taking 20 seconds. A collimator with a diameter of 2 mm was employed in the measurements.

#### 6.4.5 Developing a Micromagnetic Method for Residual Stress Measurements

Developing a nondestructive magnetic Barkhausen noise method for measuring residual stresses requires establishing calibration curves. The calibration process was performed using a bent specimen made of 1.4310. A four-point bending fixture was used to incrementally increase the applied stress with a step size of 62.5 MPa to a maximum stress of  $\pm 500$  MPa at the bottom and top of the specimen. After reaching the maximum values, the stress was relieved in the same steps down to 0 MPa. This loading sequence was repeated twice. At each step, the MBR was measured in the longitudinal and transverse directions in the loading direction. The experimental setup can be seen in figure 6.5.

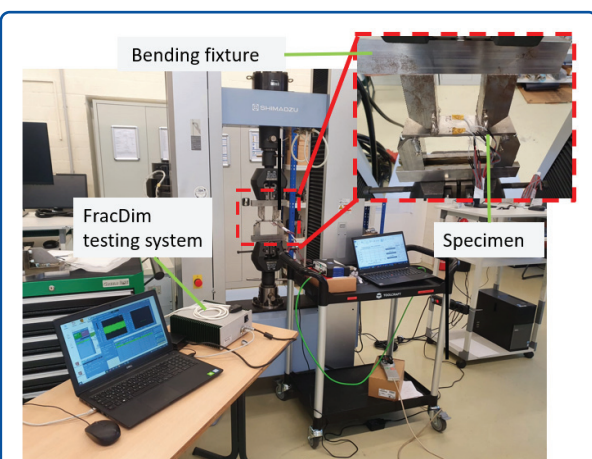


**Figure 6.5** Experimental setup for residual stress measurement.

## 6.5 Numerical Models

Microscale finite element simulations were conducted to model changes in micromechanical properties. The macroscale model is used to build up changes over the manufacturing history of the spring. The micro- and macroscale models were calibrated using experiments.

### 6.5.1 Microscale Simulation Model (CPFEM)

To model microscale changes in the material parameters, microscale FEM models based on “Crystal Plasticity” (CP) were implemented in the FE software Abaqus® using a subroutine [15, 16]. For 1.3410, both the volume of retained austenite and the mean free path of austenite dislocations influence austenite properties in strain-induced martensite transformation. Kinematic strain hardening can be calculated by stress-strain-dependent martensite formation for certain temperatures on the micro level. The stress-strains of individual crystals were homogenized and validated with experimental data. Anisotropic kinematic strain hardening was determined in the CP-FEM model, based on the work of [16, 17].

Total deformation is:

$$\mathbf{F} = \mathbf{F}^e \mathbf{F}^{tr} \mathbf{F}^p$$

$$\dot{\mathbf{F}}^{tr} = \sum_{I=1}^{N^T} \dot{\zeta}_I^{stress} \mathbf{N}_I \quad (\text{Equation 6.1})$$

Martensitic nucleation and the growth are defined as:

$$\zeta = \zeta^0 + \zeta^{strain} + \zeta^{stress} \quad 0 \leq \zeta \leq 1$$

$$(\text{Equation 6.2})$$

The thermodynamic driving force for strain-induced martensite nucleation:

$$\dot{\mathbb{N}}_I^{strain} = -[12\Delta G(\zeta_I^2 - \zeta_I^3)]$$

$$\dot{\zeta}_I^{strain} = C^{nuc} \left( 1 - \sum_{J=1}^{N^T} \zeta_J \right) \dot{P}_I \dot{\mathbb{N}}_I^{strain} \dot{\gamma}_\alpha$$

$$(\text{Equation 6.3})$$

where  $\Delta G$  is taken from [17]. The thermodynamic driving force for stress-induced martensite nucleation can be written as:

$$\begin{aligned} \aleph_I^{stress} &= \det(\mathbf{F}) \frac{\sigma}{2} \left( \mathbf{F}^e \tilde{N}_I \mathbf{F}^{e^{-1}} + \mathbf{F}^{e^T} \tilde{N}_I^T \mathbf{F}^{e^{-T}} \right) - \aleph_I^{strain} \\ \dot{\zeta}_I^{stress} &= C^{gro} (\zeta^0 + \zeta^{strain}) \left( 1 - \sum_{\beta=1}^{N^T} \zeta_\beta \right) \\ &\quad \dot{P}_I \aleph_I^{strain} \end{aligned} \quad (Equation 6.4)$$

The local CPFEM model is extended with the strain gradient approach, which leads to the flow rule of the non-local term for TRIP steels.

$$\dot{\gamma}_\alpha = \dot{\gamma}_0 \left| \frac{\tau^\alpha}{\hat{\tau}^\alpha} \right|^n \text{sign}(\tau_\alpha) \quad (Equation 6.5)$$

Flow rule of the non-local term (TRIP+TWIP):

$$\dot{\gamma}_\alpha = \dot{\gamma}_0 \left| \frac{\tau^\alpha + \tau_{GND}^\alpha}{\hat{\tau}^\alpha + \hat{\tau}_{GNDi}^\alpha} \right|^n \text{sign}(\tau_\alpha + \tau_{GND}^\alpha) \quad (Equation 6.6)$$

Lamellar hardening in flow rule:

$$\dot{\gamma}_\alpha = \dot{\gamma}_0 \left| \frac{\tau^\alpha + \tau_{GND}^\alpha}{\hat{\tau}^\alpha + \hat{\tau}_{GNDi}^\alpha + \hat{\tau}_{twip}^\alpha} \right|^n \text{sign}(\tau_\alpha + \tau_{GND}^\alpha) \quad (Equation 6.7)$$

And the lamellar structure with:

$$\hat{\tau}_{twip}^\alpha = c_{MHD} \mu \sum_{I=1}^{N^T} \dot{\psi}_I \quad (Equation 6.8)$$

$$\begin{aligned} \tau_\alpha &= \frac{\det(\mathbf{F})}{2} \cdot \sigma \cdot (\mathbf{F}^e \mathbf{F}^{tr} \mathbf{M}_\alpha \mathbf{F}^{tr^{-1}} \mathbf{F}^{e^{-1}} \\ &\quad + \mathbf{F}^{e^{-T}} \mathbf{F}^{tr^{-T}} \mathbf{M}_\alpha^T \mathbf{F}^{tr^T} \mathbf{F}^{e^T}) \end{aligned} \quad (Equation 6.9)$$

## 6.5.2 Macroscale Simulation Model

The TRIP effect, which is mapped with the Olsen-Cohen model (OC) (Equation 6.6), was modified via the parameters  $\beta$  and  $\xi$  in such a way that, in addition to the plastic strain, the strain rate and temperature influence on martensite formation are taken into account. The material model was implemented in the commercial FE software Abaqus® as

a subroutine; the coefficients were determined by inverse simulation and published in [18, 19]. This sigmoidal function relates the martensitic volume fraction and the plastic strains [20]:

$$f_{\alpha'} = 1 - \exp\{-\beta_0(1 - \exp(-\xi\varepsilon)^n)\} \quad (Equation 6.10)$$

The rate of the shear-band formation is controlled by the parameter  $\xi$  with increasing strain and is dependent on the stacking fault energy. The variation of parameter  $\beta_0$  controls the probability that a martensitic nucleus will be generated from the embryo. It is governed by the chemical driving force of the transformation  $\gamma \rightarrow \alpha'$ . The term  $n$  acts as a fitting parameter and is taken as 2 [21]. The transformation rate of the model is mathematically represented as:

$$\frac{df_{\alpha'}}{d\varepsilon} = -\frac{n\xi(1 - f_{\alpha'}) \ln(1 - f_{\alpha'})}{\exp(\xi\varepsilon) - 1} \quad (Equation 6.11)$$

The incremental formulation used to calculate the volume fraction of the martensite:

$$\begin{aligned} \dot{f}_{sb} &= \xi(1 - f_{sb}) \dot{\varepsilon}_p \\ \mathcal{M} &= \xi \beta_0 n f_{sb}^{n-1} (1 - f_{sb}) \\ \dot{f}_{nm} &= \mathcal{M}(1 - f_{nm}) \dot{\varepsilon}_p \\ V_{nm} &= V_{a0} f_{nm} \end{aligned} \quad (Equation 6.12)$$

where  $f_{sb}$ ,  $f_{nm}$  denote the normalized shear band and transformed volume fraction of martensite. The incremental plastic strain ( $\varepsilon_p$ ) is provided by the constitutive framework. The shear band formation and nucleation of martensite are functions of the temperature.

$$\begin{aligned} \alpha &= A_2^\alpha + \frac{A_1^\alpha - A_2^\alpha}{1 + \exp\left(\frac{T-T^\alpha}{\Delta T^\alpha}\right)} \\ \beta &= A_2^\beta + \frac{A_1^\beta - A_2^\beta}{1 + \exp\left(\frac{T-T^\beta}{\Delta T^\beta}\right)} \end{aligned} \quad (Equation 6.13)$$

In Equation 6.11 and Equation 6.12, the terms  $A_1^\alpha$ ,  $A_2^\alpha$ ,  $A_1^\beta$ ,  $A_2^\beta$ ,  $T^\alpha$ ,  $\Delta T^\alpha$ ,  $T^\beta$ , and  $\Delta T^\beta$  are fitted parameters and  $T$  is temperature. Because of the chemical composition of retained austenite, the eight parameters in Equation 6.11 and Equation 6.12, could be fitted as a function of Mn, Si, Al, and C content of the retained austenite [22]. The flow

stress is a combination of each constituent phase calculated as [18]:

$$\sigma_f = \sigma_{y,\gamma}(1 - f_{\alpha'}) + \sigma_{y,\alpha'}f_{\alpha'} \quad (\text{Equation 6.14})$$

where  $\sigma_{y,\gamma}$  and  $\sigma_{y,\alpha'}$  are the flow stress of the austenite and martensite, respectively.

The elastoplastic behavior is achieved for each phase by using the von Mises yield function F with an isotropic hardening law. The yielding is described as follows:

$$\sigma = \sigma_{eq} - \sigma_0 - R \quad (\text{Equation 6.15})$$

$\sigma_{eq}$  represents equivalent von Mises,  $\sigma_0$  indicates the initial yield stress, and  $R$  is the isotropic hardening parameter. The  $\sigma_{eq}$  is derived as follows:

$$\sigma_{eq} = \sqrt{\frac{3}{2}S_{ij}S_{ij}} \quad (\text{Equation 6.16})$$

here  $S_{ij}$  is the deviatoric part of the stress tensor. Where the isotropic hardening parameter can be calculated as:

$$R = Q_0 \left( 1 - e^{-b\varepsilon_{ep}^p} \right) \quad (\text{Equation 6.17})$$

where  $Q_0$  and  $b$  are material constants depending on the constituents.  $\varepsilon_{ep}^p$  is the equivalent strain.

### 6.5.3 Machine Learning

As shown in figure 6.6, the input variables into the network at the first stage (rolling process) are the rolling degree and the temperature. The martensite content and residual stresses are predicted. A neural network with a single hidden layer having 10 neurons was used in the prediction. The experimental results were interpolated to 336 experiments, 300 datasets were used for training and 36 for validation. The training dataset was randomly divided into 70 %, 15 %, and 15 % for training, validation, and testing, respectively, during training.

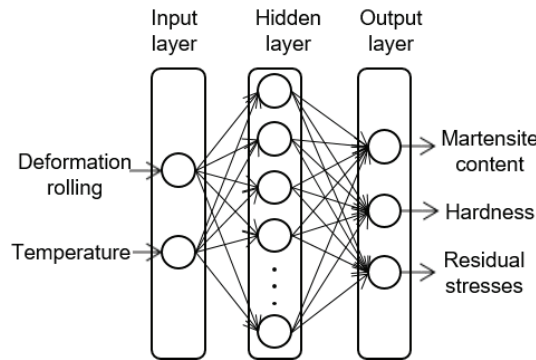


**Figure 6.6** Neural network architecture of the rolling process

## 6.6 Results and Discussion

### 6.6.1 Experimental Results of the Rolling Process

The mechanical properties of the rolled blanks were characterized by the grain size and uniaxial tensile tests performed in the blank rolling direction. Due to the formation of strain-induced martensite, the stress-strain curves show significant strain hardening (figure 6.7). The grain size and ductility increase with increasing rolling temperature and yield strength decreases for the material 1.4310 and 1.4401. More results can be found in [23].

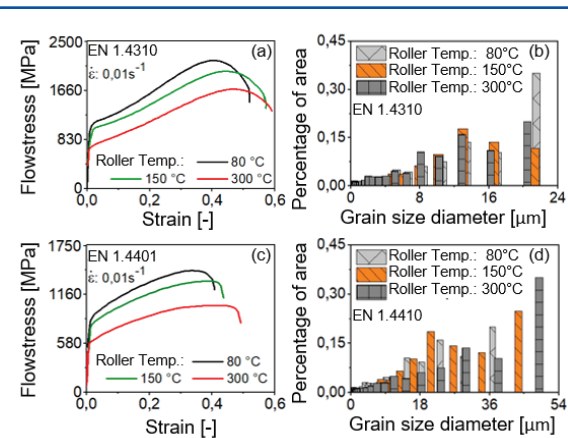


**Figure 6.7** Dependence of flow stress and grain size diameter on rolling temperature.

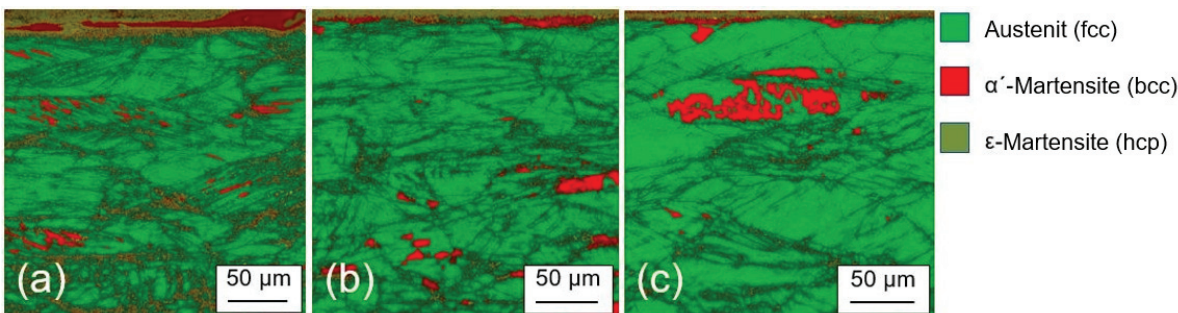


**Figure 6.8** EBSD micrographs of 1.4310 sheet blanks rolled at (a) 80°, (b) 150° and (c) 300°.

EBSG investigations (figure 6.8) revealed a decline in martensite content with increasing rolling temperature. Despite using identical incremental sheet forming parameters, variations in martensite content within the surface layer of the sheet blanks lead to different levels of induced residual stresses, which in turn produce different spring force-deflection curves.

### 6.6.2 Microscale Simulations of Material Properties

The onset of plastic deformation, flow curves, and phase change were calculated from the RVE with the aid of CP-FEM. The microscopic material properties of the RVE (grain sizes and orientation, phase assignment, etc.) were determined using the corresponding EBSD analyses and values obtained from the literature. In figure 6.9 the RVE is shown under tensile loading.

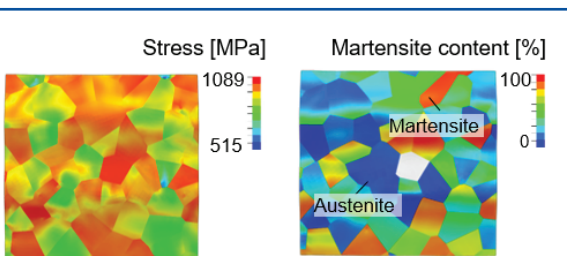


**Figure 6.9** Stress distribution of the RVE under load and b) martensite content.

The flow curves change due to the heterogeneous phenomena (TRIP/TWIP). Figure 6.10 a shows the calibration of the CP-FEM to the yield curve,

martensite content and figure 6.10 b the cyclic loading. The evolution of the martensite content depends on the loading conditions. The effect of the changing martensite volume fraction on the homogenized yield curve (uniaxial tension) is visible in figure 6.10 b.

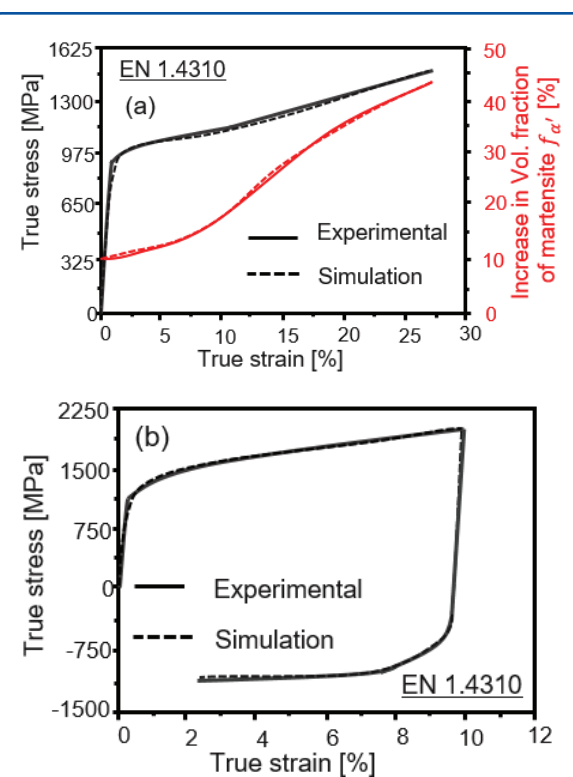


**Figure 6.10** Calibration of the flow curve and martensite development under a) static and cyclic load. Stress distribution of the RVE under load and b) martensite content.

The yield loci can be calculated for various strain rates and temperatures in the CP-FEM. The cali-

bration of the CP-FEM model was performed for the material at room temperature. Significant deviations were observed when using the calibrated material model to match experimental investigations measured at high temperatures. Further calibration is required. The small values were obtained for the yield locus in the CP-FEM because of early plasticization of individual grains. As discussed in the working group (see chapter 5), the measurement result for determination of Young's modulus and the yield locus is very strongly dependent on the measurement method and evaluation method.

### 6.6.3 Macroscale Simulations of the Rolling Process

The flow curves of the austenitic and martensitic components of the stainless steel AISI 301 were determined using the mixture rule in a parametric study. The parameters were varied to match experimentally determined phase fractions and flow curves of tensile tests performed at room temperature (RT), 80 °C, and 300 °C. The results of the parametric study are presented in table 6.2. Figure 6.11 shows the results of the parametric study on the macroscopic material model.

The cold rolling process was simulated for different rolling degrees and temperatures with the aid of the extended Olson-Cohen model. Figure 6.12 a represents the distribution of the martensite volume fraction for different rolling degrees. The variation of the martensite content in the blanks is explained by variable friction and deflection of the rollers. The average value of the martensite volume fraction and residual stresses from the experiments and FE simulations are compared in figure 6.12 b. The values were determined over the plate thickness and at the blank centers. The temperature-dependent TRIP effect and its influence on the residual stresses were reproduced with high accuracy.

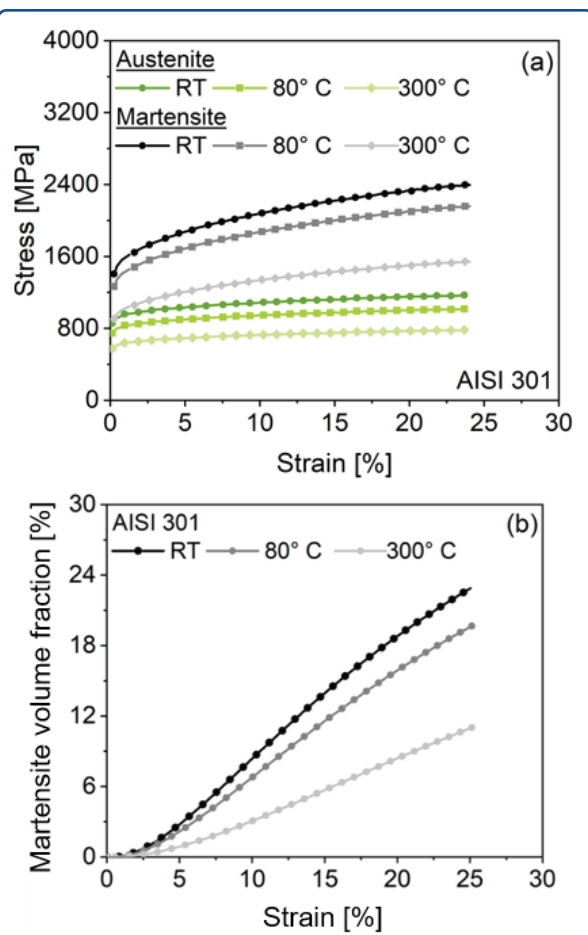


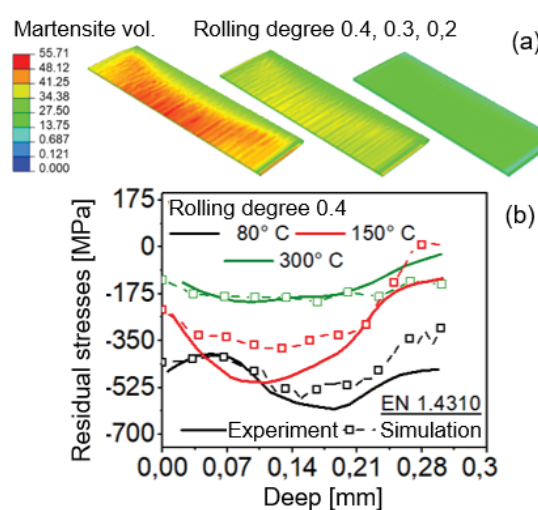
**Figure 6.11** Calculated a) flow-curves for martensite and austenite b) martensite evolution for different temperatures.

### 6.6.4 Finite Element Based Temperature Control in High-speed Incremental Forming

To obtain forming times suitable for industrial applications, a robot's speed should be increased to about 200 mm/min, which implies a processing time of about 80 seconds. High tool travel speeds lead to a temperature rise of up to 100 °C and above, depending on the lubrication cooling conditions (figure 6.13 a). Thus, an increased forming rate and temperature lead to changes in residual stresses figure 6.13 (b) and martensite fractions figure 6.13 (c).

**Table 6.2** Parameters of the macro-scale material model

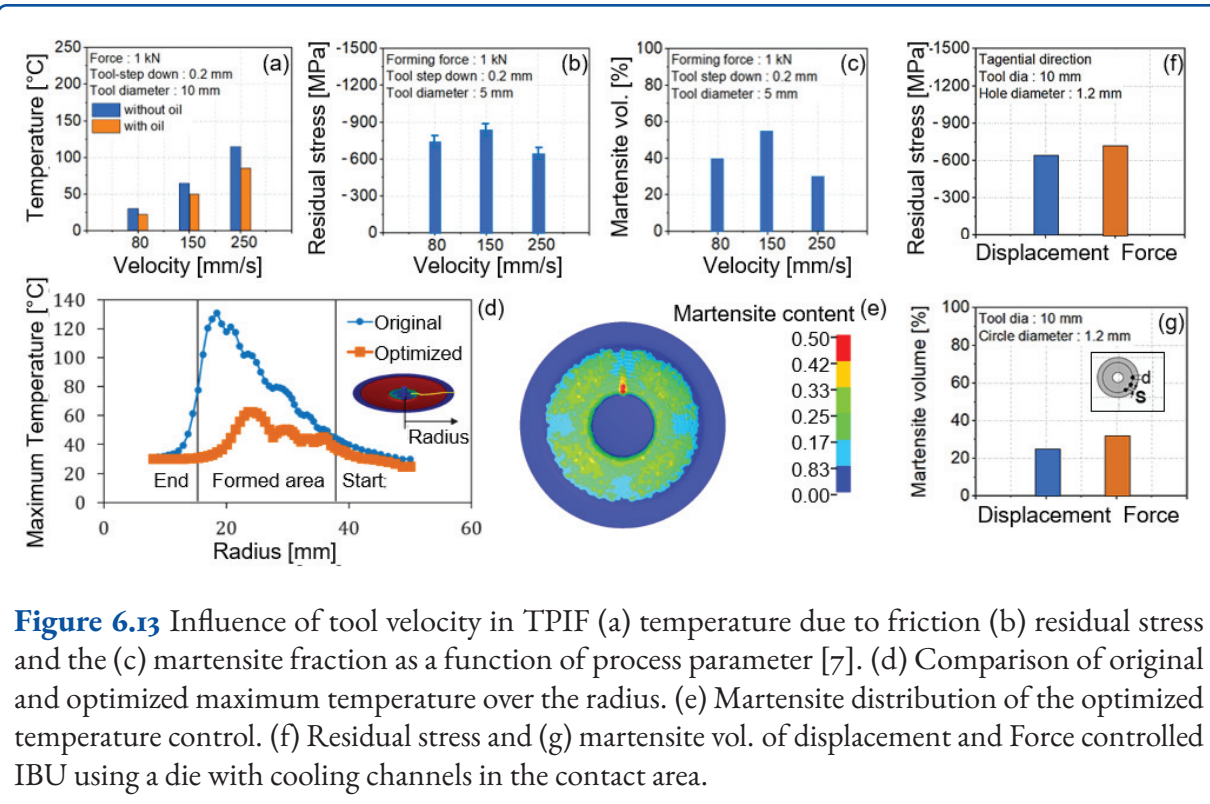
Temp. [°C]	$\sigma_{y_0,\gamma}$ [MPa]	$Q_{o,\gamma}$ [MPa]	$b_\gamma$	$E_\gamma$ [GPa]	$\nu_\gamma$
RT	856	302.7	19.97	188	0.31
	$\sigma_{y_0,\alpha'}$	$Q_{o,\alpha'}$	$b_{\alpha'}$	$E_{\alpha'}$	$\nu_{\alpha'}$
	1,460	1,005	10.22	217	0.28
Temp. [°C]	$\sigma_{y_0,\gamma}$ [MPa]	$Q_{o,\gamma}$ [MPa]	$b_\gamma$	$E_\gamma$ [GPa]	$\nu_\gamma$
80 °C	764	-	-	175	0.3
	$\sigma_{y_0,\alpha'}$	$Q_{o,\alpha'}$	$b_{\alpha'}$	$E_{\alpha'}$	$\nu_{\alpha'}$
	-	-	-	201	0.27
Temp. [°C]	$\sigma_{y_0,\gamma}$ [MPa]	$Q_{o,\gamma}$ [MPa]	$b_\gamma$	$E_\gamma$ [GPa]	$\nu_\gamma$
300 °C	600	-	-	169	0.3
	$\sigma_{y_0,\alpha'}$	$Q_{o,\alpha'}$	$b_{\alpha'}$	$E_{\alpha'}$	$\nu_{\alpha'}$
	-	-	-	192	0.27

**Figure 6.12** Rolling simulation with different rolling degrees (0.4, 0.3, 0.2) and comparison of the numerical with the experimental results.

The blank temperature should be maintained below 70 °C during forming to maximise martensite formation.

The result of the numeric parametric study is a linear increase of the cooling power from 0.2 mW/mm<sup>2</sup>K to approximately 16 mW/mm<sup>2</sup>K in the first 4 s of the process, which is then kept constant until the end of the forming process after 8 seconds. Figure 6.13 d) shows the maximum blank temperature along the disc spring radius over the process time. The temperature increases toward the center of the disk spring when the forming process proceeds from the outside of the disk toward the inside due to heat conduction (figure 6.13 d), original curve). A comparison of the temperatures in the original and optimised FE cooling parameters shows the ability of adaptive cooling to achieve a maximum temperature within the desired limits. Thus, springs with high martensite volume fractions and a homogenous distribution over the diameter can be formed at very high speeds (8 s, figure 6.13 e). Details on the parametric study are presented in [24].

It is therefore required to cool the blank in the forming operation to enhance martensite formation. In FE simulations, the convection boundary conditions and the start time of cooling are controlled.



Temperature control by the use of cooled dies is slow. Additionally, the top of the spring surface can be cooled using fluids. Additional simulations with cooling fluids were applied to the blank surface via holes in the die surface. The effect of the hole geometries on the residual stresses of formed springs at the location of the holes is presented in [25]. To determine the hole shape that has the least influence on residual stresses at a constant cross-section. FE simulations were conducted to compare the residual stresses in blanks formed using dies with no holes (reference) and dies having rectangular, elliptical, and circular holes.

To prevent the blank material from flowing into the holes on the die surface, the tool paths executed by the robot at the holes were adjusted using displacement rather than force controls. The displacement tool path control resulted in lower residual stresses and martensite content, as shown in figure 6.13 g). In the experimental work, we used cooling from the top side only.

### 6.6.5 Simulation of the Residual Stresses and Properties of the Disc Springs

The material model of macroscopic FE simulations was quantitatively validated by residual stress measurements at 80 °C, 150 °C, and 300 °C rolling temperatures. The material model of macroscopic FE simulations was further used to simulate the forming, cutting, and load simulations. The results of the rolling simulations (stresses, strains, and phase fractions) were used as the initial state of the incremental forming simulation, whereby they were mapped to a mesh optimised for ISF. In figure 6.14, the tangential residual stresses are plotted. The peak of each tool revolution is visible. The maximum values of the residual stress and martensite content from the FE simulations converge toward the experimental measurements as the forming process progresses. The deviations are mainly attributed to contact stiffness in the tool. Finally, static loading of the springs was simulated. For example, the force-displacement curves of a disk spring made of 1.4310 using a 5 mm diameter tool, a step size of 0.1 mm, and at 80 °C and 300 °C are presented in figure 6.14. Significant changes may

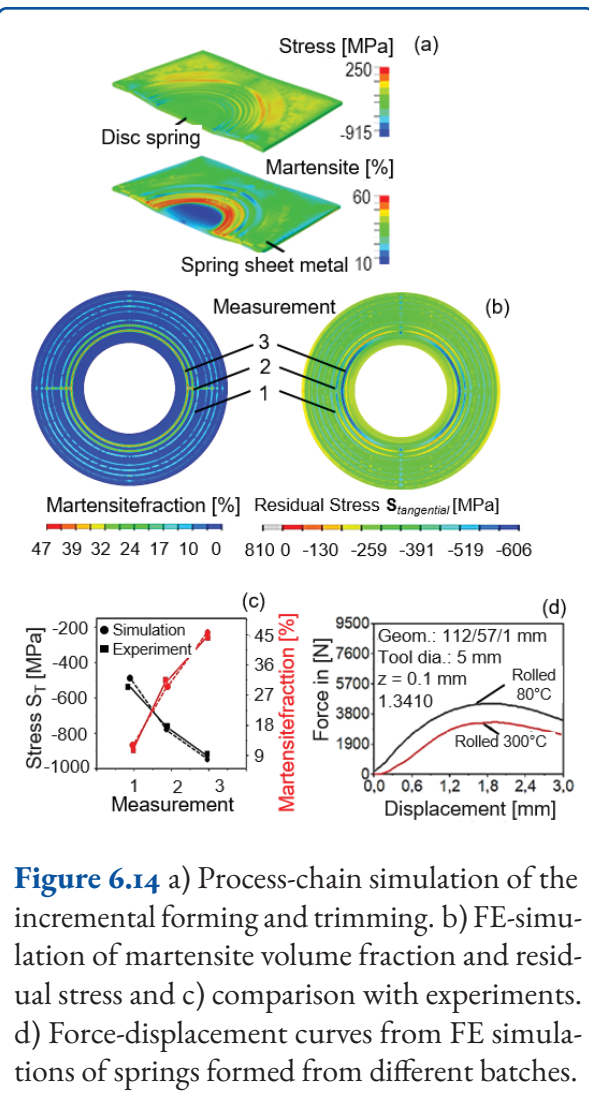


**Figure 6.14** a) Process-chain simulation of the incremental forming and trimming. b) FE-simulation of martensite volume fraction and residual stress and c) comparison with experiments. d) Force-displacement curves from FE simulations of springs formed from different batches.

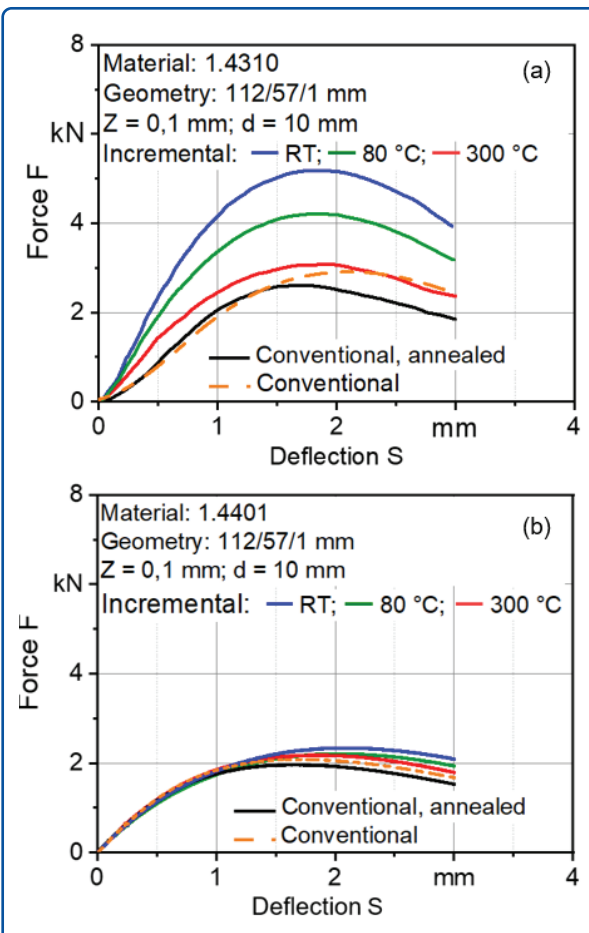


**Figure 6.15** Force-deflection capacity in disc springs formed under different process parameters. a) incrementally formed, b) conventionally formed.

occur in the properties of the springs for different batches, which was also the case in the tests.

### 6.6.6 Mechanical Testing of the Disc Springs

Incrementally formed springs from both materials demonstrated significantly improved force-deflection characteristics. The highest spring forces were found in incrementally formed springs from cold-rolled sheets. These results are consistent with the residual stress measurements so higher residual compressive stresses imply higher compressive strengths. These findings are close to the residual stress measurements, demonstrating that a rise in residual compressive stress results in an increase in compressive strength.

Up to the maximum number of cycles,  $N = 2.5 \times 10^{+6}$ , no failures occurred during the fatigue testing. However, the analysis of the residual stress stability showed that the stresses decreased significantly after a few cycles. Two disc springs, one manufactured conventionally and one incrementally, were studied. The geometry of both springs was 112/57/1 mm ( $D_e/D_i/t$ ). They were manufactured from AISI 301 sheet metal blanks. The fatigue experiments were conducted at 80 % of the conventionally manufactured springs' maximum force. For the initial 100 cycles, a frequency of  $f = 1$  Hz was used, followed by 10 Hz.  $R = 10$  was the load ratio for all stages. Using an X-ray diffractometer and Feritscope, the disc springs' residual stress content and martensite volume fraction were measured at the onset and intermittently after 1, 10,  $10^2$ ,  $10^3$ ,

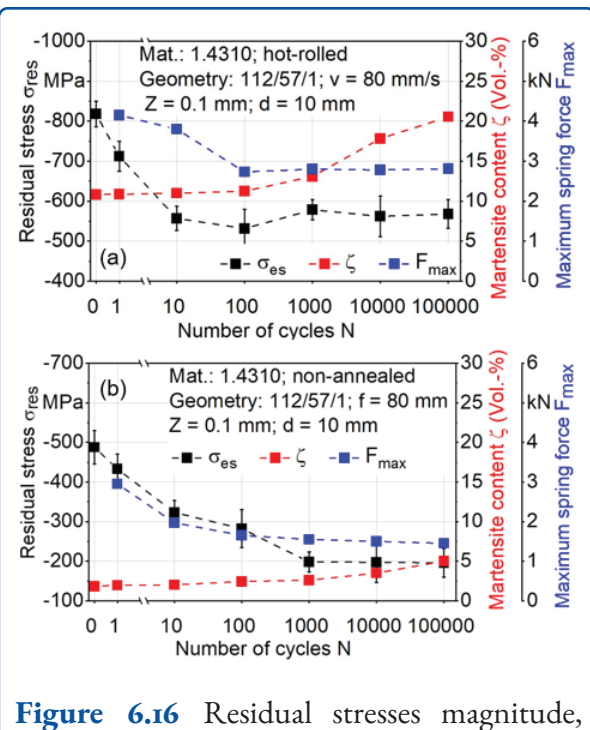


**Figure 6.16** Residual stresses magnitude, martensite volume fraction and spring forces over load cycles. a) Incrementally formed disc spring, b) conventionally formed disc spring.

$10^4$ , and  $10^5$  loading cycles. Disc compression tests were also used to determine the maximum spring force at each of the phases outlined above.

The maximum spring force in the incrementally formed disc spring stabilized after the initial 100 load cycles, as illustrated in figure 6.16. The observed stabilization was connected with an increase in its ferromagnetic properties. Martensite formation increased and stabilized the residual stress content of the disc spring, thereby providing more consistent spring properties.

### 6.6.7 Developing a Micromagnetic Method for Residual Stress Measurements

As shown in figure 6.17, the calibration curve has a sigmoidal shape and confirms the reproducibility of the measurements. The residual stress magnitudes in a conventional disc spring were measured to verify the developed curve at three points on its inner side. There is good agreement between the results of the XRD and MBN measurements.

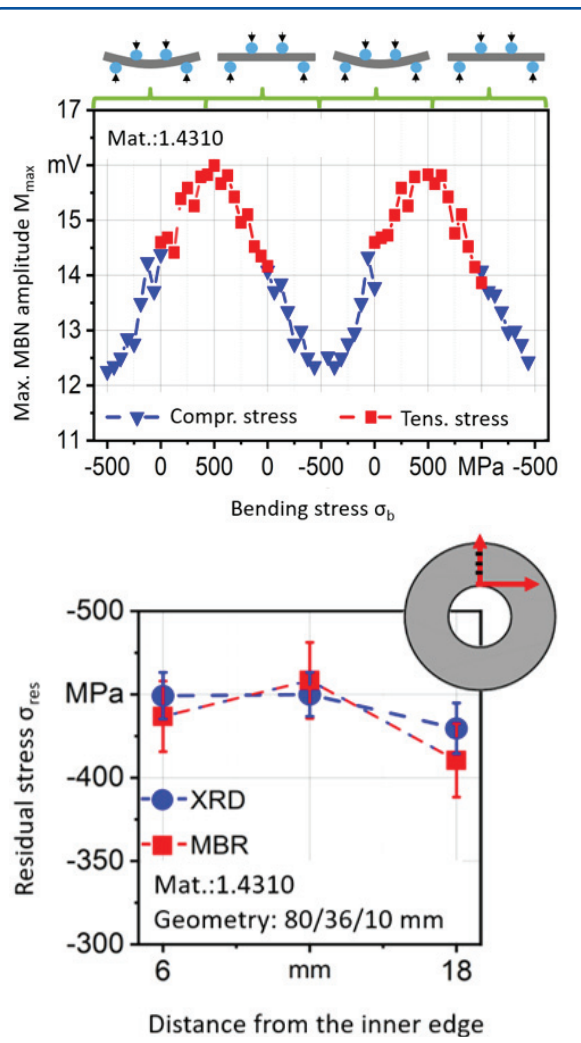


**Figure 6.17** a) Stress dependency of the max. MBN amplitude  $M_{\text{max}}$ , b) residual stress measurement results from XRD and the micromagnetic Barkhausen noise method.

### 6.6.8 Machine Learning Prediction of the Process Chain

The prediction model consists of three individual models. The first model (rolling process) was finalized by the report preparation. The regression (R-value) between the trained and target was 0.99, and the regression line was very close to 45, both of which indicate a good predictive ability of the model. To verify the performance of the trained model, the 36 validation datasets were predicted by the trained network and compared with the experimental data. Figure 6.18 shows the residual stresses of the blank center.

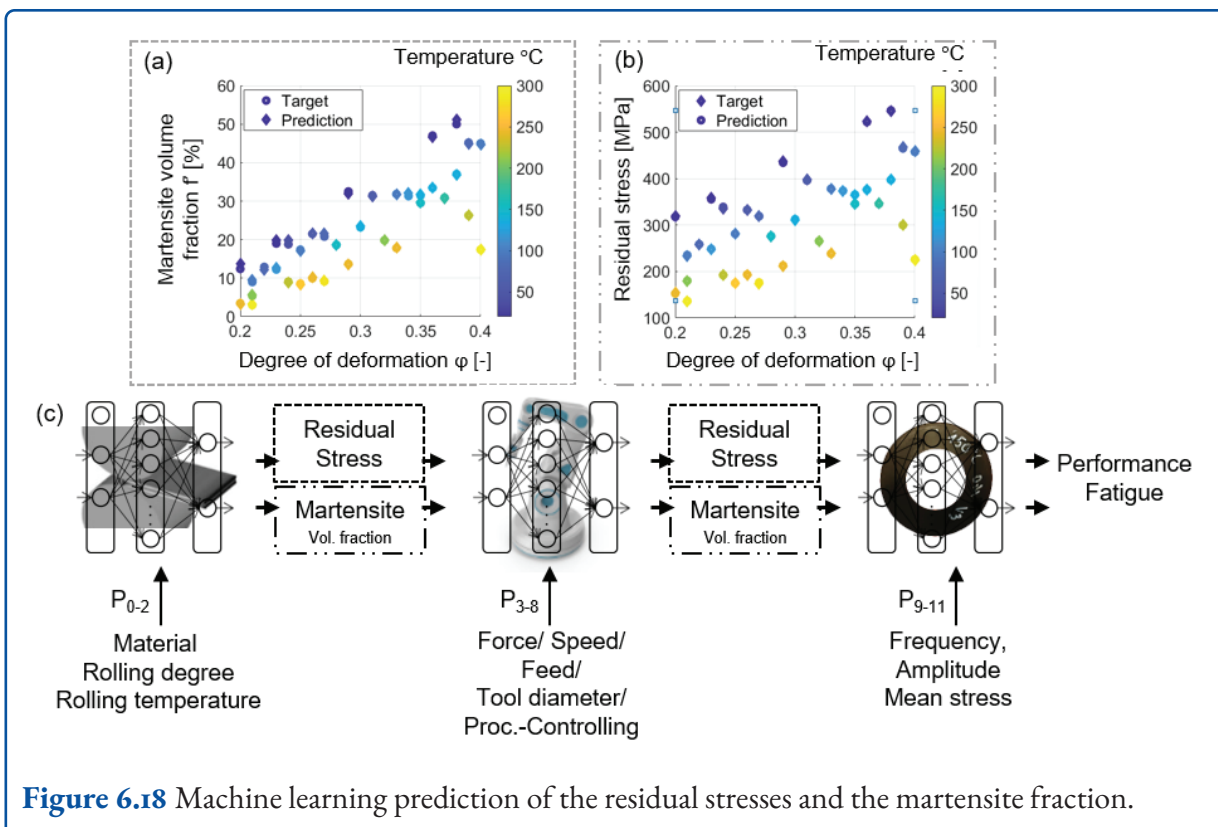


**Figure 6.18** Machine learning prediction of the residual stresses and the martensite fraction.

Due to the complex physical phenomena in TPIF, the architecture of the ANN may need to be modified to predict the residual stresses after the incremental forming process. The fatigue strength of the formed disk springs may be predicted using a neural network structure with a single hidden layer since fatigue is a less complex phenomenon than incremental forming.

## 6.7 Conclusion

The disc springs' characteristics, particularly their force-deflection capacity, can be strategically adjusted using the incremental forming technique. There is a direct correlation between the reduction of the tool diameter during incremental forming and the resulting increase in spring force. Both, I.4310 and I.4401, exhibit a correlation between residual stresses and the martensite content generated during the rolling and forming processes in the contact area. Although the conventionally and incrementally formed springs reached the specified limit load cycles without failure, the residual

stresses in the conventionally formed springs deteriorated after only a few load cycles. However, these stresses showed stability in the incrementally formed springs. The micromagnetic measurement data further emphasizes the dependencies of the residual stress properties on the martensite content of the disc springs. The developed micromagnetic approach could quantitatively measure the residual stresses in the disc springs. Macroscopic FE simulations are suitable to obtain a full field view of the rolling and forming processes and to test the deflection of the disc springs. It was shown that micromechanical models can be used to extend macro mechanical material laws, and macro FE-simulations can be used to calculate residual stresses and martensite formation. The results of the rolling process were predicted by an ANN, which will be carried out for the entire process chain by the end of the project.

## References

---

- [1] Y. Doman. "Influence of residual stress on the load-deflection curve of diaphragm springs for automobile clutches". In: *JSAE Review* 24.2 (2003), pp. 197–203. ISSN: 03894304. DOI: 10.1016/S0389-4304(02)00299-0.
- [2] Ramin Hajavifard et al. "Integrated forming and surface engineering of disc springs by inducing residual stresses by incremental sheet forming". In: *Materials (Basel, Switzerland)* 12.10 (2019). ISSN: 1996-1944. DOI: 10.3390/ma12101646.
- [3] Walter Holweger et al. "Non-destructive subsurface damage monitoring in bearings failure mode using fractal dimension analysis". In: *Industrial Lubrication and Tribology* 64.3 (2012), pp. 132–137. ISSN: 0036-8792. DOI: 10.1108/00368791211218650.
- [4] V. Llaneza and F. J. Belzunce. "Study of the effects produced by shot peening on the surface of quenched and tempered steels: roughness, residual stresses and work hardening". In: *Applied Surface Science* 356 (2015), pp. 475–485. ISSN: 01694332. DOI: 10.1016/j.apsusc.2015.08.110.
- [5] R. Fathallah. "High cycle fatigue behavior prediction of shot-peened parts". In: *International Journal of Fatigue* 26.10 (2004), pp. 1053–1067. ISSN: 01421123. DOI: 10.1016/j.ijfatigue.2004.03.007.
- [6] Nikolas Baak et al. "Characterization of residual stresses in austenitic disc springs induced by martensite formation during incremental forming using micromagnetic methods". In: *Materials Testing* 59.4 (2017), pp. 309–314. ISSN: 0025-5300. DOI: 10.3139/120.111012.
- [7] Fawad Maqbool et al. "Engineering the residual stress state of the metastable austenitic stainless steel (MASS) disc springs by incremental sheet forming (ISF)". In: *Production Engineering* 13.2 (2019), pp. 139–148. ISSN: 0944-6524. DOI: 10.1007/s11740-018-0864-6.
- [8] J. Talonen and H. Hänninen. "Formation of shear bands and strain-induced martensite during plastic deformation of metastable austenitic stainless steels". In: *Acta Materialia* 55.18 (2007), pp. 6108–6118. ISSN: 13596454. DOI: 10.1016/j.actamat.2007.07.015.
- [9] J. M. Allwood, D. R. Shouler, and A. Erman Tekkaya. "The Increased Forming Limits of Incremental Sheet Forming Processes". In: *Key Engineering Materials* 344 (2007), pp. 621–628. DOI: 10.4028/www.scientific.net/KEM.344.621.
- [10] W. C. Emmens and A. H. van den Boogaard. "An overview of stabilizing deformation mechanisms in incremental sheet forming". In: *Journal of Materials Processing Technology* 209.8 (2009), pp. 3688–3695. ISSN: 09240136. DOI: 10.1016/j.jmatprotec.2008.10.003.
- [11] Fawad Maqbool and Markus Bambach. "A modular tooling set-up for incremental sheet forming (ISF) with subsequent stress-relief annealing under partial constraints". In: AIP Conference Proceedings. Author(s), 2017, p. 080010. DOI: 10.1063/1.5008090.
- [12] Amar Kumar Behera and Hengan Ou. "Effect of stress relieving heat treatment on surface topography and dimensional accuracy of incrementally formed grade 1 titanium sheet parts". In: *The International Journal of Advanced Manufacturing Technology* 87.9-12 (2016), pp. 3233–3248. ISSN: 0268-3768. DOI: 10.1007/s00170-016-8610-8.
- [13] T. Katajärinne, S. Louhenkilpi, and S. Kivivuori. "A novel approach to control the properties of austenitic stainless steels in incremental forming". In: *Materials Science and Engineering: A* 604 (2014), pp. 23–26. ISSN: 09215093. DOI: 10.1016/j.msea.2014.03.020.
- [14] Shuji Taira, Keisuke Tanaka, and Toshiharu Yamasaki. "A method of X-Ray microbeam measurement of local stress and its application to fatigue crack growth problems". In: *Journal of the Society of Materials Science, Japan* 27.294 (1978), pp. 251–256. ISSN: 0514-5163. DOI: 10.2472/jSMS.27.251.
- [15] Anxin Ma and Alexander Hartmaier. "On the influence of isotropic and kinematic hardening caused by strain gradients on the deformation behaviour of polycrystals". In: *Philosophical Magazine* 94.2 (2014), pp. 125–140. ISSN: 1478-6435. DOI: 10.1080/14786435.2013.847290.

- [16] Anxin Ma and Alexander Hartmaier. "A study of deformation and phase transformation coupling for TRIP-assisted steels". In: *International Journal of Plasticity* 64 (2015), pp. 40–55. ISSN: 07496419. DOI: 10.1016/j.ijplas.2014.07.008.
- [17] Heung Nam Han et al. "A model for deformation behavior and mechanically induced martensitic transformation of metastable austenitic steel". In: *Acta Materialia* 52.17 (2004), pp. 5203–5214. ISSN: 13596454. DOI: 10.1016/j.actamat.2004.07.031.
- [18] Muhammad Junaid Afzal et al. "Modeling the Residual Stresses Induced in the Metastable Austenitic Stainless Steel Disc Springs manufactured by Incremental Sheet Forming by a Combined Hardening Model with Phase Transformation". In: *Procedia Manufacturing* 47 (2020), pp. 1410–1415. ISSN: 23519789. DOI: 10.1016/j.promfg.2020.04.300.
- [19] Fawad Maqbool et al. "Targeted residual stress generation in single and two point incremental sheet forming (ISF)". In: *Archive of Applied Mechanics* 91.8 (2021), pp. 3465–3487. ISSN: 0939-1533. DOI: 10.1007/s00419-021-01935-z.
- [20] G. B. Olson and Morris Cohen. "A mechanism for the strain-induced nucleation of martensitic transformations". In: *Journal of the Less Common Metals* 28.1 (1972), pp. 107–118. ISSN: 00225088. DOI: 10.1016/0022-5088(72)90173-7.
- [21] Dieter Fahr. "Stress- and strain-induced formation of martensite and its effects on strength and ductility of metastable austenitic stainless steels". In: *Metallurgical Transactions* 2.7 (1971), pp. 1883–1892. ISSN: 0026-086X. DOI: 10.1007/BF02913420.
- [22] L. Samek et al. "Influence of alloying elements on the kinetics of strain-induced martensitic nucleation in low-alloy, multiphase high-strength steels". In: *Metallurgical and Materials Transactions A* 37.1 (2006), pp. 109–124. ISSN: 1073-5623. DOI: 10.1007/s11661-006-0157-0.
- [23] Muhammad Junaid Afzal et al. "Influence of process parameters on the residual stress state and properties in disc springs made by incremental sheet forming (ISF)". In: *Forschung im Ingenieurwesen* 85.3 (2021), pp. 783–793. ISSN: 0015-7899. DOI: 10.1007/s10010-021-00491-w.
- [24] Johannes Buhl, Lemopi Isidore Besong, and Sebastian Härtel. "Temperature Control of the Two-Point Incremental Forming Process to Achieve Homogeneous Martensite Content Based on Finite Element Simulations". In: (Aug. 2023), pp. 739–747. DOI: 10.1007/978-3-031-41023-9\_74. URL: [https://doi.org/10.1007%2F978-3-031-41023-9\\_74](https://doi.org/10.1007%2F978-3-031-41023-9_74).
- [25] Muhammad Junaid Afzal and Johannes Buhl. "Numerical study to promote the residual stresses development during ISF process with improvement in two point incremental die forming". In: *Key Engineering Materials* 926 (2022), pp. 752–759. ISSN: 0015-7899. DOI: 10.4028/p-yr4vg6.

## 7 Experimental and Numerical Modeling and Analysis of Microstructural Residual Stresses in Hot Bulk Forming Parts under Specific Cooling

Behrens, B.-A.; Wester, H.; Kock, C.; Schröder, J.; Brands, D.; Hellebrand, S.

GEPRIS 374871564

### 7.1 Introduction

Almost every manufacturing process results in residual stresses in the final component. As residual stresses significantly influence the final component properties, they are of great interest. With regard to fatigue strength, residual stresses can change the cyclic deformation behavior, promote or retard crack initiation, accelerate or retard crack propagation, and have a beneficial or detrimental effect on fatigue life and fatigue strength [1]. Especially in the near-surface region, tensile residual stresses are undesirable because they promote the formation and propagation of cracks and, thus, reduce fatigue life [2]. Therefore, earlier research focused mainly on the reduction of residual stresses in the final component. The positive effects of residual stresses on component properties have already been demonstrated in research work. Studies in [3] show that the fatigue life of specimen in cyclic bending tests can be significantly increased by residual compressive stresses generated by surface treatment processes such as shot peening. In [4] the potential of manufacturing-generated residual compressive stresses to delay fatigue-induced bearing failures is substantiated. However, the targeted adjustment of residual stresses requires additional time-, cost- and energy-intensive process steps – such as the mechanical process shot peening or induction hardening following the forming process [5–7].

Due to a wide range of thermal, mechanical and metallurgical effects, see figure 7.1, hot forging processes offer great potential for targeted modification

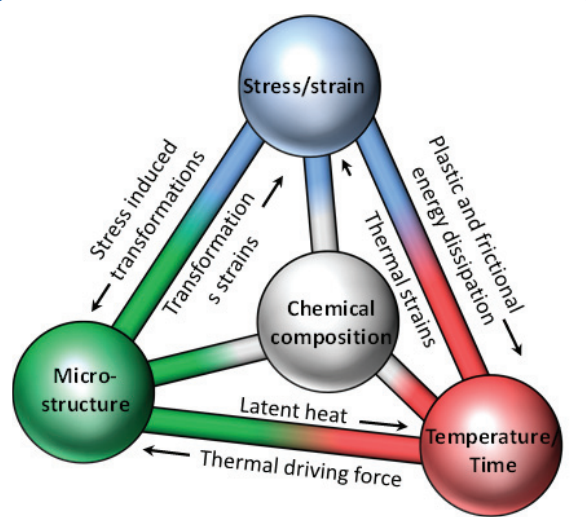


**Figure 7.1** Thermomechanical-metallurgical material interactions during hot forging.

of residual stress distribution. However, a fundamental understanding of the underlying mechanisms of residual stress generation in dependence of the forming parameters is necessary [8]. Further studies in the field of hot forging from recent years show the potential of integrating heat treatment into the forging process for the specific adjustability of microstructural properties with simultaneous cost savings due to the shortened process chain [9, 10]. However, the numerous interactions also lead to a challenging process design. In order to utilize these complex interactions in a controlled manner, it is advantageous to use numerical simulation technologies to consider the mutual influence of process parameters on residual stresses. In the field of cold forging, the prediction of residual stresses has already been demonstrated in a large number of research works [11, 12]. However, the numerical simulation of residual stress development in hot forging processes requires the consideration of thermal, mechanical as well as metallurgical effects and their interactions. Therefore, early work

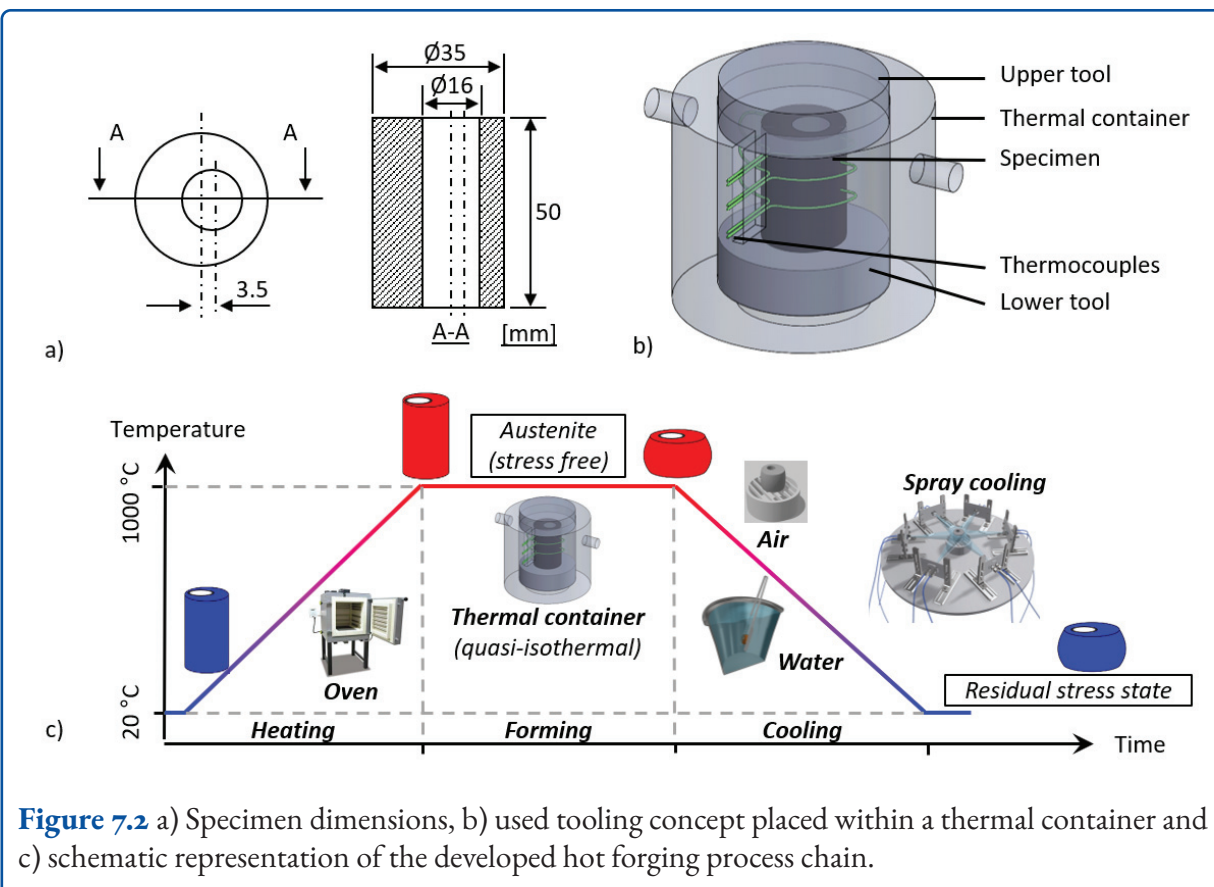


**Figure 7.2** a) Specimen dimensions, b) used tooling concept placed within a thermal container and c) schematic representation of the developed hot forging process chain.

has already modeled the formation, transformation and evolution of microstructures due to thermo-mechanical influences in numerical models and analyzed them on the basis of these models, e.g., [13–16]. In course of that, an overview on the derivation of the continuum mechanical formulation is given in [17], while [18] addresses a crystal plasticity finite element model for the computation of phase transformation. A more recent work regarding solid–solid phase transformation and its numerical description is, for example [19] where a phenomenological approach has been proposed based on an additive strain decomposition in the regime of small strains. In view of the definition of residual stress of first, second and third type, see section 1.4, the application of multi-scale methods is reasonable to account for residual stress acting on different scales. For an overview of the multi-scale modeling of residual stresses it is referred to section 4.6.1. The so-called full-field simulations with the aid of the Finite Element Method (FEM), also known as direct micro-macro transition approach or FE<sup>2</sup> method, is suitable for realizing a cross-scale simu-

lation for the analysis and consideration of residual stresses regarding their different classifications. The method was proposed by several groups in the late 1990's, see also reference on that in section 4.6.1 or [20] and [21] with references therein. With focus on thermal treatment, which is an essential aspect in hot forming processes, the works [22–24] about thermomechanical coupling in two-scale problems should be also mentioned.

The main objective of the presented research work is the adjustment of an advantageous compressive residual stress profile in hot forged components by means of intelligent process control using controlled cooling from the forging heat. The feasibility and potential are demonstrated using a hot forging process, in which cylindrical specimens with an eccentric hole, see figure 7.2 a, are formed at 1,000 °C and then undergo targeted cooling from the forging heat. The cooling is achieved by partial application of a water-air spray to the specimen. In this way, local plastification can be influenced by inhomogeneous distortions due to thermal and

transformation-induced effects to finally tailor the residual stress profile. A numerical simulation technique is used to analyze and design various process variants that are intended to generate beneficial residual compressive stresses in the near-surface. For a realistic simulation of the residual stress development, a detailed material characterization is carried out with regard to the flow behavior, the transformation behavior as well as the transformation-induced plasticity (TRIP). Since residual stresses are characterized based on the scale they act on, besides a macroscopic (single-scale) finite element (FE) model two-scale finite element ( $FE^2$ ) analyses are also performed. The overall scientific challenge is to generate different residual stresses in the surface of the samples while keeping the geometrical and microstructural properties the same.

## 7.2 Materials and Methods

### 7.2.1 Setup of Hot Forging Process Chain

Figure 7.2 shows a schematic sketch of the developed hot forging process with integrated heat treatment, which is utilized for the detailed analysis of residual stress development under variation of different process parameters such as forming speed, degree of deformation and forming temperature as well as different cooling strategies. Furthermore, the experimental tests are used for the calibration and validation of the finite element (FE) models. The investigated specimen is a cylinder with an initial diameter of 35 mm and height of 50 mm with eccentric hole. The dimensions of the specimen as well as a detailed representation of the used tooling concept placed within a thermal container is given in figure 7.2. Thermocouples are used to measure temperature development during the process.

The material investigated here is the Cr-alloyed steel 1.3505 (100Cr6) which is used in hot forging applications. In general, hot forging processes consist of three steps; heating, forming and cooling. The initial heating of the cylindrical specimen to above 1,000 °C with a suitable holding time leads to a full austenization of the material, which comes along

with a relaxation of previously present stresses. Thus, a nearly stress-free initial configuration is achieved. Afterwards, the specimen is transferred into a thermal container to ensure isothermal conditions and subsequently upset using the forming simulator DYNJS5590. The reference process results in a final height of 28 mm using a forming speed of 200 mm/s. The eccentricity leads to an inhomogeneous stress profile which is also characteristic for industrial processes [25].

A detailed description of the developed hot forging process chain is presented in [26]. With regard to the subsequent cooling, different routes and media are taken into account in order to achieve the targeted residual stress state, showing compressive stresses in regions near the outer surface. Here, either cooling in water, by air or with a spray cooling is applied to obtain the predefined, targeted residual stress state in the component. Cooling in water or air is used as reference cooling processes. Adjustable spray cooling is applied, which enables control of the cooling with respect to place and time, since the nozzles can be turned on and off individually. The six circularly arranged dual-substance nozzles of type XA PR 050 from Bete GmbH are fed by a mixture of water and air at a pressure of 0.04 MPa, which results in a water flow rate of approximately 0.2 l/s. The solenoid valves in front of the nozzles are controlled with the NI-9375 digital I/O module from National Instruments and programmed with Lab-View software.

### 7.2.2 Numerical Process Design

In order to design the manufacturing process for targeted residual stresses, single-scale FE simulations are a valuable tool. Promising cooling routes are afterwards analyzed with the two-scale FE model to obtain information with respect to microscopic residual stresses and phase-specific contributions. A schematic illustration of the numerical analyses is given in figure 7.3. The used single-scale model as well as two-scale model are presented in the following.

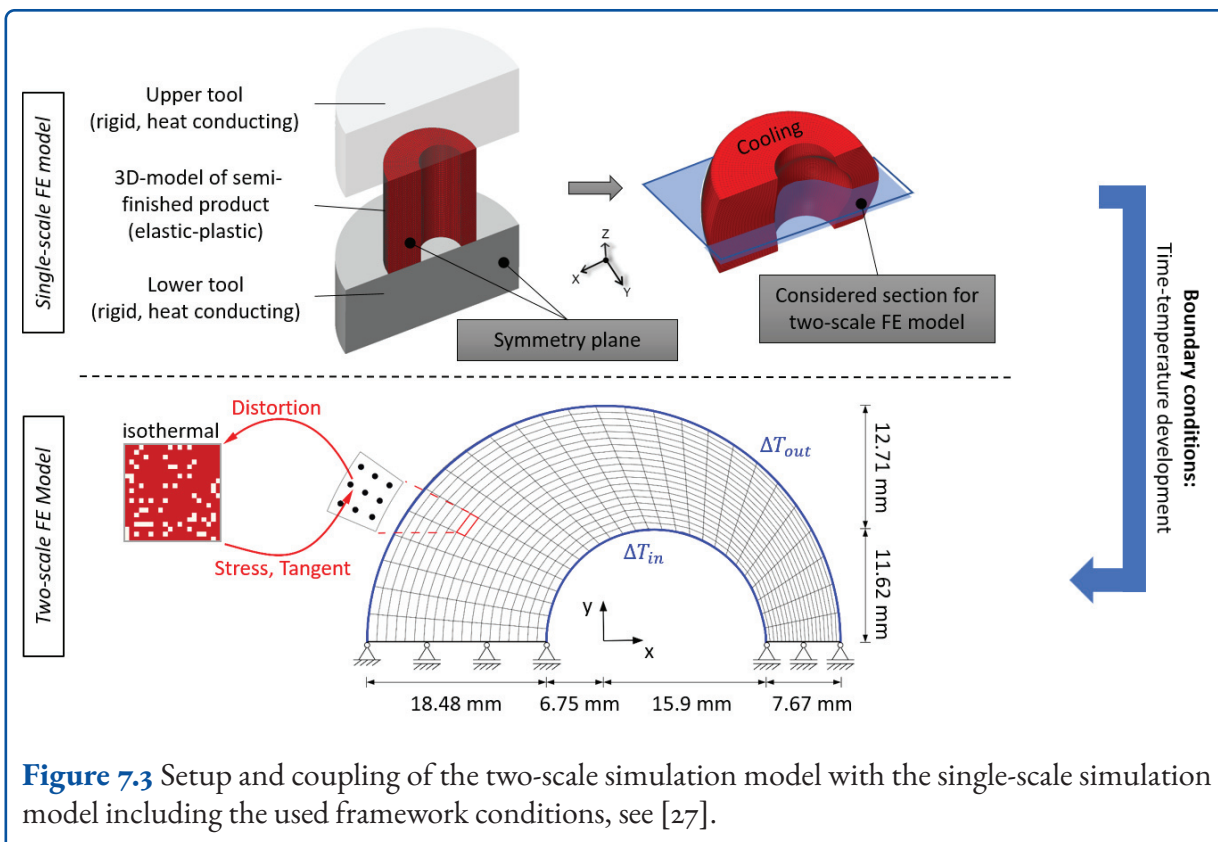


**Figure 7.3** Setup and coupling of the two-scale simulation model with the single-scale simulation model including the used framework conditions, see [27].

### 7.2.3 Single-scale Model

The previously described process, see section 7.2.1, is numerically investigated utilizing Simufact.forming v16 with an implicit MSC.Marc solver. To account for the occurring and interacting thermomechanical-metallurgical effects, the strain tensor is decomposed additively into five terms: elastic, plastic, thermal, transformation volumetric and TRIP strains

$$\varepsilon = \varepsilon^e + \varepsilon^p + \varepsilon^\theta + \varepsilon^{tv} + \varepsilon^{\text{TRIP}} \quad (\text{Equation 7.1})$$

according to [28, 29]. The developed single-scale, i.e., macroscopic, model is presented in detail in [27]. At the beginning of the simulation, i.e., at the start of the forming step, the specimen is thermally expanded at 1,000 °C and the microstructure is assumed to be fully austenitic. The tools are modeled as thermally conductive rigid bodies made of the material AISI Inconel 718 (DIN 2.4668) with a specific heat capacity of 435 J/kgK and a thermal conductivity of 11.4 W/mK according to the specifications of the material supplier [30]. The workpiece is modeled as a cylindrical

3D half model exploiting symmetry and discretized with 8-node hexahedron elements with an element length of 1 mm. The friction between workpiece and tools are considered using combined friction models with friction coefficient  $\mu = 0.1$  and friction factor  $m = 0.4$ . The strain, temperature and strain rate dependent yield stress is modeled using the GMT model (Gesellschaft für Maschinen-technik mbH), which is presented and calibrated by cylinder compression tests at various temperatures and strain rates [31]. Furthermore, the time-temperature-transformation (TTT) diagrams with and without superimposed deformation are determined and used for modeling phase transformation behavior. Detailed descriptions of experimental tests and results are given in [32, 33]. Required parameters regarding transformation plasticity are determined by numerical experiment considering the material and the occurring phases [26, 27].

Since an experimental determination of many material parameters for pure microstructural phases is

difficult, the software JMatPro<sup>1</sup>, which allows for calculation of temperature-dependent and phase-specific material parameters based on the composition of the material is utilized. Thereby, the polymorphism of the material is incorporated. Data is generated regarding Young's modulus, Poisson's ratio, specific heat capacity, heat conductivity, thermal expansion coefficient, latent heat and hardness. In case of the steel 1.3505 (100Cr6) the considered chemical composition is listed in table 7.1 and the obtained data is published in [26].

**Table 7.1** Chemical composition (wt.%) of the investigated steel alloy 1.3505 used for material data generation with JMatPro.

C	Si	Mn	P	S	Cr	Mo	Fe
0.99	0.25	0.35	0.025	0.015	1.475	0.1	bal.

For numerical mapping of the different cooling routes, the temperature-dependent heat transfer coefficients (HTCs) are needed, which are determined by an iterative experimental numerical procedure. Therefore, the temperature is measured at certain points on the specimen's surface during the cooling experiments to obtain the associated time-temperature relation. Subsequently, numerical simulations of the cooling process are carried out with varying HTCs in Simufact.forming until a good agreement between numerical and experimental data is achieved. The obtained HTC values for water and spray cooling are exemplary depicted in figure 7.4. Particularly high values are observed for spray in regions below 300 °C due to the atomization of water droplets. The methodology as well as validated results can be found in [26].

The single-scale FE model has been evaluated and validated with experimental measurements. Comparisons of microstructure distributions as well as residual stress measurements using X-ray diffraction show a good agreement. Detailed information regarding the validation procedure and results are presented in [27, 31, 34]. Furthermore, a more

thorough analysis of the residual stress distribution inside the forged specimen resulting from the multiaxial loading is performed on the basis of experimental data using the contour method. The residual stress distributions after air and water cooling in the specimen are predicted in a good agreement with experimental results by the single-scale simulation [34]. Overall, the ability of this model to provide good predictions with respect to the residual stress distribution inside the component is shown. Thus, it is used to compare the different cooling media (air, water, spray) and cooling routes (different spray cones) in order to obtain the targeted stress state, i.e., compressive stresses in regions near the outer surface.

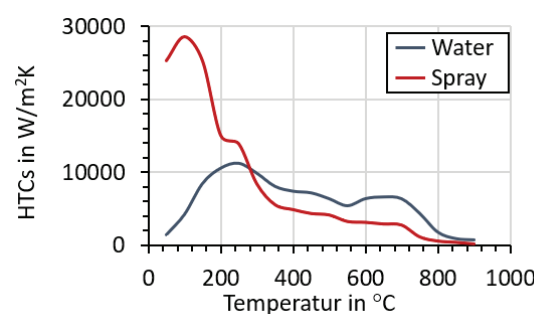


**Figure 7.4** Temperature-dependent heat transfer coefficient (HTC) for cooling in water and cooling with spray.

## 7.2.4 Two-scale Model

Based on single-scale results [35], promising cooling routes, which give the targeted residual stress state, are subject to two-scale FE<sup>2</sup> simulations, utilizing the direct micro-macro transition approach. Regarding these two-scale simulations, focus lies on the cooling step of the hot bulk forming process. In order to take into account the previous process steps, i.e., heating and forming, an equivalent plastic strain, which is obtained by the single-scale simulations after the forming is initialized [36]. The numerical analysis is carried out in the Finite Element Analysis Program (FEAP)<sup>2</sup>, using the PAR-

<sup>1</sup> JMatPro. "Practical software for materials properties" In: (Aug. 2018). <https://www.sentesoftware.co.uk/jmatpro>.

<sup>2</sup> R.L. Taylor. FEAP - A finite element analysis program, Version 8.2. Department of Civil and Environmental Engineering, University of California at Berkeley. Berkeley, California 94720-1710, 2008.

DISO solver provided by the Intel MKL library to solve the linear system of equation<sup>3</sup>.

As thermo-mechanically coupled macroscopic boundary value problem, a cross-sectional slice taken from the cylindrical specimen at mid-height is considered exploiting symmetry conditions, such that the displacement in  $x$ -direction is fixed for all nodes along the cut, see figure 7.3. On the inner and outer lateral surface, the cooling is applied via Dirichlet boundary conditions, following the single-scale simulations. Depending on the considered cooling route, these time-temperature relations differ, since inhomogeneous temperature distributions are to be modeled on the lateral surface in case of spray cooling. Therefore, the boundary is divided into sections of  $10^\circ$ , so that on each of them one temperature evolution is defined [37]. Additionally, a zero heat flux is set along the cut, since only a small impact of the heat flux in circumferential direction is assumed compared to the radial direction. Analogously to the single-scale FE model, thermal, elastic and plastic strains, the volumetric expansion due to the phase transformation and the influence of TRIP are taken into account. Moreover, the measurement of the final phase fractions of the phases present serve as input parameter required to compute the actual phase distributions considering the Koistinen-Marburger differential equation for martensitic transformation.

The microscopic boundary value problem is defined as a square RVE with periodic boundary conditions. Since it is attached to one macroscopic integration point, it is assumed that the temperature gradient over the RVE vanishes and an isothermal problem is formulated. The actual macroscopic temperature serves as input to determine the temperature-dependent phase-specific material parameters. A random distribution of martensitic inclusions in the austenitic matrix is taken into account [38, 39]. Therefore, based on the actual martensitic volume fraction, the number of finite elements that are switched from initially austenite to martensite is determined to comply with the

<sup>3</sup> O. Schenk and K. Gärtner. "Solving unsymmetric sparse systems of linear equations with PARDISO". In: Journal of Future Generation Computer Systems 20 (2004), pp. 475–487.

phase fractions [40, 41]. According to detailed studies regarding the mesh density and time step size in [40], the macroscopic boundary value problem is discretized with 270 elements, while the RVE consists of  $20 \times 20$  elements in a structured manner. The time step size is set to 0.1 s with a refinement during the phase transformation to 0.01 s.

Such a two-scale method enables the analysis of physical quantities on different scales. Here, the division of the resulting residual stresses into macroscopic (1st type) and microscopic (2nd and 3rd type) residual stresses is of special interest. Additionally, measures of the microscopic stress fluctuations on the macroscopic scale can be advantageous, since the influence of the microscopic fluctuation on the macroscopic stresses can be displayed and evaluated on the upper scale [41]. The impact of the microscopic fluctuations on the macroscopic properties of the component, e.g., strength or durability, can be analyzed. Consequently, the origin of the evolving macroscopic stresses can be determined occurring due to the cooling and a superimposed phase transformation. Since the volume average of the microscopic fluctuations of the stresses are zero by definition, quadratic measures are formulated as

$$\|\tilde{\sigma}_{\text{tang}}\|_{\mathcal{L}^2}^V := \left( \frac{1}{V} \int_{RVE} \tilde{\sigma}_{\text{tang}}^2 dV \right)^{\frac{1}{2}}$$

(Equation 7.2)

where  $V$  denotes the volume of the RVE. Note that the dimensions of the RVE are small compared to the size of the macroscopic specimen, i.e., a scale separation is assumed. In this sense, the microscopic tangential component of the stress fluctuations is defined as the projection of the microscopic stress fluctuations onto a fixed (macroscopic) tangential vector  $\bar{s}$ , i.e.,  $\tilde{\sigma}_{\text{tang}} := \tilde{\sigma} : (\bar{s} \otimes \bar{s})$ .

## 7.3 Results

First, the influence of varying process variables on the residual stress distribution is investigated using the experimental process route. As stated, it is essential to ensure that occurring residual stresses are a direct consequence of the different cooling routes

and media and are not evoked by a change of the microstructure or geometry, for instance. Thus, to investigate the influence of various forming parameters on the resulting residual stress state, they are varied individually. Based on the findings, a large number of cooling routes are analyzed by means of numerical simulations with the aim to generate compressive residual stresses in the near outer surface regions. In a first step, different cooling media and spray field variants are compared using single-scale simulations, see section 7.2.2. The cooling is finished, when the temperature gradient vanishes in the component. Due to the absence of outer forces, the resulting stress distribution can be interpreted as that of residual stresses. The focus here is on the tangential stresses, which are known to have the most impact on the strength or wear resistance.

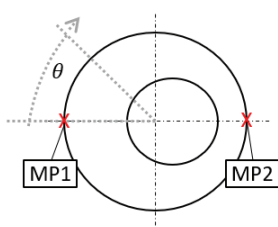


**Figure 7.5** Measuring points (MP) on the circumference of the specimen as a function of the angle  $\theta$ .

Experimental tests are carried out on selected cooling variants and the geometry, microstructure and residual stresses are investigated and compared with the numerical results. Afterwards, promising cooling routes are examined in a two-scale FE<sup>2</sup> model to achieve information regarding the microscopic residual stress distribution. On the experimentally produced specimen, the near-surface residual stresses on the circumference of the specimen as a function of the position angle  $\theta$  are measured by X-ray diffraction. A schematic representation of the measurement points can be found in figure 7.5.

### 7.3.1 Influence of Forming and Disturbance Parameters

The variation of process parameters shows, that all investigated process parameters such as forming rate, forming temperature, the degree of deformation or the cooling medium has a reciprocal impact on the formed microstructure and further on the phase transformation and the resulting stress distribution. For example, the influence of different strokes which result in varying degree of deformation within the sample is depicted in figure 7.6 a. Consequently, it is of great importance that the forming and cooling parameters be adjusted to each other. Furthermore, disturbance parameters such as different tool temperatures or quenching directly after the forming significantly influence the resulting stresses, see figure 7.6 b. Detailed results on the parameter studies are presented in [42]. By varying the assumed material composition in JMatPro, the influence of batch variations is also considered. The numerical simulations performed using the modified material data show only a small negligible influence on the resulting residual stress distribution, see figure 7.6 c.

### 7.3.2 Comparative Study of Different Cooling Media

In a first step, numerical simulations of the heated and formed cylindrical specimen cooled by air or in water are performed. The resulting tangential stresses are investigated over the respective cooling time. Exemplary results of two investigation points on the outer surface on both sides of the specimen are shown in figure 7.7. As it can be seen, the cooling medium air leads to overall small tensile residual stresses in the component. Cooling in water results also in tensile stresses in the final state, but of higher magnitude. The microstructure of the water-cooled sample consists of a large proportion of martensite and a small proportion of retained austenite, resulting in a component with high strength. Detailed description of the numerical simulation and an experimental validation are given in [34].

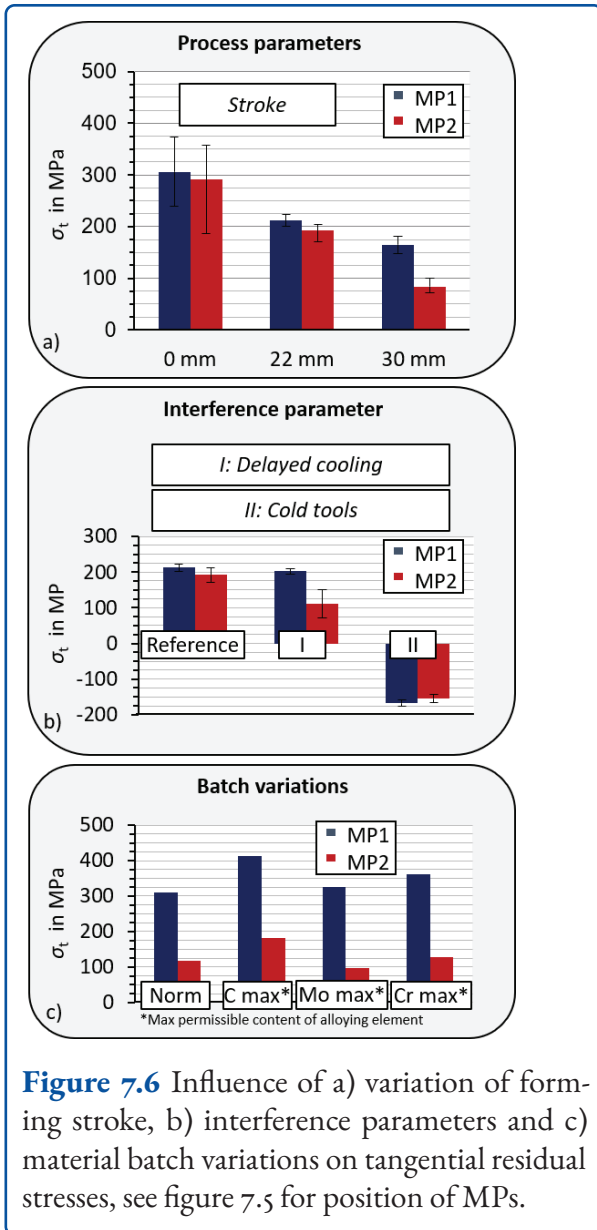


**Figure 7.6** Influence of a) variation of forming stroke, b) interference parameters and c) material batch variations on tangential residual stresses, see figure 7.5 for position of MPs.

A further investigated cooling strategy is based on the application of a spray as mixture of water and air. For the comparison of different spray cooling strategies, a martensitic microstructure is aimed at. The focus here is to verify that only a change in the cooling route and not the microstructure or geometry leads to the changed residual stress state.

Exemplarily considered spray cooling strategies “spray total”, “spray side”, “spray thin” and “spray thick” are depicted in figure 7.8. Each blue region is directly exposed to the spray. The resulting tangential stresses on the outer lateral surface in dependence of the angle  $\theta$  are illustrated in figure 7.9. For better evaluation, the results for water are depicted additionally. As can be seen, “spray total” and “spray thin” strategies evoke mostly tensile stresses analogously to cooling in water, while “spray side” and “spray thick” strategies result in tensile and compressive stresses. The latter strategies especially show high compressive stresses in the spray-exposed region around  $\theta = 0^\circ$  and is therefore object of further analysis.

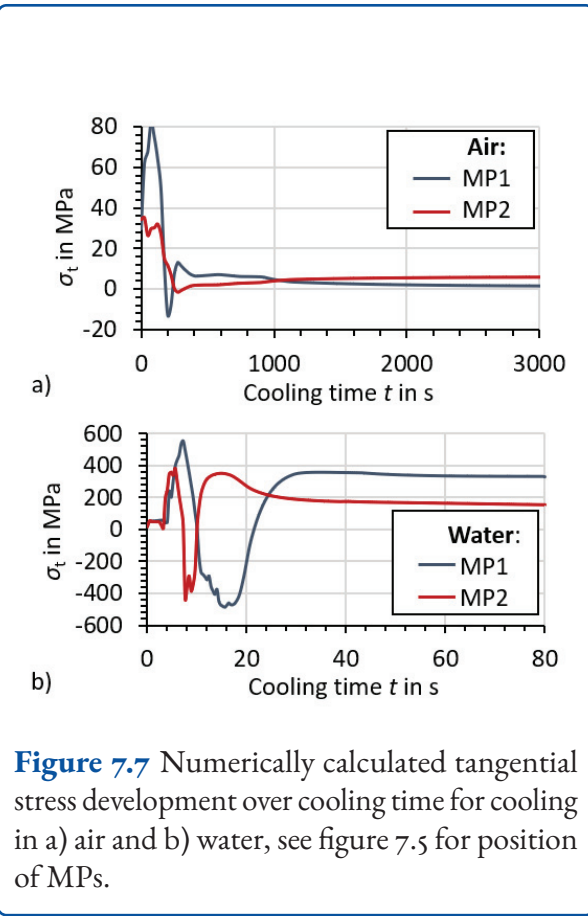


**Figure 7.7** Numerically calculated tangential stress development over cooling time for cooling in a) air and b) water, see figure 7.5 for position of MPs.

dence of the angle  $\theta$  are illustrated in figure 7.9. For better evaluation, the results for water are depicted additionally. As can be seen, “spray total” and “spray thin” strategies evoke mostly tensile stresses analogously to cooling in water, while “spray side” and “spray thick” strategies result in tensile and compressive stresses. The latter strategies especially show high compressive stresses in the spray-exposed region around  $\theta = 0^\circ$  and is therefore object of further analysis.

### 7.3.3 Experimental Realization

Since the single-scale simulation predicts a compressive residual stress profile for the cooling strategy “spray thick”, this cooling route is to be experimentally realized in a next step and compared to cooling in water as reference. Afterwards, the residual stresses near the surface on the circumference of the specimen are determined as a function of the position angle  $\theta$  by means of X-ray diffraction. The results of the experimental and the single-

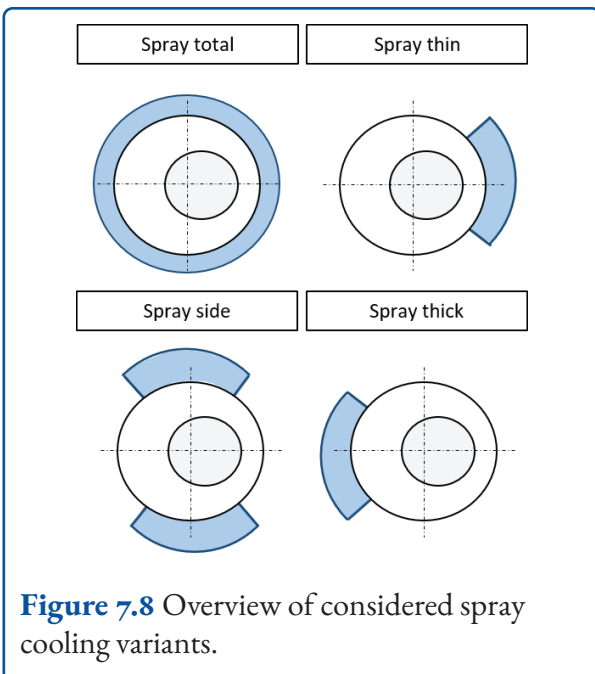


**Figure 7.8** Overview of considered spray cooling variants.

scale numerical investigations are illustrated in figure 7.10.

As can be seen, on the thick-walled side, starting from the angle  $\theta = 0^\circ$  at MP1 up to  $\theta = 45^\circ$ , compressive tangential stresses of  $\sigma_t = -407 \text{ MPa}$  and  $\sigma_t = -223 \text{ MPa}$ , respectively, are experimentally generated with the strategy “spray thick”, as predicted by the simulations. Thus, the residual stresses at these positions are significantly modified, compared with the tensile residual stresses of  $\sigma_t = 216 \text{ MPa}$  for  $\theta = 0^\circ$  and  $\sigma_t = 146 \text{ MPa}$  for  $\theta = 45^\circ$  produced by cooling in water. Above  $\theta = 90^\circ$ , both strategies produce tensile residual stresses.

On the thin-walled side, the experimental results of the strategy “spray thick” show higher tensile stresses compared to the simulation. For example,  $\sigma_t = 222 \text{ MPa}$  are measured for MP2, in contrast to the calculated stress of  $\sigma_t = 65 \text{ MPa}$ . This may be due to the fact that the influences from metallurgical effects such as dislocation density due to austenite transformation, local gradients of yield stress at phase boundaries, or forced dissolution of carbon atoms in the martensitic lattice are only considered in the material characterization at constant boundary conditions. For example, the TTT-diagrams according to the German standard are

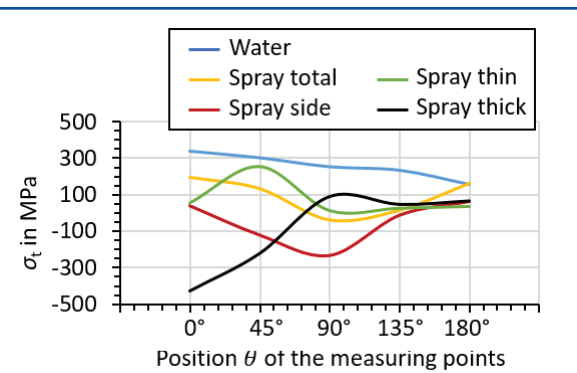


**Figure 7.9** Numerically calculated tangential residual stresses  $\sigma_t$  for different cooling variants over the circumference of the specimen, see figure 7.5 for position of MPs.

determined for a microstructure after a ten-minute holding time at austenitization temperature and direct quenching. The same applies for the transformation plasticity constants, which are determined by an experimental-numerical approach for continuous cooling from the austenitization temperature. This explains a higher deviation between experimental and numerical results, especially at the locations that experience delayed cooling, as is the case on the thin-walled side of the specimen.

Furthermore, metallographic examinations and optical geometry analyses are carried out in order to exclude the possibility that the modifications of the residual stresses in the specimen from the strategy “spray thick” compared to water cooling are influenced by the microstructure composition or a changed geometry, see [26]. Specimen produced by both of these strategies show hardness values of approximately 800 HV in the entire specimen’s cross section and the optical microscopy images indicates a fully hardened martensitic specimen. The contour plot of the deviation  $e$  in figure 7.11 on this surface illustrates the three-dimensional distance in the direction perpendicular to the surface of the geometry of a specimen produced with the “spray thick” process strategy. The sign of the deviation value indicates whether the corresponding area of the geometry from the strategy “spray thick” lies outside (positive) or inside (negative) the workpiece shape from the cooling in water. The

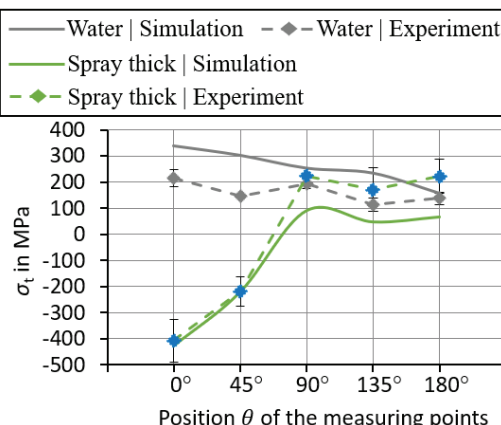


**Figure 7.10** Comparison between experimentally measured and numerical calculated tangential residual stresses  $\sigma_t$  over circumference of the specimen for different cooling variants, see figure 7.5 for position of MPs.

different thermomechanical strategies result in local deviations of less than 0.5 mm. Although the specimen are produced in different ways, they still have almost identical geometrical and microstructural properties. Hence, it is shown that only the residual stresses are changed comparing the cooling strategies “spray thick” and water. Consequently, it can be concluded that modification of the residual stresses is possible by advanced process control.

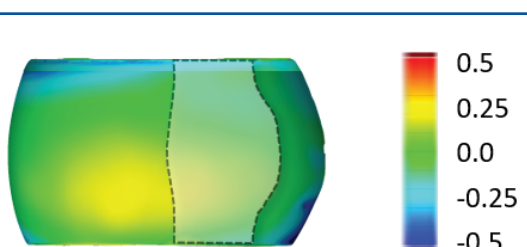


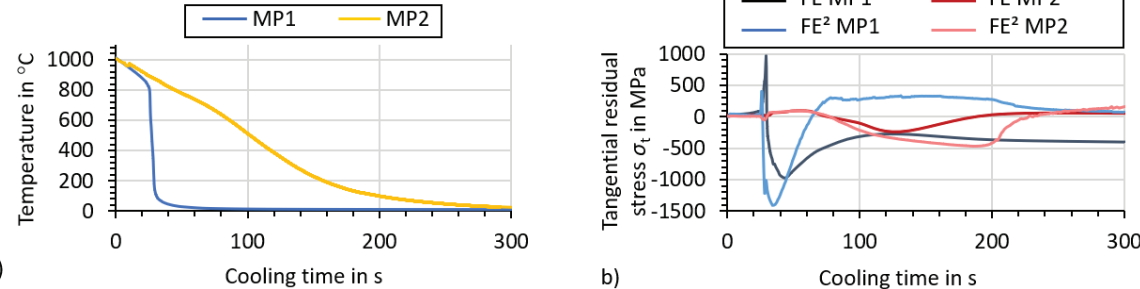
**Figure 7.11** Geometric deviation  $e$  in mm of the samples from water and spray cooling.

### 7.3.4 Investigation on Microscopic Residual Stresses

In the previous sections, an improved cooling strategy “spray thick” is found numerically regarding the final, macroscopic residual stress distribution

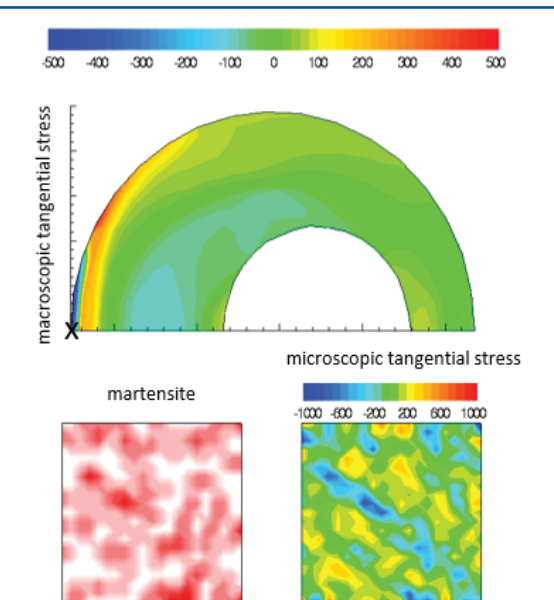
and the results are validated experimentally. Now, the aim is to analyze microscopic (residual) stresses and their respective effects on the macroscopic residual stresses, which are known to cause or promote microcracks and thereby influence the overall properties, especially lifetime prediction. The two-scale FE<sup>2</sup> model together with its temperature boundary condition, see figure 7.3, which results from single-scale analysis, has been validated regarding the cooling strategy water [43]. Qualitatively, the presented results of the two-scale and the single-scale model are in good agreement. The small quantitative differences are likely due to the disregard of heat dissipation perpendicular to the section plane, the averaged temperature boundary conditions, and the lack of consideration of latent heat generation in the microscopic material modeling. It is to be noted, that the two-scale model analyses 2D geometries in contrast to the 3D single-scale computations. In section 7.3.3, the good agreement between the single-scale simulation and the experimental realization for cooling in water has already been shown. Consequently, the respective stress evolution is considered as a reference for further analysis in the following.

Figure 7.12 shows the temperature evolution and the development of the macroscopic tangential stresses  $\sigma_t$  at measuring points MP1 and MP2 over the cooling time, resulting from the single-scale and the two-scale simulations for the cooling strategy “spray thick”. With the onset of spray cooling, the material at the surface of the thick-walled side (MP1) contracts, leading to tensile stresses in both numerical models. After a sufficient cooling time, martensitic phase transformation takes place in regions close to the surface around MP1, which is accompanied by volumetric expansion as well as a local increase of the yield strength of the material. At this point, high compressive stresses are already present, which are also represented by both numerical models, albeit with a slight time offset. In the single-scale simulation, these compressive stresses weaken as soon as the martensitic transformation front subsequently continues in the direction of the bulk and volumetric expansion also takes place. In contrast, the two-scale simulation shows a renewed changeover of the tangential stress to the positive range of values intermediately. In the final



**Figure 7.12** a) Temperature evolution and b) tangential stresses in MP1 and MP2 for cooling with strategy “spray thick” utilizing single-scale (FE) and two-scale (FE<sup>2</sup>) methods, see figure 7.5 for positions of MP1 and MP2.

state, the single-scale models predict compressive stresses at MP1, which is in good accordance with the experimental realization, while the two-scale model results in small tensile stress values.



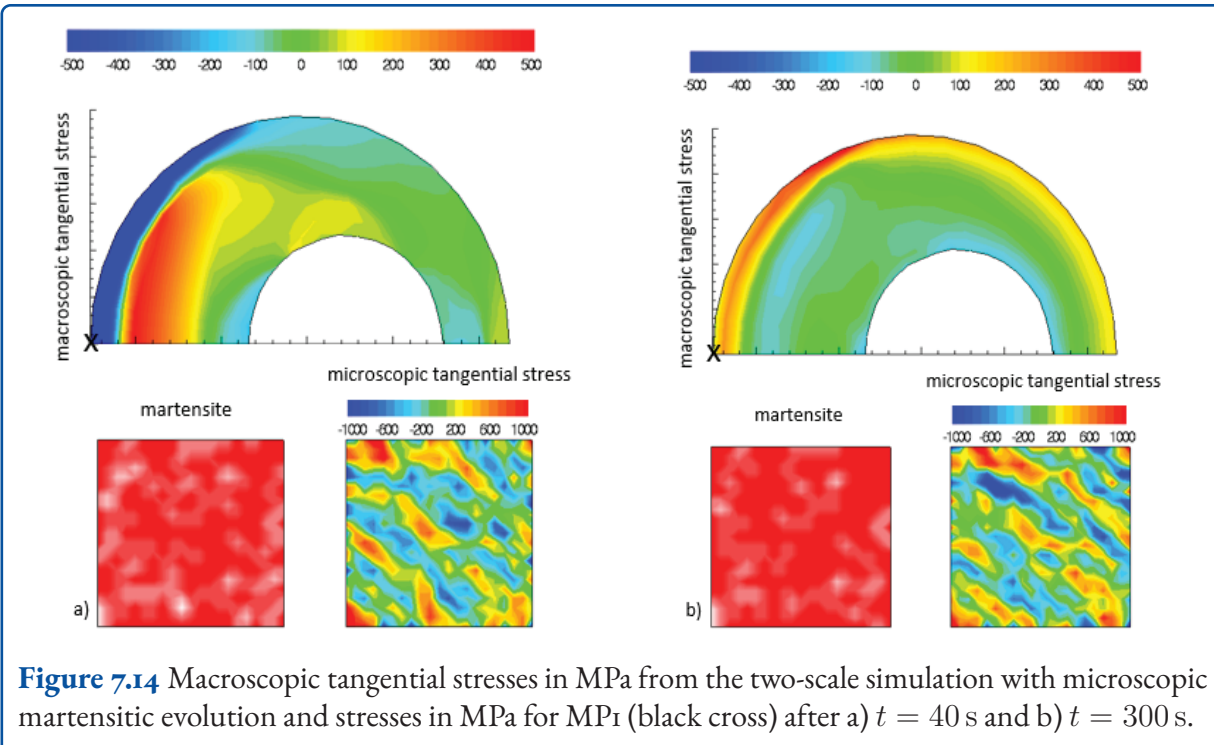
**Figure 7.13** Macroscopic tangential stresses in MPa from the two-scale simulation with microscopic martensitic evolution and stresses in MPa for MP1 (black cross) after  $t = 27$  s.

With a delay, the martensitic phase transformation also takes place at the thin-walled side, where previously compressive stresses are present at MP2 due to the preceding volumetric expansion as a result of the martensite transformation in the neighboring regions. The phase transformation at MP2 takes place under superimposed compressive stresses,

which, in accordance with the transformation plastic effect, clearly reduce the volumetric expansion in the circumferential direction. The thermal contraction at MP2 leads to tensile residual stresses contrary to the resistance of the already cooled surrounding material. Regarding both measuring points, the qualitative assessment is in good agreement.

By analyzing microscopic quantities, which is of particular interest when an RVE based on a real microstructure is used, it is possible to draw conclusions about the influence of microstructure evolution and the effects on the residual stress state. These quantities include, for example, the distribution of tangential stresses and the martensitic volume fraction. Thus, for characteristic states during spray cooling, figures 7.13 and 7.14 show the macro- and microscopic tangential stress evolution and the martensitic evolution at MP1. Before the onset of phase transformation, tensile stresses arise due to thermal contraction, afterwards compressive stresses are present, see figure 7.13. A compressive stress peak is reached before the bulk undergoes phase transformation, see figure 7.14a. Then, the stresses in the examined point are weakened as depicted in figure 7.14 b for the final state.

By definition, macroscopic stresses are calculated from the volume average of the microscopic stresses. In order to measure the impact of the microscopic on the macroscopic residual stresses, quadratic measures are evaluated as introduced in section 7.2.4, here for cooling in water. Before the onset of phase



transformation, the quadratic measure is equal to zero, i.e.,  $\|\tilde{\sigma}_{\text{tang}}\|_{\mathcal{L}^2}^V = 0$ . In case martensite starts to form near the outer lateral surface, the measures result in high values in regions of phase transformation, see figure 7.15 a+b. After the austenite-to-martensite phase transformation has been initiated in the whole specimen, the value for the quadratic measure becomes nearly homogeneous in the whole structure, see figure 7.15 c.

In contrast to the heterogeneous distribution of the macroscopic tangential stresses, which have been investigated before, the microscopic stress fluctuations of the residual stresses are independent of their associated macroscopic position. In general, such a quadratic measure can be useful to determine the influence of microscopic quantities on the macroscopic performance or to depict the phase transformation on the macroscale. However, it is to be noted that the sign of the microscopic residual stresses is omitted by definition, see *Equation 7.2*.

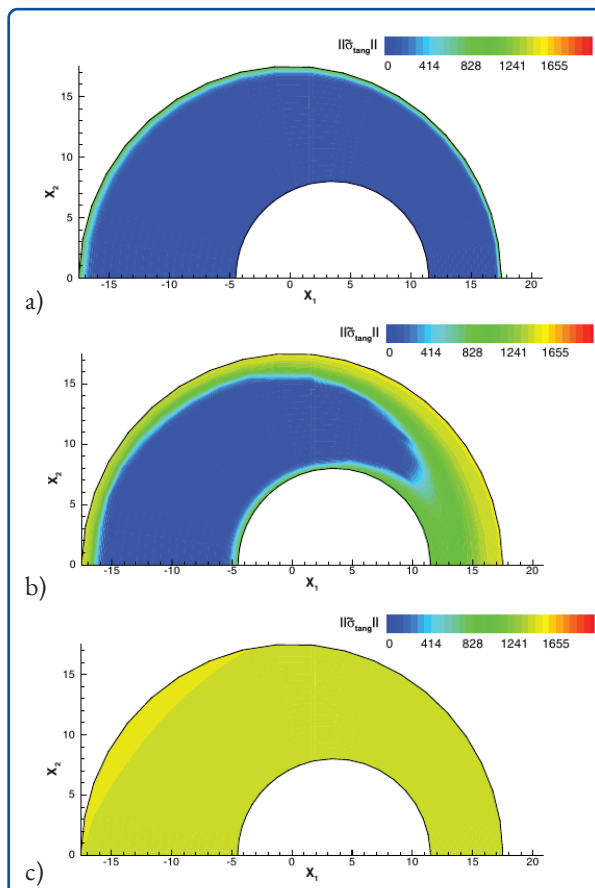


**Figure 7.15** Quadratic measure of tangential part of stress fluctuations  $\|\tilde{\sigma}_{\text{tang}}\|_{\mathcal{L}^2}^V$  after a)  $t = 9$  s, b)  $t = 12$  s and c)  $t = 80$  s for cooling in water.

### 7.3.5 Properties improved by residual stresses

In order to prove the positive influence of compressive residual stresses close to the surface on the component properties, experimental tests are carried out on samples produced with different spray field configurations resulting in tensile or compressive residual stresses. In order to analyze the increased wear resistance assumed by compressive residual stresses reducing the crack opening, experimental wear tests are carried out with the Triboindenter Hysitron TI 950. A comparison of the wear volumes shows the potential of the compressive residual stresses, see figure 7.16. Regardless of the microstructure, all specimen with modified residual stress show a significantly reduced wear volume. Subsequently, quasi-static compression tests are carried out at room temperature on samples with a pearlitic microstructure, again with tensile and compressive residual stresses. After compression with a stroke of 10 mm, 60% of the specimen with tensile residual stresses but only 28% of the specimen with compressive residual stresses show cracks.

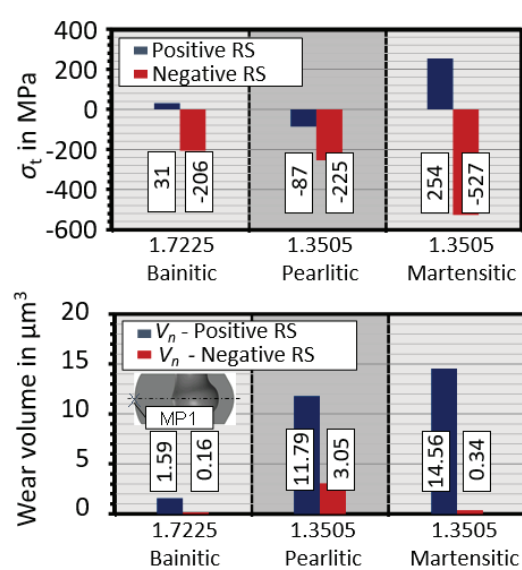


**Figure 7.16** Proof of improved wear resistance at MP1 of the specimen due to advantageous near-surface compressive residual stresses.

### 7.4 Conclusion

As part of the work, a hot forging process with integrated heat treatment is developed to analyze the development of residual stresses. The focus is on the targeted adjustment of residual compressive stresses by modifying the process parameters and cooling route. A targeted controllable spray field is used to modify the cooling process from the forging heat. Due to the complex thermo-mechanical-metallurgical interactions, FE models are developed and parameterized to enable efficient process design and analysis. For this purpose, the required material data are determined experimentally and supplemented by calculations with JMat-Pro. The multi-scale simulation approach allows for residual stresses to be taken into account at all scales and extensive fundamental knowledge to be gained. Additionally, the experimental realization of selected process routes enables a successful validation of the numerical models. The numerical and experimental parameter studies performed show an influence of the process variables as well as the cooling strategy on the resulting residual stresses. Thus, the forming process and the heat treatment have to be specifically adjusted to each other. Finally, it is demonstrated that residual stresses can be specifically influenced by targeted cooling in the spray field without changing the microstructure and geometry. The potential of numerical simulation for the design of complex thermo-mechanical-metallurgical coupled processes is also emphasized.

## References

---

- [1] D. Löhe, K.-H. Lang, and O. Vöhringer. "Residual Stresses and Fatigue Behavior". In: *Handbook of Residual Stresses and Deformation*. Ed. by G. Totten, M. Howes, and T. Inoue. Novelty, Ohio, USA, ASM International, 2002.
- [2] P.J. Withers. "Residual stress and its role in failure". In: *Reports on Progress in Physics* 70 (2007), pp. 2211–2264.
- [3] D. Löhe and J.E. Hoffmann. "Influence of Macro Residual Stresses on the Fatigue Behavior Smoothed and Notched Specimens Made from a High Strength Steel". In: *Journal of Materials and Manufacturing* III (2002), pp. 704–710.
- [4] F. Pape et al. "Influence of residual stresses introduced by manufacturing process on bearing endurance time". In: *Tribology Letters* 65.70 (2017).
- [5] J. Kritzler and W. Wübbenhorst. "Inducing Compressive Stresses through Controlled Shot Peening". In: *Handbook of Residual Stresses and Deformation*. Ed. by G. Totten, M. Howes, and T. Inoue. ASM International, 2002.
- [6] J. Grum. "Induction Hardening". In: *Handbook of Residual Stresses and Deformation*. Ed. by G. Totten, M. Howes, and T. Inoue. Novelty, Ohio, USA, ASM International, 2002.
- [7] G. Totten, M. Howes, and T. Inoue. *Handbook of Residual Stress and Deformation of Steel*. Harlow, England and New York: ASM International, 2002.
- [8] A. Franceschi et al. "Strategies for residual stress adjustment in bulk metal forming". In: *Archive of Applied Mechanics* (2021).
- [9] F.-W. Bach and K. Kerber. *Prozesskette Präzisionsschmieden*. Berlin, Heidelberg: Springer Vieweg-Verlag, 2014.
- [10] B.-A. Behrens et al. "EcoForge: Resource-efficient process chains for high performance parts". In: *Key engineering materials*. Vol. 504/506. 2012, pp. 151–156.
- [11] R.M. McMeeking and E.H. Lee. "The generation of residual stresses in metal-forming processes. Residual stress and stress relaxation". In: (1982), pp. 315–329.
- [12] A.E. Tekkaya, J. Gerhardt, and M. Burgdorf. "Residual stresses in cold-formed workpieces". In: *Manuf. Technol.* 34 (1985), pp. 225–230.
- [13] V.I. Levitas. "Condition of nucleation and interface propagation in thermoplastic materials". In: *Le Journal de Physique IV* 5 (1995), pp. 41–46.
- [14] V.I. Levitas. "Thermomechanics of martensitic phase transitions in elastoplastic materials". In: *Mechanics research communications* 22 (1995), pp. 87–94.
- [15] V.I. Levitas. "The postulate of realizability: formulation and applications to post-bifurcation behavior and phase transitions in elastoplastic materials. Part I and II." In: *International Journal of Engineering Science* 33 (1995), pp. 921–971.
- [16] V.I. Levitas. "Phase transitions in inelastic materials at finite strains: a local description". In: *Journal de Physique IV Proceedings* 6 (1996), pp. 55–64.
- [17] F.D. Fischer et al. "Continuum mechanical aspects of phase transformations in solids". In: *Archive of Applied Mechanics* 64 (1994), pp. 54–85.
- [18] F. Roters et al. "Overview of constitutive laws, kinematics, homogenization and multiscale methods in crystal plasticity finite-element modeling: theory, experiments, applications". In: *Acta Materialia* 58 (2010), pp. 1152–1211.
- [19] R. Mahnken, A. Schneidt, and T. Antretter. "Macro modelling and homogenization for transformation induced plasticity of a low-alloy steel". In: *International Journal of Plasticity* 25 (2009), pp. 183–204.
- [20] M.G.D. Geers, V.G. Kouznetsova, and W.A.M. Brekelmans. "MultiScale First-Order and Second-Order Computational Homogenization of Microstructures towards Continua". In: *International Journal for Multiscale Computational Engineering* 1 (2003).
- [21] J. Schröder. "A numerical two-scale homogenization scheme: the FE<sup>2</sup>-method". In: *Plasticity and Beyond - Microstructures, Crystal-Plasticity and Phase Transitions*. Ed. by J. Schröder and K. Hackl. Vol. 550. CISM Courses and Lectures. Springer, 2014, pp. 1–64.

- [22] I. Özdemir, W.A.M. Brekelmans, and M.G.D. Geers. “FE<sup>2</sup> computational homogenization for the thermo-mechanical analysis of heterogeneous solids”. In: *Computer Methods in Applied Mechanics and Engineering* 198 (2008), pp. 602–613.
- [23] I. Temizer and P. Wriggers. “Homogenization in finite thermoelasticity”. In: *Journal of the Mechanics and Physics of Solids* 59 (2011), pp. 344–372.
- [24] A. Sengupta, P. Papadopoulos, and R.L. Taylor. “A multiscale finite element method for modeling fully coupled thermomechanical problems in solids”. In: *International Journal for Numerical Methods in Engineering* 91 (2012), pp. 1386–1405.
- [25] C. Simsir and C.H. Gür. “3D FEM simulation of steel quenching and investigation of the effect of asymmetric geometry on residual stress distribution”. In: *Journal of Materials Processing Technology* 207 (2008), pp. 211–221.
- [26] B.-A. Behrens et al. “Experimental and numerical investigations on the development of residual stresses in thermo-mechanically processed Cr-alloyed steel 1.3505”. In: *metals* (2019).
- [27] B.-A. Behrens, A. Chugreev, and C. Kock. “Macroscopic FE-simulation of residual stresses in thermo-mechanically processed steels considering phase transformation effects”. In: *XIV International Conference on Computational Plasticity. Fundamentals and Applications*. Barcelona, Spain, 2019, pp. 211–222.
- [28] S. Denis et al. “Stress-phase-transformation interactions - Basic principles, modelling and calculation of residual stress prediction”. In: *Mater. Sci. Technol.* 1 (1985), pp. 805–814.
- [29] W. Mitter. *Umwandlungsplastizität und ihre Berücksichtigung bei der Berechnung von Eigenspannungen*. Vol. 7. Materialkundlich-Technische Reihe. Berlin, Germany: Bornträger Verlag, 1987.
- [30] Special Metals Co. “New Hartford, New York, USA”. In: (Jan. 2019). [www.specialmetals.com/assets/smc/540/documents/pcc-8064-sm-alloy-handbook-v04.pdf](http://www.specialmetals.com/assets/smc/540/documents/pcc-8064-sm-alloy-handbook-v04.pdf).
- [31] B.-A. Behrens et al. “Experimental and numerical investigations on the development and stability of residual stresses arising from hot forming processes”. In: *Proceedings of the 13th International Conference on Technology and Plasticity*. Columbus, OH, USA, 2021.
- [32] B.-A. Behrens, A. Chugreev, and C. Kock. “Experimental-numerical approach to efficient TTT-generation for simulation of phase transformations in thermomechanical forming processes”. In: *IOP Conference Series, Materials Science and Engineering*. Bristol, UK, 2018.
- [33] D. Brands et al. “On the analysis of microstructural residual stresses in hot bulk forming parts under specific cooling”. In: *Proceedings of Applied Mathematics and Mechanics* 18.1 (2018), e201800256.
- [34] B.-A. Behrens et al. “Investigations on Residual Stresses within Hot-Bulk-Formed Components using Process Simulation and the Contour Method”. In: *metals* (2021).
- [35] S. Uebing et al. “Residual Stresses in Hot Bulk Formed Parts - A Phenomenological Approach for the Austenite-to-Martensite Phase Transformation”. In: *Proceedings of the 13th International Conference on Technology and Plasticity*. Columbus, OH, USA, 2021.
- [36] S. Hellebrand et al. “Numerical investigation of hot bulk forming processes with respect to the resulting residual stress distribution”. In: *Proceedings in Applied Mathematics and Mechanics* 22.1 (2022), e202200155.
- [37] S. Hellebrand et al. “A multiscale approach to investigate residual stresses due to targeted cooling of hot bulk formed parts”. In: *Current Perspectives and New Directions in Mechanics, Modelling and Design of Structural Systems: Proceedings of the 8th International Conference on Structural Engineering, Mechanics and Computation (SEMC 2022)*, Cape Town, South Africa. Ed. by A. Zingoni. 2022.
- [38] S. Uebing et al. “A numerical study of the effect of phase evolution on residual stresses during cooling”. In: *Proceedings of Applied Mathematics and Mechanics* 20.1 (2020), e202000236.

- [39] S. Uebing et al. "On the evolution of residual stresses due to cooling considering martensitic phase transformation". In: *Proceedings in Applied Mathematics and Mechanics* 21,1 (2021), e202100031.
- [40] S. Uebing et al. "Residual stresses in hot bulk formed parts - Two-scale approach for austenite-to-martensite phase transformation". In: *Archive of Applied Mechanics* 91 (2021), pp. 542–562.
- [41] S. Uebing et al. "Residual stresses in hot bulk formed parts - Microscopic stress analysis for austenite-to-martensite phase transformation". In: *Archive of Applied Mechanics* 91 (2021), pp. 3603–3625.
- [42] B.-A. Behrens et al. "Experimental investigations on the interactions between the process parameters of hot forming and the resulting residual stresses in the component". In: *Procedia Manufacturing* 50 (2020), pp. 706–712.
- [43] B.-A. Behrens et al. "Numerische Prozessauslegung zur gezielten Eigenspannungseinstellung in warmmassivumgeformten Bauteilen unter Berücksichtigung von Makro- und Mikroskala". In: *Forschung im Ingenieurwesen* (2021).

## 8 Forming Generation of Residual Compressive Stresses During Wire Drawing for the Production of Heavy-duty Springs

Reimers, W.; Kräusel, V.; Baumann, M.; Bergmann, M.; Selbmann, R.

GEPRIS 372788207

### 8.1 Introduction

Essential factors for the optimization of components are the improvement of parameters relevant to use as well as the increasing requirements regarding the available installation space and the size of the components. In the manufacture of torsion bar springs, this means the realization of small bending radii which currently cannot be achieved without failure using conventionally manufactured spring wires. The aim of the research project was to modify the wire drawing process by means of an innovative tool geometry, which is characterized by geometry elements incorporated in the forming zone, to thereby improve the formability of the wires in the subsequent process stages for the manufacture of torsion bar springs. In the research project, the targeted and reproducible induction of compressive residual stresses close to the surface was intended to substitute post-processes such as heat treatment and shot peening realized in conventional production routes and to improve the properties of the components produced by forming technology as well as to make them usable by adjusting the residual stresses in the wire. The smaller bending radii as well as the static and dynamic properties of the wire serving as starting material were to be optimized by the defined adjustment of residual stresses during wire drawing and, as a result, the load capacity of the formed torsion bar springs was to be improved. The research project was carried out within the framework of the priority program SPP2013 of the German Research Foundation by the research partners Fraunhofer Institute for Machine Tools and

Forming Technology (IWU) Chemnitz, the Chair for Forming and Joining (UFF) of the TU Chemnitz and the TU Berlin, Department of Metallic Materials (MW). On the part of IWU, the main tasks were the process adaptation of the tension-compression forming as well as the setup and use of the experimental device for wire drawing to produce the wire samples. The focus of the UFF chair was the creation of the material model and the simulation of the impact extrusion and wire drawing tests, the optimization of the simulation models with regard to property predictions, and the implementation of the bending tests with a suitable bending tool. The MW department dealt with the characterization of the starting material, the determination of residual stresses and textures, the investigation of the stability of the residual stresses by loading experiments and the validation of the measurement methods. Within the scope of the numerical and experimental investigations, the relevance of disturbance variables and material fluctuations had to be analyzed and the quantification of the property improvements of the components had to be considered.

With the funding decision for the 1st funding phase, the experts requested that the model material S235J be replaced by the multiphase material 1.4301. This made it easier to transfer the findings from the 1st and 2nd funding phases to the overall objective. This meant that the findings from the 1st and 2nd funding phases were better applied to the overall objective but resulted in considerable additional work in material characterization and residual stress measurement, which could not have been foreseen when the project was applied for. As a result, there were delays in individual phases of project processing.

**Table 8.1** Depth-resolved residual stresses in the starting material and after solution annealing after two electrolytic removal steps (3 and 6 mm)

Material removal [mm]	Axial residual stress [MPa]		Tangential residual stress [MPa]	
	Output	annealed	Output	annealed
0	-250 ± 15	-15 ± 70	-160 ± 30	-100 ± 45
3	+190 ± 30	-60 ± 70	+220 ± 10	-160 ± 6
6	-80 ± 20	+10 ± 100	+50 ± 10	+90 ± 130

## 8.2 Work and Results

### 8.2.1 Presentation of the Results and Discussion

The results listed below represent excerpts from the main findings of the funding periods. A detailed description of the project results can be found in the publications mentioned in section 1.6. Reference is made to the publications in the report.

#### Define Target Properties

Within the project, the expected load and favorable residual stress distributions over the cross-section of the specimens for the semi-finished products and bent springs under consideration were first coordinated. Distinct compressive residual stresses at the immediate component surface and tensile residual stresses in the core of the specimens were defined as target properties to be induced by the wire drawing process using a specially developed tool geometry. If this not possible, at least a significant reduction of the tensile residual stresses at the component surface was to be aimed for. As a result of the intended residual stress distribution, a better formability of the wires to produce the torsion bar springs by means of bending was expected by preventing the formation of cracks close to the surface, especially at small bending radii. The superposition of the bending stresses with the adapted residual stresses of the wire resulted in the improved properties of the component under load.

#### Characterization of the Starting Material

The model material 1.4301 used was characterized and investigated in detail using various methods in its initial state and formed states. In its initial state, the material exhibited an austenitic microstructure. As a result of forming at high degrees of deformation, martensite is formed, which increases the amount of work required in the analysis. In order to characterize the 1.4301 material used and its preloads, X-ray phase analyses were carried out on the cross-sectional area of the bar profile, which showed exclusively austenite reflex layers both at the edge and in the core of the bar material, corresponding to a purely austenitic initial material state. The initial microstructure exhibited a homogeneous average grain size both at the specimen edge and in the volume of the bar material of  $15 \mu\text{m} \pm 4 \mu\text{m}$ . Vickers hardness determination showed a hardness at the edge of the bar material of  $292 \pm 9 \text{ HV0.5}$  and a hardness in the volume of  $290 \pm 8 \text{ HV0.5}$ . Manufacturing-related preloads in the starting material were investigated and detected using depth-resolved residual stress and texture determinations. In order to reduce the preloads in the microstructure, the bar material was subjected to a heat treatment. The starting material was solution annealed at  $1,050^\circ\text{C}$  for 15 min (+6 min heat treatment) and cooled in air. Following solution annealing, metallographic examination revealed an average grain size of  $28 \mu\text{m} \pm 9 \mu\text{m}$ . The Vickers hardness determination yielded a mean hardness of  $164 \pm 18 \text{ HV0.5}$ . In table 8.1 the residual stresses determined at the surface (0 mm removal) and by electrolytic layer removal of 3 mm and 6 mm, re-

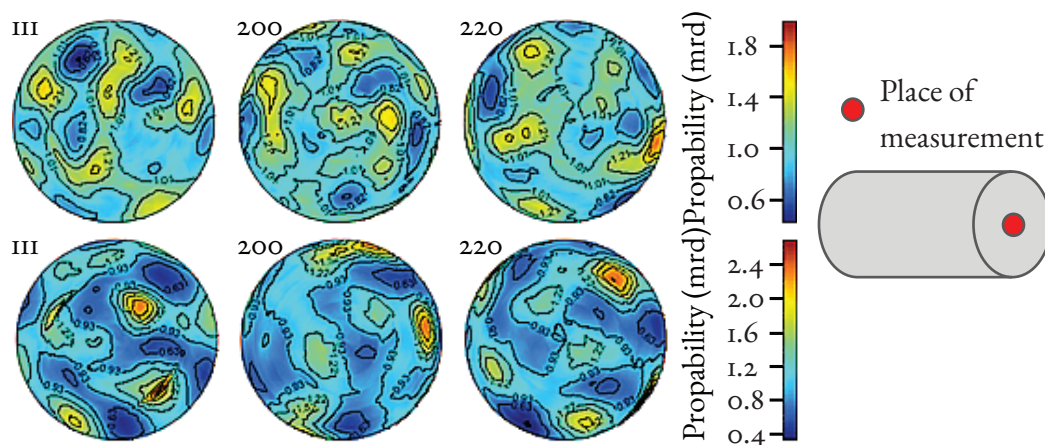


**Figure 8.1** 111, 200 and 220 pole figures of the starting material (left), 111, 200 and 220 pole figures after solution annealing (right).

spectively, are shown. The specimen preparation is explained in the publications [1, 2].

Depth-resolved texture measurements were made on the samples at the German Electron Synchrotron (DESY) in Hamburg. The texture due to the heat treatment is shown in figure 8.1. Compared to the non-heat-treated initial state, the occupancy density exhibits higher maximum intensities in the pole figures shown. In addition, a change in the localization of the pole maxima can be observed because of the heat treatment.

By means of compression tests with the Gleble System 3800, stress-strain curves were recorded at different temperatures and strain rates for both the starting material and the annealed material, based on which flow curves were created by approximating the curve progressions for higher degrees of deformation for the simulation. The evaluation is carried out in WP5 as part of the development of the material model.

### Production of Graded Semi-finished Products by Means of a Pressure Forming Process

The experimental investigations were carried out with an existing extrusion die, with which the influence of the developed geometry elements on extrusion was first investigated. The same geomet-

try elements were used as for wire drawing, which were developed in the FE simulation (WP5). The compression tests were performed on a hydraulic press in a modular column guide frame with active parts, which were designed, engineered and manufactured as part of the research project. The press speed was 10 mm/s in each case. Lubrication consisted of a combination of a solid lubricant containing MoS<sub>2</sub> (LOCTITE LB 8191) on the specimens and an addition of high-alloy drawing oil (Multidraw CF 4) to the forming process. In order to generate as homogeneous a single-phase material state (austenite) as possible and low residual stresses in the specimens of the starting material, annealing was again performed. The specimens (12 mm,  $L = 32$  mm) were successively pressed through the die with the specific geometry element for the respective series of tests, always with at least three repetitions. The procedure and results are shown in graphs and pictures in [1] and published. In summary, it can be reported that with the three dies used, it was possible to influence the residual stresses during extrusion without ejection in the desired way and to generate residual compressive stresses with the geometry elements.

## Process Adaptation to a Tensile-pressure Forming Process

Based on the studies on impact extrusion, the wire drawing equipment was designed for transfer to the wire drawing process. The theoretical principles of the tension-compression process were systematically worked through and the resulting forming in the local areas was analyzed by correlation with the forming elements. The design and manufacture of the dies with the corresponding geometry elements (conventional, convex, concave) were based on feedback between the design and the findings obtained in the FE simulation. For the design, additional simplified preliminary drawing tests were carried out using the dies already manufactured for the extrusion die. Both the heat treatment of the specimens before forming and the lubrication were carried out in the same way as the compression tests. In each case, the specimens were drawn from an initial diameter of  $\varnothing$  12 mm to  $\varnothing$  10.8 mm at a press speed of 10 mm/s. Based on these findings, the preliminary analytical considerations and the parallel FE investigations, a wire drawing die for short wire sections was developed in AP6.

## Development and Validation of a Material Model and Process Simulation of Impact Extrusion and Wire Drawing

As already mentioned in WP2, compression tests were performed to generate flow curves. The strain rates and the test temperatures were varied. Furthermore, different flow curve approaches for the approximation were investigated, finally the approach according to Swift was chosen due to the best mapping and the parameters were determined and combined by means of the method of least squares. A selection of the results of the compression tests and the general procedure for deriving the flow curves are described in [1, see figure 4] and [2, see figure 3] and the respective following text passages. Extensive additional investigations were necessary due to the observance of the experts' instructions and the selection of the model material 1.4301, which exhibits a deformation-induced microstructural transformation. The further adaptation of the material model therefore had to be

shifted to the 2nd funding phase. The validation of the material model was initially based on the process data for force and displacement recorded during the experimental investigations. Based on the friction values and the friction model, the FE simulation was adapted. The procedure and numerical values are described in [1–3]. However, the predictability of residual stresses showed deviations, which were also discussed in the publications [1, 3, 4].

In the FE simulations, it was first possible to detect fundamental relationships such as the sensitivity to the mesh sizes and the boundary conditions, and to analyze elastic and rigid tools comparatively [1]. For the further FE simulations, the rigid tools were selected due to the shorter computation times and approximately equal results [1].

FE calculations were performed in the FE program Abaqus using a 2D axisymmetric model setup as well as the explicit calculation method. The specimens were defined in a simplified way with an initial state free of residual stresses on the macroscale. For the evaluation of the resulting residual stresses after forming, an implicit calculation after forming and unloading of the specimen followed. As a friction model, the friction factor model according to Coulomb and Tresca was applied [1–3]. In this model, a frictional shear stress, which depends on the yield stress, is defined with a coefficient  $m$  and the coefficient of friction  $\mu$  is adjusted.

For the further development of the die geometry, a diameter reduction of the starting material during forming from  $D = 12$  mm to  $D = 10.8$  mm was specified. In order to generate a database, the forming of the bar material was first fundamentally investigated in the FE simulations with convex, concave and step-shaped geometry elements in the dies. Based on [4], a convex as well as a concave geometry variant was selected for the further investigations in addition to the conventional one. The developed die geometries as well as the specific dimensions are shown in figure 8.2 shown.

In the analysis of the FE simulation it becomes clear that during impact extrusion strong differences in the formation of the forming degrees in the edge

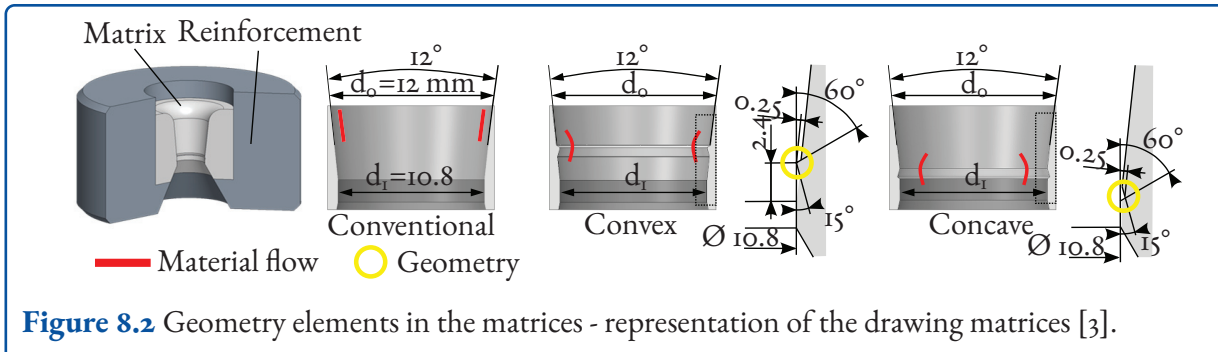


**Figure 8.2** Geometry elements in the matrices - representation of the drawing matrices [3].

zone are achieved, which is shown in [1, see figure 8]. Due to the convex and concave geometry elements, the degree of deformation in the edge zone increases significantly. However, this area is very narrow, which was also determined in the metallographic investigations by the deformation-induced martensite formation shown and [1, see figure 5].

In the evaluation of the residual stress curves, the radial component is not taken into account in the FE simulation because it runs against a stress value of zero at the edge and cannot be determined experimentally. The evaluations of the curves for the axial and tangential residual stresses from the FE simulation [1, see figure 9] show that the conventional variant achieves axial compressive stresses in the specimen in the edge zone, but these quickly transform into tensile residual stresses.

The axial proportions of the convex and concave geometry in the edge region of  $0.75 - 1$  relative distance from the specimen center to be considered show that initially compressive residual stresses can be generated, but these change again to tensile residual stresses in the outermost zone. This may also be related to the numerics, here specifically to the contact model. It can be concluded from further FE simulations not shown that residual stresses can be specifically adjusted with the geometry elements. The deviations between simulation and experiment can partly be explained by the complicated manufacturing of the geometries in the matrices.

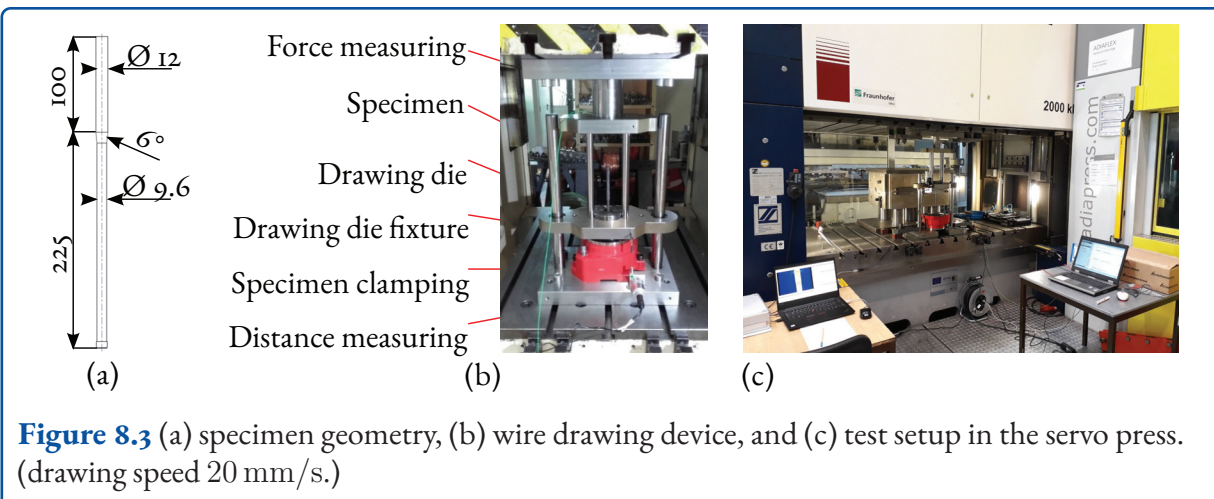
In the experiments, the deformation-induced transformation of austenite into martensite was demonstrated, which could not be represented in the simulation because the material model had not yet been

developed. As already mentioned, this was an objective of the 2nd funding phase.

Based on the results for compression forming, a tensile device for wire drawing was designed, which is described in WP6. In the FE analyses for wire drawing of the material 1.4301, which were also carried out in this context, it was shown that the tensile-compression forming of wire drawing results in significantly different residual stress curves in the axial and tangential components compared to the compression forming of extrusion as a result of the changed degrees of deformation [2].

## Experimental Device Wire Drawing

The basis for the design and construction of the experimental device for tension-compression forming, including change parts, was described in WP4. Funding was provided as part of the research project. The experimental device has a modular design and is presented in [2]. The results of the process design and the forming simulation form the basis of the tool development. In addition to the recording of the process variables force and displacement and the specimen clamping, the experimental device also includes an insert for the exchangeable drawing dies. In figure 8.3 shows the die, including measuring instruments, installed in the press. The drawing dies were developed in WP5 as part of the FE simulations. The steel frame of the geometrically modified drawing dies corresponds to the standardized series production status, so that they can be transferred to an industrial plant without additional design modifications, taking into account the increased drawing force requirement. Process



integration into a series production process would thus be possible.

### Basic Test Wire Drawing

Based on the wire drawing device and the FE simulations, the specimen geometry was defined with an initial diameter of 12 mm and the specimen length was adjusted to 100 mm to achieve an analysis range with constant properties. For the specimen clamping, a length of 225 mm with a diameter of 9.6 mm is added. An inclination of 6° is used to achieve a transition to drawing [2]. The specimen geometry is shown in figure 8.4 clarified.

In the test apparatus the specimens are clamped vertically, and the drawing die is pulled upwards over the specimen. This enables a homogeneous distribution of the lubricant (drawing oil or drawing soap). The wire drawing device can be used flexibly in various forming machines. The process variables are recorded via the integrated displacement (draw wire sensor) and force (Kistler load cell) measurements. After the annealing process described above and subsequent cooling in air, the specimens are clamped in the device and drawn to a diameter of  $D = 10.8$  mm and a length of  $L = 125$  mm at room temperature. Initial tests were carried out first in a servo press (figure 8.3, right). The device was firmly connected to the press table. The drawing force was applied via the return stroke of the press ram. The advantage of this operation can be explained by a defined speed profile. The move-

ment speed was 20 mm/s, and the drawing speed was constant. The specimens were prepared for characterization and for further processing by wire bending.

### Development of Methodology for Residual Stress Analysis in Graded Wires

The preliminary investigations have shown that complex material states exist in graded specimens. These are characterized by gradients of the macro-residual stresses from the surface to the specimen depth. Furthermore, gradients of micro-residual stresses, which show an increasing orientation dependence with increasing depth are also present. The gradients of the integral intensities also show an increasing directional dependence with increasing depth. The latter indicate increasing anisotropy with increasing distance from the surface. The measurement methodology for determining the residual stresses of formed specimens was adapted with the aim of recording and evaluating the macro-residual stresses, but especially the micro-residual stresses and texture effects, which are also important for the material properties, at selected measurement depths and directions. The measurement methodology was extended with synchrotron investigations at DESY so that depth-resolved texture data were included in the analysis of the complex material states.

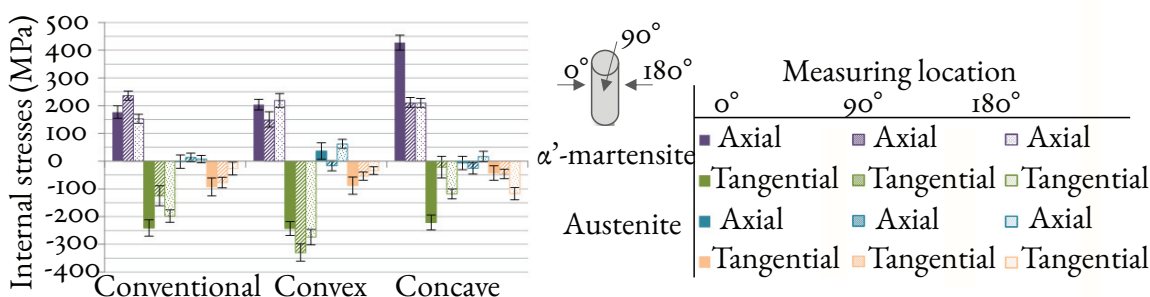


**Figure 8.4** Residual stresses corresponding to the reflective layers on the lateral surface of the wire drawing specimens in as a function of the die (geometry element) and the measuring location on the specimen's circumference.

### Determination of Residual Stresses on Extrusion Test Specimens, Drawn Wires and Bent Wires

The results, evaluations and illustrations of the extruded specimens were published in [1]. Forming induced martensite formation near the surface [1, see figure 5]. The determined residual stress states for the martensite and austenite phases show different values, depending on the different matrices (figure 8.4). For the example of the martensite phase in the tangential direction using the convex die, significant compressive residual stresses occur with up to  $-490$  MPa, whereas for the martensite phase using the conventional die in the tangential direction, significant tensile residual stresses were determined with  $+400$  MPa. It was found that the phase-specific residual stresses are not homogeneous over the circumference of the specimens and vary in their magnitude and sign [1, see figure 6].

For wire-drawn specimens, the location-dependent distribution was reduced. The results and procedure for slowly drawn wires are partly explained and published in [2]. The test series were still carried out in the first project phase, the measurement and evaluation of the residual stresses were only carried out extensively in the 2nd funding phase and is, however, already presented here, as the focus was placed on the higher drawing speed in this project phase. Compared to extrusion, the measurements on the wire surface show a slight increase in tensile residual stresses when using the convex geometry.

With the concave geometry, the axial tensile residual stresses can be slightly reduced.

### Characterization of Samples (Property and Microstructure Characterization)

Comprehensive investigations were carried out on the material. In addition to microstructural investigations by light and scanning electron microscopy and, in particular, electron backscatter diffraction (EBSD) analyses, investigations were carried out using X-ray and neutron diffraction methods. The metallographic preparation of the transverse sections was implemented by means of an individual adaptation of the etching recipe based on the Lichtenegger and Bloech recipe to identify the deformation-induced phase transformation of the austenite in the deformed edge zone based on transverse sections and to analyze their expression and homogeneity [1, see figure 5]. The results of the color etching show that the microstructure, especially in the deformed edge zone, differs in depth expression and homogeneity depending on the die used. The X-ray phase analysis confirms this result. It is evident that a deformation-induced martensite phase is formed in the immediate edge zone of the specimens. This can be observed both during impact extrusion and wire drawing. The formation and expression of the deformation-induced martensite in the volume of the specimens are inhomogeneous for all geometry elements investigated (conventional, convex and concave). The expression of the martensite layer at the edge of the speci-

**Table 8.2** Residual stresses near the surface of the martensite phase for two geometry elements (convex and concave) before and after 10.000 load cycles in a fatigue test.

Geometry element	Residual stresses [MPa] - martensite phase			
	Initial state		After 10.000 load changes	
	Axial	Tangential	Axial	Tangential
Convex	204 ± 19	-243 ± 25	250 ± 31	-246 ± 19
Concave	427 ± 27	-221 ± 27	488 ± 23	-248 ± 21

mens varies in thickness in the ranges from 5 µm to 60 µm. Furthermore, it can be noted that residual austenite components and intermediate phases due to deformation ( $\epsilon'$  martensite) also coexist with the martensite phase in the edge region. The martensite phase is also weaker in the edge region of the 180° measurement location. The inhomogeneous martensite formation across the cross-section of the samples due to the deformation was also detected in neutron diffraction experiments using the dark-field image (DFI) signal with depth resolution. The neutron diffraction experiments were implemented at the Heinz Maier-Leibnitz research neutron source in Munich. Neutron diffraction takes place under the same geometric laws as the diffraction of X-rays by crystals (Laue equations, Bragg's equation). The peculiarity lies in the interaction of the neutrons not only at the atomic nuclei (atomic scattering factor), but, because of their magnetic moment, also with the magnetic moment of the unpaired shell electrons. The diffraction pattern is then determined not only by the chemical but also by the magnetic order of the sample. The investigations by means of neutron diffraction illustrate that an inhomogeneous phase distribution is present over the cross-section of drawn wire samples. It should be noted that a lower DFI signal indicates more scattering, which in turn is attributed to scattering at the magnetic domains in the martensite. With the aid of EBSD measurements, the microstructural investigations were supplemented and the observations presented were confirmed.

### Determination of the Stability of Residual Stresses under Dynamic Loading

The dynamic load tests were performed on the MTS 810 servo-hydraulic universal testing machine with the MTS Hydraulic Wedge Grips fixture using MTS 647.10 Wedge Set Assy (10.9 mm–16.5 mm) jaws. Additional sleeves were fabricated and used to appropriately clamp the specimens. In table 8.2 a selection of results with a load interval of 10.000 load cycles and a load amplitude of 5 kN is shown. From table 8.2 the residual stresses near the surface introduced by the forming process by means of concave and convex dies, taking the martensite phase as an example, do not show any significant changes in their magnitudes during dynamic loading with the selected load amplitude. Thus, the residual stresses remain stable.

### Determination of the Process Window and Derivation of the Optimized Process

The results of the process simulation, the basic forming tests and the residual stresses determined were evaluated and an optimum was derived. When determining the process parameters, attention was already paid to later industrial feasibility. The grading process must be integrable into a typical process chain for wire production in order to be economically feasible for a wide range of applications later on. The convex and concave die geometry proved promising for introducing the desired residual stress state into the component.

## Spring Wire Bending Test with Residual Compressive Stresses

In the 1st funding phase, the modular bending tool financed from the project funds was developed and initial bending tests were carried out. The aim was to record the process forces during forming in addition to the 3-point bending and folding that are particularly prevalent in the manufacture of torsion bar springs. An integrated load cell (Kistler) and a laser triangulation displacement sensor (Micro-Epsilon) were used. The bending radii were varied by alternating active parts, allowing the influences of different residual stress states of the wires on the bending behavior, specifically on the possible bending radii (0.9; 1 and 1.1 times the wire diameter) to be investigated. The comprehensive experiments with the various residual stress states in the wire were shifted to the 2nd funding phase, while the commissioning of the tool and initial preliminary investigations were still carried out in the 1st funding phase. For 3-point bending, a bending angle of  $80^\circ$  was defined and, depending on the bending radii, the traverse paths of the servo press in which the bending tool was operated were adjusted. In [2] the design of the tool was published and the respective bending variant was shown [2, see figure 9]. In figure 8.8 (2nd FÖP, AP6) the tool can be seen.

## Evaluation and Consolidation of the Results

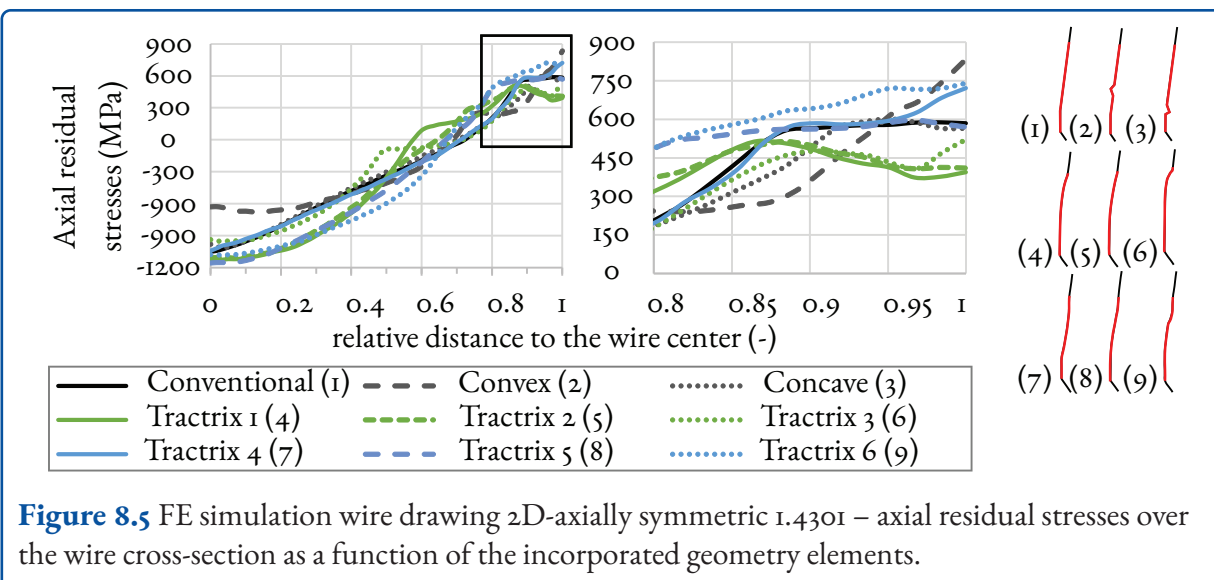
### Definition of Favorable/Desirable Residual Stress Conditions in the Workpiece Based on the Findings from the 1<sup>st</sup> Funding Phase

Based on the findings from the 1st funding phase, the residual stress states to be aimed for were defined for the torsion bar spring. As mentioned above, the convex and concave die geometries were selected as suitable for achieving the desired residual stress state. The consideration of other geometries was carried out by means of FE simulation. At this point, it should be emphasized once again that the residual stresses in the edge region can be specifically adjusted in such a way that, although no compressive residual stresses were adjustable during wire drawing, the tensile residual stresses can be reduced. This was regarded as progress and further

pursued. The goal was now defined as further minimizing the tensile residual stresses and including high-speed drawing, as in industrial wire drawing, in the machining process. Since the research approach should not be limited to austenitic steels, additional reference tests were carried out with a ferritic steel 1.0579 (S355J2+). For this material, phase-independent flow curves were first recorded, and the isotropic hardening behavior was extrapolated using the Swift approach for higher degrees of deformation. These data were published in [3, see figure 4].

## FE Simulations for the Design of Further Drawing Dies

The incorporated geometry elements in the drawing die cause a forming-induced change in the residual stress distribution in the wire, with the same main geometric dimensions of the wire after wire drawing. Further 2D axisymmetric as well as 3D FE process simulations of wire drawing with rigid dies were performed to investigate and analyze targeted geometry elements for the drawing dies. In the material definitions, the elaborated material models with isotropic hardening behavior (1.4301, S355) and without mapping of the phase transformation were used for the material 1.4301 since the models for the phase transformation were still under development and were to be elaborated by a cooperation in SPP2013 in the 3rd funding phase. The residual stresses were calculated based on the hardening behavior. In figure 8.5 calculated residual stress values for the axial component are illustrated for a selection of geometry elements in the drawing matrices. The tractrix shapes (4–6) represent drag curves whose formation varies, thus affecting the degree of deformation and the resulting residual stresses differently. With Traktrix shapes 1 and 2, the residual stresses in the boundary region can be specifically and significantly adjusted. The Traktrix-1 die was therefore also investigated experimentally to some extent. Selected results of the FE simulations, such as the calculation of the degree of deformation, are published in [2, see Fig. 5]. It is evident from the curves of the degree of deformation as a function of the matrix variant that these influence the layer



near the surface and that the degree of deformation is increased with the geometry elements.

The material characterization and further validation are the focus of further work. To more accurately represent the material behavior in a multi-stage process as well as in downstream wire bending, further investigations for the material models with the integration of kinematic hardening will be carried out as part of a student thesis after completion of the project.

### Determination of the Geometry of the Drawing Dies

The manufactured drawing die geometries were measured tactilely at four measuring points ( $0^\circ$ ,  $90^\circ$ ,  $180^\circ$ ,  $270^\circ$ ) distributed around the circumference in the forming zone using a coordinate measuring machine and an additional combination of a highly sensitive roughness gauge. Based on this measurement data and the production-related deviations from the nominal geometry, the FE simulation models were revised, and a comparative evaluation was performed. This made it clear how these geometry deviations affect the wire drawing process. This contributed to the quantification of the relevance of disturbance variables and to the further validation of the FE simulations. The procedure was described in the publications [2, 3].

### Production of Wire Semi-finished Products with Tension-compression Forming Processes

After the transition from modified impact extrusion [5] to a wire drawing process, the experimental investigations of the temperature influence and the validation of the FE simulations of the wire drawing process continued to be carried out in the servo press. In order to reproduce realistic forming conditions of a classical wire drawing process at a speed of 2,000 mm/s, tests were subsequently carried out in a high-speed testing machine.

For the temperature investigations, the emissivity was first determined for relevant temperature ranges during wire drawing by measuring the samples in an oven. These were heated to  $200^\circ\text{C}$  and cooled down to  $180^\circ\text{C}$  during transport and installation in the device. The drawing of the specimens was monitored with the thermal camera. At a drawing speed of 20 mm/s, the wire temperatures were constant over the drawing area after an approximately 30 mm run-in area at approximately  $160^\circ\text{C}$  (conventional, concave die) and at approximately  $175^\circ\text{C}$  (convex die). A slightly reduced force requirement was observed for the drawing forces.

For the tests on the high-speed testing machine, both the die mounting, and the specimen clamping

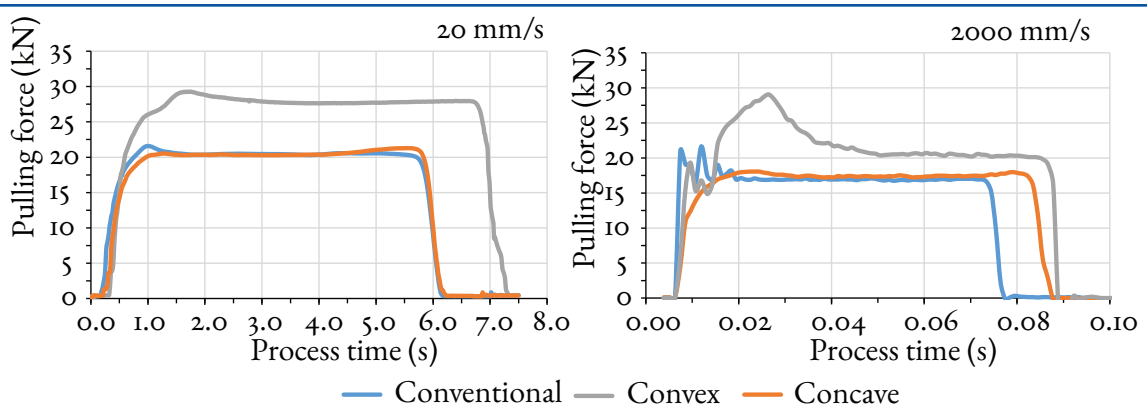


**Figure 8.6** Force-time curves for drawing tests at 20 mm/s and 2,000 mm/s.

had to be adapted. In [2, see figure 8] the die setups are published and shown comparatively.

In figure 8.6 shows force-time curves using three die shapes for a selection of the tests. Due to the increased drawing speed, the required force decreases. The evaluation and analysis of these extensive wire drawing tests and the resulting residual stresses are currently the content of a planned publication.

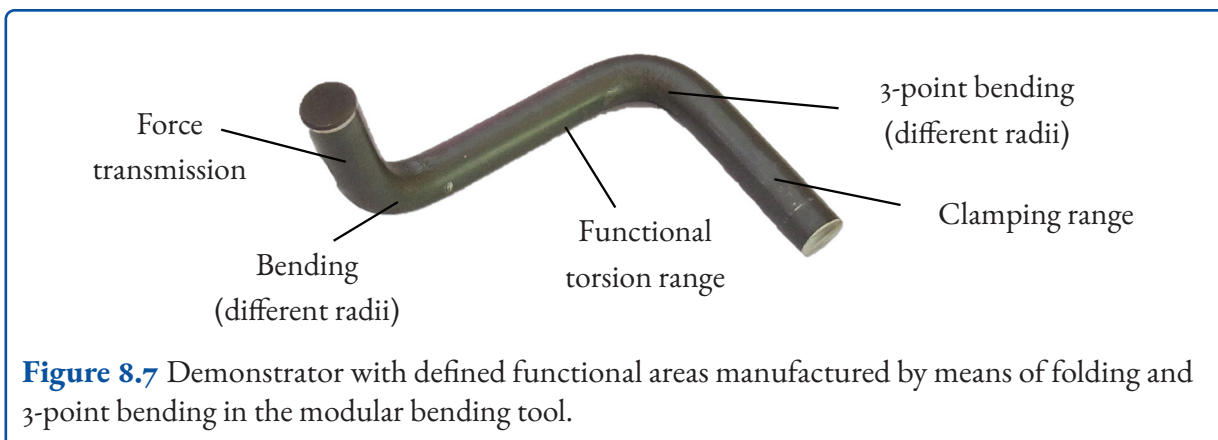
#### Design of a Demonstrator (Torsion Bar Spring) and the Corresponding Process Chain for Manufacturing

Based on the FE simulation models and the experience gained from the bending tests, a representative demonstrator was developed along the lines of a torsion bar spring. The specifications were wire bending by means of folding and 3-point bending as well as the integration of a functional torsion area. Furthermore, it had to be possible to manufacture the demonstrator from the drawing specimens produced with the wire drawing fixture using the specific dies. After testing the production possibilities on an industrial bending machine, it was determined that the machine could not apply sufficient force due to the wire diameter of  $D = 10.8 \text{ mm}$ . Thus, the demonstrator was designed for production with the modular bending tool on the servo press, considering the specified functional ranges and manufacturability. In the design, the following was considered as shown in figure 8.7; a component area for force application and a functional

area defined at  $90^\circ$  to each other. In addition, a sufficiently long clamping area was provided for testing the spring or functional capability. By examining the different bending radii, the lengths of the defined areas change. It was determined that the functional torsion range should always have the same length of 45 mm for the comparability and evaluation of the vibration tests, regardless of the bending radius. Depending on the bending radius ( $R 7.6\text{--}11.9 \text{ mm}$ ), the component areas of force application and clamping range vary in this respect. The bending angle of  $80^\circ$  for 3 point bending was left the same. The process chain for manufacturing the demonstrator provides for the force application area to be produced first by bending after wire drawing in the first step and then the functional and clamping area to be produced in the second step by 3-point bending. Extensive load tests were planned for the 3rd production phase. In this respect, a concept was also already designed in this funding phase, which is additionally presented in WP10. However, the 3rd funding phase was not approved, so that these investigations could not be carried out.

#### Simulation Models and Validation for Wire Bending

The FE simulation models were built on the basis of 3D models with symmetry plane and taking into account the travel values of the press of the experimental bending tests in order to be able to compare the force-displacement curves as well as



the angles of springback. In addition to bending, wire drawing was also simulated in advance in the models using the measured die data. The results of the calculations were used to design the bending radii and the experimental bending tests (figure 8.8). In comparison, the evaluation of springback shows similar behavior for both materials 1.4301 and S355. Depending on the bending radius, the springback is reduced at smaller bending radii. The absolute values agree better in the tests with the material S355. This is also evident in the force values. Further necessary work, which was started at the end of the 2nd funding phase, is to develop a kinematic hardening model and a damage model, as well as to further develop the material model for the material 1.4301 in order to represent martensite formation and thus to calculate the force values in a comparable way.

### Experimental Bending Tests with Wire for Validation of the Simulation

With the modular bending tool, basic investigations on the bending of the wires have been realized. The wires made of 1.4301 and S355 were drawn at 2,000 mm/s and the various dies conventional (Ref), convex (Kov), concave (Kok) and tractrix (Tra). Force and displacement curves were recorded via the measuring sensors of the bending tool. The variation of the bending radii was performed via the alternating active elements [R 7.6 (0.7xD); R 8.6 (0.8xD); R 9.7 (0.9xD); R 10.8 (1xD); R 11.9 (1.1xD)]. Bending with a nominal angle of 90° and 3-point bending with a nominal angle of 80° were investigated. In addition to the forming force, the angles of the springbacks due to the superposition

of the residual stresses and the stresses caused by bending, as well as any material failure, were evaluated. When bending the 1.4301 wires, it was determined, as with the measured residual stresses, that the wires drawn with the concave geometry exhibited lower bending forces and also reduced springback compared to the reference process due to the lower tensile residual stresses. This applies to all bending radii. The specimens drawn with the other geometries do not show this reduction, or in the case of the convex variant there is an increase in the values of bending force and springback due to the higher martensite content in the edge region. In 3-point bending, the reductions in bending force and springback are not observed to the same extent. However, it can also be seen here that the forces and springbacks increase in the convex variant.

### Fabrication and Characterization of the Torsion Bar Spring/Demonstrator

The demonstrators were manufactured in the modular bending tool according to the concept developed in AP5 (figure 8.9). The rationale for the change from the industrial bending machine is explained in AP5. In addition to material 1.4301, demonstrators were also recovered for material S355. In the process, the characteristic values of displacement, by means of a laser sensor, and force, by means of an integrated force ring, were recorded via measurement data acquisition. In addition to the initial wires, which were manufactured using conventional, convex, concave as well as the Tractrix geometry, a variation of the bending radii was

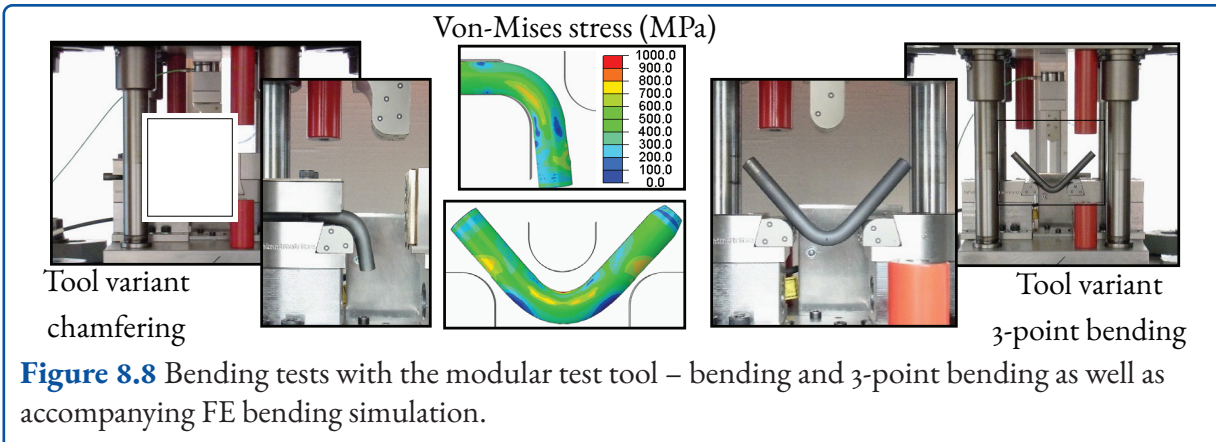


**Figure 8.8** Bending tests with the modular test tool – bending and 3-point bending as well as accompanying FE bending simulation.

carried out as indicated in AP5. The springback and the assessment of any cracks were evaluated. In addition to the demonstrators, the fabrication of pure bevel specimens and 3-point bend specimens was also performed in AP7 to determine interactions due to further bending. No influence could be detected.

### Simulation of the Load on the Torsion Bar Spring

Within the scope of AP9 and AP10, a device for load investigations of the torsion bar springs was designed. Due to postponements in the personnel months and material models that have not yet been fully developed, the investigations were to be carried out in the 3rd funding phase. Since a manufacturing of the device was not possible and therefore the execution of experimental investigations could not be realized, values for the validation of the FE-simulations were missing. Furthermore, complete 3D elements and models are necessary, which result in a high computational effort. In combination with the material model with kinematic hardening, which is currently still under development and necessary in this application, it was foreseeable that an exact representation of the load would not be possible. However, the FE models have already been developed and can be calculated after completion of the material model.

### Vibration Tests on Wires and Springs

The aim of the AP was to carry out dynamic load tests on torsion, tension-compression and alternating elastic bending on selected variants of drawn wires and torsion bar springs, taking into account defined intervals and load collectives. Based on the previous tests, it was decided to conduct only tension-compression tests and to focus on the torsion and bending tests in the 3rd funding phase. Residual stress analyses (macro, micro-residual stresses) were performed at selected measuring points before and after the vibration tests to check the stability of the residual stress states. The residual stress state was determined specifically after 10.000 and 100.000 load cycles at 5 Hz and 5 kN load spectrum in order to analyze the effects of the dynamic load on the residual stresses and thus draw conclusions about their stability. The investigations revealed a stable residual stress state in the fatigue test with a slight reduction in residual stresses. A concept for testing the demonstrator has already been developed in conjunction with WP9, which is shown in figure 8.10. With the same setup of the testing machine, bending, torsion and bending with additional torsion are to be investigated by the respective clamping and bearing of the demonstrator.

### Depth-resolved Determination of Residual Stresses

The investigations within the 1st funding phase showed that the formed samples exhibit complex

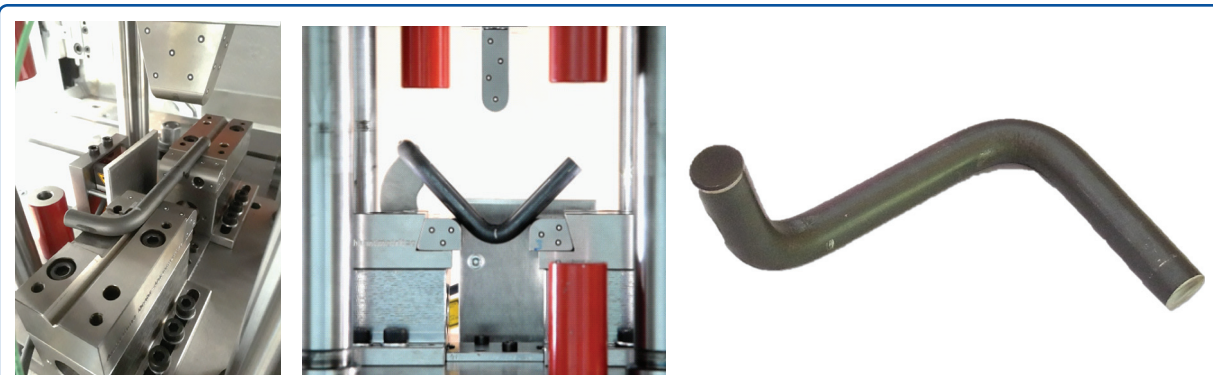


**Figure 8.9** Fabrication of the demonstrator by means of folding and subsequent 3-point bending.

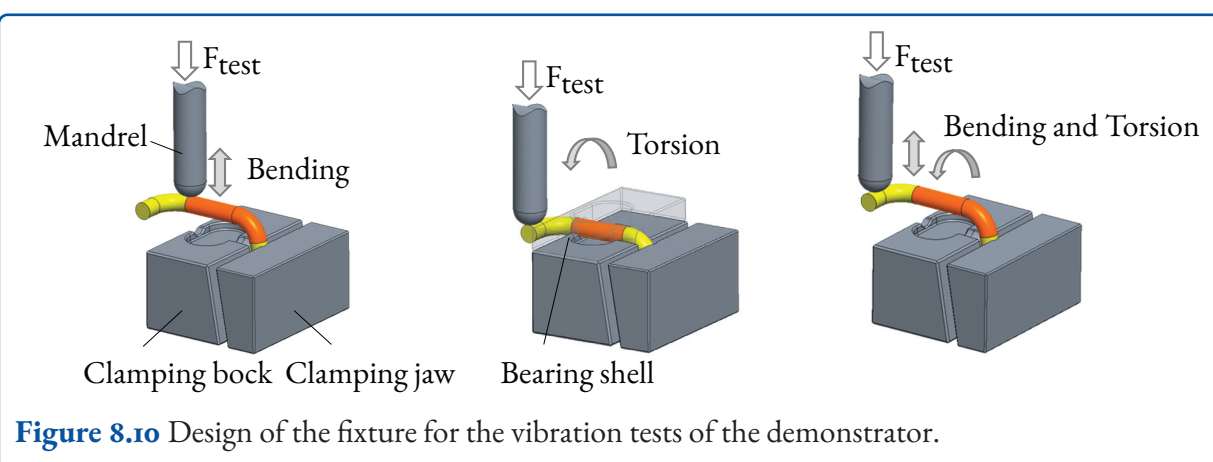


**Figure 8.10** Design of the fixture for the vibration tests of the demonstrator.

material states, in particular at the sample surface. Due to the cross-linking in SPP2013, the analyses were extensively expanded in the 2nd funding phase through a collaboration with KIT. The influence of the deformation-induced phase transformation and the degree of deformation on the residual stress state at the specimen surface were first determined by means of depth-resolved residual stress determination. In addition, integral intensities and half-widths were evaluated, providing conclusions about the degree of deformation of the specimen as a function of the selected process parameters. Radiographic investigations were carried out on the specimens with respect to macro and micro-residual stresses as well as texture. For the analysis of the near-surface properties, measurements were performed with laboratory X-rays and the reflection intensities, positions and profiles were evaluated at different specimen tilts and rotations. To analyze the gradients of micro- and macro-residual stresses, measurements were performed after step-

wise electrochemical removal. The deformation-induced microstructural transformations that occur in the material 1.4301 during wire drawing must be taken into account in the experimental analysis of residual stresses. These processes also depend on the drawing speed. In order to investigate this relationship, measurements using the borehole method (BLM) were included in addition to phase-specific XRD measurements. The aim was to analyze the macro-residual stresses at a greater component depth in addition to the XRD measurements in the near-surface region. Due to the characteristic martensite formation during cold forming of 1.4301 and the high degree of deformation at the specimen edge, an X-ray residual austenite analysis was also carried out with evaluation according to the Rietveld method. Examined and compared in this comprehensive evaluation were drawn wires produced with the geometry variants conventional (Ref), convex (Kov) and concave (Kok), both with drawing speeds of 20 mm/s and 2,000 mm/s.

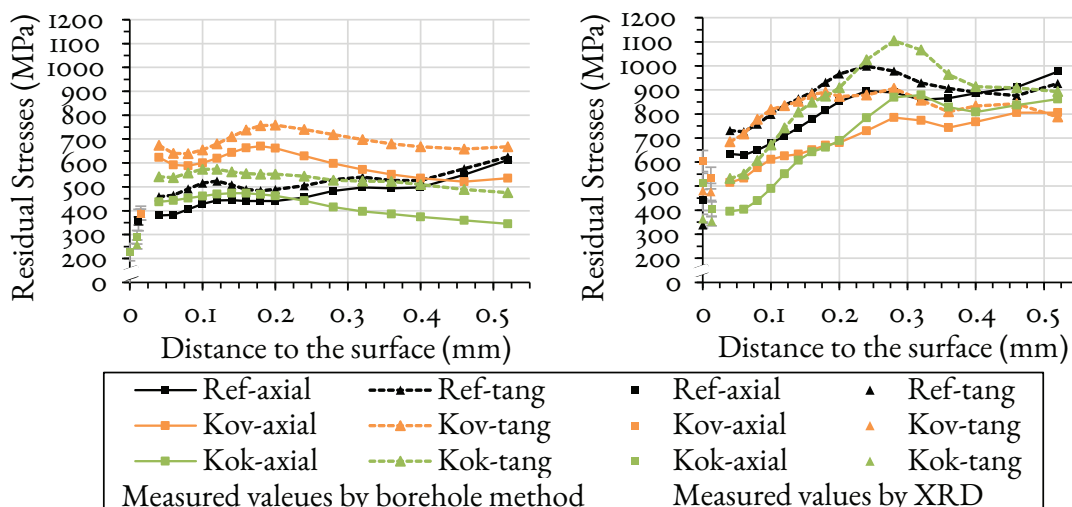


**Figure 8.11** Experimental results I.4301 – X-ray diffraction (XRD) and borehole method (BLM). Left: Wire drawing at 20 mm/s. Right: Wire drawing at 2,000 mm/s with the geometry variants conventional (Ref), convex (Kov) and concave (Kok).

From a depth of about 30 µm (Kov and Kok) below the wire surface, an approximate 90 % austenite content could already be detected. For the reference condition (Ref), 85 % austenitic microstructure was already present from a depth of 15 µm. At greater depths, the samples exhibit the initial microstructure with an austenite content of 100 %. The residual austenite analyses at the specimen surface gave the following values: Ref 81 %, Kov 72 %, Kok 74 % for the specimens drawn at 2,000 mm/s. For the samples drawn at 20 mm/s, no martensite reflex was measurable by XRD analysis at the surface. For the analysis of depth distributions, successive electrochemical layer removal was performed in combination with renewed XRD analysis on the newly formed surface in each case. Phase-specific XRD residual stress analyses were performed for both the martensite phase (lattice plane  $\alpha'211_0$ ) and the austenite phase (lattice plane  $\gamma220$ ) using Cr-K $\alpha$  radiation and a 1 mm mm round collimator. The BLM measurements were performed with a face mill  $D = 0.8$  mm and a strain gauge rosette: EA-06-031RE-120. The measuring points were located in the center of the drawn specimen and thus in the stable range, which were determined and verified in the FE simulation. Figure 8.11 summarizes the residual stresses determined by X-ray on the dominant austenite phase in the immediate vicinity of the sur-

face (two ablation depths) and the results of the mechanical macro-residual stress analyses (BLM) for the two main directions axial and tangential for the drawn wires.

Differences are shown with regard to the absolute values in the comparison of the two drawing speeds. A publication of the results is currently being prepared. When analyzing the results, it becomes clear that there are significant influences on the residual stress states during wire drawing with geometry elements in the layer close to the surface. Thus, for the high drawing speeds, it can be read that the axial and tangential residual stresses in the surface region initially assume significantly lower numerical values and, in addition, the tangential residual stresses have lower values than the axial residual stresses. With increasing distance to the surface, this relationship changes. In order to be able to compare these with the FE simulation, the residual stress analyses in the immediate vicinity of the surface alone are insufficient; moreover, the values near the surface can be influenced by shear and friction effects. In addition, the evaluation of residual stresses due to multiphase near-surface in the case of material I.4301 always requires measurement in both phases (austenite and martensite) to provide macro-residual stress values for simulation match-

ing. Incremental BLM directly allows the residual stress depth distribution to be determined to great depths, providing the macro-residual stresses needed for the adjustment. For the high drawing rate, a good agreement regarding the material behavior between the XRD and BLM measurements can be recognized, which also speaks for the validation of the measurement methods.

In the evaluations of the FE simulations and in the comparison with the residual stress analyses, it becomes apparent that there are clear influences of the residual stress states after wire drawing, especially in the edge region. In order to reasonably evaluate the residual stress distributions influenced by the deformation-induced phase transformations, it is absolutely necessary to apply a combination of phase-specific XRD (surface proximity) and BLM (greater depths). In order to analyze the geometry variations in this respect, the complementary use of both analysis methods will also be a focus in further investigations. The depth distributions presented clearly show that the residual stresses depend on the drawing speed present and the geometry variant. For the wire drawing step from  $D_0 = 12$  to  $D = 10.8$  mm and a degree of deformation of  $\phi = 0.26$  for the conventional variant, a high level of tensile residual stress occurs in the surface region at a drawing speed of 2,000 mm/s. The conventional geometry (Ref) exhibits tensile residual stresses of well over 600 MPa (BLM) near the surface. By using the geometry elements with concave additional element, this axial tensile residual stress is reduced by up to 28 %, especially in the area of approximately 0.1 mm depth; on the other hand, there is a peak at approximately 0.3 mm. The residual stress curve in specimens drawn in the mold with a convex additional element shows a reduction in the axial tensile residual stress of up to 15 % at depths of 0.04– 0.32 mm. Thereby, the course corresponds qualitatively to that with the conventional geometry. The quantification of the property improvement with respect to the residual stress distribution in the wire can thus be demonstrated and the behavior, in particular with the wires drawn with the concave geometry, is also shown in the bending tests (AP7).

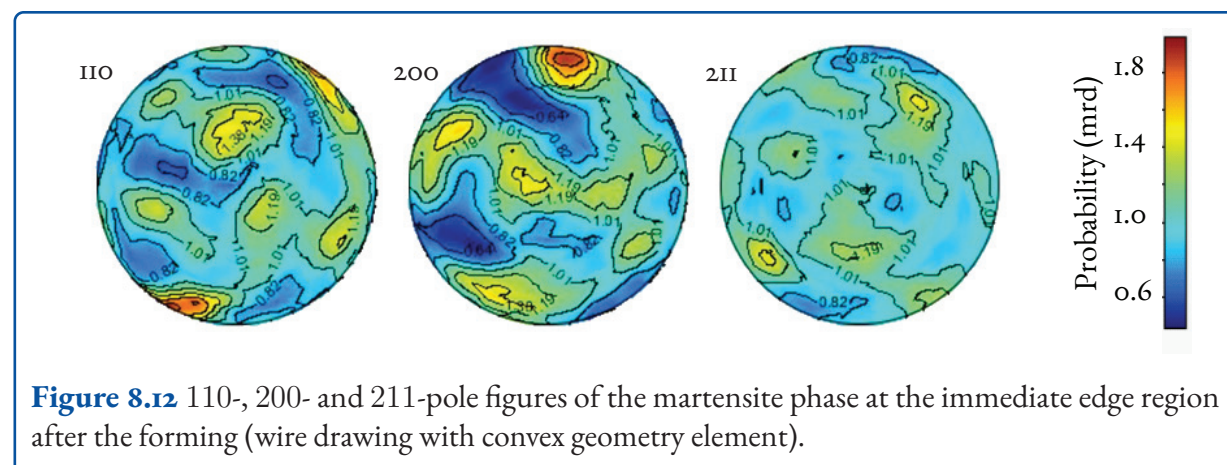
In the experimental investigations with the material S355, it was possible to prove at a drawing speed of 20 mm/s that the residual stresses can be specifically adjusted by forming with a geometry element in one drawing stage. Compared to drawing with a conventional drawing die, the convex geometry element was able to adjust the axial residual stresses at the wire surface on average from about 330 MPa to about 222 MPa and to about 301 MPa with the concave forming element [3]. At higher drawing speeds, this difference can no longer be observed, which is also reflected in the bending tests. Further investigations and publications are planned here across projects.

### **Validation of Measurement Methods for Residual Stresses**

Within the framework of SPP2013, an interlaboratory test was initiated in which the validation of the measurement method for the radiographic determination of residual stresses was made possible. Mutual validation of the experimental measurement methodology was implemented by means of a mutual exchange of residual stressed steel samples with subsequent X-ray, depth-resolved residual stress analysis. The results of the residual stress analysis were compared with each other and no significant deviations were found with regard to measurement and evaluation strategy.

### **Validation of the Simulation by Building Models to Represent Phase Transformation**

In order to build a material model that represents deformation-induced martensite formation, research was first carried out and various approaches were considered. In the course of the WP, the cross-linking in SPP2013 was used and a macromechanical material model was built with colleagues from BTU Cottbus using literature values to represent the material 1.4301. Extensive outstanding investigations for the construction and validation of the model were planned for the 3rd funding phase. Due to the high complexity of such a computational model with a high workload, the calibration with literature values of the subroutine in LS-DYNA was performed in this funding phase. First



evaluations showed about 40 volume percent of deformation induced martensite as homogenized value from the bar surface to 0.4 mm towards the core. Axial and tangential tensile residual stresses between 300 MPa and 600 MPa occurred, but averaged through the element size. Thus, a direct comparison with the measurements of the residual stress analyses using XRD and BLM was not possible, although the results based on literature data are already in the correct order of magnitude. Further work is needed here to validate the FE simulations.

### Material Investigations for the Construction of the Phase Models

The material characterization of the formed specimens made of 1.4301 showed that forming-induced martensite formation occurs on the specimen surface. For this purpose, X-ray phase determination is used to analyze the martensite content as a function of the process parameters on the specimen surfaces. By means of electrolytic ablation, specifically graded depth-resolved residual stress determination was realized. In addition, metallographic preparations were carried out to further investigate the forming-induced phase by means of color etching on transverse sections, and their expression into the sample interior was analyzed. Additional EBSD investigations on the transverse section allowed the orientation of the phases to be determined as a function of specimen depth. Depth-resolved texture measurements were performed on the deformed samples at the German Electron Synchrotron. Due

to the relatively low degree of deformation, the expression of a characteristic deformation texture can only be detected to a limited extent. In figure 8.12 the 110-, 200- and 211-pole figures of the martensite in the edge region of the bar material for convex deformation are shown as examples.

### Investigation of Disturbance Variables in the Forming Process

This work package served to quantify the relevance of disturbance variables and material variations for the selected forming process. Using the example of forming temperature and lubrication, it was found that increased forming temperature affected lubrication such that the surface of the specimens exhibited significant residues of lubricant after the forming process that were difficult to remove. This had a negative effect on the near-surface, radiographic determination of residual stresses. Surface properties could also be affected by the lubricant layer present, which was about 10 µm thick. Furthermore, no significant change in residual stresses after wire drawing was observed by varying the forming temperature. Variations in the geometry of the drawing dies also have a strong effect on the level and homogeneity of residual stresses over the circumference of the specimens. It was found that asymmetric die design leads to inhomogeneous residual stress states. Furthermore, the internal geometries of the drawing dies were determined and incorporated into the FE simulations (WP3). Thus, the deviations could also be analyzed and taken into account for the validation.

## 8.2.2 Statement on the Economic Usability of the Results

The project carried out involved a modification of the wire drawing process by means of an innovative die geometry in order to improve the formability of the wires in subsequent process stages for the production of torsion bar springs and to optimize the end properties. The findings obtained support future process parameter selection with regard to application-optimized wire semi-finished products. In particular, the possibilities for reducing the tensile residual stresses at the wire surface should be emphasized. No industrial partner was involved in the project and no patents were filed. In further activities, interest has already been shown by industrial partners in transferring the technology developed in a transfer project for large-scale production. Further investigations into the load capacity of the optimized torsion bar springs are to be carried out in advance.

## 8.2.3 Cooperation Partners at Home and Abroad

In the context of the 2nd funding phase, cooperation took place with colleagues from SPP2013 Dr.-Ing. Johannes Buhl - BTU Cottbus (FE simulation of phase transformation) and Dr.-Ing. Jens Gibmeier - KIT Karlsruhe (XRD analyses and BLM). Within the scope of the joint publication in the expert group "Thick Walled" [5], the colleagues Prof. Merklein - FAU Erlangen, Prof. B. Kuhfuß - bime Bremen, Prof. W. Volk - TU Munich, Prof. B. Behrens - Leibniz Universität Hannover and Prof. P. Groche - TU Darmstadt cooperated.

## 8.2.4 Qualification of Young Scientists in Connection with the Project

Within the framework of the project, student assistants were employed for the evaluation of the metallographic investigations and the FE simulations, which enabled them to expand their scientific work skills. Currently, a master's thesis on the topic of material map generation under considera-

tion of kinematic hardening has emerged from the project.

## 8.3 Summary

The aim of the joint project was to use geometry elements in the drawing dies to specifically influence the stress curves over the specimen cross section during wire drawing and thus to reproducibly generate stress states that have a positive effect on the manufacture and use of torsion bar springs. In the 1st funding phase, the material 1.4301 was analyzed. In order to design the geometry elements, FE simulations were set up and various geometry elements for extrusion and wire drawing were considered in the calculations. Based on this, it was possible to develop a wire drawing device and carry out tests. In order to investigate the further processing into torsion bar springs and the influence of the adapted residual stress states of the component in the bending process, a modular wire bending tool was developed, with which bending and 3-point bending operations can be investigated using different bending radii. During the investigations, it was numerically and experimentally demonstrated that the geometry elements in the dies influence the distribution of residual stresses across the wire cross-section. The phase-specific residual stresses were determined radiographically, depth-resolved and demonstrated qualitatively. With the aid of metallographic examinations and texture analyses, the effect on the near-surface deformation-induced martensite formation was analyzed. Due to the geometry elements, residual compressive stresses are generated in the edge region during extrusion. During wire drawing, the tensile residual stresses were reduced. The stability of the residual stresses was demonstrated in the fatigue test. The results were used to validate the FE simulations and to assess the effect of the modified residual stress distribution on the bending process. The objective of the 2nd funding phase was to deepen the specific adjustment of residual stresses during the drawing process and to investigate the relevance of disturbance variables and material variations. The resulting influence on the near-surface residual stress states was demonstrated phase-specifically using X-ray residual stress

analysis ( $\sin 2 \psi$ -method) and made available for the validation of the FE simulations. Furthermore, the macro-residual stresses could be analyzed using the borehole method. The wires were drawn at different temperatures and drawing speeds using the developed drawing matrices. In addition, the development of a demonstrator was carried out, which shows characteristic component areas of a torsion bar spring and was manufactured with different bending radii in the bending tool. The evaluation of the wires was carried out with regard to failure and influence of springback and proved a possible improvement of the properties of the components. This was followed by further development of the FE simulations for wire drawing and bending with regard to predictability and investigations into the mapping of phase transformation. Furthermore, work was carried out on the material map generation for kinematic hardening. Dynamic loading in the form of vibration tests was used to quantify and confirm the stability of residual stresses. The interaction between the residual stresses introduced into the wire by the geometry elements and the bending deformation to form the torsion bar spring was investigated in the project and demonstrated with regard to property formation.

An aim of the research project was to influence the residual stress distribution over cross-section during wire drawing by geometric elements in the drawing dies. This creates residual stress conditions in a reproducible process that have a positive effect on the production and application of torsion bar springs. First, the material was analyzed. In order to design geometric elements in the dies, FE simulations were set up and specific geometric elements were considered. The experiments were developed and carried out on the basis of a wire drawing device. To investigate further processing to torsion bar springs and the influence of the adapted residual stress states of components in the bending process, a modular bending tool was developed. Folding and 3-point bending operations can be analyzed using different bending radii. Based on investigations it was demonstrated that the geometric elements in the dies influence the distribution of the residual stresses over the wire cross-section. The phase-specific residual stresses were determined by X-ray, depth-resolved and qualitatively

verified. Using metallographic and texture analyses, the effect on deformation-induced martensite formation near the surface was evaluated. The geometric elements were able to reduce residual tensile stresses, ideally compressive stresses are generated. The stability of residual stresses was verified in fatigue tests. Results were used to validate the FE simulations and assess the effect to change residual stress distribution on the bending process. In the second funding phase the controlled adjustment of residual stresses during the drawing process was intensified. Investigations of the relevance of disturbance variables and material fluctuations were performed. The borehole method for analyzing the macro-residual stresses complemented the X-ray analysis. The wires were drawn with the developed drawing dies at different temperatures and drawing speeds. A demonstrator, which has characteristic component areas of a torsion bar spring was designed and produced. The evaluation of the wires was focused on failure and the influence of the spring back and represent a potential improvement of component properties. The FE simulations were further developed with regard to predictability and investigations into the depiction of phase transformation. In addition material cards for kinematic hardening were prepared. The stability of the residual stresses was quantified and confirmed by dynamic loads in fatigue tests. The interaction between the residual stresses introduced into the wire by the geometry elements and the bending deformation to the torsion bar spring were investigated in the project and demonstrated with regard to the property formation.

## References

---

- [1] René Selbmann et al. "Concept for controlled adjustment of residual stress states in semi-finished products by gradation extrusion". In: *Archive of Applied Mechanics* 91.8 (Apr. 2021), pp. 3627–3636. DOI: 10.1007/s00419-021-01937-x. URL: <https://doi.org/10.1007/s00419-021-01937-x>.
- [2] Markus Baumann et al. "Gezielte Beeinflussung umformtechnisch induzierter Eigenspannungen beim Drahtziehen". In: *Forschung im Ingenieurwesen*

*nieurwesen* 85.3 (July 2021), pp. 773–781. DOI: 10.1007/s10010-021-00501-x. URL: <https://doi.org/10.1007/s10010-021-00501-x>.

[3] Markus Baumann et al. “Adjusting the Residual Stress State in Wire Drawing Products via In-Process Modification of Tool Geometries”. In: *Materials* 14.9 (Apr. 2021), p. 2157. DOI: 10.3390/m14092157. URL: <https://doi.org/10.3390/ma14092157>.

[4] Baumann, Markus et al. “Influence of a modified drawing process on the resulting residual stress state of cold drawn wire”. In: *MATEC Web Conf.* 190 (2018), p. 04004. DOI: 10.1051/matecconf/201819004004. URL: <https://doi.org/10.1051/matecconf/201819004004>.

[5] A. Franceschi et al. “Strategies for residual stress adjustment in bulk metal forming”. In: *Archive of Applied Mechanics* 91.8 (Feb. 2021), pp. 3557–3577. DOI: 10.1007/s00419-021-01903-7. URL: <https://doi.org/10.1007/s00419-021-01903-7>.

## 9 Targeted Introduction of Residual Stresses via Local Embossing of Structures in Sheet Normal Direction to Improve Component Properties

Böhlke, T.; Gibmeier, J.; Heinzelmann, P.; Liewald, M.; Riedmüller, K. R.; Simon, N.; Krause, M.; Erdle, H.

GEPRIS 374768210

### 9.1 Introduction

In the field of automotive manufacturing, sheet metal components are used both as cladding or exterior panels and as structural parts with load-bearing functions in various assemblies. Currently, these structural parts are conservatively designed due to vibrations and repeated load changes during operation, resulting in relatively large sheet thicknesses. Modern lightweight design requires that the sheet thickness must be reduced while keeping high operational strength. One promising and effective approach to meet these requirements is to locally adjust defined stress conditions in the sheet metal component, which positively impact static and dynamic loads during operation and allow for a reduction in sheet thickness.

This research project aims to enhance the properties of sheet metal structural components through targeted forming techniques that introduce homogeneous compressive residual stress (RS) distributions. The approach followed here is to implement local embossings in areas subjected to high loads. The homogeneous compressive RS distributions generated through the embossing technique counteract static and cyclic loads during component operation, resulting in a significant improvement in the fatigue strength of such load-bearing sheet metal components. This allows for a reduction in sheet thickness while maintaining the same operational durability.

To enable reliable prediction of the RS distributions arising from the combination of sheet metal forming and local embossing, suitable models are being developed to simulate the generation of local RS and their stability under mechanical loading. These models consider various scales and types of RS, i.e., RS on all length scales (RS of I<sup>st</sup> to III<sup>rd</sup> kind). By employing a two-scale simulation approach using a mean-field concept and considering the local material texture, the local embossing is simulated to design the optimal forming processes for component manufacturing.

This collaborative project focuses specifically on the production of thin-walled sheet metal structural components for battery enclosures in electric vehicles. Due to the operational conditions and requirements of the forming process, these components primarily consist of high-strength, corrosion-resistant sheet materials with good formability. One suitable group of materials that offers this combination of properties is duplex stainless steel, which is being specifically investigated in this research project. The multiphase structure of these materials and their phase-specific crystallographic texture pose a particular challenge for the numerical simulation and experimental analysis of RS. Therefore, it is necessary to consider the phase-specific micro-RS of these sheet materials. Within this project, appropriate measurement and evaluation strategies are being developed to analyze the local RS at various length scales. At the same time, a simulation model is being developed to enable reliable prediction of the RS in multiphase materials with large phase fraction of the contributing phases with phase-specific crystallographic texture.

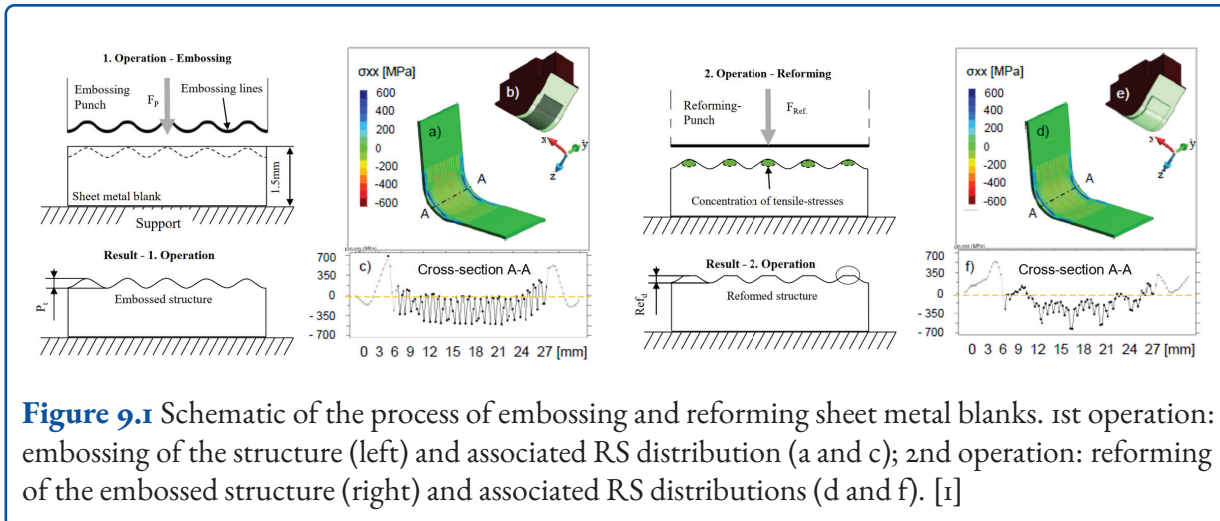


**Figure 9.1** Schematic of the process of embossing and reforming sheet metal blanks. 1st operation: embossing of the structure (left) and associated RS distribution (a and c); 2nd operation: reforming of the embossed structure (right) and associated RS distributions (d and f). [1]

## 9.2 Studies of the Design of the Combined Forming and Embossing Process

To specifically increase the fatigue strength of sheet metal components, the objective of process development was to introduce compressive residual stresses (RS) with the most homogeneous distribution possible into the sheet metal material by using near-surface embossing. Embossing was only to be applied superficially to ensure that the basic component geometry was not changed by the process, as is the case, for example, when beads are introduced. Concretely, the embossing indents were applied to blanks with a sheet thickness of 1.5 mm with a depth of between 50  $\mu\text{m}$  and 100  $\mu\text{m}$ .

As part of the process design, different embossing structures consisting of truncated pyramids, hemispheres or line composites were numerically investigated in terms of their potential for specifically introducing compressive RS into sheet metal materials. For this, simplified FE simulation models were created, allowing different punch geometries, embossing strategies and embossing depths to be investigated using flat sheet samples as examples. Here, it was found that soft contours lead to fewer stress peaks and thus more homogeneous RS distributions within the sheet metal material. Based on these results, the geometry of embossing was determined as a groove structure. To further optimize this structure, different groove distances and depths

were simulated in the next step. As a result of this structural optimization, embossing grooves with a spacing of 0.5 mm and a penetration depth of 100  $\mu\text{m}$  were obtained as the best variant regarding compressive RS introduction. Furthermore, the simulation results of the optimized embossing process showed that a single embossing stroke was not capable of producing sufficiently homogeneous RS distributions. For this reason, a so-called reforming operation was established after the actual forming and embossing process, leading to a more uniform distribution of RS (see figure 9.1).

Based on these first numerical investigations on flat sheet samples, a specific embossing geometry was implemented in a real forming tool, enabling simple bending specimens to be formed and embossed simultaneously and finally reformed in a subsequent step. During the design process for this tool, static-structural mechanical analyses were carried out with an unembossed specimen before the forming and embossing simulations to identify critical component areas with increased stress concentrations. Subsequently, embossing structures were numerically determined for this area to compensate for these stress concentrations via compressive RS superposition. This embossing structure was implemented at the end of the forming process by pressing the bending punch equipped with embossing dimples into the specimen. In contrast, forming a pre-stamped sheet would lead to a rearrangement and reduction of the compressive RS distribution or could even generate balancing ten-

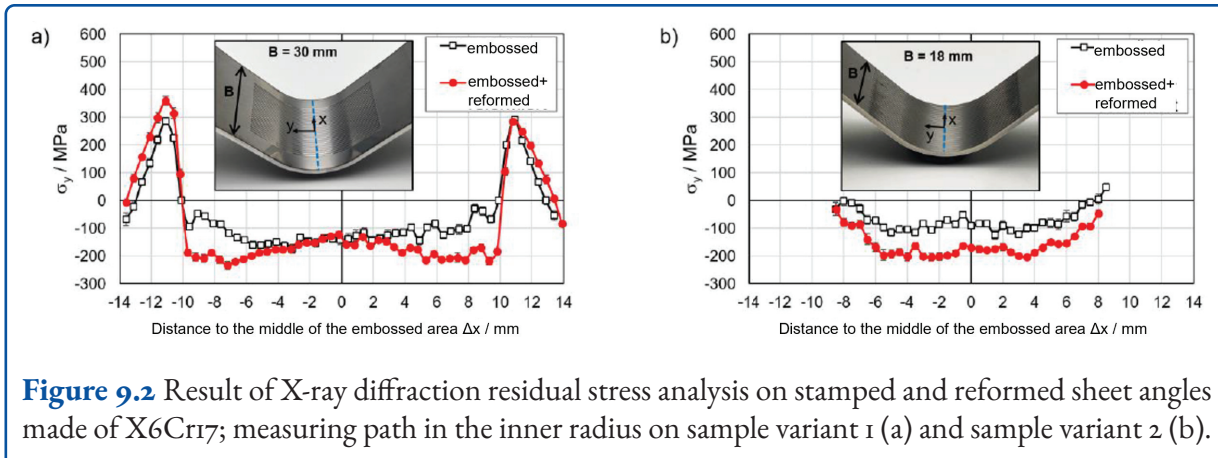


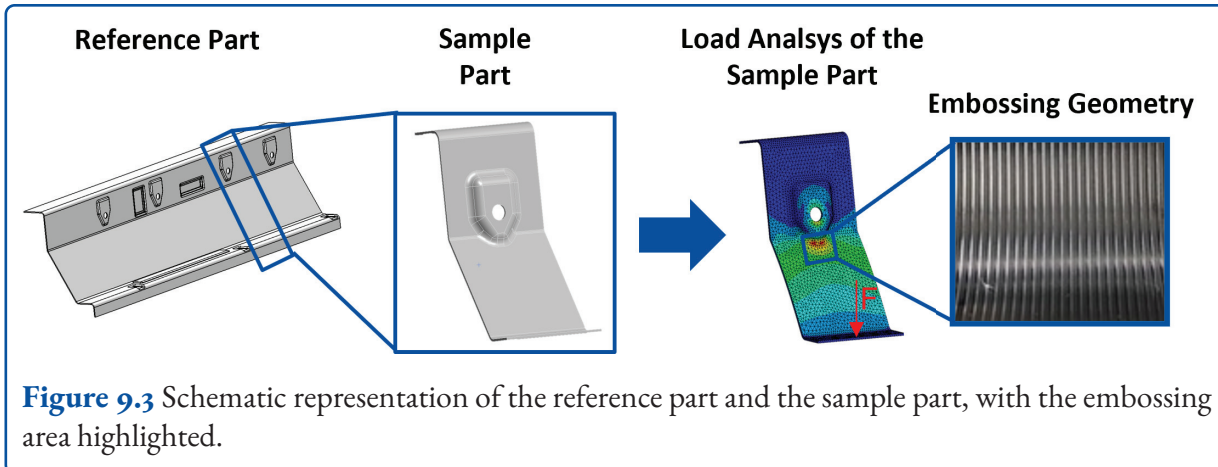
**Figure 9.2** Result of X-ray diffraction residual stress analysis on stamped and reformed sheet angles made of X6Cr17; measuring path in the inner radius on sample variant 1 (a) and sample variant 2 (b).

sile RS in areas adjacent to the actual embossing zone. A further advantage of this approach is that the embossing process can be integrated into conventional sheet metal forming processes, such as deep drawing and crash forming [2]. This avoids a separate step for the specific introduction of compressive RS into the sheet metal surface. The investigations showed that the compressive RS induced into the sheet sample strongly depended on the embossing depth and the embossing surface. Higher embossing depths led to plastic deformations in the width and length of the sheet specimen, which resulted in a decrease in the compressive RS. To determine the optimum amount of compressive RS induced by the approach for the considered part, a sensitivity analysis was carried out. Based on the results of this analysis, a die tool with interchangeable inserts was developed to produce embossed and subsequently reformed bending angles. Two inserts with different embossing structures were designed. The tool allowed conventional bending of the sheet sample at the beginning of the process. During the last 0.1 mm of travel, the punch head pressed the embossing structure into the sheet surface. Subsequently, only the elevations of the embossed surface were reformed by a few 10 µm with a reforming punch in a second process step. The developed process was evaluated using the single-phase ferritic corrosion-resistant stainless steel X6Cr17 (1.4016) and the two-phase duplex stainless steel X2CrNiN-23-4 [3]. Both materials reveal comparable mechanical properties. Furthermore, two variants of bending samples were produced, differing only in the specimen width

(18 mm and 30 mm). Afterwards, the embossed bending samples were handed over for further experimental X-ray analyses of phase-specific RS and for performing alternate bending tests. The X-ray RS analyses showed an RS distribution across the embossing field that was assessed for being sufficiently homogeneous, which was balanced by tensile RS at the edge of the embossing zone. The compressive RS were measured along a measurement path transverse to the embossed structures. It was found that the combined forming-embossing step already produced an approximately homogeneous distribution of compressive RS in the embossing field. Subsequent reforming further increased the compressive RS in the first sample variant, while the balancing tensile RS in the areas at the edge of the embossing remained almost unchanged. In the smaller sample variant, the reforming led to an increase in the compressive RS at the sample surface. No tensile RS were observed at the specimen surface, indicating that the compressive RS in depth were compensated by tensile RS (see figure 9.2). The alternate bending tests further showed that the induced compressive RS in the sheet metal sample were produced stably and reproducibly.

### 9.3 Numerical Design of the Tool Concept

Finally, the results were transferred to a more complex and realistic part. Here, a section of a support plate used to fix battery housings in the frame structure of an electrically driven vehicle was se-



lected as a sample part (refer to figure 9.3, left side). Again, static-structural mechanical analyses were performed to identify the most suitable areas for introducing compressive RS. For this, areas were determined to show the highest tensile stresses and thus a high probability of failure under continuous loading.

Once the part geometry and critical areas were defined, the next step was to determine the tool's working surfaces. As the developed process involved separate operations for combined forming and embossing as well as for reforming, tool working surfaces were numerically designed for each of these two operations. To evaluate the working surface of combined forming and embossing, additionally, a simulation with working surfaces for an unembossed part was conducted as a reference. Figure 9.4 shows the simulation results of the forming operation without embossing and additional load. On the left side, the  $x$  stresses and, on the right side, the  $y$  stresses are displayed. For validation, this simulation was compared with real measured data obtained from the residual stress measurements. Subsequently, the validated simulation of the unembossed bending specimen was used as starting point for the simulations of the embossing and reformation operations.

Best compensation of the tensile stresses prevailing in the not-embossed bending specimen was achieved with a total of 35 groove-shaped embossings aligned with the load direction of the sample and introduced in the marked area in figure 9.3

(right side). The embossing die was designed to create embossings that penetrated the component by approximately 100  $\mu\text{m}$ . Figure 9.5 illustrates the simulated embossing process, showcasing stress components in  $x$  (left) and  $y$  (right) direction.

The simulation result shown in figure 9.5 still revealed an inhomogeneous distribution of RS over the embossed surface in the  $x$  and  $y$  directions. To achieve a satisfactory homogenization of the RS distribution, an additional reforming operation was introduced. Here, the reforming die indented the embossings by 20  $\mu\text{m}$ . This resulted in a more uniform distribution of RS across the embossing surface, as shown in fig. 9.6. These simulation results were finally validated by real experiments.

## 9.4 Tool Concept Design

The tool concept was derived from the aforementioned sequence of operations. Another criterion was to design the tool in a single stage, meaning that the tool's working surfaces could be changed for each operation. In addition to the embossing and reforming operations, a forming operation without the embossings was needed to assess and quantify the fatigue behavior due to the embossing and reforming. To fulfill these requirements, it was decided to manufacture three inserts representing the three operations (forming, combined forming and embossing, and reforming).

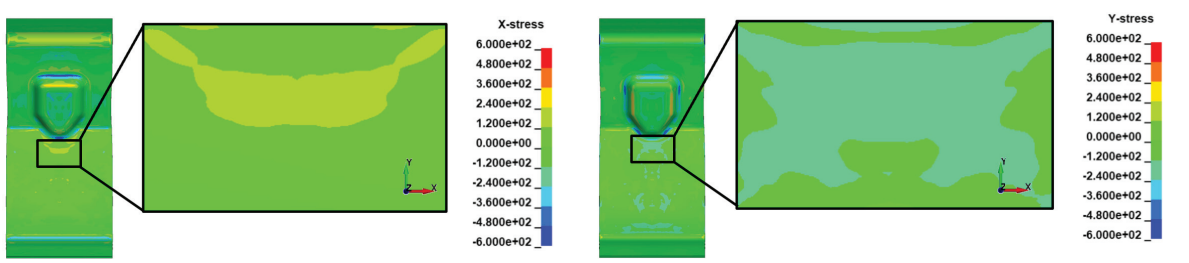


**Figure 9.4** Numerical results of the bending process simulation.

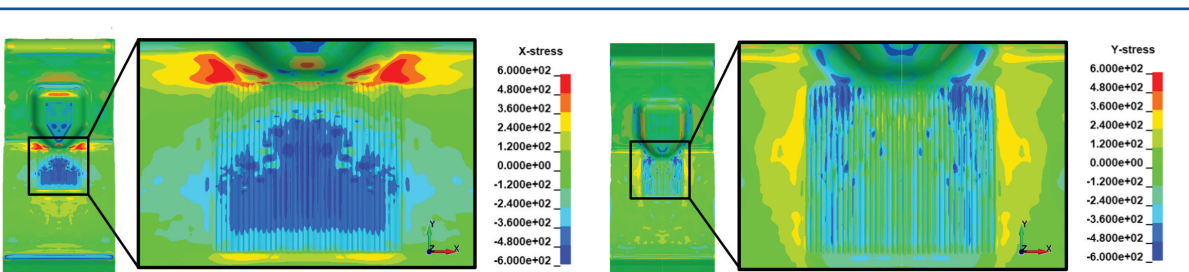


**Figure 9.5** Numerical results of the embossing process simulation.

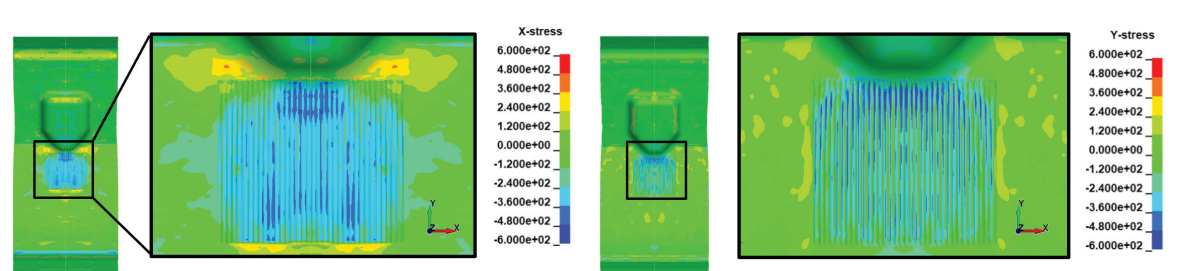


**Figure 9.6** Numerical results of the reforming process simulation.

The tool was designed to be compatible with a single-acting press at IFU. Based on the specified tool requirements, the tool was manufactured (see figure 9.8 a). The different inserts were manufactured for the tool, as shown in figure 9.7. The resulting components are displayed in figure 9.8 b, illustrating forming with and without embossing as well as reforming from left to right.

## 9.5 Experimental Analysis of Residual Stresses on Textured, Multi-phase Sheet Metal Materials

The problem with local experimental analysis of forming-induced RS distributions in thin-walled sheet metal components is, in addition to the thin walls as such, that crystallographic textures are usually introduced during manufacturing and must be taken into account. In the case of multi-phase material states with large phase fractions of the contributing phases, such as duplex steels, there are also phase-specific textures. In order to evaluate the RS,

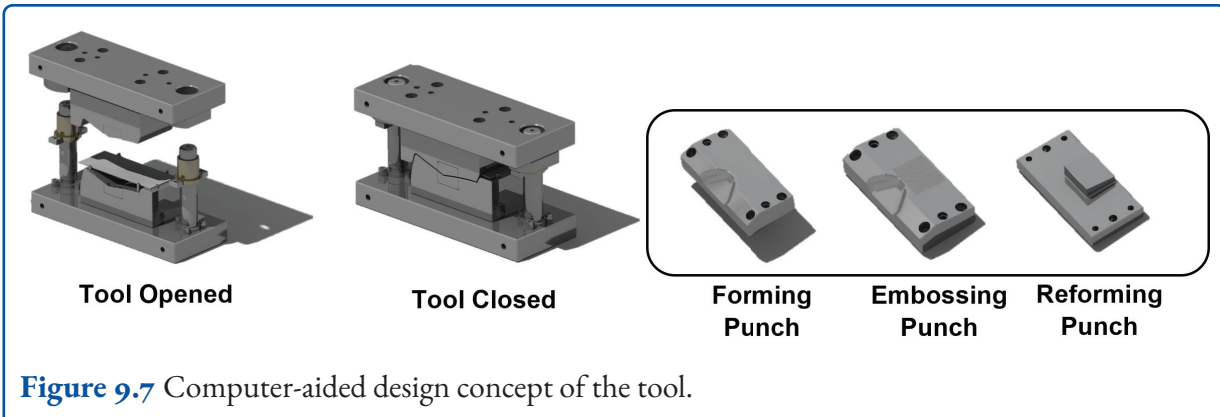


**Figure 9.7** Computer-aided design concept of the tool.

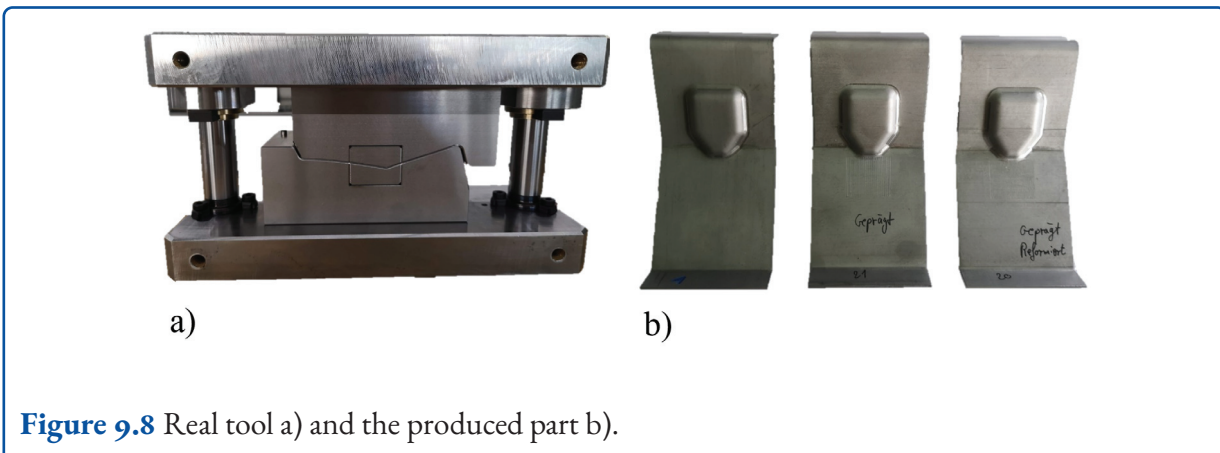


**Figure 9.8** Real tool a) and the produced part b).

it is necessary to carry out phase-specific RS analyzes based on diffraction methods (e.g., X-ray or neutron diffraction) and to take the phase-specific texture and texture gradients into account both in the measurement and in the evaluation.

In the present sub-project, the duplex stainless steel X<sub>2</sub>CrNiN<sub>23</sub>-4 (material number 1.4362) in cold-rolled condition with a sheet thickness of 1.5 mm was used as the model material. This stainless steel has a ferritic-austenitic structure with a phase content of approximately 50 %. Figure 9.9 shows an example of the results of EBSD (electron back scatter diffraction) analyses that were carried out in the plane of the sheet and in longitudinal and transverse sections of the initial material state. Both phases have grains that are elongated in rolling direction, with the ferrite phase having a significantly larger average grain size (see figure 9.9).

To determine the crystallographic texture, pole figures were determined by means of X-ray diffrac-

tion for both phases of the duplex stainless steel, in the ferrite and austenite phase, in addition to the local EBSD analyses and the orientation density distribution function (ODF) was calculated from them. In combination with sequential, electrochemical material removal, the depth gradient of the local texture over the entire sheet thickness was determined in this way. Both phases show a typical rolled texture for the respective crystal structure (ferrite: cubic body-centered (bcc), austenite: cubic face-centered (fcc)) and a slight decrease in texture sharpness toward the middle of the sheet.

The basic problem with the X-ray analysis of RS on elasto-plastic formed components made of duplex stainless steel is shown in the following illustrations. While the RS analyses using the incremental bore-hole method are hardly influenced by the phase-specific crystallographic texture, the results using a case-specific numerical calibration [5] the depth gradients of the local macro RS were represented very well. However, the X-ray phase-specific RS analy-

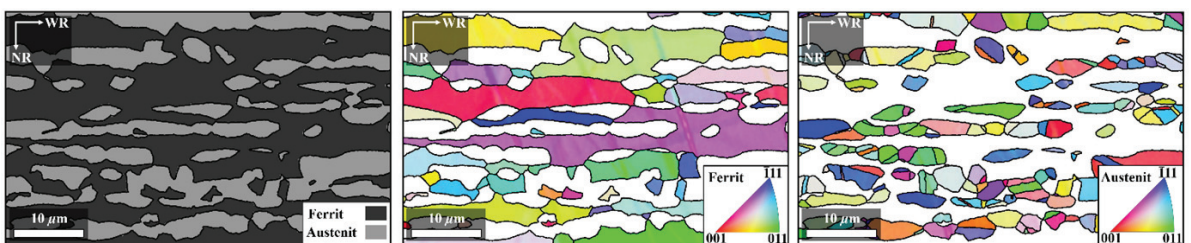


**Figure 9.9** EBSD analysis of the cross section of the X<sub>2</sub>CrNiN<sub>23-4</sub> stainless steel sheet: phase distribution (left) and orientation maps of the phases ferrite (middle) and austenite (right) [4].

ses are significantly more problematic. Figure 9.10 shows the geometry of a cup manufactured by deep-drawing with indication of a measuring point on the outside of the radius in the area of the cup base on the outside of the cup.

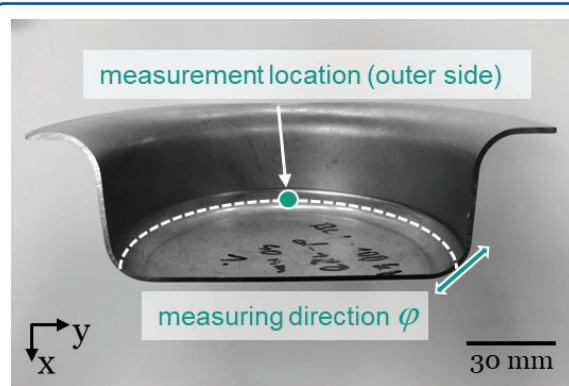


**Figure 9.10** Geometry of a deep-drawn cup (cut open for illustration purposes) with indication of a measuring point for local X-ray residual stress analyses.

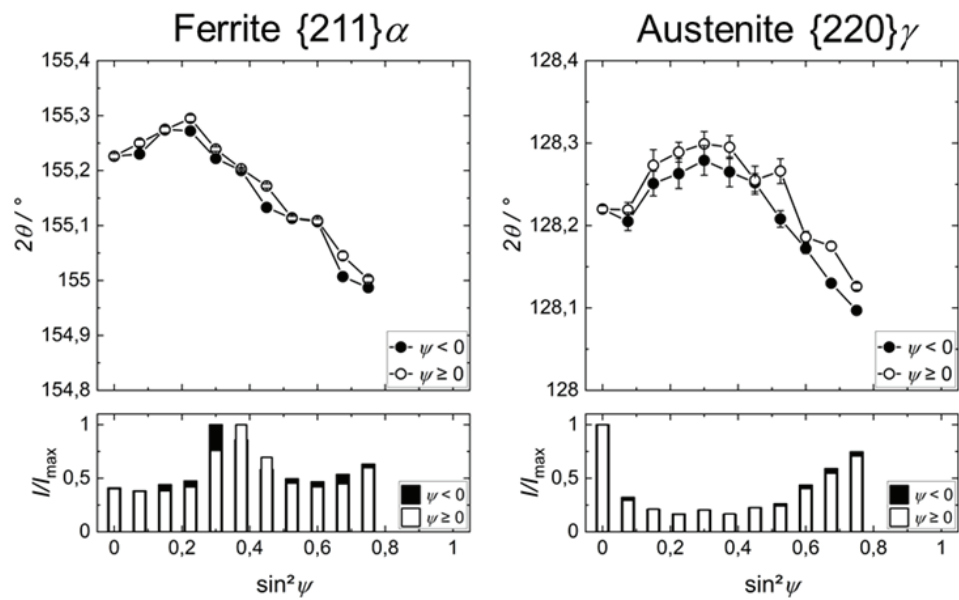
The presentation of the results in figure 9.11 clearly shows that at the measurement location shown in figure 9.10, where relatively high plastic deformations occur, strong non-linearities in the  $2\theta$  vs.  $\sin^2 \psi$ -distribution were observed. One reason for these distribution oscillations can be seen in the crystallographic textures.

For the further evaluation of these distributions, special methods for considering the crystallographic texture (crystallite group method [6], stress factors  $F_{ij}$  [7]) are proposed in the relevant literature. The applicability of these methods was examined in detail for the present material condition of

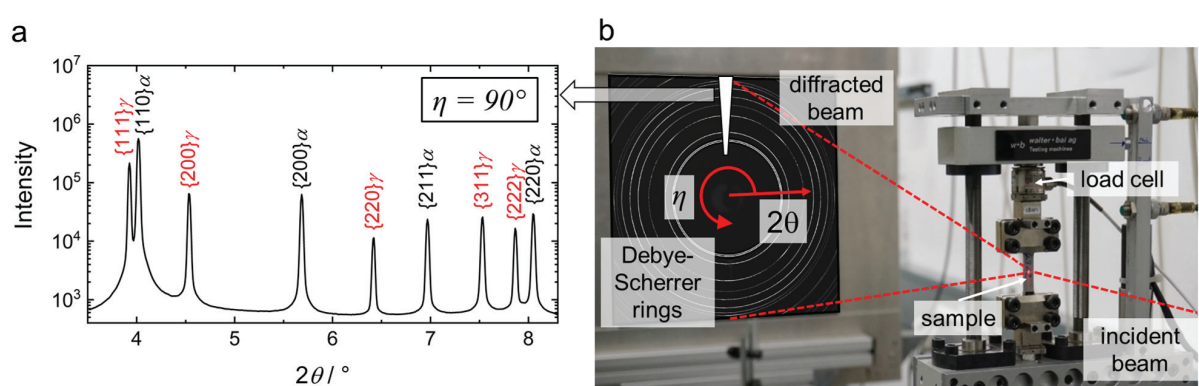
the duplex sheet in the sub-project described here. According to the present texture characteristics, the measurement and evaluation approach according to the literature using the stress factors  $F_{ij}$  should preferably be used. The fundamental investigations mentioned were carried out for the duplex stainless steel by means of defined in situ load stress analyses both in the laboratory using laboratory X-ray sources and using high-energy synchrotron X-rays at Petra III at DESY (Hamburg). In the following, selected results of measurements are presented as an example, which were carried out on the beamline Po7B@Petra III at DESY (Deutsches Elektronen Synchrotron = German Electron Synchrotron) in transmission geometry using monochromatic synchrotron X-ray radiation with photon energies of 87.5 keV.

Figure 9.12 b shows the basic setup used at the DESY measurement campaign. The uniaxial tensile loading up to a total elongation of about 12 % was carried out using a specially adapted 10 kN miniature tensile/compression apparatus. Complete diffraction rings of both phases were recorded using a 2D flat panel detector. During the evaluation, these rings were integrated in sections. Figure 9.12 a shows an example of the diffraction rings resulting from this integration for the angle  $\eta = 90^\circ$  over a circular segment of about  $10^\circ$ , i.e., for the direction of stress. The different  $\{hkl\}$ -diffraction lines of the two phases ferrite and austenite are marked in the illustration.

For the direction of loading ( $\eta = 90^\circ$ ), transverse to the direction of loading ( $\eta = 0^\circ$ ) and at an angle of  $45^\circ$  to the direction of loading ( $\eta = 90^\circ$ ), the



**Figure 9.11** Results of the local X-ray residual stress analyzes on the deep-drawn cup made of duplex stainless steel X<sub>2</sub>CrNiN<sub>23-4</sub> using the  $\sin^2 \psi$  method at the measurement position from figure 9.2 for the phase-specific measurements on the immediate sample surface for the components in the circumferential direction.



**Figure 9.12** Setup of the in situ diffraction experiment under uniaxial tensile loading at the beamline Po<sub>7</sub>B@Petra III at DESY (Deutsches Elektronen Synchrotron) (b) and diffractogram after segment-by-segment integration of the diffraction rings over a ring segment of  $10^\circ$  in the direction of stress ( $\eta = 90^\circ$ ) (a).

line positions calculated from the diffractograms for the individual  $\{hkl\}$ -diffraction lines as an example for the austenite phase in figure 9.13 and for the ferrite phase in figure 9.14 plotted directly over the stress (total strain). In addition to the experimental data, calculated curves are entered, which can be expected taking into account the texture (ODF) on

the basis of the stress factors  $F_{ij}$ . The curves shown in figure 9.13 and figure 9.14 show that, as expected, the stress factors are very well suited to describing the courses in the purely elastic stress range.

With the onset of plastic deformation, depending on the  $\{hkl\}$  diffraction line, both phases are partly

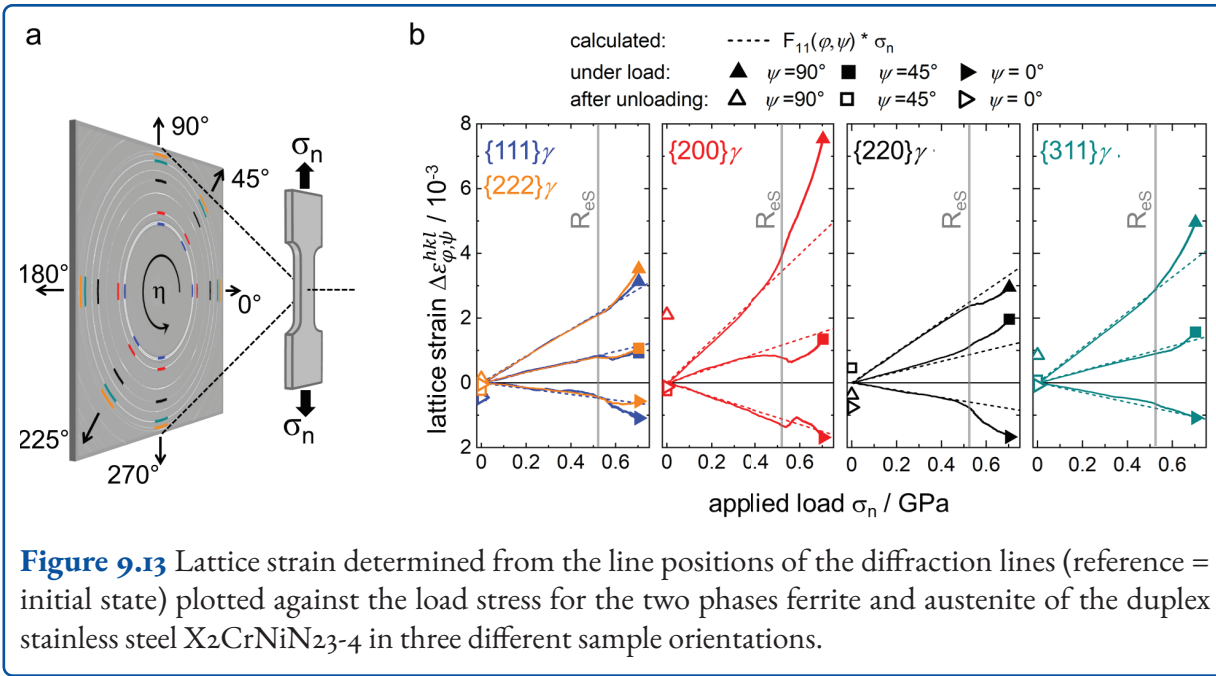


**Figure 9.13** Lattice strain determined from the line positions of the diffraction lines (reference = initial state) plotted against the load stress for the two phases ferrite and austenite of the duplex stainless steel X<sub>2</sub>CrNiN<sub>23-4</sub> in three different sample orientations.

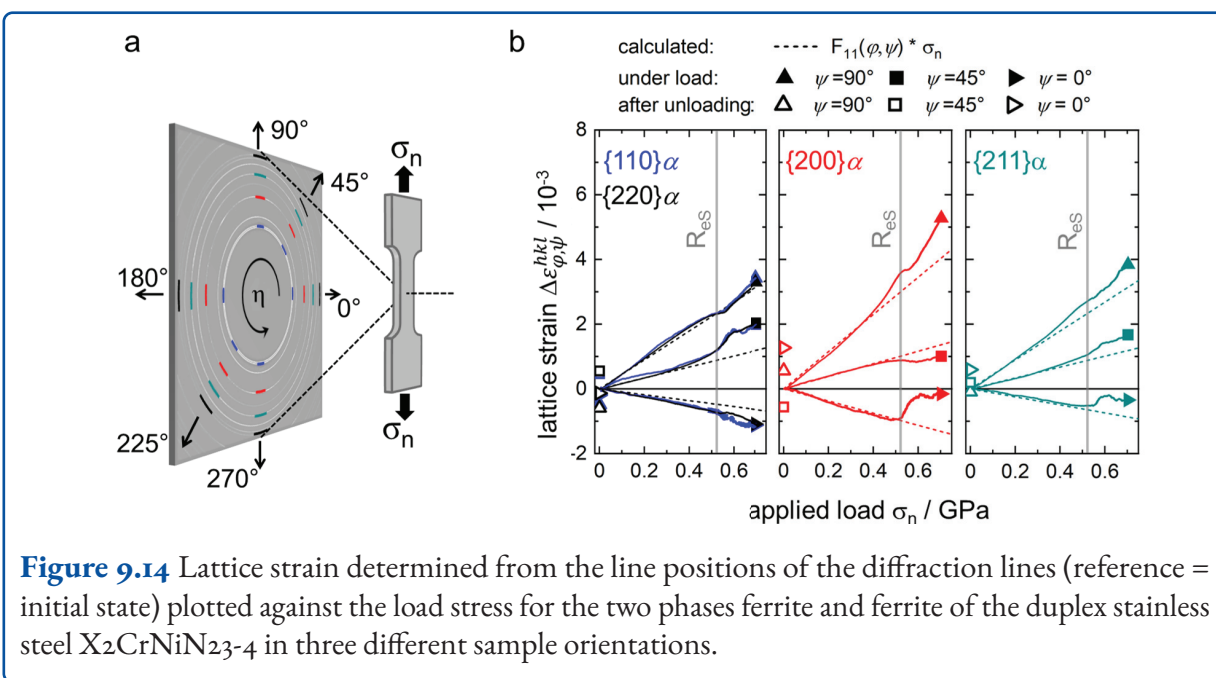


**Figure 9.14** Lattice strain determined from the line positions of the diffraction lines (reference = initial state) plotted against the load stress for the two phases ferrite and ferrite of the duplex stainless steel X<sub>2</sub>CrNiN<sub>23-4</sub> in three different sample orientations.

strongly deviating from the approximately linear distribution from the purely elastic range. The reason for this strong non-linearity, which cannot usually be described with the stress factors, is that in the plastic range (above the yield point  $R_{eS}$ ) additional intergranular strains occur (plastic anisotropies), which are additively superimposed on the effects of elastic anisotropy. Conversely, this means that for the material condition of the duplex steel examined here, a residual stress evaluation for an elastic-

plastically stressed condition can sometimes only be carried out reliably if the extent of this plastic anisotropy is known. As the presentation of the results in figure 9.13 and figure 9.14 shows, this is of course strongly dependent on the observed hkl diffraction line of the two phases.

For the relatively small diffraction angle  $2\theta$ , the diffraction rings can also be evaluated in such a way that the line positions from the segment-by-

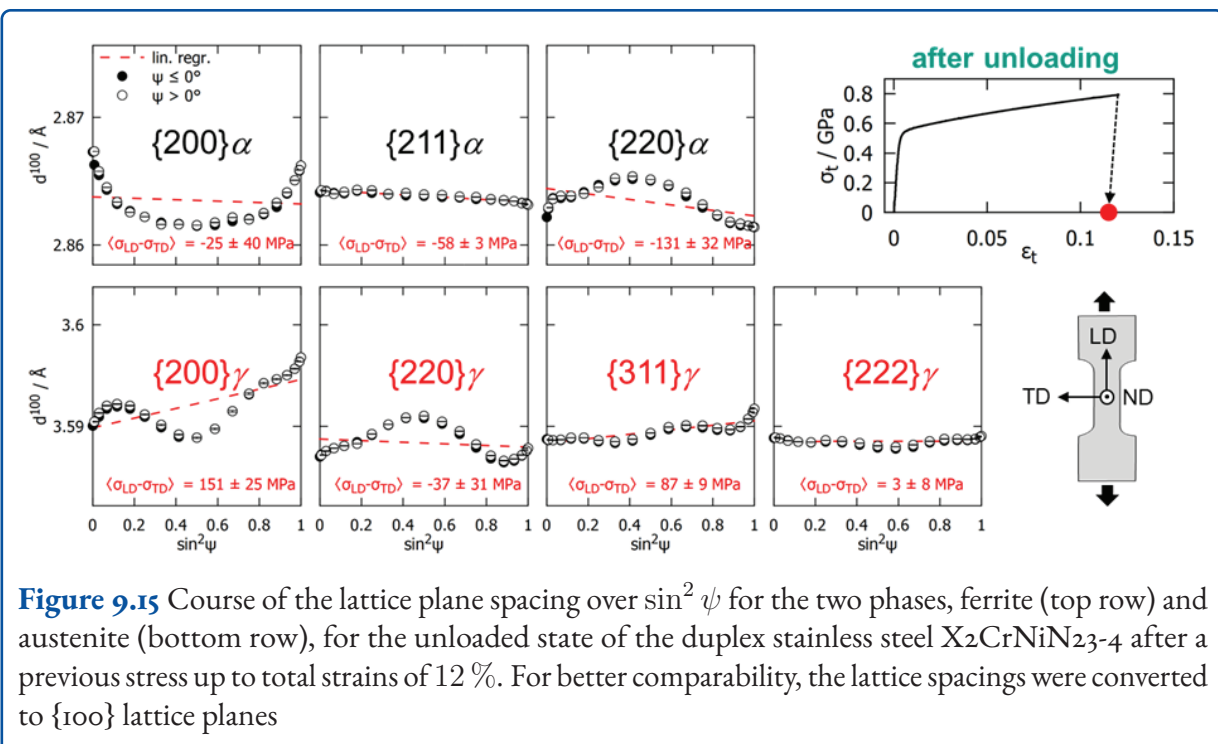


**Figure 9.15** Course of the lattice plane spacing over  $\sin^2 \psi$  for the two phases, ferrite (top row) and austenite (bottom row), for the unloaded state of the duplex stainless steel X<sub>2</sub>CrNiN<sub>23-4</sub> after a previous stress up to total strains of 12 %. For better comparability, the lattice spacings were converted to  $\{100\}$  lattice planes

segment integration are also applied directly to the square of the sine of the orientation angle in the plane of the sheet. In this way,  $d_{hkl}$  vs.  $\sin^2 \psi$  distributions can be displayed over the entire orientation range  $\psi$ , i.e. over the entire range  $0 \leq \sin^2 \psi \leq 1$ , and the resulting non-linearities in the distributions can be discussed. Figure 9.15 shows this representation for selected hkl diffraction lines of both phases for the unloaded state after a previous elastic-plastic stress up to 12 % total strain. The presentation of the results, in which the lattice plane distances for the two cubic phases were converted into the  $\{100\}$  lattice planes for better comparability, clearly shows that the  $\{hkl\}$  lattice planes are influenced to different extents by the intergranular strains. For the body-centered cubic (bcc) ferrite phase, it is confirmed that the  $\{211\}$  lattice plane, which is often used for RS analyses, deviates only slightly from the ideal linear distribution. For example, for the face-centered cubic austenite phase, the lattice plane recommended for residual stress analyzes is the  $\{311\}$  plane. Due to the diffraction structure in the laboratory, measurements are often taken at the  $\{220\}$  lattice planes. In both cases it is shown that despite the relatively weak crystallographic texture in the austenite phase, both lattice planes sometimes result in very large errors if one

tries to approximate the measurement data with a linear distribution. This is also reinforced by the fact that the tilt angle range in laboratory setups is severely limited when using mobile diffractometers, sometimes only up to tilt angles of just 45° (corresponds to  $\sin^2 \psi = 0.5$ ). In these cases, the existing non-linearity in the  $\sin^2 \psi$ -distribution may not even be recognized and incorrect RS are sometimes calculated as a result of the crystallographic texture and the additional occurrence of intergranular strains.

Based on the very extensive datasets from the in situ synchrotron diffraction analyses during the defined uniaxial tensile stress up to the elastic-plastic range (up to total strains of 12 %) for a large number of lattice plane families  $\{hkl\}$ , detailed knowledge about the direction-dependent, phase-specific hardening behavior and the development of the crystallographic texture obtained. These results are important for the understanding of materials but also for the optimization of material models in technical mechanics. In particular, these test data offer the possibility of applying the complex approach for calculating harmonic strain and stress functions, which also enables a reliable ES analysis for highly plastically deformed, textured material

states [8]. This is the subject of ongoing work in the sub-project presented here.

## 9.6 Theoretical Framework for the Simulation of Phase-specific Residual Stresses

For accurate simulation of material properties, which depend on RS, the influence of RS on the macro- and microscale needs to be taken into account. Numerical simulations of a fully resolved microstructures (full-field simulations) are not feasible on the part scale with current finite element methods. Therefore, a multiscale approach is used. RS of first kind are characterized on the part scale via FEM simulations using ABAQUS/Standard. These simulations make use of an integration-point material model which takes into account the phase interaction in the duplex steel leading to RS of second kind through micromechanical relations. Each of the two phases is treated as a homogenized polycrystal model for which the influence of RS of third kind has been investigated through separate full-field simulations. Because only respective mean stresses and strains of each polycrystalline phase are taken into account, the model can be considered a mean-field model (MFM) with two separate scale transitions.

In the first scale transition, local quantities  $\phi(\mathbf{x})$  in the polycrystals, e.g., Cauchy stress or strain, are averaged within each phase  $\xi$  with corresponding volume  $V_\xi$  by

$$\phi_\xi = \langle \phi(\mathbf{x}) \rangle_\xi = \frac{1}{V_\xi} \int_{V_\xi} \phi(\mathbf{x}) dV. \quad (\text{Equation 9.1})$$

Each polycrystalline phase is then modeled elastically using an anisotropic Hooke's law

$$\boldsymbol{\sigma}_\xi = \mathbb{C}_\xi [\boldsymbol{\epsilon}_\xi - \boldsymbol{\epsilon}_\xi^p], \quad (\text{Equation 9.2})$$

where the phase stiffness  $\mathbb{C}_\xi$  and the phase plastic strain  $\boldsymbol{\epsilon}_\xi^p$  are not simple averages due to the heterogeneous orientation distribution in each phase. The viscoplastic behavior is specified with

an anisotropic dissipation potential

$$\Phi_\xi = \frac{\dot{\varepsilon}_{0\xi}^p \sigma_\xi^F}{m_\xi + 1} \left( \frac{\sqrt{\frac{3}{2} \boldsymbol{\sigma}_\xi \cdot \mathbb{H}_\xi[\boldsymbol{\sigma}_\xi]}}{\sigma_\xi^F} \right)^{m_\xi + 1}, \quad (\text{Equation 9.3})$$

where flow stresses  $\sigma_\xi^F$ , stress exponents  $m_\xi$  and the reference strain rates  $\dot{\varepsilon}_{0\xi}^p$  are introduced as material parameters.

The flow stress  $\sigma_\xi^F$  is modeled by phenomenological approaches based on phase-specific equivalent strain measures

$$\varepsilon_\xi^{\text{eq}} = \int_0^t \|\dot{\varepsilon}_\xi^p(\tau)\| d\tau. \quad (\text{Equation 9.4})$$

A common approach for the flow stress is the Voce-type hardening approach

$$\sigma_\xi^F = \sigma_\xi^{F0} + \Theta_\xi^\infty \varepsilon_\xi^{\text{eq}} + (\sigma_\xi^{F\infty} - \sigma_\xi^{F0}) \times \left( 1 - \exp \left( \frac{-(\Theta_\xi^0 - \Theta_\xi^\infty) \varepsilon_\xi^{\text{eq}}}{\sigma_\xi^{F\infty} - \sigma_\xi^{F0}} \right) \right), \quad (\text{Equation 9.5})$$

where the initial yield stress  $\sigma_\xi^{F0}$ , the saturation stress  $\sigma_\xi^{F\infty}$ , the initial hardening modulus  $\Theta_\xi^0$ , and the saturation hardening modulus  $\Theta_\xi^\infty$  are introduced as material parameters. For monotonic loading processes, it can be shown that a direct connection exists between the Voce-type hardening and the dislocation-density-based Taylor formulation of hardening [9] with a Kocks-Mecking evolution law for the dislocation density [10], see, e.g., Bayerschen [11].

Both the anisotropic stiffness tensor and the Mises-Hill comparison stress are influenced by the texture of the polycrystal. Homogenizing the polycrystal using the geometric mean according to Matthies et al. [12] leads to

$$\mathbb{C}_\xi = \mathbb{C}_\xi^{\text{iso}} + \zeta_\xi \mathbb{V}_\xi \quad (\text{Equation 9.6})$$

where the isotropic stiffness  $\mathbb{C}_\xi^{\text{iso}}$  and the anisotropy factor  $\zeta_\xi$  depend on single crystal elastic parameters, and the fourth-order texture coefficient  $\mathbb{V}_\xi$  is related to the experimentally characterized orientation distribution function

$f_\xi(\mathbf{Q})$  via

$$\begin{aligned} \mathbb{V}_\xi = & \frac{\sqrt{30}}{30} \left( \mathbf{I} \otimes \mathbf{I} + 2\mathbb{I} \right. \\ & \left. - 5 \int_{SO(3)} f_\xi(\mathbf{Q}) \mathbb{D}(\mathbf{Q}) d\mathbf{Q} \right). \end{aligned} \quad (Equation \ 9.7)$$

Based on the representation theory argument by Man and Huang [13], the Hill tensor  $\mathbb{H}_\xi$  is given by Böhlke et al. [14] as

$$\mathbb{H}_\xi = \mathbb{P}_2 + \eta_\xi \mathbb{V}_\xi. \quad (Equation \ 9.8)$$

The plastic anisotropy parameter  $\eta_\xi$  can be obtained by an optimization problem based on the experimentally characterized macroscopic plastic anisotropy, as shown in Simon et al. [4].

All other parameters are available from uniaxial tension experiments. For two-phase steels, phase-wise stresses need to be measured in situ, e.g., by using diffraction methodology, also shown by Simon et al. [4].

In the second scale transition, two separate polycrystal models for austenite and ferrite are further homogenized to yield the duplex steel model described by Hofinger et al. [15]. Phase-dependent quantities  $\phi_\xi$  are homogenized to macroscopically effective quantities  $\bar{\phi}$ . Those quantities which are homogenized via simple averages can be expressed as a weighted sum

$$\bar{\phi} = \langle \phi(\mathbf{x}) \rangle = \frac{1}{V} \int_{V_{RVE}} \phi(\mathbf{x}) dV = \sum_\xi c_\xi \phi_\xi \quad (Equation \ 9.9)$$

by the use of the phase volume fractions  $c_\xi = V_\xi / V_{RVE}$  of a representative volume element (RVE) with volume  $V_{RVE}$ .

In deep-drawing simulations, the deformation of a material body  $\mathcal{B} \in \mathbb{R}^3$  must be considered under the assumption of large deformations. Based on the deformation gradient  $\mathbf{F}$ , an incrementally objective macroscopic strain increment  $\Delta\bar{\varepsilon}$  is constructed using a midpoint integration rule

$$\Delta\bar{\varepsilon} = \text{sym} \left( 2 (\mathbf{F}^{n+1} - \mathbf{F}^n) (\mathbf{F}^{n+1} + \mathbf{F}^n)^{-1} \right) \quad (Equation \ 9.10)$$

see Miehe et al. [16]. The strain increment is assumed to be additively decomposed into an elastic strain increment  $\Delta\bar{\varepsilon}^e$  and a plastic strain increment  $\Delta\bar{\varepsilon}^p$ , i.e.,  $\Delta\bar{\varepsilon} = \Delta\bar{\varepsilon}^e + \Delta\bar{\varepsilon}^p$ . On the macroscopic scale of the RVE a purely energetic effective Cauchy stress increment  $\bar{\sigma}$  is assumed, which results in the incremental Hooke law on the macroscale

$$\Delta\bar{\sigma} = \bar{\mathbb{C}} [\Delta\bar{\varepsilon} - \Delta\bar{\varepsilon}^p], \quad (Equation \ 9.11)$$

with macroscopic fourth-order stiffness tensor  $\bar{\mathbb{C}}$ . The localization relations

$$\begin{aligned} \Delta\varepsilon_\xi &= \mathbb{A}_\xi [\Delta\bar{\varepsilon}] - \Delta\mathbf{a}_\xi, \\ \Delta\sigma_\xi &= \mathbb{B}_\xi [\Delta\bar{\sigma}] - \Delta\mathbf{b}_\xi, \end{aligned} \quad (Equation \ 9.12)$$

introduces for each phase  $\xi$  the strain localization tensor  $\mathbb{A}_\xi$  and the stress localization tensor  $\mathbb{B}_\xi$ , as well as the corresponding fluctuation field increments  $\Delta\mathbf{a}_\xi$  and  $\Delta\mathbf{b}_\xi$ . As shown in Hofinger et al. [15], for a two-phase material, explicit expressions of the localization tensors and fluctuation fields can be constructed based on the Mandel-Hill lemma

$$\langle \boldsymbol{\sigma} \cdot \boldsymbol{\varepsilon} \rangle = \langle \boldsymbol{\sigma} \cdot \boldsymbol{\varepsilon} \rangle. \quad (Equation \ 9.13)$$

This two-scale approach requires the assumption that an anisotropically homogenized polycrystal model satisfactorily represents the behavior of the polycrystal without explicitly modeling RS of third kind. Krause and Böhlke [17] validate this assumption for duplex steels using the Maximum-Entropy Method (MEM), an analytical approximation of local stress distributions based on homogenized quantities due to Kreher and Pompe [18]. The MEM considers one-point probability distributions of stress, strain and material properties without an explicit representation of any microstructure. By maximizing the information-theoretic entropy

$$S = - \iint p(\mathbb{C}, \boldsymbol{\varepsilon}) \ln p(\mathbb{C}, \boldsymbol{\varepsilon}) d\mathbb{C} d\boldsymbol{\varepsilon}, \quad (Equation \ 9.14)$$

a joint probability distribution of material properties and local strains  $p(\mathbb{C}, \boldsymbol{\varepsilon})$  is retrieved, see Krause and Böhlke [19], which is parametrized by phase properties, effective properties and effective stresses. Applied to the elasto-plastically deformed austenite steel, the MEM allows for an approximation of residual stresses of third kind based on mean fields,

which supports modeling the present material system using homogenized polycrystal phases. These results were quantitatively validated using full-field simulations of the duplex microstructure based on the fast-Fourier-transform approach as outlined by Wicht et al. [20].

## 9.7 Validation of the Simulation Strategy

In Maassen et al. [21] the presented MFM is applied to the finite element simulation of a four-point bending test under the assumption of plastic isotropy. The resulting distribution of phase-specific stresses over the height of the bending beam is compared to results obtained by a Taylor approximation for the localization of the macroscopic strains onto the individual phases. Both simulation strategies are validated with experimental results.

Figure 9.16 shows the comparison between MFM and experimental results. The phase-specific Cauchy stress component in the longitudinal direction of the beam, evaluated in the region of highest bending stress in the fully loaded state, is plotted over the height of the bending beam.

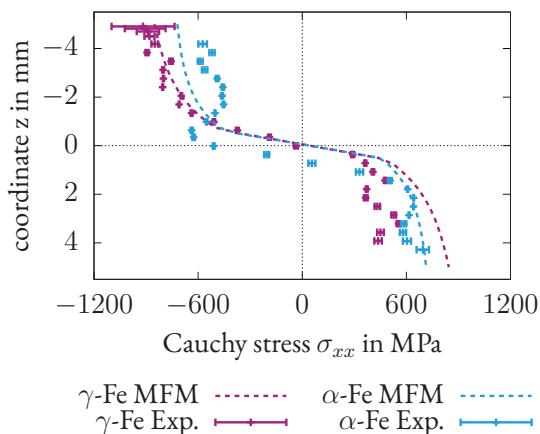


**Figure 9.16** Distribution of phase-specific stress over the height of the bending beam. The simulation results of the MFM are shown in comparison to the experimental data obtained by means of neutron diffraction analysis [21].

Qualitatively the numerical results align with the experimental data, however, a deviation in magnitude can be observed. The experimental data shows a non-symmetry over the cross section height and an additional shift of the zero crossing for the ferrite phase. This non-symmetry is explained by the phase-specific texture analysis. Here, in particular for the ferrite phase, a significantly heterogeneous distribution of the phase-specific crystallographic texture was observed over the bending height, see Maassen et al. [21]. In the numerical model, however, a homogeneous crystallographic texture is assumed. This results in a symmetric stress distribution over the bending height and consequently leads to deviations in comparison to the experimental results.

In Simon et al. [22] the simplified MFM based on the assumption of a vanishing plastic anisotropy is applied on the component level of a deep drawing process. In addition to the incremental hole drilling method to determine the effective RS state, X-ray diffraction was used to experimentally determine phase-specific RS.

In a first simulation step the effective material behavior was simulated based on tensile test data using Hill's anisotropic material behavior. The effective RS state obtained in this first simulation step was found to agree well with the effective RS determined experimentally via the incremental hole drilling method. In a second simulation step the effective stress-strain state of three measurement points was transferred to the MFM for the determination of the phase-specific RS. The corresponding material behavior of the individual phases was characterized based on literature values. Due to the weak crystallographic texture of the plate in the initial state, the simulation strategy for isotropic materials was applied, i.e., the crystallographic texture and its evolution during the forming process was disregarded. Texture development, however, was observed experimentally by comparing the orientation distribution function of the grains before and after forming. This inevitably leads to a discrepancy of the simulation results, especially at points with a strong plastic deformation.

A second study of RS in deep-drawn cups was performed in Simon et al. [23]. Hereby, in contrast to the two-step simulation approach of the previous study, the MFM is applied for the numerical efficient prediction of the effective and phase-specific RS at every integration point of the entire component. In figure 9.17 the simulated distribution of RS at half-cup height are shown in comparison to experimentally determined RS by X-ray diffraction. Although calculation and measurement at the outside wall are in very good agreement, the RS state at the inside wall is overestimated in the simulation. Nevertheless, the study shows that despite the increased numerical effort of a component-level simulation, the efficient two-scale simulation approach of the MFM makes the qualitative and quantitative prediction of phase-specific RS feasible.

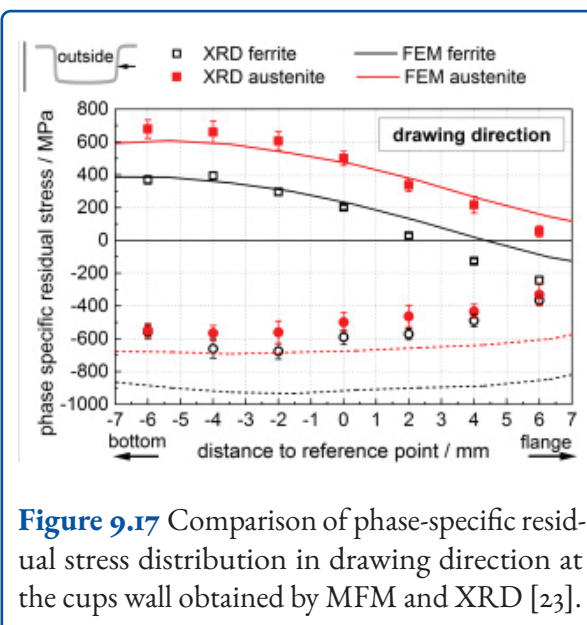


**Figure 9.17** Comparison of phase-specific residual stress distribution in drawing direction at the cups wall obtained by MFM and XRD [23].

Experimental studies of the deep drawing processes showed that the crystallographic texture and its evolution with plastic deformation are important for the prediction of micromechanical RS. In Simon et al. [4] the anisotropic phase-specific strain hardening behavior of cold rolled duplex stainless steel sheets of type X<sub>2</sub>CrNiN<sub>23-4</sub> is investigated. Uniaxially loaded tensile tests are performed on specimens with a varied orientation toward the rolling direction of the sheet metal. The development of phase-specific RS is analyzed experimentally via X-ray diffraction and compared to simulation results obtained by the MFM. In figure 9.18 the eval-

uated phase-specific stress in the ferrite and austenite phase is shown for a varying specimen orientation. The predicted load partitioning of the MFM is in accordance with the experimental results for all three loading directions.

## 9.8 Summary and Conclusions

The research project has yielded a comprehensive strategy for introducing RS in sheet metal materials through localized forming operations, achieved by employing precise embossings. The experimental material of choice, lean duplex stainless steel X<sub>2</sub>CrNiN<sub>23-4</sub>, has successfully demonstrated the achievement of uniformly distributed compressive RS within the component's surface region. Customized stamping tools have facilitated multiple embossing indentations on various formed sheet structures, resulting in stable RS characteristics even under cyclic loading conditions. To reliably predict phase-specific RS formation, a two-scale simulation model utilizing an efficient Mean-Field approach has been developed. By comparing locally determined macroscopic RS distributions and phase-specific measurements, the validity of the model has been established for lean-duplex steel. Several important considerations have emerged from the project, shaping future investigations. Firstly, the influence of phase-specific local texture, previously overlooked in simulations and experiments, must be taken into account to comprehensively understand RS behavior. Process design and tool concepts should prioritize a combined approach that integrates sheet metal forming and localized indentation techniques. Two strategies warrant further investigation: deep drawing followed by stamping deformation, and sheet-holder-free forming employing a specially designed stamping tool. Additionally, extending the project's findings to complex component profiles beyond flat sheet metal is crucial for a more realistic representation of RS phenomena. Furthermore, an integrated process encompassing forming, stamping, and reforming has been developed to achieve a homogeneous RS state in simplified sheet metal geometries. Cyclic loading tests have demonstrated the stability of RS and improvements in cyclic load-bearing

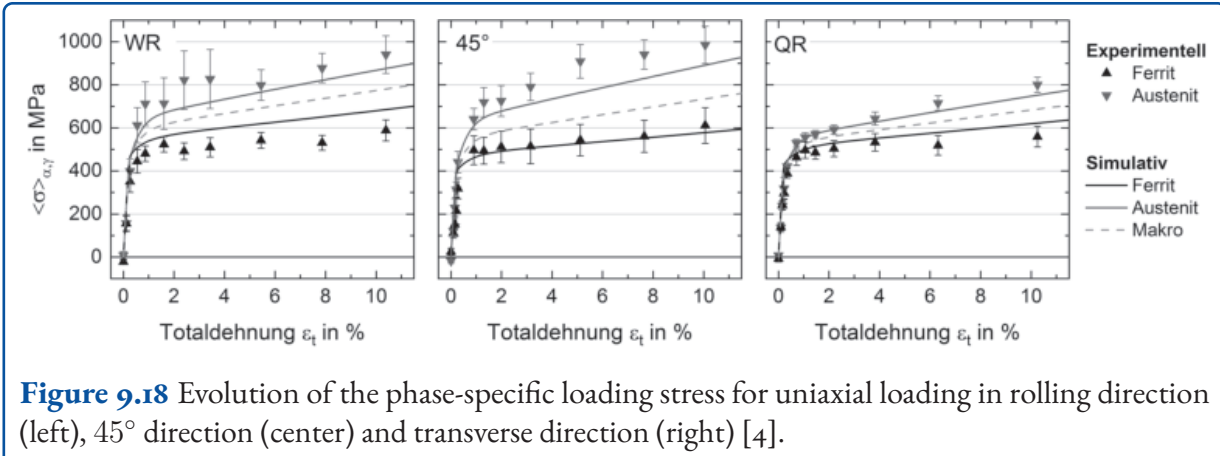


**Figure 9.18** Evolution of the phase-specific loading stress for uniaxial loading in rolling direction (left), 45° direction (center) and transverse direction (right) [4].

capacity. The transferability of this process to duplex steel, along with the refinement of evaluation methodologies for textured duplex steel, is being pursued. Notably, simulation methods have been devised to predict RS at various scales, considering crystallographic texture and plastic anisotropy. However, accurately simulating and analyzing RS phenomena pose challenges due to deformation-driven texture evolution.

Shifting the focus to the design process, the information provided describes the development of a tool used in the manufacturing of support plates for battery housings in electric vehicles. The design process commences with a thorough load analysis to identify critical areas within the component. Subsequently, RS analysis is conducted to determine the optimal location for introducing compression RS through the embossing technique. The tool design encompasses the definition of three distinct working surfaces dedicated to bending, embossing, and reforming operations. To account for springback, the bending operation is simulated using software, enabling compensation for this phenomenon. The obtained results are then utilized to design the remaining die surfaces. Through simulation, it is determined that the critical area requires the implementation of 35 embossings covering a surface region of approximately 250 mm. Accordingly, the embossing die is designed to penetrate the component by 100  $\mu\text{m}$ . As the RS resulting from the embossing process are unevenly distributed, a reforming operation is introduced to homogenize the RS on the embossing surface. The tool con-

cept is designed to accommodate the prescribed sequence of operations, necessitating the utilization of different inserts for each distinct operation. Subsequently, the tool is manufactured with the appropriate inserts to facilitate bending, embossing, and reforming procedures. The manufactured components are subsequently subjected to experimental verification to validate the simulation results and evaluate fatigue strength. The design process of the tool encompasses component analysis, simulation of operations, design of tool working surfaces, and manufacturing of the tool for subsequent experimental testing and verification.

Systematic X-ray diffraction studies on texture and texture evolution, on load partitioning behavior and on RS development in duplex stainless steels indicated that for the duplex steel sheet metals phase-specific crystallographic textures were determined, which leads to rather strong non-linearities in the  $2\theta$  vs.  $\sin^2 \psi$ -distribution in both phases, i.e., in the ferrite and the austenite phase. Furthermore, it was shown that common approaches to account for elastic anisotropy as, e.g., the usage of stress factors is not sufficient to explain and describe these non-linearities. Instead plastic anisotropy effects caused by so-called intergranular strains significantly contribute to these non-linearities once the onset of plastic deformation is exceeded. The investigations showed that this must be taken into account for evaluation of the results of X-ray diffraction stress analysis also for  $\{hkl\}$  lattice planes, which are expected for being not strongly affected by this means.

Regarding simulations, a state-of-the-art approach is to model duplex steel as a single macroscopic phase with empirically determined material properties. Through XRD methods, phase-specific RS are experimentally accessible, which makes it necessary to simulate phase-specific RS as well. To that end, a model was derived and implemented, which uses micromechanical relations to explicitly localize phase-wise incrementally small stress and strain increments. The exact micromechanical relations for stress and strain localization used for the two phases can be tailored to a given homogenization method. Each phase is modeled as an anisotropic viscoelastoplastic material model motivated via homogenization of polycrystalline crystal plasticity on the microscale. By taking into account both elastic and plastic anisotropies in terms of texture tensors, the influence of texture on the material behavior can be captured. As stresses and strains for both phases are fully available, the single-phase material can be arbitrarily complex, including additional refinements in terms of texture evolution descriptions. All necessary material parameters are experimentally accessible through tensile tests with *in situ* X-ray diffraction measurements. Additional tensile tests with varying loading directions relative to the sheet rolling direction were used to validate the anisotropy of the stress-strain relationship.

In conclusion, this research project contributes to understanding RS induction and distribution in sheet metal materials. The findings underscore the importance of incorporating phase-specific local textures, exploring combined process design approaches, and extending investigations to complex component profiles. The ultimate aim is to advance manufacturing processes by improving the control and management of RS.

## References

- [1] Stefan Walzer et al. "Improvement of Sheet Metal Properties by Inducing Residual Stresses into Sheet Metal Components by Embossing and Reforming". en. In: *Applied Science and Engineering Progress* 15.1 (2021). ISSN: 2673-0421. DOI: \url{10.14416/j.asep.2021.09.006}. URL: %5Cu r1%7Bhttps://ph02.tci-thaijo.org/index.php/ijast/article/view/245643%7D.
- [2] Stefan Walzer and Mathias Liewald. "Studies on the influence of embossing on the mechanical properties of high-strength sheet metal". In: *Proceedings of the 22nd International ESAFORM Conference on Material Forming: ESAFORM 2019* (Vitoria-Gasteiz, Spain, May 8–10, 2019). AIP Conference Proceedings. AIP Publishing, 2019, p. 160006. DOI: \url{10.1063/1.5112703}.
- [3] Stefan Walzer et al. "Local Creation of Uniform Residual Stresses Into Sheet Metal Components by Means of Multiple One-Side Embossing". In: *Forming the Future. Proceedings of the 13th International Conference on the Technology of Plasticity*. Ed. by Glenn Daehn et al. 1st ed. 2021. The Minerals, Metals & Materials Series. Cham: Springer International Publishing and Imprint Springer, 2021, pp. 2357–2368. ISBN: 978-3-030-75380-1. DOI: \url{10.1007/978-3-030-75381-8\_197}.
- [4] Nicola Simon et al. "Phase-Specific Strain Hardening and Load Partitioning of Cold Rolled Duplex Stainless Steel X<sub>2</sub>CrNiN<sub>23-4</sub>". In: *Crystals* 10.11 (2020). ISSN: 2073-4352. DOI: 10.3390/crys10110976.
- [5] S Schuster and J Gibmeier. "Incremental hole drilling for residual stress analysis of strongly textured material states—a new calibration approach". In: *Experimental Mechanics* 56.3 (2016), pp. 369–380.
- [6] Viktor Hauk. "Eigenspannungen in Kristallitgruppen texturierter Stähle". In: *Zeitschrift für Metallkunde* 76.2 (1985), pp. 102–107.
- [7] H Behnken and Viktor Hauk. "Berechnung der röntgenographischen Spannungsfaktoren texturierter Werkstoffe: Vergleich mit experimentellen Ergebnissen". In: *Zeitschrift für Metallkunde* 82.2 (1991), pp. 151–158.
- [8] H Behnken. "Strain-Function Method for the Direct Evaluation of Intergranular Strains and Stresses". In: *physica status solidi (a)* 177.2 (2000), pp. 401–418.
- [9] G. I. Taylor. "The mechanism of plastic deformation of crystals. Part I. - Theoretical". In: *Proceedings of the Royal Society of London A: Mathematical, Physical and Engineering Sciences* 145.855

- (1934), pp. 362–387. ISSN: 0950-1207. DOI: 10.1098/rspa.1934.0106.
- [10] Fred Kocks and H. Mecking. “Physics and phenomenology of strain hardening: The FCC case”. In: *Progress in Materials Science* 48 (2003), pp. 171–273. DOI: 10.1016/S0079-6425(02)0003-8.
- [11] Eric Bayerschen. *Single-crystal Gradient Plasticity With an Accumulated Plastic Slip: Theory and Applications*. Karlsruhe: Doctoral thesis, KIT Scientific Publishing, 2016. ISBN: 978-3-7315-0606-5. DOI: 10.5445/KSP/1000062103.
- [12] S. Matthies and M. Humbert. “On the Principle of a Geometric Mean of Even-Rank Symmetric Tensors for Textured Polycrystals”. In: *Journal of Applied Crystallography* 28.3 (June 1995), pp. 254–266.
- [13] Chi-Sing Man and Mojia Huang. “Identification of material parameters in yield functions and flow rules for weakly textured sheets of cubic metals”. In: *International Journal of non-linear mechanics* 36.3 (2001), pp. 501–514.
- [14] Thomas Böhlke, Albrecht Bertram, and Erhard Krempl. “Modeling of deformation induced anisotropy in free-end torsion”. In: *International Journal of Plasticity* 19.11 (2003). Finite Plasticity and Viscoplasticity - Theoretical, Experimental and Computational Aspects, pp. 1867–1884. ISSN: 0749-6419. DOI: 10.1016/S0749-6419(03)00043-3.
- [15] J Hofinger, H Erdle, and T Böhlke. “Prediction of residual stresses of second kind in deep drawing using an incremental two-scale material model”. In: *Philosophical Magazine* (2020), pp. 1–21. DOI: 10.1080/14786435.2020.1798533.
- [16] C. Miehe, D. Rosato, and I. Frankenreiter. “Fast estimates of evolving orientation microstructures in textured bcc polycrystals at finite plastic strains”. In: *Acta Materialia* 58.15 (2010), pp. 4911–4922. DOI: 10.1016/j.actamat.2010.05.004. URL: <https://doi.org/10.1016/j.actamat.2010.05.004>.
- [17] Maximilian Krause and Thomas Böhlke. “Stochastic evaluation of stress and strain distributions in duplex steel”. In: *Archive of Applied Mechanics* 91.8 (2021), pp. 3527–3540. ISSN: 1432-0681. DOI: 10.1007/s00419-021-01925-1.
- [18] W. Kreher and W. Pompe. *Internal Stresses in Heterogeneous Solids*. Berlin: Akademie Verlag, 1989. ISBN: 3-05-500669-0.
- [19] Maximilian Krause and Thomas Böhlke. “Maximum-Entropy Based Estimates of Stress and Strain in Thermoelastic Random Heterogeneous Materials”. In: *Journal of Elasticity* 141.2 (2020), pp. 321–348. ISSN: 1573-2681. DOI: 10.1007/s10659-020-09786-5.
- [20] Daniel Wicht, Matti Schneider, and Thomas Böhlke. “An efficient solution scheme for small-strain crystal-elasto-viscoplasticity in a dual framework”. In: *Computer Methods in Applied Mechanics and Engineering* 358 (2020), p. 112611.
- [21] S. F. Maassen et al. “Numerical characterization of residual stresses in a four-point-bending experiment of textured duplex stainless steel”. In: *Archive of Applied Mechanics* 91.8 (2021), pp. 3541–3555. ISSN: 1432-0681. DOI: 10.1007/s00419-021-01931-3.
- [22] Nicola Simon et al. “Phase-specific residual stresses induced by deep drawing of lean duplex steel: measurement vs. simulation”. In: *Production Engineering* 13.2 (2019), pp. 227–237. DOI: 10.1007/s11740-019-00877-4.
- [23] Nicola Simon et al. “Residual stresses in deep-drawn cups made of duplex stainless steel X<sub>2</sub>CrNiN<sub>23-4</sub>”. In: *Forschung im Ingenieurwesen* 85.3 (2021), pp. 795–806. ISSN: 1434-0860. DOI: 10.1007/s10010-021-00497-4.

## 10 Experimental Characterization and Numerical Analysis of Increasing Fatigue Strength by Residual Stresses for Cross-rolled Parts

Brosius, A.; Guilleaume, C.; Kästner, M.; Schneider, T.; Kalina, M.; Kühne, D.

GEPRIS 374767659

### 10.1 Motivation and Objective

In line with the focus of the priority program, this project aimed to advance the targeted use of the strength-increasing effect of residual stresses. In addition to experimental characterization, numerical methods for qualitative prediction of the influence of material and process control on the induced residual stresses and their effect on crack initiation and propagation under cyclic loading have been developed as a main priority.

Starting with the forming process, process parameters and resulting residual stress distributions in the components are discussed and analyzed using FE-analysis. Experimental investigations regarding the residual stress level and triaxiality of the components as well as their fatigue properties will be presented and analyzed. The developed fatigue models are briefly described and utilized to show how residual stress affects fatigue life through comparison of the experimental findings with numerical simulations.

### 10.2 The Cross-rolling Process

The process investigated in this project is an innovative cross-rolling process that combines the flexibility of incremental bulk forming with the ability to combine different materials into hybrid assembled drive shafts using a joining-by-forming process. In many cases the required properties for the shaft itself and the mounted components differ

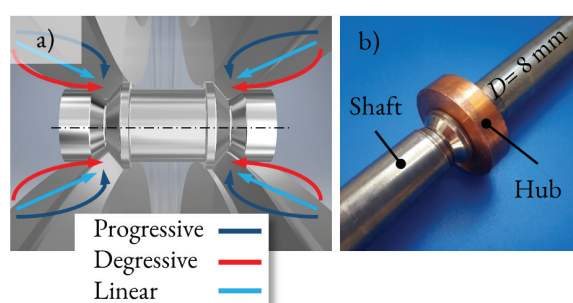


**Figure 10.1** Schematic of the rolling process a) [1] and joint part with steel shaft and copper hub b) joined by rolling process [2].

greatly. Therefore, a hybrid build for these shafts and axles is desirable. The hybrid shaft-hub combination displayed in figure 10.1 b) is manufactured using a modified cold cross-rolling process. The cold rolling process positively influences fatigue life of the shaft component by inducing compressive residual stresses and surface strain hardening while reducing surface roughness and creating a combined form and interference-fit with the hub. In the center of this research project is the analysis and prediction of the influence of residual stresses on the fatigue life of such components under different loading types.

#### 10.2.1 Process Kinematic and Parameters

This modified cross-rolling process variant is characterized by an incremental kinematic forming of the geometry that is highly flexible and can be used to join various material combinations. Here, two symmetrically positioned pairs of actively driven work rolls are used in a transverse rolling process, see figure 10.1 a). Both sets of work rolls can travel in the axial as well as the radial direction. These symmetric kinematics are used to control the material flow in the axial and radial direction without an

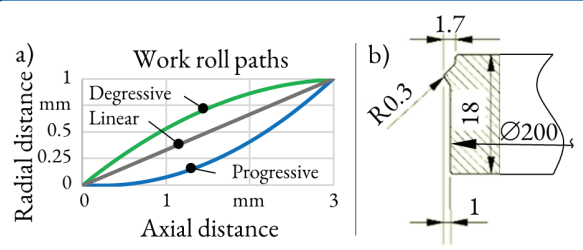


**Figure 10.2** a) Different work roll paths with linear, progressive and degressive movement and b) detail of work roll geometry [3].

additional clamping device for the workpiece. The workpiece itself is not actively driven. The rotation is introduced via friction forces in the contact area between the work rolls and rod. The radial movement of the work rolls pushes them into the workpiece, creating a circumferential notch. The synchronized axial movement then forms the material toward the joining partner, creating two material shoulders that keep the drive wheel for example in place, see figure 10.1 b). Due to the process kinematics, the formation of a circumferential indentation is unavoidable and even necessary for the joining process.

The rolling path of the work roll pairs, as a combination of their radial and axial movement, can be varied from strong degressive to strong progressive, thereby changing the material flow during the rolling process, see figure 10.2 a), and consequently the resulting strains and stresses in the workpiece. The variation of this rolling path is used within this project in order to selectively influence the resulting residual stress profiles and resulting expected fatigue life.

The cold rolling process carried out on the Profiroll 2-PR-15e shoulder rolling machine has a number of process parameters that can be used to influence the final result and the material flow during rolling, see table 10.1. These parameters mostly affect process stability and overall achievable surface quality.

Additionally, the rolling process can be adapted to different shaft diameters or hub widths within the parameter range of the shoulder rolling machine. More importantly, the work roll paths can be var-

**Table 10.1** Range of rolling process parameters

Rotational speed of work rolls	Res. rotational speed of workpiece
20 – 80 rpm	300 – 1300 rpm
Process time	Calibration time
2 – 10 s	0 – 5 s

ied, see figure 10.2 a), so that the material flow and consequently the resulting residual stress state can be altered. This is important for the joining process, because it directly influences the resulting interfacial stresses in the interference-fit and also the residual stress distribution in the notch area, as shown in [2]. The progressive work roll path finishes with a dominantly radial movement toward the workpiece axis, while the degressive work roll path moves mainly in axial direction toward a possible joining partner in the last stages of the process.

### 10.2.2 Material Selection

The obvious disadvantage of this joining by forming process is the resulting circumferential notch in the shaft of the component that is inherent to the process kinematic. Small improvements are conceivable by modification of the work roll geometry (figure 10.2 b), but the general challenge remains. This notch is especially relevant for high cycle fatigue strength, because its effect cannot be compensated by substituting a higher-strength material, since the notch factor has much greater influence on the achievable fatigue life than does the chosen material [4]. Considering the relatively high notch factor of about  $K_t = 3.6$  in the current work-roll set-up, little improvement can be expected by substituting the shaft material. Additionally, high strength steels have a higher mean stress and residual stress sensitivity [5]. Conversely, however, a larger increase of endurable stress amplitude than for mild steels can be observed in the presence of compressive mean stresses [4]. Therefore, a 42CrMo4 steel was chosen as the main material for this project, because it exhibits a high level of strain hardening during cold forming. In combina-

tion with the cold rolling process, that induces high compressive residual stresses in the critical notch area, the notch effect can be significantly reduced. As an additional benefit, residual stresses should be more stable due to the high yield strength of the material. Therefore, higher loads can be sustained for more cycles by lowering the effective mean stress in the notch with this selected process-material combination.

### **10.3 Joining Mechanism and Achievable Joint Strength**

The design of the process for a joint component follows two steps. First, the planned loading conditions and life cycles of the component have to be transferred into a geometric design, considering aspects such as material combinations and respective yield strength and Young's modulus. A guideline for interference-fit dimensioning of shaft hub joints can be found in DIN 7190. Secondly, the process parameters of the rolling process itself have to be determined depending on the required interfacial pressure and geometric form-fit.

The joint strength of the component is the result of a combination of force- and form-fit. The main focus here will be on the force-fit mechanism of the joint, because it is the more relevant component regarding torque transmission. Coulomb's friction law determines the maximum joint strength for such a joint, as discussed by [6]. This means the friction coefficient between joining partners, the area of the joining zone and the interference pressure in the contact area can be used to estimate the transmissible torque. This applies to all force-fit joints regardless of the chosen joining process. Therefore, conventional and well established design and dimensioning methods can be applied to this novel joining process.

For a shaft-hub connection, the diameter of the shaft and the width of the joined hub or gear geometrically determine the contact area. The friction coefficient is mainly influenced by the material combination and surface roughness of the components. The third determining factor in Coulomb's law –

the interference pressure in the joining zone – is the link to the specific processes used to manufacture the joint. Each process results in a characteristic stress distribution in the joining zone. In reality, the interference pressure is typically not uniform over the entire contact area and depends on the joining process. For the rolling process presented here, the stress distribution in the joining zone is influenced by process parameters such as the geometry of the work rolls, the chosen work roll paths (figure 10.2), the material combination and rotational speed during rolling. Regarding possible material combinations, the limiting factor for the formation of strong force-fit is the relative yield strength of the inner and outer joining partner. Ideally, as demonstrated by [7], the outer joining partner should have a higher yield strength than the inner shaft material so that the deformation remains fully elastic and a high clamping force can be generated after joining. A high Young's modulus increases the interfacial pressure in the joining zone thereby increasing the load bearing capacity.

### **10.4 Process Simulation**

Numerical process simulations in this project were used for two different purposes. In the first and second project phase, the main focus was on the analysis of residual stress profiles in the characteristic circumferential notch. Here, different rolling paths were numerically compared with regards to resulting residual stress profiles. In the third project phase, the focus shifted to the application of the rolling process for a joining by forming. Therefore, it was analyzed numerically focusing on the stress distribution in the joint area that determines the interference fit.

#### **10.4.1 Material Characterization and Model**

For the material formulation, a linear piecewise approximation of the flow curve in combination with an isotropic hardening behavior was used for plasticity. This simplified material formulation is sufficient as shown by tensile-compression tests carried out on the 42CrMo4 (1.7225) used for the

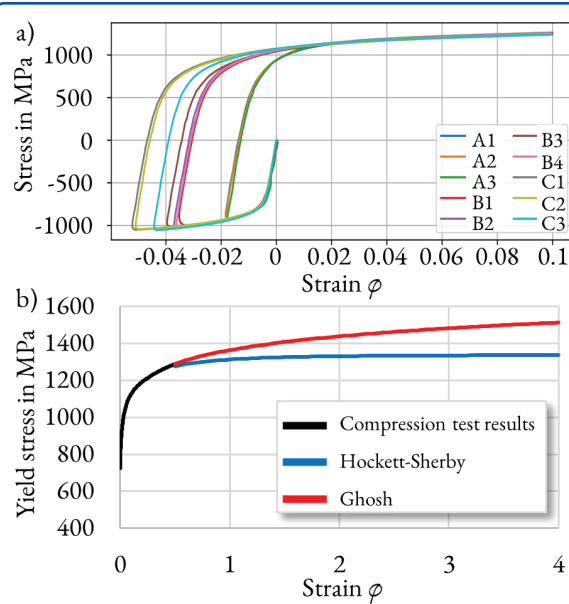


**Figure 10.3** Material characterization of 42CrMo4 (1.7225) with a) results of tensile-compression tests and b) results of compression tests including extrapolation according to Hocket-Sherby and Ghosh according to [1].

shaft. The material exhibits a slight reduction of yield stress after pre-strain in tensile direction during the transition from elastic to plastic deformation. However, this effect quickly dissipates, and the stress-strain curves fall on the same trajectory again, see figure 10.3 a). Therefore, the Bauschinger effect can be ignored. The flow curve for 42CrMo4 (1.7225) was acquired via compression tests up to  $\varphi = 0.5$  and extrapolation using a Hocket-Sherby flow curve approximation [8], see figure 10.3 b). An extrapolation according to Ghosh was also considered, but results have shown an overestimation of residual stresses [1]. This is especially relevant for the analysis of the joint, because the interference force of the force-fit is the direct result of residual stresses in both parts of the joint component. The joining partner (hub) was modeled as a generic elastic material with a Young's modulus of 210 GPa, which is a typical value for common steels.

#### 10.4.2 Simplified FE-model

For both analyses, the cross-rolling process was simulated with a simplified  $2\frac{1}{2}$ -D model using LS-

Dyna RII.1.0 with an implicit solver. Two symmetry boundary conditions are applied. Firstly, the rotational axis of the shaft is used for rotational symmetry, meaning process is modeled as a circumferential indentation of the shaft. The point-wise loading of the material, as it is the case in reality, is disregarded. Secondly, an additional symmetry plane is placed in the middle of the hub and shaft in axial direction. For the material formulation, a linear piecewise approximation of the flow curve in combination with an isotropic hardening behavior was used for plasticity.

A fine mesh with an element size of 0.05 mm is used in combination with remeshing triggered at fixed intervals to avoid large distortions of the elements in the forming zone. The strain in this process is very localized at the nose of work roll, see figure 10.2 b), that has a radius of only 0.3 mm leading to localized very high degrees of strain. This simplified approach is significantly faster than a full 3D model that has a runtime of several days on the TU Dresden High Performance Cluster and is, therefore, better suited to vary parameters during process analysis.

As a result, there may be deviations compared to the actual forming, especially regarding the exact geometric component shape. However, the relevant influences on the residual stress distribution in the notch base can be qualitatively and in the order of magnitude qualitatively analyzed. The overall stress state considered in this approach differs from the stress state of a 3D model, but the actual forming zone is very small in relation to the workpiece. Only in this zone, the yield stress is reached both in reality and in a full 3D model. The surrounding material, on the other hand, behaves elastically, i.e., comparably with a very stiff support. This results in a stress state in the circumferential direction which is very similar to the stress state in the axisymmetric model used here. The principal stresses in the radial and tangential direction in the  $2\frac{1}{2}$ -D simulation are directly interdependent. In the axial direction, both models behave equally stiff, therefore the stress states are similar. In contrast, the overall stress distribution shows deviations which, however, have no negative influence on the notch-

relevant local residual stress profiles due to the very localized forming zone.

## 10.5 Residual Stress Analysis

The results of the simulations with progressive and degressive rolling paths indicate that the notch geometry is formed slightly differently, resulting in a notch factor of  $K_t = 2.7$  for the degressive path and  $K_t = 3.2$  for the progressive path according to Neuber. This difference is important for the subsequent simulation of the expected service life using the local strain approach, see section 10.7.1. On real components, the difference in notch geometry between the different rolling paths is so small that it cannot be detected by optical measurement using 3D scans. The deviation in the simulation results is likely due to the simplifications made with regard to rotational symmetry in the model, see section 10.4.2. The residual stress results of the simulation are used for qualitative comparison between the different rolling paths while the absolute level should only be considered as a comparative parameter. The residual stress profiles are analyzed as a combination of the von Mises equivalent stress and the triaxiality distribution, as this allows the prevailing three-dimensional stress state to be evaluated.

The maximum level of residual stress of about 1,150 MPa is higher than the initial yield stress of the material. The forming zones at the notch base, where the peak stresses are present, however, show a very high degree of deformation up to  $\varphi = 4$  which explains the higher local yield stress of about 1,300 MPa, see figure 10.3 b). The highest comparative residual stresses are obtained directly in the notch base just below the workpiece surface, see detailed views figure 10.4 a) and b). The evaluation of the respective triaxiality in these areas indicates compressive residual stresses, which means that a positive influence on the fatigue strength can be expected. The scale for triaxiality is chosen so that tensile residual stresses are shown in red and areas with more pronounced compressive residual stresses are shown in blue.

The notch base is the critical zone regarding crack formation. Here, high compressive residual stresses should lead to a significant improvement in service life. In the contact area between shaft and hub, a zone of predominant compressive residual stresses is formed on the shaft side, as indicated by the blue zone of triaxiality. This is the driving influence for the frictional connection to the hub. However, this zone of compressive residual stress narrows toward the center of the hub, corresponding to a drop in the joint pressure, see circular markings A in figure 10.4 a) and B in figure 10.4 b). This area, therefore, has a lower contribution to the transmission of forces and moments by the joint. The evaluation of the process with hollow tube shaft, see figure 10.4 c) and d), shows a similar residual stress profile. However, the stress peaks in the area of the notch are less pronounced, while compressive residual stresses continue to dominate in the progressive rolling path. In the case of the degressive rolling path, on the other hand, a tensile stress state tends to dominate in the notch base. According to current research, this is rather unfavorable for the service life of components. For the manufacture of joined shaft-hub connections, there is therefore a possible conflict of objectives between an advantageous rolling path with regard to the joining process and a rolling path which leads to an advantageous residual stress distribution in the shaft. Particularly interesting in terms of the joining process are the joining zones C in figure 10.4 c) and D in figure 10.4 d). Here, when joining with a tubular shaft, a more uniform stress distribution is formed across the width of the joining gap and the zone of compressive residual stresses is wider and extends into the center of the hub. This indicates that more favorable joining properties can be set when joining with a hollow tube shaft.

## 10.6 Experimental Validation

### 10.6.1 Residual Stress Measurements

The residual stresses of real components were measured using a Prism borehole measurement system from Stresstech. This system determines the displacements on the sample surface around the bore-

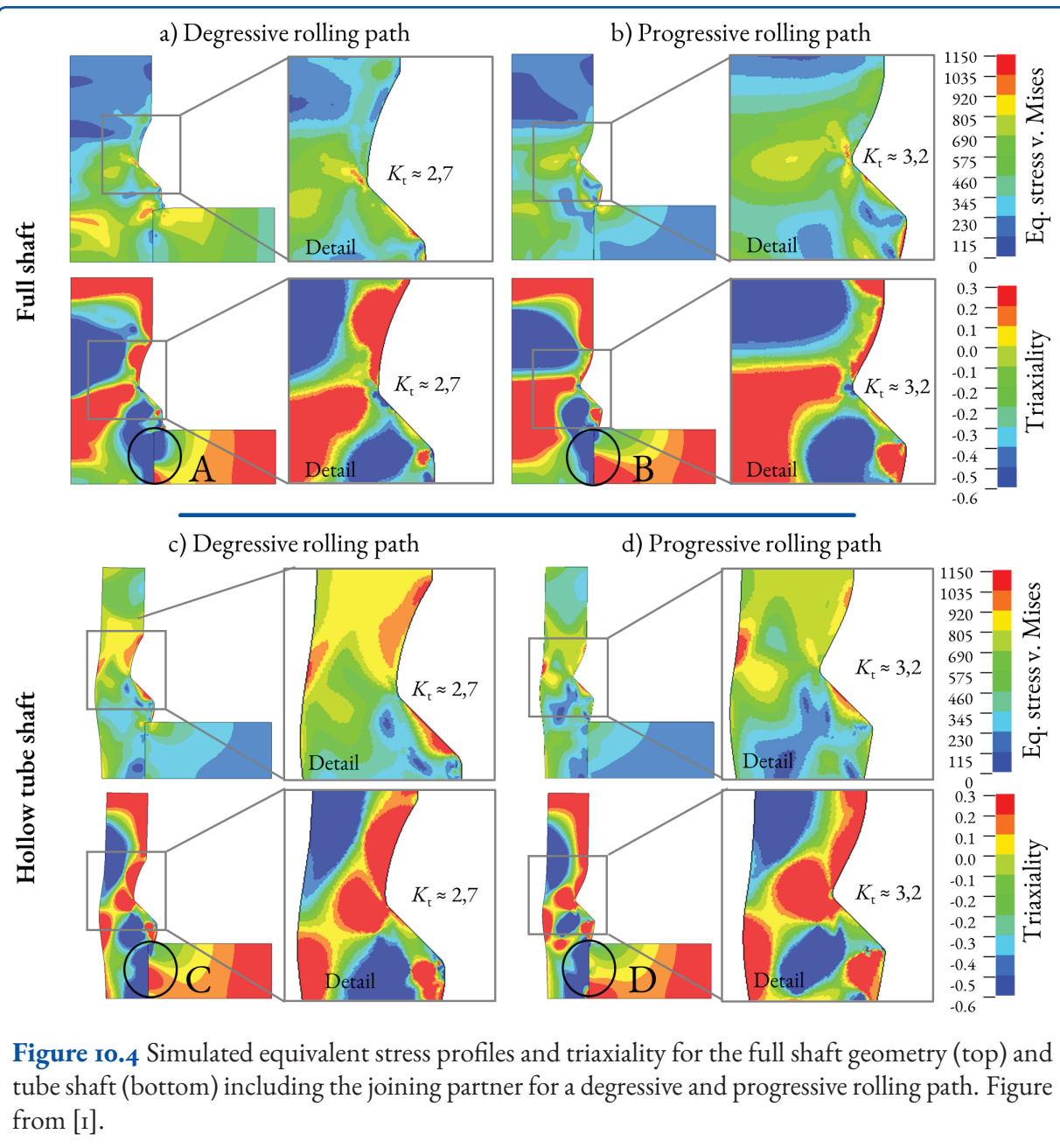


**Figure 10.4** Simulated equivalent stress profiles and triaxiality for the full shaft geometry (top) and tube shaft (bottom) including the joining partner for a degressive and progressive rolling path. Figure from [1].

hole by ESPI (Electronic Speckle Pattern Interferometry). A thin white spray film was applied for sample preparation. Drilling was performed using a 0.8 mm drill bit in increments of 0.04 mm to a total depth of 0.4 mm. Shown here are exemplary measurements on a specimen rolled with a degressive rolling path both with a full and tube profile. The measuring points were distributed around the circumference at the shoulder of the notch as close to the base as technically possible.

There is a clear change compared to the initial measured residual stress profile on unrolled specimen (not shown here) with tensile residual stresses between 0 – 200 MPa in both axial and radial direction. In the near-surface region, residual compressive stresses of 600 – 1000 MPa are detected. This is in good agreement with the results of the simulations, see section 10.5. Quantitatively, direct comparability is not possible due to the simplifications made to the model, as discussed in section 10.4.2. However, the general level of residual stresses is comparable with the results from the numerical

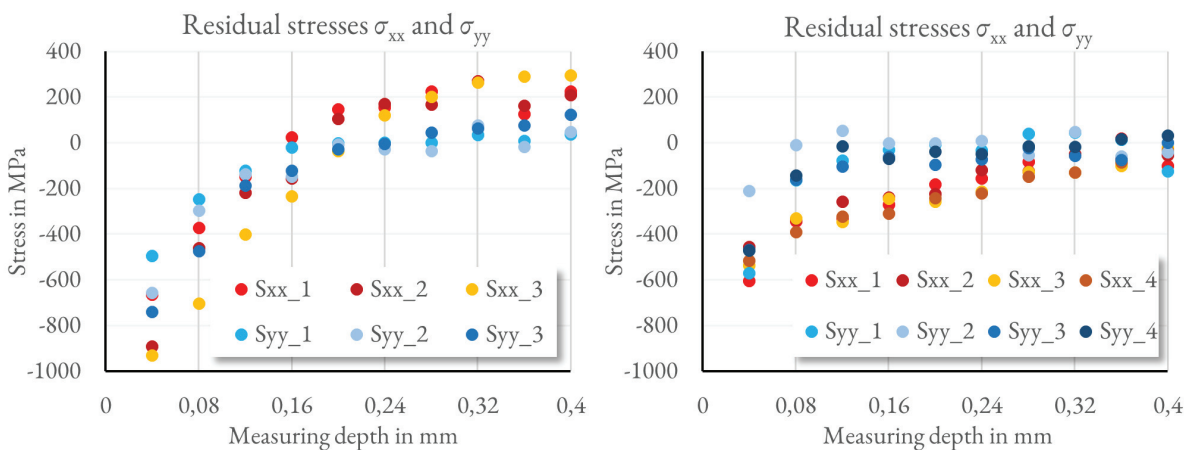


**Figure 10.5** Residual stress measurements in axial (red) and tangential direction (blue) for degressive rolling path on full specimen (left) and tube specimen (right).

analyses. With increasing drilling depth, the residual stresses approach the initial state, indicating that the influence of the rolling process is limited in depth, which again underlines the very localized forming zone of the process.

### 10.6.2 Experimental Fatigue Life Tests

The full shaft components underwent experimental fatigue tests using servohydraulic testing machines. Cyclic tests with the given specifications were carried out at exemplary load horizons for tensile and torsional loading, respectively. Progressively and degressively rolled components were investigated. The results and specifications of the experimental fatigue characterizations are displayed in figure 10.6. First, the progressively rolled components show a higher fatigue strength than the degressively rolled ones. This holds true for both, tensile and torsional loading of the specimens. Interestingly, the scatter range of the tests were higher in the torsion tests. A possible reason could lie in the manufacturing tolerances of the specimen and the higher sensitivity of the torsional shear stresses to varying diameters compared to the tensile stresses in the tension and compression tests.

In a second step, the experimental results were compared to the residual stress fields predicted by the forming simulation. As depicted in figure 10.4,

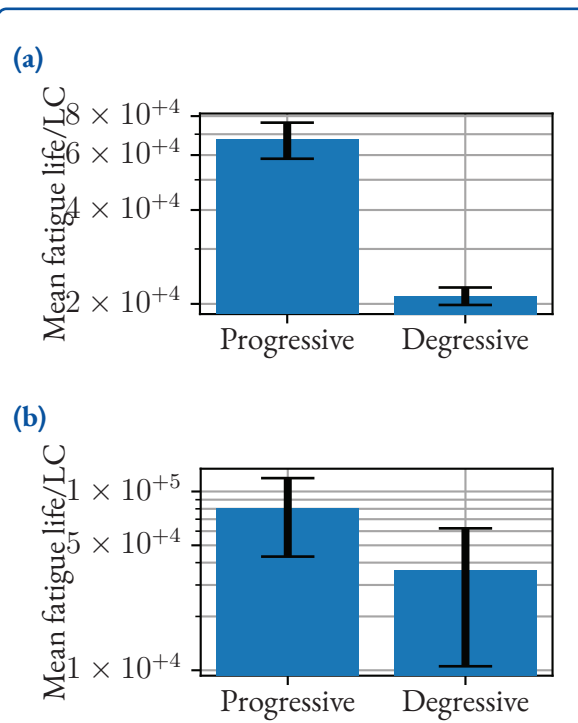


**Figure 10.6** Results of (a) tensile fatigue tests at load level  $F_a = 11$  kN with  $R_\sigma = 0$  and (b) torsion fatigue tests at  $M_{t,a} = 19$  N m with  $R_\tau = -1$  for the two roll paths using the full shaft geometry.

the degressively rolled components were found to exhibit the maximum compressive residual stress closer toward the flank of the rolled notch. The progressive roll path results in a compressive residual

stress peak directly in the vicinity of the notch root. The high compressive residual stresses prevailing there counteract the load induced notch stresses and thus lead to an increase in fatigue life of the progressively rolled components when compared to the degressively rolled specimens. This may at least qualitatively explain the differences in fatigue life of both variants, especially when we take into account the slightly greater notch factor of the components that have been progressively rolled.

### 10.6.3 Thermal and Mechanical Stability of Residual Stresses

The thermal stability of the residual stresses induced by cross-rolling into the workpieces was analyzed in cooperation with other projects focused on bulk metal forming as part of the activity of the corresponding working group. The detailed results are discussed in section 3.5 of this report.

In summary, the specimen manufactured by cross-rolling from 42CrMo4 displayed a good residual stress stability over the course of the temperature treatment up to 240° C with holding times of several hundred hours – resembling the temperature profiles workpieces might typically be subjected to in real-life applications, see section 3 for details and graphs.

The mechanical stability of residual stresses in general was addressed in the Bending Benchmark of the priority program described in section 4.8. Focusing on microscopic elastic-plastic loading of the material in the investigated bending setup, it was shown that the stability of residual stresses was reached after an initial stabilization phase. However, the simulation of residual stresses evolution under cyclic loading in order to predict their change remains a challenging task. The parametrization and the material model used may especially influence the resulting prediction's quality. For more details see Sec. 4.8.

### 10.6.4 Joint Quality Testing

All tested components displayed have the same basic geometry, as shown in figure 10.7 a) with a shaft diameter and hub width of 8 mm and an outer hub diameter of 30 mm with a material combination of 42CrMo4 for the shaft material and C60 for the hubs. The same rolling parameter set was used as identified in pre-tests by means of a cross-section analysis. The criterion was a good shoulder formation, see figure 10.7 c). For a selected shaft material and diameter, a series of tests is necessary to establish the correct machine settings regarding radial and axial movements, which will then be kept constant throughout a series of experiments.

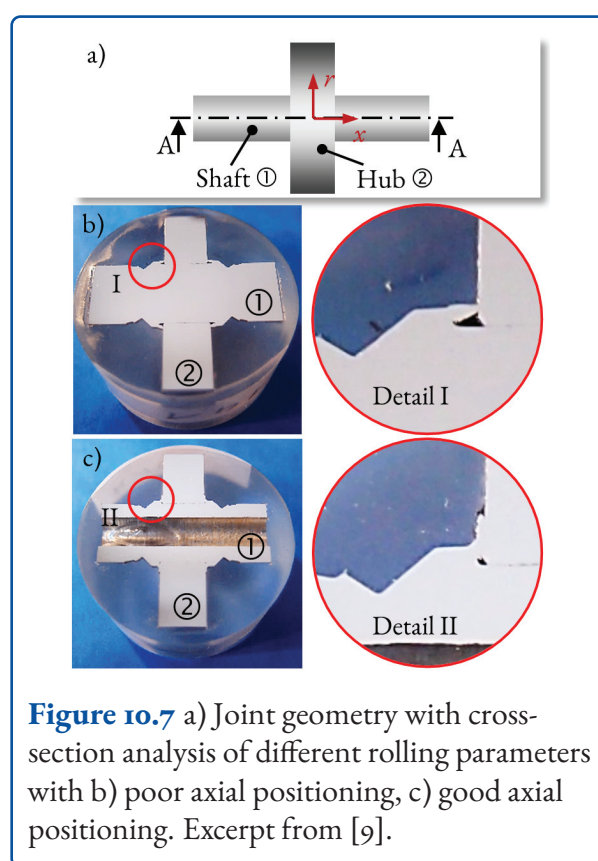


**Figure 10.7** a) Joint geometry with cross-section analysis of different rolling parameters with b) poor axial positioning, c) good axial positioning. Excerpt from [9].

When testing a joint, generally two failure modes are possible: detachment of the two joining partners in the joining area or failure in form of cracking of one of the joining partners. In order to quantify the joint quality and identify the dominant failure mode, torque tests were carried out on a stick-slip testing stand. It is equipped with a 450 N m Atlas-Copco EC-spindle and an open-loop control. During the angle-controlled test, the resulting torque

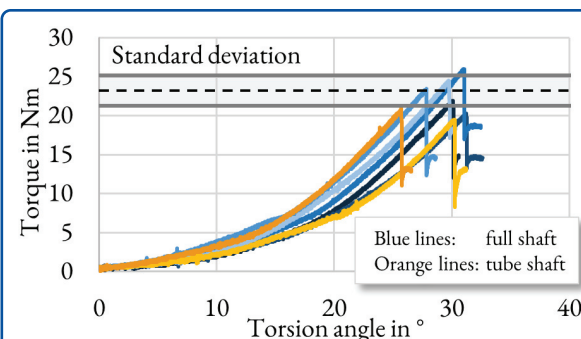


**Figure 10.8** Results of the torque tests on components manufactured by cross-rolling [9].

was measured continuously until a sharp drop in the torque curve was detected indicating component failure.

All components remained visually intact during tests, indicating that the failure occurs in the interference-fit. This is to be expected, since the shaft material has a very high yield stress. The torque measurements of both solid shaft (blue curves) and hollow shaft (orange curves) components are shown in figure 10.8. The arithmetic mean of the failure torque for the solid shafts is approximately 23 N m with a standard deviation of about 2 N m. The hollow shafts performed slightly worse.

The variation in the maximum bearable torque between each specimen group has two possible reasons. First of all, the hydraulic shoulder rolling device has a limited positioning accuracy, which can cause small variations of the final axial position of the work rolls. Secondly, the transmitted torque is directly dependent on the friction conditions within the joint, which also can have small variations.

When analyzing the torque test results in relation to the corresponding analyzed cross-sections, it appears that the difference in the maximum transmissible torque between the components with good and with insufficient axial positioning is caused by the additional contact area that contributes to the load bearing capacity of the joint, see figure 10.9. Ideally, both the axial contact zones (orange) and the cylindrical contact zone (blue) form a force-fit

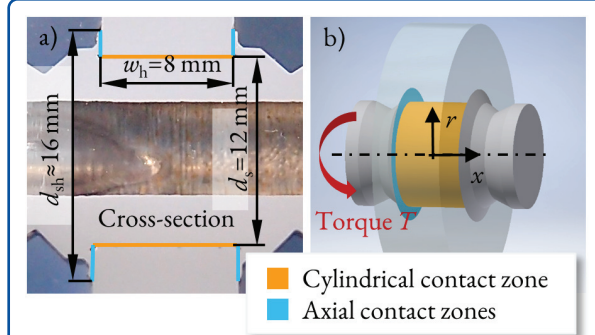


**Figure 10.9** a) Cross-section with color indicated contact areas and b) 3D model of a joined component with color indicated contact areas [9].

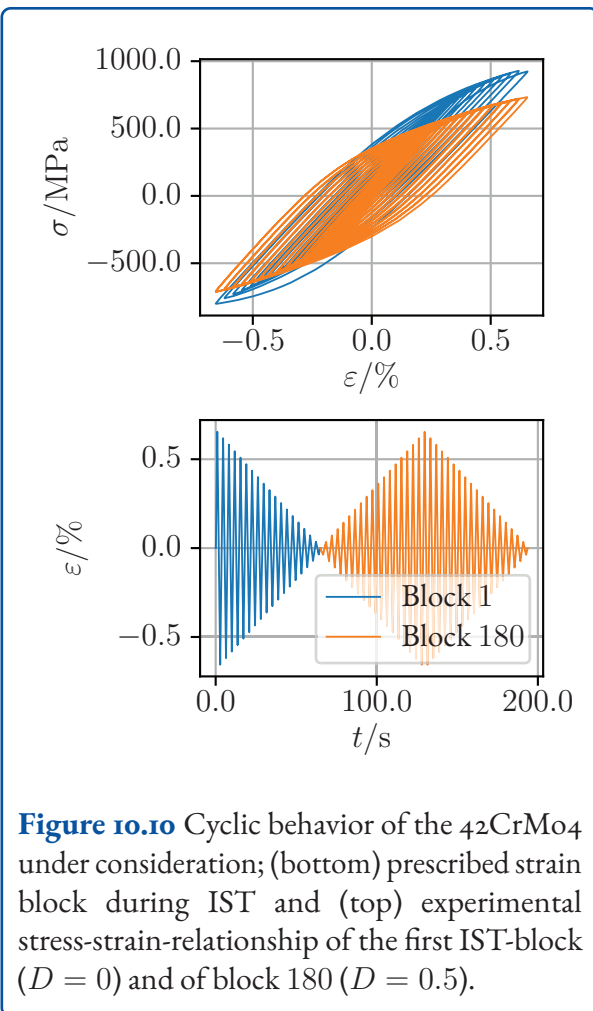
with the hub thereby increasing the contact area and resulting maximum load bearing capacity, see figure 10.9. A more detailed discussion on the geometric interference-fit parameters for this joining by rolling process can be found in [3].

In summary, the axial force-fit significantly contributes to maximum bearable torque of the joint. Overall, the transmissible torque of the rolled components is still not sufficient for an industrial application. The high-strength 42CrMo4 is not an ideal choice for this type of joining by rolling process, because its yield stress is too high and therefore not enough radial material flow can be generated into the contact areas. Since for most shaft-hub connections the contact zones are the most likely point of failure during loading, the shaft material can be exchanged for a more ductile material in order to reach better joining conditions.

## 10.7 Fatigue Life Calculations Considering Residual Stresses

### 10.7.1 Extension of Local Strain Approach

In the following, an extension of the state of the art Local Strain Approach (LSA) for fatigue life analysis, see section 4.7 and figure 4.8, which is capable of capturing effects resulting from the process history, especially the influence of forming induced resid-

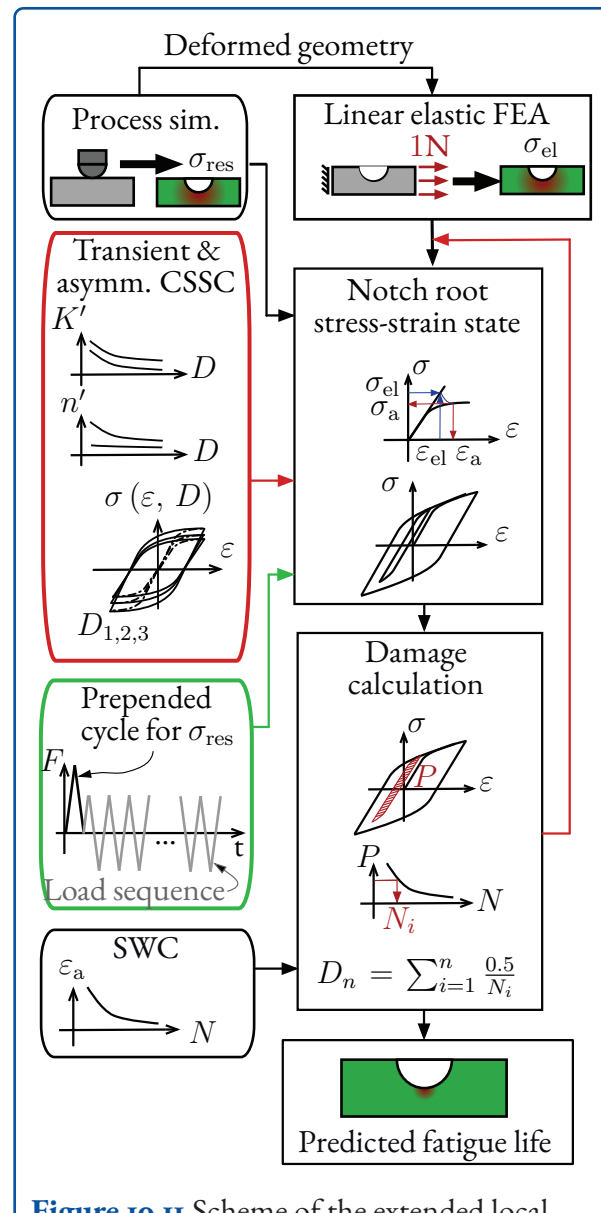


ual stresses is presented. Additionally, an extension for modeling the transient material behavior under cyclic loading is provided. For more detailed information see the works of Kühne et al. [2, 10].

### Extension to Transient Material Behavior

For the 42CrMo4 material under consideration, the results of an Incremental Step Test (IST) indicate a cyclic softening behavior as well as asymmetry in tension/compression, see figure 10.10.

First, the material law must be generalized to distinguish between tension and compression in order to account for both effects. Consequently, an asymmetric stress-strain relationship is introduced by applying different cyclic hardening parameters  $K'_+$  and  $K'_-$  and  $n'_+$  and  $n'_-$  for tensile and compressive stresses



$$K' \rightarrow \begin{cases} K'_+ & \sigma \geq 0 \\ K'_- & \sigma < 0 \end{cases} \quad n' \rightarrow \begin{cases} n'_+ & \sigma \geq 0 \\ n'_- & \sigma < 0 \end{cases} \quad (\text{Equation 10.1})$$

in the commonly used Ramberg-Osgood equation [11] of the CSSC. In order to represent the transient behavior over the course of the fatigue life, they also need to be connected to the damage variable  $D$ . The Ramberg-Osgood equation can

therefore be expressed as

$$\Delta\varepsilon_{\pm}(\Delta\sigma, \gamma) = \dots$$

$$\dots \text{sign}(\Delta\sigma) \left( \frac{|\Delta\sigma|}{E} + \gamma_{\pm} \left( \frac{|\Delta\sigma|}{K'_{\pm}(D)} \right)^{1/n'_{\pm}(D)} \right)$$

(Equation 10.2)

for stress ranges  $\Delta\sigma$  [2]. In a second step, the transient material behavior can be modeled by choosing appropriate dependencies  $K'_{\pm}(D)$ ,  $n'_{\pm}(D)$ , e.g., from a fit to each IST loading block. For an asymmetric stress-strain relationship, as displayed in figure 10.10, the hysteresis curves must be adjusted. The reloading curve for tension and compression is therefore described by the newly introduced parameters  $\gamma_+$  and  $\gamma_-$ . Since the hysteresis closure no longer necessarily takes place at the beginning of the hysteresis and thus the determination of the damage is no longer trivial, the evaluation with the damage parameter is now performed for half hystereses instead of closed hystereses. As a result, the linear damage accumulation hypothesis is modified to

$$D = \sum_{i=1}^n \frac{0.5}{N_i}$$

(Equation 10.3)

where  $0.5/N_i$  is the damage contribution of one half hysteresis and  $N_i$  results from the comparison of the Strain Wöhler Curve (SWC) with its parameters  $\sigma'_f$ ,  $\varepsilon'_f$ ,  $b$ ,  $c$  and the used damage parameter, e.g.,  $P_{SWT} = \sqrt{E \sigma_o \varepsilon_a}$ , for a considered half-hysteresis. The overall procedure extending the LSA from section 4.7 is summarized in figure 10.11.

### Incorporation of Residual Stresses

In order to consider the forming induced residual stresses in the fatigue life calculation they have to be properly introduced in the modeling approach. By prepending an additional loading cycle with  $R_{\sigma} = 0$  in the load sequence, as shown in figure 10.12, residual stresses  $\sigma_{\text{Res}} \neq 0$  can be applied.

The amplitude of the elastic stress  $\sigma_{1\text{st LC},\text{el}}$  for the extra load cycle can be calculated if the forming induced residual stresses  $\sigma_{\text{res}}$  are known, e.g., from a forming simulation or an experimental residual

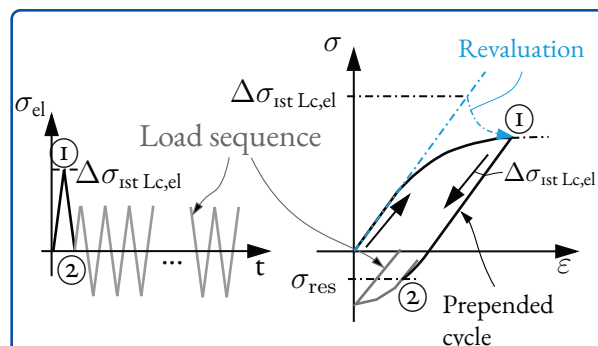


**Figure 10.12** Scheme of prepended load cycle with  $R_{\sigma} = 0$  (black) and the subsequent load sequence (gray) in their temporal evolution and the corresponding stress-strain plot.

stress measurement. The  $\sigma_{1\text{st LC},\text{el}}$  produces an elastic-plastic estimated stress  $\sigma_{1\text{st LC}}$  when Neuber's reevaluation rule is used. The resulting residual stress directly affects the load sequence starting after the prepended load cycle. Finding the necessary  $\sigma_{1\text{st LC},\text{el}}$  for matching  $\sigma_{\text{res}}$  may require the calculation of several constant amplitude loading sequences in an iterative procedure.

### Fatigue Life Calculation of the Cross-rolled Component

In the following, the developed concept is applied for the fatigue life calculation of the cross-rolled component. The required results of the cyclic material characterization of the 42CrMo4 under consideration are depicted in table 10.2.

**Table 10.2** Material properties of the 42CrMo4 steel under investigation [10]

from IST

	First Cycle	Cyclic stabil. ( $\circ$ )'
$K/\text{MPa}$	1,308.70	2,227.89
$n$	0.047	0.2168

from CA testing

$\sigma'_f/\text{MPa}$	$\varepsilon'_f$	$b$	$c$
1502.3	-0.0862	0.1319	-0.45132

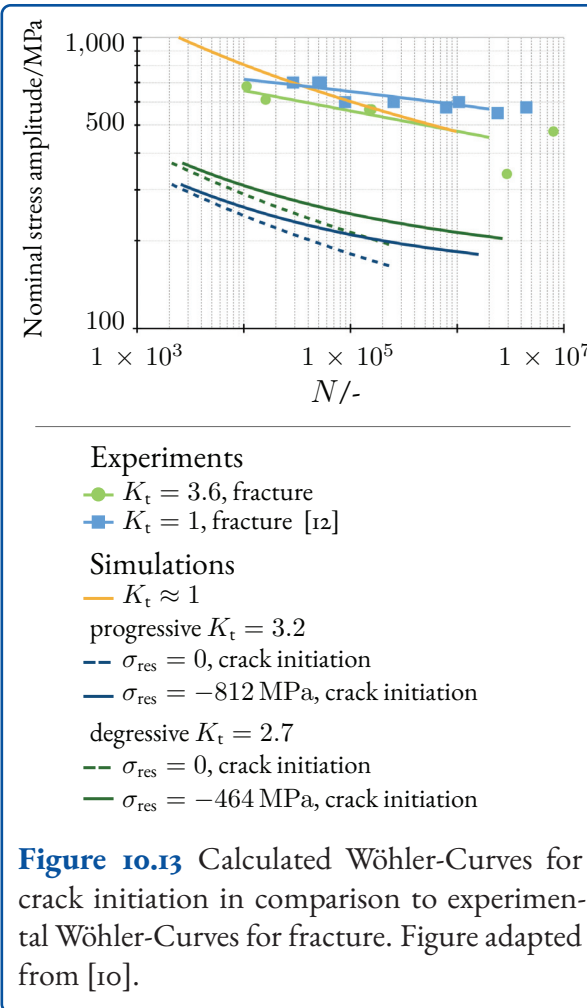


**Figure 10.13** Calculated Wöhler-Curves for crack initiation in comparison to experimental Wöhler-Curves for fracture. Figure adapted from [10].

The transient behavior is proposed to be described using a simplifying approach without asymmetry in tension/compression. Thus,  $K'_{\pm}(D), n'_{\pm}(D) \rightarrow K'(D), n'(D)$  and  $\gamma_{\pm} = 0$  hold in *Equation 10.2*. The transient dependencies on  $D$  are modeled according to table 10.2 from IST data. The transition from the initial material response to the as stabilized assumed state at  $N_F/2$  is simplified to a linear relationship. Afterwards, no further change in material behavior is assumed due to stabilization. The calculation results are shown in figure 10.13 next to comparative experimental results.

Comparing the simulations with and without residual stresses, the qualitative increase in fatigue life due to the compressive residual stresses is matched correctly. This effect is evident especially for high load cycle numbers. Interestingly, the degressive component's simulation predicts a higher fatigue

strength than the one from the progressive part. This is contrary to the experimental findings for the total fatigue life in section 10.6.2. Additionally, in figure 10.13 there is a discrepancy between the experimental curve for cross-rolled specimens and the simulations leading to conservative results of the proposed approach.

Possible reasons for the discrepancy are the influence of strain hardening and the improved surface roughness due to the cross-rolling process which were not yet taken into account for the simulation. Besides, the experimental results in figure 10.13 are associated with the total fatigue life for specimen fracture. The simulations in turn predict the crack initiation life. Compressive residual stresses may lead to retardation of fatigue cracking after initiation and thus lead to structural integrity reserves which are not predictable with the LSA at all.

### 10.7.2 Phase-field Model for Fatigue Fracture

For using possible structural integrity reserves one needs to consider fatigue crack growth under residual stress influence. In recent years, the numerical phase-field method especially has gained popularity within the fracture community because of its ability to describe complex crack patterns such as crack branching and merging and even crack initiation within one single model [13].

The consideration of fatigue influences makes changes in the standard phase-field model for brittle fracture necessary. For detailed information on the standard model, see [13]. An overview of possible extensions to fatigue can be found in Kalina et al. [14].

The fatigue fracture model developed here [15, 16] assumes that the material's crack resistance depends on the experienced fatigue damage in terms of a local lifetime variable  $D$ . Thus, the energy functional of a cracked domain  $\Omega$  with sharp crack surface  $\Gamma$  considering fatigue [15] can be expressed by deploying the widely known Griffith criterion [17]. Using the principle idea of the phase-field method for fracture,  $\Gamma$  is regularized by introducing the phase-field

variable  $d \in [0, 1]$  and the crack surface density  $\gamma_{\ell_c} = \frac{1}{2\ell_c}d^2 + \frac{\ell_c}{2}|\nabla d|^2$  [18]. The resulting functional of the now coupled field problem without external loading reads

$$\Pi_D = \int_{\Omega} \psi \, dV + \int_{\Omega} \alpha(D) \mathcal{G}_c \gamma_{\ell_c} \, dV. \quad (\text{Equation 10.4})$$

It is  $\psi$ , the Helmholtz energy density, and  $\alpha(D) = (1 - \alpha_0)(1 - D)^{\xi} + \alpha_0$  the fatigue degradation function with its parameters  $\alpha_0$  and  $\xi$ , leading to local and gradual degradation of the model's critical energy release rate or fracture toughness  $\mathcal{G}_c$  with increasing  $D$ . The characteristic length of the phase-field  $\ell_c$  describes the width over which the crack is smeared.

From a phenomenological point of view, the emerging crack leads to local degradation or loss of the material's stiffness. Accordingly, the energy density of the undamaged, isotropic linear elastic material  $\psi_0$  is degraded with increasing  $d$ . As a result, the dependency  $\psi(\varepsilon, d) = g(d)\psi_0(\varepsilon)$  using the degradation function  $g(d) = (1 - d)^2$  is introduced in *Equation 10.4* [19].

The governing differential equations of the coupled problem follow from demanding  $\delta\Pi = 0$  for the displacement field and the phase-field. The equations are the balance of linear momentum for quasi static loading, see *Equation 1.1* in section 1.2 and the phase-field differential equation considering fatigue

$$\begin{aligned} \alpha(D)d - \ell_c^2 \nabla \alpha(D) \cdot \nabla d - \alpha(D) \ell_c^2 \Delta d &= \dots \\ \dots 2(1-d) \underbrace{\psi_0}_{\mathcal{H}} \frac{\ell_c}{\mathcal{G}_c}. \end{aligned} \quad (\text{Equation 10.5})$$

In order to ensure the irreversibility of the crack during unloading, a damage mechanics inspired approach of Miehe et al. [19] using the crack driving force  $\mathcal{H} = \max_{\tau \in [0, t]} \psi_0(\varepsilon, \tau)$  instead of  $\psi_0$  is deployed. As one can show, the usage of  $\mathcal{H}$  in *Equation 10.5* prevents the phase-field variable from decreasing and ensures a fully irreversible evolution of  $d$ .

## Calculation of the Local Lifetime Variable

The calculation of  $D$  follows the standard local strain approach, see figure 4.8. As the damage parameter the  $P_{\text{SWT}}$  using the equivalent von Mises stress is adopted. It is applied at each material point in order to calculate load cycle wise contributions to the local lifetime variable  $D$ . Using the linear damage accumulation rule for damage contributions  $D_i$  of load cycle  $i$  we can define the  $D = \sum_i D_i$  as current local lifetime variable  $D$ . By assuming only slight changes of the stress-strain states over  $\Delta N$  consecutive load cycles starting from cycle  $i$ , the simulation is accelerated and  $D$  can be approximated as  $D \approx \sum_{j=1}^{i-1} D_j + \Delta N D_i$  what states that we skip the calculation of the next  $\Delta N$  load cycles and thus save computational cost. The ability of the proposed model to reproduce typical fatigue crack growth phenomena is shown in Seiler et al. [15]. Furthermore,  $D$  could principally be calculated according to any fatigue damage concept available. This makes the approach very flexible and modular and enabled the application of the developed framework to the complex high cycle fatigue phenomenon Tooth Flank Fracture in gears [20].

## Incorporation of Residual Stresses

In general, residual stresses originate from the forming process of the specimen. The stress remaining after unloading is the residual stress  $\sigma_0$ . The associated strain

$$\varepsilon_0 = \varepsilon_{0,\text{el}} + \varepsilon_p \quad (\text{Equation 10.6})$$

can be decomposed into an elastic part  $\varepsilon_{0,\text{el}}$  and a plastic part  $\varepsilon_p$ , see figure 10.14 a). Only the elastic part  $\varepsilon_{0,\text{el}}$  of the residual strain  $\varepsilon_0$  is of relevant for the phase-field fatigue life simulation. The plastic forming process is treated as completed and is not modeled. Hence, all material points are assigned the same material parameters initially, regardless of their (plastic) history. The total stress-strain state  $(\sigma, \varepsilon)$  in the model is the sum of the initial state  $(\sigma_0, \varepsilon_{0,\text{el}})$  and the stress-strain state caused by the cyclic loading  $(\sigma_c, \varepsilon_c)$ . Hence, the total strain in the fatigue simulation is  $\varepsilon = \varepsilon_{0,\text{el}} + \varepsilon_c$  as shown

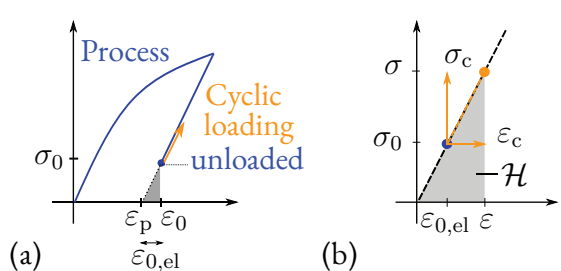


**Figure 10.14** (a) Formation of residual stresses through plastic deformation. (b) Material law for cyclic simulation. Figure from [16].

in figure 10.14 b). Here, the strain  $\varepsilon_c$  is

$$\varepsilon_c = \frac{1}{2} (\nabla u + (\nabla u)^\top). \quad (\text{Equation 10.7})$$

The elastic residual strain  $\varepsilon_{0,el}$  is known initially from the residual stress field  $\sigma_0$  and enters the strain determination as an offset. On the one hand, this offset in stress and strain influences the determination of  $P_{SWT}$  and consequently the calculation of  $D$ . It results in a shift of hysteresis due to residual stresses and thus increases or lowers the resulting  $D$ , as clearly depicted in figure 4.8 (Point ③). On the other hand, the governing phase-field fatigue equation in *Equation 10.5* is influenced. Therein, the crack driving force is replaced by the temporal maximum of the strain energy density of the total stress strain state

$$\mathcal{H}(t) = \max_{\tau \in [t_0, t]} (\psi^e(\varepsilon_{0,el} + \varepsilon_c(\tau))). \quad (\text{Equation 10.8})$$

The initial state at the time  $t_0$  is hereby  $\varepsilon = \varepsilon_{0,el}$ ,  $\sigma = g(d) \sigma_0$ .

A realization using experimentally measured residual stresses requires the calculation of an equilibrium stress field since the experimental results are not a priori equilibrium ones. A load free simulation needs to be carried out prior the fatigue simulation using the measured residual stresses as initial stress field. Subsequently, the resulting equilibrium stresses  $\sigma_0$  are used as an initial stress field for the phase-field simulation.

### Numerical Example with Comparison to Experiment

The model's principal behavior will be shown using the example of a *Compact Tension* (CT) specimen according to ASTM E647 with a width of 100 mm. The initial crack length is increased to 25 mm (20 mm notch plus 5 mm pre-crack) by the introduction of a 5 mm pre-crack. After that, forming induced residual stresses are introduced to some specimens by Laser Shock Peening (LSP) in front of the initial crack [16], see figure 10.15 a). Using this setup the influence of residual stress on the fatigue crack growth is investigated. Throughout the FCG test, the applied load ratio  $R_\sigma = 0.1$  remains constant. The maximum applied force for the fatigue load load cycles is 1.65 kN for the specimens with a thickness of 2 mm. A representative aluminum AA2024-T3 is used [16]. For the model parametrization, specimens without LSP induced residual stresses are used. Therefore we fit the model parameters  $\alpha_0$  and  $\xi$  to the resulting crack growth curve of the experiment, see the grey curves in figure 10.15 b). The crack length of the specimen is denoted as  $a$ . Obviously, for the parametrization dataset a good agreement between simulation and experiment is reached.

In order to test the model's prediction for residual stress influence, CT specimens which undergone LSP are considered.

A comparison of crack growth curves from the experiments with the ones from the phase-field simulation for fatigue fracture is given in figure 10.15 b). With regard to the compressive residual stresses depicted in figure 10.15 a) the simulation predicts the qualitative crack growth well: In the peened area a decrease in crack growth rate is observed. Accelerated crack growth occurs in front of and behind the peened area as a result of tensile residual stresses filling equilibrium. However, the quantitative result differs from the experiment. Possible reasons are the simplified modeling in 2D and the therefore as constant over the thickness assumed residual stresses in the simulation. Nevertheless, principal effects of residual stresses influencing crack

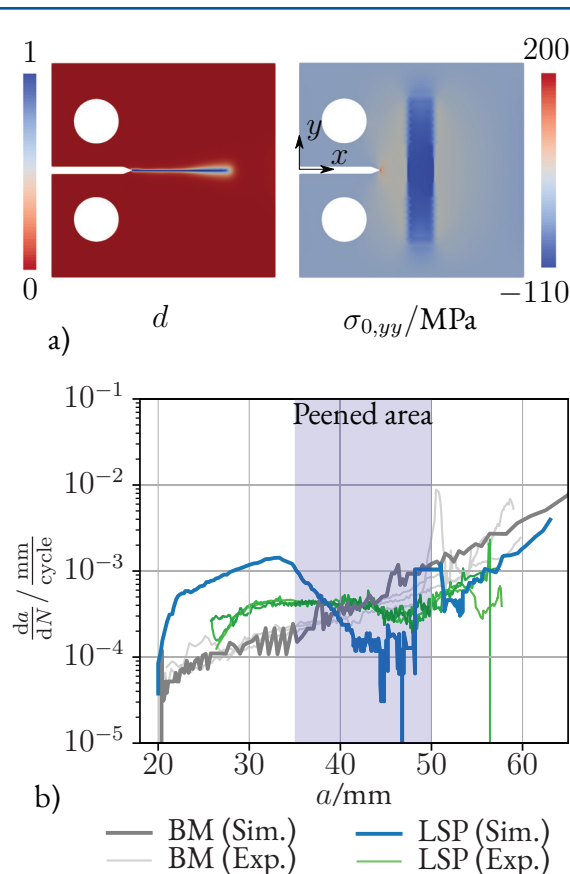


**Figure 10.15** Fatigue crack growth in peened (LSP) and unpeened (BM) specimens. **a)** Phase-field  $d$  at the end of simulation and imposed residual stress component  $\sigma_{0,yy}$  from residual stress measurements after LSP **b)** Crack growth rate. Figure adapted from [16].

growth can be shown using the presented modeling approach.

## 10.8 Conclusion

The procedure described in the project has led to comprehensive findings on the relationship between the targeted process control in the rolling forming process, the residual stresses that arise, their influence on varying rolling paths and the resulting properties of the cross-rolled components. This applies both to experimental work, which involves the generation of the necessary data and findings from material characterization, component testing and residual stress measurements, and to the

accompanying numerical simulations, which are aimed at predicting residual stresses and performing final service life analyses. Overall, methodical, transferable findings are thus available for the evaluation and investigation of steel components with regard to their behavior under residual stresses and their targeted influence by the forming process.

Questions to be answered in future work are the influences of the forming process on the fatigue life of the component. The quantitative effect of residual stresses compared to the effect of surface roughness as well as the strain hardening effect is still to be investigated. Especially the separation of the effect of strain hardening from the effect of residual stresses is a challenging task since both result from the elastic-plastic forming history of the material and thus are closely related.

## References

- [1] Christina Guilleaume et al. "Eigenspannungsorientiertes Fügen von hybriden Bauteilen mittels Radial-Walzen". de. In: *Forschung im Ingenieurwesen* 85.3 (Sept. 2021), pp. 745–755. ISSN: 0015-7899, 1434-0860. DOI: 10.1007/s10010-021-00486-7.
- [2] David Kühne et al. "Fatigue analysis of rolled components considering transient cyclic material behaviour and residual stresses". en. In: *Production Engineering* 13.2 (Apr. 2019), pp. 189–200. ISSN: 0944-6524, 1863-7353. DOI: 10.1007/s11740-018-0861-9.
- [3] Alexander Brosius and Christina Guilleaume. "New cross-rolling process for joining of hybrid components". en. In: *CIRP Annals* 69.1 (Jan. 2020), pp. 245–248. ISSN: 0007-8506. DOI: 10.1016/j.cirp.2020.04.034.
- [4] C. M. Sonsino. "Light-weight design chances using high-strength steels". en. In: *Materialwissenschaft und Werkstofftechnik* 38.1 (2007), pp. 9–22. ISSN: 1521-4052. DOI: 10.1002/mawe.20060090.
- [5] E Macherauch and H Wohlfahrt. "Residual stresses and fatigue (Eigenspannungen und Ermüdung)". In: *Fatigue behavior of metal-*

- lic materials. Oberursel, West Germany, DGM-Informationsgesellschaft mbH 86.23-26 (1985), pp. 237–283.
- [6] Ken-ichiro Mori et al. “Joining by plastic deformation”. en. In: *CIRP Annals* 62.2 (Jan. 2013), pp. 673–694. ISSN: 0007-8506. DOI: 10.1016/j.cirp.2013.05.004.
- [7] R. Jantscha. “Über das Einwalzen und Einpressen von Kessel- und Überhitzerrohren bei Verwendung verschiedener Werkstoffe”. Deutsch. PhD thesis. Darmstadt: Technische Hochschule Darmstadt, 1929.
- [8] J. E. Hockett and O.D. Sherby. “Large strain deformation of polycrystalline metals at low homologous temperatures”. In: *J. Mech. Phys. Solids* 23 (1975), pp. 87–98. DOI: 10.1016/0022-5096(75)90018-6.
- [9] Christina Guilleaume and Alexander Brosius. “Cross-rolling process for manufacturing lightweight hybrid components”. en. In: *Journal of Advanced Joining Processes* 3 (June 2021), p. 100063. ISSN: 26663309. DOI: 10.1016/j.jajp.2021.100063.
- [10] David Kühne et al. “Consideration of cyclic hardening and residual stresses in fatigue life calculations with the local strain approach”. en. In: *Archive of Applied Mechanics* 91.8 (Aug. 2021), pp. 3693–3707. ISSN: 0939-1533, 1432-0681. DOI: 10.1007/s00419-021-01950-0.
- [11] W. Ramberg and W. R. Osgood. “Description of Stress-Strain Curves by Three Parameters”. In: 1943.
- [12] K.H. Kloos. “Größeneinfluss. Einfluss der Probengröße auf das Ermüdungsverhalten bauähnlicher Kerbproben unter einstufigen und zufallsartigen Beanspruchungsabläufen”. In: *Ab schlussbericht Vorhaben Nr. 145-2, Forschungskuratorium Maschinenbau e.V., Heft 192* (1995).
- [13] Marreddy Ambati, Tymofiy Gerasimov, and Laura De Lorenzis. “A review on phase-field models of brittle fracture and a new fast hybrid formulation”. en. In: *Computational Mechanics* 55.2 (Feb. 2015), pp. 383–405. ISSN: 0178-7675, 1432-0924. DOI: 10.1007/s00466-014-1109-y .
- [14] Martha Kalina et al. “Overview of phase-field models for fatigue fracture in a unified framework”. en. In: *Engineering Fracture Mechanics* 288 (Aug. 2023), p. 109318. ISSN: 0013-7944. DOI: 10.1016/j.engfracmech.2023.109318.
- [15] Martha Seiler et al. “An efficient phase-field model for fatigue fracture in ductile materials”. en. In: *Engineering Fracture Mechanics* 224 (Feb. 2020), p. 106807. ISSN: 00137944. DOI: 10.1016/j.engfracmech.2019.106807.
- [16] Martha Seiler et al. “Phase-field modelling for fatigue crack growth under laser shock peening-induced residual stresses”. en. In: *Archive of Applied Mechanics* (Mar. 2021). ISSN: 0939-1533, 1432-0681. DOI: 10.1007/s00419-021-01897-2.
- [17] G.A. Francfort and J.-J. Marigo. “Revisiting brittle fracture as an energy minimization problem”. en. In: *Journal of the Mechanics and Physics of Solids* 46.8 (Aug. 1998), pp. 1319–1342. ISSN: 00225096. DOI: 10.1016/S0022-5096(98)00034-9.
- [18] B. Bourdin, G.A. Francfort, and J-J. Marigo. “Numerical experiments in revisited brittle fracture”. en. In: *Journal of the Mechanics and Physics of Solids* 48.4 (Apr. 2000), pp. 797–826. ISSN: 00225096. DOI: 10.1016/S0022-5096(99)00028-9.
- [19] C. Miehe, F. Welschinger, and M. Hofacker. “Thermodynamically consistent phase-field models of fracture: Variational principles and multi-field FE implementations”. en. In: *International Journal for Numerical Methods in Engineering* 83.10 (Sept. 2010), pp. 1273–1311. ISSN: 00295981. DOI: 10.1002/nme.2861.
- [20] Tom Schneider et al. “Phase-field modeling of fatigue crack growth during tooth flank fracture in case-hardened spur gears”. en. In: *International Journal of Fatigue* 163 (Oct. 2022), p. 107091. ISSN: 01421123. DOI: 10.1016/j.ijfatigue.2022.107091.

# 11 Requirement-specific Adjustment of Residual Stresses During Cold Extrusion

Groche, P.; Oechsner, M.; Franceschi, A.; Hoche, H.; Jäger, F.; Siedbürger, C.

GEPRIS 374584412

## 11.1 Introduction

The large, inhomogeneously distributed degrees of deformation that usually appear in cold forging lead to large residual stresses. In the industrial environment, these residual stresses (RS) are primarily perceived as a concern with potentially undesirable effects. Especially during extrusion, (partially) plastic deformations, subsequent elastic recovery as well as heating and cooling lead to uncontrolled or partly unknown RS states [2, 3]. The forming-induced RS affect various properties of mechanical components, the main effects being fatigue life, distortion, and corrosion [4–6]. Up to now, countermeasures have mainly been aimed at limiting the influences during the production chain [7]. In particular, the negative effects of tensile RS on the surface are to be avoided. Among other things, undesired RS are reduced by stress relief by means of intermediate heat treatment. Performance increases that can be achieved without additional process steps through targeted RS adjustment are often not taken into account. Approaches that specifically adapt the RS condition have so far only existed in the form of additional operations such as deep rolling, machine hammer peening or shot peening and the associated increase in machining times and production costs, see chapter 3 and [8–10]. These modifications are primarily aimed at the area close to the surface and are intended to change the RS from tension to compression. The size and distribution of the RS in the depth direction can hardly be influenced.

For this purpose, an inline controlled process control was developed for the modification of the cold

forming-induced RS state, the so-called TaReS strategy (Tailored residual stress strategy) [1]. A schematic illustration of this strategy is shown in figure 11.1. Classified as a forming strategy, two process extensions are used for conventional extrusion, see chapter 3. Compared to project 5 in chapter 10, in which the influence of the tool geometry and different lubricants on the RS state are analysed, for this project the focus lies on active elements for the inline controlled influencing of the RS state [11]. A first process extension refers to the use of the ejector as a counterpunch during the main forming process to generate a counterforce. The second process extension refers to the inline adjustable die preload to influence the degree of forming in the ejection phase. Both forming strategies together allow the modification of the RS state with two independent degrees of freedom. Under the hypothesis that an optimal RS condition exists for a characteristic load, a desired RS profile is derived. A characteristic load is understood to be, for example, a specific bending, tensile or torsional load. The desired RS state corresponds to the requirements placed on the cold extruded component and results from the component property improvements, which correlate with the forming-induced RS. Subsequently, simulation-supported models can be used to derive a suitable RS profile and the optimum process parameters, which are set in the forming process.

The introduction of the TaReS strategy is also intended to contribute to an industrial paradigm shift in RS-optimized components: Forming-induced RS are no longer to be considered a problem, but their advantages and potentials are to be used for future industrial applications. In particular, the performance increase of products and the shortening of process chains through inline controllable RS states are to be considered. The methodologies and models of the TaReS strategy as well as the experimental and numerical validation of the RS settings are presented and summarized in the fol-

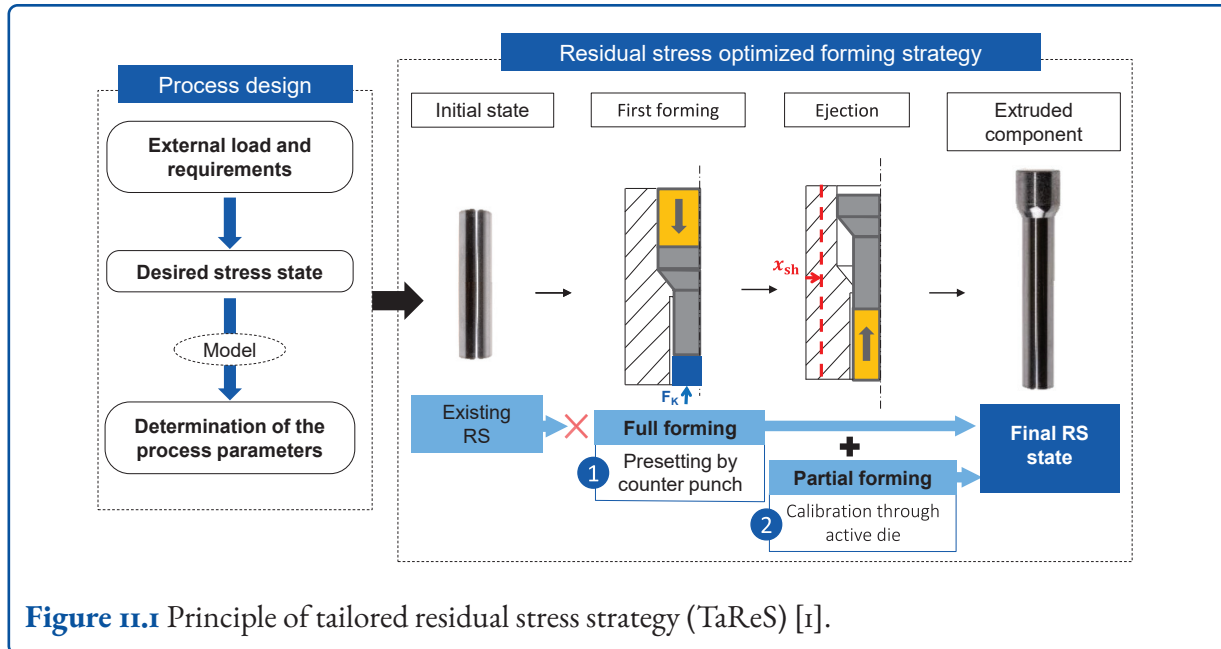


**Figure II.1** Principle of tailored residual stress strategy (TaReS) [i].

lowing chapter. The overall objective of the project is the fundamental scientific analysis and utilization of the influence of forming-induced RS on product quality improvement in cold forging. For this purpose, the forming strategies are primarily focused on the metastable austenitic steels 1.4404 and 1.4307. The selection of these materials is based on the fact that the strength is adjusted exclusively by the hardening mechanisms resulting from cold forming and not by heat treatment. [i]

## 11.2 Formation of Residual Stresses During Conventional Extrusion

In order to gain a deeper understanding of the TaReS strategy, RS development in the conventional process is addressed. The focus is on the description of the development of RS through inhomogeneous deformation, where the RS state can be explained very well through 2D FE simulations. [12]

The typical RS profile and associated flow lines of a full forward extruded sample are shown in figures II.2 a) and b). Below the extrusion shoulder of the specimen, it can be seen that there is high tensile RS in the near-surface region and compressive RS in the core after cold forming. The occurrence of RS

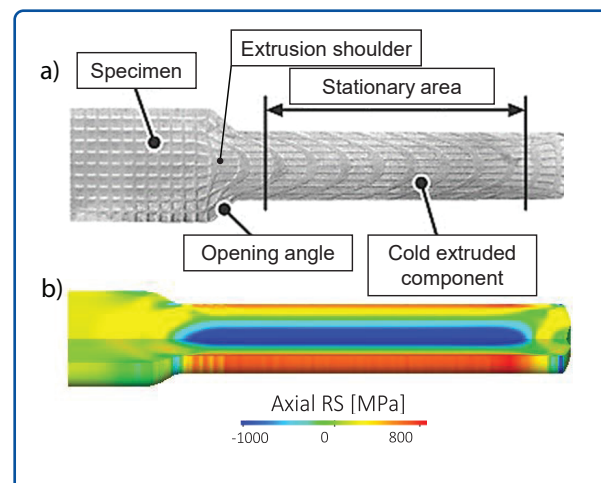


**Figure II.2** Conventional process of full forward extrusion: a) material flow [i3]; b) axial RS in FE simulation [i4].

is primarily due to the inhomogeneous deformation in the taper zone of the die [15]. The material flow in the edge zone is retained compared to the core zone of the specimen due to wall friction as well as deflection through the die shoulder. This can be seen in figure II.2 a). The inhomogeneous deformation prevents a complete elastic recovery, which leads to RS being retained in the molded part due to the newly established equilibrium. Below the opening angle of the specimen, a stationary region is formed, which must be taken into account

as an important feature in the investigations of RS formation [13].

A second superimposed effect on RS formation relates to the sample ejection process. The study of RS formation must therefore take into account the various sub-steps of the full-forward extrusion process, which are summarized in figure II.3. In particular, Tekkaya states in his investigations that the high tensile RS on the surface of the components in the axial and tangential directions can be significantly reduced after ejection [2]. This effect is due to the fact that a second deformation in the opposite direction takes place in the area close to the surface.

The second plastification due to pressing through the calibration zone forces a new RS equilibrium state, which reduces the surface RS. Although the tensile RS are reduced after ejection, a non-negligible tensile component remains, which can also be validated experimentally by X-ray diffraction [16]. A more detailed explanation of this effect is based on the thought experiment of Tekkaya [17], which is described in chapter 3. In order to achieve an accurate modeling of the final stress state, e.g., in FE simulations, the consideration of the ejection phase is thus of great importance.

### 11.3 Material Characterisation

In order to correctly represent the material behavior of samples made of 1.4404 and 1.4307, compression tests and incremental step tests were carried out. Furthermore, a suitable kinematic hardening model is necessary for the FE modeling in order to obtain a suitable springback after the first forming [18]. For the following investigations, a Chaboche material model was used with a restraint that proportionally takes into account the isotropic and kinematic hardening [19]. The general material model is defined as follows, see *Equation II.1* to *Equation II.3*.  $\sigma_i$  represents the isotropic and  $\sigma_k$  the kinematic hardening.

$$\sigma = \sigma_i + \sigma_k \quad (\text{Equation II.1})$$

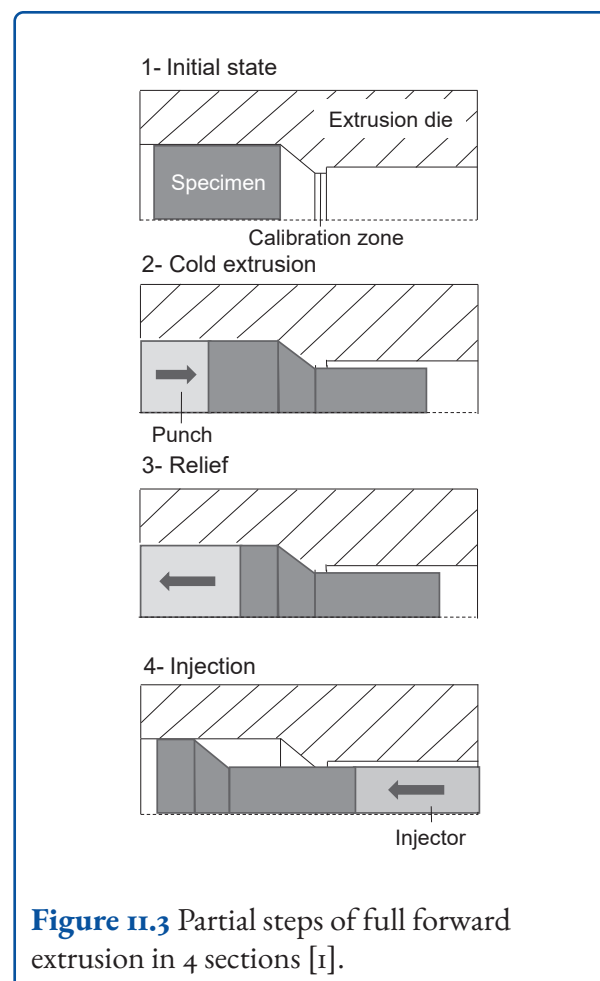


**Figure II.3** Partial steps of full forward extrusion in 4 sections [1].

$$\sigma_i = \sigma_{y0} + Q \cdot (1 - e^{-b_0 \cdot \epsilon_p}) + P \cdot e^{-b_0 \cdot \epsilon_p} \quad (\text{Equation II.2})$$

$$\sigma_k = i \cdot \sum_{i=1}^M \frac{C_i}{\lambda_i} (1 - e^{-\lambda_i \cdot \epsilon_p}) \quad (\text{Equation II.3})$$

Here  $\sigma_{y0}$  is the initial yield strength,  $\epsilon_p$  is the plastic strain and  $Q$ ,  $P$  and  $b_0$  are coefficients for isotropic hardening.  $C_i$  and  $\lambda_i$  describe the kinematic hardening.  $M$  is the number of restraints. Only one restraint is needed to account for subsequent ejection. Accordingly, the coefficients for  $i = 1$  are evaluated.

The interpolated results are iteratively improved with the help of FE simulation of the same test. A detailed description of the procedure can be found in the chapter 2 as well as in [1]. The results of the

**Table II.1** Results of material characterization tests on solution annealed samples [1].

Material	I.4307	I.4404
$\sigma_{y0}$ in MPa	278.00	244.00
$P$ in MPa	-93.9	-22.0
$Q$ in MPa	1513.4	1424.1
$b_0$	1.41	1.97
$C_1$ in MPa	176.43	134.67
$\lambda_1$	3.47	2.36
$\sigma_k / (\sigma_k + \sigma_i)$	6 %	3 %

tests are summarized in table II.1 and in figure II.4 below. The results apply to the solution-annealed condition. From the results, two differences can be identified between the materials studied. On the one hand, the proportion of kinematic to isotropic hardening is higher for the material I.4307. Secondly, the material I.4404 has an overall higher yield stress  $\sigma$ , which will be considered in a later discussion, see figure II.4. [1]

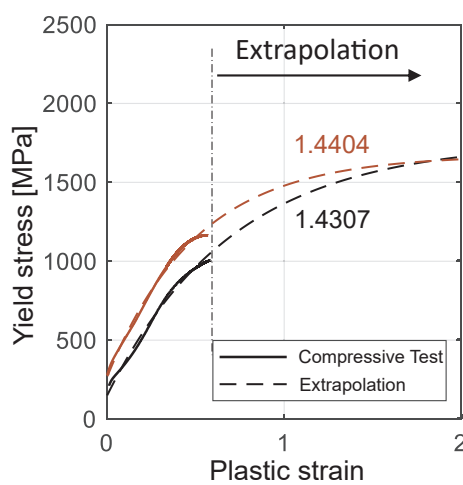


**Figure II.4** Results of the material tests: Flow curves of I.4404 and I.4307 [1].

## 11.4 Methodology for Reducing Residual Stresses Due to a Counter Punch

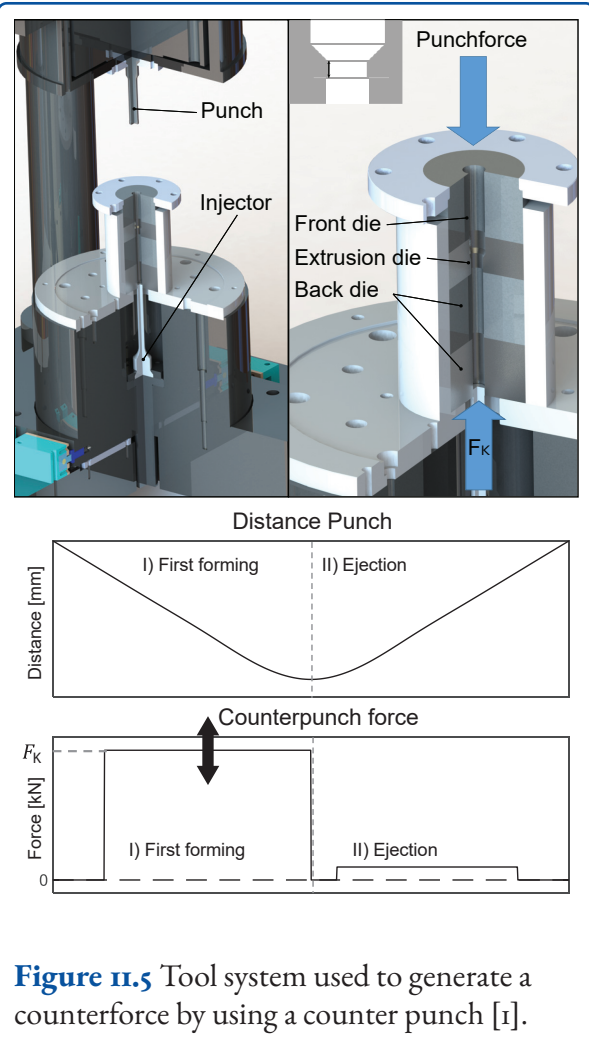
Based on the first mechanism for RS generation in conventional full forward extrusion, the use of the ejector as a counterpunch was developed.

### Description of the Process

The tool system shown in figure II.5 is used to implement this process control. A force- or path-controllable die cushion of the PtU's spindle press enables the ejector to be used as a counterpunch: Within the main forming phase, a force-bound counterforce controlled to constant values is generated opposite to the flow direction. In the ejection phase, the force control is then switched back to displacement control. The die consists of a total of four components: front die, extrusion die and two back dies connected in series. All components are clamped inside a long sleeve. The specimens discussed in this chapter have an initial diameter of 14.5 mm and are extruded to approximately 10.78 mm in the die. The opening angle of the die used has an angle of 60°, whereby the calibration zone has a length of 2 mm. [20]

The die material used was carbide G20 with a TiAlN surface coating. In addition to the experimental investigations, numerical FE simulations are carried out in order to be able to investigate the 2D distributions in depth. Especially in the depth direction, the experimental determination of the RS is limited by X-ray diffraction up to 1 mm.

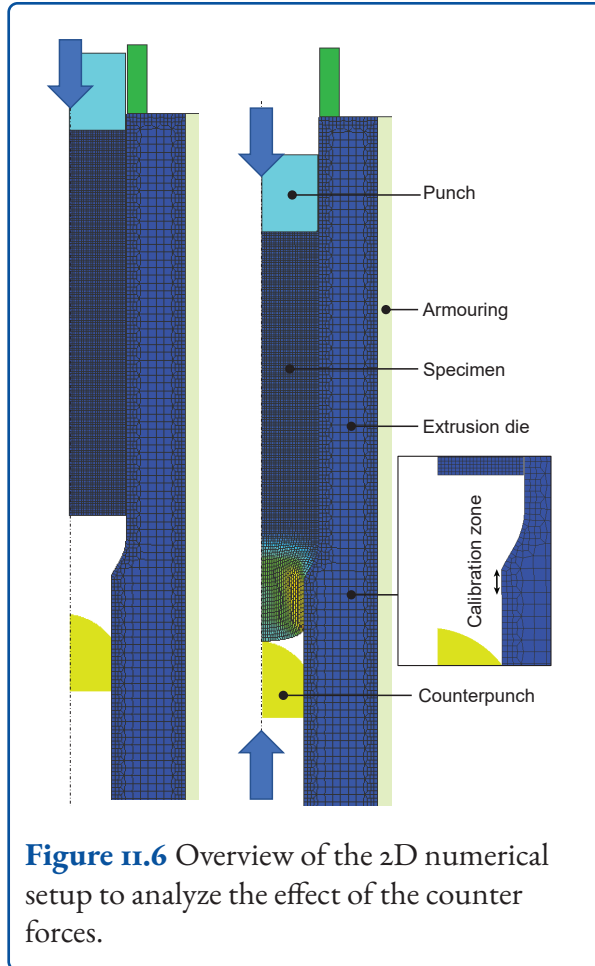
The numerical models for the analysis of RS are calculated with the software Simufact Forming 21® with implicit solver, based on an axially symmetric 2D model. The structure of the model and relevant components are summarized in figure II.6. The three-part die is designed as a solid body to avoid extrusion into the intermediate gap. The contact zone between tool and workpiece is defined as segment-to-node contact and without user-defined contact tolerance. Furthermore, due to the small



diameter reduction of the elements, remeshing and rezoning are omitted. In this way, no stress smoothing is generated during the simulation.

The required friction coefficients were determined experimentally via the PtU's *Sliding Compression Test Stand* and are assumed to be constant for all simulations. For a combined friction model,  $\mu_R = 0,31$  for Coulomb and  $m_R = 0,5$  for shear friction were derived from the tribological studies. For simplicity, only the die and specimen are deformable bodies, while the other components are modeled as rigid bodies. To avoid possible distortion during the deformation, the edge lengths of the mesh grid of the deformable bodies are set equal.

For the ejection of the specimen as well as for the forming with the punch, a path-dependent forming is used. In this case, the force represents a re-



sult variable. For the simulation of the counter force during the forming process, a second ejector is designed as a spring element to which a time-dependent force profile is assigned. The value of the counter force is set due to the time-dependent force profile. The optimal starting position of the counter punch during the main forming process was determined by numerical simulations. At the counterpunch position in figure II.6, the most effective RS degradation is achieved and is located below the calibration zone. [14]

For the investigations, counterforces of zero to 80 kN were used on the specimens made of 1.4404 and 1.4307, whereby the case with zero corresponds to the conventional process without counterpunch. Intuitively, it is clear that, as the counterforce increases, the required total force of the press must also increase to compensate for the counteracting internal pressure. The relationship between the punch force of the press and the counterforce is

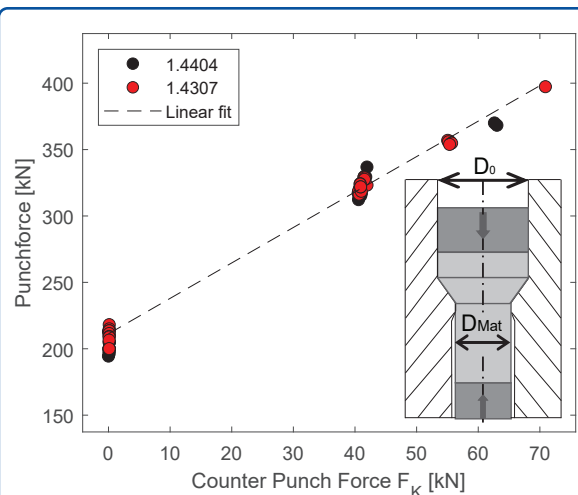


**Figure II.7** Relationship between punch force and counterpunch force.

shown in figure II.7. Assuming a linear correlation between counterpunch force and force of the press results in a slope of approximately 2, 66. This phenomenon cannot be explained by a force or pressure equilibrium alone, as the area ratio in the taper zone  $D_0/D_{Mat}$  is only 1, 36. The larger slope is due to the higher contact normal stresses to overcome the counterforce. The specimens upset in the front bushing are pressed more strongly against the die wall, resulting in increased frictional shear stresses. The higher friction ratios must in turn be compensated for by an increased pressing force. Furthermore, the higher tribological stresses have a considerable influence on tool life. In the experimental tests, the tools in counterpunch operation showed an increased tendency to fail due to cracking or wear.

## Working Principle

The general effect on the final stress state due to the counterpunch is shown by the 2D distribution of the RS in figure II.8 from the FE simulations. By using a counterpunch, the high tensile RS at the surface are reduced from about 650 MPa to 200 MPa at a counter force of  $F_k = 80$  kN after forming. The RS gradients are also reduced in all other principal stress directions [1]. The principle of operation of the counterpunch on the RS formation can be explained by two mechanisms. Firstly,

the material flow in the core area of the specimens is impeded by the counterforce applied, so that a stronger homogenization of the plastic deformation at the extrusion shoulder is achieved. At the same time, the hydrostatic stress state is increased. Due to the more uniform springback after unloading, less pronounced tensile RS are achieved in the surface area. For reasons of equilibrium, the high compressive RS in the core area are also reduced. This principle of operation can be visualized by numerical FE simulations in figure II.9 a), where the complete RS depth profile in radial direction is shown over selected counter forces. With larger counter force, the RS gradients are flattened in the radial direction. The homogenization effect is enhanced by a convex curved counterpunch shape at the tip and is preferable for the structural design of a counterpunch. The second principle is based on the subsequent ejection of the specimen. Since the counterpunch also compresses the extruded specimens, the effective specimen diameter is increased with increasing counter force [1].

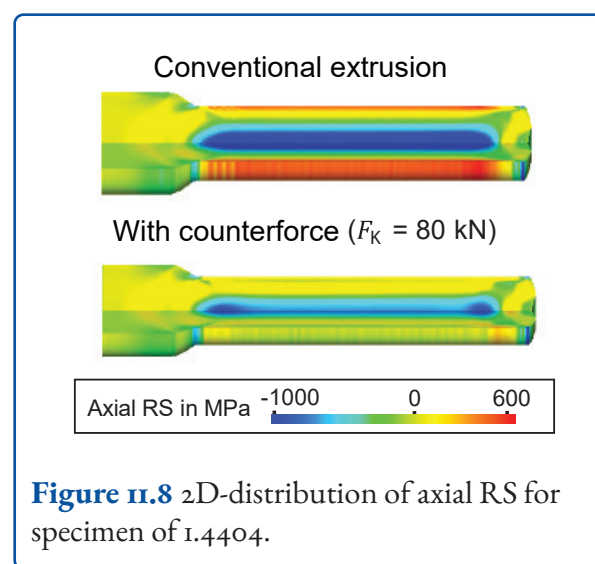


**Figure II.8** 2D-distribution of axial RS for specimen of 1.4404.

The compression of the specimens occurs below the calibration zone of the die. This effect is consistent with the experimental measurement of the specimen diameter by optical 3D measurement technology, see figure II.9 c). The results confirm an effective increase of 21  $\mu\text{m}$  at a counterforce of  $F_k = 80$  kN. When ejecting the specimens with increased effective diameters, reverse extrusion takes place, whereby the resulting degree of deformation

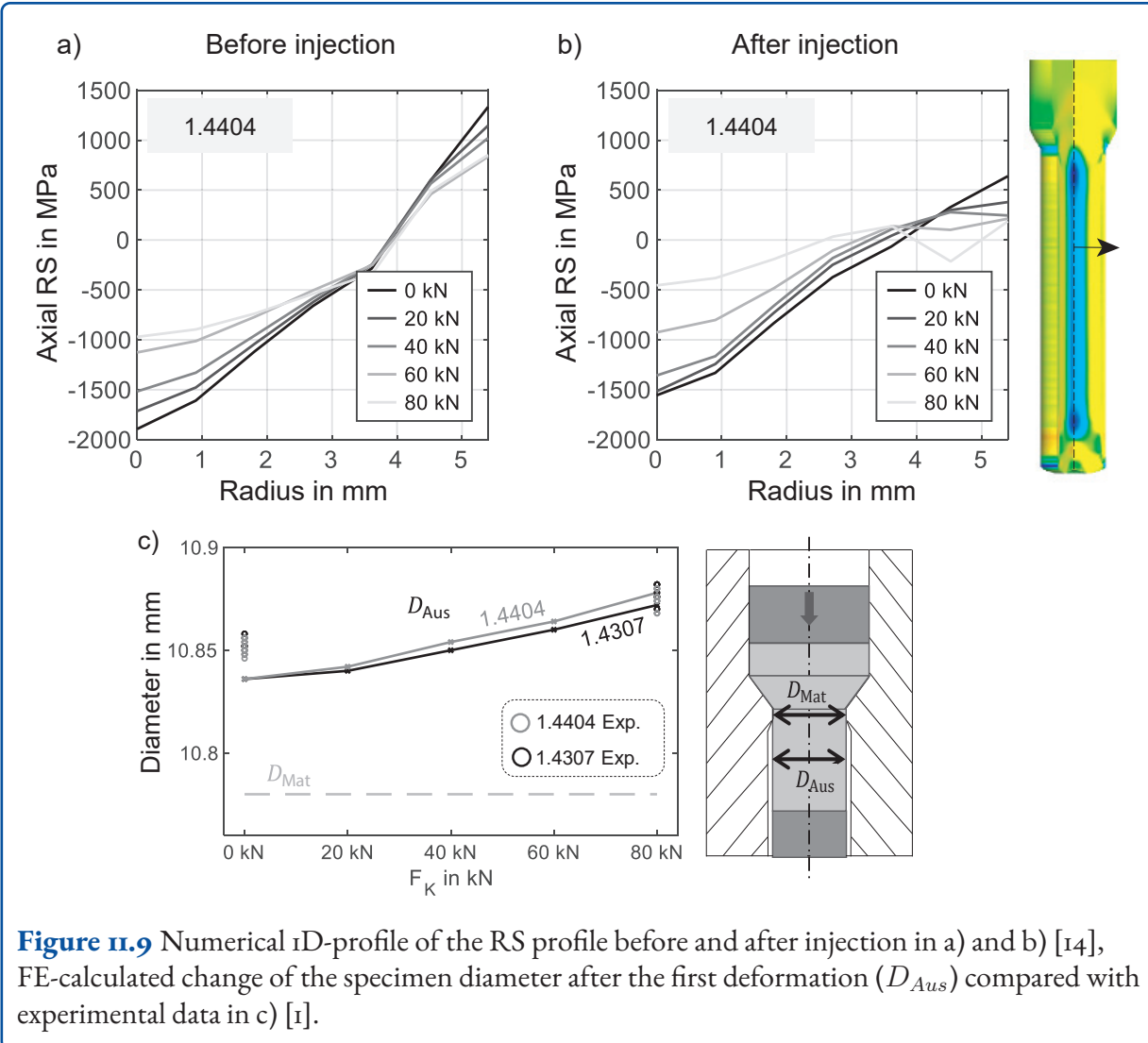


**Figure 11.9** Numerical 1D-profile of the RS profile before and after injection in a) and b) [14], FE-calculated change of the specimen diameter after the first deformation ( $D_{Aus}$ ) compared with experimental data in c) [1].

results from the counterforce. The plastic deformation with subsequent springback further reduces the tensile RS near the surface. Overall, the stress state before ejection is superimposed on that after ejection and results in an overall lower RS state, see chapter 3. A comparison between figure 11.9 a) and b) demonstrates this mechanism, whereby a further redistribution of the RS distribution takes place in the depth direction.

### Validation with X-ray Diffraction

To validate this forming strategy, X-ray diffraction measurements using the  $\sin^2\Psi$  method were carried out on both materials 1.4307 and 1.4404. As an example, some results are shown in figure 11.10 a), b) for axial RS. In figure 11.10 a), RS profiles

are recorded from the surface to a depth of 1 mm. With the exception of the measuring point at the surface, the RS curves of the materials 1.4307 and 1.4404 differ significantly when a counterpunch is used during the process. After conventional extrusion without a counter punch, high tensile RS, which are above 500 MPa even at a depth of 1 mm remain in the surface area. Due to the counterforce applied during forming, both materials show clearly decreasing tensile RS, which tend toward zero at 1 mm depth. However, the measurement results show similar values in the measuring points close to the surface up to a depth of 50  $\mu\text{m}$ . This result is not to be expected from the numerical simulations. The reasons for this difference are not yet understood. One conceivable explanation is process-related, as the surface layer undergoes a more complex plastic forming than the rest of the

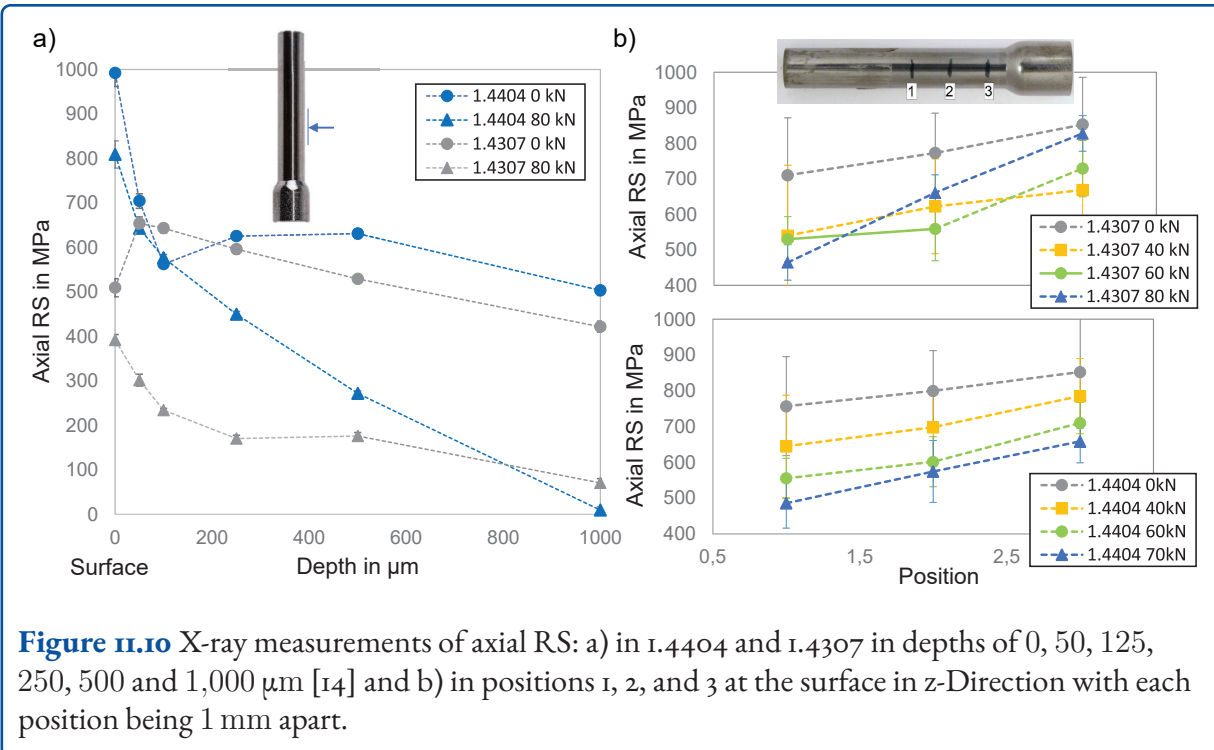


**Figure II.10** X-ray measurements of axial RS: a) in 1.4404 and 1.4307 in depths of 0, 50, 125, 250, 500 and 1,000  $\mu\text{m}$  [14] and b) in positions 1, 2, and 3 at the surface in z-Direction with each position being 1 mm apart.

sample due to direct contact with the forming tool. This behavior is difficult to reproduce in the FE simulations. A second possible reason is related to the measurements in this area, which are also very complex. RS calculations from X-rays can be influenced by various parameters, such as the anisotropy caused by extrusion, which leads to linearity deviations of the strains via the  $\sin^2\Psi$  method, or inhomogeneous grain refinement on the sample surface. While measurement data shows some minor non-linearity of the  $\sin^2\Psi$  plots, there were no depth-dependent differences in grain size seen in microsections. Another explanation is due to the structure of the numerical model. In particular, only the austenitic phase is modeled in the FE simulations, so that no forming martensite is modeled, see chapter II.5. [1, 14, 20]

With regard to the RS on the surface recorded by X-ray diffraction in figure II.10 b), it can be seen that with increasing counterforce there is a decrease in the near surface tensile RS based on the average values. The result validates the effect already observed in the numerical simulations, see figure II.9 b). The main difference is that in the material 1.4404 a continuous decrease occurs for all counterforces up to 70 kN. For the material 1.4307 it can be seen that

deterioration starts at approximately 60 kN. In particular at positions 2 and 3 there are significantly higher tensile RS compared to the case at 40 kN. This phenomenon clearly shows that the improvement due to the counterpunch has a limit value. It appears that this limit is material dependent [1].

Comparing the error bars in figure II.10 a) and b), it can be seen that in b) there are higher calculated standard deviations due to the large number of specimens. The cause of the higher fluctuations in the experimental RS measurements can be attributed to several factors, so that no clear explanation can be given: From the point of view of forming technology, the local friction is not uniform due to different lubricant distributions, which consequently leads to different pressing forces, see figure II.7 [21]. Furthermore, there are control fluctuations in the generation of the counterforce. From the point of view of materials science, the high standard deviations are due to the different formation of forming martensite and deviations in the yield stress curve, see chapter II.5.

## Process Limits

The experimental results as well as the FE simulations clearly show that the application of a counterforce reduces the tensile RS at the surface of the extruded specimens. However, the reduction of the RS state is subject to a limit from the counterforce at which a maximum reduction of the tensile RS is achieved. Based on FE simulations, this limit can be determined iteratively by parameterizing the counterforce. For the investigated specimen configuration with the material 1.4307, a maximum RS reduction at approximately 80 kN was determined from numerical simulations. For the material 1.4404 with the identical numerical setup, this reversal point is reached later at approximately 110 kN, which is illustrated in figure II.11. This result agrees with the X-ray diffraction measurements based on the average values from figure II.10 b): As the counterforce increases, the tensile RS near the surface are reduced. With a further increase in the counterforce, the reduction mechanism reverses again, so that higher tensile RS are again generated at the surface.

The reason for the repeated increase in the RS near the surface is the expansion of the plastic deformation in the ejection process for strongly compressed specimens. Since the effective specimen geometry after the first deformation increases with increasing counterforce, the range of influence of the second deformation during ejection also increases. From the limit value  $F_{K,max}$  the range of fully plastic deformation begins, in which plastic deformation also starts in the workpiece core. The existing RS state is completely substituted by the second forming process during ejection, i.e., the final RS state depends only on the ejection process. A more detailed explanation of this model theory for fully-/partially plastic forming is given in chapter 3 and in [22]. In summary, with a higher yield stress, a higher degree of forming is necessary to achieve fully plastic forming, which shifts the limit  $F_{K,max}$  to higher values.

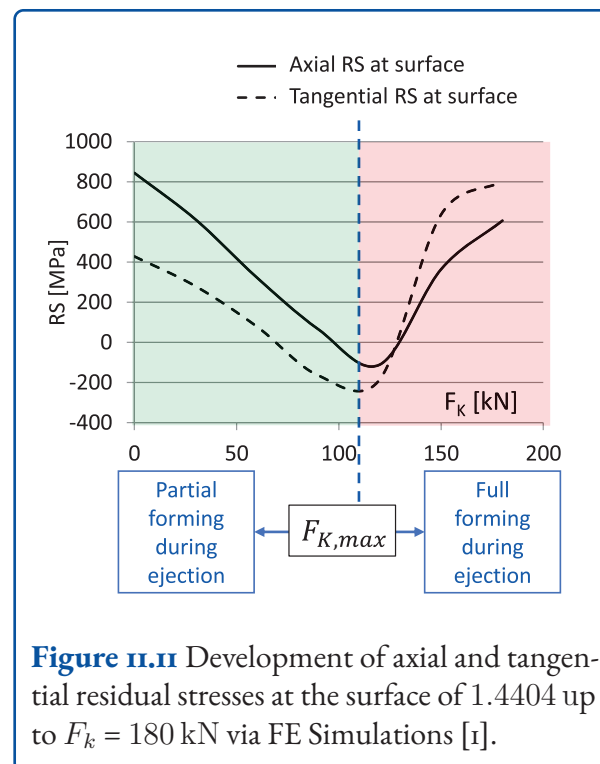


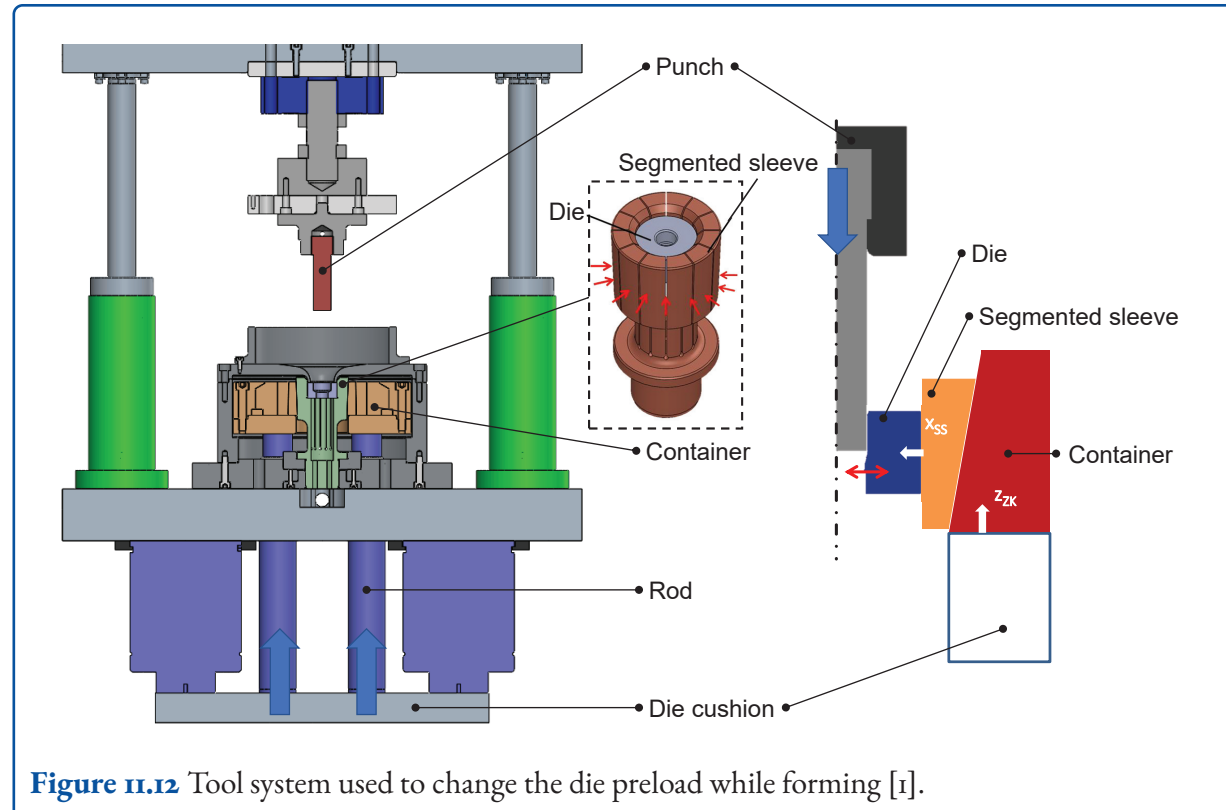
**Figure II.11** Development of axial and tangential residual stresses at the surface of 1.4404 up to  $F_k = 180$  kN via FE Simulations [1].

## 11.5 Methodology for Reducing Residual Stresses through an Active Die

Based on the effect of ejecting the specimens to modify the RS state, a second forming strategy was designed. Fine adjustment of the degree of deformation during ejection leads to superposition of the RS state, resulting in a final setting of the final RS state.

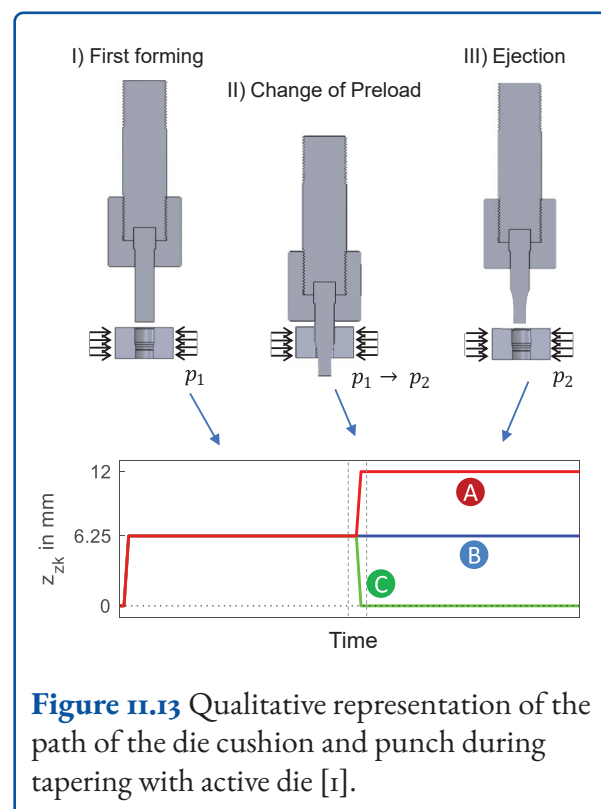
### Description of the Process

The process idea here refers specifically to the partial forming in the ejection process in order to fine-tune the final RS state. The tooling system and associated components in figure II.12 are used to actively influence the die preload. The mechanism for inline adjustable pre-stressing is based on a rotationally symmetrical wedge gear, which is coupled to the PtU's spindle press via the die cushion. An axial upward movement of the die cushion pushes the conically shaped 3-part reinforcement onto the segmented sleeve. Due to the transmission, the forming die is tensioned in the segmented sleeve so that



the inner diameter of the calibration zone of the forming die is adjusted. In this way, the degree of forming for the partial forming during ejection is also calibrated. For the investigations, a total of 3 cases with variable ejection conditions are examined, whereby the identical pressurising takes place in the main forming in all cases:

- **Case A – Preload increase:** In case A, the preload on the die is increased during the ejection phase.
- **Case B – Conventional method:** In case B, the preload on the forming die remains constant throughout the process. It is a conventional full forward extrusion process.
- **Case C – Preload decrease:** In case C, the position of the die cushion is lowered during ejection. In this way, the diameter of the die is increased after forming the workpiece.



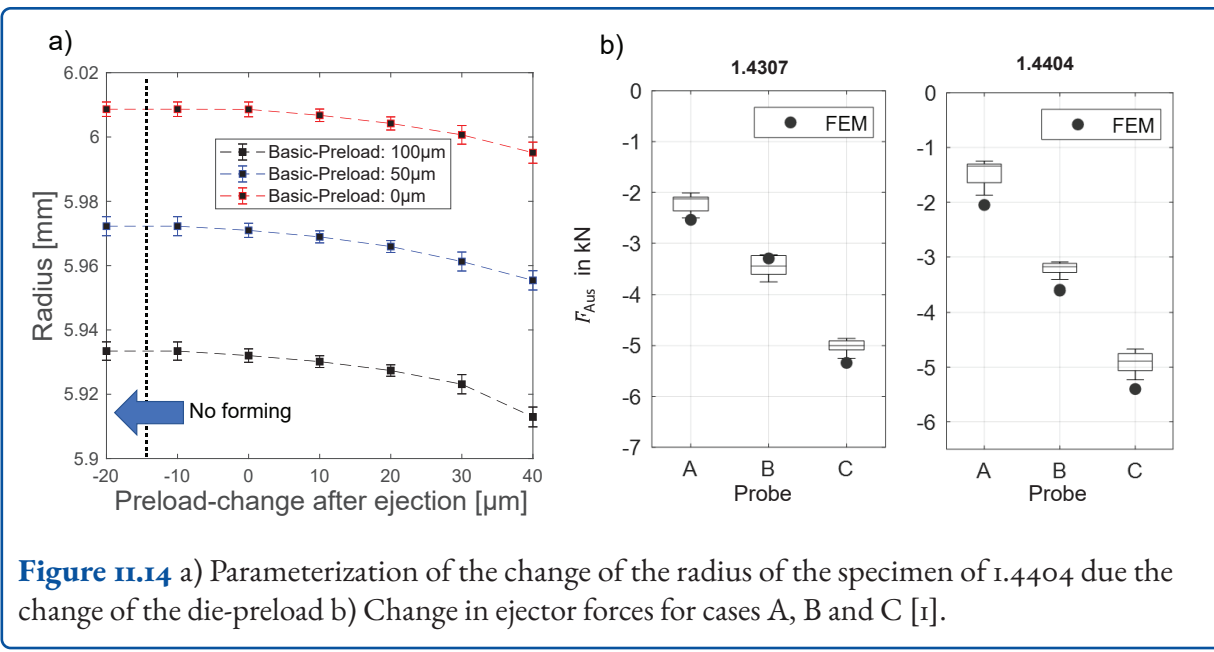


**Figure II.14** a) Parameterization of the change of the radius of the specimen of 1.4404 due the change of the die-preload b) Change in ejector forces for cases A, B and C [1].

For all cases, the punch and the die cushion are path-controlled. To illustrate the die movement, these are summarized in figure II.13. Compared to the tooling system for the counter punch, in this setup the samples to be examined are clamped at the punch, i.e., the ejection of the samples is done by pulling them out over the punch. The numerical setup of this process is based on the setup of chapter II.4, whereas more details can be found in the following literature sources [14] and [1].

## Working Principle

As described earlier, changing the die preload during ejection results in the change in degree of deformation. Fine-tuning the degree of deformation also controls the second plastic deformation during ejection, so that the ejection process is considered a partially plastic forming [22]. The final RS results from this superposition. The resulting change in the diameter of the die is in the order of microns. Therefore, great care must be taken while modeling this effect, as small errors could lead to large deviations in the predicted RS state [1]. An illustration of the diameter change is provided in figure II.14 a), where a simulated parameterization of the preload has been performed. Intuitively, it is clear that an increase in the basic preload within the main forming will result in a decrease in the diameter of the

die in the calibration zone. Therefore, the extruded parts will have a slightly different diameter depending on the process conditions. Conversely, as the base preload is reduced, the die relaxes, resulting in larger diameters. Based on the preload changes during ejection in figure II.13, the identical effect is shown by analogy. The influence of the variable degree of deformation also affects the ejector forces, which are listed in figure II.14 b). Here, a comparison of the average forces during ejection  $F_{Aus}$  for cases A, B and C is made and shown in box plots. The experimental data are from seven samples for each case studied. The ejection forces are significantly lower in case A than in case B. It should be noted that ejection is not eliminated in case A, but merely occurs with a lower degree of deformation. Compared to the conventional process, the forming forces in case C are slightly higher. The higher ejection forces of 1.4307 compared to 1.4404 can be attributed to the formation of martensite and the resulting volume expansion after the first forming [20]. Overall, the experimental and numerical data are in good agreement, confirming the FE simulations for the investigations. A first process limit can be derived by considering the diameter change and the ejector forces. As the preload is progressively reduced during ejection, no forming occurs during ejection above a certain specimen diameter. The calibration zone of the die no longer touches the sample surface, which is why there is a stationary

area in the negative x-direction in figure II.14 a). Beyond this limit, it is assumed that the resulting RS state corresponds only to the main deformation: For very small changes in preload, there is no deformation during ejection and hence no plastic deformation occurs in the region close to the surface. Figure II.15 shows the numerical results of the axial RS profiles for the materials 1.4404 and 1.4307. In addition to the experimentally investigated cases A, B and C, the results of the stresses for the process without ejection are also shown. Firstly, the results confirm that in all the experimental cases A, B and C a reduction in the tensile RS is obtained in the surface region, due to the inclusion of the ejection process. For the material 1.4404, the axial RS at the surface decreases from an initial value of about 850 MPa to 600 MPa in case C, 200 MPa in case B and 150 MPa in case A, with the last case showing almost zero RS up to a large specimen depth [8]. The same behavior is observed for the material 1.4307, whose curves are also quantitatively very similar to the first material [8]. In summary, an increasingly greater degree of deformation during ejection causes a shift of the axial RS into the pressure range. From these results it is evident how the control of the degree of deformation by the active forming tool allows a specific calibration of the RS state. It is also noticeable that plastic deformation is limited to the near-surface region, i.e., partial deformation takes place, while the central part of the specimen is subject to a constant elastic relaxation of the RS to maintain the overall equilibrium.

A second process limit can be derived from the observation: As RS redistribution occurs with larger changes in preload during ejection due to near-surface plastic deformation, fully plastic deformation will occur above a limit. Analogous to chapter II.4, fully plastic deformation again leads to high tensile RS at the surface. The identical behavior due to a fine calibration of the degree of deformation can also be described by an analytical model, which is discussed in [22]. Here a coupled reverse shrink-fit model is used to determine the resulting RS state.

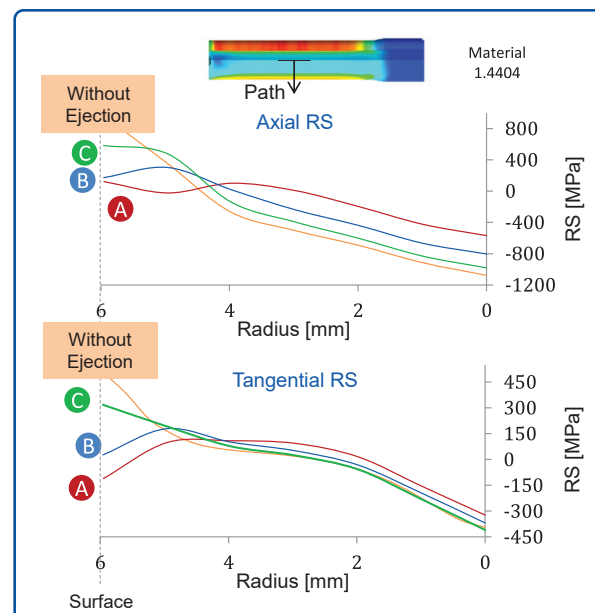


**Figure II.15** Numerical evaluation of the RS curves in the axial direction for the examined cases A, B and C for 1.4404 [8, 23].

## Validation with X-ray Diffraction

Figure II.17 shows the results of X-ray diffraction measurements on the tapered samples 1.4404 with the analysis of the three elementary cases A, B, and C. RS measurements are performed on the remolded samples using the  $\sin^2 \Psi$  method in the depth direction. If the RS profile of case B is used as a reference, it can be seen that a lower preload as in case C causes higher tensile RS. On the other hand, a more ideal stress state can be observed in case A. Here, even near-surface compressive RS up to -100 MPa were measured, which are particularly desirable as they can improve the fatigue strength of these extruded parts.

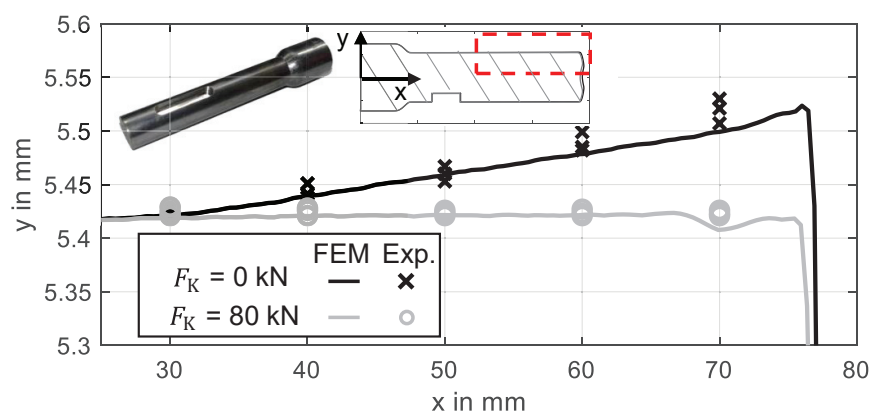


**Figure II.16** Milling of a feather key on the RS optimized specimens to demonstrate distortion reduction [1].

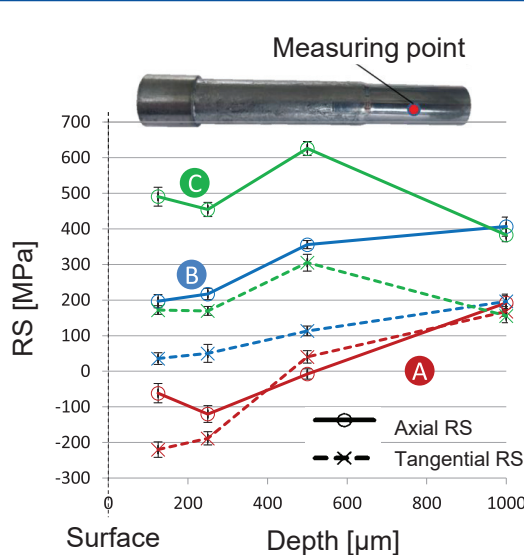


**Figure II.17** RS measurements with X-rays in axial and tangential directions on samples of 1.4404 in the austenitic phase, using higher (A), identical (B), and lower (C) pre-stresses during ejection [8].

As the sum of all RS in a workpiece in each direction must be zero, the curves are expected to cross at a certain point in the depth to reach equilibrium. In particular, the striking high slope of curve C indicates that the high compressive RS at the surface is compensated by increased tensile RS inside. Overall, the results agree very well with the simulations. The largest discrepancy is in the axial RS

in case A, which are slightly overestimated in the simulations. [8]

In contrast to 1.4404, the lower content of austenite-stabilizing elements in 1.4307 leads to the formation of deformation-induced martensite even at low degrees of deformation. For this reason, the respective phase fractions on the surface were determined by X-ray according to ASTM E975 [24]. The values are between 35 % and 44 % and are listed in table II.2. The different prestressing forces of the die do not lead to a significant increase in the proportion of deformation-induced martensite. [20]

**Table II.2** Martensite contents on the surface of the samples made of 1.4307, according to ASTM E975 [20]

Specimen	Martensite content on the surface in %	Martensite content in 1 mm depth in %
A	$35.1 \pm 4.5$	$18.0 \pm 2.1$
B	$42.7 \pm 5.9$	$9.6 \pm 3.3$
C	$43.6 \pm 0.6$	$14.6 \pm 0.8$

From the investigations for the material 1.4307, a reduction of the tensile RS due to the deformation-induced martensite phase was observed. This is further described in [20]. No significant trend

was observed in the austenite phase of material 1.4307 with a changing die preload. One explanation is that deformation-induced martensite is found mainly in areas where large deformations occur since the phase transformation is caused by deformation. Due to the greater degree of deformation and the volume expansion during the phase change, the martensitic phase has greater tensile RS. In the martensitic phase, the effect of greater preloads causes compressive stresses up to a depth of 1 mm. [20]

## 11.6 Validation of Improvement of Material Properties

Component properties that are influenced by the RS state were already described in the introduction. In order to specifically validate the effect of the methods presented in this chapter for industrial application, two case studies are focused on.

### Reduction of Distortion

The high RS gradients created during cold extrusion are highly undesirable within a process chain, for example, as slight disturbances of this equilibrium can easily lead to plastic deformations. To minimize the risk of distortion, the component should ideally be free of internal stresses. To demonstrate the effect of the forming strategies presented in this chapter, a post-processing on a sample with and once without optimised RS condition is considered. In this case, samples are produced with and once without a counterforce and then a key is milled on the extruded components. The keyway is designed according to DIN 6885-1 [25]. The resulting geometry is determined via a dial gauge and simulated in parallel via FE simulations. Figure II.16 shows the numerical and experimental results comparing the deformation due to the manufacture of the keyway on cold extruded specimens made of 1.4404 with  $F_k = 0 \text{ kN}$  and  $F_k = 80 \text{ kN}$ . The maximum radial displacement at the specimen tip is  $\Delta d/l_0 = 1.37\%$ . In contrast, when using a counterpunch with  $F_k = 80 \text{ kN}$ , the deformation

is almost completely avoided. These experimental results are also confirmed by the FE simulations.

### Improvement of Fatigue Life

The fatigue life of the extruded components is investigated by means of rotating bending tests. This test reproduces the cyclic loading to which many axisymmetrical extruded components are subjected during their use, i.e., a cyclic bending moment. This type of stress frequently occurs, for example, in shafts where radial cyclic loads are applied by the bearings, such as railway axles. The superposition of external loads and the RS state in this configuration is of great importance due to the high number of accidents caused by fatigue failure. [4]

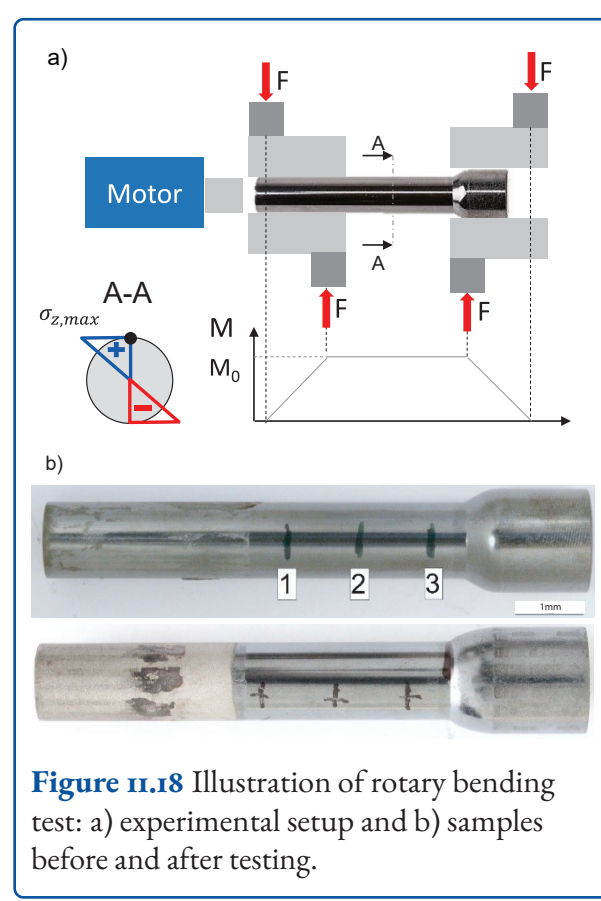


**Figure II.18** Illustration of rotary bending test: a) experimental setup and b) samples before and after testing.

The test setup of the rotating bending tests is shown in figure II.18. The test specimen is fixed by clamps at one end in the undeformed area and at the other end over a length of 30 mm. The prestressing systems rotate at constant speed and are connected to an external structure via bearings. Radial forces are applied to these bearings, which exert a bending

moment on the specimen. The stress profile thus corresponds to that of a 4-point bending process, whereby the central area is subjected to a constant torque  $M_0$ . The specimen is loaded with pure alternating stresses in the axial direction, i.e., the average stress level is zero.

In particular, because one of the two end sections of the extruded specimens has the same cross-section as the test section, failure in the clamped section is likely. To prevent fractures in this area, compressive RS were introduced into this section by hammer peening. From RS measurements it was shown that the hammer peening did not affect the RS in the test section [i]. Additional shot peening was needed for the high cycle fatigue measurements to prevent failure in the clamping region during higher cycles. Consequently, the experimental setup is suitable to perform the fatigue life tests.

The difference in RS has effects on the material properties. To achieve different material responses, various bending stress levels are used for the tests. Additionally, the results of 1.4404 are utilized to optimize the bending stresses for 1.4307 to achieve more meaningful results. Figure II.19 a) shows the Wöhler plot of 1.4404. At 350 MPa, all results are in the low cycle fatigue area. There is no significant difference between the samples with no counterpunch (0 kN) and those with a counterpunch (40 kN) at this bending stress level, although there is a slight tendency of the 40 kN samples to exhibit higher cycle numbers. At 150 MPa, no sample experiences failure until the cut-off cycle number of  $10^7$ . Thus, no difference in the failure behavior can be found due to the different forming parameters. At a bending stress of 250 MPa, differences are evident. From 0 kN to 40 kN there is an increase of the average cycle number of 82 % caused by the improved RS state generated by the modified forming process. A counterpunch force of 60 kN has even better results with one of the three data points sustaining a whole series of cycles more before failure occurs. This trend does not continue with even greater counterpunch forces. At 70 kN the results are comparable to a force of 40 kN. This implies that there exists a maximum beneficial counterforce, despite the continuing reduction in surface tensile RS (see figure II.10).

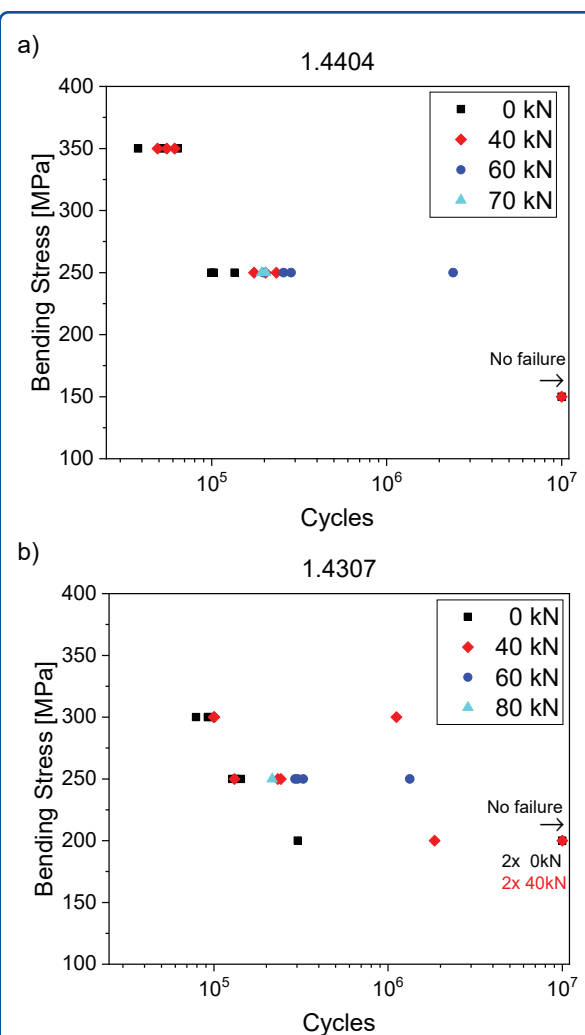


**Figure II.19** Results of the fatigue life test: Wöhler-Plots of Material 1.4404 and 1.4307 with different bending stresses applied.

Figure II.19 b) shows the results of the 1.4307 samples. Due to the trivial results for the 150 MPa and 250 MPa bending stress horizons for 1.4404, the bending stresses for 1.4307 were adjusted to 200 MPa and 300 MPa. While there is a lot of overlap between the data points at 200 MPa, a single point with a force of 40 kN lasted for  $10^6$  cycles. At the 300 MPa threshold it is similar. There is a large overlap of samples without failure (2 x 0 kN and 2 x 40 kN), but of the samples that fail, the 40 kN sample endures six times as many cycles before breaking. Similar to the 1.4404 results, the effects were well pronounced at the 250 MPa stress level. There is a marked increase in cycle numbers going from 0 kN to 40 kN. Using a counterpunch with a force of 60 kN increase the results even fur-

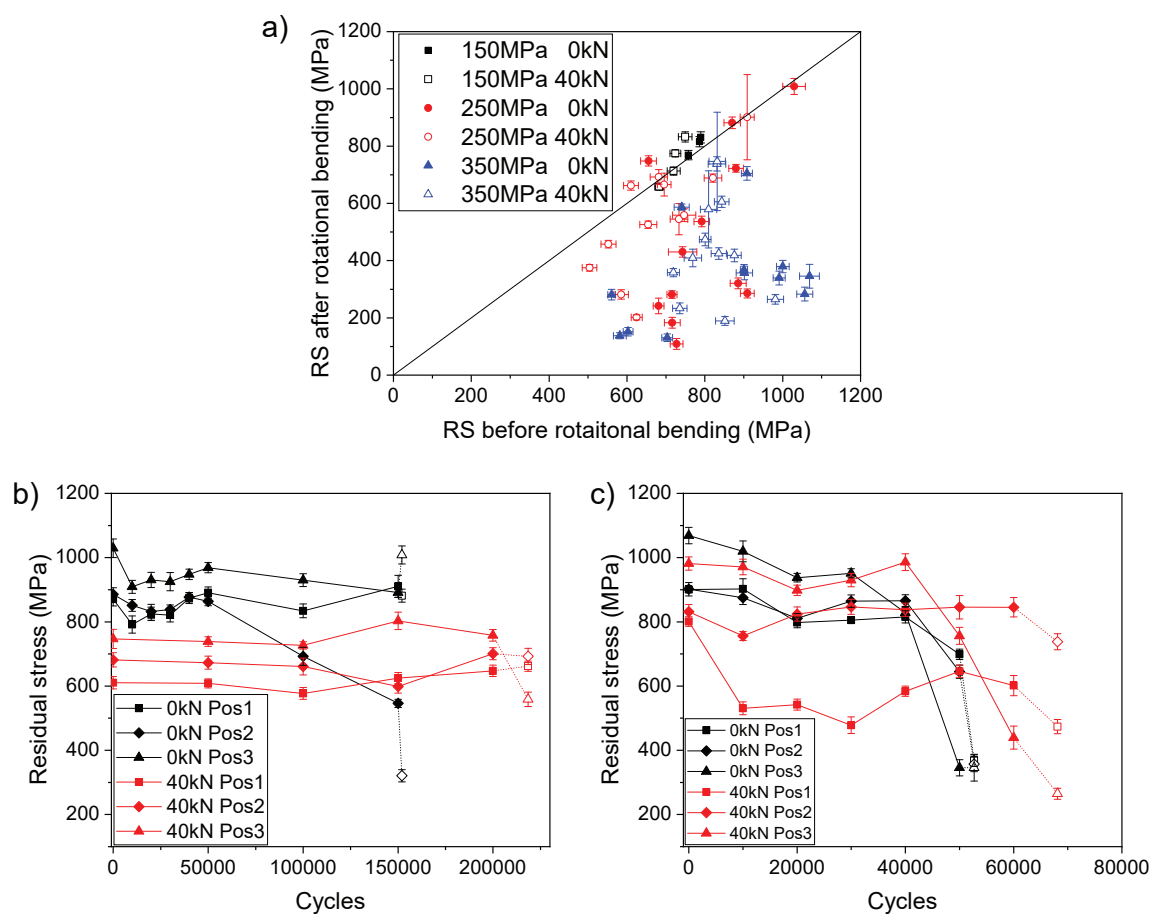


**Figure II.20** Results of rotary bending test: a) Residual stresses before and after failure by rotational bending for 1.4404, b) 1.4404 at 350 MPa. Failure occurs at positions 2.7 (0 kN) and 2.0 (40 kN). c) 1.4404 at 250 MPa. Failure occurs at positions 2.3 (0 kN) and 2.6 (40 kN).

ther. At 80 kN, however, the number of cycles to failure is again comparable to that of the 40 kN case. Research for the reasons of this decrease in fatigue properties is a current topic. As the effect is relevant for both 1.4404 and 1.4307, it is not related to deformation-induced martensite. Higher counterforces have no hardness increasing effect up to 40 kN, which makes it unlikely that a greater notch sensitivity due to increased hardness would be relevant at higher forces.

### Mechanical Residual Stress Stability

Mechanical residual stress stability is understood as the change in RS over time under a cyclic load. The associated investigation aims to determine the

extent to which the RS state changes under real operating conditions [26].

Figure II.20 a) shows the RS before and after failure by rotational bending for the different load levels and for the two main counterpunch forces. The diagonal line marks the area where no change would take place. At first, it can be seen that the reduction in RS scales with the bending stress. 150 MPa leads to almost no reduction in RS. There are some data points at 250 MPa where the RS state remains stable, but most times a reduction is caused. A stress of 350 MPa leads to even greater reductions. In addition to the lower tensile RS during the forming process, the use of a counterpunch causes a lower reduction of RS as well. This can be seen in that the RS after failure are higher for 40 kN than for 0 kN

despite the initial values being lower. This speaks for a better ability to retain beneficial RS states.

At first, the in-situ measurements were undertaken every 10.000 cycles. The results for material 1.4404 and bending stress levels of 350 MPa can be seen in figure II.20 b). For the 0 kN sample, there is a slow decline of the RS which accelerates after 40.000 cycles. At 50.000 cycles the RS at position 3.0, which is closest to the failure point of 2.7 (0.7 mm from position 2 and 0.3 mm from position 3), shows the lowest RS, which are equal to the later failure at 52.700 cycles. The RS at other positions are higher at 50.000 cycles, but nearly identical after failure. The 40 kN sample behaves differently. The initial RS states are much lower, as already discussed for figure II.10. During the rotational bending test, the RS of position 1.0 is already at 530 MPa after the first 10.000 cycles. It stays at that much lower level when compared to positions 2.0 and 3.0, which do not experience failure of RS stability until after respectively 40.000 and 60.000 cycles. Here it is notable that position 3.0, which had the highest RS at the beginning, ends up with the lowest RS. Position 2.0, the point of failure, showed the most stable RS evolution. At 250 MPa (see figure II.20 c), the RS split happens the other way. Here the 0 kN sample splits at failure with low values at position 2.0 (close to the failure position of 2.3) and stable values at position 1.0 and 3.0. For 40 kN, all positions retain a stable RS state despite failure occurring at position 2.6. Due to the placement of the data points, it can be seen that the number of cycles between measurements increased. This was due to the large number of measurements in the beginning of the testing period that did not show any significant RS change.

In conclusion it can be observed that the use of a counterpunch does not only improve the RS state right after forming, but also leads to a better stability of that RS state. The same effect can be seen for 1.4307 for both the austenitic and martensitic phases. At counterforces of 60 kN there is barely any reduction of the RS except in the area of failure.

## 11.7 Modeling the TaReS Strategy

After the introduced definition of the TaReS strategy, a desired RS profile can be set by means of the two described forming strategies. The combination of the counterforce and the infeed by the active die offers two independent degrees of freedom for this. However, in order to generate the desired RS profile, an exact prediction of the forming parameters to be set is crucial. For this reason, modeling of the combination of both forming strategies is required. Therefore, a parameterization was carried out in an FE simulation with the sample configuration discussed in this chapter. On the one hand, the counterforce in the main forming and, on the other hand, the infeed of the active die during the ejection process are varied. The process window resulting from the combination of both parameters is shown in figure II.21 a) with essentially 4 areas to highlight. In this case, the parameterization of the parameters for the material 1.4404 was chosen, with the resulting sample gauge shown on the y-axis. As already gathered in the previous chapters,  $D_{Mat}$  is adjusted by the infeed within the active die with  $z_{zk}$ . On the other hand, the diameter of the specimen  $D_{Aus}$  after the main forming is a function of the counterforce, which is due to the compression below the calibration zone. Thus, the change in the degree of deformation during ejection is a function of the form  $\varphi = f(D_{Mat}, D_{Aus})$ . These two geometric parameters can be used to define the 4 areas for the ejection process, which represent the process window of the combined forming strategy:

1. **No forming** – If  $D_{Mat} > D_{Aus}$  no deformation takes place because the sample and the matrix do not come into contact.
2. **Elastic forming** – If  $D_{Mat} < D_{Aus}$  so that  $\varphi$  remains below a certain limit, pure elastic deformation occurs. In this case, the stress state is not changed.
3. **Partial forming** – If  $D_{Mat} < D_{Aus}$  so that  $\varphi$  is within a certain range, partial deformation occurs.
4. **Full forming** – If  $D_{Mat} \ll D_{Aus}$  a full forming occurs.

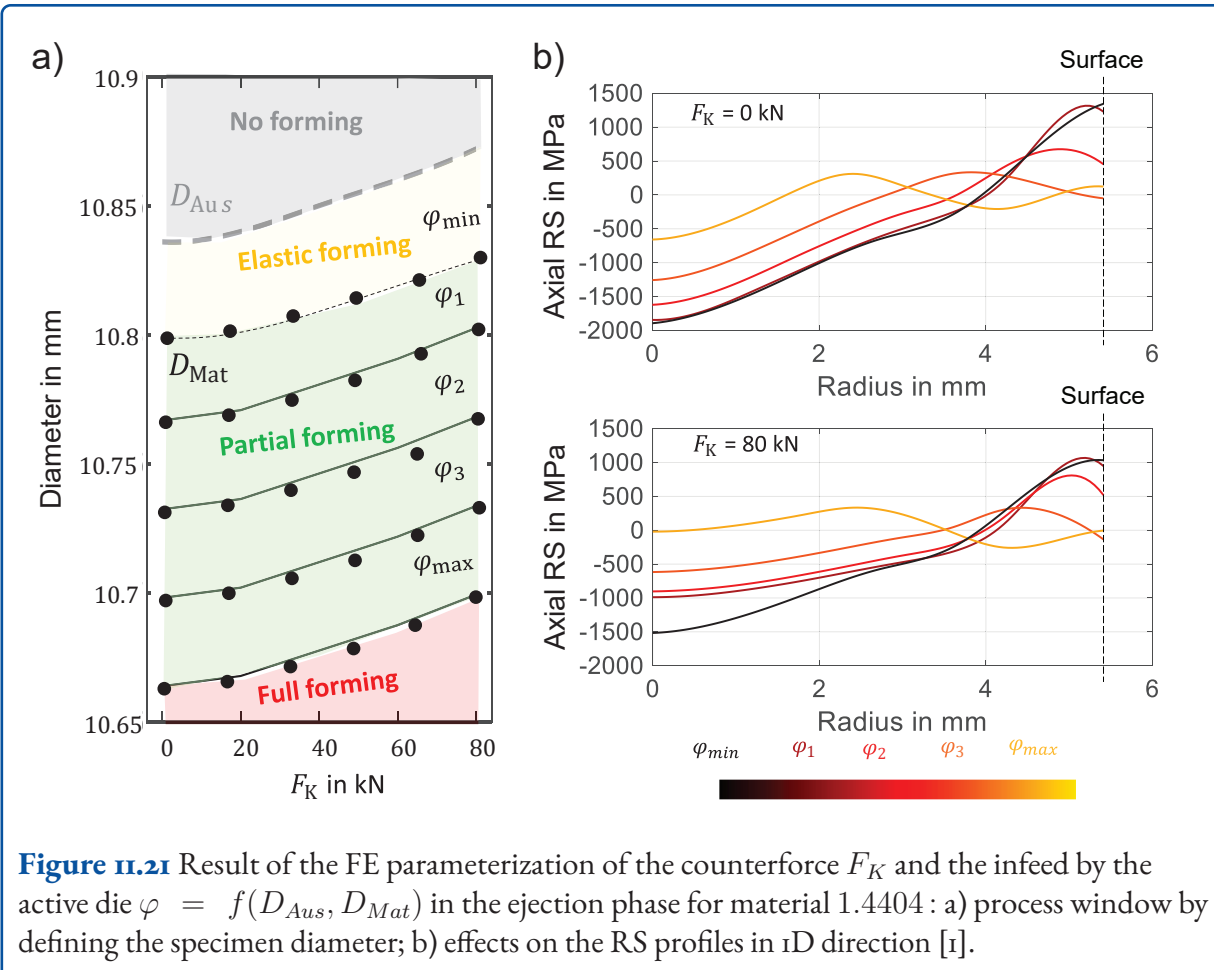


**Figure II.21** Result of the FE parameterization of the counterforce  $F_K$  and the infeed by the active die  $\varphi = f(D_{Aus}, D_{Mat})$  in the ejection phase for material 1.4404 : a) process window by defining the specimen diameter; b) effects on the RS profiles in 1D direction [1].

The simulated RS profiles resulting from the combination are listed in figure II.21 b), whereby only the counterforce for 0 kN and 80 kN was used. A comparison between the two graphs in b) shows that regardless of the counterforce a large adjustment range is possible by adjusting the active die, see chapter II.5. By increasing the counterforce, the family of curves can even be shifted further into the compressive range, with a significantly less infeed by the active die required. In this way, it is possible to dimension the actuators smaller for both forming strategies in order to achieve the identical level of RS close to the surface. For the modeling of the forming process in area 3. *Partial forming* from figure II.21 a) an analytical approach can be created to describe the resulting RS state. Assuming that the ejection is a partial forming, the stress state is superimposed from the main forming. This results in the final axial RS  $\sigma_{z,End}$  as a superposition of the two process steps:

$$\sigma_{z,End} = \sigma_{z,Aus} + \sigma_{z,Over} \quad (\text{Equation II.4})$$

where  $\sigma_{z,Aus}$  are the axial stresses after the first forming and  $\sigma_{z,Over}$  are the superimposed stresses during ejection. To determine  $\sigma_{z,Aus}$ , family of curves is simulated with a progressive counterforce at identical basic pre-stress, see figure II.9 a). These results are interpolated using a higher-order polynomial of the form  $\sigma_{z,Aus} = f(r, F_k)$ . Furthermore, the infeed of a RS-free specimen is varied, where the varied degree of deformation is determined  $\varphi$  from the diameter ratio of  $D_{Mat}$  and  $D_{Aus}$ , see chapter II.5. The results of the second parameterization are analogously adjusted by an interpolation of the form  $\sigma_{z,Over} = f(r, \varphi)$ . Substituting both interpolation rules into Equation II.4 yields an equation of the form  $\sigma_{z,End} = f(r, F_k, \varphi)$ . With this approach, the final RS state can be determined by specifying the two process parameters. The procedure for the development of the interpolation rules is exemplarily demonstrated in [1].

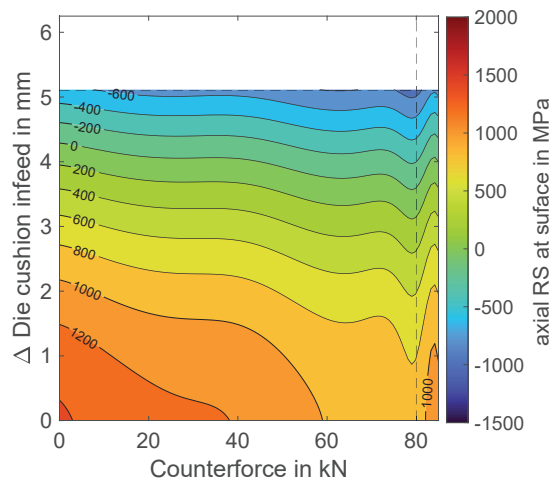


**Figure II.22** Contour map to represent possible RS states on the surface of the material 1.4404 for the given specimen geometry, derived from the superposition approach in *Equation II.4* [1].

The isoline diagram (operating diagram) in figure II.22 shows the possible combinations for the RS near the surface. The degree of deformation  $\varphi$  to be set during ejection is described in this case by the transmission through the die cushion. From this diagram, a desired RS state can be read, fulfilling the basic requirement for the TaReS prediction strategy.

surface tensile RS was reduced, and fatigue life (particularly in the low cycle fatigue range) and corrosion resistance were increased, see chapter 3 and [1]. The combination of the two process designs allows an extension of the possible RS states that can be explained by the partial/full plastic deformation model theory. In an intelligent and efficient manufacturing system, the RS introduced should be considered together with other component properties in the design of the manufacturing process. Accordingly, the RS state of a component should be tailored to the specific requirements of its application. This manufacturing strategy is referred to in this chapter as the "TaReS strategy". The main challenge for the industrial application of a tailor-made RS setting system in manufacturing is the development of economically viable systems. In order to transfer the promising approaches and knowledge to the industrial environment, it is therefore necessary to adapt the developed tooling system for in-line control of the RS state. For the tools, the effects of any necessary auxiliary elements (e.g., spring systems) on the RS profile must also be investigated. In this way, the optimum of possible product quality improvements through tailor-made RS and a load-appropriate design of the tool systems must be determined in order to guarantee an industrial application of the manufacturing strategy.

## 11.8 Conclusion

Strategies for the targeted control of RS during forming processes offer enormous potential for the improvement of component properties which is not yet sufficiently exploited. In the investigations, this was demonstrated by integrating forming strategies into conventional process control. The influence of the counterpart and the active die on the RS state of full-forward extruded components was scientifically described and validated numerically and experimentally. The active die was able to induce compressive RS even close to the surface. The positive influence of process control on component performance was demonstrated. Unwanted distortion due to the reduction of near-

## Symbols

$b_0$	Coef. of isotropic hardening (-)
$C_i$	Coef. of kinematic hardening (kN)
$D_{Aus}$	specimen diameter after first forming (mm)
$D_{Mat}$	variable die diameter in the ejection phase (mm)
$D_0$	initial diameter of specimen (mm)
$\Delta d$	radial displacement (mm)
$F_K$	counterforce (kN)
$F_{K,max}$	maximum counterforce (kN)
$i$	counter variable (-)
$l_0$	length of extruded specimen (mm)
$m_R$	Shear stress friction factor (-)
$P$	Coef. of isotropic hardening (kN)
$Q$	Coef. of isotropic hardening (kN)
$x_{SS}$	radial infeed of the die ( $\mu\text{m}$ )
$z_{ZK}$	infeed of the die cushion (mm)
$\lambda_i$	Coef. of kinematic hardening (-)
$\mu_R$	Coulomb friction factor (-)
$\sigma_z$	axial residual stresses (MPa)
$\sigma_{z,Aus}$	residual stress before ejection (MPa)
$\sigma_{z,End}$	residual stress after ejection (MPa)
$\sigma_{z,Over}$	super-positioned residual stress in the ejection phase (MPa)
$\sigma_{y0}$	initial yield stress (MPa)

540-16498-2. DOI: 10.1007/978-3-642-82799-0\\$\backslashtextunderscore.

- [3] P. J. Withers. "Residual stress and its role in failure". In: *Reports on Progress in Physics* 70.12 (2007), pp. 2211–2264. ISSN: 0034-4885. DOI: 10.1088/0034-4885/70/12/R04.
- [4] Hans-Jakob Schindler. "Effect of Residual Stresses on Safe Life Prediction of Railway Axles". In: *Procedia Structural Integrity* 4 (2017), pp. 48–55. ISSN: 24523216. DOI: 10.1016/j.prostr.2017.07.008.
- [5] Volodymyr Okorokov et al. "Corrosion Fatigue of Low Carbon Steel under Compressive Residual Stress Field". In: *Procedia Engineering* 213 (2018), pp. 674–681. ISSN: 18777058. DOI: 10.1016/j.proeng.2018.02.063.
- [6] Klaus-Dieter Thoben et al. "'Distortion engineering': a system-oriented view on the distortion of component-parts". In: 29 () .
- [7] Mackenzie D. "Metallurgical Aspects of Distortion and Residual Stresses in Heat Treated Parts: Conference: 23rd IFHTSE Congress on Heat Treatment and Surface Engineering". In: (2016).
- [8] Alessandro Franceschi et al. "Calibration of the residual stresses with an active die during the ejection phase of cold extrusion". In: *International Journal of Material Forming* 14.2 (2021), pp. 223–233. ISSN: 1960-6206. DOI: 10.1007/s12289-020-01572-x.
- [9] V. Schulze et al. "Surface modification by machine hammer peening and burnishing". In: *CIRP Annals* 65.2 (2016), pp. 809–832. ISSN: 00078506. DOI: 10.1016/j.cirp.2016.05.005.
- [10] Christian Schieber et al. "Modeling of Deep Rolling as a Distortion Compensation Strategy during Profile Grinding". In: *Key Engineering Materials* 926 (2022), pp. 897–905. DOI: 10.4028/p-k1033k.
- [11] Andreas Jobst. *Influence of material delivery condition on residual stresses and part properties during forward rod extrusion*. 2020. DOI: 10.31224/osf.io/9wuzm.

## References

- [1] A. Franceschi. "Anforderungsspezifische Einstellung des Eigenspannungszustands in der Kaltmassivumformung". Dissertation. TU Darmstadt, 2022.
- [2] A. Erman Tekkaya. "Eigenspannungen in Kaliumgeformten Massivteilen". In: *Ermittlung von Eigenspannungen in der Kaltmassivumformung*. Ed. by Kurt Lange and A. Erman Tekkaya. Vol. 83. Berichte aus dem Institut für Umformtechnik der Universität Stuttgart. Berlin, Heidelberg: Springer Berlin Heidelberg, 1986, pp. 67–103. ISBN: 978-3-

- [12] Philipp Landkammer et al. "Investigations on residual stress generation in full-forward-extrusion". In: *Production Engineering* (2019). ISSN: 0944-6524. DOI: 10.1007/s11740-019-00892-5.
- [13] Stefan Ossenkemper. *Verbundfließpressen in konventionellen Fließpresswerkzeugen*. [1. Auflage]. Vol. Band 100. Reihe Dortmunder Umformtechnik. Aachen: Shaker Verlag, 2018. ISBN: 978-3-8440-6175-8.
- [14] A. Franceschi and Hoche, H., Kaffenberger, M., Oechsner, M., Groche, P. "Effects of a counter-punch system for cold full-forward extrusion. NUMIFORM 2019: The 13th International Conference on Numerical Methods in Industrial Forming Processes". In: (2019).
- [15] H. Zhang et al. "Investigation of material flow during friction extrusion process". In: *International Journal of Mechanical Sciences* 85 (2014), pp. 130–141. ISSN: 00207403. DOI: 10.1016/j.ijmecsci.2014.05.011.
- [16] A. Franceschi and P. Groche. "Verzugsarme Kaltmassivumformung". In: *wt Werkstattstechnik online* 109.10 (2019). ISSN: 1436-4980. DOI: 10.37544/1436-4980-2019-10.
- [17] A. E. Tekkaya, J. Gerhardt, and M. Burgdorf. "Residual Stresses in Cold-Formed Workpieces". In: *CIRP Annals* 34.1 (1985), pp. 225–230. ISSN: 00078506. DOI: 10.1016/S0007-8506(07)61761-2.
- [18] Shinobu Narita et al. "Effect of Hardening Rule for Spring Back Behavior of Forging". In: *Procedia Engineering* 207 (2017), pp. 167–172. ISSN: 18777058. DOI: 10.1016/j.proeng.2017.10.756.
- [19] J. L. Chaboche. "Constitutive equations for cyclic plasticity and cyclic viscoplasticity". In: *International Journal of Plasticity* 5.3 (1989), pp. 247–302. ISSN: 07496419. DOI: 10.1016/0749-6419(89)90015-6.
- [20] Fabian Jaeger et al. "Optimierung des Eigenspannungszustands kaltfließgepresster austenitischer Stähle durch einen kontrollierten Ausstoßvorgang". In: *Forschung im Ingenieurwesen* 85.2 (2021), pp. 691–702. ISSN: 0015-7899. DOI: 10.1007/s10010-021-00483-w.
- [21] Fabian Jaeger et al. "Statistical analysis of the reproducibility of residual stress measurements in cold extruded parts". In: *Archive of Applied Mechanics* 91.8 (2021), pp. 3665–3677. ISSN: 0939-1533. DOI: 10.1007/s00419-021-01953-x.
- [22] Peter Groche and Alessandro Franceschi. "Residual stress evolution in partial and full axisymmetric forming processes". In: *CIRP Annals* 70.1 (2021), pp. 227–230. ISSN: 00078506. DOI: 10.1016/j.cirp.2021.03.003.
- [23] A. Franceschi and P. Groche. "Towards tailored residual stresses through cold forging processes: Conference-Paper". In: 2021 (13 - 15 September 2021).
- [24] PEo4 Committee. *Practice for X-Ray Determination of Retained Austenite in Steel with Near Random Crystallographic Orientation*. West Conshohocken, PA. DOI: 10.1520/E0975-13.
- [25] DIN 6885-1:2020-01, *Mitnehmerverbindungen ohne Anzug, Passfedern, Nuten - Hobe Form - Teil\_1: Maße, Toleranzen, Masse*. Berlin. DOI: 10.31030/3121665.
- [26] A. Franceschi et al. "Observations on the stability of the residual stresses after cold forming and unidirectional loading". In: *Production Engineering* 13.2 (2019), pp. 157–167. ISSN: 0944-6524. DOI: 10.1007/s11740-018-00871-2.

## 12 Increased Efficiency of Electrical Steel by Targeted Residual Stress

Neuwirth, T.; Schauerte, B.; Gilch, I.; Sebold, S.; Hartmann, C.; Volk, W.; Leuning, N.; Hameyer, K.; Schulz, M.

GEPRIS 374548845

### 12.1 Introduction

The ongoing climate crisis necessitates a sharp reduction in the emission of CO<sub>2</sub> to limit the temperature increase. A critical factor is fossil energy usage. One major contributor to fossil energy usage is the transportation sector, which is still highly dependent on fossil fuels. In particular, battery electric vehicles, powered by renewable energies, are seen as an option to reduce emitted CO<sub>2</sub>. Together with the capacity and longevity of the battery, the energy efficiency and energy density of electric drives determine the range and lifetime of the vehicle. The energy density of an electric drive is coupled to its rotational speed, where higher speeds result in higher energy densities. Typical electric drive topologies used in electric vehicles are synchronous reluctance machines (SynRM) and permanent magnet synchronous machines (PMSM). During the operation of these topologies, the magnetic flux inside the rotating magnetic core (rotor) of the electric drive has to be guided, the stray fluxes reduced, or a magnetic anisotropy created. The magnetic core for these types of electric drives typically comprises stacked non-grain-oriented electrical steel (NGOES) sheets.

In conventional drives, flux guidance is achieved by cutting out material of the core, locally reducing its high relative magnetic permeability  $\mu_r$  of NGOES ( $\mu_r \approx 10000$ ) significantly toward the permeability of air ( $\mu_r \approx 1$ ) [1]. As a result of the reduced permeability and, therefore, the increased magnetic resistance, the magnetic flux is forced around the cutout. This technique can be used to guide the magnetic

flux and suppress stray fluxes. However, efficient flux guidance by cutouts leads to thin structures in the cross-section of the rotor, consequently reducing the mechanical stability. During the operation of an electric drive, centrifugal forces and torques act on the rotor, which the remaining thin structures have to withstand. Therefore, a compromise between magnetic flux guidance and achievable rotational speed has to be found for both PMSM and SynRM.

The concept of cutouts for magnetic flux guidance has been highly optimized. Hence for further optimizations, a new approach to magnetic flux guidance is required. The introduction of residual stresses is avoided during the manufacture of conventional magnetic core topologies. Residual stresses reduce the material's magnetic permeability and degrade other magnetic properties. These degraded magnetic properties increase losses during the operation of the electric drive (iron losses). The reduction of magnetic permeability due to residual stresses is called the inverse magnetostrictive effect or the Villari effect [2]. However, by carefully introducing residual stress, the local magnetic properties can be tuned to achieve similar magnetic flux guidance as provided by cutouts. In this project, this novel approach to magnetic flux guidance was studied.

Residual stresses are introduced into the material by embossing. Embossing makes it possible to tune the residual stress state depending on the requirements by adjusting the embossing points' size, shape, and density. This creates localized areas of increased residual stresses and decreased magnetic permeability, which guide the magnetic flux. Due to the replaced cutouts, the material cross-section increases, improving the rotor's mechanical strength and enabling higher rotational speeds.

Common standardized global magnetic measurement systems such as the Epstein frame and single-sheet-testing (SST) are not sufficient to quantify the local change in magnetic properties, as they average over the full volume of the sheet metal. To analyze the local magnetic properties, neutron grating interferometry (nGI) was applied. nGI is a non-destructive neutron imaging technique allowing analysis of the local magnetic properties with sub-millimeter resolution in the bulk of the material. The residual stress state of the material was modeled by mechanical simulations of the embossing process. This residual stress distribution was then used to perform magnetic simulations taking the directional effect of the residual stress distribution on the magnetic properties into account. The global and local measurements of the magnetic properties were used to validate the magnetic and mechanical simulations. The residual stress state, in turn, was verified using nanoindentation.

The following will give an overview of the research methods and project results. The developments will be split into parts: The Chair of Metal Forming and Casting (*utg*) analyzed the embossing process and the numerical and experimental evaluation of residual stress. The measurement of global magnetic properties and the simulation of the magnetic flux resulting from embossing was evaluated by the Institute of Electrical Machines (IEM). Finally, the measurements of local magnetic properties were performed and evaluated at Heinz Maier-Leibnitz Zentrum (MLZ). In a separate part, we will discuss the results concerning the project's goals and the development of the foundations for more effective electric drives.

## 12.2 Embossing Process

To manufacture alternative magnetic flux barriers embossing was selected as a metal-forming process. Embossing is a local bulk metal forming process. The embossing punch penetrates the material's surface, which is plastically deformed. Typically the process is used to produce coins or to inscribe products. [3]

Due to the strong local deformation, dislocations appear, and residual stresses increase. The challenge of embossed flux barriers is that a restricted area with high residual stresses is necessary. In contrast, no mechanical and magnetic material properties change is desired outside the flux barrier. The embossed electrical steel sheets should be stackable to a rotor or stator. The study was performed with a NGOES with 2.4 wt% silicon and a sheet thickness of 0.35 mm.

Different embossing processes were analyzed in the research project. Large embossing points with a diameter of 3 mm are compared to small patterns with an embossing point distance of 0.5 mm and 1.0 mm. In figure 12.1, the embossing strategy with large embossing points is shown. The die is comparable to a shear-cutting tool, and the punch is cylindrical, spherical, or conical. The diameter of one embossing point is 3 mm. [4, 5]

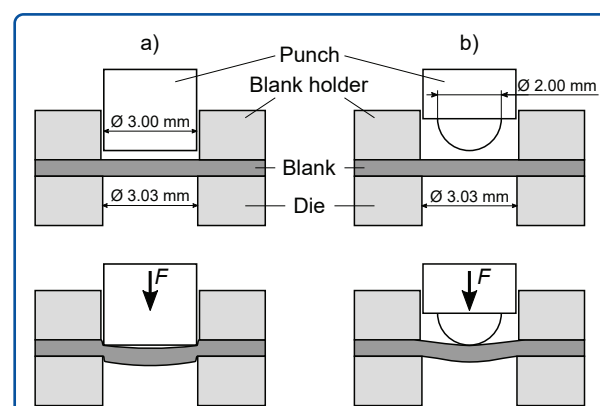


**Figure 12.1** Schematic illustration of the embossing tool and the embossing of the blank with **a** cylindrical punch and **b** spherical punch [4].

The second embossing strategy is a sequential process with small pyramidal or spherical embossing points (see figure 12.2). It differs between a punch with only one embossing point and one with ten embossing points for a sequential embossing process. A flux barrier assembles several embossing points with a distance of 0.5 or 1.0 mm. [6–8]

To scale the embossing to an industrial process, an embossing tool for embossing patterns of 30 mm × 60 mm was designed. Pyramidal emboss-

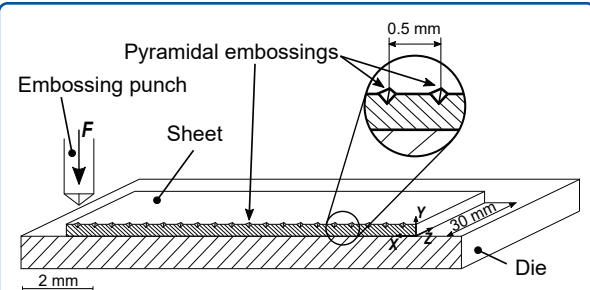


**Figure 12.2** Schematic illustration of the sequential embossing process with a flat die and pyramidal punch [6].

ing points with a tip angle of  $70^\circ$  are arranged in a grid with a distance of 0.5 mm. Due to the tool's construction, embossing on the top of the sheet and both sides of the sheet is possible. Four other different embossing patterns are feasible; see figure 12.3. The pyramidal tips of the top embossing can be directly opposite the bottom embossing (A-A) or shifted in (B-A) or transverse (A-B) to the direction of magnetization or shifted in both directions (B-B).

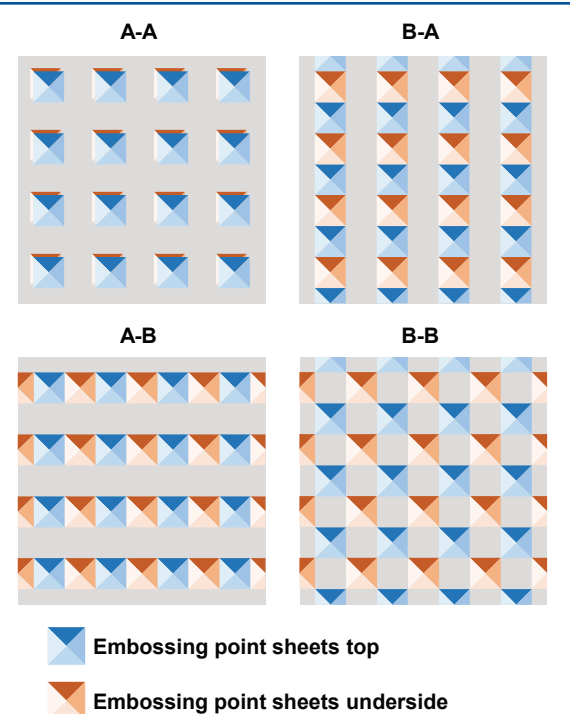


**Figure 12.3** Schematic illustration of the embossing patterns manufactured with embossing process scaled to industrial manufacturing.

## 12.3 Mechanical Material Behavior of Embossed Flux Barriers

### 12.3.1 Embossed Flux Barriers under Tensile Load

To emphasize the advantages of the alternative magnetic flux barrier design, the mechanical behavior of embossed and cut flux barriers are compared using tensile tests. The t-bone samples have a width of 20 mm and length of 250 mm [9]. The quadratic flux barrier has a size of  $10 \text{ mm} \times 10 \text{ mm}$  and is in the sample's center. The sample contour and the conventional flux barrier are laser cut. The embossed flux barrier is embossed sequentially with 100 pyramidal embossing points. The strain-force curves are evaluated as the sample's cross-section of the cut flux barrier is not constant. Strain is examined with an optical measurement system.

In figure 12.4, the strain-force curves of the reference sample and the samples with embossed and

cut flux barriers are displayed. Three samples are compared for each configuration, and the mean curve and derivation are plotted.

Due to its reduced cross-section, the samples with cut flux barrier reach a higher strain at lower forces, and plastic behavior appears at low loads. The embossed sample shows a similar behavior compared to the reference. The cross-section is constant, and the embossing process results in strain hardening in the area of the flux barrier. Consequently, the elasticity of the embossed material is reduced, and the elastic deformation concentrates on the unembossed material volume. In the enlarged sector in figure 12.4, it can be remarked that the elastic behavior of the embossed sample ends at approximately 2.000 N whereas the reference sample shows up to 2.500 N the linearity of an elastic curve. Because of strain hardening in the embossed material volume, higher loads are necessary for the plastic deformation of the embossed material volume.

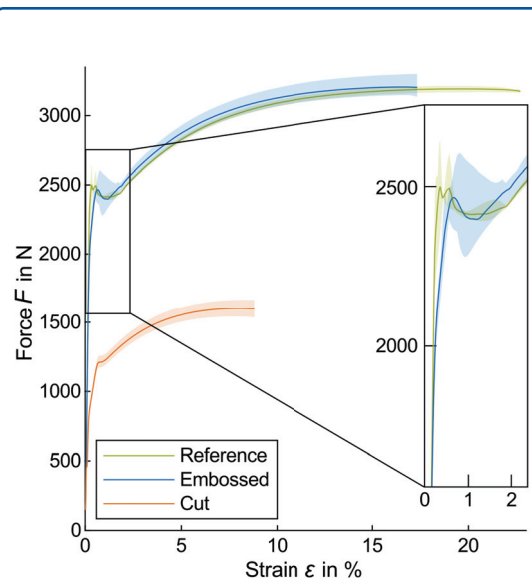


**Figure 12.4** Mechanical behavior under tensile strain of embossed and cut flux barriers compared to an unworked reference sample. [10]

This shows that the mechanical strength of the sample is strongly reduced by the cutout. Plastic deformation starts at a load of 36 % compared to the reference sample. The embossing leads to strain hardening in the embossed material volume, which affects the elastic and plastic deformation of the sample. [10]

### 12.3.2 Embossing Induced Residual Stresses

Embossed flux barriers are based on the Villari Effect, which describes that increased mechanical stresses lead to reduced magnetizability. Therefore, the residual stress distribution evaluation is essential to show the functionality of embossed flux barriers. The numerical analysis and the experimental approach with nanoindentation are applied to examine the residual stress distribution.

Nanoindentation is a tool to evaluate hardness and residual stresses by indenting the sample on a micro or nano scale using the principle of hardness tests. The detected indentation curves – depth to force – can be compared to reference curves of an unworked reference sample. A high number of

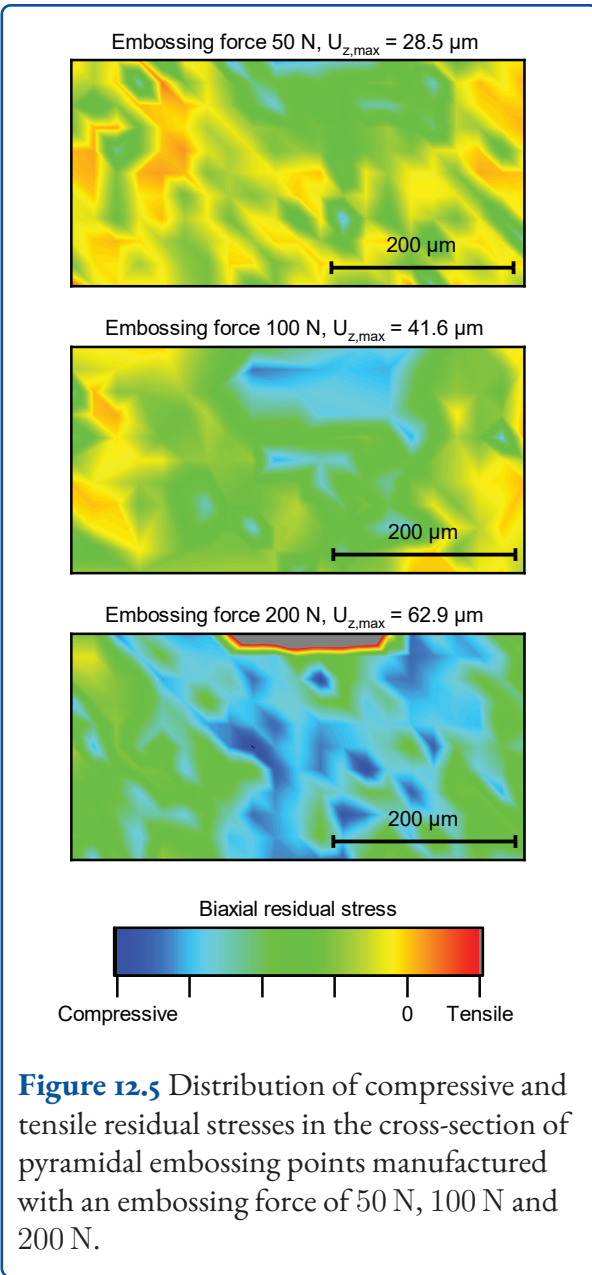
nanoindents is necessary to evaluate a residual stress distribution. Consequently, only a very local evaluation in the cross-section of the sample is possible [11].

Figure 12.5 shows the distributions of tensile and compressive residual stresses in the cross-section of pyramidal embossing points which are manufactured with an embossing force of 50 N, 100 N and 200 N. The evaluated embossing point is located in a line of embossing points manufactured according to figure 12.2. The different embossing forces result in an embossing depth of 28.5 µm, 41.6 µm and 62.9 µm in the electrical steel with a thickness of 0.35 mm. To analyze the residual stress distribution, the sample's cross section is polished, and a grid of nanoindents is performed with a distance of 25 µm. Referencing indents are made in unworked polished material to evaluate the residual stress distribution.

The experimental analyzed residual stress distributions show that compressive residual stresses are concentrated directly below the embossing point. Left and right of the embossing point – hence between the single embossing points – there are almost no residual stresses for the embossing forces 50 N and 100 N. For 200 N, compressive residual stresses dominate between the embossing points. Generally, higher embossing forces – hence increased deformation – result in higher compressive residual stresses below the embossing point.

As the experimental evaluation of residual stress distribution requires complex experiments, Finite Element Analysis (FEA) is preferable for comparing different embossing strategies. According to the nanoindentation results, the line of pyramidal embossing with two different embossing forces is simulated. The residual stresses are evaluated as hydrostatic stresses and averaged over the sheet thickness; see figure 12.6.

Because of the sequential embossing process (figure 12.2), the residual stresses vary in each embossing point and along the whole embossing line. The higher embossing force – 200 N – leads to a larger difference between compressive and tensile residual stresses along the embossing line compared to



**Figure 12.5** Distribution of compressive and tensile residual stresses in the cross-section of pyramidal embossing points manufactured with an embossing force of 50 N, 100 N and 200 N.

the embossings with 100 N. Additionally, the area with increased residual stresses enlarges with higher embossing forces. The results are described in detail in [6].

The residual stress distributions of embossed flux barriers can be evaluated numerically and with nanoindentation. Additionally, the residual stresses can be qualified indirectly by measuring the change in magnetic material properties originating from the residual stresses through the Villari Effect. Therefore different embossing strategies – embossing process, pattern, and force – are systematically

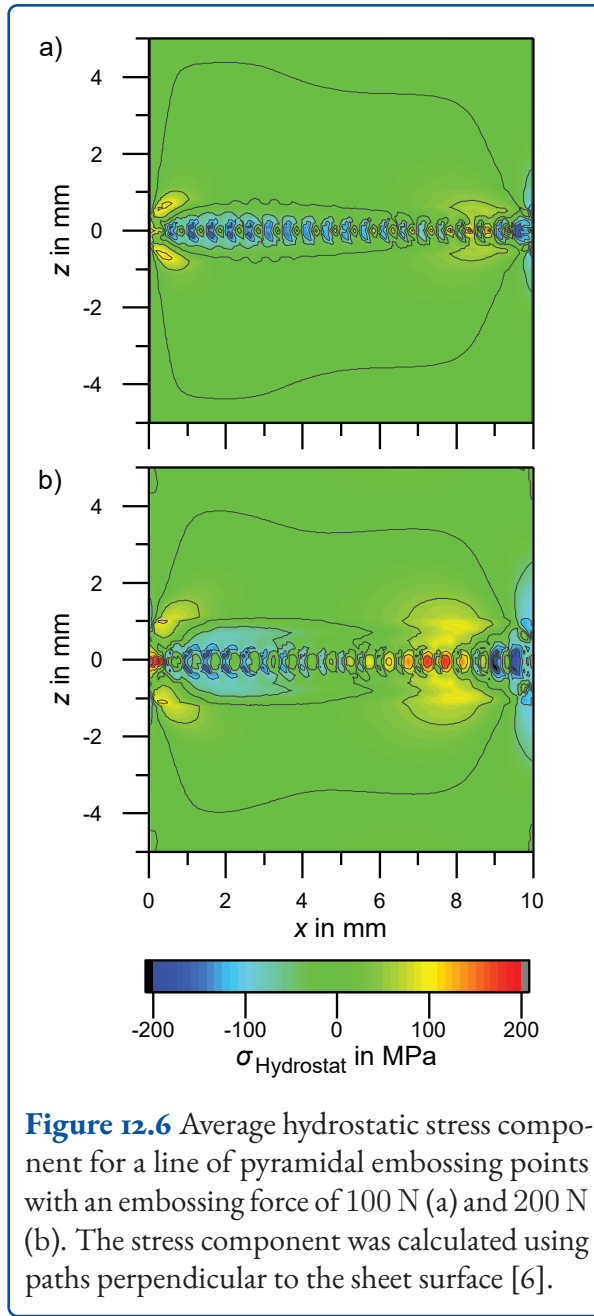


**Figure 12.6** Average hydrostatic stress component for a line of pyramidal embossing points with an embossing force of 100 N (a) and 200 N (b). The stress component was calculated using paths perpendicular to the sheet surface [6].

compared by the measured magnetic permeability or the magnetic domain distribution.

## 12.4 Advances in the Characterization and Simulation of Magneto-mechanical Coupling

Conventional measuring systems for characterizing the magneto-mechanical coupling of electrical

steel allow measurement either only in a limited range of mechanical stresses or only unidirectionally, which means that the combinations of magnetization and voltage that occur are only displayed to a very limited extent. While SST topologies expanded by a tension-compression unit only allow scalar measurements with parallel main mechanical stress, vectorial systems that allow different orientations suffer from the fact that the maximum stress range is severely restricted ( $\pm 30$  MPa).

As a combination of both conventional measurement methods for the characterization of the magneto-mechanical effect, a novel measurement topology was developed as part of the project. A universal testing machine with a maximum force of 20 kN is used as a loading unit. A rotatable magnetization yoke, which is equipped with a pair of needles for measuring the magnetic flux density ( $B$ ) and an H-coil for determining the magnetic field strength ( $H$ ) in the vicinity of the sample serve as the magnetic measuring system. The sample itself is held by a support frame, which prevents the sample from bending under compressive loads and thus enables a significant extension of the measuring range of up to  $-70$  MPa. The measurement setup allows a vector hysteresis sensor to be pressed on the opposite side of the magnetization yoke in order to record the magnetic field quantities magnetic flux density  $B$  and magnetic field  $H$  vectorially.

The measurements on the developed measuring stand have revealed a significant influence of the angle between magnetization and the mechanical main stress direction  $\gamma_{\sigma,B}$ . To transfer this observed material behavior to magneto-mechanical FEA of electrical steel in general and rotating electrical machines in particular, a magnetization model is necessary. For this purpose, the measurements are processed to guarantee convergence of the FEA. Magnetic flux density  $B$  is first considered as a function of magnetic strength  $H$ , mechanical stresses  $\sigma$  and set angle  $\gamma_{\sigma,B}$ . After setting up and homogenizing the system matrix, the system matrix is transformed:

$$\nu = f(B^2, \sigma, \gamma_{\sigma,B}) \quad (\text{Equation 12.1})$$

so that reluctance  $\nu$  serves as the input variable for the FEA model. Due to the needle probes, it is



**Figure 12.7** Developed sensor with loading unit, support frame and vector hysteresis sensor for vectorial characterization of magneto-mechanical effect at high mechanical stress.

possible, in contrast to the first prototype built, to apply sinusoidal curves of the magnetic flux density using the control unit. It is now also possible to use the measured iron losses to parametrize an iron loss model. The parameters of the IEM core loss model  $x_k$ , which enables the core losses to be separated into different phenomenological effects, are identified as a function of existing mechanical stresses  $\sigma$  and angle  $\gamma_{\sigma,B}$ . Thus, in the post-processing of the magneto-mechanical FEA, conclusions can be drawn about the effects of the mechanical stresses introduced by embossing on the efficiency of the drive.

## 12.5 Analysis of the Local Magnetic Properties in the Bulk of the Material

The interaction of the magnetic moment of neutrons with the magnetic domain structure in non grain-oriented electrical steel gives rise to scattering

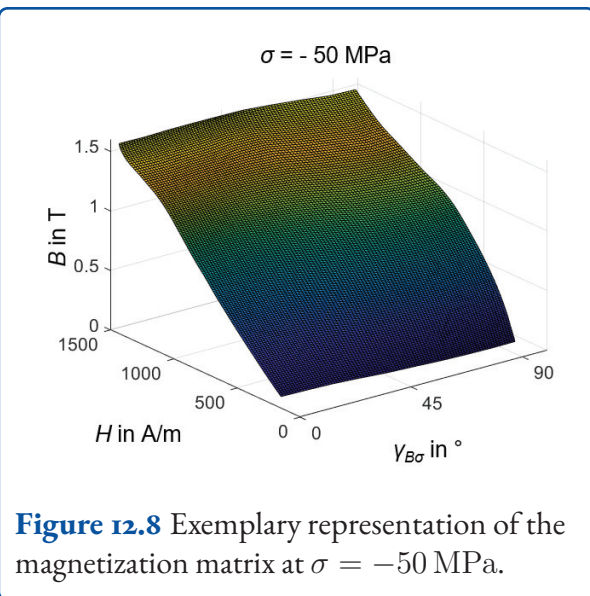


**Figure 12.8** Exemplary representation of the magnetization matrix at  $\sigma = -50 \text{ MPa}$ .

of neutrons at ultra small angles (ultra small angle neutron scattering (USANS)). Neutron grating interferometry (nGI) is an advanced neutron imaging technique relying on a micrometer-sized intensity modulation of the neutron beam to detect neutrons scattered by USANS. Changes in this modulation originating from USANS are measured spatially resolved in the dark-field image (DFI) of a neutron grating interferometer [13]. The DFI signal in each detector pixel is dependent on the average magnetic structure size present along the neutron beam path through the electrical steel sheet in the area covered by this pixel. The magnetic domain structure size changes depending on the local state of magnetization, with higher magnetization states resulting in overall larger domain structures compared to states of lower magnetization. This enables us to judge the spatial distribution of the magnetization state in electrical steel and therefore gain qualitative knowledge of the local magnetic flux distribution across the sample.

### 12.5.1 Upgrade of the Neutron Grating Interferometer

The intensity modulation used to resolve USANS in nGI is commonly generated by the interference pattern of three gratings of a Talbot-Lau type interferometer: a source grating  $G_0$  ensuring the spatial coherence of the beam, a phase grating  $G_1$  and

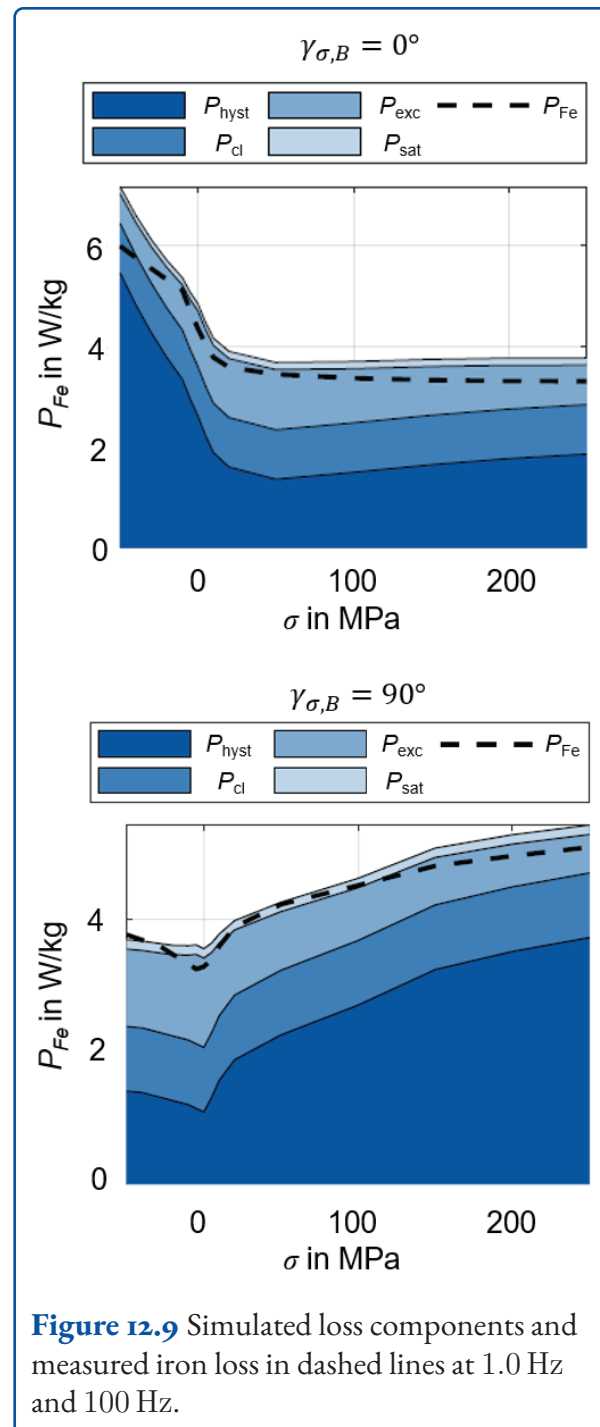


**Figure 12.9** Simulated loss components and measured iron loss in dashed lines at 1.0 Hz and 100 Hz.

an analyzer grating  $G_2$ , where source and analyzer gratings are binary absorption gratings. The quality of this stripe-pattern modulation is quantified by the ratio of the change in intensity between dark and bright stripes to the mean intensity; this ratio is referred to as the visibility of the setup and is represented as a number between 0 and 1. The signal-to-noise ratio of the DFI signal is strongly dependent on visibility. By adapting a grating man-

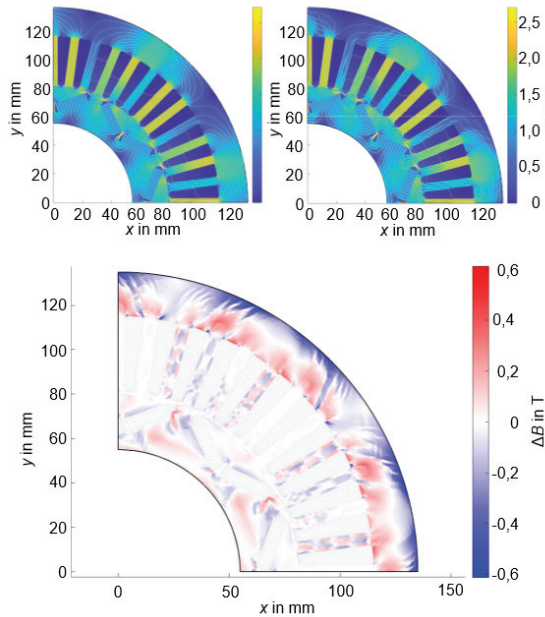


**Figure 12.10** Simulation of a PMSM with shrunk stator at 5000 rpm and 200 Nm without consideration of magneto-mechanical effect (top left), a vectorial magneto-mechanical magnetization model (top right) and resulting difference in flux density (bottom) [12].

ufacturing technique used in X-ray grating interferometry to nGI [14] and redesigning the parameters of the setup, unprecedented visibility of 0.74 was achieved [15]. Figure 12.11 shows the simulated and measured visibility over the neutron wavelength of two configurations of the new interferometer (blue, orange) compared to the previous setup (green). The excellent performance of the new setup enabled the measurements shown in the following.

### 12.5.2 Influence of Residual Stresses on DFI

It was possible to separate the influence of residual stress states from embossing on the DFI signal by normalizing the signal of an embossed sample to a non-embossed reference sample for each pixel. This results in a relative signal indicating an increase (decrease) in domain structure size by embossing if it is greater (less) than 1 and eliminates potential contributions of scattering by other structures. Figure 12.12 a shows the normalized DFI signal of

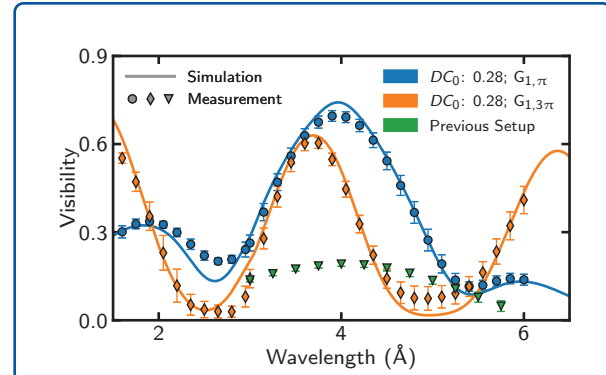


**Figure 12.11** Comparison of simulation to measured visibility [15].

a sample embossed with a spherical punch while applying an external magnetic field of 3.330 A/m. The red ring marks the diameter of the spherical punch and the position of the embossing. The embossed area shows significantly decreased normalized DFI, indicating lower states of magnetization in the embossed sample compared to the non-embossed reference. This was shown to be a direct result of the residual stress states by comparing to an identically embossed and annealed sample shown in figure 12.12 b. The embossing is again marked with a red circle and a slight change in normalized DFI can be observed in the embossed area. However the entire large surrounding area is now in a state of magnetization comparable to the reference sample. This shows that the change DFI signal is indeed originating from residual stress states in the electrical steel sheet.

### 12.5.3 Determination of Optimal Embossing Punch Shape

To determine the ideal shape of the embossing punch, several options were compared using DFI. Figure 12.13 a shows the resulting normalized DFI signal for embossing with spherical (A), cone-shaped (B), and cylindrical (C) punch at an external magnetic field of 3.330 A/m. This DFI signal was averaged azimuthally, shown in figure 12.13b. This indicates a similar maximum reduction in DFI for the spherical and cone-shaped punch but a larger area of influence for the spherical punch. The cylind-

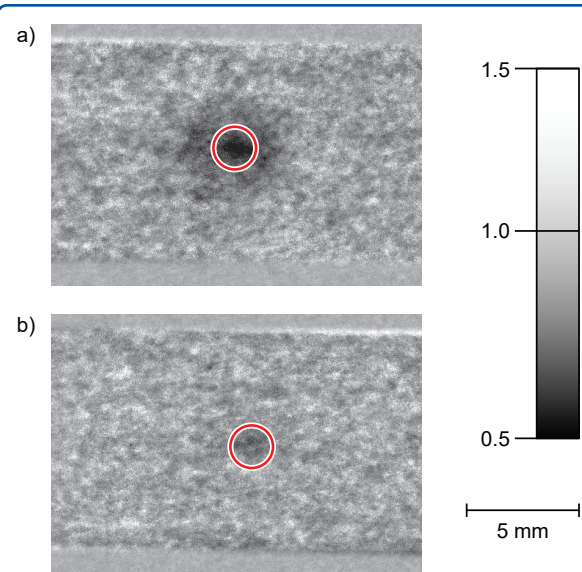


**Figure 12.12** Comparison of (a) an electrical steel sheet and (b) an annealed electrical steel sheet in an applied magnetic field of  $3.330 \text{ A/m}$  [5].

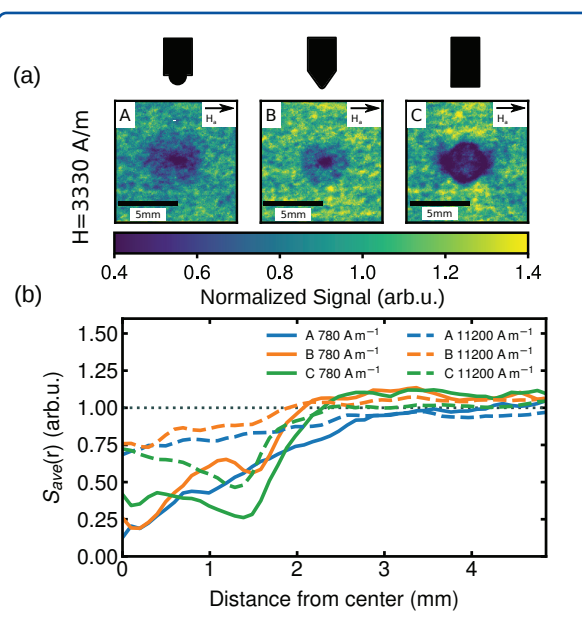


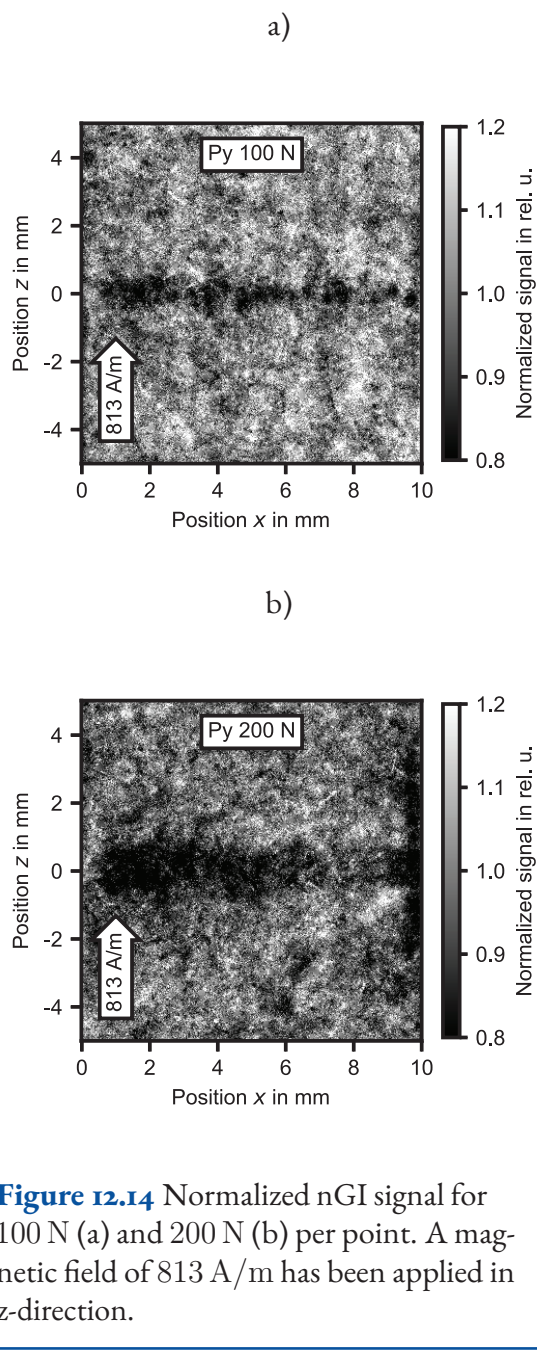
**Figure 12.13** Analysis of the influence of different embossing shapes on the scattering contrast [15].

drical punch has a strong reduction, albeit not as strong as the others, on the edge of the punch, leveling off toward the center. This shows that pointed punches are beneficial compared to large flat areas to achieve high degradation of the local magnetic

properties while minimizing the effect on adjacent non-embossed regions.

#### 12.5.4 Validation of Mechanical Simulations

The data presented in figure 12.13 indicates that it is beneficial to perform multiple small embossings with sharp-edged punches to form magnetic flux barriers. Consequently, the area of steel affected by the embossing can be controlled and high degradation of the magnetic properties is achieved. Barriers were therefore manufactured by sequential embossing using a pyramidal punch as shown in figure 12.2. This process was simulated and performed for different embossing forces. The average hydrostatic stress component taken from simulations is shown in figure 12.6 and shows strong variations perpendicular as well as parallel to the embossing line between compressive and tensile stress states. As compressive stress states show significantly higher degradation of magnetic properties compared to tensile stress states of a similar level [16], the spatial distribution of compressive stresses can be seen in the DFI map of sequentially embossed steel sheets, as shown in figures 12.14 a and 12.14 b for 100 N and 200 N, respectively. At  $x = 0 \text{ mm}$  to  $x = 0.5 \text{ mm}$  a small stripe of tensile stresses in  $z$ -direction is present which is matched by a high normalized DFI signal, followed in  $x$ -direction by low normalized DFI originating from a large area with compressive stress. The higher embossing force in figure 12.14 b results in a larger area being affected in  $z$ -direction as well as lower DFI compared to the lower force in figure 12.14 a. The stress states change from compressive to tensile in the range of  $x = 6 \text{ mm}$  to  $9 \text{ mm}$  for both forces accompanied by higher normalized DFI values. Above  $x = 9 \text{ mm}$  an area of compressive stresses elongated in  $z$ -direction is present and especially pronounced for 200 N, resulting in a reduction of normalized DFI signal. The local change in DFI signal originating from changes in the magnetic properties due to residual stresses matches the simulations of the stress state due to the manufacturing process very well. We, therefore, conclude that the simulations accurately depict the stress state in the material and that nGI is very well



suited to map even complex distributions of magnetization states influenced by residual stress.

## 12.6 Results

### 12.6.1 Repeatable Results

The decisive criterion concerning the usability of residual stress-based flux barriers is the reproducibil-

ity of the embossing process and the stability of their effectiveness during operation. Extensive studies were carried out to examine the two criteria mentioned as part of the second project phase. A circular section was cut out of a sample to ensure reproducibility and enable comparison between conventional and stress-based flux barriers. The comparison samples provided the same area with sequentially executed embossing points. The embossing force was varied between 50, 100 and 200 N. The embossing with 100 N was carried out five times to examine the reproducibility of the process. An unprocessed reference sample of the same geometry is compared to the conventional cutout and the flux barriers embossed with different forces. As can be seen from figure 12.15, the residual stress-based flux barriers already have an effect comparable to that of the cutout sample on the magnetizability of the sample at an embossing force of 50 N. With increasing embossing force, the residual stress-based flux barriers show a greater reduction in  $\mu_r$  than the cut barrier. Although the identically designed samples with an embossing force of 100 N show slight deviations in the area of low magnetization, in the overall picture the deviations are negligibly small so that sufficient stability of the flux barriers can be stated. [8]

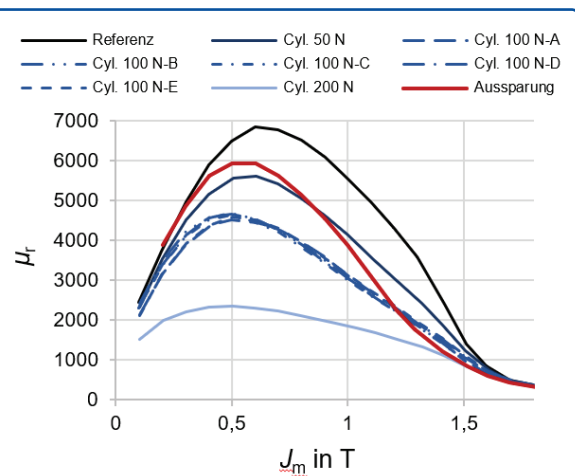


**Figure 12.15** Relative permeability  $\mu_r$  of sequentially executed circular embossing geometries against an unprocessed reference sample and cutout circle at 50 Hz [8].

### 12.6.2 Magnetic Flux Guidance

In chapter 12.6.1 the influence of embossing on the magnetic behavior of the electrical steel is shown. To validate the functionality of embossings as magnetic flux barriers the magnetic flux guidance was evaluated. The magnetic flux barriers lead to a concentration of magnetic flux, indicated by a normalized DFI signal greater than 1 above and below the barrier (areas 3 and 4), see figure 12.16. The flux concentration is stronger for the cutout (area 3) compared to the embossed flux barrier (area 4). This is to be expected, as while the local magnetic permeability in the embossed barrier is strongly reduced due to the Villari effect, it is still higher than the permeability of air. Area 1 exhibits high normalized DFI signal due to missing sheet material, whereas area 2 shows low normalized DFI because of the deteriorated magnetic properties from embossing with multiple small punches. The flux guidance with large embossing points is shown in [4, 5].

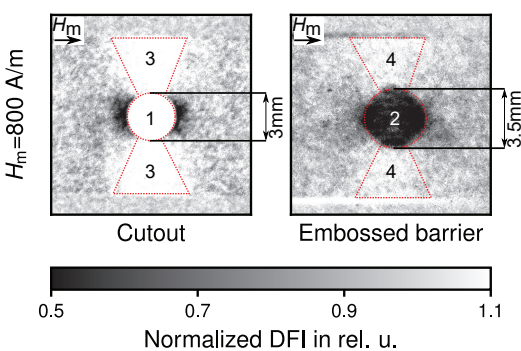


**Figure 12.16** Comparison of magnetic flux distribution using cutout and embossed flux barrier under magnetic field of  $H_m = 800 \text{ Am}^{-1}$  [8].

### 12.6.3 Embossing Patterns and Embossing Force

Using the new die-based embossing device, samples were embossed from the top and bottom in various patterns. The magnetic permeability of samples embossed with patterns A-A and B-A (figure 12.3) with varying embossing forces are presented exemplarily in figure 12.17. Both graphs show the ex-

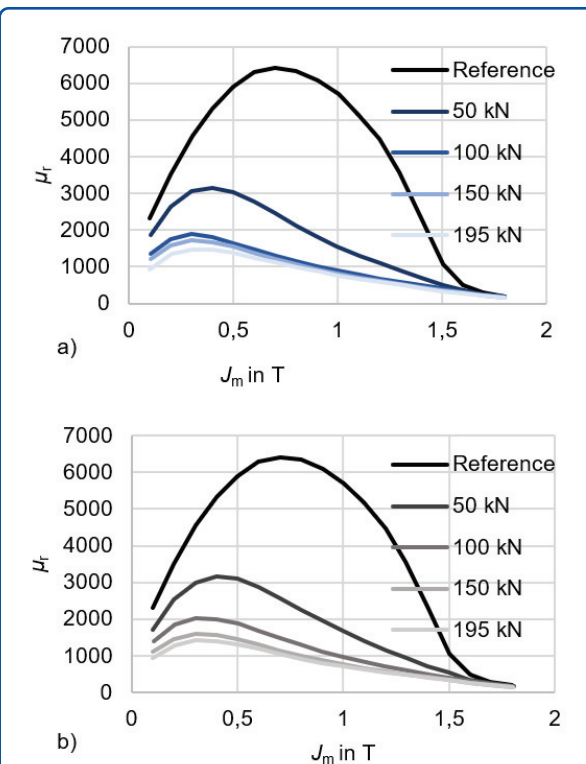


**Figure 12.17** Measurement results of embossed sheets with embossing patterns A-A (a) and B-A (b).

cellent controllability of the magneto-mechanical flux displacement through the respective embossing forces and the resulting residual stresses in the material. Compared to the unembossed reference sample shown in black in both figures, a significant reduction in the relative permeability  $\mu_r$  of up to 87 % can be seen for the offset embossing pattern B-A.

For a better comparison of different embossing patterns and their effect on relative magnetic permeability, the impact of the embossing patterns on magnetizability at an embossing force of 150 kN is presented in figure 12.18. The blue curve of the sample embossed from above and below in the same position (sample A-A) shows the highest relative magnetic permeability ( $\mu_r(J_m)$ ). In comparison, the pattern A-B has the lowest relative permeability due to the offset of the embossing points orthogonally to the direction of magnetization. Especially concerning the stackability of the electrical laminations, the offset pattern B-B is assumably best

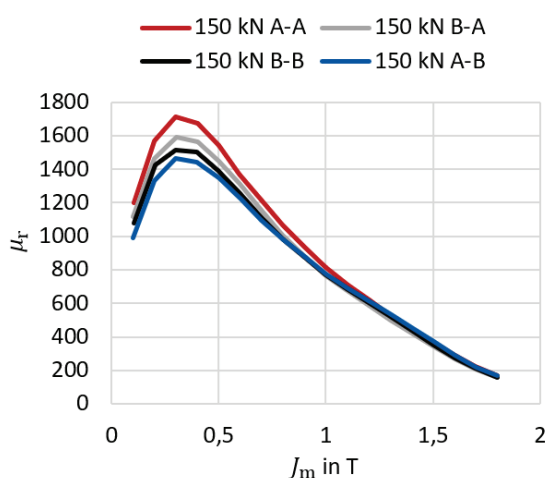


**Figure 12.18** Comparison of the four different embossing patterns with an embossing force of 150 kN.

because of minimum warping and almost the highest reduction magnetic of magnetic permeability. This version of the embossing process is the method of choice for building direction-independent flux barriers with symmetrical embossing patterns.

Another point of interest is the difference between the two anisotropic embossing strategies. The sample with the embossing lines (A-B) aligned orthogonally to the magnetization direction has the lowest magnetic permeability of all four embossing patterns examined. In comparison, the permeability of the sample with embossed lines (B-A) aligned parallel to the direction of magnetization is less reduced but can still be considered superior to the sample embossed with pattern A-A in terms of its effectiveness as a flux barrier.

These results demonstrate the possibility of inducing some form of magnetic anisotropy in the residual stress-based flux barriers using specific embossing patterns. Adjusted process parameters such as line spacing, embossing dot density, and embossing force create further exciting possibilities for using residual stress-based flux barriers in certain areas of the magnetic circuit of rotating electrical machines. Other embossing patterns are shown in [8].

#### 12.6.4 Residual Stress Distribution and Magnetic Behavior under Tensile Load

Since the rotors of electrical machines are exposed to considerable centrifugal forces with increasing speeds, the residual stress's stability and effectiveness over a wide range of tensile stresses must be guaranteed. For this purpose, an unembossed reference sample, an embossed flux barrier, and a homogeneously embossed sample were subjected to different tensile loads and characterized numerically and magnetically.

In figure 12.19, the consequences of tensile load on the residual stress distribution of an embossed flux barrier are shown. The key parameters are the hydrostatic  $\sigma_{\text{hydrostatic}}$  and normal stresses  $\sigma_{11}$  in the direction of magnetization averaged in the direction of sheet thickness. Additionally, nGI measurements were performed during in-situ tensile loading of embossed magnetic flux barriers to verify the spatial distribution of the residual stress states.

In general, the hydrostatic tensile stresses increases due to tensile load. The high compressive stresses close to the embossing points remains. Hence the functionality of the flux barrier is given. A tensile stress concentration is detected in the unembossed area when the normal stress value  $\sigma_{11}$  is examined. Hence, the tensile load results in a high magnetic material deterioration of the areas without embossing. This effect will be stronger for samples with conventional magnetic flux barriers because the smaller cross-section is under the same load. [10]

Single-sheet-tests are performed on unembossed and homogeneously embossed samples to evaluate the effect on the magnetic properties. In this case, relative permeability  $\mu_r$  is the comparison criterion. Figure 12.20 shows that the relative permeability  $\mu_r$  of the homogeneously embossed sample decreases less with increasing mechanical tensile stresses than the reference sample. However, the measured permeability is below the reference sample at every tested mechanical tensile stresses  $\sigma$ .

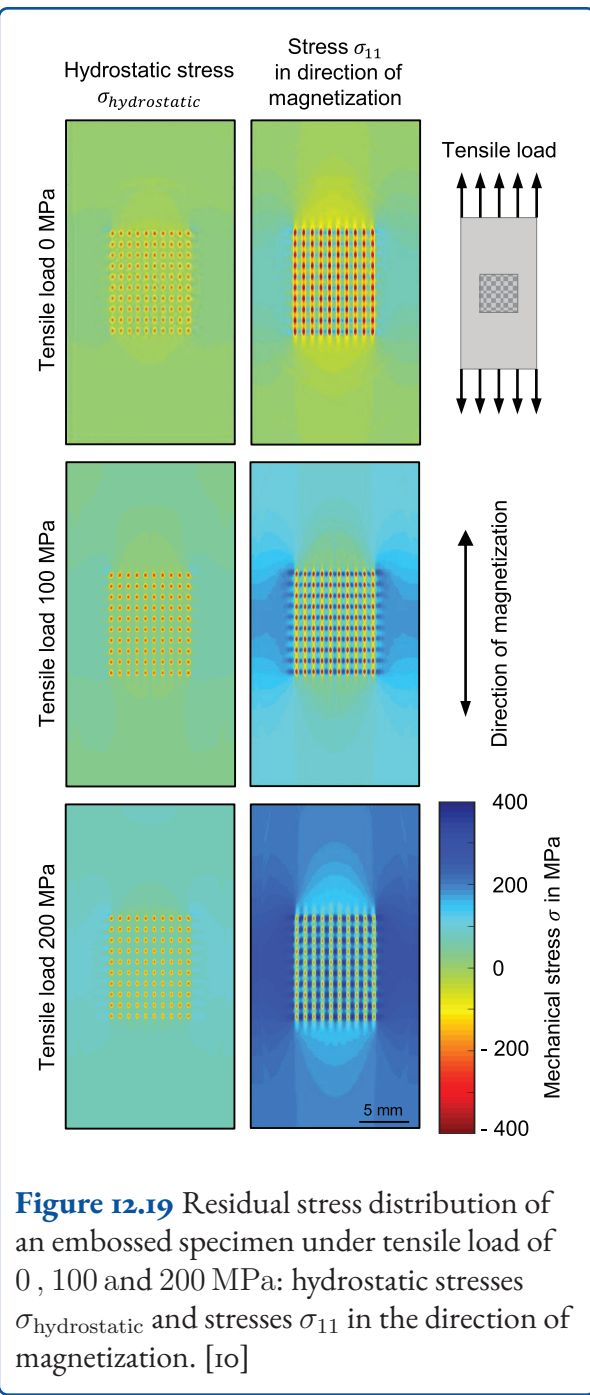


**Figure 12.19** Residual stress distribution of an embossed specimen under tensile load of 0, 100 and 200 MPa: hydrostatic stresses  $\sigma_{\text{hydrostatic}}$  and stresses  $\sigma_{11}$  in the direction of magnetization. [10]

These results are in good agreement with the DFI data. By selecting and averaging over distinct areas of the DFI map the difference in magnetization state due to increasing tensile load and applied field for non-embossed and embossed regions can be shown, see figure 12.21 a. The resulting magnetization curves show an apparent decrease in DFI with increasing tensile load, especially for low magnetic field (figure 12.21 b). However, the magnetization state of the embossed barrier (blue) is lower than

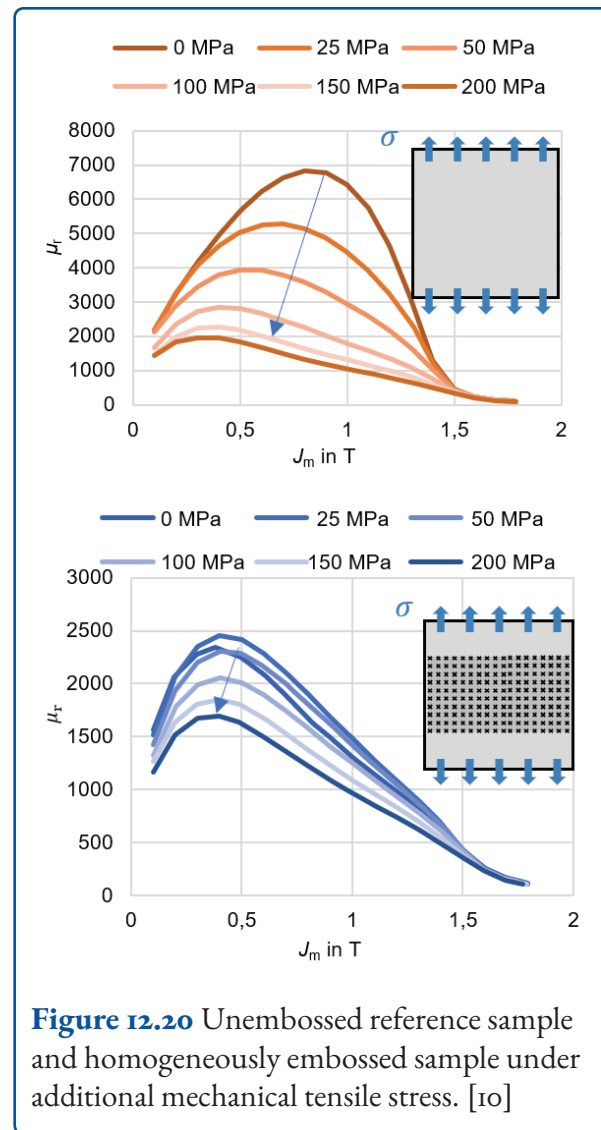


**Figure 12.20** Unembossed reference sample and homogeneously embossed sample under additional mechanical tensile stress. [10]

the non-embossed region (grey) for every given tensile load. To sum up, mechanical tensile loads, such as those that arise due to the centrifugal forces during operation in the rotor lamination stack, do not reduce the effectiveness of the residual stress-based flux barriers but rather increase them. [10]

## 12.7 Summary

In the project, embossing-induced residual flux guidance was analyzed to enhance the energy efficiency of electric drives. The results show that the principle of magnetic flux guidance with embossing-induced residual stresses works. The embossing of electrical steel leads to a change in residual stresses, and the residual stress distribu-

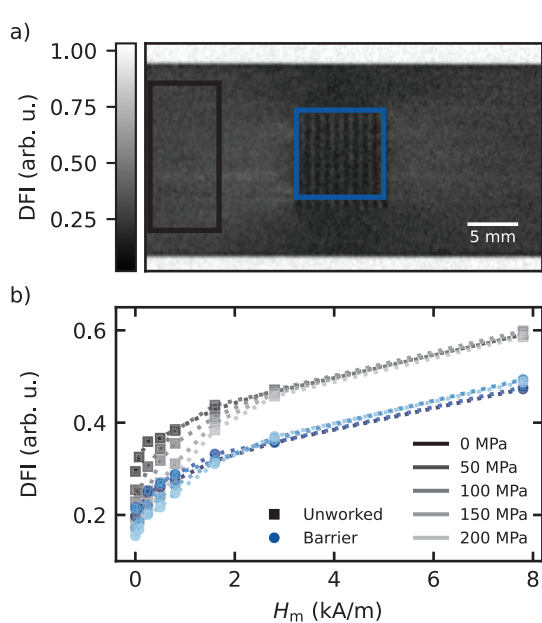


**Figure 12.21** Influence of tensile loading on the DFI signal of embossed flux barriers.

tion can be adjusted by embossing parameters. The residual stresses were evaluated numerically with finite element analysis and experimentally with nanoindentation tests. Succeeding the sample production, the impact of embossing-induced residual stresses on the magnetic material properties was evaluated. Single sheet tests measure the magnetic permeability, which is reduced for embossed electrical steel. Variations of embossing patterns – the distance between and number of embossing points – and the embossing force reduce the magnetic permeability differently. Additional to the measurements of global magnetic material properties, local measurements with neutron grating interferometry and vector-hysteresis measurements were performed. The dark field images validated the local deterioration of magnetic material properties and the magnetic flux guidance. With vector hysteresis, the path of the magnetic flux was visualized. Based on these results, the functionality of embossed magnetic flux barriers is validated, and the process and measurement procedures were optimized.

The research in the DFG priority program focused on the fundamental analysis of embossed magnetic flux barriers. The first evaluations of the applicabil-

ity in electric drives were made, such as the behavior of embossed electrical steel under tensile strain, which was used to model the centrifugal forces acting on the rotor of an electric drive. The industrial manufacturing process with a stamping tool also produces wear on the embossing geometry. The change in the tool geometry varies only on a small scale in the residual stress distribution. To enable the application of embossed magnetic flux barriers in industrially produced electric drives, further research in cooperation with industry is necessary.

## Abbreviations

$B$	magnetic flux density
DFG	German Research Foundation
DFI	dark-field image
FEA	Finite Element Analysis
$\gamma_{\sigma,B}$	angle between magnetization and mechanical main stress direction
$G_0$	source grating
$G_1$	phase grating
$G_2$	analyzer grating
$H$	magnetic field strength
IEM	Institute of Electrical Machines
MLZ	Heinz Maier-Leibnitz Zentrum
$\mu$	magnetic permeability
$\mu_r$	relative magnetic permeability
nGI	neutron grating interferometry
NGOES	non-grain-oriented electrical steel
PMSM	permanent magnet synchronous machines
$\sigma$	mechanical stress
$\sigma_{11}$	normal stress in direction of magnetization
$\sigma_{\text{hydrostatic}}$	hydrostatic stress
SynRM	synchronous reluctance machines
SST	single-sheet-testing
USANS	ultra small angle neutron scattering
utg	Chair of Metal Forming and Casting
$x_k$	core loss model

## References

---

- [1] Richard M Bozorth. *Ferromagnetism*. 1993.
- [2] Nora Leuning, Simon Steentjes, and Kay Hameyer. "Effect of magnetic anisotropy on Villari Effect in non-oriented FeSi electrical steel". In: *International Journal of Applied Electromagnetics and Mechanics* 55.S1 (2017), pp. 23–31.
- [3] Hartmut Hoffmann, Reimund Neugebauer, and Günter Spur. *Handbuch Umformen*. [2., vollständig neu bearbeitete Auflage]. Edition: Handbuch der Fertigungstechnik. München: Hanser, 2012. ISBN: 9783446430044.
- [4] I. Gilch et al. "Analysis of Cylindrically and Spherically Embossed Flux Barriers in Non-oriented Electrical Steel". In: *The Minerals, Metals & Materials Series* (2021). DOI: 10.1007/978-3-030-75381-8\_193.
- [5] S. Vogt et al. "Extent of embossing-related residual stress on the magnetic properties evaluated using neutron grating interferometry and single sheet test". In: *Production Engineering* 13.2 (2019), pp. 211–217. DOI: 10.1007/s11740-018-0863-7.
- [6] I. Gilch et al. "Impact of residual stress evoked by pyramidal embossing on the magnetic material properties of non-oriented electrical steel". In: *Archive of Applied Mechanics* 91.8 (2021), pp. 3513–3526. DOI: 10.1007/s00419-021-01912-6.
- [7] I. Gilch et al. "Influence of pyramidal and spherical embossing on residual stress distribution and magnetic material properties of non-oriented electrical steel". In: *Forming Technology Forum* (2022).
- [8] Benedikt Schauerte et al. "Alternative Magnetflussführung in Elektromotoren". In: *Forschung im Ingenieurwesen* 53.3 (2021), p. 1948. DOI: 10.1007/s10010-021-00493-8.
- [9] DIN Deutsches Institut für Normung e.V. *DIN 50125:2016-12: Prüfung metallischer Werkstoffe - Zugproben*. Berlin.
- [10] I. Gilch et al. "Residual stresses and magnetic material properties of embossed and cut magnetic flux barriers in non-oriented electrical steel under tensile strain". In: *Electric Drive Production Conference* (2023).
- [11] S. Vogt et al. "Method for highly spatially resolved determination of residual stress by using nanoindentation". In: *Production Engineering* 13.2 (2019), pp. 133–138. DOI: 10.1007/s11740-018-0857-5.
- [12] Benedikt Schauerte et al. "Consideration of the spatial orientation of magnetic field quantities and tensile mechanical stress in the Finite Element Analysis of electrical machines". In: *Archives of Electrical Engineering* 71.4 (2022).
- [13] C. Grünzweig et al. "Bulk magnetic domain structures visualized by neutron dark-field imaging". In: *Applied Physics Letters* 93.11 (2008), p. 112504. DOI: 10.1063/1.2975848.
- [14] A. Gutschin et al. "Fabrication of gadolinium particle-based absorption gratings for neutron grating interferometry". In: *Review of Scientific Instruments* 89.10 (2018), p. 103702. DOI: 10.1063/1.5047055.
- [15] Tobias Neuwirth et al. "A high visibility Talbot-Lau neutron grating interferometer to investigate stress-induced magnetic degradation in electrical steel". In: *Scientific Reports* 10.1 (2020), p. 1764. ISSN: 2045-2322. DOI: 10.1038/s41598-020-58504-7.
- [16] N. Leuning et al. "Effect of elastic and plastic tensile mechanical loading on the magnetic properties of NGO electrical steel". In: *Journal of Magnetism and Magnetic Materials* 417 (2016), pp. 42–48. ISSN: 0304-8853. DOI: <https://doi.org/10.1016/j.jmmm.2016.05.049>.

## 13 Targeted Introduction of Residual Stresses through Suitable Forming Processes to Produce Bistable, Metallic, Fully Closed Tube Profiles

Hirt, G.; Pavliuchenko, P.; Ringel, A.

GEPRIS 374688658

### 13.1 Introduction

Bistable structures are mechanical systems or devices characterized by two stable equilibrium states or configurations. These structures are widely used in various applications, particularly in mechanical and electromechanical devices that undergo state transitions. They are also of great importance in the field of deployable structures, offering the possibility of designing mechanisms capable of reliable transitions from their compacted form to the desired operational configuration.

Generally, deployable structures can be monostable, bistable or multistable, depending on whether they have one, two or more stable geometric states. Prominent examples of monostable structures are conventional steel tape measures. However, monostable structures with a cross section angle of more than  $360^\circ$  are also used in space as STEMs (Stored Tubular Extendable Members) [1]. The stable state is the extended state, and for storage and transport (in the rolled-up, unstable state) a housing is required to prevent uncontrolled unfolding (figure 13.1 a). However, this enclosure is typically much heavier and bulkier than the lightweight structure itself, thus contributing to the transport weight and ultimately the transport cost [2, 3]. Unlike monostable structures, bistable structures inherently have two stable states, eliminating the need for a housing and thus reduce the transport weight and volume (figure 13.1 b).

Bistable, fully closed profiles can be used as long support structures that can be coiled into a com-

pact transport geometry and uncoiled on site. This has several potential applications, such as support structures for roll-out photovoltaic modules [4] or portable antenna masts [5]. The volume and weight advantages mentioned above are crucial for space applications, offering improved dimensional stability during launch and a significant reduction in inertia during space manoeuvres [6]. Thus, using bistable, fully closed profiles allows the construction of larger systems such as satellite antennas [7] and the deployment of solar sails [8].

Bistable, fully closed tube profiles made from fiber composites are already on the market. The bistability is not due to residual stresses but to the

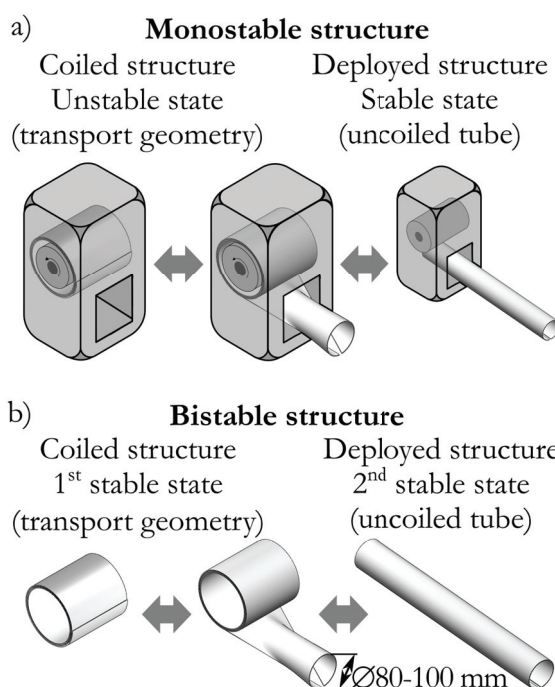


**Figure 13.1** Schematic representation of a monostable tube with housing (a) and a fully closed bistable shell without housing (b) [9].

anisotropic properties of the composite and a special layer structure [10]. The main objective of this research project is to develop a manufacturing process for the targeted introduction of residual stresses during continuous forming of metallic high strength strip materials in order to produce metallic, bistable, fully closed tube profiles.

## 13.2 Bistability in Thin Metal Sheets

Residual stresses can be introduced into the metal sheet by plastic deformation such as bending. In the case of pure bending, there is a linear distribution of strain  $\varepsilon(y)$  across the thickness of the sheet as a function of distance from the neutral axis (figure 13.2 a). Positive strains (tension) occur on the convex side and negative strains (compression) on the concave side. The stress-strain relationship gives the corresponding stress  $\sigma(y)$  curve under load. After the applied load is removed, the spring-back effect takes place, causing the sheet metal to quickly transition to a deformed equilibrium geometry. The residual stress  $\sigma_{res}(y)$  and strain  $\varepsilon_{res}(y)$  after springback is depicted in figure 13.2 b [II].

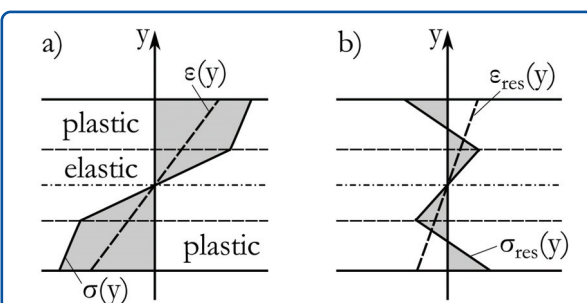


**Figure 13.2** Residual stress due to bending. Stress and strain distribution through the sheet thickness after deformation (a) and after springback (b) [II].

The approach described above could allow the production of monostable tubes (see figure 13.1 a), which are stable only in the unfolded state. Bistability can be reached in a two-step deformation process. Kebadze et al. [3] bent BeCu sheet material into a cylindrical stable structure in a first forming step. A suitable heat treatment removed the existing residual stresses. In a second step, the sheet was

bent in the opposite direction and also perpendicularly to the first bending axis [3, 12]. This forming step is performed at room temperature to maintain the residual stresses, which create the bistable structure with two stable states. To avoid changes in the material properties and simplify the process, the heat treatment has been omitted for steel materials. The residual stress distribution will look as shown in figure 13.3. The stresses in y-axis ( $\sigma_y$ ) are responsible for the first stable state (figure 13.3 a). Since they are comparably large, a small stable radius will result. The rather small stresses in x-axis ( $\sigma_x$ ) of the second stable state produce a larger radius (figure 13.3 b).

Although the basic research into the possibility of producing bistable metal sheets had already been carried out, there was a gap in the knowledge about the influence of different material and manufacturing process parameters on the bistability and on the radii of stable geometries. By knowing the relationship between these parameters and the radii of stable geometries, it is possible to design the manu-

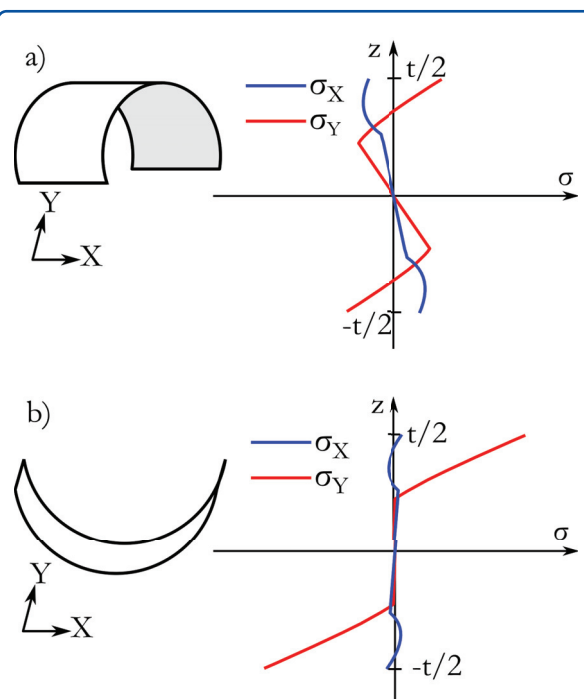


**Figure 13.3** Sheet geometry and distribution of residual stresses along the sheet thickness in the first (a) and second (b) stable states of the bistable sheet [13].

...

**Table 13.1** Material properties

Steel	Young's modulus (GPa)	Yield strength (MPa)	Q	b	C	$\gamma$
1.1274 (1 <sup>st</sup> batch)	208	1689	250	122	30643	122
1.1274 (2 <sup>nd</sup> batch)	212	1810	235	154	36349	154
1.4310	192	908	158	172	27132	172

factoring process to produce bistable, fully closed metal tubes. Consequently, this research deals with various experimental and simulation-based methods used to manufacture those bistable profiles and to investigate the aforementioned relationships.

### 13.3 Materials

Materials with high yield strength and low thickness are used as starting materials for the production of bistable sheets. The level of the yield strength determines the size of the elastic deformation range. The thickness together with the yield strength defines the maximum strain in the sheet surface at a given bending radius [14].

Two main materials were considered for the production of bistable metal tubes: the martensitic spring steel 1.1274 and the austenitic steel 1.4310. Figure 13.4 shows the averaged flow curves from six tensile tests per material or material batch with two samples taken at 0°, 45° and 90° to the rolling direction. Finally, flow curve equations were fitted from the experimental results (see figure 13.4). Since accurate knowledge of Young's modulus and yield strength is essential for predicting residual stresses, tensile tests were also carried out with simultaneous measurement of temperature change. During the tensile test, the specimen temperature decreases in the elastic region (volume increase) and increases in the plastic region (dissipation). By measuring the temperature minimum, the onset of plastic defor-

mation can be determined more accurately. The material property data is given in table 13.1.

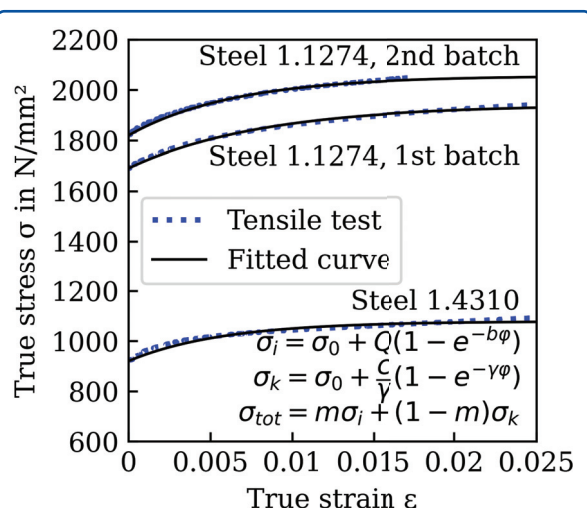


**Figure 13.4** Flow curves and fitted flow curves for the isotropic-kinematic hardening law:  $\sigma_0$  – yield point, Q – maximum change in isotropic yield area, b – rate of change in isotropic yield area, C – kinematic hardening modulus,  $\gamma$  – rate of change in kinematic hardening.

### 13.4 Considered Production Process Strategies

The bistability of a metal sheet can be reached by plastic bending of the sheet around two perpendicular axes in two opposite directions [13]. Initial tests showed that small bending radii were required to induce sufficient plastification in the thin, high-

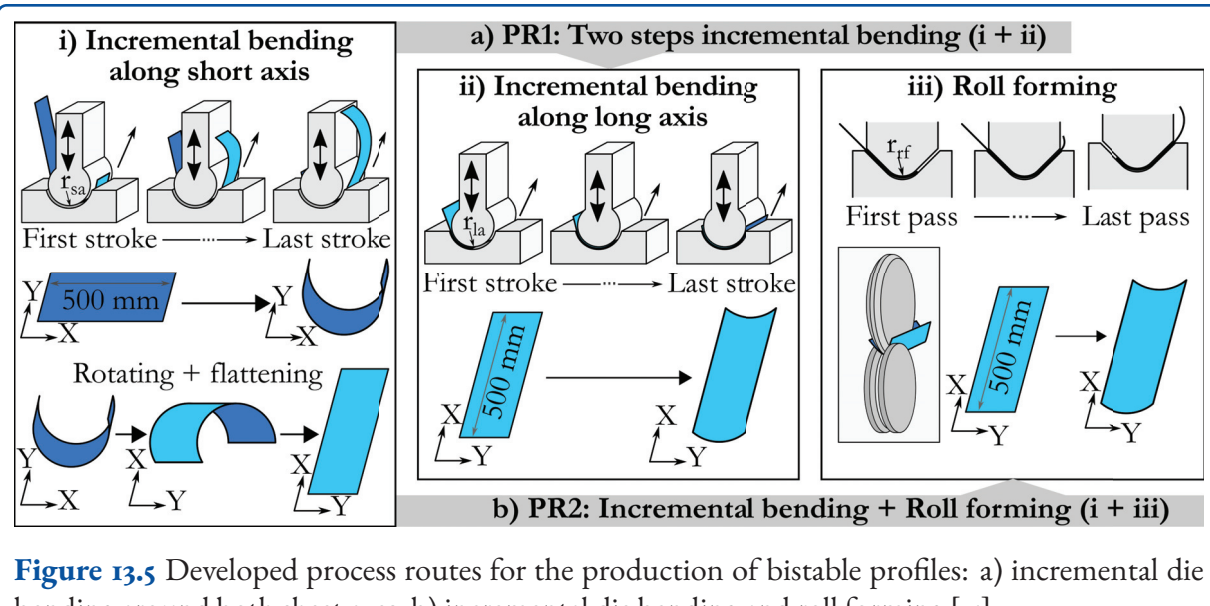


**Figure 13.5** Developed process routes for the production of bistable profiles: a) incremental die bending around both sheet axes, b) incremental die bending and roll forming [15].

strength sheet, making it impossible to bend the sheet into the tube in one step. To overcome this obstacle, early production attempts used an incremental die bending process over small bending radii (see figure 13.5 a). This production process allowed the manufacturing of bistable sheets with a fully closed geometry in one of the stable states [9].

On the other hand, the incremental die bending process is not suitable for the production of bistable tubes of arbitrary and theoretically infinite length, since the maximum length of the tube is limited by the length of the die. Therefore, a process for roll-forming the sheet in the longitudinal direction was established as a second production step after incremental bending in the transverse direction [16]. However, it should also be noted that roll forming of thin, high yield strength sheet metal requires rolls with small forming radii and therefore a large number of roll stands [15].

Therefore, two main production routes are proposed: two-step incremental die bending along two orthogonal axes in two opposite directions (PR<sub>1</sub>, figure 13.5 a) and initial incremental bending along the shorter side of the sheet and subsequent roll forming in orthogonal direction within several passes (PR<sub>2</sub>, figure 13.5 b).

### 13.4.1 Two-step Incremental Bending PR1

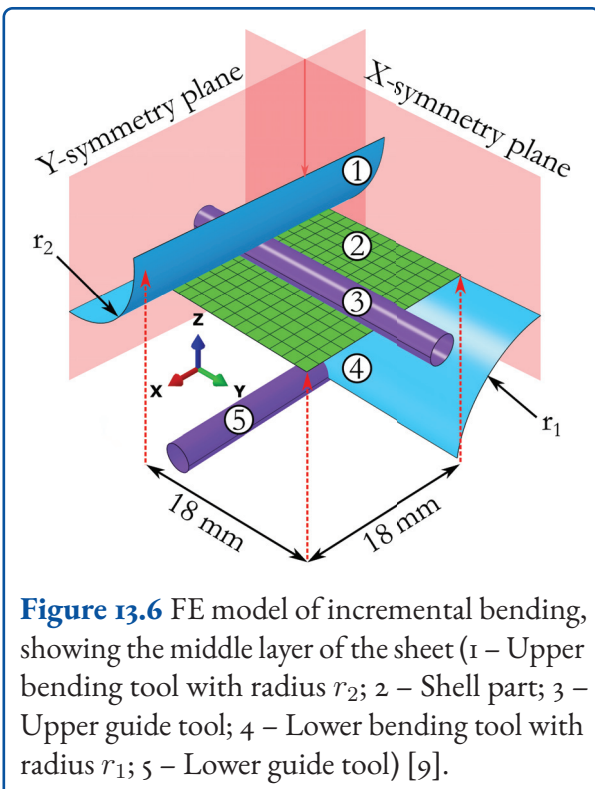
The production of the bistable tubes with the incremental die bending process (see figure 13.5 a) was investigated by numerical simulations, semi-analytical modeling and experimental approaches. With those methods the influences of the production process and of the material properties on the bistability and the radii of stable states was investigated.

#### Numerical Simulations

In order to investigate the influence of bending radii on bistability a three-dimensional FE model was built using Abaqus/CAE software incorporating the material data. The model consists of two bending and two guide tools, reproducing the kinematics of the bending process (see figure 13.6). The model covers the following steps:

- Step 1: Initial state.
- Step 2: The upper guide tool moves downwards and bends the sheet over the lower bending tool of radius  $r_1$  around the y-axis.
- Step 3: After springback and flattening of the shell, the lower guide tool moves upwards and bends the shell in opposite direction around the x-axis over the upper bending tool of radius  $r_2$ .

...



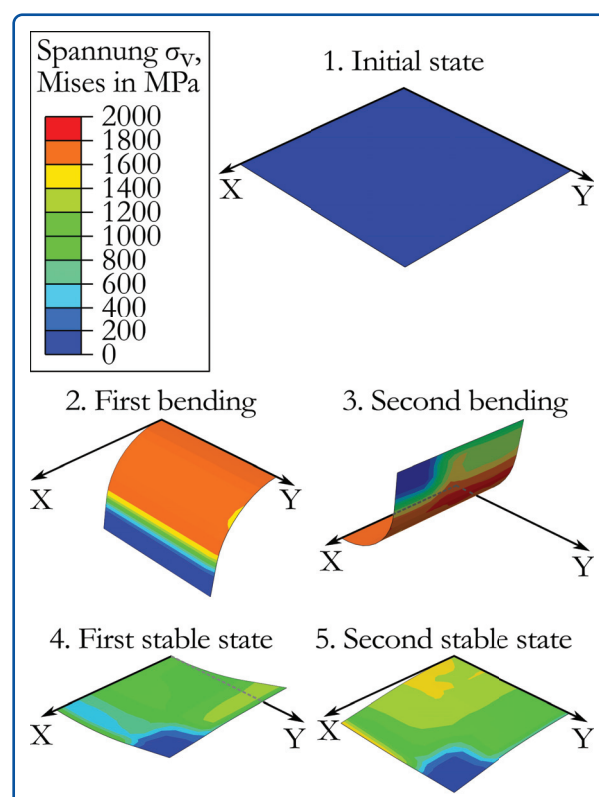
- Step 4: Springback and achievement of the first stable state.
- Step 5: Bending the shell slightly around the y-axis using the upper guide tool with the aim of testing for a second stable state.

The model was used to examine which combinations of bending radii led to a bistable structure. The results (see figure 13.7) of the parameter study show the possibility of producing bistable sheets using a single stroke die bending process [9]. The model showed that it is possible to produce bistable structures with a curvature in the stable states [9]. Thus, a fully closed tubular geometry is theoretically possible.

The single stroke FE model could only be employed to define the parameters leading to bistability. In order to reflect the incremental die bending process in numerical simulations, an improved FE model, which can model the individual die strokes over the length of the sheet was required. The model was created using Abaqus/CAE software and designed to further investigate the influencing process parameters (see figure 13.9 a). The whole simulation process is divided into the following steps (fig-

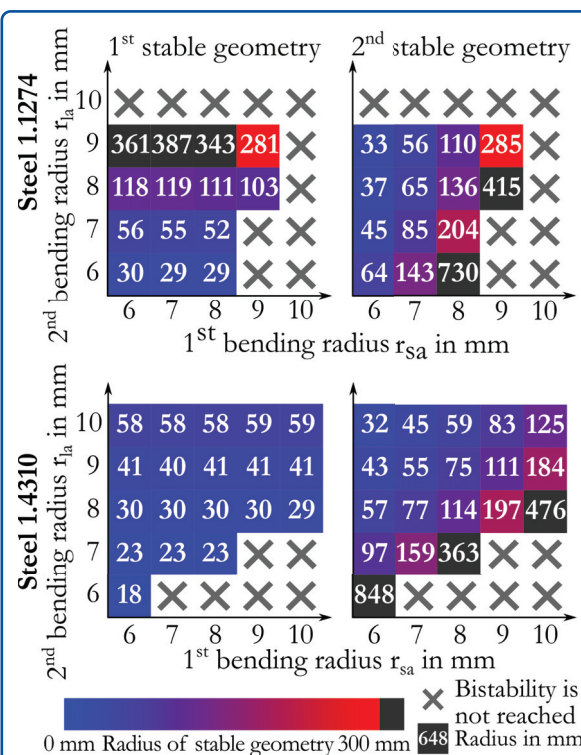
ure 13.5 a): incremental bending of the sheet along the y-axis in the positive z-direction → flattening of the sheet → incremental bending of the sheet along the x-axis in negative z-direction → flattening of the sheet → bistability test by bending the sheet slightly in positive z-direction. The feed distance between the bending strokes (lateral displacement of the sheet) is kept constant and is equal to the current bending radius. The step size and the sheet size thus determine the number of bending operations. In the parameter study, the influence of the bending radii  $r_{sa}$  (bending radius along the short axis) and  $r_{la}$  (bending radius along the long axis) is examined in the range from 6 to 10 mm [15].

Figure 13.8 shows the simulation results (achieved bistability, radii of both stable geometries) for the steels 1.1274 and 1.4310. In general, bistable properties can be achieved with different radii of stable geometries for both steel grades. The relationship between the combinations of bending radii and the radii of the resulting stable geometries is not linear.



**Figure 13.7** Main simulation steps and related von Mises equivalent stress distribution on the visible surface.

However, it can be generally concluded that using the smallest possible combinations of bending radii ( $r_{sa} = r_{la} = 6 \text{ mm}$ ) could result in a smallest radius of the first stable geometry, but a large radius in the second one (e.g., 30 mm and 64 mm for 1.1274 steel and 18 mm and 848 mm for 1.4310 steel). By increasing the second bending radius, the combination of the smallest possible stable geometries can be achieved (e.g., 56 mm and 45 mm for 1.1274 steel and 41 mm and 43 mm for 1.4310 steel). For a 300 mm wide sheet the fully closed geometry is achieved at a 48 mm radius. As the simulation results show, it is possible to produce a fully closed tubular geometry in at least one stable state.



**Figure 13.8** Results of simulations of steels 1.1274 (1<sup>st</sup> batch) and 1.4310 for both stable states by PR1 [15].

Also the following observations can be made:

- Larger first bending radii can be used for steel 1.1274 compared to 1.4310 to achieve bistable properties.
- Steel 1.4310 allows larger radii within the second bending than 1.1274. The reason for these two observations lies in the influence and interaction of parameters such as Young's modulus,

yield strength, bending radii etc. on the residual stress distribution in the sheet.

- Since the residual stresses introduced in the individual bending operations are superimposed, there are differences in the profile radii achieved depending on the used bending radii.

### Semi-analytical Model

Although FE models can be used to simulate complex manufacturing processes and provide reliable results, the main disadvantage of such models is the long simulation time. A semi-analytical model can essentially capture the influence of material parameters such as sheet thickness, Young's modulus, yield strength and yield curve and process parameters such as bending radius combinations and return the achievability of bistability and the radii of the stable geometries. Such a model could calculate the result for a given set of parameters in seconds and thus perform an initial parameter study to define the appropriate process and material parameters for further investigations with FE models and experiments.

Therefore, an appropriate semi-analytical model was set up. The model assumes that the bending is uniform over the whole sheet, making it more suitable for incremental bending tests. It takes the bending moments into account to calculate the stable geometries. To account for isotropic and kinematic hardening during plastic deformation, a combined isotropic-kinematic hardening model based on material parameters was added. Several assumptions are made to allow fast calculation and to solve the equations describing the deformation during bending [3, 17], which can be summarised as follows:

- Plane stress condition due to the large ratio of sheet width to sheet thickness.
- No stresses perpendicular to the sheet surface.
- Application of pure bending load.
- No change in sheet thickness during bending.
- The neutral bending axis is always in the centre of the sheet.
- The stress-strain characteristic of the material is the same for tension and compression.

...

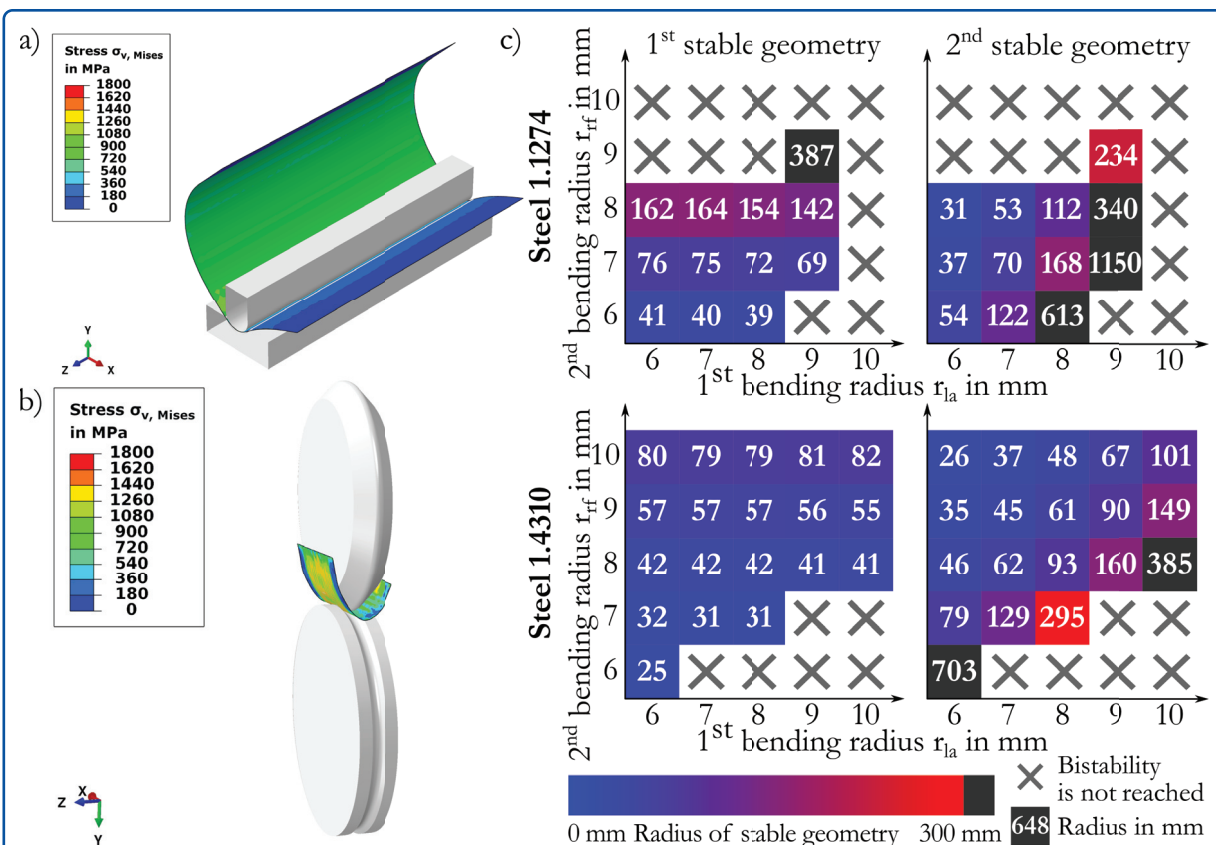


**Figure 13.9** FE simulations: a) incremental die bending, b) roll forming and c) simulated radii of curvature of steels 1.1274 (1<sup>st</sup> batch) and 1.4310 for both stable states by PR2 [15].

- The planes perpendicular to the neutral axis remain perpendicular to this axis during bending.

The whole chain of the bending process is shown in figure 13.10 using the stress state and the von Mises yield criteria. The yield point represents the stresses on the sheet surface. Point A corresponds to the unstressed flat sheet. At the start of the first bend about the y-axis, the sheet initially deforms elastically until the stress state reaches point B. This is followed by plastic deformation to point C. During plastic deformation, hardening occurs and the yield curve shifts from its initial position. After plastic deformation, the material relaxes linearly to point D. After springback, the sheet continues to bend to the flattened state (point E). From the flattened state, bending about the x-axis begins. This step also consists of elastic deformation up to point F and plastic deformation up to point G. Point H corresponds to the configuration after springback after the second bend. By bending the sheet to the

flat geometry (point I) and further bending in the opposite direction around the y-axis, the second stable state is reached at point J [13, 18].

During plastic deformation, the yield locus shifts (kinematic fraction) and increases (isotropic fraction). The ratio of kinematic and isotropic fractions was determined for each material using an inverse modeling approach. The model parameters of the simulations were iteratively adjusted until a minimum deviation from the experimental results was obtained.

Due to the short computation times, the semi-analytical model was used for sensitivity analysis. The influence of the bending radius combination on the bistability was investigated for steel 1.1274 with bending radii from 4 mm to 12 mm in increments of 0.1 mm. The results are shown in figure 13.11. It can be seen that the results of the semi-analytical model are in good agreement with the

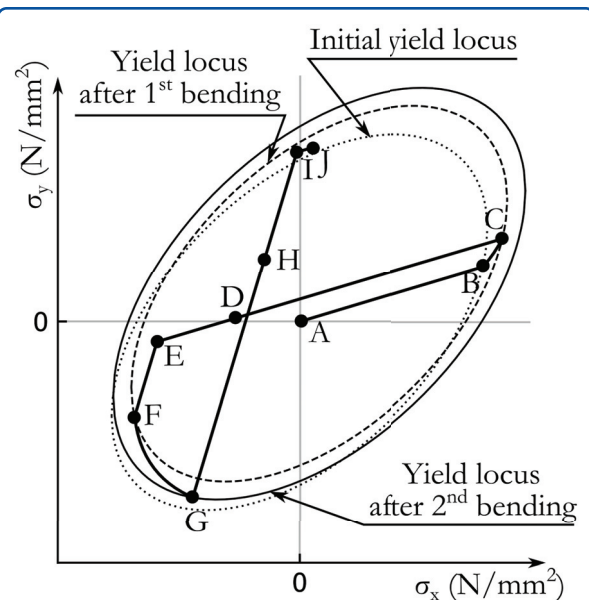


**Figure 13.10** Yield locus shift and stress evolution during bending operations [13].

numerical model (figure 13.8). By reducing the first and second bending radii, the smallest geometry in the first stable state could be achieved, but the geometry of the second stable state will increase. On the other hand, by increasing the second bending radius, the geometry of the second stable state could be reduced.

Figure 13.12 a generally shows the effect of yield strength for 1.1274 over a range from 1.500 MPa to 1.900 MPa. As an example, the results are shown for an equal first and second bending radius ( $r_1 = r_2$ ). While the influence is hardly noticeable for small bending radius combinations ( $r_1 = r_2 = 6$  mm), for larger bending radius combinations ( $r_1 = r_2 = 9$  mm) almost no residual curvature (corresponding to very large stable geometries) can be observed in both stable states. Forming with small bending radii allows plastic deformation to be achieved despite high yield strength and a higher overall process reliability can be observed. At the same time, these results explain why there are sometimes larger deviations between simulation and experiment for larger bending radii (e.g., from  $r_1 = r_2 = 7$  mm), since even small fluctuations between simulated and real yield strength lead to significant changes in the radii of stable states.

Figure 13.12 b shows the radius of curvature of the first and second stable layers as a function of sheet thickness varying from 0.175 to 0.225 mm for steel 1.1274. It can be seen that the radii of stable geometries decrease with increasing sheet thickness. For small bending radii, the influence of the sheet thickness is small because there is still sufficient plasticity to introduce residual stresses.

### 13.4.2 Incremental Bending Followed by Roll Forming PR2

PR2 consists of an initial incremental die bending along the shorter side of the sheet followed by roll forming in the orthogonal direction (see figure 13.5 b). In this process, the length of the bending die only limits the profile width and the profile length is theoretically unlimited. However, this process route requires two machines.

### Numerical Simulations

Three-dimensional FE models of the incremental bending and roll forming processes were used to determine the attainability of bistable properties and to estimate the achievable curvature radii of the structures more accurately (see figure 13.5 b). The feed distance is kept constant and equals the current bending or rolling radius, respectively. After each roll forming pass the sheet is flattened and rolling tools are positioned for the next pass. The numerical roll forming model is depicted in figure 13.9 b.

In the parameter study the influence of the bending radius  $r_{sa}$  of incremental bending and rolling radius  $r_{rf}$  of roll forming is investigated in the range of 6 to 10 mm. Figure 13.9 c shows the simulation results (achieved bistability, radii of stable geometries). Bistable properties were achieved for both steels. The results show similar tendencies as for PR1: (1) larger radii can be used in incremental bending for 1.1274 compared to 1.4310 to achieve bistable properties; (2) 1.4310 allows larger radii within the roll forming step (2<sup>nd</sup> bending) than 1.1274. Comparing PR1 and PR2 it can be found that PR1 produces smaller first stable radii

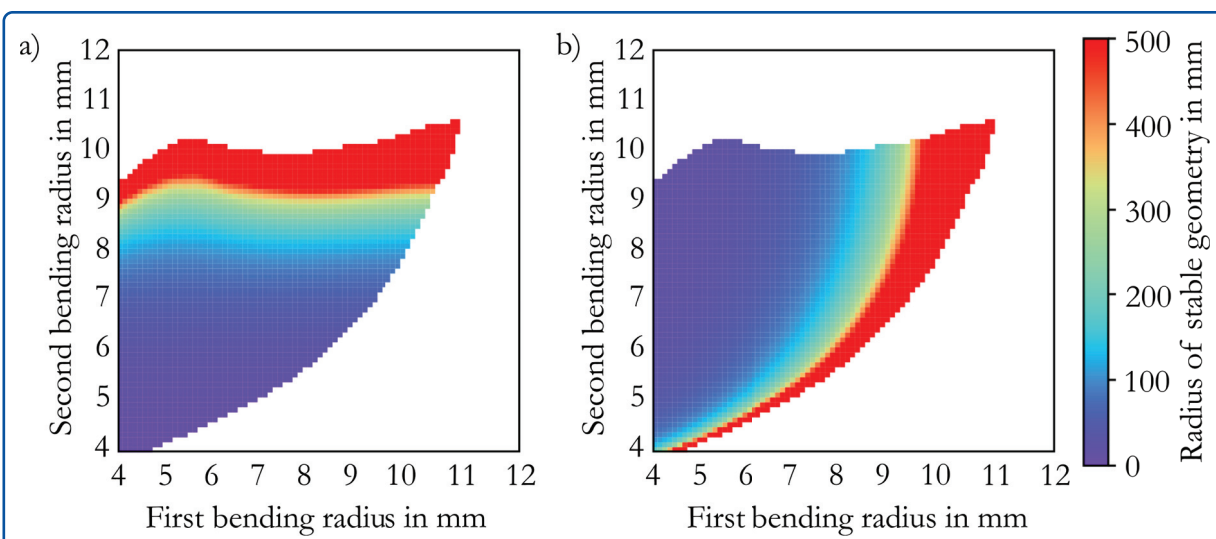


**Figure 13.11** Bistability and radii of a) first and b) second stable geometries for steel 1.1274 (1<sup>st</sup> batch) as a function of different combinations of bending radii [16].

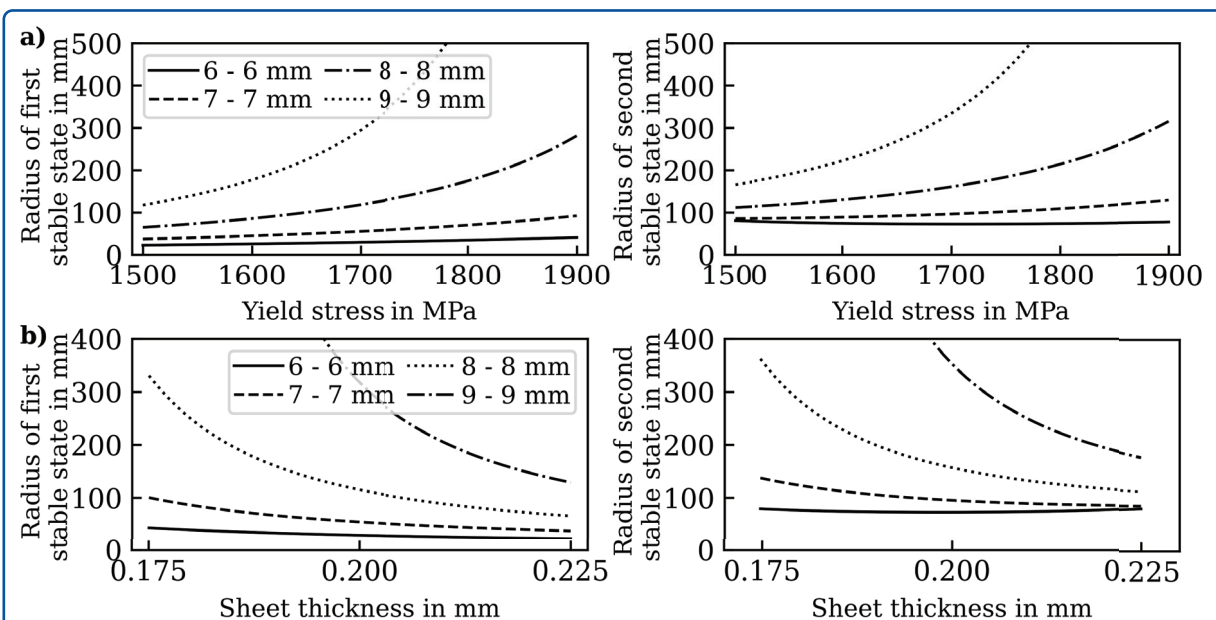


**Figure 13.12** a) Dependence of the first and second stable radius of curvature on the yield strength for different bending radii combinations for 1.1274; b) dependence of the first and second stable radius of curvature on the sheet thickness for different bending radii combinations for 1.1274.

and larger second stable radii compared to PR<sub>2</sub> for both materials.

### 13.4.3 Validation of the Models

In order to validate the simulations, experiments were carried out to produce bistable sheet struc-

tures. The experiments were carried out for both production routes PR<sub>1</sub> [15] and PR<sub>2</sub> [16]. Several combinations of bending radii were tested, resulting in the successful manufacturing of bistable sheets with a fully closed tubular geometry and a folded transport geometry [9]. Two steels with two different initial yield strength (1.1274 with 1.690 MPa and 1.4310 with 870 MPa, see fig-



**Figure 13.13** Bistable tubes produced by two step incremental die bending process.

ure 13.4) and comparable strain hardening are used in experiments. The experimental results show good qualitative agreement with the simulated results. The fabricated bistable tubes are shown in figure 13.13.

#### 13.4.4 Experimental Determination of Residual Stress Distribution

The residual stress distribution introduced by the forming processes is crucial to achieve bistable properties. At the IWT in Bremen, residual stress measurements were carried out on deformed sheets of steels 1.1274 (1<sup>st</sup> batch) and 1.4310 to determine the residual stress distribution across the entire sheet thickness. For this purpose, the material was chemically removed and the residual stresses were then measured by X-ray diffraction approximately every 0.02 mm. The samples were selected from the two-stage die bending process (PR<sub>1</sub>, see figure 13.5 a) and from incremental die bending followed by roll forming (PR<sub>2</sub>, see figure 13.5 b). The selected and measured samples had the smallest radius of curvature in the unfolded state, which were achieved by the respective process routes so far. For profiles produced by PR<sub>2</sub> (see figure 13.14, blue) the stresses, particularly in the y-direction, are lower near the surface compared to the profiles produced by PR<sub>1</sub> (black). The reason for the different expression of residual stresses must be the different way in which residual stresses are introduced into

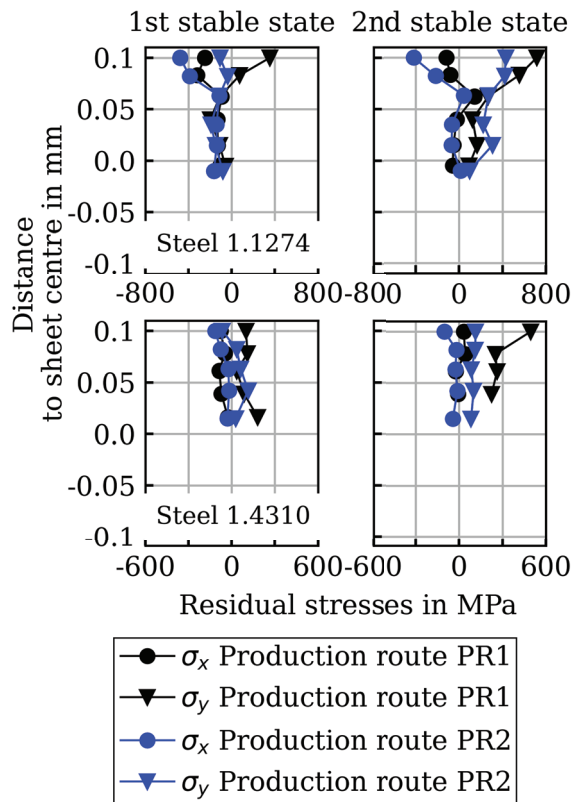


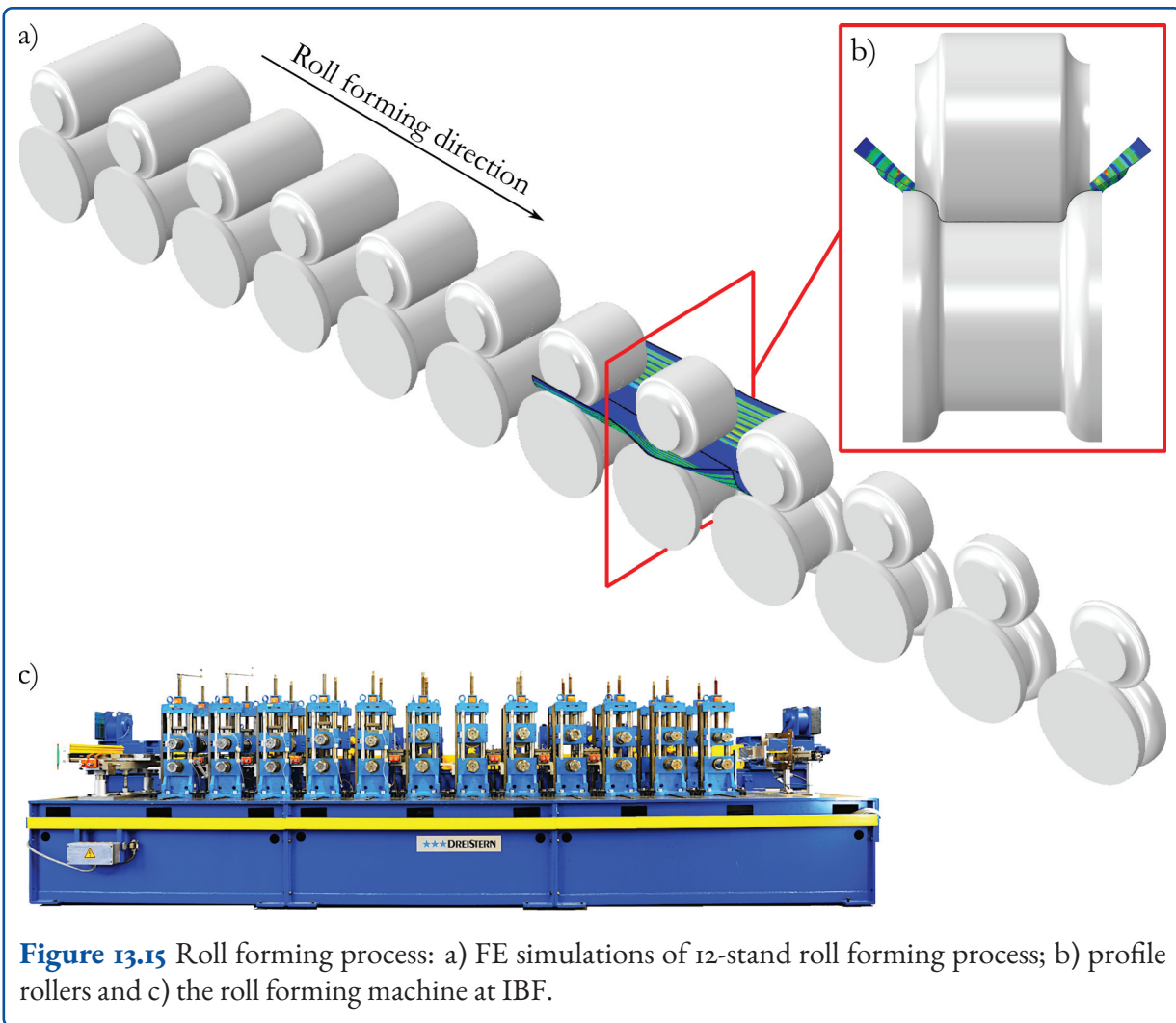
**Figure 13.14** Comparison of the residual stresses generated (measured at IWT Bremen) and radii of stable states of steels 1.1274 (1<sup>st</sup> batch) and 1.4310 for both stable states and both production routes.

the sheet during roll forming, as the first process step (incremental die bending) is identical for both process routes.

#### 13.5 12-stand Roll Forming Process

The roll forming process of PR<sub>2</sub> only uses one pair of rollers and the sheet must be positioned manually. This leads to a time consuming process chain and problems with the repeatability of the bending. Therefore, an improvement of the roll forming process is required. The final design includes numerical calculation of the optimum arrangement of several pairs of rolls so that bistable, fully closed tubes can be produced using all 12 roll stands of the roll forming machine available at IBF. The use of additional rolls and roll stands inevitably results in better sheet guidance. However, this also results

...



in a mutual influence of the material inside the upstream and downstream roll stands, so that a numerical design of all roll pairs used in the entire roll forming machine is necessary (figure 13.15).

The numerical FE model of the roll forming process consists of the 12 roll stands and was created using Abaqus/CAE. The model consists of 12 pairs of rolls made as analytical rigid parts and the deformable sheet part. To prevent the free edges of the sheet from coming into contact with the shafts during roll forming, the rolls were designed with a modified geometry. The material sides were bent with a large radius in a more horizontal position. The results of the model show the general applicability of the proposed roll geometry in the 12-roll stand forming machine for the production of tube profiles.

## 13.6 Properties of the Bistable Profiles

In the previous chapters, the produced bistable structures were evaluated only in terms of achieving bistable properties and final radii of stable geometries. However, it is also important to investigate the mechanical properties of such structures. Therefore, the stiffness of the bistable structures as well as the residual stress stability was investigated.

### 13.6.1 Stiffness of the Deployed Structure

The stiffness of the bistable structure is essential for an usage as load-bearing part. Thus, the stiffness of different circular arc profiles and their behav-

ior under different loads is of great interest. Analytical equations provide a way to determine the critical axial, lateral and rotational loads of cylindrical metal tubes [19]. However, when dealing with bistable sheets, these equations cannot be applied directly due to the effects of residual stresses and the open geometry. Even in fully closed structures, there is an open seam where the sheet edges only touch or overlap. Sheets with a smaller curvature or width will not result in a fully closed tube profile, but rather a circular-arc profile with a reduced load-bearing capacity. But a circular-arc profile may be of interest for weight saving reasons or adapted manufacturing processes.

In order to investigate the stiffness of the bistable structure under different conditions, numerical FE models were developed using Abaqus/CAE software. Figure 13.16 shows three different approaches: axial buckling, lateral buckling with two supports and free edges, and lateral buckling with a fixed edge. In addition, the corresponding residual stresses are imported over the sheet thickness. The sheet length of 1.000 mm and width of 300 mm are constant, only the radius of the stable geometry varies from 48 mm (fully closed tube profile) to 500 mm (virtually flat profile).

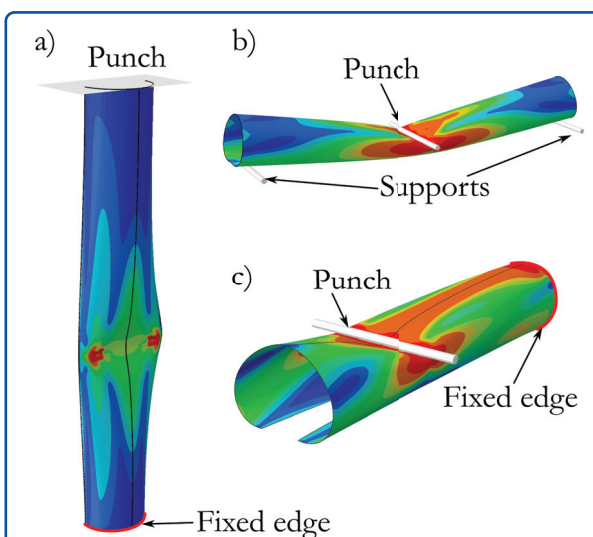


**Figure 13.16** Numerical simulations for the critical buckling force of bistable structures: a) axial buckling; b) lateral buckling with two supports, and c) lateral buckling with a fixed edge.

### Maximum Axial Load

This performance criteria is a measure of the maximum axial force that can be applied to the structure in deployed state without causing failure or collapse (see figure 13.16 a). It is an important measure of the structure's performance under loading, particularly for applications that involve significant axial forces.

In this model, one edge of the bistable structure in the deployed state is fixed and the compressive force is applied to the other edge by means of a punch (see figure 13.16 a). The reaction forces on the punch are measured. The axial buckling forces are displayed as a function of the different radii of stable states and of the sheet thickness in figure 13.17. As it can be seen, the critical buckling force is maximum at the smallest radius, which corresponds to a fully closed profile. As the radius of the stable geometry increases, the force decreases rapidly. However, it should be noted that even for a half pipe profile (around 96 mm radius) the force is around 10 kN, making it suitable for various applications such as antenna masts.

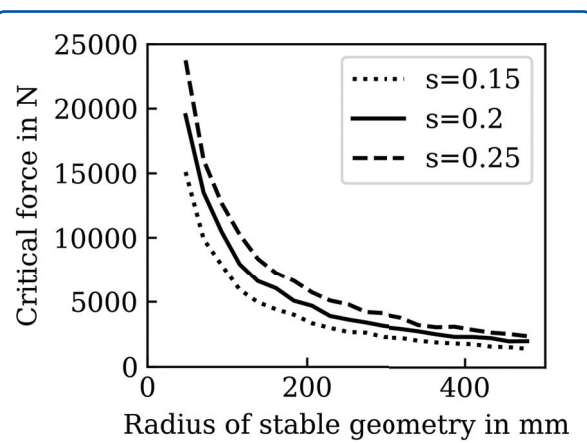


**Figure 13.17** Critical axial buckling force as a function of radius in the unfolded stable state and sheet thickness.

### Maximum Lateral Load

This criteria refers to the maximum lateral force that the unfolded structure can withstand before collapsing. This is a critical measure of the struc-

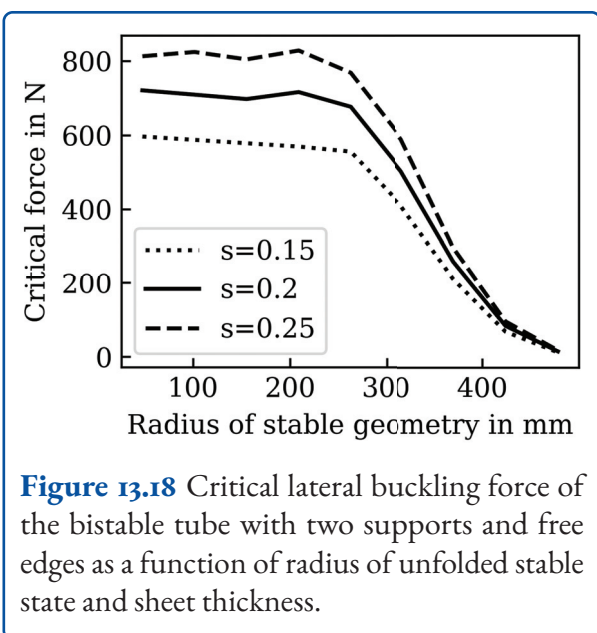


**Figure 13.18** Critical lateral buckling force of the bistable tube with two supports and free edges as a function of radius of unfolded stable state and sheet thickness.

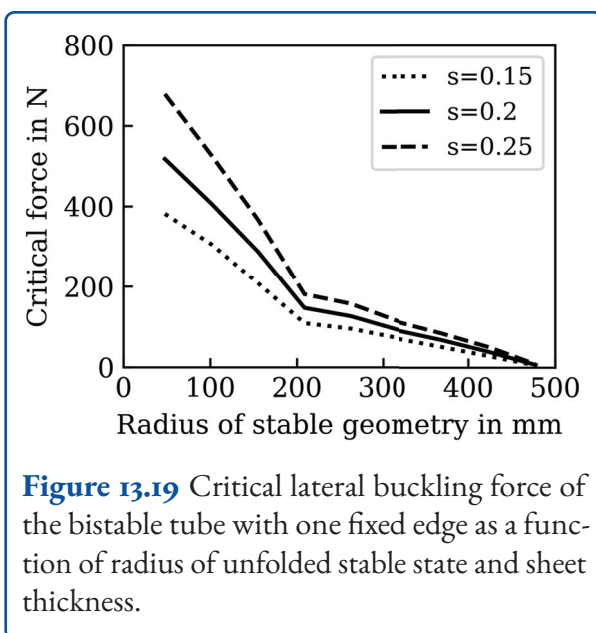


**Figure 13.19** Critical lateral buckling force of the bistable tube with one fixed edge as a function of radius of unfolded stable state and sheet thickness.

ture's resistance to lateral loading and its overall stability, especially in applications where the structure may be subjected to substantial lateral forces. The maximum lateral load was investigated for two different cases using FE simulations. For one model (see figure 13.16 b), the bistable sheet in the unfolded state is placed on two supports and the force is applied in the middle. The results show (see figure 13.18), that the critical buckling force is maximum at the smallest radius (fully closed profile) and does not change significantly with increasing radius until approximately a 250 mm radius. This means that the critical buckling force is the same for the fully closed profile and the half-pipe profile in this case.

In the second case (see figure 13.16 c), the bistable sheet is fixed on one edge in the unfolded state and the force is again applied by a punch (figure 13.19). For this type of test the critical buckling force is maximum for the fully closed profile and drops rapidly with an increase in the radius of stable state. At around a 200 mm stable state radius a change in the slope can be observed.

### 13.6.2 Thermal Stability of Forming-induced Residual Stresses

Thermal stability testing was carried out over a temperature range of 150 °C to 400 °C for both stable geometries of the steel 1.1274 (1<sup>st</sup> batch). The bistable structures were heated to the target temperature in the inert argon atmosphere of a furnace and kept there for approximately 20 min. This was followed by slow cooling to room temperature in approximately 24 hours to avoid introducing further thermally induced residual stresses. The results in figure 13.20 a show that the bistable property of the sheet treated in the deployed tube geometry is already lost at 150 °C, as the sheet can no longer be transferred to the transport geometry. Therefore no profile radius curve can be plotted. Figure 13.20 b shows the improved stability of properties when annealed in the transport geometry. Bistability is maintained at high temperatures, although the profile radius increases significantly above 250 °C.

### 13.6.3 Stability of Residual Stresses at Room Temperature under Cyclic State Changes

The aim of the investigations was to analyze the stability of residual stresses after several changes

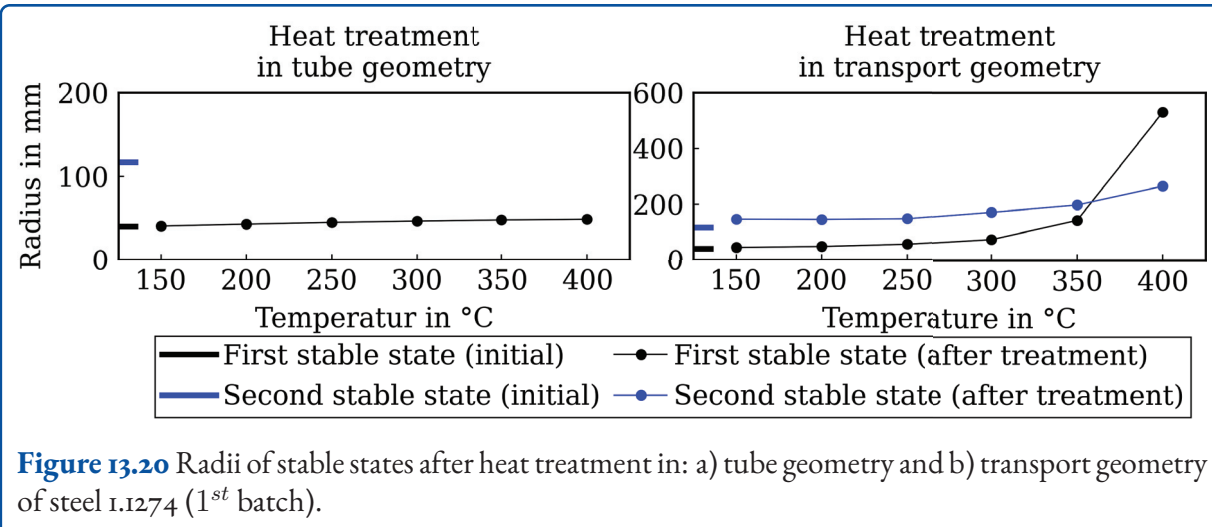


**Figure 13.20** Radii of stable states after heat treatment in: a) tube geometry and b) transport geometry of steel 1.1274 (1<sup>st</sup> batch).

of state. The investigations were carried out on bistable sheets produced by two-step incremental die bending and incremental die bending followed by roll forming with forming radii of  $r_1 = r_2 = 6$  mm. Different numbers of changes between the stable states of the produced bistable sheets were carried out. In addition, the profile diameter was measured after predefined change cycles. Since the radii of the stable states are defined by the residual stress distribution, the change in the radii of the stable states should imply the change in the residual stresses. The investigations showed that, even after 100 changes between stable states, no modification was detected and the residual stresses could therefore be considered to be stable.

## 13.7 Conclusion

This research project focused on investigating the effect of residual stresses for the manufacturing of bistable metal tube profiles. The aim was to demonstrate that residual stresses can result in a specific geometry of the structure, develop appropriate manufacturing processes and analyze the properties of the bistable structures. The results show that it is possible to produce the bistable tube profiles from sheet metal using a two-step production process. The two-step bending of the thin 1.1274 steel sheet around the bending radii of 6 mm could produce bistable fully closed tubular profiles with the radius of the profile in the deployed state of 41 mm and

in the coiled state of 101 mm. In addition, two different production routes involving incremental die bending and roll forming are developed. The developed process models allow the evaluation of the appropriate production parameters, such as the radius of the bending die and the number of roll forming passes, in order to produce a bistable tube profile from the material of given thickness and mechanical properties. Furthermore, the structures properties such as stiffness as well as thermal and mechanical stability were analyzed. The knowledge gained during the project could be directly applied to the production of bistable metal profiles.

## References

- [1] E. Groskopfs. "Storable tubular extensible member device". Patent US3434674A. Assignee: De Havilland Aircraft of Canada Ltd. 1969.
- [2] A.D. Norman et al. "Multistable Textured Shell Structures". In: *Advances in Science and Technology* 54 (2008), pp. 168–173. DOI: 10.4028/www.scientific.net/AST.54.168.
- [3] E. Kebadze, S.D. Guest, and S. Pellegrino. "Bistable prestressed shell structures". In: *International Journal of Solids and Structures* 41.11 (2004), pp. 2801–2820. ISSN: 0020-7683. DOI: 10.1016/j.ijsolstr.2004.01.028.
- [4] B. Hoang et al. "Commercialization of Deployable Space Systems' roll-out solar array (ROSA)

...

- technology for Space Systems Loral (SSL) solar arrays". In: *2016 IEEE Aerospace Conference*. 2016, pp. 1–12. DOI: 10.1109/AERO.2016.7500723.
- [5] Q.M. Compton-Bisho, A.J. Daton-Lovett, and R.G. Curry. "Industrial and commercial applications of bistable reeled composites". In: *Smart Structures and Materials 2000: Industrial and Commercial Applications of Smart Structures Technologies*. Vol. 3991. International Society for Optics and Photonics. SPIE, 2000, pp. 335–343. DOI: 10.1117/12.388176.
- [6] A. Pagani, R. Augello, and E. Carrera. "Numerical simulation of deployable ultra-thin composite shell structures for space applications and comparison with experiments". In: *Mechanics of Advanced Materials and Structures* 30.8 (2023), pp. 1591–1603. DOI: 10.1080/15376494.2022.2037173.
- [7] Hakan Kayal et al. "Next Level Autonomous Nanosatellite Operations". In: *2018 SpaceOps Conference*. DOI: 10.2514/6.2018-2690.
- [8] M Leipold et al. "Solar sail technology development and demonstration". In: *Acta Astronautica* 52.2 (2003). Selected Proceedings of the 4th IAA International conference on Low Cost Planetary Missions, pp. 317–326. ISSN: 0094-5765. DOI: 10.1016/S0094-5765(02)00171-6.
- [9] P. Pavliuchenko et al. "Production of bistable fully closed metallic shells by introducing residual stresses during bending processes". In: *Production Engineering* 13.2 (2019), pp. 201–209. ISSN: 1863-7353. DOI: 10.1007/s11740-019-00875-6.
- [10] K. Iqbal, S. Pellegrino, and A. Daton-Lovett. "Bi-stable Composite Slit Tubes". In: *IUTAM-IASS Symposium on Deployable Structures: Theory and Applications*. Ed. by S. Pellegrino and S. D. Guest. Dordrecht: Springer Netherlands, 2000, pp. 153–162. ISBN: 978-94-015-9514-8. DOI: 10.1007/978-94-015-9514-8\_17.
- [11] K. Lange and M. Liewald. *Umformtechnik. Handbuch für Industrie und Wissenschaft. Band 3: Blechbearbeitung*. 2., völlig neubearb. und erw. Aufl. Springer Berlin, 1990. ISBN: 978-3-540-50039-1.
- [12] S.D. Guest, E. Kebadze, and S. Pellegrino. "A zero-stiffness elastic shell structure". In: *Journal of Mechanics of Materials and Structures* 6.1–4 (2011), pp. 203–212. DOI: 10.2140/jomms.2011.6.203.
- [13] P. Pavliuchenko et al. "A Semianalytical Model for the Determination of Bistability and Curvature of Metallic Cylindrical Shells". In: *Journal of Manufacturing and Materials Processing* 3.1 (2019), p. 22. ISSN: 2504-4494. DOI: 10.3390/jmmmp3010022.
- [14] S. Pellegrino. In: *Deployable Structures*. 2001. Chap. Deployable Structures in Engineering, pp. 1–35. ISBN: 978-3-7091-2584-7. DOI: 10.1007/978-3-7091-2584-7\_1.
- [15] P. Pavliuchenko, G. Hirt, and M. Teller. "Analysis and manufacturing of bistable metallic profiles". In: *Archive of Applied Mechanics* 91.8 (2021), pp. 3501–3511. ISSN: 1432-0681. DOI: 10.1007/s00419-021-01916-2.
- [16] P. Pavliuchenko, M. Teller, and G. Hirt. "Voruntersuchungen zur Einsetzbarkeit des Walzprofilierens zur Herstellung bistabiler dünner Bleche". In: *Forschung im Ingenieurwesen* 85.3 (2021), pp. 817–825. ISSN: 1434-0860. DOI: 10.1007/s10010-021-00488-5.
- [17] S.D. Guest and S. Pellegrino. "Analytical models for bistable cylindrical shells". In: *Proceedings of the Royal Society A: Mathematical, Physical and Engineering Sciences* 462.2067 (2006), pp. 839–854. DOI: 10.1098/rspa.2005.1598.
- [18] P. Pavliuchenko, M. Teller, and G. Hirt. "Analysis of Influencing Factors on the Achievability of Bistable Fully Closed Shells by Semi-Analytical Modeling". In: *Forming the Future. The Minerals, Metals and Materials Series*. 2021, pp. 2319–2330. ISBN: 978-3-030-75381-8.
- [19] W. Young, R. Budynas, and A. Sadegh. "Roark's Formulas for Stress and Strain". In: 8th Edition. McGraw-Hill Education, 2012. Chap. Elastic Stability, pp. 709–742. ISBN: 978-0-07-174247-4.

## 14 Control of Component Properties in the Rotary Swaging Process

Langstädtler, L.; Schenck, C.; Kuhfuss, B.; Epp, J.; Charni, D.

GEPRIS 374789876

### 14.1 Introduction

Rotary swaging is widely used for near-net-shape serial production of axisymmetric components from tubes or rods and is known to produce close geometrical tolerances in a process-safe manner. Additionally, mechanical properties such as static and dynamic strengths of the parts are positively influenced by the introduction of work hardening as well as residual stresses during the process. Infeed rotary swaging produces a complex material flow with incrementally occurring locally varying degrees of elongation and compression of the material. The material flow can be influenced by the process control. However, the interaction of the different influencing variables is only partially known and in practice leads to a purely geometrical design of the components. The residual stresses introduced and the resulting mechanical component properties have so far not been considered in the process design for rotary swaging. They do, however, have the potential of further improving service properties, in particular enhance fatigue life.

The central hypothesis of the present project was that residual stresses at the surface and in the bulk of workpieces can be controlled by process modifications during infeed rotary swaging and that fatigue strength can be improved by the targeted generation of compressive residual stresses in highly loaded regions.

Suitable methods for investigation and measurement had to be developed/adapted for this purpose in order to understand and modify the generation of the residual stresses. Modifications of the process

were defined to influence the state and amplitude of stresses as well as their distribution at the surface and in the depth of the workpieces.

The influence on the mechanical properties of the introduced material modifications, in particular residual stresses, had then to be assessed, as well as their stability during service conditions.

During the project, the main investigated material was the steel grade S355/E355 as rods/tubes with ferrite-pearlite microstructure, since it has a good formability and is widely used in rotary swaging. On the other hand, austenitic stainless steel 1.4305 and 1.4310 with a different capability of forming strain induced martensite were also investigated due to their higher strength and therefore higher sensitivity to residual stresses regarding the fatigue properties.

### 14.2 Rotary Swaging Process

Rotary swaging is an incremental open die forging process. The used swaging machine was a Felss HU 32V with fully hydrostatic feed with linear direct drive. The machine is equipped with different measurement systems to measure forces and displacement. Processible workpiece initial diameters  $d_0$  were  $\varnothing 32$  mm for tubes and  $\varnothing 20$  mm for rods swaging to a diameter  $d_1$ . The standard length of the swaged workpieces was 300 mm in the following investigations. Depending on the forming stages different final geometries and diameters are formable. Furthermore, mandrels can be used to influence the wall thickness distribution as well as the workpiece geometry. Depending on the process properties (parameters, contact conditions between the workpiece and the die) and the formed material, the workpiece can heat up to around 100 °C.

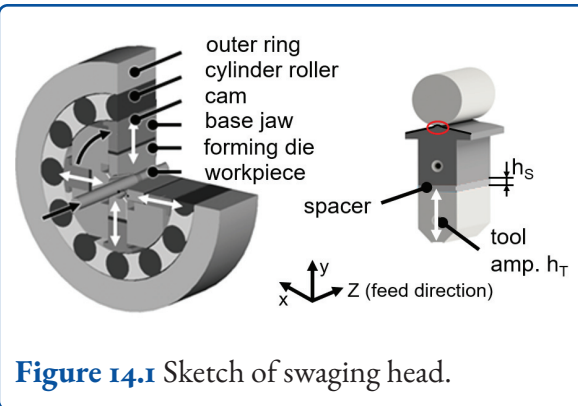


**Figure 14.1** Sketch of swaging head.

The process kinematics are based on a revolving of the base jaw with a cam along cylinder rollers that causes an oscillation of the forming die in radial direction (stroke), figure 14.1. With each stroke the material flows elastic-plastically by stretching and upsetting. The material flow is maintained as the cylinder roller, the base jaw, the spacer with height  $h_s$  and forming die are supported on the outer ring, thus creating a pressure column defining the amplitude and gradient of local plastic deformation and induced stresses. In this research the spacer height was set to 5.08 mm as a standard value. The generated closing pressure and closing time with contact time  $t_k$  depend on the rotational speed of the swaging axle which is around 300 1/min as well as the base jaws and die dimensions and can be varied by the height of the spacers. The stroke following angle  $\Delta\Phi$  is the relative rotation angle of workpiece and die between two consecutive strokes. The rotational speed of the machine resulting in approximately 34 strokes per second and the relative feeding of the workpiece to the swaging head, influences the material flow history.

In infeed rotary swaging, the sample is fed axially into the swaging head and afterwards axially retracted with standard infeed rate of 1,000 mm/min and retraction speed of 2,000 mm/min. However, if required due to the swaged material properties or the material flow, the infeed rate can be changed. Furthermore, the retraction speed was kept as high as possible due to a reduction of process time. Thus, according to its effect on workpiece calibration the retraction speed can be reduced.

The forming dies feature a reduction zone in which the main deformation takes place with an opening angle  $\alpha$  ( $5^\circ \leq \alpha \leq 15^\circ$ ). In the adjacent calibration zone, the final geometry (diameters/shape, roundness, cylindricity, surface quality) is generated, see figure 14.2 [1].

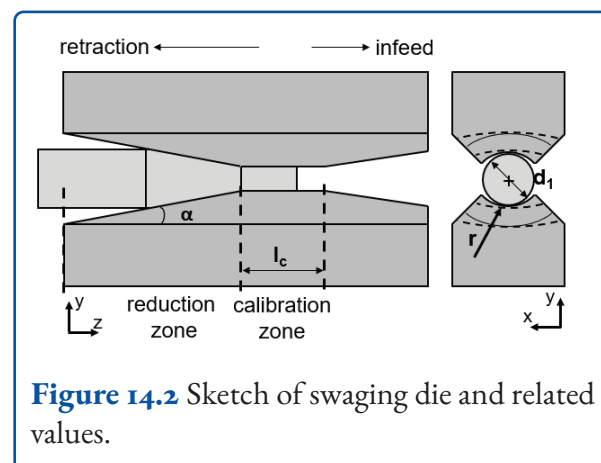


**Figure 14.2** Sketch of swaging die and related values.

The opening angle of the reduction zone was  $\alpha = 10^\circ$  and the length of the calibration zone was 20 mm in the dies used in this research. The reduction zone and the calibration zone were connected by a transition radius 20 mm. In the exit zone, the workpiece was gradually unloaded. The zones were equipped with a round shape crosswise to the infeed direction [2], but also flat dies can be used to produce round [3] as well as polygonal cross sections [4]. As a standard value for round shaped dies a slightly increased – approximately 2 – 6 % higher – die radius  $r$  is given. According the workpiece diameter  $d_1$  which is defined by the set of dies, the forge value  $S$  can be calculated by the following equation.

$$S = \frac{\frac{d_1}{2}}{r} \leq 1 \quad (\text{Equation 14.1})$$

With this it is possible to achieve a particularly good surface finish and at the same time avoid material damage [5]. The surfaces of the different die zones can be modified by coatings. Here for example a tungsten-carbide coating can be spray-coated on the reduction zone to increase friction. Diamond-like carbide coatings (DLC) on dies can be used to reduce friction, e.g., for lubricant-free dry rotary swaging. As an overview the different dies are given in the following table.

**Table 14.1** Swaging dies for experimental investigations

type	$r$ [mm]	$d_1$ [mm]	$S$	material
1	7.5	round	1.00	1.3395
		15		WC
2	7.5	round	1.00	1.2379
		15		DLC
3	7.5	round	1.00	carbide
		15		
4	8.1	round	0.93	1.2379
		15		
5	-	square	0	1.2379
		15		
6	4.0	round	1.00	carbide
		8		
7	9.1/8.1	round	0.93	1.2379
		17/15		

The rotary swaging process was simulated with a 2D-axis-symmetric model [6] and with a 3D model [7]. The simulation analysis was carried out using the FEM software Abaqus-explicit (Version 6.14). The mesh consisted in the 2D model of *CAX4R* and in the 3D model of linear *C3D8R* elements using distortion control and hourglass control. The dies oscillated according to the real process with stroke height  $h_T$  of 1 mm and a frequency of 37.5 Hz. In order to represent the combined kinematic and isotropic strain hardening, the non-linear combined hardening material model of Chaboche was used. To evaluate and visualize the residual stresses during the process, the tools were virtually retracted at the end of each stroke and the simulation was continued with a static general unloading step to allow the springback. The contact conditions between the workpiece and dies were simplified in the simulation by use of Coulomb's law with a constant friction coefficient of 0.1 in penalty contact method.

## 14.3 Residual Stress Analysis

For the experimental analysis of residual stress distributions at different length scales, complementary methods of X-ray diffraction, neutron diffraction and micromagnetic methods were used and adapted to the special requirements of rotary swaged components. The experimental methods were used to validate FEM simulations of the process, allowing the analysis of (residual) stress generation along the process. For this purpose, among other things, measurements were carried out in the volume of solid rods and tubes.

### 14.3.1 X-Ray Diffraction

X-ray diffraction (XRD) is a nondestructive technique for residual stress analysis. Due to its low penetration depth in steel (in general few micrometers) this method was applied extensively for surface residual stress measurement as well as to assess gradients within the first few millimeters by means of local material removal (depth profile). The residual stress measurements were performed with a commercial 8-axis diffractometer Type ETA 3003 from GE Inspection Technologies, equipped with a position sensitive detector. A beam of 1 mm diameter of vanadium filtered Cr-K $\alpha$  radiation was used. In the case of steel grade E355/S355, all residual stresses were determined using the  $\sin^2 \psi$ -method with the {211} diffraction peak of  $\alpha$ -iron along 13  $\chi$ -angles between  $-45^\circ$  and  $+45^\circ$  and X-ray elastic constant  $1/2S_2 = 5.8110 - 5\text{ MPa}^{-1}$  [8].

Annealed E355 steel tubes ( $\varnothing 20 \times 3\text{ mm}^2$ ; 700 °C for 2 hours) were swaged with die type 1 to 15 mm. Figure 14.3 shows the distribution of the axial and tangential residual stresses along a line at the surface of a workpiece generated by rotary swaging. The residual stresses were compressive at the outer surface with values between  $-300\text{ MPa}$  and  $-400\text{ MPa}$  in axial direction with slight fluctuation and between  $-250\text{ MPa}$  and  $-300\text{ MPa}$  in tangential direction. This showed that the residual stress measurements can be inhomogeneously distributed along the axial position. Since mainly bending fatigue was considered, mainly axial resid-

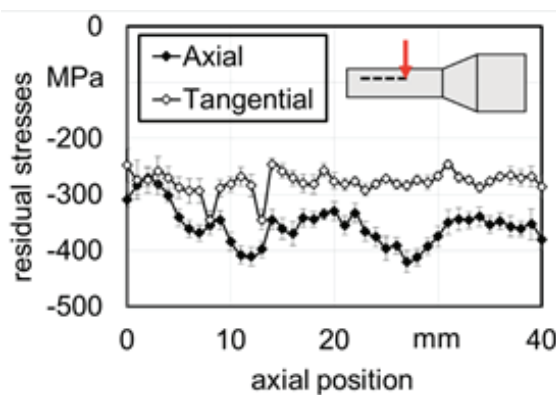


**Figure 14.3** Axial and tangential residual stress distribution measured at the outer surface of rotary swaged annealed E355 steel tube along a path in the axial direction.

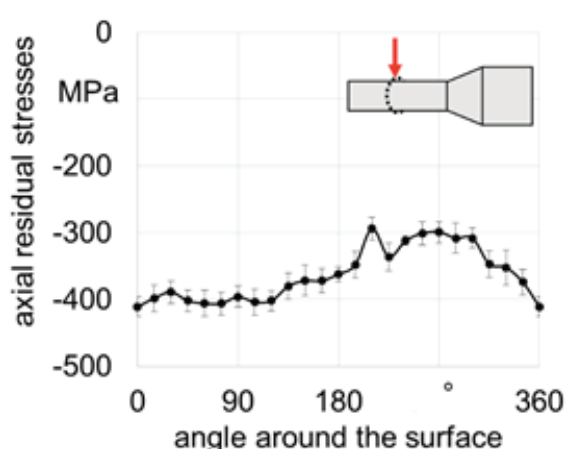


**Figure 14.4** Axial residual stress distribution measured at the outer surface around the circumference of rotary swaged annealed E355 steel tube at a fixed axial position.

ual stresses were measured, in order to save time. Therefore, further results will focus only on the axial residual stresses.

The residual stress state generated by rotary swaging was also investigated around the circumference of the same rotary swaged annealed E355 steel tube at a fixed axial position, see figure 14.4. The results show that at a fixed axial position, the axial residual stresses vary also between  $-300$  MPa and  $-400$  MPa as already observed in axial direction. Due to the nature of the process, a helical distribution of the strokes takes place at the outer surface of the samples. This can result in a corresponding distribution of residual stresses, thus showing fluctuations along the axial and circumferential axes.

### 14.3.2 Neutron Diffraction

For the analysis of bulk residual stresses induced by rotary swaging, nondestructive measurements were performed by neutron diffraction at the reactor BER II, HZB Berlin. Several beam times were granted at the instrument E3 during the project and measurements were performed using  $2 \times 2 \times 2$  mm $^3$  gauge volume. The {211} diffraction peak of  $\alpha$ -iron at  $78^\circ$  with a wavelength of 0.1486 nm was analyzed to determine the lattice spacing. The stress-free lattice parameter  $d_0^{hkl}$  was determined at small cubes ( $2 \times 2 \times 2$  mm $^3$ ) of

the same material prepared by electrodischarge machining. Due to the difficulties associated with the analysis of surface-near residual stresses by neutron diffraction, complementary semi-destructive measurements were performed by XRD and combined with the neutron diffraction data to obtain a full view of residual stresses along the diameter of tubes/rods. For the correction of the stress-free lattice parameter  $d_0^{hkl}$ , a force balance criterion was also applied on combined X-ray/neutron stress dataset [9]. The analysis of the diffraction pattern was performed using the software Stresstex developed by C. Randau of FRMII/TUM. The diffraction peak was obtained by integrating the 2-dimensional diffraction frames. The fitting of the diffraction pattern was performed using pseudo-Voigt function after background subtraction.

Results regarding the residual stress distribution of full rods are published in [7]. When examining tubes, the small wall thickness posed a particular challenge when carrying out and evaluating measurements with neutron radiation due to surface effects generating pseudo-strains, caused by partial immersion of the gauge volume in the material. To eliminate these pseudo-strains, all the measurements were repeated with the path of the primary beam and the diffracted beam switched, where the sample was rotated by  $180^\circ$  after the first

measurement. Taking the average of both measurements cancels out the pseudo-strain, since the geometrically induced peak shift is in opposite direction for both configurations. The pseudo-strain distribution was also numerically evaluated with the model-based ray tracing software SIMRES developed by Saroun et al. [10]. This evaluation was performed using a stress-free iron powder with a simplified geometry of a flat thin plate representing the tube wall with the same thickness (3.6 mm). A scan through the thickness was simulated and the resulting strain distribution was considered as pseudo-strains originating from the surface effect. After comparing the pseudo-strains evaluated by numerical and experimental methods, it was found that the pseudo-strains were in a good agreement and in the range between 0.001 and -0.001, which can result into significant residual stress errors, see figure 14.5. Along with pseudo-strains, partial immersion of the gauge volume in the material causes a shift of the real position of the gauge volume. This gap between the real position and the theoretical position of the entire gauge volume was corrected by determining the center of gravity of the immersed part of the gauge volume.

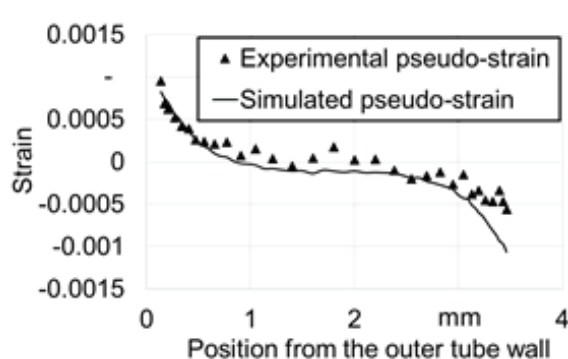


**Figure 14.5** Pseudo-strain distribution in the tube wall thickness.

$\varnothing 20 \times 3 \text{ mm}^2$  diameter E355 steel tubes were annealed at  $890^\circ\text{C}$  for 5 hours and then were rotary swaged to 15 mm diameter using type 1 dies with infeed rate of 1,000 mm/min and no retraction. In figure 14.6, the axial residual stresses calculated by the FEM 3D-simulation as described before is presented in comparison with neutron diffraction and complementary XRD results.

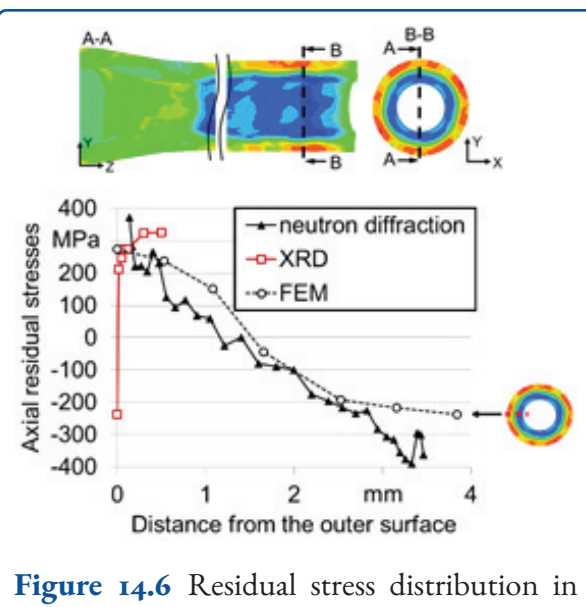


**Figure 14.6** Residual stress distribution in swaged tube analyzed by finite element simulation and neutron/X-ray diffraction.

At the inner surface, high compressive residual stresses were present, which continuously increase over the thickness toward the outer surface. Overall, very good agreement can be observed between the calculated and the experimentally determined residual stress distribution. Close to the inner surface, slight discrepancies of the neutron data and of the calculated values can be observed, which can be related to the inhomogeneity of the stress distribution in the swaged tubes. Directly at the outer surface, the FEM simulation does not present a drop to compression as does the XRD data. This is attributed to the friction model and its boundary conditions as well as to the FE mesh size, which did not allow the resolution of surface-near stress states precisely (0.5 mm FE size).

### 14.3.3 Micromagnetic Method

Micromagnetic measurements with high spatial resolution were performed using a Barkhausen eddy current microscope (BEMI) at IWT. Thanks to the miniaturized sensor technology and the external magnetization, it was possible to acquire micro-magnetic characteristics with a lateral resolution of  $20 \mu\text{m}$  and thus to analyze entire surfaces with several thousands of points [11]. Reference values from X-ray measurements were used for the cali-

bration for a quantitative analysis of the residual stresses. Two-dimensional maps of tangential residual stresses in the range of  $2 \times 10 \text{ mm}^2$  at the surface of a flat swaged full rod with flat dies were obtained and the integrated results are shown in figure 14.7.

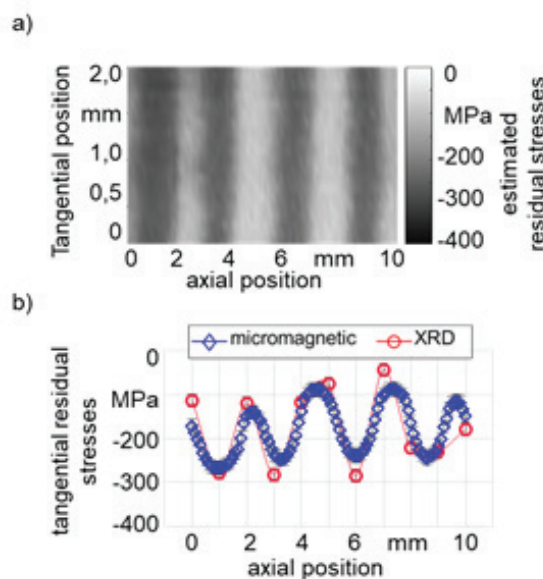


**Figure 14.7** Micromagnetic measurement: a) 2D surface tangential residual stresses measured by micromagnetic method on a rotary swaged sample with high fluctuations; b) averaged distribution and comparison with XRD [7].

Thanks to the fast measurements and high spatial resolution, the micromagnetic results could show clear periodic fluctuating tangential residual stress distribution, which agree well with the XRD results. In the present case, micromagnetic method was further employed for fast assessment of local or large-scale residual stress state using macro-sensor. However, it is worth mentioning that this method requires careful calibration with suitable reference samples from the same material, since further material properties such as hardness also strongly influence the measured signals. Further difficulties were also encountered in measuring round surfaces or hollow tubes due to disturbance of the magnetic coupling with the sensor.

#### 14.3.4 In-Situ Synchrotron XRD

In-situ synchrotron experiments were performed at Deutsches Elektronen Synchrotron (DESY) in two granted beamtimes at P07 – EH3 from HZG Hereon to investigate the transient (residual) stress evolution at different individual strokes during swaging. For this, a custom-built recess rotary swaging device was developed allowing forming tube sections, which is a special process variation. The experimental device developed and built within the project allowed transmission measurements as shown in figure 14.8.

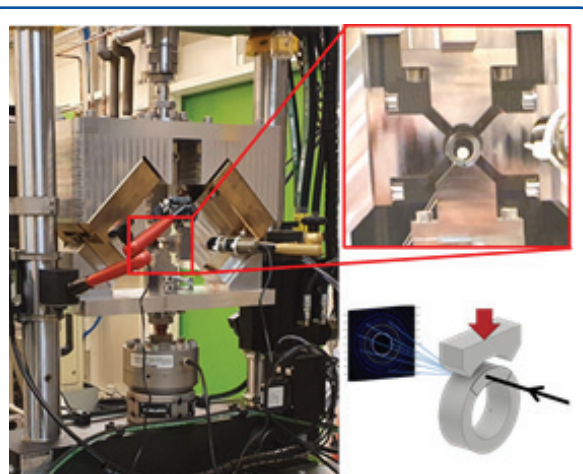


**Figure 14.8** Overview of in-situ recess rotary swaging setup and a sketch of the beam path.

This device was powered by hydraulic tensile tester of type Instron 100 kN, which allows adjustable stroke height to perform the gradual reduction of the cross-section diameter. The bottom die is fixed and only the upper die can be moved by the tensile tester simultaneously with the side dies. Tube sections of 6 mm length were formed by means of recess swaging. The in-situ synchrotron experiments were performed using a high-energy beam (103 keV) with a cross-section of  $50 \times 50 \mu\text{m}^2$  to obtain spatially resolved data on the stress state during and after individual forming steps. Heat-treated (at  $890^\circ\text{C}$  for 5 hours) and therefore residual stress-free specimens made of  $\varnothing 20 \times 3 \text{ mm}^2$  E355 steel tubes and 6 mm length were reduced to a target diameter of 15 mm without a mandrel. With radial feeds of 0.1 mm/stroke, the diameters were progressively reduced until the four jaws were

fully closed. After that, several calibration strokes were carried out. Additionally, the sample was rotated after each stroke by  $30^\circ$  to change the impact surface.

The images of the diffraction rings obtained by the 2D detector had a  $2\Theta$ -range of  $0^\circ - 10^\circ$  including the  $\alpha$ -iron diffraction rings from  $\alpha \{110\}$  to  $\alpha \{321\}$ . The strain components values were determined by analyzing the diffraction ring of  $\alpha$ -iron  $\{211\}$  after radial transformation and azimuthal integration of the data through pyFAI software. The azimuthal integration was done over 72 segments of  $5^\circ$  slices before fitting the obtained diffraction pattern with a pseudo-Voigt function to obtain the peak positions [12]. In this case, the material was assumed to be in plane strain state since the contact is established along the whole material thickness and, based on that, several strain components can be assumed to be zero, i.e.,  $\epsilon_{zz} = 0$ ,  $\epsilon_{xz} = 0$  and  $\epsilon_{zy} = 0$ . This approach was validated for in-situ XRD transmission experiments during orthogonal cutting by Uhlmann et al. by FEM-simulation [13].

The stress calculations posed a challenge due to the movement of the sample thus slightly changing the sample/detector distance, resulting in significant pseudo-strains. To eliminate this effect, residual stresses were corrected by an offset determined using the boundary condition stating that stresses normal to surfaces are zero without external forces (unloaded). In this case, the surface stresses in the radial direction are considered to be zero at the outer surface after unloading, so the calculated radial stress value near the surface is used as a correction parameter for each individual stroke. For the stress calculation under load, the same offset as for the unloaded state was used. Also, measurements close to the inner/outer surface are very sensitive to the ring orientation. If the specimen is slightly tilted and not perfectly aligned with the beam, additional pseudo-strain can greatly affect the stress results. Therefore, obtained measurements in the first 200  $\mu\text{m}$  near the outer or inner surface should not be considered.

Figure 14.9 shows mappings of the tangential stresses with about 4,000 data points during the

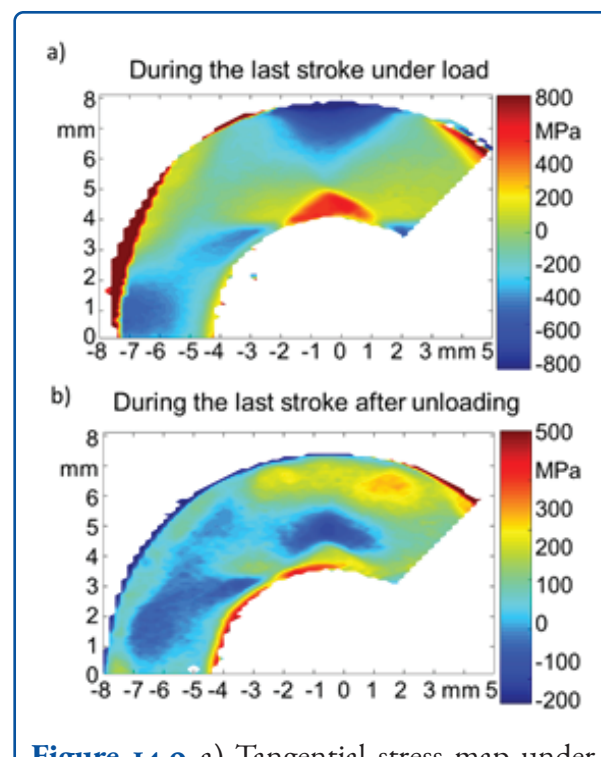


**Figure 14.9** a) Tangential stress map under load at the final calibration stroke; b) Tangential residual stress map after unloading after the final calibration stroke.

final calibration stroke under load and after unloading (residual tangential stress).

Under load, local inhomogeneity of tangential stress occurs across the wall thickness and in circumferential direction with stress concentrations below the dies (vertically and at  $90^\circ$ ) with values ranging between  $-700$  MPa at the outer surface and  $+600$  MPa at the inner surface. After unloading, inhomogeneous residual stresses with values between  $-150$  MPa and  $+300$  MPa are present. In this case, it was shown that the final residual stress distribution is not necessarily axisymmetric.

#### 14.4 Insight into Residual Stress Generation

Due to the process speed and accessibility of the forming zone, in-process observations of the real forming process have not been feasible so far. The complex material flow induces material modifica-

tions such as work hardening and residual stresses in the workpiece incrementally with each forming stroke. To understand the resulting specific distribution of residual stresses, better insight can be given by simulations and dedicated in-situ experiments. Therefore, process simulations by FEM were performed.

#### 14.4.1 2D-Simulation Results

In 2D-simulation, the influence of spacer height on the swaging process was investigated. Here, the difference in spacer height was numerically represented by a changed tool path. With thicker spacer the axial residual stresses at the workpiece surface increased. Furthermore, in the depth profile the values decreased toward the compressive range, figure 14.10.

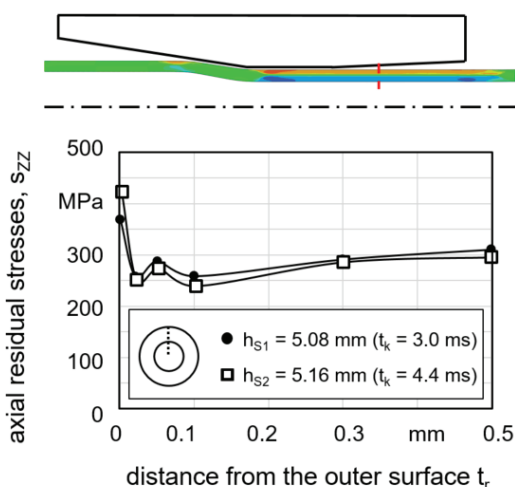


**Figure 14.10** 2D simulation results: residual stresses depth profile for different spacer height and contact time.

As described in [6] the simulated tensile values at the surface correlate with the measured distribution of the axial residual stresses at the surface of the swaged tubes with flat dies to square cross-section. Here, an increase of values in axial residual stresses occurs with thicker spacer and thus with a higher closing time. Swaging of tubes with round-shaped dies lead to compressive residual stresses at the surface which does not correlate with the simulation,

which could be explained by the simplified friction model and material flow in the 2D axisymmetric simulation. However, a correlation can be found by the relative change of residual stresses for swaging tubes with round dies. Here, residual stresses at the surface increase to higher compressive values for a thicker spacer. Another interesting observation in the simulations was that, before entering the dies, significant axial residual stresses were generated in the tube. However, it was shown that they were almost reduced to zero in the subsequently passed reduction zone. In the calibration zone, residual stresses were generated again to their final values in the steady-state zone.

#### 14.4.2 In-Situ Recess Swaging of Rings

The complex material flow induces material modifications such as work hardening and residual stresses in the workpiece incrementally with each forming stroke. To understand the resulting specific distribution of residual stresses, better insight can be given by simulations and dedicated in-situ experiments. The details of the in-situ experiments are as shown in a previous section and figure 14.11 shows the determined field of stresses over a small 2D-map of  $4 \times 4\text{ mm}^2$  centered below the upper swaging die at different steps of the process.

The upper images (figure 14.11 a) show the tangential stresses in the loaded state, while the resulting tangential residual stresses after unloading are presented below (figure 14.11 b). With each stroke, compressive loading stresses increase below the upper die while high tensile stresses increase on the inner side of the ring. During the final calibration stroke, high and inhomogeneous stress distribution is still observed, which should be mostly elastic, with superimposed residual stresses. The resulting residual stresses in tangential direction after unloading show a stress gradient over the wall thickness with tensile residual stresses near the inner and outer surface and compressive residual stresses near the middle. This gradient increases with the strokes. However, after the final calibration stroke, the residual stresses are slightly reduced compared to residual stresses during previous forming strokes and are inhomogeneously distributed along the circum-

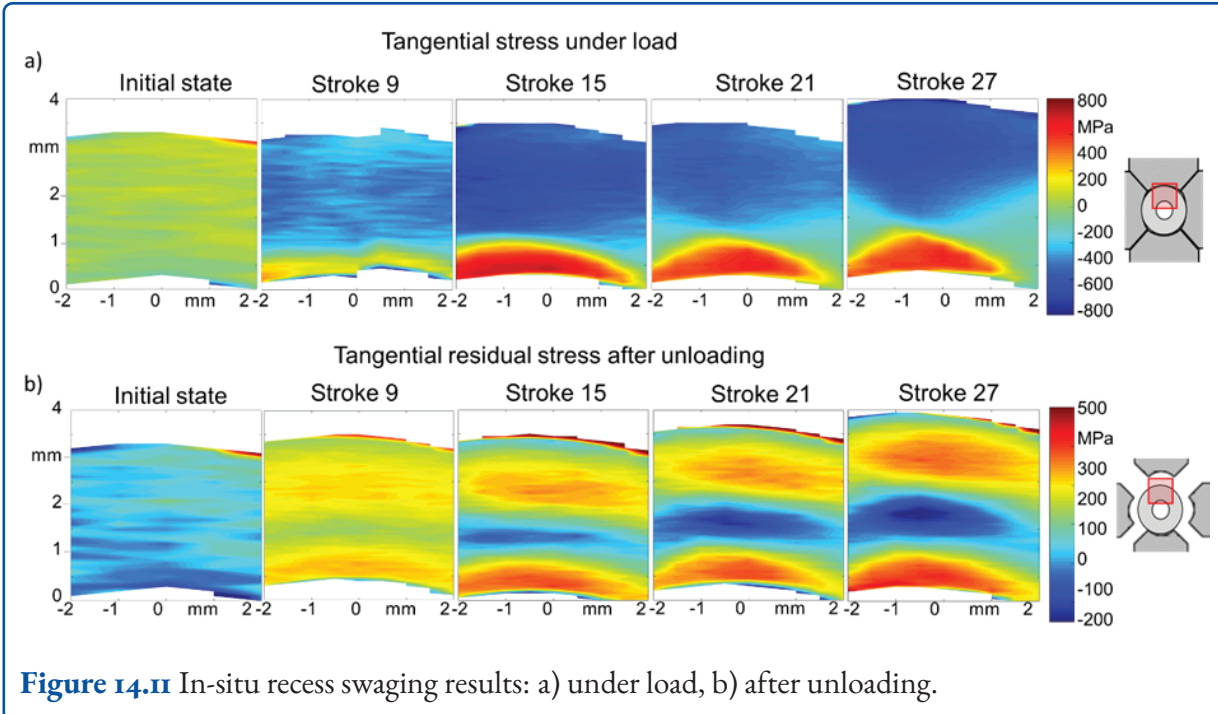


**Figure 14.11** In-situ recess swaging results: a) under load, b) after unloading.

ference. The same effects were observed in the further experiments performed with a stroke height of 0.2 mm and a stroke following angle of 60°. The stress gradients were slightly higher with a larger stroke height.

## 14.5 Experimental Studies of Process Influence on Residual Stress Generation

In the following, variations in the rotary swaging process and their effect on the residual stress state, in particular amplitude and distribution along the surface and in the depth are shown.

As open-die forging process, rotary swaging gives the material a certain freedom to flow during each stroke. Within each stroke the pressure column in the swaging head provides the forming force on the workpiece. This causes a certain stress state and amplitude while the material flow ends up in the arising residual stresses. The influence of the process (shape of dies; spacer height; use of mandrel; rod/tube forming; forming stages) on the residual stress depth profile was investigated.

On the other hand, due to the incremental forming characteristic, the residual stresses within the workpiece can also exhibit local varying distribution or random fluctuations, as shown previously. Hence, the influence of key process parameters (calibration strokes by reduced retraction speed; variations in machine parts) on local distribution of residual stresses was also investigated.

### 14.5.1 Process Variations Influencing the Residual Stress Depth Profile

In the following, rotary swaging from  $\varnothing 20$  mm to  $\varnothing 15$  mm with an infeed rate of 1,000 mm/min and a retraction rate of 500 mm/min was performed, if not stated otherwise. Swaging was performed with annealed E355 tubes with different forge value S to investigate their influence on residual stresses, figure 14.12. The variation of the respective forge value S from 1 to 0.93 resulted in a changed contact area, hence changed pressure conditions between die and workpiece. As a consequence, the stress state within the workpiece is expected to be different for each stroke. Due to the used die material and surface finishing, a difference in friction coefficient between die and workpiece was also expected. In the case of the DLC coat-

ing of die type 2, a lower friction coefficient was assumed compared to the spray-coated tungsten-carbide layer on die type 1 and the uncoated die type 4. With die type 4 axial residual stresses were close to zero at the workpiece surface. Comparing these results with die type 1 and 2, compressive residual stresses arose at the surface up to 100  $\mu\text{m}$  depth. At higher depth tensile range was achieved. The slightly difference in the die height of approximately 40  $\mu\text{m}$  due to manufacturing accuracy introduced a slightly changed pressure column and correlates with further change in residual stresses below the surface. The forge value has an impact on near-surface axial residual stresses in swaged tubes.

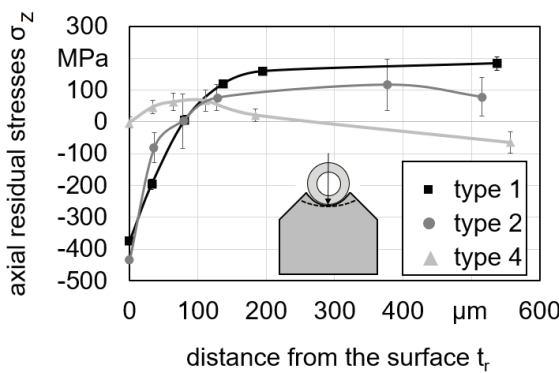


**Figure 14.12** Axial residual stresses  $\sigma_z$  depth profiles for different dies (annealed E355  $\varnothing 20 \times 3 \text{ mm}^2$  tubes).

Swaging of tubes and rods with the same swaging dies (type 2) and process parameters (infeed rate 1,000 mm/min; no retraction) led to the same compressive stresses at the surface according to the used swaging die. However, a clear change in depth profile was observed at higher depth, figure 14.13. The change in the compressive range in depth profile correlated to changed material flow resulting in an increase of the stress amplitude respectively pressure.

In contrast to swaged rods, swaged tubes generally exhibited tensile residual stresses in the outer region. This is attributed to the radial material flow to the inner hole, resulting in a modification of the overall elastic-plastic deformation within the work-piece. A method to influence the residual stresses

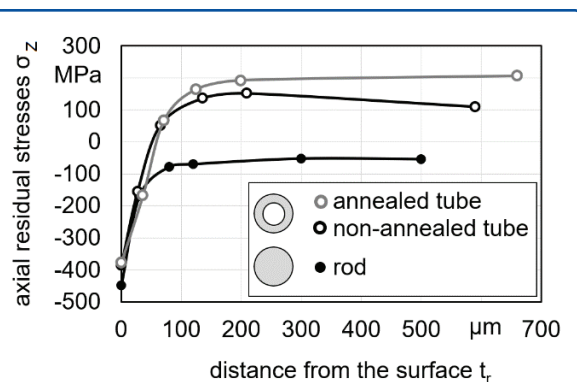


**Figure 14.13** Axial residual stresses  $\sigma_z$  depth profiles for tubes and rods (die type 2; annealed E355;  $\varnothing 20 \text{ mm}$  rods;  $\varnothing 20 \times 3 \text{ mm}^2$  tubes).

depth profile by swaging of tubes with mandrels was found. Conventionally, mandrels are used to obtain a well-defined inner diameter of tube with high surface finish. Here, this method also gave the opportunity to modify the material flow and thus the stress conditions in the tubes. During infeed rotary swaging to 15 mm diameter of non-annealed E355 tubes ( $\varnothing 20 \times 3 \text{ mm}^2$ ) with round shaped dies (type 2) on hardened warm-working-steel cylindrical mandrels with varied diameter  $d_m$ , the depth profile of axial residual stresses changed significantly, figure 14.14. At the surface, homogeneous and reproducible residual stresses  $-300$  to  $-400$  MPa were induced for different mandrel diameters which correlated with the standard deviation as shown by the measurements in the previous chapter. On the other hand, the depth profile of residual stresses was strongly affected, going from tensile without mandrel down to  $-300$  MPa with a mandrel of  $\varnothing 8.2 \text{ mm}$ . This effect could even be maintained after the mandrel has been removed mechanically after the process. For higher mandrel diameters, the residual stresses below the surface decreased again to lower compressive values. This can be explained by a hindered material flow due to an increased friction force between mandrel and tube. The changed material flow was as well observed in process observation data where the backpushing of the workpiece out of the swaging head with each stroke increased for thicker mandrels.

Additional swaging tests (die type 2 and 4) with conical (diameter  $\varnothing 8.2$  mm; 1 : 100) mandrels were conducted as this geometry simplifies the removal of the mandrel after swaging. The additional variation of dies confirmed that mandrels are usable to influence the residual stresses depth profile separately to the residual stresses at the surface, see figure 14.15. The die type 4 was used. As shown in previous tests it caused residual stresses close to zero at the workpiece surface. However, residual stresses below the surface remained at comparable values as for  $d_m = 8.2$  mm cylindrical mandrel as well as conical mandrel.

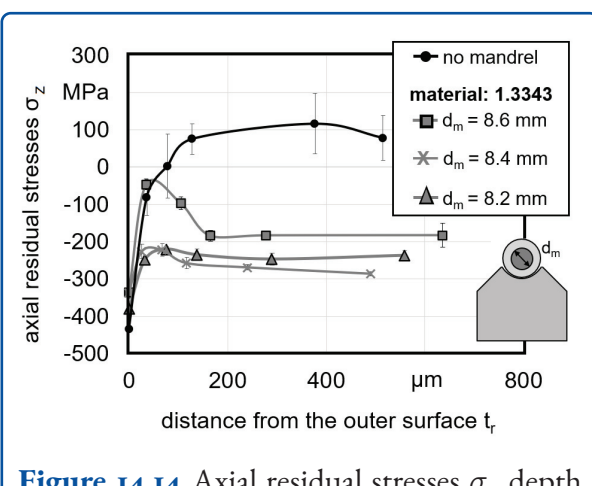


**Figure 14.14** Axial residual stresses  $\sigma_y$  depth profiles for different mandrel diameter (die type 2; non-annealed E355  $\varnothing 20 \times 3 \text{ mm}^2$  tubes).

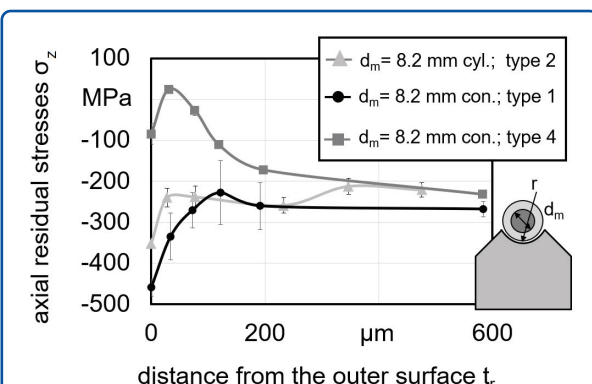


**Figure 14.15** Axial residual stresses  $\sigma_y$  depth profiles for 1 : 100 conical mandrel and die variation (die type 2 and 4; annealed E355  $\varnothing 20 \times 3 \text{ mm}^2$  tubes).

#### 14.5.2 Surface Residual Stress Distribution and Fluctuations

Due to the complex process kinematic and its possible influence on the material flow, effects on residual stresses distribution and fluctuations by process parameters and machine characteristics were investigated. Tubes  $\varnothing 20 \times 3 \text{ mm}^2$  were swaged with an infeed rate of 1,000 mm/min, but stopped without retraction and no additional calibration strokes respectively in order to better evaluate the effects on distribution and fluctuation on residual stresses. For this, softer E355 material was generated by an increased annealing time (at 890 °C for 5 hours). The basic assumption was that differences in individual strokes in soft material cause larger changes that are easier to detect. The measurement of residual stresses was performed at the surface along a 40 mm line. In addition to the normalized condition, non-annealed E355 tubes in condition as cold drawn were swaged with round-shaped dies (type 2). The initial material condition affected the fluctuations of residual stresses at the surface, figure 14.16. Given by process observations measuring a certain backpushing of the workpiece with each stroke, a change was also observed in backpushing depending on the initial material conditions. The residual stresses of the annealed tubes showed fluctuations, while the stresses on non-annealed tubes were almost homogeneous over the entire investigated areas at high compression.

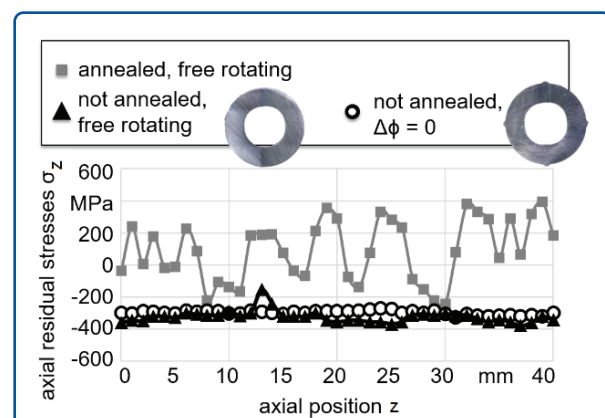


**Figure 14.16** Axial residual stresses  $\sigma_y$  at  $\varnothing 20 \times 3 \text{ mm}^2$  E355 tubes surface (die type 1; annealed and non-annealed, with and without free rotation).

These differences were mainly attributed to the near-surface microstructure caused by the special long-term annealing, as slight decarburization of about  $10 - 20 \mu\text{m}$  was observed during annealing [14]. This can lead to locally changed plastic deformation of the softer ferrite grains and thus changed residual stresses, which does not occur in the non-annealed tubes. The third condition in figure 14.16 visualizes a representative case where the stroke following angle was kept constant to zero. The slight material flow into the gaps between the dies (start of wing formation) led to a forced rotation of the specimen with the swaging unit (stroke following angle was zero) and homogeneous residual stresses at the surface resulted. This was mainly attributed to the increased number of calibration strokes on the same workpiece position and volume.

In a further investigation, the residual stresses of the annealed E355 tubes, which were swaged to  $\varnothing 15 \text{ mm}$  with infeed rate of  $1,000 \text{ mm/min}$  and round shaped dies (type 2) with different spacers height of  $5.02 \text{ mm}$  and  $5.16 \text{ mm}$ , were analyzed along the workpiece surface. Here, small changes in final diameters were found, which correlates with the changed spacer thickness for one stage swaging, figure 14.16. However, in the case of swaging with thicker spacers in one stage, fluctuations of the residual stresses at the surface were not reduced. These fluctuations were reduced by an additional calibration step (2 stage, black dots see figure 14.17). The calibration was carried out in such a way that after a full process with thin spacers ( $h_s = 5.02 \text{ mm}$ ), a second process was performed with thicker spacers ( $h_s = 5.16 \text{ mm}$ ). Calibration represents a special variant of swaging with only a small reduction of the workpiece diameter in the  $\mu\text{m}$  range with low local strain and can be seen as analogous to shot peening or hammering, thus increasing compressive residual stresses in the surface region by local repeated strokes.

A further process variant of calibration can be carried out by retracting the workpiece with reduced speed out of the swaging die. With a reduction of retraction speed the number of calibration strokes was increased. Tests were carried out for swaging annealed tubes (E355,  $\varnothing 20 \times 3 \text{ mm}^2$ ) with round shaped dies (type 2) to  $\varnothing 15 \text{ mm}$ . Starting

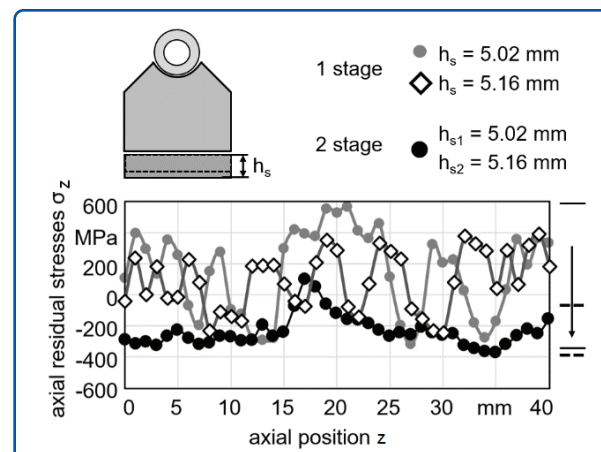


**Figure 14.17** Axial residual stresses  $\sigma_y$  at  $\varnothing 20 \times 3 \text{ mm}^2$  E355 tubes surface for different spacer thickness (die type 1).

from a value of  $350 \pm 100 \text{ MPa}$ , it was shown that more stable compressive residual stresses were generated at the surface with increasing calibration strokes, see figure 14.18. In this calibration variant, no change in spacer height was necessary, whereas with the increase of calibration strokes a small decrease of the mean value was observed, which can be related to stress relaxation.

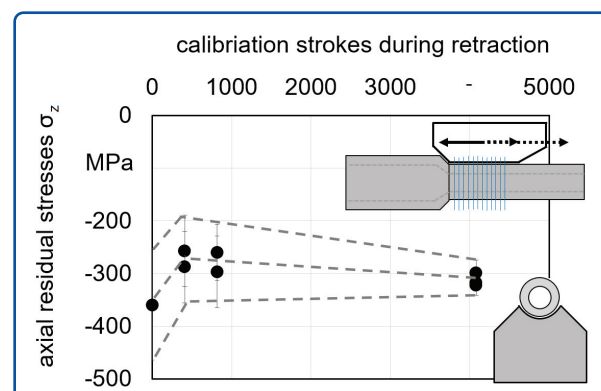


**Figure 14.18** Axial residual stresses  $\sigma_y$  at  $\varnothing 20 \times 3 \text{ mm}^2$  E355 tubes surface as a function of calibration strokes (die type 2).

### 14.5.3 Residual Stresses in Multi-stage Rotary Swaging

One further process variation was investigated in multi-stage swaging of annealed  $\varnothing 20 \times 3 \text{ mm}^2$  tubes to  $\varnothing 8 \text{ mm}$ . In the tests, the workpieces

passed through different sets of forming dies. In the three forming stages, the diameter changed with different forming histories. One-stage forming was carried out within one die with an infeed speed of 100 mm/min and a forge value of 1. Two-stage forming was carried out in each case with a forge value of 1 in the first step to Ø15 mm (die type 2) with an infeed rate of 1,000 mm/min and subsequently to Ø8 mm with an infeed rate of 100 mm/min. Three-step forming was carried out from Ø20 to Ø15 mm with an intermediate step to 17 mm within a two-step forming die with forge value of 0.93 (die type 7). The subsequent diameter change to 8 mm was performed with an infeed rate of 100 mm/min and a forge value of 1 (die type 6). The retraction speed was set to 500 mm/min for all forming stages. The different forming histories resulted in different depth profiles of the residual stresses in all variants in the intermediate stages, figure 14.19. Fluctuations as shown by the scattering of each measurement point in residual stresses were reduced. Regarding the reduction to Ø8 mm, after one-stage, two-stage and three-stage swaging comparable residual stresses in depth profile arose in the compressive range. The residual stresses in one-step forming were slightly lower, which can be related to thermal relaxation as the samples temperature was higher after one-stage forming.

#### 14.5.4 Residual Stresses Generation in Austenitic Steel

In addition to ferritic pearlitic E355 steel, two different austenitic semi-finished products were examined (1.4310 and 1.4305). In the first case, deformation-induced martensite formation during rotary swaging which could induce strong work hardening can occur. The second material mostly experiences work hardening of the austenite through lattice defects, but can also contain some amount of martensite. 1.4305 and 1.4310 austenitic steel bars were rotary swaged from an initial diameter of 18 mm to 15 mm diameter with infeed speed of 1,000 mm/min using round-shaped hard metal dies with forge value 1 (die type 3). The distribution of the axial residual stresses along a line at the surface in both austenite and martensite phases of

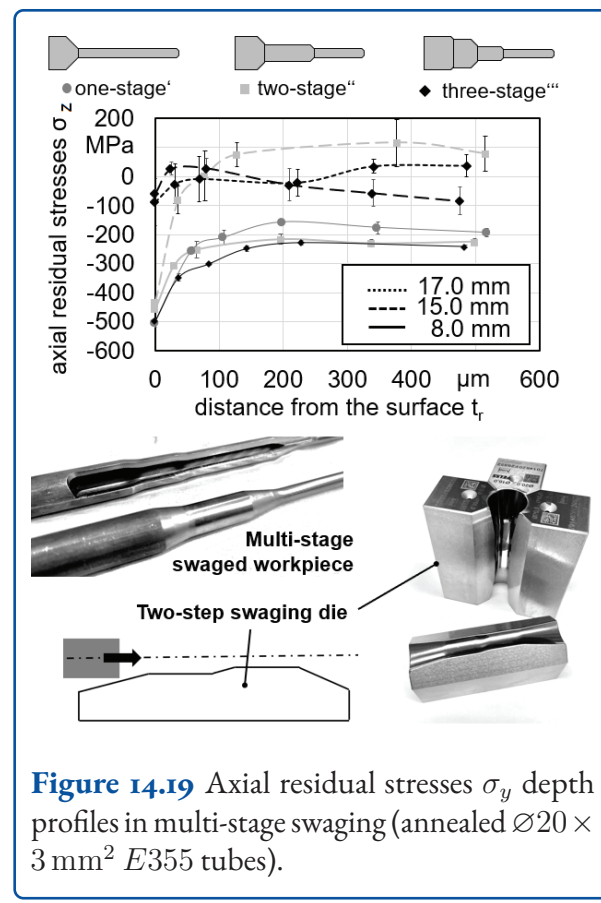


**Figure 14.19** Axial residual stresses  $\sigma_y$  depth profiles in multi-stage swaging (annealed  $\varnothing 20 \times 3 \text{ mm}^2$  E355 tubes).

workpieces generated by rotary swaging measured by XRD is given by figure 14.20 a.

## 14.6 Further Material and Parts Properties

In order for the residual stresses to have an effect on component properties, in particular on fatigue strength, they must not be fully relaxed under load [15]. However, it has been reported in literature that low-strength materials cannot achieve pronounced fatigue strength enhancement by residual stresses, as these can relax under load close to the plastic range [16]. Moreover, thermal stability under service conditions might also be relevant for several industrial application. Therefore, the stability of the residual stresses in rotary swaged samples was investigated at elevated temperature and after cyclic loading.

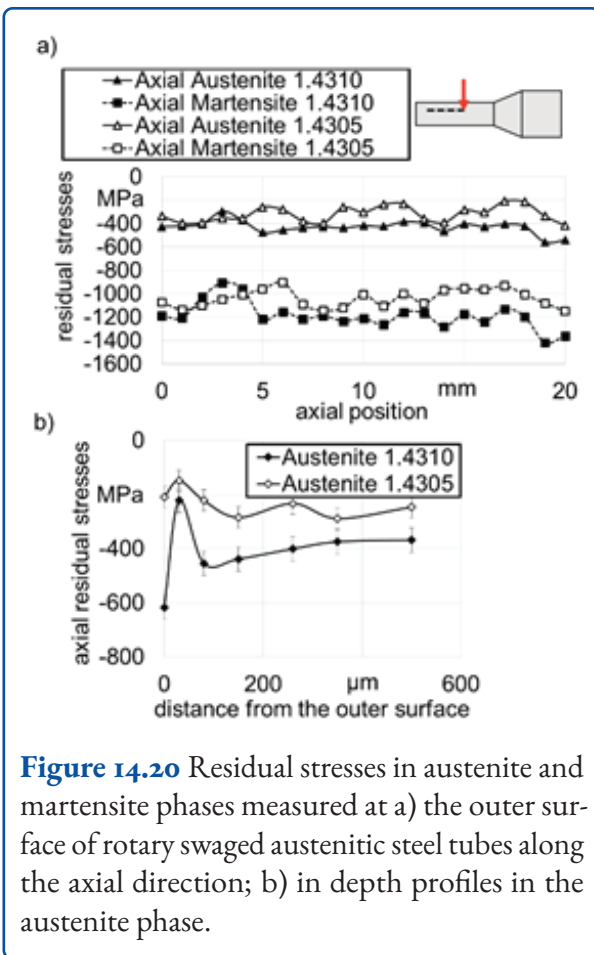


**Figure 14.20** Residual stresses in austenite and martensite phases measured at a) the outer surface of rotary swaged austenitic steel tubes along the axial direction; b) in depth profiles in the austenite phase.

### 14.6.1 Hardness

To investigate the work hardening induced by rotary swaging, microhardness measurements were performed over the tube thickness at longitudinal sections. The hardness was measured on E355 cold drawn steel tubes with and without annealing (at 890 °C for 5 hours) before and after rotary swaging using round-shaped dies (die type 1) to reduce the initial diameter from 20 mm to 15 mm, see figure 14.21. For the annealed tubes, hardness increased by about 46 % by rotary swaging and was mostly homogenous across the tube thickness. However, in the case of cold drawn tubes, hardness remained unchanged by rotary swaging indicating that no additional work hardening was introduced by rotary swaging.

Microhardness measurements were also performed in the longitudinal section in the case of austenitic rotary swaged bars featuring deformation-induced

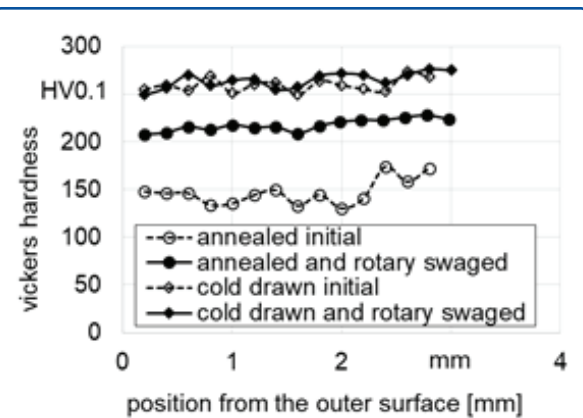


**Figure 14.21** Hardness depth profile measured over the radial position.

martensite formation. The rotary swaging was performed to reduce the initial diameter from 18 mm to 15 mm using round-shaped dies. For the 1.4305 alloy, the results show an increase in hardness from  $307 \pm 14\text{HV}0.1$  (below 5 % martensite content) before rotary swaging to  $377 \pm 19\text{HV}0.1$  (up to 15 % martensite content) after rotary swaging. In the case of 1.4310 steel, the hardness increase was from  $378 \pm 32\text{HV}0.1$  (below 10 % martensite content) to  $464 \pm 37\text{HV}0.1$  (up to 40 % martensite content).

### 14.6.2 Fatigue Properties

To evaluate the modification of the fatigue properties by rotary swaging, three-point bending fatigue tests were performed and S/N curves were determined for different conditions. The number of cycles corresponding to the fatigue strength was set to 5 million cycles and the loading ratio was 0.1. It was assumed that fatigue strength obeys the Weibull distribution function. This function was fitted to the experimental results to determine the fatigue strength which corresponds to 50 % probability of fatigue failure. The S/N curves were determined using the Basquin line method [17]. The cyclic tests were carried out using an electromagnetic pulser Rumul 50 (Russenberger, Switzerland). As a reference, stress-free annealed steel bars were tested (initial state) and compared with rotary swaged bars (square-shaped cross section, using two different infeed rates 1,000 mm/min and 3,000 mm/min).

The stress-free steel bars before rotary swaging had a hardness of  $150HV0.1$  and the rotary swaged bars of both variants had a hardness around  $250HV0.1$  (Hardness increased by 33 % by cold working), with surface axial residual stresses close to 315 MPa for the 3,000 mm/min infeed rate variant and -287 MPa for the 1,000 mm/min feeding speed variant. The determined Wöhler curves are presented in detail in [14]. The results show that the rotary swaged samples have a fatigue strength 15 % higher than the reference state. It was found that the samples which led to the highest fatigue strength with increased infeed rate while the hardness in both rotary swaged series was comparable. In addition to increasing fatigue strength, and fatigue resistance was also significantly improved in the low cycle compared to the reference state. From the investigations of the mechanical stability of the residual stresses, it was observed that they remain mostly stable even at high bending stress amplitudes, at least on the tensile loaded side. An effect of residual stresses on the fatigue strength of swaged E355 steel tubes by targeted introduction of residual stresses can therefore be expected. However, clear separation of the respective effect of work hardening and residual stress is difficult. Therefore, an additional condition was investigated after annealing of rotary swaged samples at moderate temperature to eliminate most of the residual stresses while preserving work hardening induced by rotary swaging. For this, prior tests with varying temperatures and durations were performed and the optimal parameters to achieve the desired properties was defined as a temperature of 500 °C with a holding time of 1 hour. This heat treatment showed good reduction of surface axial residual stresses (from -400 MPa down to around -30 MPa) with only a slight hardness loss of about 260 to  $240HV0.1$ . The Wöhler curve is shown in figure 14.22. The results do not show a clear change of the fatigue strength with only a small decrease of fatigue resistance in the low cycle region. This might be attributed to the slight loss of hardness due to annealing. Based on these results it seems that the effect of the residual stresses on the fatigue life is not very pronounced. This can be explained by the relatively low yield strength of the material, for which very low residual stress sensitivity was already observed after shot peening [15].

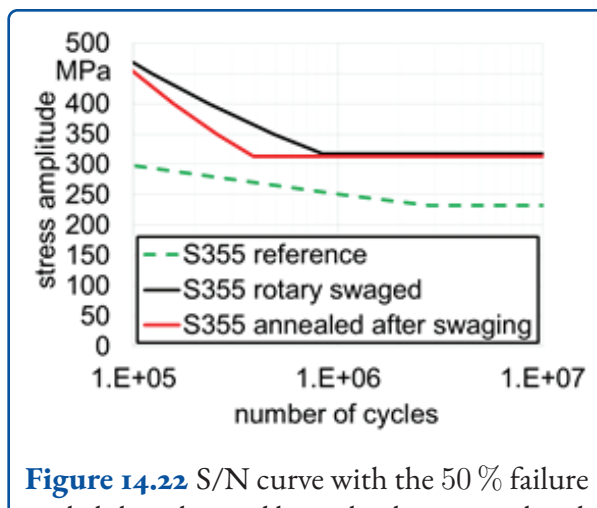


**Figure 14.22** S/N curve with the 50 % failure probability obtained by cyclic three-point bending for three material conditions of S355 steel grade.

Investigations of rotary swaged material with higher yield strength such as austenitic steel grades 1.4305 and 1.4310 were performed. 18 mm-diameter bars of these materials were rotary swaged to 15 mm diameter with infeed rate of 1,000 mm/min. Three point bending cyclic test results are shown in figure 14.23. It has to be remarked that the plotted data are based on a reduced number of fatigue tests. The results show that the rotary swaged 1.4305 samples have a significantly higher fatigue resistance than the 1.4305 reference state, which is due to combined effect of cold working and higher martensite content (increased from 5 % to 15 %), as well as to induced compressive residual stresses. The 1.4310 grade show almost similar fatigue strength but lower low-cycle fatigue properties compared to 1.4305 despite having higher compressive residual stresses and higher hardness as shown previously. This is a result of the strong embrittlement of the rotary swaged 1.4310 bars due to formation of high martensite content (around 40 %) by rotary swaging. This effect could also be observed in fracture surfaces, showing brittle failure across all samples, whereas 1.4305 showed ductile fractures. This shows that competition between a beneficial hardness increase and compressive residual stresses and embrittlement due to martensite formation has to be considered carefully for the selection of the steel grade.

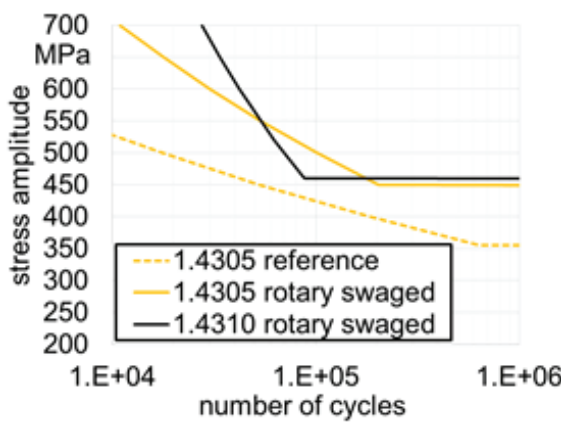


**Figure 14.23** S/N curve with the 50 % failure probability obtained by cyclic three-point bending of rotary swaged austenitic steel bars.

In order to complement the bending fatigue investigation, torsion loading of tubes produced with and without mandrels (diameter Ø8.2 mm) was performed. All samples were machined to have the same geometry regardless of the process parameters. Hardness tests were also performed on all sample variants showing virtually no difference in hardness, around 220HV0.1. The results show that the samples rotary swaged with mandrel have increased fatigue resistance in the low-cycle region compared to the samples rotary swaged with mandrel, figure 14.24. This can be directly attributed to the generated compressive residual stress over a large depth of the outer surface in the samples formed with mandrel. In comparison, the investigations of samples rotary swaged without mandrel with and without subsequent annealing after the process show lower, but almost comparable, fatigue properties. The non-annealed condition even exhibits a slightly lower fatigue limit than does the annealed state as a result of the generated tensile stresses at the outer surface.

#### 14.6.3 Mechanical Stability of Residual Stresses

Measurements were made at the surface of austenitic round steel 1.4310, which were formed with infeed rate of 1,000 mm/min (surface macro axial residual stresses after swaging about -600 MPa). Three-point bending tests were

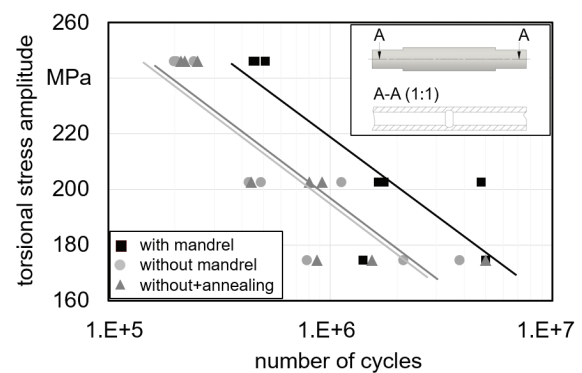


**Figure 14.24** Residual stress stability at the surface of rotary swaged E355 steel tubes under cyclic torsion.

performed for assessment of the fatigue properties. Axial residual stresses on the surface in both phases were examined on one sample at the tensile load region after 1, 10, 100, 10,000 and 100,000 cycles with a stress amplitude of 456 MPa (maximum stress about 98 % of the yield strength). The axial compressive stresses remained relatively stable until the failure of the sample before reaching 1,000,000 cycles, see figure 14.25.

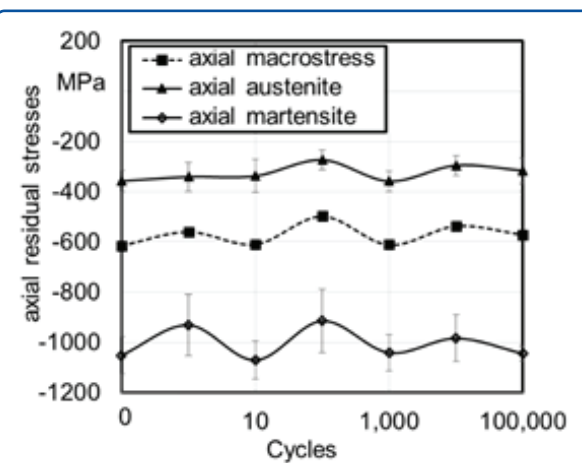


**Figure 14.25** Residual stress stability at the surface of a rotary swaged 1.4310 steel rod under cyclic three-point bending.

Previous residual stress mechanical stability analysis was performed by three-point bending tests on E355 square-shaped steel bars rotary swaged from 20 mm initial diameter to 15 mm diameter using flat shaped dies. The results are published in

[14]. The surface compressive axial residual stress remained stable after 1 million cycles with maximum bending stress of 81 % of the yield strength. However, at a higher maximum bending stress of 105 % of the yield strength, the surface compressive axial residual stress decreased in the first 100 cycles before increasing slightly with more cycles, indicating the effect of plasticity during testing.

## 14.7 Summary

---

Methods for investigation and measurement were developed to understand and modify the generation of the residual stresses in infeed rotary swaging. Modifications of the process were found to influence the state and amplitude of stresses in the forming zone as well as their distribution at the surface and in the depth of the workpieces. Residual stresses at the workpiece surface were modified by swaging dies. This process is related to a change in material flow, which results in a certain distribution of stress and pressure in the forming zone. The depth profiles of swaging tubes were pushed to the compressive range by the use of mandrels, which is due to hindered radial material flow. Multi-stage forming was performed with several dies as well as combined in one die. Here, residual stresses at the surface remained constant. With the reduction to smaller diameters, the residual stresses depth profile shifted to the compressive range, which can be explained by the increased pressure in the forming zone resulting in an increased depth of the material flow. Different effects of the process on residual stresses fluctuation were also investigated. One of the main influences was found by the initial condition of the material which, in the case of very soft material, tends to higher fluctuations. However, adjustments must be made depending on the incremental process characteristics and various parameters influencing the final surface distribution. Hence, as a practical way to reduce fluctuations, calibration strokes were found to homogenize the residual stresses at the surface. Finally, it has to be mentioned that for industrial application the residual stresses and the resulting mechanical properties of the workpiece as well as geometrical and surface properties of the workpieces have to be adjusted

and considered together in process design. The effect of residual stresses on the bending fatigue of rather soft material E355 was not found to be pronounced. On the other hand in torsion loading of tubes produced with mandrels, it is clear that an improvement of fatigue properties could be achieved compared to tube formed without mandrel (with and without subsequent annealing). This is due to generation of compressive residual stresses in deeper regions from the outer surface, which gives a concrete possibility to influence the process for the manufacturing of parts with increased fatigue properties. The analysis of 1.4310 austenitic steel with higher yield strength exhibited strong embrittlement due to the generation of a high amount of martensite, which was shown to be detrimental for the fatigue properties. In the case of the austenitic steel grade 1.4305, showing only small amount of martensite formation during swaging, a beneficial effect of the rotary swaging process on the bending fatigue properties could be observed, showing promising possibility for further research activities.

## References

---

- [1] B. Kuhfuss and E. Moumi. *Incremental forming*. Ed. by F. Vollertsen. Springer, 2013, pp. 104–113.
- [2] M. Herrmann, B. Kuhfuss, and C. Schenck. *Dry Rotary Swaging—Tube Forming*. 2015, pp. 1042–1047.
- [3] S. Ishkina et al. *Eccentric rotary swaging*. Vol. 18(7). 2017, pp. 1035–1041.
- [4] S. Ishkina et al. *Influence of process fluctuations on residual stress evolution in rotary swaging of steel tubes*. Vol. 12(6). 2019, pp. 1035–1041.
- [5] C. Kienhöfer and P. Grupp. *Rundknettechnik - Verfahren, Vorteile, Möglichkeiten*. 2003.
- [6] S. Ortmann-Ishkina et al. *Development of residual stresses by infeed rotary swaging of steel tubes*. 2021.
- [7] D. Charni et al. *Complementary methods for assessment of residual stress fields induced by rotary swaging of steel bars*. 2021.

- [8] I. C. Noyan and J. B. Cohen. *Residual Stress Measurements by Diffraction and Interpretation*. Springer, 1987.
- [9] M. Hunkel J. Epp T. Hirsch and R. Wimpory. *Combined Neutron and X-ray Diffraction Analysis For The Characterization Of A Case Hardened Disc*. Vol. 652. 2010, pp. 37–43.
- [10] J. Gibmeier J. Saroun J. Rebelo-Kornmeier and M. Hofmann. *Treatment of spatial resolution effects in neutron residual strain scanning*. 2018.
- [11] K. Szielasko et al. *Ortsauflösende Charakterisierung ferro- und ferrimagnetischer Schichten für magnetoresistive und magnetooptische Sensoren*. 2014.
- [12] J. Epp H. Meyer. *Spatial Internal Material Load and Residual Stress Distribution Evolution in Synchrotron In Situ Investigations of Deep Rolling*. 2020.
- [13] E. Uhlmann et al. *An extended shear angle model derived from in situ strain measurements during orthogonal cutting*. Vol. 7. 2013, pp. 401–408.
- [14] D. Charni et al. *Mechanical properties of rotary swaged steel components*. Vol. 85. 2021, pp. 723–732.
- [15] B. Scholtes. *Eigenspannungen in mechanisch randschicht-verformten Werkstoffzuständen. Ursachen, Ermittlung und Bewertung*. 1991.
- [16] V. Schulze. *Modern mechanical surface treatment: states, stability, effects*. John Wiley & Sons, 2006.
- [17] O. H. Basquin. *The exponential law of endurance tests*. Vol. 652. 1910, pp. 625–630.

## 15 Investigation of Residual Stress-related Elementary Processes for Cold Forged Components in the Manufacturing and Operating Phase

Jobst, A.; Lara, J.; Steinmann, P.; Merklein, M.

GEPRIS 374688875

### 15.1 Introduction

Cold forward rod extrusion is used for the production of rotationally or cyclically symmetric steel components such as screws, bolts or axles in large quantities. In this process, a billet is shaped within a die by a three-dimensional stress and strain state. By forming at room temperature, a high material and energy efficiency is achieved due to the omission of the heating step. Compared to hot forging, the extensive work hardening during production leads to highly resilient components [1]. However, high plastic strains and work hardening lead to residual stresses remaining in the formed components.

Residual stresses are known to influence the fatigue behavior of components [2]. Tensile stresses often enhance crack initiation and propagation, while compressive stresses counteract applied load stresses [3]. In corrosive environments, tensile residual stresses promote stress corrosion cracking in the component surface [4]. During cold forming, residual stresses are generated by inhomogeneous plastic deformation [5]. The characteristic work hardening in combination with a high material strength and the limited possibility of thermal stress relief lead to particularly pronounced residual stress states. They remain in the produced components and are in an equilibrium state across the material volume. Interfering with this equilibrium, for example through subsequent machining steps, leads to a redistribution of the residual stresses, which may result in geometrical changes [6].

If residual stress states generated by forming are not known, additional process steps are necessary to prevent unexpected behavior. One possibility is the removal of the unknown residual stress state, which is possible, for example, by stress relief annealing at half the absolute melting temperature or by mechanical methods [7]. Thermal residual stress relaxation is based on a temperature-induced reduction of the yield strength of the material. This leads to residual stresses being able to relax by plastic deformation [8]. Subsequent slow cooling prevents the generation of thermally induced residual stresses. For stress relaxation without energy-intensive thermal annealing processes, mechanical stress relief is used [9]. This method is based on local plastic deformation in specific component areas, leading to a new residual stress state after unloading [10]. In order to additionally generate a beneficial stress condition, finishing processes such as shot blasting are used to generate compressive near-surface residual stresses [11]. All these steps share the characteristic that they are additional effort, require additional resources and energy and extend the process chain. The ability to create a defined residual stress state during the forming process can therefore help to improve the resource and energy footprint of components.

In forward rod extrusion, the material flows along the die shoulder during forming. The material in the edge area moves in the radial and axial direction, while the material in the core only moves in the axial direction. This inhomogeneous deformation leads to residual stresses remaining in the formed components [12]. The characteristic residual stress state arising from this process consists of compressive axial, tangential and radial stresses in the core, which are in equilibrium with tensile stresses near the surface [13]. The tensile residual stress maximum is not at the surface, but underneath [12]. This forming-induced residual stress state is influenced by the

ejection from the forming die. The elastic spring-back of the die leads to a reduced die land diameter which necessitates additional forming of the component surface with a small reduction of area during the ejection [14].

The evolution of the residual stress field throughout the metal forming process can be further investigated by means of simulations replicating the manufacturing operation. Due to the complexity of the physical phenomena and their interaction occurring during the forming process, the fidelity of the numerical results requires a robust mathematical model and numerical implementation. Relevant to forward extrusion is the ability of the model to describe what is known as secondary yielding [15] which occurs during unloading. Furthermore, the modeling of the other components of the tool system also affects the numerical results, e.g., considering the die rigid or elastic [16]. The frictional contact between components also plays an important role in forming operations and its adequate modeling is required to numerically replicate the material's behavior, e.g., as shown in [17] with their proposed model. A summary of the important considerations and possible error sources when modeling bulk forming process is presented in [18].

In order to be capable of influencing the operating properties, residual stresses need to be stable under operating conditions [19]. Although plastic deformation removes the residual stresses in the affected material volume, load stresses below the yield strength may also influence the residual stress state [20]. In the early stage of testing, cyclic loading with positive mean stresses may result in a high stress relaxation rate [21]. It is known for welding-induced residual stresses that the number of load cycles, the mechanical properties of the material as well as the interaction between the stress ratio, the magnitude of the mechanical load and the initial stress state influence the residual stress relaxation [22].

While basic findings are available, little work exists on targeted adjustment of the residual stresses during the forming process and its subsequent use for component improvement in the service phase.

## 15.2 Objectives and Methodology

The motivation for the research in this project is to generate an understanding of residual stress-related elementary processes in cold formed components in the forming and operating phase. For this, the following objectives are defined.

- Identification of basic principles of residual stress generation during cold extrusion.
- Development of methods for controlling residual stresses during forming.
- Evaluation of process robustness against disturbing factors.
- Determination of residual stress stability under typical operating load.
- Assessment of residual stress-related influences on the operating and fatigue behavior.

### Methodology

In order to study the residual stresses that result from the manufacturing process and their effect on the operating behavior of the mechanical component, the joint experimental-numerical approach shown in figure 15.1 is followed in the project. It is based on the analysis of the shown forward extrusion process in simulation and by measurements of the residual stresses of experimentally formed workpieces. A selected set of adjustable parameters in the forming process are varied in value in order to obtain different residual stress profiles. The profiles are tested for their mechanical and thermal stability and, subsequently, their effect on the lifetime of a cyclically loaded workpiece is assessed. Based on the results, the process can be designed in such a manner that the desired qualities of the formed workpiece are achieved.

The considered manufacturing process is the cold extrusion of rod elements following the sequence shown in figure 15.2. During part production, a cylindrical billet undergoes inelastic deformations by being forced through a forming die in order to reduce its diameter. The material is subjected to a triaxial compressive stress state. Once the desired dimensions are obtained, the billet is pushed out

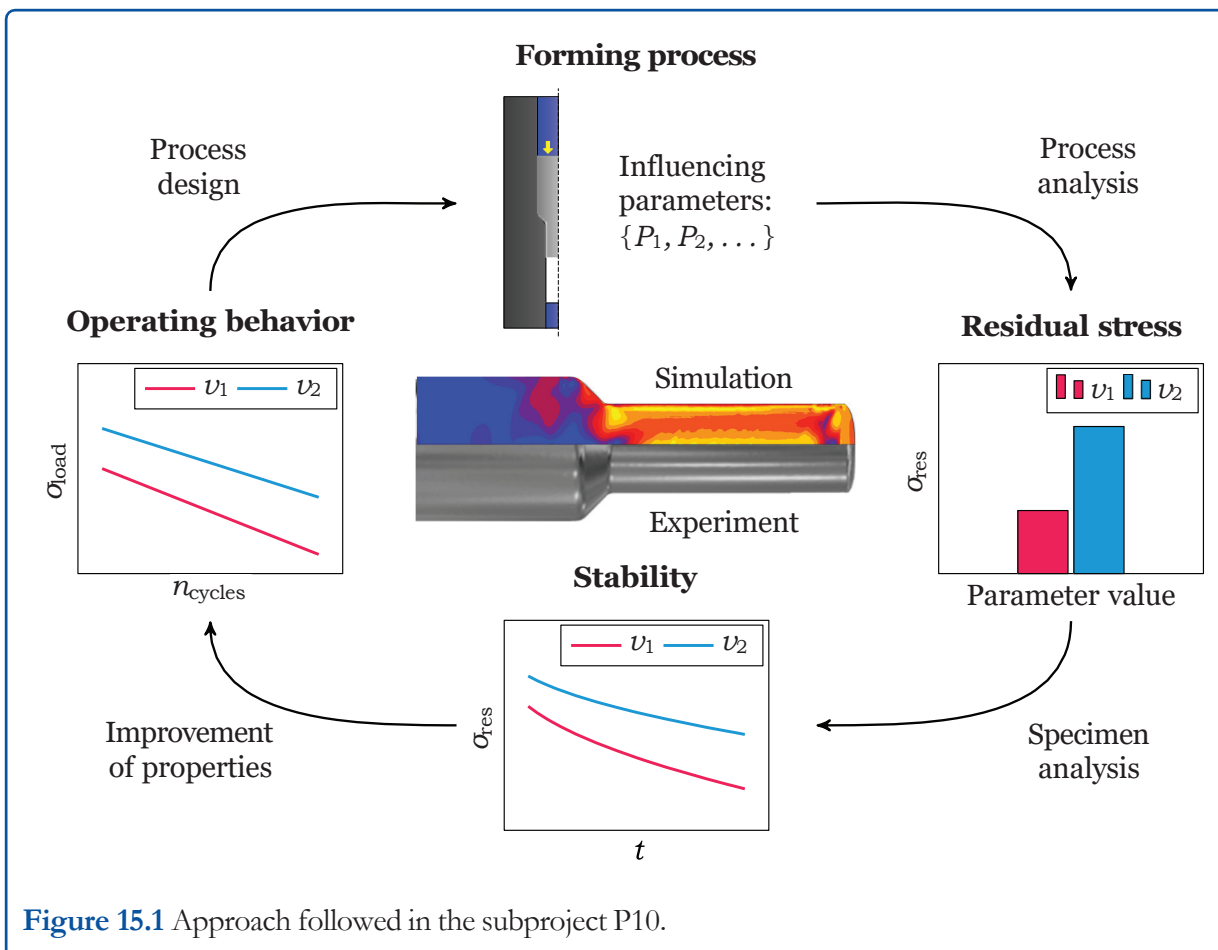


Figure 15.1 Approach followed in the subproject P10.

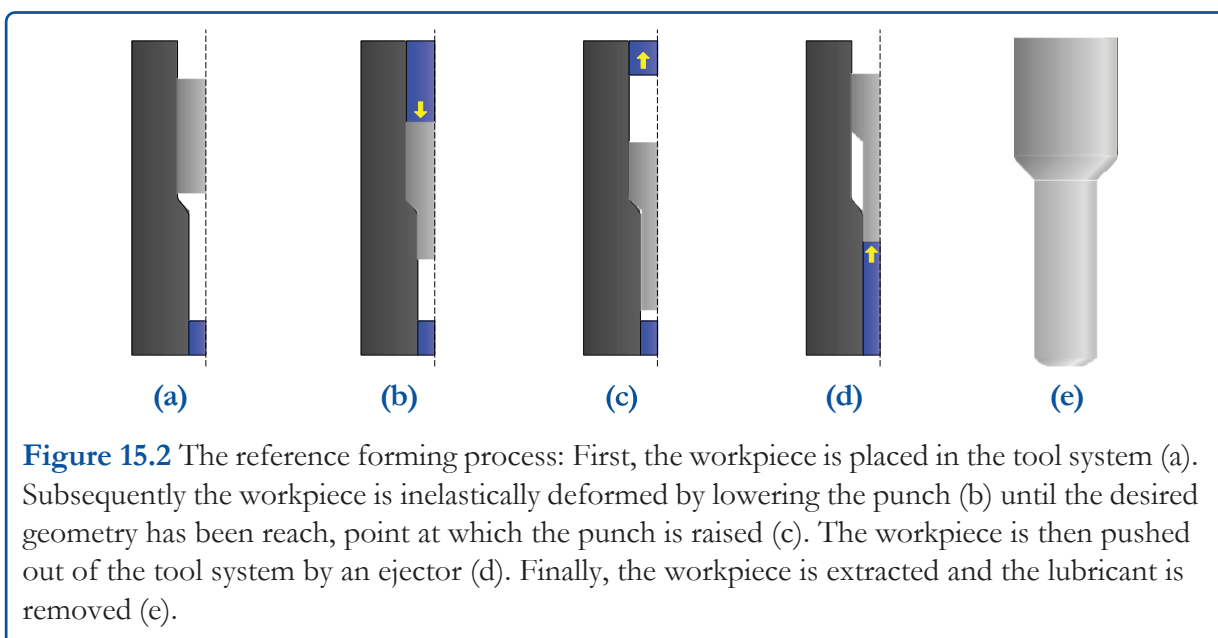


Figure 15.2 The reference forming process: First, the workpiece is placed in the tool system (a). Subsequently the workpiece is inelastically deformed by lowering the punch (b) until the desired geometry has been reached, point at which the punch is raised (c). The workpiece is then pushed out of the tool system by an ejector (d). Finally, the workpiece is extracted and the lubricant is removed (e).

by an ejector in the opposite direction to the punch direction. Due to its industrial relevance, the forward rod extrusion process, which is used for the

manufacturing of bolts, axles or other cylindrical bulk metal formed products is investigated. In this representative forming operation, the die diame-

ter of the billet is reduced from 25 mm to 15 mm, which corresponds to a reduction of area of 64 % or an overall plastic strain of 1.02.

### Experimental Setup and Software

For part production, billets of ferritic stainless steel X6Cr17 (DIN 1.4016) with a diameter of 25 mm and a height of 50 mm are cut from bars. To enable forming and to reduce tool loads, the billets are coated with a high-performance tribological system, which consists of an iron-III-oxalate lubricant carrier layer *ZWEZ-Coat 1039* and a molybdenum-disulfide-based lubricant *ZWEZ-Lube MD 230*. The coated billets are formed in a die made of high-speed steel *ASP 2012*, which is pressed into a shrink ring made of hot working steel X37CrMoV5-1. The test setup is shown in detail in [23]. The die opening angle in the reference variant is  $2\alpha = 90^\circ$ . For the studies, further component materials such as X5CrNi18-10 and X2CrNiMoN22-5-3, lubricants (soap, polymer) and die opening angles ( $60^\circ$ ,  $120^\circ$ ) are used in addition to the reference variant.

The residual stresses on the surface of the formed parts are determined by X-ray diffraction. For this, a diffractometer type *Seifert XRD 3003* is used. The X-rays are generated by a chromium anode, guided by glass capillary optics and projected on the surface with a spot size diameter of 0.8 mm. The diffracted beam is detected by a line detector *Meteor 1D*, with the  $K_\beta$  fraction removed by a vanadium filter. For a single measurement, axial and tangential stresses are identified with 13  $\psi$ -tilts performed per measuring direction. The line positions of the recorded peaks are determined by fitting with a Pseudo-Voigt function. The well-established  $\sin^2 \psi$ -method is used for the evaluation. A detailed overview of the measurement setup is given in [23]. For the ferritic-austenitic dual-phase steel X2CrNiMoN22-5-3, stress determination is possible only specifically for the ferritic and the austenitic phase. In [24], a method was developed with which a determination of the macro stress from the phase stresses is possible.

The numerical reproduction of the forming process is realized in *MSC Marc*, a commercial soft-

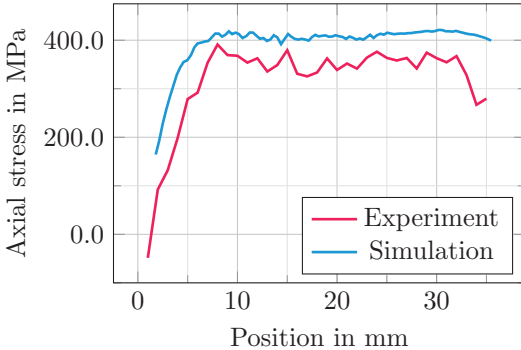
ware specialized in solving non-linear problems using the finite element method. The mathematical model used to investigate the material response at the microscopic scale was numerically implemented using the open-source finite element library *deal.II* [25].

### 15.3 Residual Stress Generation during Forming

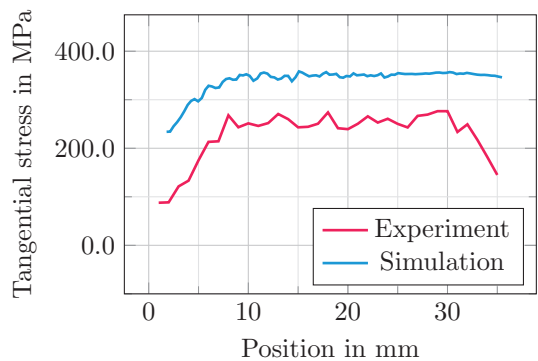
In the forming process, the billet is first pressed into the die and formed at the die shoulder. In the process, the material flows in the axial and radial directions in the edge area and only in axial direction in the core. This results in differences in the strains between the edge and core areas, which leads to residual stresses remaining. During forming, the die experiences elastic expansion due to the internal pressure and elastically springs back after removal of the punch force. As a result, the diameter of the die land is slightly reduced during ejection opposite to the punch direction. This affects the component surface and the corresponding residual stresses near the surface. The arising residual stresses are compared to the numerically predicted stresses in figure 15.3.

The residual stresses at the surface of the formed shaft after forming without ejection are shown in figure 15.3 a) and b). Near the shoulder, minor axial compressive stresses and tangential tensile stresses occur, which change into constant and distinct tensile residual stresses along the formed shaft. The axial stresses have a value of approximately 350 MPa, the tangential stresses are around 250 MPa. From a distance of 8 mm from the part shoulder, constant residual stresses are present. This corresponds to the literature, where a constant stress state is expected at a distance of the half diameter [12].

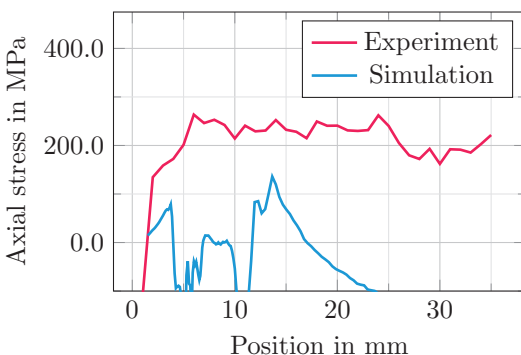
Figure 15.3 c) and d), which represent the resulting residual stress with ejection, shows that the ejection from the die reduces the tensile residual stresses. In the axial direction, they are reduced by approximately 100 MPa. In the tangential direction, only minor stresses of 50 MPa are present after ejection. This is attributed to the elastic springback of the



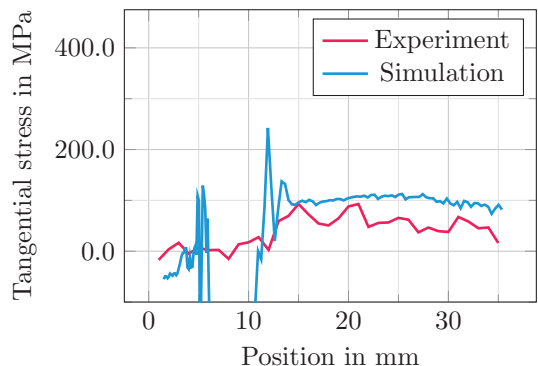
(a) Axial stress without ejection



(b) Tangential stress without ejection



(c) Axial stress with ejection



(d) Tangential stress with ejection

**Figure 15.3** Comparison of experimentally determined and numerically obtained residual stresses along a portion of the formed shaft [26].

die. Due to the resulting reduction of the die land diameter, the formed shaft is formed again with a slight reduction of area during ejection.

### Modeling of the Forming Process

The mathematical model of the forward rod extrusion has to reproduce the finite inelastic deformation intrinsic to forming processes and also to capture the Bauschinger effect due to the load reversal that occurs when the workpiece is extracted from the machine via an ejection punch. To this end, an in *MSC Marc* built-in combined hardening plasticity formulation based on the work of Chaboche [27] was used. It is characterized by the yield function

$$f = \sqrt{\frac{3}{2} \|s^{\text{red}}\|^2 - [R + \sigma_{y0}]} \quad (\text{Equation 15.1})$$

where  $s^{\text{red}}$  is the deviatoric part of the reduced stress defined as  $\sigma^{\text{red}} := \sigma - \mathbf{X}$ ,  $\mathbf{X}$  is the back stress tensor,  $R$  is the isotropic hardening parameter and  $\sigma_{y0}$  the initial yield stress. The evolution of the plastic strain and the backstress are given by

$$\dot{\epsilon}^p = \kappa \frac{\partial f}{\partial \sigma}, \quad \dot{\mathbf{X}} = \kappa \left[ \frac{C}{R + \sigma_{y0}} \sigma^{\text{red}} - \gamma \mathbf{X} \right] \quad (\text{Equation 15.2})$$

where  $\kappa$  denotes the plastic multiplier. Furthermore, the isotropic hardening parameter is given by

$$R = R_\infty [1 - \exp(-bp)] \quad (\text{Equation 15.3})$$

with  $p$  being the accumulated plastic strain. The material parameters  $\{R_\infty, b, C, \gamma\}$  are calibrated using experimental data from uni-axial tests as detailed in [28]. Two sets of material parameters are calibrated: one for the combined hardening model and for the same model but without the kinematic

hardening part, i.e.,  $C = 0$  and  $\gamma = 0$ , further referred as the isotropic hardening model.

Forming process simulations are challenging due to the intrinsic finite deformations and the interaction between components through contact forces. The complexity of the model requires that the discretization schemes used sufficiently resolve both spatial and temporal scales in order to produce reliable results. This was investigated in [26] by simulating the forward extrusion process while varying the mesh and the load step size for the cases with and without the ejection of the workpiece. For the latter it was determined that, as the load step size is reduced, the solution does not change noticeably; thus, a coarse discretization sufficiently resolves the temporal scale. While varying the mesh size, it was observed that the spatial scale of the problem requires fine discretizations to obtain mesh-independent results. The temporal and spatial scales of the forming process with an ejection step were found to require a finer discretization than without ejection. Adaptive discretization schemes may provide a way to reduce the computational costs needed to fully resolve the scales and thus obtain trustworthy results.

Using the calibrated model and the appropriate discretization, the full-forward extrusion process was reproduced in *MSC Marc*. An extensive description of the simulation and the numerical considerations can be found in [28]. The workpiece was subjected to three load steps: a forming step, an ejection step and an unloading step. The stress field at the end of the latter corresponds to the residual stresses. In figure 15.3, the numerical results as predicted by the combined hardening model and the experimental data measured alongside a path starting at the end of the shoulder and running axially down the deformed shaft are shown for the case with and without ejection. A good qualitative agreement can be observed between the numerical and the experimental values for the case without ejection. The mathematical model leads to overestimated values of the residual stresses. When considering the ejection step the model provides good qualitative – yet overestimated – results for the tangential stress in the range [15 mm, 35 mm]. Outside this range and also for the axial stresses, the formulation leads

to different stress profiles. As reported in [28], the isotropic hardening model provides better results, both quantitatively and qualitatively, than the combined hardening model. This is more noticeable for the case when the workpiece is ejected. This unexpected behavior hints that a more complex material model is required to describe the plastic flow that occurs during the load reversal and thus obtaining accurate predictions of the residual stress field when the workpiece is ejected from the tool system.

The residual stress field, being the product of inhomogeneous inelastic deformations, evolves dynamically as the material experiences local hardening and softening throughout the loading history. This progression can not be captured by conventional means since the residual stress field can only be determined when all the loads acting on the deformable body are completely removed. As such, in order to observe the evolution of the residual stresses, the workpiece has to be unloaded throughout the forming process. Whereas this is not feasible in an experimental setting, it can be achieved numerically. This can be done through a post-processing scheme as proposed in [23], in

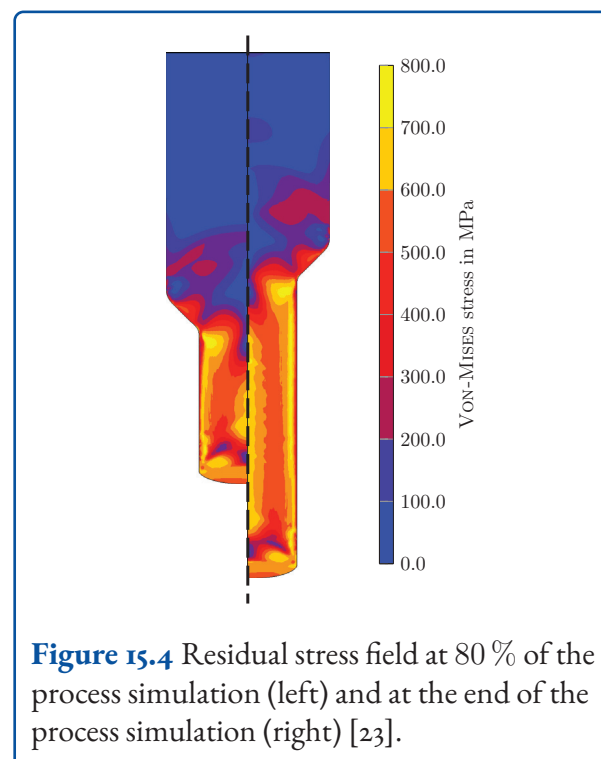


**Figure 15.4** Residual stress field at 80 % of the process simulation (left) and at the end of the process simulation (right) [23].

which a snapshot of the solution is taken at each load step. Subsequently, the snapshot undergoes an unloading step resulting in the residual stress field, as shown by way of example in figure 15.4. The agglomerate of these unloading steps provides the evolution of the residual stresses throughout the simulation, and thus making it possible to obtain a valuable insight to the generation of the residual stresses during the forming process.

## 15.4 Adjustment of Residual Stresses

For a targeted and reliable adjustment of the residual stresses, influencing factors and their effects and relevance need to be known. In this project, the influence of the parameters material, die opening angle and lubricant are analyzed among others.

### Material

Forming the reference geometry with both the austenitic steel X<sub>5</sub>CrNi<sub>18</sub>-10 and the duplex steel X<sub>2</sub>CrNiMoN<sub>22</sub>-5-3 has led to distinctly higher tensile residual stresses compared to the reference material X<sub>6</sub>Crr<sub>7</sub> [24]. This is due to the fact that an increased material strength facilitates higher residual stresses due to the extended elastic range. However, when forming materials with different strength and work hardening properties, differences in residual stress generation mechanisms may arise. When forming duplex steel X<sub>2</sub>CrNiMoN<sub>22</sub>-5-3, it is shown in [24] that the residual stresses are less reduced during ejection compared to the single phase ferritic steel X<sub>6</sub>Crr<sub>7</sub>. This is attributed to the interaction between die springback and material strength. With lower part material strength, the strain generated by die springback is able to plastically deform the component during ejection, while parts with higher strength are not deformed.

### Die Opening Angle

In industrial practice, the die opening angle is an important parameter for forming process design. Increasing the die opening angle reduces the subse-

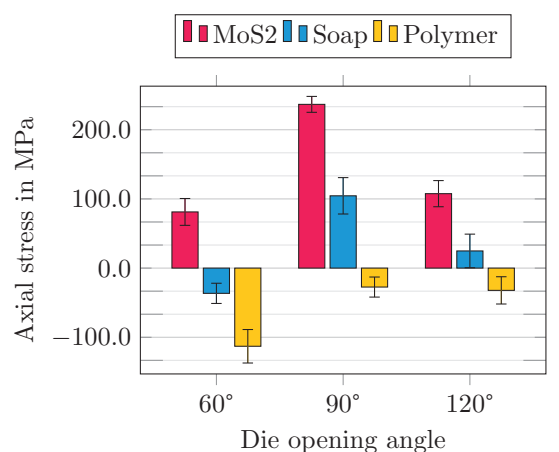


**Figure 15.5** Experimentally determined influence of die opening angle and lubrication on residual stresses.

quent machining work, but leads to an increase in the required forming energy [29]. The influences of the die opening angle with the reference geometry on the residual stresses generated during part production are shown in figure 15.5. The use of a die opening angle of  $2\alpha = 90^\circ$  leads to the highest tensile residual stresses. Both a reduction to  $2\alpha = 60^\circ$  and an increase to  $2\alpha = 120^\circ$  result in lower residual stresses in the formed shaft [26]. The forming induced part temperature, which is lowest for  $2\alpha = 90^\circ$ , is unlikely to be the cause for these differences, since the temperatures only have a variation of 20 °C [30]. Instead, the change of the die opening angle leads to differences of the plastic strain distribution in the interior of the specimen. Furthermore, the contact pressures are influenced, which changes the near-surface stresses and the tribological conditions during forming.

### Lubrication

For cold forming with high material strengths and contact pressures, the billets are coated with a two-part lubrication system. Its main task is to separate the tool and workpiece surfaces and to enable sliding. In this project, the effects of three typical cold forming lubricants are investigated. In the double cup extrusion test, the MoS<sub>2</sub>-based lubricant exhibited the highest friction factor ( $m = 0.126$ ), while

soap ( $m = 0.116$ ) and polymer ( $m = 0.098$ ) provide better lubrication. Using MoS<sub>2</sub>, the highest tensile residual stresses are achieved for all die opening angles, as shown in figure 15.5. The use of lubricants with reduced friction factors leads to a reduction of the residual stress values. Forming with a die opening angle of  $2\alpha = 60^\circ$  and the polymer lubricant results in the highest near-surface compressive residual stresses. This reduction is explained by an improved sliding of the workpiece on the tool and thus reduced shear stresses, which leads to a decreased plastic deformation inhomogeneity in the near-surface areas and thus to decreased residual stress values [26]. However, the application of the lubricants in practice is limited. While it has been possible to successfully manufacture parts with all lubricants for the reference material, only MoS<sub>2</sub> can be used for higher material strengths and therefore higher contact pressures and part temperatures [30].

## 15.5 Residual Stress Stability

To estimate the influences on fatigue strength, not only the magnitude and sign of the residual stresses, but also their stability under typical operating loads are relevant [19]. During operation, mechanical load stresses are typical during the intended use of the component. Thermal exposure can also be encountered in the event of malfunctions or for special components. In this project, the influences of mechanical [31] and thermal [32] loading on the component residual stresses were analyzed experimentally.

### Thermal Load

Residual stresses in components are often specifically eliminated by thermal processes such as stress relief annealing [8], which is based on a thermal reduction of the yield stress and therefore a transformation of the elastic residual stresses into plastic strains. It is usually performed with temperatures of 550 °C to 650 °C and soaking times of one to two hours. At lower temperatures, different mechanisms such as a thermally activated dissolution

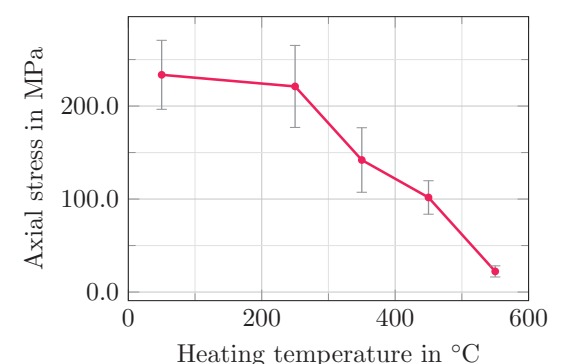


**Figure 15.6** Residual stress stability for single heating in the surface of the formed shaft of each  $n = 3$  specimens of the reference variant (material X6Cr17, MoS<sub>2</sub>-based lubricant,  $2\alpha = 90^\circ$ ).

of dislocation accumulations, which also lead to a residual stress relaxation may occur [33].

When analyzing the thermal stability of residual stresses, the temperature and soaking time are to be considered. Figure 15.6 shows the residual stress stability for a single heating of the components of the reference variant. For a temperature of 550 °C, single heating leads to 22 MPa remaining in the component, which is considered stress-free. Temperatures of 450 °C and 350 °C significantly reduce the stresses. Below 250 °C, no distinct influence of single heating is detected. This temperature-dependent residual stress relaxation is attributed to a reduced material strength with elevated temperatures [32]. For temperatures of 200 °C and below, small changes of the residual stresses were detected in the surface for soaking times of up to 100 h. Possible reasons for these observed changes are the measurement uncertainty or a minor reduction of tensile and compressive stress maxima in the inside. However, due to the minor amplification of the near-surface residual stresses, they are considered stable at 200 °C and below [32].

### Mechanical Load

When subjected to a mechanical load, residual stresses are removed due to plastic deformation if the sum of load and residual stresses exceeds the

yield stress. After unloading and elastic recovery, a new residual stress state is generated due to the necessary stress equilibrium in the specimen. As a part of this project, a modified three-point-bending setup was used in a resonance pulsator to investigate the residual stress stability under a cyclic mechanical load. The bending of the formed shaft leads to a tensile load stress at the surface, which is superimposed on the residual stress in the test area. Depending on the load stress and the number of load cycles, three different stress relaxation mechanisms shown in figure 15.7 have been identified [31].

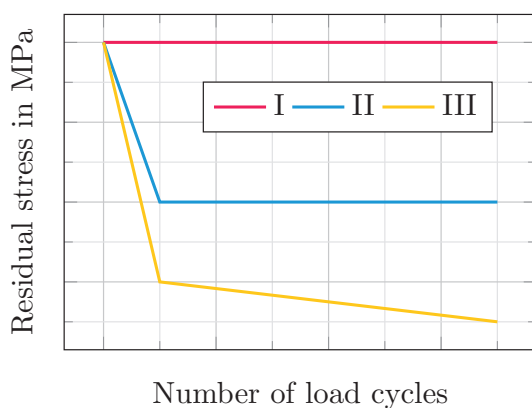


**Figure 15.7** Residual stress stability mechanisms under cyclic mechanic loading. I. Stability in all cycles, II. Relaxation with subsequent stability, III. Relaxation with subsequent relaxation.

- Constant residual stresses for all loading cycles are found in mechanism I. This is the case if the effective load stress as the sum of nominal load and residual stresses does not exceed the yield stress of the material [31].
- A change in the first cycle and subsequent stability occur in case II. This is explained by specific part areas being plastically deformed in the first loading cycle. If the sum of load and residual stress exceeds the yield stress, the affected material volume is plastically deformed and the resulting strain hardening leads to an increase in load-bearing capacity. If the sum of load stress and the new residual stress is less than the yield stress, the residual stresses remain stable in the further course [31].

■ Residual stresses are changed both in the first and in further cycles for mechanism III. If the generated work hardening is not sufficient to increase the material strength to a level equal to the load stress, plastic deformation occurs in every load cycle, resulting in a persistent reduction of the residual stress values during cyclic loading [31].

## 15.6 Operating Behavior

For the identification of the fatigue strength of the formed components with S-N-curves, the experimental setup for the analysis of the residual stress stability is used. The experimental procedure follows DIN 50100, using the pearl string method [34]. The S-N-curve is defined by

$$N = C \times L_a^{-k} \quad (\text{Equation 15.4})$$

where  $N$  is the number of load cycles to rupture,  $L_a$  is the applied load amplitude, position  $C$  and slope  $k$ . The high-cycle fatigue (HCF) regime is limited by the low-cycle fatigue (LCF) regime with approximately  $10^4$  cycles and the knee point, which represents the transition to the long-life fatigue (LLF) regime. In the latter, a horizontal course is expected for the ferritic steel. For the specification of the operating properties, the evaluation variables used are the slope  $k$ , the cycle number at the knee point  $N_K$  and the load amplitude of the LLF regime.

The influence of the forming induced residual stress state is identified by testing specimens produced with the reference variants and a comparison to stress-relief annealed specimens. The effect of forming-related residual stress changes is determined using specimens formed with die opening angles of  $60^\circ$  and  $120^\circ$ . The results are shown in figure 15.8.

In the reference variant formed with a die opening angle of  $2\alpha = 90^\circ$ , the highest tensile stresses are present after forming and ejection. This leads to the lowest LLF stress amplitude with a value of 350 MPa. With  $2\alpha = 60^\circ$  and  $120^\circ$ , significantly lower tensile stresses are present, leading

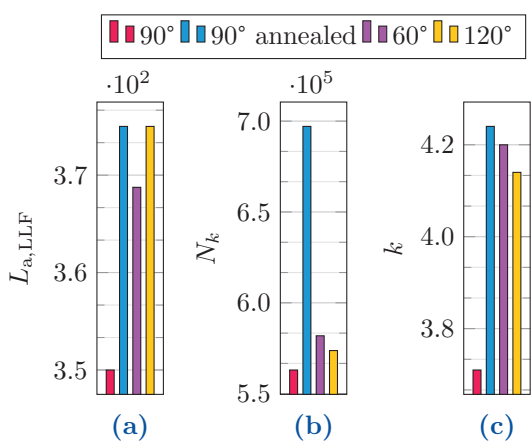


**Figure 15.8** Experimentally determined parameters of the S-N-curves for different specimen variations. a) load amplitude of the long-life fatigue  $L_{a,LLF}$  (MPa), b) cycle number at the knee point  $N_K$ , c) slope  $k$  of the S-N-curve

to an increased LLF stress amplitudes of 369 MPa and 375 MPa, which is in the range of the annealed reference specimens with 375 MPa. Furthermore, an increased slope of the S-N-curves occurs with reduced residual stresses, which leads to a flatter course. These effects are attributed to the superimposition of the load stresses and the residual stresses. During loading, these add up and therefore increase the effective load stress, leading to reduced load bearing capacity of the component.

Comparing the achievable cycle numbers at the knee point, the residual stress-free variant shows 20 % to 24 % higher values than the unannealed variants. The reason for this is the residual stress state of the formed components. Although the residual stresses in the surface are reduced by the adaption of the die opening angle of the forming tool, there are still tensile residual stresses below the surface. By superimposition with the load stresses, they reduce the achievable number of operating cycles.

This leads to the conclusion that tensile residual stresses are detrimental to operating behavior. A full removal of the residual stress state increases fatigue strength. Forming methods to reduce tensile residual stresses near the surface offer the potential

to increase the load bearing capacity of the components.

### Material Behavior at the Microscopic Scale

The abrupt failure of mechanical components characteristic of high-cycle fatigue can be traced back to the propagation of microscopic cracks that originate at imperfections within the material, e.g., at the grain boundaries of polycrystalline materials. Therefore, in order to numerically assess the influence of the residual stress field on the lifetime of the mechanical component, the gradient crystal plasticity formulation presented in [35] is augmented to consider damage driven by cyclic loading and the mechanical contact between grains. The formulation is built upon the work of Gurtin [36–38], which introduces vectorial and scalar microstresses,  $\xi_\alpha$  and  $\pi_\alpha$  respectively, of the  $\alpha$ -th slip system as energetic conjugates of the plastic slips  $\gamma_\alpha$  and their gradients. The principle of virtual work renders, in addition to the linear momentum balance, the microforce balance

$$\operatorname{div} \xi_\alpha + \tau_\alpha - \pi_\alpha = 0, \quad (\text{Equation 15.5})$$

where  $\tau_\alpha$  is the resolved shear stress. Equation 15.5 acts as a non-local yield condition, which is to be solved simultaneously to the linear momentum balance when plastic flow occurs. The gradient enhancement introduces an energetic length scale to the formulation that allows consideration of size-dependent effects. Furthermore, the theory reproduces the dislocation pile-up occurring at the grain boundaries. The grain boundaries can be modeled as a cohesive zone; thus, allowing an organic introduction of a damage variable that affects the interaction between adjacent crystals as proposed in [35]. Therein, the thermodynamic framework and constitutive equations of the formulation can be found in a detailed manner. The mechanical contact between grains is numerically implemented through the penalty method using a quadratic energy potential. To account for damage in a cyclic loading regime, the evolution equation

$$\dot{d} = c [1 - d] \zeta_d \langle \delta \rangle \quad (\text{Equation 15.6})$$

is proposed where  $d$  is the damage variable,  $c$  is the damage accumulation constant,  $\zeta_d$  is the thermo-

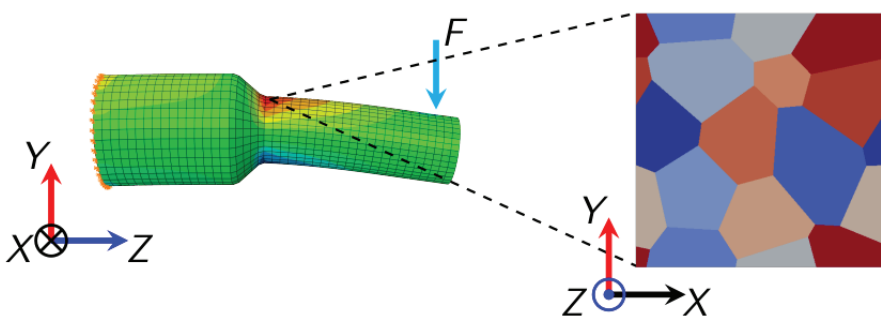


**Figure 15.9** The formed billet is loaded as shown in the figure by a force  $F$  with a cyclically varying magnitude. Based upon the obtained Von-Mises stress field, a critical point is identified, in which a representative volume element consisting of 12 crystals is inserted. Picture taken from [28]

dynamic force related to the damage variable and  $\delta$  the norm of the opening displacement at the grain boundary.

This enhanced formulation was employed to build upon the preliminary work presented in [28], in which the microscopic scale in the context of forward rod extrusion was first investigated using a uncoupled multi-scale approach. In [28], the formed billet was cyclically loaded inside the material's elastic domain, as shown in figure 15.9, and the location of a critical point was then identified based on the von Mises stress. At this point, a representative volume element (RVE) consisting of 12 randomly oriented face-centered cubic crystals, as pictured in figure 15.9, is inserted to analyze the microscopic material response. In the following, the RVE undergoes a kinematic process driven by the macroscopic strain

$$\boldsymbol{\varepsilon}^M = \begin{bmatrix} -0.02 & 0 & 0 \\ 0 & -0.02 & 0 \\ 0 & 0 & 0.04 \end{bmatrix}_{ij} \mathbf{e}_i \otimes \mathbf{e}_j \quad (\text{Equation 15.7})$$

via a half sinus wave in order to simulate the residual stress resulting from the manufacturing process. Afterwards, the RVE is gradually loaded with

$$\boldsymbol{\varepsilon}^M = 2 \times 10^{-3} \mathbf{e}_2 \otimes \mathbf{e}_3, \quad (\text{Equation 15.8})$$

using a linear function. The macroscopic strain in Equation 15.8 corresponds to the mean value of the cyclic load representing the load acting on the billet.

The amplitude of the cyclic loading is  $2 \times 10^{-4}$ . After 10 cycles a gradual linear unloading process occurs in order to determine the residual stresses.

In figure 15.10 the residual stress field before and after the cyclic loading can be seen. An overall reduction, which coincides with the hypothesis made in the preliminary work presented in [28] can be clearly observed. Furthermore, the proposed formulation identifies the grain boundaries as a critical area in the microstructure as the magnitude of the stress field is considerably higher than inside the grains.

The numerical implementation of the mathematical model introduces a rate dependency through the approximation of the scalar microscopic stress

$$\pi_\alpha = \sigma_\alpha \operatorname{sgn}(\dot{\gamma}_\alpha) \approx \sigma_\alpha \operatorname{erf} \left( \frac{\sqrt{\pi}}{2} \frac{\dot{\gamma}_\alpha}{\xi} \right) \quad (\text{Equation 15.9})$$

where  $\sigma_\alpha$  is the slip resistance and  $\xi$  is the regularization parameter. The approximation based on the error function was determined to better match the rate-dependent limit for a given values of  $\xi$ . The rate-dependent approximation leads to a constant plastic flow throughout the simulation. This fictitious effect can be reduced by small values of  $\xi$ . Nonetheless, a better approximation leads to a higher computational cost, especially in polycrystalline domains and 3D problems.

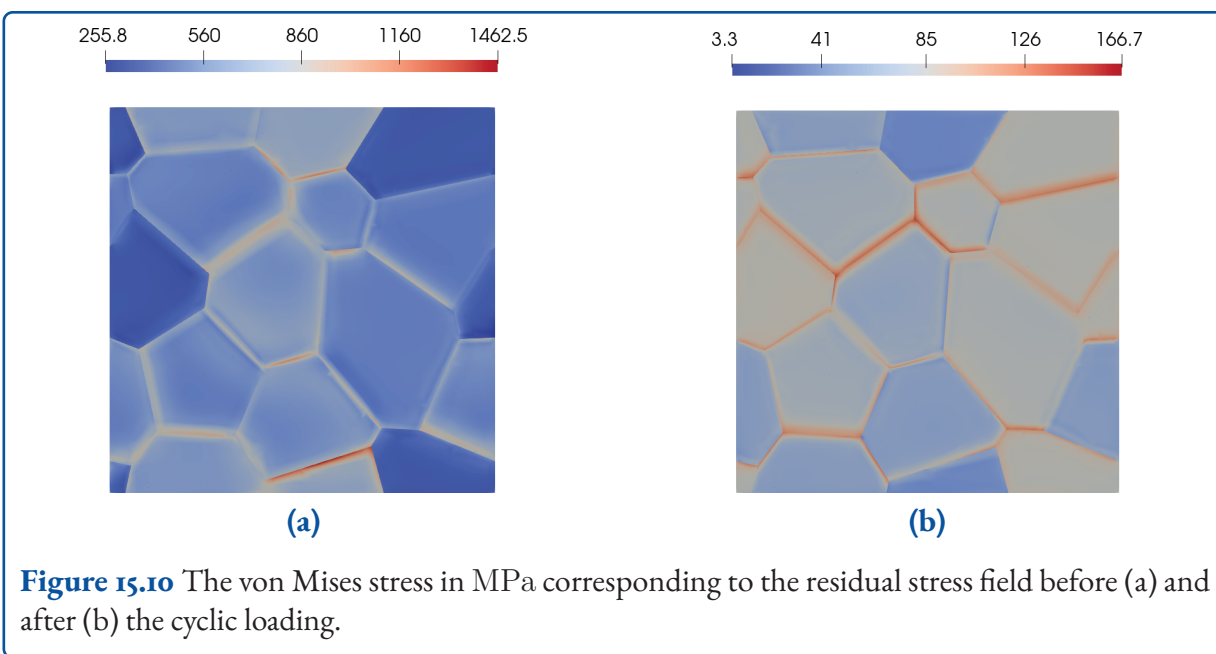


**Figure 15.10** The von Mises stress in MPa corresponding to the residual stress field before (a) and after (b) the cyclic loading.

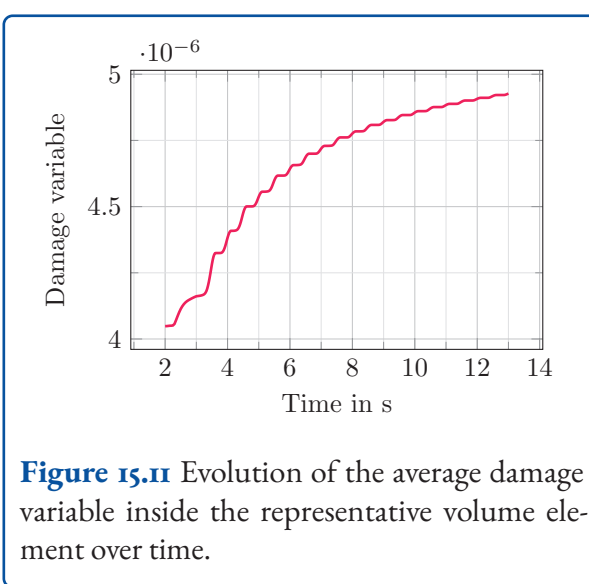


**Figure 15.11** Evolution of the average damage variable inside the representative volume element over time.

The damaged enhancement leads to a gradual increase of the average damage experienced by the representative volume element each cycle, as shown in figure 15.11. The average damage, i.e., the macroscopic damage allows the establishment of a framework to approximate the lifetime of the billet in a high-cycle fatigue regime.

## 15.7 Implications for Component and Process Design

During forming and ejection, residual stresses are generated in the components due to inhomogeneous plastic deformation. In the center of the extruded shaft, compressive residual stresses, which are in equilibrium with tensile residual stresses near the surface are present.

The residual stresses in the surface can be controlled by adjustments to the die opening angle and the lubricant. A high friction factor and a die opening angle of  $2\alpha = 90^\circ$  lead to tensile residual stresses in the surface. A reduction of the near-surface stresses and in some cases even a shift to compressive stresses can be achieved by using lubricants with low friction factors in combination with a high die opening angle of  $120^\circ$  or a low angle of  $60^\circ$ .

During operation, the forming induced residual stresses are stable under the influence of temperature as long as it does not exceed  $200^\circ\text{C}$ . Heating to  $550^\circ\text{C}$  results in a total relaxation of the residual stresses. Between these two limits, there is a time-dependent correlation between temperature and stress relief.

If the sum of load and residual stresses does not exceed the yield stress of the material, the residual stresses are not influenced. On the other hand, if the yield stress is exceeded, a new residual stress state, which will be stable if the sum of the new residual stresses and the load stress does not exceed the yield stress will be created. Otherwise, an unstable residual stress state, which changes during the operating time of the component is present.

The tensile residual stresses generated by forming reduce the achievable number of load cycles during fatigue testing. An increase of the achievable fatigue cycles can be achieved by removing the sub-surface tensile residual stresses. Generating reduced tensile residual stresses in the part surface by an adaption of the forming strategy increases the load-bearing capacity in the long-life fatigue range despite a reduced work hardening.

## 15.8 Summary and Outlook

Cold forming of steel leads to the generation of residual stresses, which are known to influence the fatigue behavior of formed components. In this project, residual stress-related effects in the life of a cold-formed stainless steel component were investigated.

In a combined numerical and experimental approach, residual stress generation was analyzed using a forward rod extrusion process. In the reference variant, a pronounced residual stress state, which was due to inhomogeneous plastic deformation during forming occurred. Besides the forming, the die springback and the ejection of the component in particular showed significant impacts. The experimentally monitored mechanics were reproduced in the simulation. Furthermore, a numerical tool, which allows the development of residual stresses to be traced already during forming was developed.

Based on this, influencing variables for the targeted setting of a residual stress state were investigated. In particular, the reduction of friction and the use of die opening angles of 60° and 120° were identified

for generating a compressive residual stress state close to the surface, while high friction and a die opening angle of 90° lead to distinct tensile residual stresses.

The forming induced residual stresses proved to be stable in the long term when subjected to a thermal load of 200 °C, while 550 °C resulted in an instant and full relaxation. Between these limits, a time- and temperature-dependent influence occurred. When subjected to a mechanical load, three basic mechanisms for residual stress relaxation were identified. Depending on load and residual stress state, a stable stress state, a one time change or an instable stress state may occur.

Distinct tensile residual stresses in the surface led to a reduced fatigue strength in the components. Thermal removal of the full residual stress state resulted in an improvement of fatigue behavior. By using forming methods for the reduction of near-surface tensile residual stresses, it was possible to increase the load-bearing capacity of the specimens in long-life fatigue.

Based on these results, implications have been derived for the numerical simulation and the component and process design.

In future work, the transferability of the identified findings to more complex component geometries and processes is to be investigated. Furthermore, the measured temperature of the workpiece after ejection can reach up to values in the range from 55 °C to 125 °C depending on the material, die shoulder angle and lubricant. These temperature changes can lead to consequential variations of the model's material parameters; thus, rendering a purely mechanical mathematical model insufficient. The intrinsic thermal effects at play may become more relevant in real-world applications where mechanical components are subjected to consecutive forming processes. Additionally, a more elaborate model for the frictional contact could lead to an increased fidelity of the results. Lastly, a computationally robust and efficient numerical implementation of the multi-scale problem to predict the lifetime of the workpiece is required to perform a fully coupled analysis in a fea-

sible computing time. Hereby, the rate-dependent approximation should match the behavior of the rate-independent behavior to a great extent to be able to simulate over several cycles without having the fictitious effects caused by the introduced rate dependency noticeably affecting the material response. Furthermore, the role of a time integration scheme capable of spanning cycles is of vital importance in order to greatly reduce computational costs.

## References

- [1] Oliver Hering and A. Erman Tekkaya. "Damage-induced performance variations of cold forged parts". In: *Journal of Materials Processing Technology* 279 (2020), p. 116556. DOI: <https://doi.org/10.1016/j.jmatprotec.2019.116556>.
- [2] M.N. James et al. "Residual stresses and fatigue performance". In: *Engineering Failure Analysis* 14.2 (2007). Papers presented at the 22nd meeting of the Spanish Fracture Group (Almargro, Spain, March 2005), pp. 384–395. DOI: <https://doi.org/10.1016/j.engfailanal.2006.02.011>.
- [3] P.J. Withers. "Residual stress and its role in failure". In: *Reports on Progress in Physics* 70.12 (Nov. 2007), p. 2211. DOI: [10.1088/0034-4885/70/12/R04](https://doi.org/10.1088/0034-4885/70/12/R04).
- [4] J. Toribio. "Residual Stress Effects in Stress-Corrosion Cracking". In: *Journal of Materials Engineering and Performance* 7.2 (Apr. 1998), pp. 173–182.
- [5] Z. Wang and B. Gong. "Residual stress in the forming of materials". In: *Handbook of residual stress and deformation of steel* (2002), pp. 141–49.
- [6] Lars Ingvarsson. "Cold-forming residual stresses effect on buckling". In: (1975).
- [7] Otmar Vöhringer. "Relaxation of residual stresses by annealing or mechanical treatment". In: *Pergamon Press, Advances in Surface Treatments. Technology—Applications—Effects*. 4 (1987), pp. 367–396.
- [8] Claudia Barile et al. "Feasibility of Local Stress Relaxation by Laser Annealing and X-ray Measurement". In: *Strain* 49 (July 2013). DOI: [10.1111/str.12045](https://doi.org/10.1111/str.12045).
- [9] Jijin Xu, Ligong Chen, and Chunzhen Ni. "A study on the mechanical stress relieving and safety assessment without post-weld heat treatment". In: *Materials Science and Engineering: A* 443.1 (2007), pp. 107–113. DOI: <https://doi.org/10.1016/j.msea.2006.08.022>.
- [10] Muhammad Mubashar Siddique and Muhammad Abid. "Numerical simulation of mechanical stress relieving in a multi-pass GTA girth welded pipe-flange joint to reduce IGSCC". In: *Modelling and Simulation in Materials Science and Engineering* 13 (Dec. 2005), p. 1383. DOI: [10.1088/0965-0393/13/8/013](https://doi.org/10.1088/0965-0393/13/8/013).
- [11] M.A.S Torres and H.J.C Voorwald. "An evaluation of shot peening, residual stress and stress relaxation on the fatigue life of AISI 4340 steel". In: *International Journal of Fatigue* 24.8 (2002), pp. 877–886.
- [12] A. Tekkaya. *Ermittlung von Eigenspannungen in der Kaltmassivumformung*. Springer Berlin Heidelberg, 1986.
- [13] Anke Kaysser-Pyzalla and W. Reimers. "Residual Stress and Texture Due to Cold and Hot Extrusion Processes". In: *Textures and Microstructures* 33 (Jan. 1999). DOI: [10.1155/TSM.33.291](https://doi.org/10.1155/TSM.33.291).
- [14] P. S. Midha and G. F. Madlen. "Residual stresses in cold-extruded rods". In: *Metals Technology* 3.1 (1976), pp. 202–207.
- [15] A. Rosochowski and R. Balendra. "Effect of secondary yielding on nett-shape forming". In: *Journal of Materials Processing Technology* 58.2-3 (Mar. 1996), pp. 145–152.
- [16] Y. Qin and R. Balendra. "FE simulation of the influence of die-elasticity on component dimensions in forward extrusion". In: *International Journal of Machine Tools and Manufacture* 37.2 (Feb. 1997), pp. 183–192.
- [17] Bernd-Arno Behrens et al. "Advanced friction modeling for bulk metal forming processes". In: *Production Engineering* 5.6 (Sept. 2011), pp. 621–627. DOI: [10.1007/s11740-011-0344-8](https://doi.org/10.1007/s11740-011-0344-8).

- [18] A. Tekkaya. "A guide for validation of FE-simulations in bulk metal forming". In: *The Arabian Journal for Science and Engineering* 30 (Jan. 2013), pp. 113–136.
- [19] R. C. McClung. "A literature survey on the stability and significance of residual stresses during fatigue". In: *Fatigue & Fracture of Engineering Materials and Structures* 30.3 (Mar. 2007), pp. 173–205. DOI: 10.1111/j.1460-2695.2007.01102.x.
- [20] Takyuki Yonezawa, Hiroshi Shimanuki, and Takeshi Mori. "Influence of cyclic loading on the relaxation behavior of compressive residual stress induced by UIT". In: *Welding in the World* 64 (Nov. 2019), pp. 1–8. DOI: 10.1007/s40194-019-00821-1.
- [21] Wyman Z. Zhuang and Gary R. Halford. "Investigation of residual stress relaxation under cyclic load". In: *International Journal of Fatigue* 23 (2001), pp. 31–37. DOI: [https://doi.org/10.1016/S0142-1123\(01\)00132-3](https://doi.org/10.1016/S0142-1123(01)00132-3).
- [22] Qiang Wang et al. "On the mechanism of residual stresses relaxation in welded joints under cyclic loading". In: *International Journal of Fatigue* 105 (2017), pp. 43–59. DOI: <https://doi.org/10.1016/j.ijfatigue.2017.08.016>.
- [23] Philipp Landkammer et al. "Investigations on residual stress generation in full-forward-extrusion". In: *Production Engineering* (Mar. 2019). DOI: 10.1007/s11740-019-00892-5.
- [24] Andreas Jobst, Christoph Kiener, and Marion Merklein. "Investigations on Residual Stress Generation in Extruded Steel Components". In: *Production at the leading edge of technology*. Springer Berlin Heidelberg, 2019, pp. 83–92. DOI: 10.1007/978-3-662-60417-5\_8.
- [25] Daniel Arndt et al. "The deal.II Library, Version 9.3". In: *Journal of Numerical Mathematics* 29.3 (2021), pp. 171–186.
- [26] Andreas Jobst et al. "Component residual stress control in forward rod extrusion by material flow and tribology—experiments and modeling". In: *Forschung im Ingenieurwesen* 85.3 (July 2021), pp. 733–744. DOI: 10.1007/s10010-021-00509-3.
- [27] J.L. Chaboche. "Constitutive equations for cyclic plasticity and cyclic viscoplasticity". In: *International Journal of Plasticity* 5.3 (Jan. 1989), pp. 247–302.
- [28] Dimosthenis Floros et al. "Towards an holistic account on residual stresses in full-forward extruded rods". In: *Archive of Applied Mechanics* 91.8 (Mar. 2021), pp. 3649–3664. DOI: 10.1007/s00419-021-01917-1.
- [29] Kurt Lange et al. *Fließpressen*. Springer Berlin Heidelberg, 2008.
- [30] Andreas Jobst and Marion Merklein. "Applicability of Solid Lubricant Coatings in Cold Rod Extrusion of Stainless Steels". In: *Defect and Diffusion Forum* 404 (Oct. 2020), pp. 95–100. DOI: 10.4028/www.scientific.net/ddf.404.95.
- [31] Andreas Jobst and Marion Merklein. "Stability of forming induced residual stresses in stainless steel components under mechanical load". In: *North American Manufacturing Research Conference* 51. 2023.
- [32] Andreas Jobst and Marion Merklein. "Stability of forming induced residual stresses in stainless steel parts at elevated temperature". In: *11th International Conference on Residual Stresses*. 2022.
- [33] Xianglong Wang et al. "Improvement on room-temperature ductility of 6.5wt.% Si steel by stress-relief annealing treatments after warm rolling". In: *Materials Characterization* 122 (2016), pp. 206–214. DOI: <https://doi.org/10.1016/j.matchar.2016.11.006>.
- [34] Rainer Masendorf and Christian Müller. "Execution and evaluation of cyclic tests at constant load amplitudes – DIN 50100:2016". In: *Materials Testing* 60.10 (2018), pp. 961–968.
- [35] Lucie Spannraft et al. "Grain boundary interaction based on gradient crystal inelasticity and decohesion". In: *Computational Materials Science* 178 (June 2020), p. 109604. DOI: 10.1016/j.commatsci.2020.109604.
- [36] Morton E. Gurtin. "On the plasticity of single crystals: free energy, microforces, plastic-strain gradients". In: *Journal of the Mechanics and Physics of Solids* 48.5 (May 2000), pp. 989–1036. DOI: 10.1016/s0022-5096(99)00059-9.

[37] Morton E. Gurtin. "A gradient theory of single-crystal viscoplasticity that accounts for geometrically necessary dislocations". In: *Journal of the Mechanics and Physics of Solids* 50.1 (Jan. 2002), pp. 5–32. DOI: 10.1016/s0022-5096(01)00104-1.

[38] Morton E. Gurtin. "A theory of grain boundaries that accounts automatically for grain misorientation and grain-boundary orientation". In: *Journal of the Mechanics and Physics of Solids* 56.2 (Feb. 2008), pp. 640–662. DOI: 10.1016/j.jmps.2007.05.002.

# 16 Improvement of Product Properties by Selective Induction of Residual Stresses in Incremental Sheet Metal Forming

Tekkaya, A. E.; Lampke, T.; Winter, L.; Mehner, T.; Maaß, F.; Hahn, M.; Bergelt, T.

GEPRIS 372803376

## 16.1 Introduction

The residual stress state of metal components manufactured by incremental forming processes has a significant influence on component properties, in particular on fatigue strength and corrosion resistance. The prediction of the forming-induced residual stress state with suitable finite element models is therefore essential for the product design phase. Incremental sheet metal forming (ISF) is characterized by low tool costs and low process forces with an increased formability compared to conventional forming processes. ISF enables the induction of locally defined residual stresses in geometrically identical components by adjusting the process parameters that influence the forming mechanisms. The origin of the resulting residual stress state in relation to the forming mechanisms of shearing, bending, and the membrane component is mostly unknown. The relationships between process parameters, forming mechanisms, resulting residual stress state, and fatigue strength of parts manufactured by ISF are analyzed in the joint project "Improvement of product properties by selective induction of residual stresses in incremental sheet metal forming" by the Institute of Forming Technology and Lightweight Components (IUL) of TU Dortmund University and the Materials and Surface Engineering Group (WOT) of the Institute of Materials Science and Engineering of TU Chemnitz University. In particular, the influence of the relative step-down increment on the forming mechanisms and the residual stresses of the component are identified. Based on these results, concepts of

tensile and compressive stress-superposition are analyzed numerically and tested experimentally to increase the range of targeted residual stress adjustment through the forming process. Additionally, the influence of the forming-induced residual stress state on corrosion resistance during fatigue testing is analyzed. With this knowledge, forming-induced residual stresses can be used to maximize the component's stability under static and cyclic loads under given boundary conditions to meet the requirements of robust lightweight constructions.

## 16.2 Incremental Sheet Metal Forming

In incremental sheet metal forming (ISF), a sheet metal is formed by the continuous movement of a non-geometry dependent forming tool while the metal sheet is clamped at the edges (figure 16.1). The forming tool is moved along a predefined tool path derived from the desired CAD geometry and only a small area of the sheet is in contact with the forming tool. Due to the localized deformation zone, very high strains occur locally and a higher formability compared to conventional forming processes can be achieved [1].

The forming tool with a hemispherical tip of tool radius  $R_{\text{tool}}$  is moved stepwise in the  $z$ -direction with a constant step-down increment  $\Delta z$  (figure 16.2). The advantages of the non-geometry-dependent forming tool are low tooling costs and a flexible manufacturing process that is particularly suitable for small batch sizes and rapid prototyping [2]. The ISF process was patented by Leszak in 1967 and was further developed to multiple process variants with and without using a supporting die or supporting tools. Single-point incremental forming (SPIF) as described by Jeswiet et al. [3] can be performed on

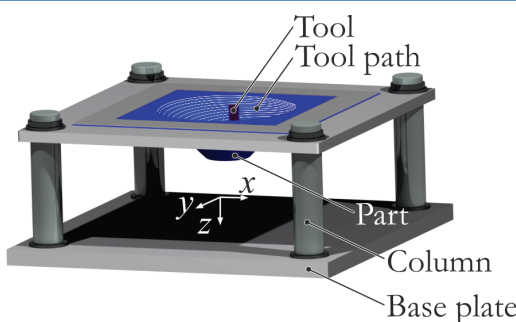


**Figure 16.1** Single point incremental forming process setup.

a conventional 3-axis CNC milling machine to produce complex parts without using partial or solid dies. SPIF is the most flexible ISF process, but the occurring springback leads to a comparatively poor geometrical accuracy. Two-point incremental forming (TPIF) as presented by Powell and Andrew [4] can improve the geometrical accuracy of the manufactured components by using additional supporting tools or solid dies with reduced flexibility [1]. A common disadvantage of ISF processes is a high process time compared to conventional forming processes. The process combination of ISF and stretch forming presented by Taleb Araghi et al. [5] can lead to a noticeable reduction of process time. In a two step-process the sheet metal is stretch formed over a positive die using a servo-driven movable blank holder. After the stretch forming process, features can be formed into the pre-formed part using ISF to achieve the final part geometry. A more uniform thickness distribution with a reduced amount of maximum thinning was observed using this process combination.

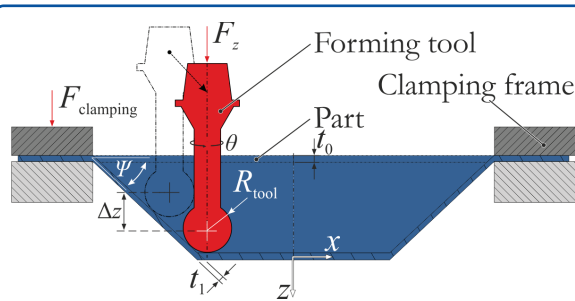


**Figure 16.2** Incremental forming process.

### 16.2.1 Forming Mechanisms

The high formability in incremental sheet metal forming is due to the superposition of the forming mechanisms bending and shearing, and the membrane component [1], which enables forming of high-strength materials and complexly shaped components compared to conventional forming processes. The influence of each forming mechanism on the forming process has been discussed in several publications and is still not fully clear. Silva et al. [6] indicated the influence of membrane stretching as an important mechanism in SPIF related to sheet thickness reduction. Sebastiani et al. [7] demonstrated experimentally membrane stretching perpendicular to the tool movement. This effect increases with decreased vertical tool step-down increments and forming tool radii [8]. The influence of the bending mechanism as an essential forming mechanism is proposed by Emmens et al. [9]. Larger strains on the tool side than on the non-tool side and non-linear stresses on the tool side are shown as results of the bending mechanism during the forming operation [10]. In SPIF, bending always occurs in combination with a stretching component perpendicular to the tool feed. Therefore, additional tensile residual stresses on the tool side can be measured. Sebastiani et al. [7] detected larger plastic strains perpendicular to the tool feed on the tool side than on the non-tool side. The importance of the shearing mechanism for this process is related to the comparison of SPIF and the process of metal spinning [11]. Three different types of shearing that are relevant for SPIF can be distinguished: in-plane shear [12], shearing through the sheet thickness [13], and out-of-plane shear [7]. Maqbool et al. [8] demonstrated increasing through-thickness shear in the tool direction with decreasing step-down increment, increasing sheet thickness, or increased friction. Additionally, through-thickness shear increases with higher wall angles [14]. The shear due to the tool feed leads to a shear gradient in through-thickness direction [15], but is not an essential forming mechanism for incremental sheet metal forming [16]. Silva et al. [6] explained by membrane theory that stretching, not shear, is the dominant forming mechanism in the SPIF process. Out-of-plane shear was only pro-

posed by numerical investigations and not yet validated [17]. The contact pressure of the forming tool during the forming operation leads to additional compressive stresses in the forming zone. These compressive stresses stabilize the forming process and lead to the increased formability of the material [2].

### 16.2.2 Residual Stress Analysis in Incremental Sheet Forming

Tanaka et al. [18] demonstrated the influence of the tool radius on the residual stress state of an incrementally formed rotor blade based purely on numerical process simulations. The prevailing tensile residual stresses in the near-surface edge layers of the component and the compressive stresses in the deeper layers were increased in amplitude by decreasing the tool radius. An experimental analysis of the residual stress was done by Radu et al. [19] using incrementally formed aluminum (Al99.5) truncated cones and pyramids. The state of residual stress in the component was determined using the hole-drilling method for thin-walled components ( $t_0 = 0.6$  mm) and correlated to the process parameters tool radius  $R_{\text{tool}}$ , tool step-down  $\Delta z$ , feed rate  $v_f$  and rotational speed of the tool  $\theta$ . The literature demonstrates the potential of influencing residual stresses by the incremental forming process. Separately, experimental and numerical results show the influence of several process parameters on the resulting residual stress. The consideration as a phenomenological effect of the process parameters on the residual stresses without involving the forming mechanisms limits the transferability of these findings. A validation of the numerical models to predict residual stresses is also not given. Overall, residual stresses largely determine the product properties of manufactured components. Especially near-surface residual stresses can reduce or increase the fatigue strength of a component under static and cyclic loads although the influence of forming-induced residual stresses by incremental forming on fatigue strength has not been investigated yet. The targeted adjustment of residual stresses in components to improve the component performance, especially through near-surface compressive residual stresses or the targeted reduction

of residual stresses to reduce geometric distortion, is widespread in industry. To adjust the residual stresses, subsequent processes, such as shot peening or heat treatment processes that need additional resources are used. The use of targeted forming-induced residual stresses can possibly make these subsequent processes superfluous if transferable knowledge about the formation of residual stresses and reliable residual stress prediction models are available.

## 16.3 Analysis of the Single Point Incremental Forming Process

### Experimental and Numerical Procedure

The initial material for the following investigations is the cold-rolled wrought aluminum alloy AA5083 (AlMg4.5Mn) in the H111 state with an initial sheet thickness  $t_0 = 1.0$  mm. Uniaxial tensile tests and cyclic in-plane torsion tests are performed for material characterization (figure 16.3).

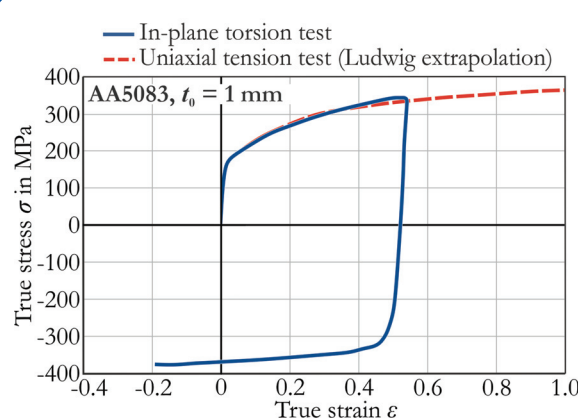
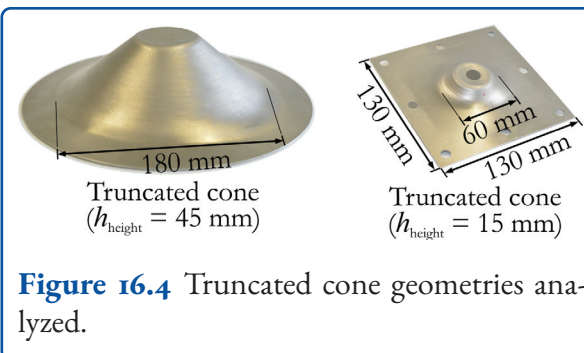


Figure 16.3 Material characterization of AA5083.

Since the material properties required for the numerical analysis exceed the range of the uniaxial tensile test, an extrapolation approach according to Ludwig is used [20]:  $k_f = 159.9 + 220 \cdot \varphi^{0.41}$  MPa. A numerical process model in *ABAQUS* is set up according to [21] to analyze the process. The explicit model uses solid elements for the deformable sheet.



**Figure 16.4** Truncated cone geometries analyzed.

The material model including combined isotropic-kinematic hardening based on Chaboche [22] is used to analyze the process. Two different truncated cone geometries are manufactured by SPIF. The dimensions of the truncated cone geometries are shown in figure 16.4. In this project, the dependence of the forming mechanisms shearing, bending, and the membrane component on the process parameter  $\Delta z$  is shown for truncated cone geometries [21]. A conventional 5-axis milling machine DMU 50 from DMG Mori is used to perform the SPIF process according to figure 16.5. Production is carried out with a bidirectional tool path and a driven forming tool with a tool radius  $R_{\text{tool}} = 5 \text{ mm}$ . The step-down increment is varied in three steps:  $\Delta z_{24} = 1.875 \text{ mm}$ ,  $\Delta z_{12} = 3.750 \text{ mm}$ , and  $\Delta z_8 = 5.625 \text{ mm}$ . All other process parameters are kept constant. The sheet is fixed with a clamping frame (figure 16.5). A deep-drawing oil (Castrol Iloform PN 226) is applied to the sheet metal surface as a lubricant.

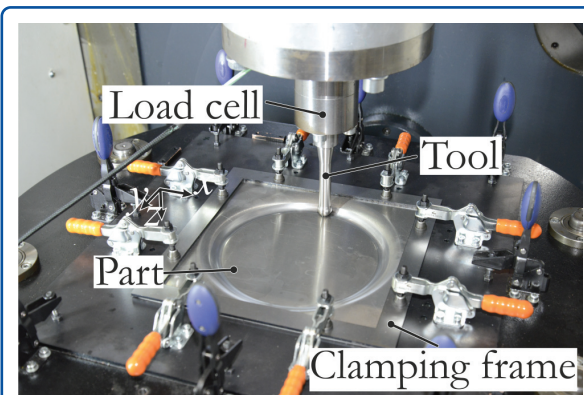


**Figure 16.5** SPIF process setup.

### 16.3.1 Forming Mechanisms

In addition to the experiments, the step-down increment  $\Delta z$  is varied in a numerical process model while the tool radius  $R_{\text{tool}}$  and the other process parameters as well as the final geometry are kept constant. The determination of the resulting residual stresses and their development with regard to the forming mechanisms, as a result of the process parameter adjustment, is carried out numerically. Quantitative values for the forming mechanisms are derived by the output of the stress and strain components of the numerical model. The relevant stress and strain components of each volume element are evaluated at the measuring point in the center of the cone wall (figure 16.6). The principle stress components taken into account for the membrane component ( $m$ ) are the average values  $\sigma_{11}^m$ ,  $\sigma_{22}^m$ ,  $\sigma_{33}^m$  and for shearing  $\sigma_{12}$ ,  $\sigma_{23}$  and  $\sigma_{13}$ . The values for bending ( $b$ ) cannot be output directly from the numerical model, so the following relationship is defined  $\sigma_{ii} := \sigma_{ii}^m + \sigma_{ii}^b$  respectively strain-wise  $\varphi_{ii} := \varepsilon_{ii}^m + \varepsilon_{ii}^b$  for  $i = 1, 2, 3$ . Therefore, the bending components are calculated by stress and strain superposition according to  $\sigma_{ii}^b = \sigma_{ii} - \sigma_{ii}^m$  respectively  $\varepsilon_{ii}^b = \varepsilon_{ii} - \varepsilon_{ii}^m$  for  $i = 1, 2, 3$ . The resulting plastic energy fractions of the mechanisms are validated by comparing their sum with the specific total plastic energy given by the finite element solver.

The forming mechanisms are evaluated on the inside and outside in the middle of the truncated cone wall according to figure 16.6. The near-surface element is evaluated in each case. An evaluation of the forming mechanisms on the tool side shows a significant and continuous increase of the impact of shearing with decreasing step-down increments (figure 16.7) [21]. At the same time, the influence of the bending mechanism decreases continuously with decreasing step-down increments. The proportion of the membrane component on the tool side varies in a small, almost constant range when adjusting the step-down increment size. On the non-tool side, the qualitative development of the forming mechanisms is the same as on the tool-side. However, the forming mechanisms of shearing and the membrane component are at a lower level than

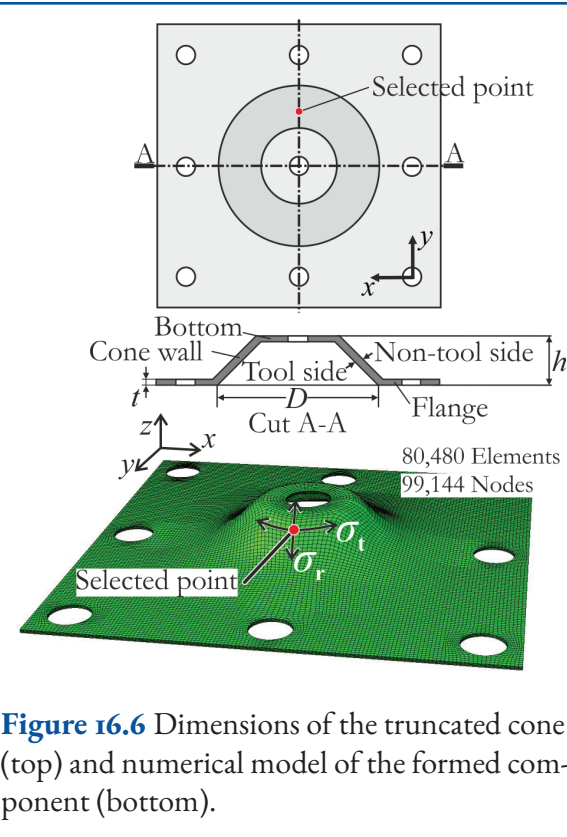


**Figure 16.6** Dimensions of the truncated cone (top) and numerical model of the formed component (bottom).

on the tool side. The bending mechanism is higher on the non-tool side, though.

The numerical results are supported by experimental texture analysis of truncated cone geometries [23]). Figure 16.8 a-d shows the determined texture of the outside of the truncated cone wall in comparison with the initial rolling texture and a reference shear texture of an in-plane torsion test sample. The {222}-pole figures on the outside of the component show the formation of a characteristic {222}-pole figure of the shear test as the size of the step-down increment decreases. Starting from the less pronounced rolling texture of the initial sheet, the center of the pole figure is distorted with decreasing step-down increment size. In addition, the six characteristic intensities of the shearing texture are formed at the edges. The truncated cones on the outside of the wall were analyzed with regard to the development of a characteristic bending texture. The {220}-pole figures in figure 16.8 e-h show the texture development with increasing step-down increment compared to the initial texture and a reference sample of a bent sheet. With increasing step-down increment size, vertical intensity bands

are formed from the initial rolling texture, which correspond to the characteristics of the experimentally measured bending specimen. The intensities increase as the increment size increases.

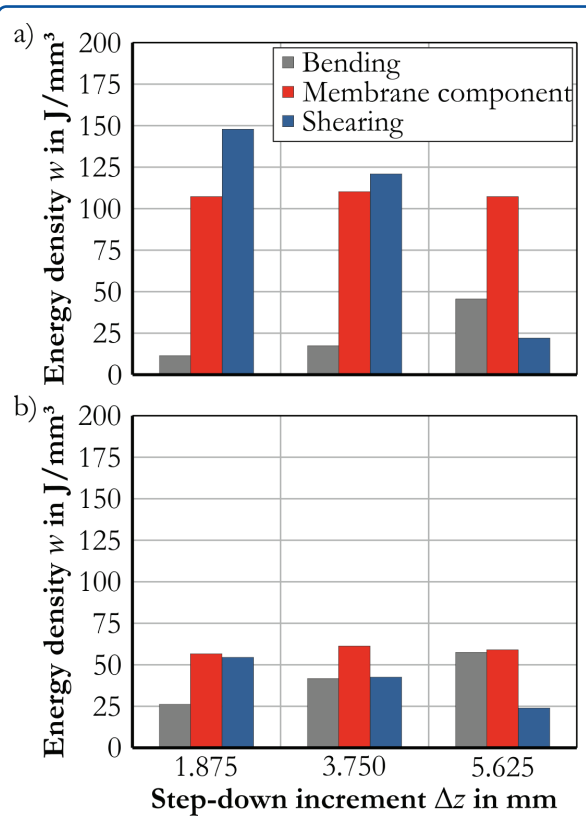


**Figure 16.7** Numerical evaluation of the forming mechanisms for a) tool side and b) non-tool side of a truncated cone wall [21].

### 16.3.2 Process Forces, Geometry, and Material Hardness

A comparison of the experimentally measured in-situ process forces  $F_z$  for the three different step-down increments  $\Delta z$  is shown in figure 16.9. An increasing step-down increment  $\Delta z$  results in a reduction in the process time. The maximum process force  $F_z$  of the considered process window corresponds to a reduction of 46 % comparing 24 increments ( $F_{\Delta z=1.875 \text{ mm}} = 1.89 \pm 0.04 \text{ kN}$ ) and eight increments ( $F_{\Delta z=5.625 \text{ mm}} = 3.49 \pm 0.07 \text{ kN}$ ). There is good agreement between the experimental and the numerical results with a maximum deviation of 8 %. The peak forces are a result of the tool step-down. The time span between two peaks decreases due to the decreasing diameter of the tool

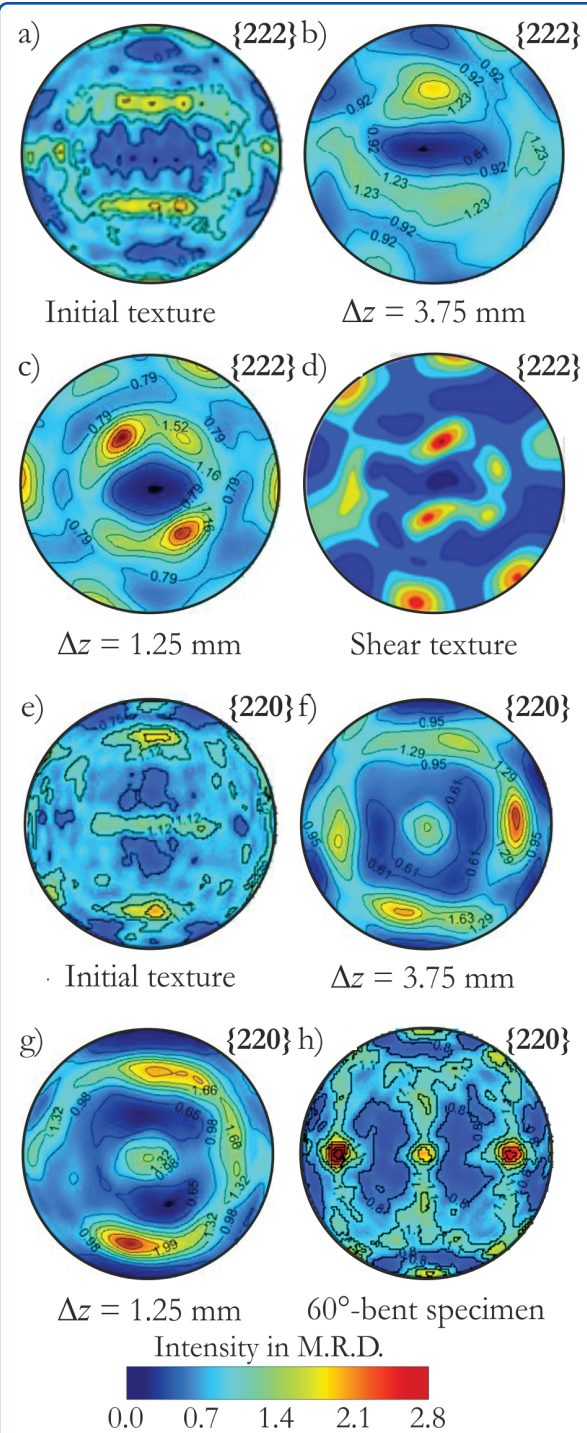


**Figure 16.8** {222}-pole figures of the a) initial sheet, truncated cone geometry b)  $\Delta z = 3.75 \text{ mm}$ , c)  $\Delta z = 1.25 \text{ mm}$  and d) shear texture of in-plane torsion test specimen and {220}-pole figures of the e) initial sheet, truncated cone geometry f)  $\Delta z = 3.75 \text{ mm}$ , g)  $\Delta z = 1.25 \text{ mm}$  and h) bending texture, sheet metal normal direction [23].

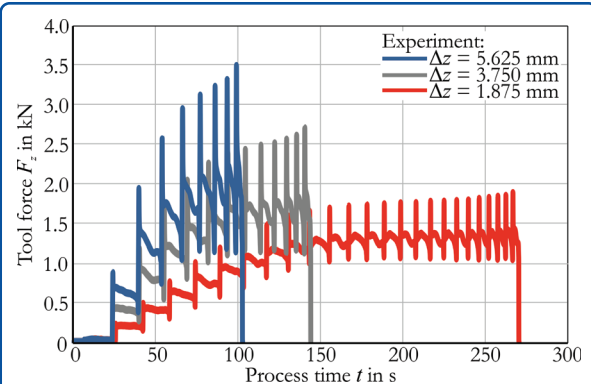


**Figure 16.9** Experimental process forces  $F_z$  for  $\Delta z = 1.875^5.625 \text{ mm}$  [21].

path circle with the increasing depth of the cone. A comparison of the geometry (cut A-A) of the experimental results is shown in figure 16.10. With a decreasing number of step-down increments, there is an increasing waviness on the inner surface.

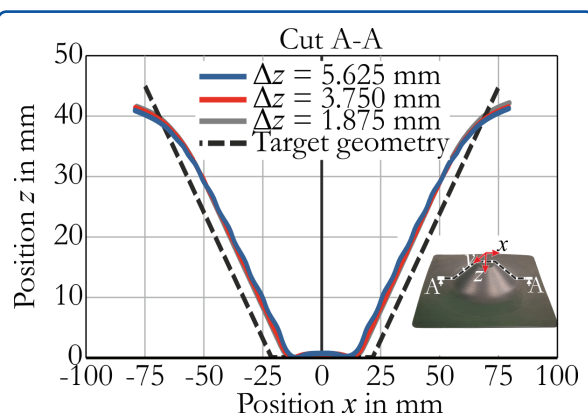


**Figure 16.10** Comparison of the cone's geometry formed with varying step-down increments  $\Delta z = 1.875^5.625 \text{ mm}$  in the cut view A-A [21].

The maximum geometric deviation from the CAD target geometry is 11 % due to process-related springback effects. The deviation is defined as the maximum distance between two points on the profiles with the same  $z$ -coordinate. The highest deviation is measured in the flange area after unclamping. However, the accuracy of the final geometry increases with a decreasing number of step-down increments due to decreased springback, the maximum deviation between the three final geometries is 4.8 %. Therefore, it can be assumed that

a variation of the step-down increment, within the examined limits, has no significant effect on the resulting geometry of the component. The sheet thickness distribution along the cut A-A is shown in figure 16.11. The initial sheet thickness of  $t_0 = 0.96 \pm 0.01$  mm decreases with an increasing number of step-down increments. The decreasing sheet thickness reduction varies between 26.8 % for  $\Delta z = 1.875$  mm and 44.7 % for  $\Delta z = 5.625$  mm (figure 16.11). The experimentally determined sheet thickness is smoothed to reduce the high level of noise due to the light reflections during the optical sheet thickness measurement using 3D-structured light projection.

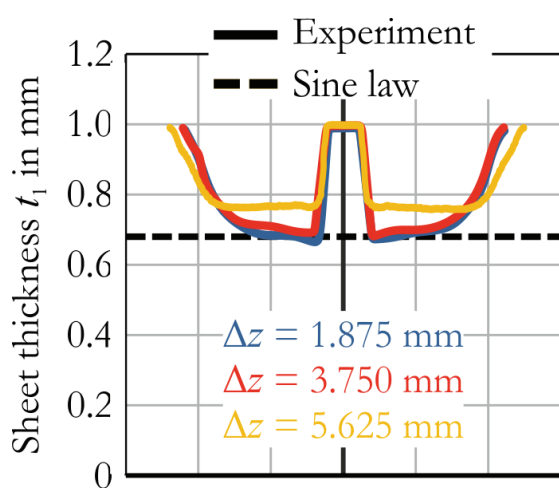


**Figure 16.11** Comparison of the cone's sheet thickness distribution with varying step-down increments  $\Delta z = 1.875\text{--}5.625$  mm in the cut view A-A of figure 16.10 [21].

The maximum deviation between experiment and numerical results is 9 % for the sheet thickness. With a decreasing number of increments, the thickness distribution along the cone wall becomes more homogeneous. Due to the incremental forming of the cone wall, the initial sheet thickness is only reduced in the cone wall area. In the clamped flange area and the unformed bottom area of the part, the initial sheet thickness remains constant. The sheet thickness predicted by the sine law for the wall angle  $\Psi = 45^\circ$  is  $t_1 = 0.68$  mm. The sine law is based on considering pure shear deformation. From figure 16.7, it can be concluded that the shearing mechanism decreases as the step-down

increment increases. This fact explains the decreasing prediction quality of the sine law with a higher number of increments. The Vickers hardness measurement corresponding to HV10 is used to determine the average hardness in the cross-sections of the component wall (figure 16.12). The material hardness of the AA5083 initial material of 69 HV10 is significantly increased by the process due to work hardening. With regard to the step-down increment, there is an increase in the material hardness in the cone wall with decreasing step-down increment, corresponding to the observed thinning. The hardness of 93 HV10 for  $\Delta z = 5.625$  mm increases monotonously up to a maximum value of 102 HV10 for  $\Delta z = 1.875$  mm. This corresponds to an increase in material hardness of 8.4 % in the middle of the cone wall.

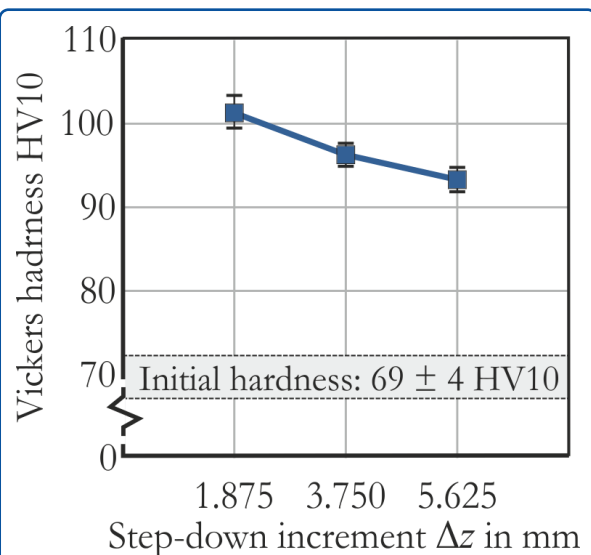


**Figure 16.12** Development of material hardness with increasing step-down increment in the cone wall cross section.

### 16.3.3 Residual Stresses

The residual stresses of the formed truncated cone geometry are numerically output in the evaluation point (figure 16.6) on the tool side and the non-tool side. Additionally, experimental residual stress measurements are carried out on the unclamped specimens using nondestructive X-ray diffraction (XRD) methods. A portable X-ray diffractometer Xstress 3000 G2R from Stresstech is used to

evaluate the near-to-surface residual stresses. The residual stresses on the inside of the truncated cones (tool side) are tensile residual stresses (figure 16.13 a). Considering the residual stresses  $\sigma_r$  perpendicular to the tool feed direction, the tensile residual stresses on the tool side decrease monotonously from  $\sigma_r = 144 \text{ MPa}$  down to almost zero with increasing step-down increment. The residual stresses on the non-tool side become less distinct with increasing step-down increment. The residual stresses in tool feed direction  $\sigma_t$  inside the component (tool side) decrease monotonously with increasing step-down increment, from  $\sigma_t = 97 \text{ MPa}$  for  $\Delta z = 1.875 \text{ mm}$  to  $\sigma_t = 43 \text{ MPa}$  for  $\Delta z = 5.625 \text{ mm}$  (figure 16.13 a).

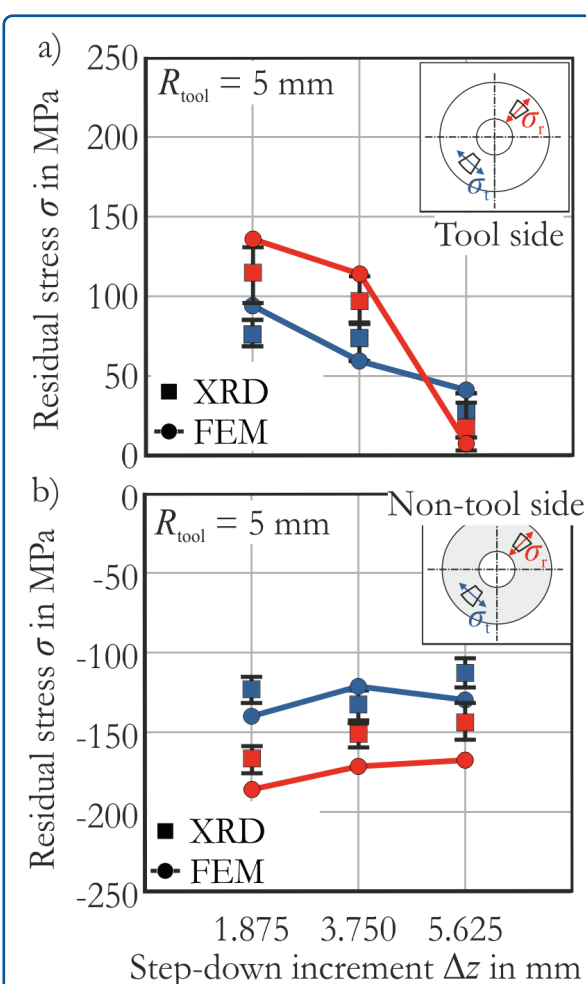


**Figure 16.13** Residual stress development at a) tool side and b) non-tool side with increasing step-down increment [21].

The residual stresses experimentally measured using XRD validate the numerically predicted resid-

ual stress development inside the cone wall with increasing step-down increment  $\Delta z$ . The residual stresses in tool feed direction  $\sigma_t$  originate from compression of the material in the circumferential direction due to bending around the forming tool. After unloading, tensile residual stresses result from the compression of the material. The compression is superposed by stretching due to the relative movement between the tool and the workpiece surface [23]. The residual stresses on the non-tool side of the cone wall are compressive residual stresses (figure 16.13 b). These compressive residual stresses are caused by the bending-induced stretching of the material around the tool as a result of the tool step-down. The bending mechanism increases with increasing step-down increment while the shearing mechanism decreases at the same time. The higher proportion of bending on the outer sheet radius around the forming tool causes stretching during forming, which leads to higher bending-induced residual stresses on the outside of the cone wall than on the tool side.

## 16.4 Analysis of the Process Enhancements

Depending on the process parameter step-down increment, the forming mechanisms and thus the forming-induced residual stresses in incrementally formed components can be adjusted. Small step-down increments cause higher tensile residual stresses on the tool side of the component. These tensile residual stresses potentially decrease the fatigue strength of cyclically loaded components. On the other hand, for large increments tensile residual stresses on the tool side are reduced. However, large increments cause an increased waviness on the component surface. In addition, the maximum size of the step-down increment is limited by the maximum forming force of the forming machine and the formability of the material. Two process enhancements are presented in order to expand the process window for setting residual stresses through incremental sheet metal forming: a concept for superposing compressive stress across the sheet thickness by using an elastic counter die (ISF with counter pressure) [24] and a concept for su-

superposing tensile stresses over the sheet metal plane during forming [25].

### 16.4.1 Incremental Sheet Metal Forming with Counter Pressure

The TPIF process developed by Matsubara [26] can improve the geometric accuracy of the manufactured components by using supporting dies [27]. However, by using dedicated solid dies, the TPIF process is less flexible than SPIF. In contrast to the SPIF process, the tool moves from the inside to the outside, while the guided clamping frame moves continuously downward. In the case of TPIF, the sheet is supported on the non-tool side either by a partial or full die or by a second forming tool [28]. In addition to TPIF with rigid dies, the use of flexible dies is gaining increasing interest. It can be distinguished between adjustable full and partial dies as in [16] and active or passive medium dies. The media can be polyurethane, oil or other viscous media or compressed air. A description of the process principle for pressure-stressed, superimposed incremental sheet metal forming using a polyurethane tool (TPIF) is shown in figure 16.14.

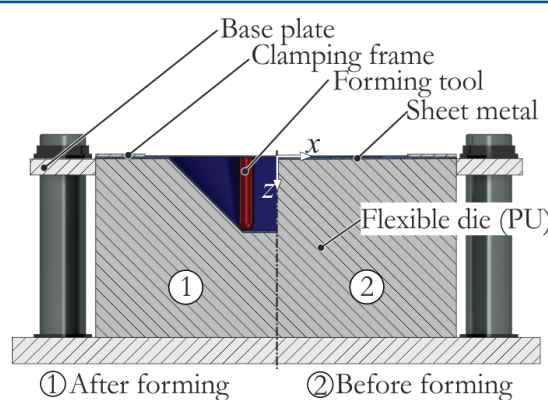


**Figure 16.14** Process setup of ISF with counter pressure [24].

The process setup for the SPIF process is enhanced to a TPIF process by integrating a polyurethane plate. A polyurethane die is placed below the unprocessed sheet metal. The polyurethane die is installed by form-fit joints and fixed in all directions. The positioned and clamped sheet metal is formed into the polyurethane die by the forming tool move-

ment in the  $z$ -direction. The concept is compared to SPIF regarding the component properties and especially the residual stresses in the following chapters.

### 16.4.2 Process Forces, Geometry and Material Hardness

Figure 16.15 shows the process force in the  $z$ -direction for the production of small truncated cone geometries. The forming force for the SPIF process increases with each tool step-down.

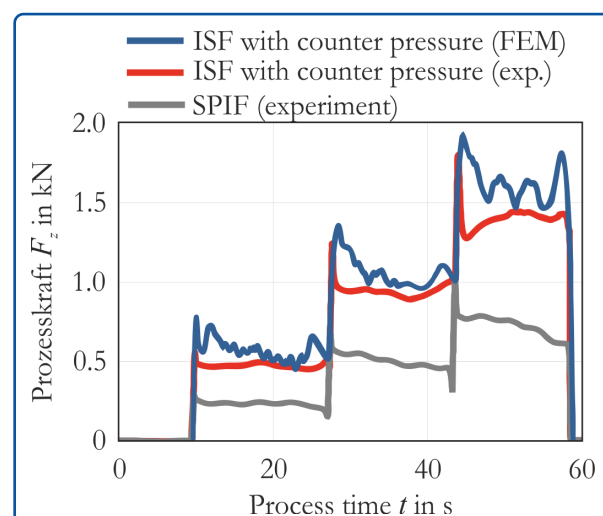


**Figure 16.15** Process forces of SPIF compared to ISF with counter pressure. [24]

Compared to the forming force of the ISF with counter pressure, the qualitative curve progression is equal to that of the SPIF process. The values of the forming forces are significantly higher for the ISF with counter pressure compared to the SPIF process forces. The maximum forming force in the  $z$ -direction for the SPIF process ( $F_z = 0.8 \text{ kN}$ ) is 79 % higher in the comparable ISF with counter pressure experiment ( $F_z = 1.8 \text{ kN}$ ). The force output in the  $z$ -direction of the ISF with counter pressure calculated by the numerical model as presented in figure 16.15 shows a satisfactory agreement with the experimental results. The die material is modeled using a hyper-elastic material model (Mooney-Rivlin). The sample with counter pressure shows a high geometrical accuracy for the bottom area, which is not achieved with the SPIF process. Therefore, three geometries are compared: the SPIF com-

ponent, a component manufactured with ISF with counter pressure using the same SPIF parameters and a component with adjusted process parameters for the SPIF process to meet the geometrical accuracy of the ISF with counter pressure (SPIF compensated). A comparison of the sheet thickness in the cone wall for the three process variants can be seen in figure 16.16 a.

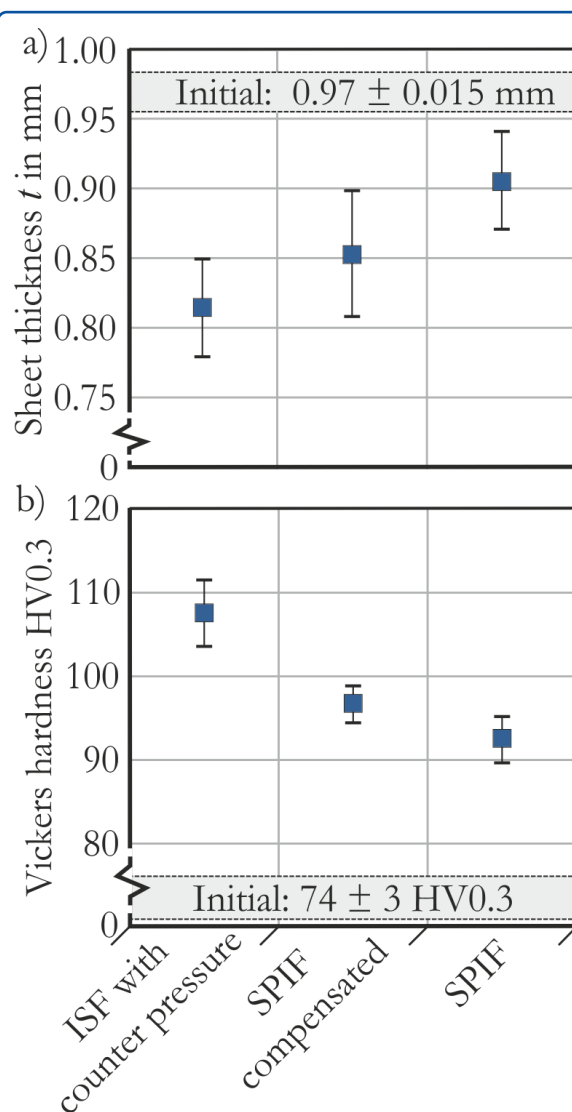


**Figure 16.16** a) Sheet thickness in the cone wall for three process variants, b) Material hardness in the cone wall for three process variants [24].

The measured thickness of the initial base material is around  $t_0 = 0.97$  mm. A sheet thickness reduction occurs for all process variants. The smallest thickness reduction of 6 % is observed for the SPIF process compared to the initial sheet thickness. The thickness reduction of 15 % for the ISF with

counter pressure process is significantly higher because of the added compression. Besides the sheet thickness, the material hardness is measured in the cross section of the cone wall at the selected point using Vickers hardness  $HV0.3$  (figure 16.16 b). All hardness values are mean values of three measurements. The initial material hardness of the AA5083 base material is measured to be  $74 \pm 3$  HV0.3. After the forming processes, all specimens have a significantly higher material hardness in the forming zone compared to the initial material hardness. The specimen with the highest thinning (ISF with counter pressure) shows the highest increase in material hardness of 31 %. In the forming zone of the SPIF specimen, the lowest material hardening of 20 % occurs correspondingly.

### 16.4.3 Residual Stresses

The measured residual stresses in the tool feed direction (figure 16.17 a) on the tool side significantly differ for the three process variants. There is a shift from tensile residual stresses to compressive residual stresses between the specimen manufactured with ISF with counter pressure and the SPIF specimens. The SPIF and SPIF compensated cones both show tensile residual stresses with equal amplitudes of approximately  $\sigma_r = 130$  MPa. In the truncated cone manufactured using compressive stress-superposed ISF notable compressive residual stresses ( $\sigma_r = -45$  MPa) occur perpendicular to the tool feed at the tool side. In the tool feed direction on the tool side the residual stresses are tensile residual stresses for all three process variants. The highest tensile residual stress can be observed in the SPIF manufactured part with approximately  $\sigma_t = 155$  MPa. The residual stress states on the non-tool side are compressive residual stresses for all stress components and process variants (figure 16.17 b). The residual stresses perpendicular to the tool feed at the non-tool side are high compressive residual stresses in the same range near  $\sigma_r = 210$  MPa. The compressive residual stresses in tool feed direction are comparatively high for the ISF with counter pressure specimen, close to  $\sigma_t = 195$  MPa. The comparable residual stresses of the SPIF compensated geometry are lower, at a level close to  $\sigma_t = 100$  MPa.

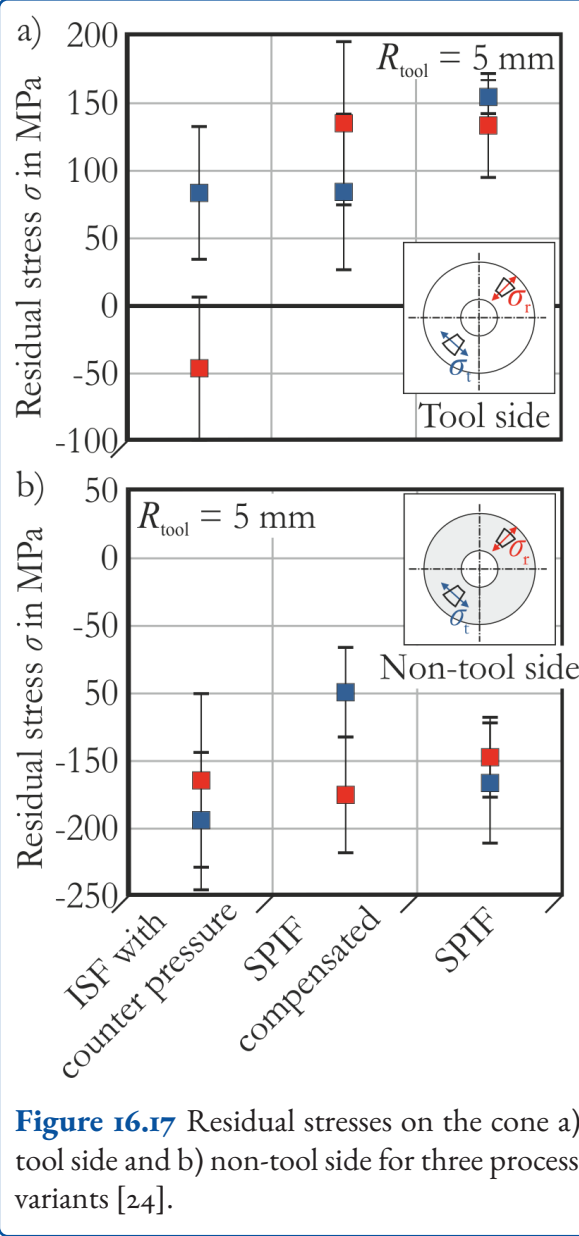


**Figure 16.17** Residual stresses on the cone a) tool side and b) non-tool side for three process variants [24].

#### 16.4.4 Tensile Stress-superposed Incremental Forming

The process setup for tensile stress-superposed incremental forming (TSSIF) is given in figure 16.18. A SPIF setup is used consisting of a forming tool  $R_{\text{tool}} = 5 \text{ mm}$  and clamping frame. Instead of a rigid clamping, an adjustable clamping is added to the SPIF setup. Two sides of the clamping can be moved by hydraulic cylinders along rails in the  $x$ - $y$ -direction independently. The forming area is not affected by the TSSIF setup. The TSSIF setup is mounted to a DMG Mori® 5-axis DMU 50 milling machine. Two different tensile prestress

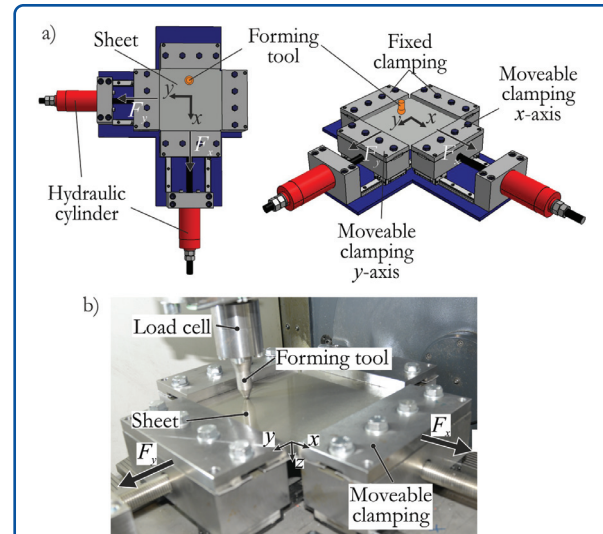


**Figure 16.18** TSSIF process setup [25].

values are applied, namely 20 % and 40 % of the initial yield stress of the AA5083 material of  $\sigma_{y,0} = 160 \text{ MPa}$ .

#### 16.4.5 Geometry and Material Hardness

Sheet thickness and material hardness evaluations are performed at the location of the selected point (figure 16.6). The resulting sheet thickness evaluation is shown in figure 16.19 a. Sheet thickness values are mean values of three repetitions. The sheet thickness reduction measured in the cone wall is almost equal comparing the three process variants. The resulting thickness is equal to the theoretical value  $t_{\text{analytic}} = 0.74 \text{ mm}$  calculated by the sine law for truncated cones with a wall angle  $\Psi = 40^\circ$ . The material hardness is measured in the cross section of the cone wall using Vickers hardness HV<sub>0.3</sub> (figure 16.19 b). All hardness values are mean values of three measurements. The initial material hardness of the delivered AA5083 material is  $74 \pm 3 \text{ HV}_{0.3}$ . After the forming processes, all specimens have a significantly higher material hardness of between 114 and 116 HV<sub>0.3</sub> in the forming zone compared to the initial material hardness. Within the accuracy of the measurements, no significant hardness difference between the process variants can be observed.

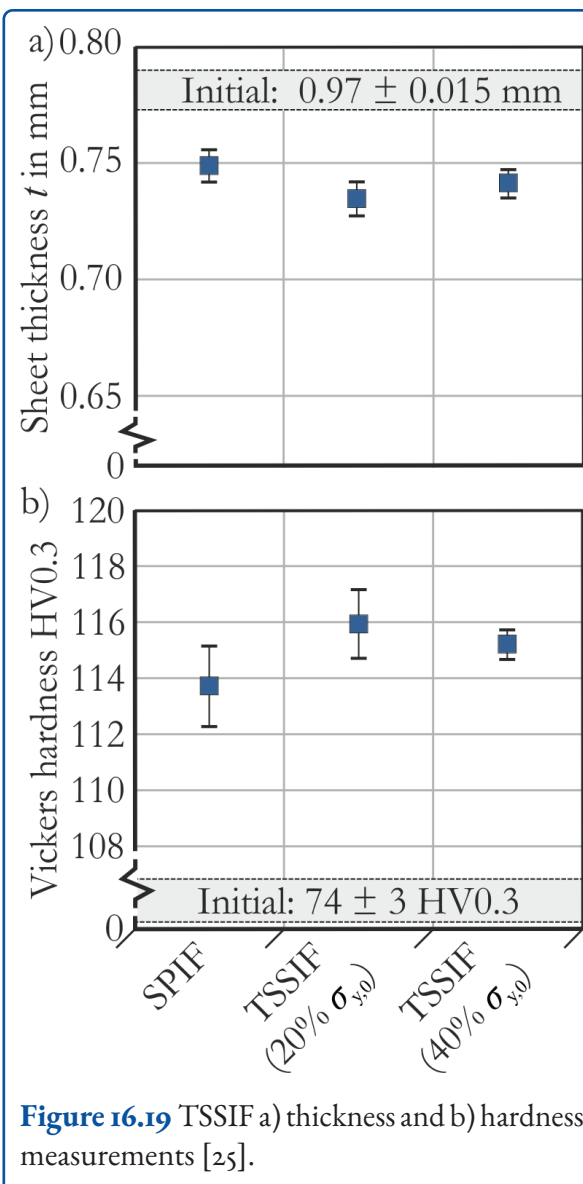


**Figure 16.19** TSSIF a) thickness and b) hardness measurements [25].

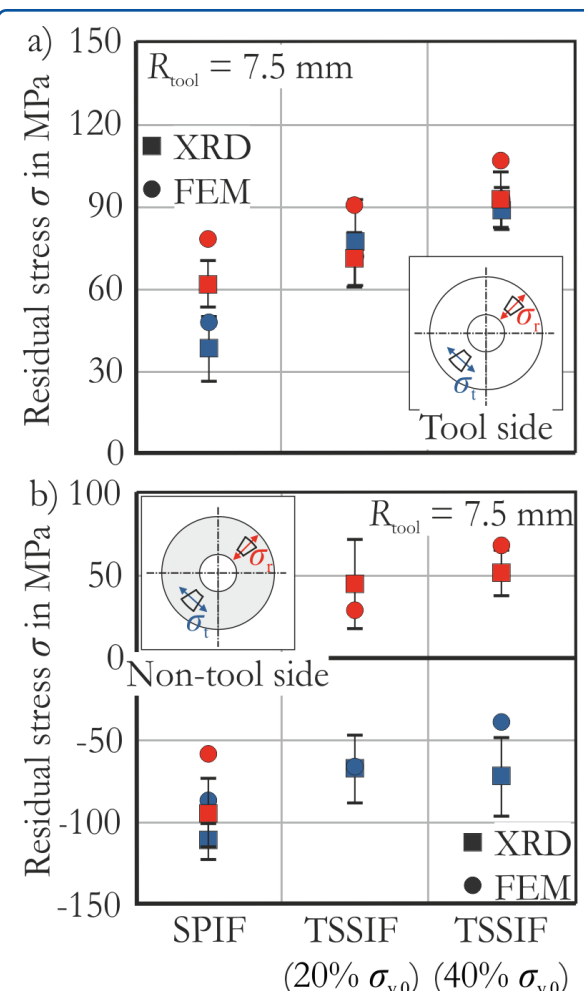


**Figure 16.20** Residual stresses on the cone a) tool side and b) non-tool side for SPIF compared to TSSIF [25].

## Residual Stresses

An evaluation of the experimentally measured residual stresses located at the selected point of the cone wall in tool feed direction and perpendicular to the tool feed on the tool side and the non-tool side was done. The residual stress evaluation of the numerical model is performed accordingly (figure 16.6). The residual stresses perpendicular to the tool feed direction on the tool side are tensile residual stresses (figure 16.20 a). The residual stresses monotonously increase with increasing superposed tensile stress. The residual stresses in tool feed direction are increased by 25 % for TSSIF with a tensile stress equal to 20 % of the initial yield stress and

49 % with a superposed tensile stress equal to 40 % of the initial yield stress.

The residual stresses perpendicular to the tool feed on the tool side monotonously increase with increasing superposed tensile stress (figure 16.20 a). The circumferential residual stresses are increased by 47 % for TSSIF with a tensile stress equal to 20 % of the initial yield stress and 57 % with a superposed tensile stress equal to 40 % of the initial yield stress. The numerical results show the same behavior qualitatively and quantitatively. An evaluation of the residual stresses in tool feed direction and perpendicular to the tool feed direction on the non-tool side of the part is shown in figure 16.20 b. The residual stresses perpendicular to the tool feed direction on the non-tool

side are compressive residual stresses for the SPIF process. The residual stresses monotonously decrease into the tensile range with increasing superposed tensile stress. The compressive residual stresses perpendicular to the tool feed direction  $\sigma_r = -89 \pm 19$  MPa are changed to tensile residual stresses for TSSIF. The compressive residual stresses in the circumferential direction on the non-tool side monotonously decrease into the tensile range with increasing superposed tensile stress. The numerical results show the same behavior qualitatively and quantitatively. Hence, TSSIF is only capable of intensifying the residual stress amplitude toward more tensile stresses.

## 16.5 Analysis of Fatigue Strength

The process analysis indicates the possibility of the targeted adjustment of the residual stresses of a component manufactured by incremental forming processes. An evaluation of the influence of the adjusted residual stress state on fatigue strength is conducted. Truncated cone specimens are clamped at the edges and at the bottom in a resonant testing machine and are loaded until a visible crack occurs at the wall of the cone geometry (figure 16.21). The crack always occurs perpendicular to the aforementioned  $\sigma_r$ -direction 16.6.

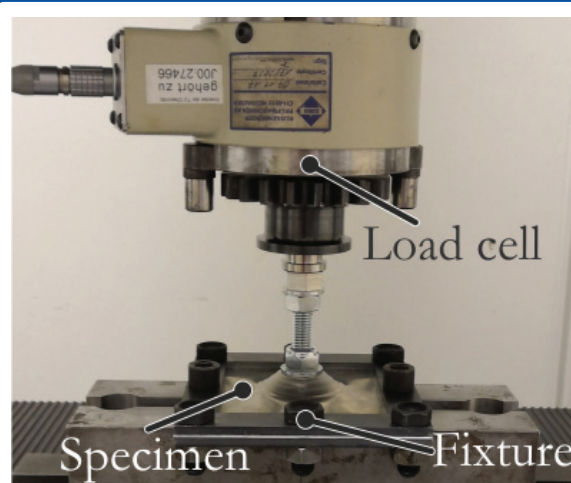


**Figure 16.21** Fatigue testing setup.

To evaluate the influence of the residual stresses on the fatigue strength of the component, reference

tests are performed with stress-relieved truncated cone components. The specimens are heat-treated for 2 min at 300 °C including 1 min holding time. Using a cyclic loading test setup for heat-treated and not heat-treated specimens, as explained in [29], with an increasing number of increments, the relationship between residual stresses on the tool side and the failure of a component is shown (figure 16.22). The failure can be clearly assigned to the residual stresses by comparing stressed specimens and stress-relieved specimens. A relationship between the tensile residual stresses on the tool side and a 42 % reduction of the lifetime in cyclic load tests until component failure is experimentally shown.

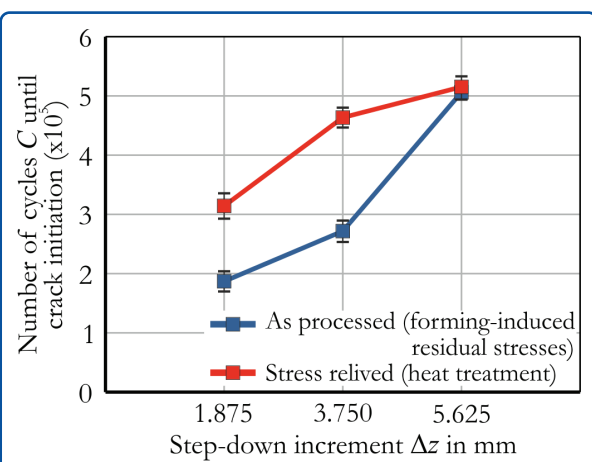


**Figure 16.22** Influence of step-down increment  $\Delta z$  on the fatigue strength of cyclically loaded truncated cones [29].

### 16.5.1 Numerical Fatigue Strength Model

The numerical model of the incremental sheet metal forming modified by cyclic load is based on the experiments. By coupling with the program *fe-safe*, fatigue strength predictions were possible for the different  $\Delta z$  (1.25 mm and 3.75 mm). The model is able to show the influence of residual stresses on the beginning of the crack on the inside of the truncated cone. The model is therefore suitable for supporting the experiments, but in order to do predictions beyond the verified limits further optimizations are needed.

### 16.5.2 Influence of Corrosion

Residual stresses strongly effect the fatigue strength of a component. Tensile residual stresses in corrosive environments especially can lead to early failure due to stress corrosion cracking [30]. Cyclic loading test are performed to analyze the influence of the residual stress state on the corrosion resistance of AA5083 truncated cones. Two geometrically identical cones are manufactured with two different sets of process parameters to generate different residual stress states. A step-down increment  $\Delta z = 1.25$  mm is used to generate comparably high tensile residual stresses in the cone wall, whereas  $\Delta z = 3.75$  mm is applied to generate comparably low tensile residual stresses (figure 16.23).

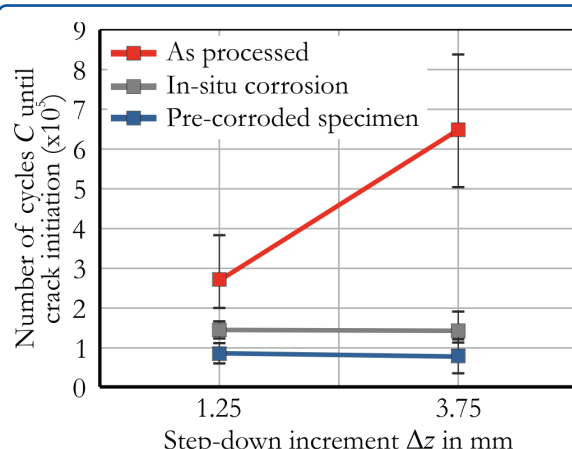


**Figure 16.23** Influence of corrosion on cyclically loaded truncated cones manufactured with two different step-down increment  $\Delta z$ .

A cyclic load with  $F_{\max} = 2,000$  N and  $F_{\min} = 200$  N is applied to the specimen with a frequency of  $f = 55$  Hz. To analyze the corrosive influence, a pre-corroded specimen dipped in corrosive medium (3.5 % NaCl, pH 3) for 7 days is compared to an in-situ corroded specimen by applying a corrosive gel electrolyte (3.5 % NaCl, pH 3) during the fatigue testing procedure. The as-produced specimens show a significant difference in the cycles until crack initiation. Due to the high tensile residual stresses inside the cone wall, the fatigue strength of the  $\Delta z = 1.25$  mm component is reduced by 46 % compared to the  $\Delta z = 3.75$  mm compo-

nent. The fatigue strength of the in-situ corroded specimen is limited to 51 % of the as-produced specimen for  $\Delta z = 1.25$  mm. There is no significant change of the fatigue strength for the in-situ corroded specimen regarding the  $\Delta z = 3.75$  mm case for two different step-down increments. Thus, the in-situ corrosion is less sensitive to the different residual stress states. A local corrosion attack (pitting) at defects or precipitates during in-situ corrosion serves as the starting point of crack growth and causes the premature cracking of the component. The fatigue resistance of the pre-corroded specimen is similar to the in-situ corroded specimen at a low level. However, the harsher conditions of pre-corrosion (i.e., long exposure time) caused pitting with deeper pits than during in-situ corrosion, which results in the lower number of cycles until cracking. Both after pre-corrosion and during in-situ corrosion, the corrosive media has a significant influence on the fatigue strength of the component. This influence is so pronounced that present residual stresses can rather be disregarded with respect to their influence on fatigue strength.

## 16.6 Transferability of the Results and Application

To analyze the transferability of the project results to other materials [31], the influence of the step-down increment on the residual stress state for austenitic-ferritic dual-phase steel 1.4462 (X<sub>2</sub>CrNiMoN<sub>22-5-3</sub>,  $t_0 = 1$  mm) is experimentally investigated. According to the findings for the aluminum AA5083 material, the residual stresses of both phases can be modified in a targeted manner by varying the size of the step-down increment (figure 16.24 a). An industrial application for the incremental forming process forms a cavity in high-strength steel seat rails for car seating as shown in figure 16.24 b. The calotte geometry is used to overcome the distance created by the carpet and insulation material to the car body at the mounting point. The cavity is exposed to quasi-static and cyclic loads during operation. The ability to influence the residual stresses of this component to enhance its fatigue strength is a suitable application for the knowledge generated in this project.

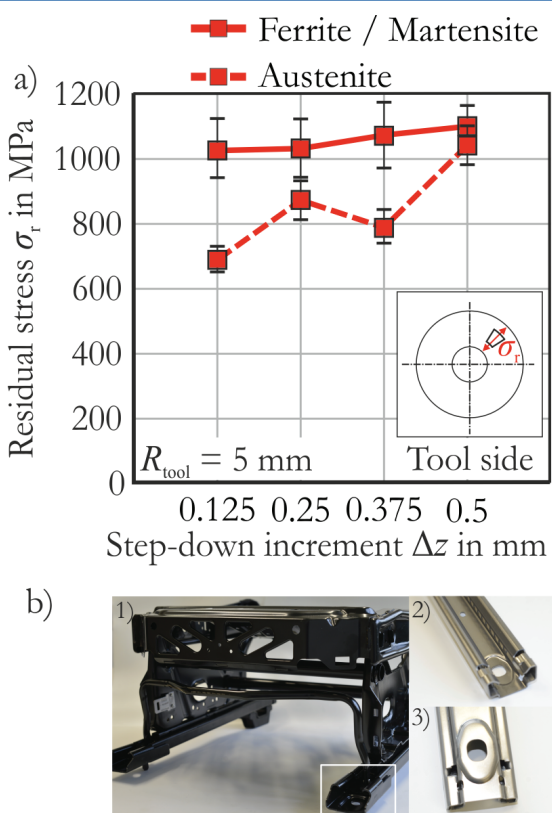


**Figure 16.24** a) Influence of the step-down increment on the residual stress state of dual-phase steel 1.4462 truncated cones. b) 1) Car seat with 2) seat rail and 3) mounting point.

## 16.7 Conclusion

In this project regarding the incremental sheet metal forming process, the relationship between the process parameters, the forming mechanisms, the resulting residual stress state and fatigue strength of formed components in a corrosive environment was analyzed. The key findings can be summarized as follows:

- The residual stress prediction model was validated by XRD measurements for the material AA5083. The prediction quality of the model was increased by considering the unclamping process and the kinematic hardening in the material model [32].
- For the analyzed geometries, near-surface tensile residual stresses on the component's tool side and compressive residual stresses on the non-

tool side are detected. The residual stress values can be set by the step-down increment  $\Delta z$  and the tool radius  $R_{\text{tool}}$ .

- The increasing reduction of sheet thickness with increasing hardening as a result of the shearing mechanism for smaller step-down increments causes an increase in the tensile residual stresses on the tool side.
- The increasing impact of the bending mechanism with an increasing tool step-down increment  $\Delta z$  causes a stretching of the non-tool side, which leads to an increase in the compressive residual stresses on the non-tool side.
- Compressive stress superposition during the process can lead to a shift to compressive residual stresses, which enables compressive residual stresses on both sides of the formed component.
- Tensile stress superposition leads to a shift of the residual stresses toward tensile residual stresses.
- Targeted forming-induced residual stresses lead to a 172 % increase in fatigue strength for AA5083 truncated cone geometries.
- The effect of the forming-induced residual stresses on fatigue strength in corrosive environments is negligible for AA5083.

## References

- [1] W. C. Emmens and A. H. van den Boogaard. "An overview of stabilizing deformation mechanisms in incremental sheet forming". In: *Journal of Materials Processing Technology* 209.8 (2009), pp. 3688–3695. ISSN: 09240136.
- [2] P.A.F. Martins et al. "Theory of single point incremental forming". In: *CIRP Annals* 57.1 (2008), pp. 247–252. ISSN: 00078506. doi: 10.1016/j.cirp.2008.03.047.
- [3] J. Jeswiet and E. Hagan. "Rapid prototyping of a headlight with sheet metal". In: *Canadian Institute of Mining, Metallurgy and Petroleum* (2001), pp. 109–114.
- [4] N. N. Powell and C. Andrew. "Incremental Forming of Flanged Sheet Metal Components Without Dedicated Dies". In: *Proceedings of the Institution of Mechanical Engineers, Part B: Journal of Engineering Manufacture* 206.1 (1992), pp. 41–47.

- ISSN: 0954-4054. DOI: 10.1243/PIME\_PROC\_1992\_206\_054\_02.
- [5] B. Taleb Araghi et al. "Investigation into a new hybrid forming process: Incremental sheet forming combined with stretch forming". In: *CIRP Annals* 58.1 (2009), pp. 225–228. ISSN: 00078506. DOI: 10.1016/j.cirp.2009.03.101.
- [6] M. B. Silva et al. "Single-point incremental forming and formability—failure diagrams". In: *The Journal of Strain Analysis for Engineering Design* 43.1 (2008), pp. 15–35. ISSN: 0309-3247. DOI: 10.1243/03093247JSA340.
- [7] Gerd Sebastiani. "Erweiterung der Prozessgrenzen inkrementeller Blechumformverfahren mittels flexibler Werkzeuge". Dissertation. Aachen: Shaker Verlag.
- [8] Fawad Maqbool and Markus Bambach. "Revealing the Dominant Forming Mechanism of Single Point Incremental Forming (SPIF) by Splitting Plastic Energy Dissipation". In: *Procedia Engineering* 183 (2017), pp. 188–193. ISSN: 18777058. DOI: 10.1016/j.proeng.2017.04.018.
- [9] W. C. Emmens and A. H. van den Boogaard. "An overview of stabilizing deformation mechanisms in incremental sheet forming". In: *Journal of Materials Processing Technology* 209.8 (2009), pp. 3688–3695. ISSN: 09240136. DOI: 10.1016/j.jmatprotec.2008.10.003.
- [10] Fritz Klocke. *Fertigungsverfahren 4: Umformen*. 6. Aufl. 2017. VDI-Buch. Berlin, Heidelberg: Springer Berlin Heidelberg, 2017. ISBN: 9783662547144. URL: <http://nbn-resolving.org>.
- [11] E. Hagan and J. Jeswiet. "A review of conventional and modern single-point sheet metal forming methods". In: *Proceedings of the Institution of Mechanical Engineers, Part B: Journal of Engineering Manufacture* 217.2 (2003), pp. 213–225. ISSN: 0954-4054. DOI: 10.1243/095440503321148858.
- [12] Ahmet Erman Tekkaya. "Equivalent strain and stress history in torsion tests". In: *Steel Research* 65.2 (1994), pp. 65–70. ISSN: 01774832. DOI: 10.1002/srin.199400928.
- [13] Wilco C. Emmens. *Formability: A review of parameters and processes that control, limit or enhance the formability of sheet metal*. 1., st edition. Springer briefs in applied sciences and technology. Heidelberg: Springer, 2011. ISBN: 978-3-642-21903-0. DOI: 10.1007/978-3-642-21904-7.
- [14] Philip Eyckens et al. "MK modelling of sheet formability in the incremental sheet forming process, taking into account through-thickness shear". In: *International Journal of Material Forming* 2.SI (2009), pp. 379–382. ISSN: 1960-6206. DOI: 10.1007/s12289-009-0458-0.
- [15] Kathryn Jackson and Julian Allwood. "The mechanics of incremental sheet forming". In: *Journal of Materials Processing Technology* 209.3 (2009), pp. 1158–1174. ISSN: 09240136. DOI: 10.1016/j.jmatprotec.2008.03.025.
- [16] Gerd Sebastiani et al. "FlexDie: A Flexible Tooling-Concept for Incremental Sheet Forming". In: *Key Engineering Materials* 504-506 (2012), pp. 883–888. DOI: 10.4028/www.scientific.net/KEM.504-506.883.
- [17] T.J Kim and D.Y Yang. "Improvement of formability for the incremental sheet metal forming process". In: *International Journal of Mechanical Sciences* 42.7 (2000), pp. 1271–1286. ISSN: 00207403. DOI: 10.1016/S0020-7403(99)0047-8.
- [18] Shigekazu Tanaka et al. "Residual Stress In Sheet Metal Parts Made By Incremental Forming Process". In: *AIP Conference Proceedings*. AIP, 17–21 June 2007, pp. 775–780. DOI: 10.1063/1.2740904.
- [19] Crina Radu et al. "The Residual Stress State Generated by Single Point Incremental Forming of Aluminum Metal Sheets". In: *Applied Mechanics and Materials* 371 (2013), pp. 148–152. DOI: 10.4028/www.scientific.net/AMM.371.148.
- [20] Paul Ludwig. *Elemente der Technologischen Mechanik*. 6. Aufl. 2017. Berlin: Springer Berlin Heidelberg, 1909. ISBN: 9783662392652. URL: <http://link.springer.com>.
- [21] Fabian Maaß, Marlon Hahn, and A. Erman Tekkaya. "Interaction of Process Parameters, Forming Mechanisms, and Residual Stresses in Sin-

- gle Point Incremental Forming". In: *Metals* 10.5 (2020), p. 656. DOI: 10.3390/met10050656.
- [22] Jean Lemaitre and Jean-Louis Chaboche. *Mechanics of solid materials*. Cambridge: Cambridge University Press, 1990. ISBN: 0521477581. URL: <http://www.loc.gov/catdir/samples/cam034/88022913.html>.
- [23] Mateus Dobecki. "Röntgenographische Analysen der Umformmechanismen und der Eigenspannungen umgeformter Bleche im Single Point Incremental Forming - Verfahren". Dissertation. Berlin: Verlag TU Berlin.
- [24] Fabian Maaß, Marlon Hahn, and A. Erman Tekkaya. "Adjusting residual stresses by flexible stress superposition in incremental sheet metal forming". In: *Archive of Applied Mechanics* 91.8 (2021), pp. 3489–3499. ISSN: 0939-1533. DOI: 10.1007/s00419-021-01929-x.
- [25] Fabian Maaß, Marlon Hahn, and A. Erman Tekkaya. "Setting Residual Stresses in Tensile Stress-Superposed Incremental Sheet Forming". In: *Key Engineering Materials* 926 (2022), pp. 655–662. DOI: 10.4028/p-232uip.
- [26] S. Matsubara. "A computer numerically controlled dieless incremental forming of a sheet metal". In: *Proceedings of the Institution of Mechanical Engineers, Part B: Journal of Engineering Manufacture* 215.7 (2001), pp. 959–966. ISSN: 0954-4054. DOI: 10.1243/0954405011518863.
- [27] Haibo Lu et al. "Part accuracy improvement in two point incremental forming with a partial die using a model predictive control algorithm". In: *Precision Engineering* 49 (2017), pp. 179–188. ISSN: 01416359. DOI: 10.1016/j.precisioneng.2017.02.006.
- [28] J. Jeswiet et al. "Asymmetric Single Point Incremental Forming of Sheet Metal". In: *CIRP Annals* 54.2 (2005), pp. 88–114. ISSN: 00078506. DOI: 10.1016/S0007-8506(07)60021-3.
- [29] F. Maaß et al. "Setting Component Properties in Incremental Forming". In: *Contributed Papers from MSE&T19*. TMS, 2019, pp. 1176–1182. ISBN: 978-0-87339-770-4. DOI: 10.7449/2019/MST\_2019\_1176\_1182.
- [30] W. H. Friske and J. P. Page. "Shot peening to prevent the corrosion cracking of austenitic stainless steels". In: *Journal of Materials for Energy Systems* 1.1 (1979), pp. 20–32. ISSN: 0162-9719. DOI: 10.1007/BF02833987.
- [31] Fawad Maqbool et al. "Targeted residual stress generation in single and two point incremental sheet forming (ISF)". In: *Archive of Applied Mechanics* 91.8 (2021), pp. 3465–3487. ISSN: 0939-1533. DOI: 10.1007/s00419-021-01935-z.
- [32] Fabian Maaß et al. "Influence of tool path strategies on the residual stress development in single point incremental forming". In: *Procedia Manufacturing* 29 (2019), pp. 53–58. ISSN: 23519789. DOI: 10.1016/j.promfg.2019.02.105.

# 17 Characterization and Utilization of Process-induced Residual Stresses for the Manufacture of Functional Surfaces by Near-net-shape Blanking Processes

Nürnberg, A.; Müller, D.; Holzer, K.; Hartmann, C.; Tobie, T.; Stahl, K.; Volk, W.

GEPRIS 374524261

## 17.1 Introduction

Near-net-shape blanking (NNSB) processes enable the production of functional complex surface contours in an economical way. The blanking processes are characterized by high plastic deformation and thus induce significant residual stresses in the produced part. Up to now, process-induced residual stresses have not been investigated with respect to their suitable use or even how to control for their tensile and compressive residual stress components to ensure targeted, part-specific residual stress profiles. Controlling the single step NNSB process-induced residual stresses offers great potential to substitute the cost-, energy- and time-intensive heat treatment and the subsequent required grinding for highly loaded parts such as gears. In the following, the main investigations and results of the six-year research project are presented. The research project consists of three funding periods. In the first period, simplified geometries helped to choose a promising NNSB process. In the second period, fineblanking was used to produce a pinion with shear cutting parameters optimized for the prevention of fatigue failure. In the last period, the results were bundled and used to produce a pinion/wheel pair from higher strength steels. Finally, it is possible to increase the load-bearing capacity of power-transmitting gears without heat treatment by process-induced residual stresses.

## 17.2 State of the Art

NNSB processes are precision cutting technologies for the production of metallic cutouts [2]. These separating manufacturing processes do not produce chips and economically produce components with cutting surfaces suitable for use as functional surfaces. With the exception of a deburring step, which may be necessary, the components can be produced ready for use in a single stroke [3].

The cutting surfaces (compare figure 17.1) of such components are characterized by a high clean cut percentage and an almost perpendicular angle to the cut part surface. Figure 17.2 shows five selected near-net-shape blanking processes. The processes illustrated use very small die clearances (the circumferential gap between punch and die) in the range of approximately  $u_{rel} = 0.5\%$  to 2 % of the sheet thickness. The die cutting edge is defined in the form of a chamfer or radius. For the fineblanking and precision blanking processes three forces act independently of each other, the v-ring force  $F_{VR}$  or blank holder force  $F_{BH}$ , the counter punch force  $F_{CP}$  and the blanking force  $F_B$ , which requires the use of special presses. [2] On the other hand,

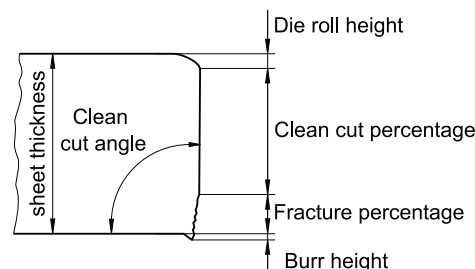


**Figure 17.1** Cutting surface characteristics of functional surfaces produced with NNSB processes [1].

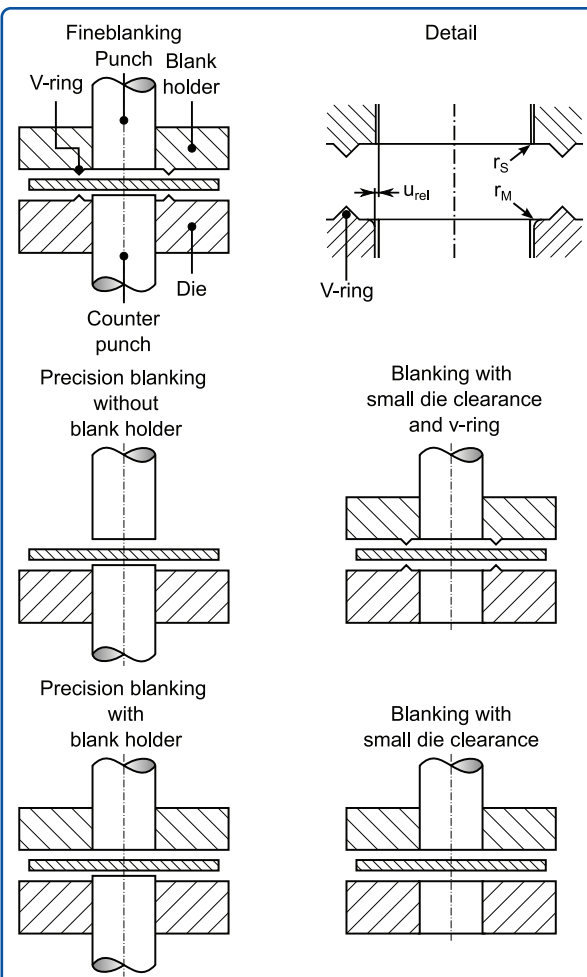


**Figure 17.2** Overview of the investigated near-net-shape blanking processes.

precision blanking without blank holder, blanking with small die clearance and blanking with small die clearance and v-ring can be carried out on single-acting presses. The forces required in addition to the cutting force can be applied passively, e.g., via springs. [4] Extensive investigations on optimized cutting surface characteristics by Hörmann [2] show that a small die clearance, a chamfer on the cutting edge of the die and the use of a v-ring on the die lead to high contact ratios on the cutting surfaces. The reason for this is said to be an increased compressive stress state in the shear area through which the fracture strength of the sheet material is reached later, resulting in a high clean cut percentage or contact ratio, respectively. In order to counteract the deflection of the cut part, the use of a counter punch shows the greatest effect. This is realized by clamping the cut part be-

tween the punch and the counter punch during the blanking process, which almost completely prevents plastic deflection. Hörmann [2] concludes that the cutting surface characteristics achieved by fineblanking are not in total reached by any of the other NNSB processes mentioned above.

The conventional manufacturing process of power-transmitting gears consists of milling, heat treatment and grinding. All three steps are costly as well as energy and time intensive. For power-transmitting gears usually helical involute gears are used in industrial applications. The gears are made of high-strength case hardened steels. For applications with significantly lower torques the use of plastic gears has been increasing recently.

The design of gears is carried out with regard to the main fatigue failure modes: tooth root breakage and pitting (see figure 17.3). Fatigue damage usually occurs after several million load cycles. The cause of damage is the formation of cracks in fatigued material areas. Standardized calculation methods for the design of gears exist, e.g., ISO 6336 [5–7]. The design methods are based on the comparison of occurring stresses, e.g., in the area of the  $30^\circ$  tangent in the tooth root or at the flank, with experimentally determined strength numbers of reference gears. Various influencing factors are considered, such as the gear size or the roughness on the load-carrying capacity. The influence of residual stresses is not yet included in standardized calculations. However, a significant influence of the residual stresses on pitting and tooth root breakage is already known. For example with shot peening the compressive residual

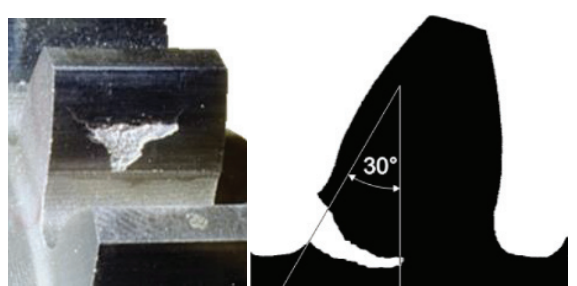


**Figure 17.3** Pitting damage on a gear flank and schematic tooth root breakage.

stresses after the heat treatment can be quadrupled within a limited material depth from approximately  $-300$  MPa to  $-1,200$  MPa. This can result in an increase of pitting strength and tooth root bending strength of up to 50 % [8] compared to an unpeened carburized gear.

Until now, there has been little research on shear cut power-transmitting gears. However, gears made of lower-strength steels have been investigated. In Niemann [9], the load-carrying capacity of involute spur gears made of sheet metal discs was investigated. In this case, however, the individual plates were first soldered or bonded and then milled. The residual stresses were not considered in these investigations.

For wrought normalized low-carbon steels the ISO 6336-5 [7] specifies stress numbers that allow the calculation of the gear load-carrying capacity. Hereby, the increase in load-carrying capacity due to compressive residual stresses is not yet considered in the ISO 6336 standards.

### 17.3 Funding Period I - Choice of NNSB Process

In the first period the main objective was to manufacture representative but simplified parts. Circular discs and C-profiles are manufactured with different NNSB processes and variations of their process parameters (compare figure 17.2) to investigate the cutting surface characteristics and residual stresses. Simulation methods and testing methods regarding the residual stresses are established as well. Further, the simplified parts are tested regarding bending fatigue in a pulsating test rig and contact fatigue in a twin disc test rig.

#### 17.3.1 Experimental Setup and Test Equipment I

Circular discs and C-profiles (see figure 17.4) made of S355MC with sheet thickness  $s = 6$  mm were manufactured using the five different NNSB processes shown in figure 17.2. Two different config-

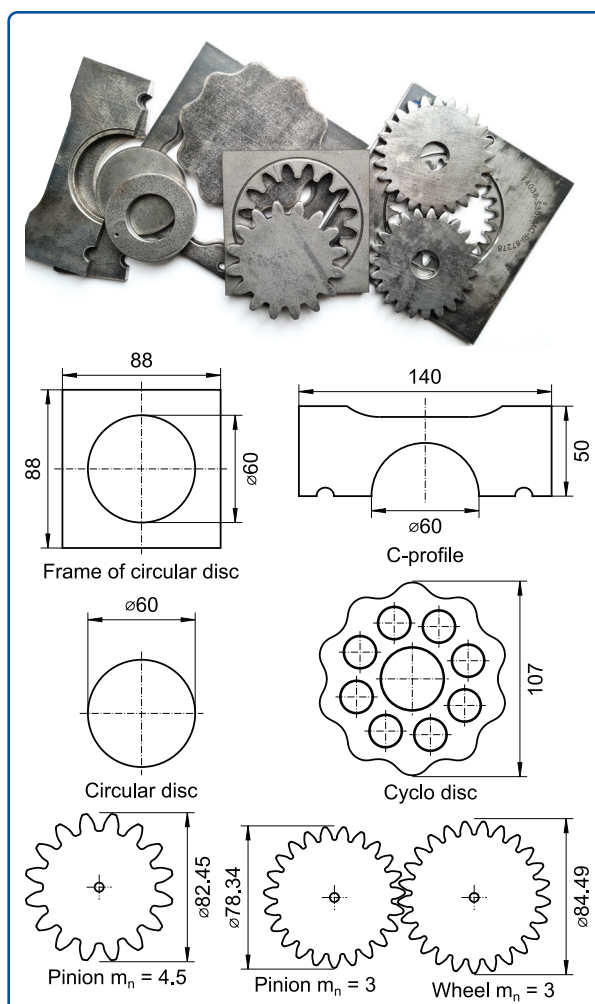


**Figure 17.4** Overview of investigated specimen geometries.

urations of punch cutting edge radius  $r_S$  and die cutting edge radius  $r_M$  were used. Furthermore, for the NNSB processes of fineblanking and blanking with small die clearance, the relative die clearances 0.5 %, 1 % and 3 % were investigated. The process parameters used are shown in table 17.1.

The more complex geometry of an equidistant of a shortened epicycloid with convex and concave cutting line (see cyclo disc in figure 17.4) was manufactured to further investigate the effects of geometry on the distribution of residual stresses along the cutting line. To determine the influenced depth for the different NNSB processes, the residual stress depth profiles were measured with x-ray diffraction. In addition, residual stress measurements along the cutting surface height were performed. To ensure a uniform initial residual stress state all

**Table 17.1** Cutting parameter configurations 1 and 2 for the circular disc and C-profile.

Process parameter	1	2
$u_{rel}$	0.5 %, 1 %, 3 %	
$r_M$	200 $\mu\text{m}$	< 20 $\mu\text{m}$
$r_S$	< 20 $\mu\text{m}$	200 $\mu\text{m}$
$F_{BH}$		200 kN
$F_{VR}$		450 kN
$F_{CP}$		200 kN
$v_B$		50 mm/s



**Figure 17.5** Bending test of the C-profile in a pulsating test rig and contact fatigue test in a twin disc test rig.

semi-finished products were stress-relieved before the blanking tests. Care was taken to ensure that the temperatures specified in [10] were not exceeded. To rule out recrystallization or other microstructural changes microstructural examinations were carried out.

Different variants of C-profiles were tested regarding bending strength in a pulsating test rig using a specially designed clamp holder (figure 17.5). More than 70 tests in the range of the limited life and endurance strength up to 6 million load cycles were carried out.

The circular discs were tested regarding contact fatigue in a twin-disc test rig that was designed and build for these investigations. The objective of these fatigue tests was the estimation of the contact fatigue strength and the evaluation of the influence of the residual stresses on the contact fatigue as well as the stability of the residual stresses. The cyclo discs were tested in a cycloidal test rig. Accompanying the experimental investigations, a simulation-supported residual stress model was built for NNSB processes, which provides information on the resulting residual stress state. In addition, load-bearing capacity models were developed to take the influence of residual stresses into account.

### 17.3.2 Results I

Most NNSB processes result in almost similar cutting surface characteristics and hardness distributions. The results of the cutting surface characteristics of the circular discs manufactured by the different NNSB processes in configuration 2  $r_S < 20 \mu\text{m}$  and  $r_M = 200 \mu\text{m}$  are shown in figure 17.6. The differences in the residual stresses of the blanks on the functional surface are given in figure 17.7. In this configuration, the residual stresses range from  $-549 \text{ MPa}$  to  $+269 \text{ MPa}$  depending on both the NNSB process and its process parameters. Compared to the other configuration, a sharp cutting punch in combination with a rounded die cutting edge results in higher compressive residual stresses for fineblanched cutouts.

Fineblanking (configuration 2:  $r_S < 20 \mu\text{m}$ ,  $r_M = 200 \mu\text{m}$  and  $u_{rel} = 0.5 \%$ ) showed tangential and axial compressive residual stresses of  $-549 \text{ MPa}$  and  $-262 \text{ MPa}$  at the circular discs and  $-285 \text{ MPa}$  and  $-384 \text{ MPa}$  at the associated stamping frame and the C-profiles, respectively, and along the cutting surface height. At depth, compressive residual stresses of up to  $0.2 \text{ mm}$  could be induced on the C-profiles. The scatter of residual stresses is in the range  $\pm 100 \text{ MPa}$ .

For the theoretical explanation of the residual stress states on the blanked functional surfaces at the circular discs and at the stamping frame, an explanatory model was developed for circular discs

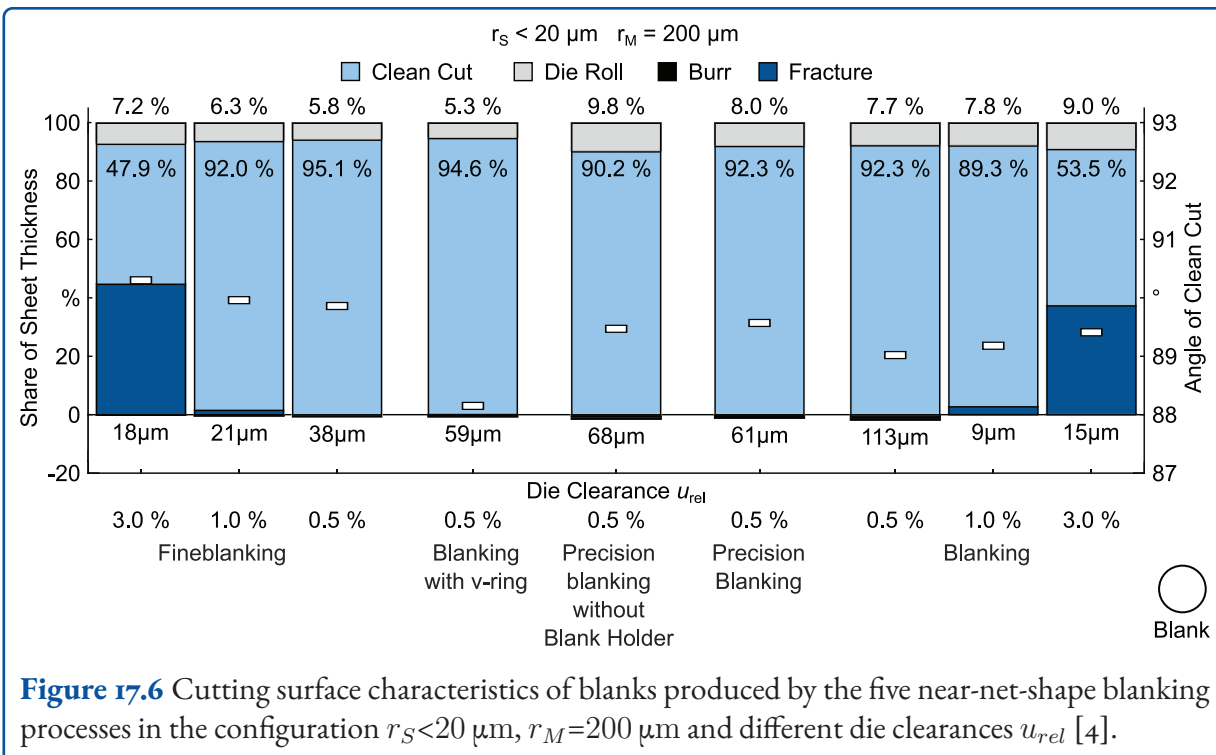


**Figure 17.6** Cutting surface characteristics of blanks produced by the five near-net-shape blanking processes in the configuration  $r_S < 20 \mu\text{m}$ ,  $r_M = 200 \mu\text{m}$  and different die clearances  $u_{rel}$  [4].

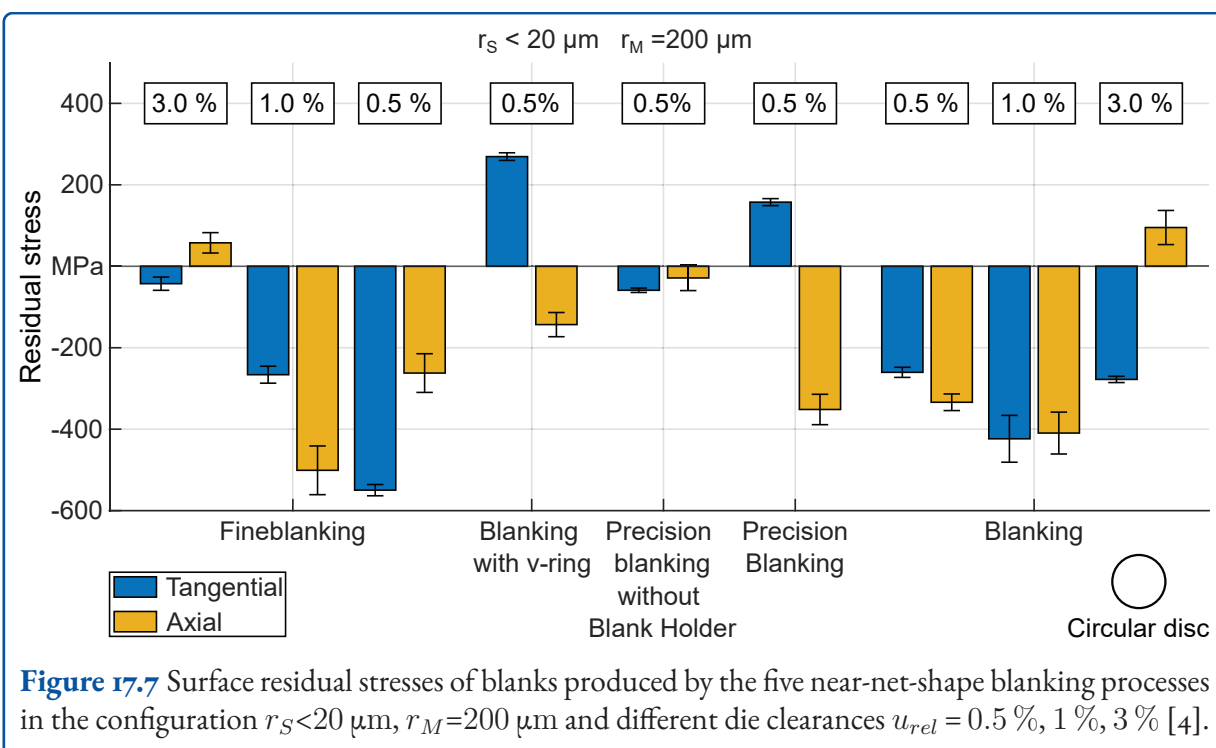


**Figure 17.7** Surface residual stresses of blanks produced by the five near-net-shape blanking processes in the configuration  $r_S < 20 \mu\text{m}$ ,  $r_M = 200 \mu\text{m}$  and different die clearances  $u_{rel} = 0.5\%, 1\%, 3\%$  [4].

which are blanked with a die clearance of  $u_{rel} = 0.5\%$ . The explanatory model is derived from macroscopic changes in the geometries of the components. It is assumed that deviations from the ideal nominal geometry after springback are caused by a change in the stress state during the blanking

process. Based on four defined springback modes (Mode I: global radial springback, Mode II: local radial springback, Mode III: bending springback and Mode IV: axial springback), the model can be used to explain the residual stress state remaining in the component after springback. By linking the

explanatory model with a FEM process simulation, it is possible to show the influences of the NNSB process parameters, cutting edge preparation, blank holder, v-ring and counter punch, leading to the following recommendations for the induction of compressive residual stresses in precision cut components.

Cutouts exhibit higher compressive residual stresses in the axial and tangential directions if the punch cutting edge is left in a nearly sharp-edged state and the die cutting edge has a rounding. The stamping frame is insensitive in this respect, but a rounded punch cutting edge and a sharp die cutting edge can further increase the compressive residual stresses.

With regard to high compressive residual stresses, it is advisable to use a blank holder, otherwise, tearing may occur and thus a tensile residual stress condition may exist in the stamping frame and in the cutout. The use of a blank holder tends to result in tangential tensile residual stresses in cutouts as opposed to the stamping frame edges. Axial residual stresses are lowered by the use of a blank holder for cutouts, but there is no influence observed on the stamping frame.

In the case of cutouts, the use of v-rings promotes compressive residual stresses in the tangential direction. In contrast, the cutting surface on the stamping frame produced by the NNSB processes tends to have tangential tensile residual stresses. The axial residual stresses remain unaffected by the v-rings.

The use of a counter punch in combination with a v-ring supports compressive residual stresses on the cutout in the tangential and axial directions. A counter punch is also recommended for the production of holes in strips, as both the axial and tangential residual stresses on the functional surface on the stamping frame are positively influenced as a result, so that compressive residual stress states are promoted.

The selection of a suitable NNSB process with appropriate process parameters offers the possibility of adjusting the residual stress state as required. However, the cutouts react much more sensitively

to changed process parameters than the stamping frame.

In this funding period, the NNSB process of fineblanking was identified as a suitable process for further investigations. The reasons for this are the high process-induced compressive residual stresses on cutouts achieved and the high-quality cutting surface characteristics, especially with respect to the clean cut percentage.

With regard to the fineblanking of the circular discs, further investigations were carried out concerning the arrangement of the v-rings. These showed that a v-ring on the die side is sufficient to generate high process-induced compressive residual stresses on the functional surface. An additional v-ring on the blank holder offers no further advantages as it does not improve the cutting surface characteristics or the hardening in the vicinity of the cutting surface.

The bending tests show that parts with higher compressive residual stresses have an increased lifetime and that the process-induced compressive residual stresses remain stable within the investigated load cycle range. The rolling contact fatigue tests showed no decrease of the compressive residual stresses as well. For variants with higher compressive residual stresses, a Hertzian pressure of  $p_H = 700 \text{ N/mm}^2$  was endured without plastic deformation. However, the lifetime in the case of pitting damage strongly depends on the elastohydrodynamic lubrication conditions including roughness, which decreased significantly within the first 100,000 load cycles depending on the sliding conditions.

Results of the funding period I are published in [4, 11–14].

## 17.4 Funding Period II – Fineblanking with Targeted Process-induced Residual Stresses

In funding period II, a pinion with module  $m_n = 4.5$  mm (see figure 17.2) was produced from the material S355MC using the NNSB process fineblanking. With variations of the process parameters smaller radii of the cutting line geometry and smaller die rolls as well as increased compressive residual stresses that lead to an increased fatigue strength should be enabled.

Consequently, the goal of funding period II was the quantification of the improvement of the shear cut characteristics and tooth root bending strength by process-induced residual stresses and a comparison with the state of the art as well as the validation of the simulation models.

### 17.4.1 Experimental Setup and Test Equipment II

Suitable fineblanking active elements were designed for creating the pinion geometry. The v-ring cross-section geometry was designed according to [15] and is not arranged equidistant to the cutting line, but follows a circle which is 6 mm larger in diameter than the tip circle. According to [16], the v-ring force and the counter punch force were set to  $F_{VR} = 611$  kN and  $F_{CP} = 291$  kN. The relative die clearance was set constant to  $u_{rel} = 0.5\%$  of the sheet thickness  $s = 6$  mm and the cutting speed was set to  $v_B = 50$  mm/s. The cutting edge of the die was divided into eight segments. Two opposite segments have an equal die cutting edge radius of the four radii  $r_M = 50 \mu\text{m}$ ,  $100 \mu\text{m}$ ,  $150 \mu\text{m}$  and  $200 \mu\text{m}$  investigated. The cutting edge of the punch was rounded with  $r_S = 50 \mu\text{m}$  at the exposed geometry elements (tooth tips). Otherwise, the punch cutting edge was left in its nearly sharp-edged state. The semi-finished products have three holes prior to fineblanking by machining and are stress-relieved as described in funding period I. Two of the holes are used to position the semi-finished product relative to the die. The third hole is located in the

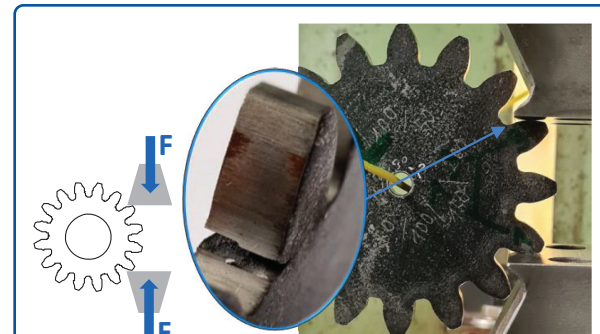


**Figure 17.8** Pulsator test of a module 4.5 mm gear.

center of the part after fineblanking and used as a centering for further examinations.

The tooth root bending strength was determined in a pulsating test rig (see figure 17.8) by a standardized test [17] and the rolling contact fatigue of the cutouts was determined under variation of sliding and lubrication conditions. Furthermore, the change of roughness and residual stresses for different load stages was investigated. This allows conclusions on the flank load-carrying capacity of gears manufactured by fineblanking.

The residual stress states of the variants were determined by x-ray diffraction and allow a quantification of the property improvement by residual stresses on an actual gear. Additionally, disturbances caused by the manufacturing process were taken into account.

### 17.4.2 Results II

For the fineblanked pinion ( $m_n = 4.5$  mm), it is shown in figure 17.10 that the compressive residual stresses increase in the axial direction with larger die radius  $r_M$ . Furthermore, the tooth root bending strength correlates with the height of the compressive residual stresses and the die edge radius as shown in figure 17.11. However, the cutting surface characteristics (see the exemplary figure 17.9) are not significantly influenced by the different die cutting edge radii. Likewise, no influence was measured in the hardening of the cutting surface, which

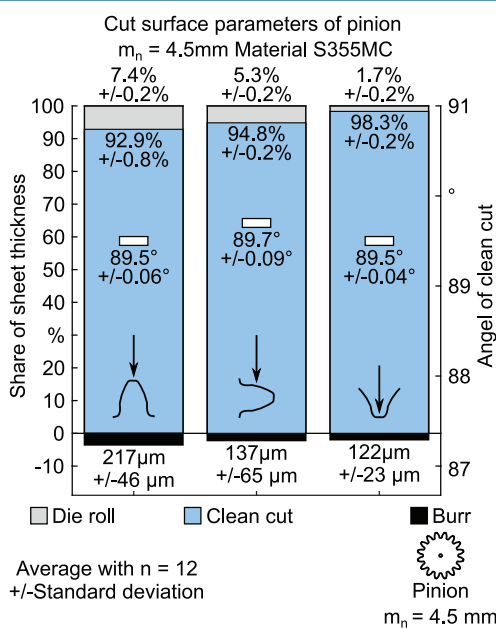


**Figure 17.9** Characteristics of the cutting surface at the measuring points tooth tip, tooth flank and tooth root of the pinion ( $m_n = 4.5 \text{ mm}$ ), fineblanked in the configuration  $r_S < 50 \mu\text{m}$ ,  $r_M = 200 \mu\text{m}$  and  $u_{rel} = 0.5 \%$ .

corresponds to about twice the base hardness of the material.

A quality class of  $Q = 4$  to  $7$  according to DIN ISO 1328 [18] was achieved for the fineblanked pinion ( $m_n = 4.5 \text{ mm}$ ). In addition, the pinions ( $m_n = 4.5 \text{ mm}$ ) correspond to grade  $Q = 6$  in the case of the pitch deviation. The fineblanked pinions are thus in the quality range of the milled and case-hardened pinions after grinding.

The determined tooth root bending strength for the four die edge radii variants is within  $\sigma_{Flim} = 318$  to  $327 \text{ N/mm}^2$  and thus significantly higher than specified in ISO 6336-5 [7] for this material (compare figure 17.18). Sample tests of variants manufactured with unfavorable process parameters such as lower counter punch force or without compressive residual stresses showed lower fatigue limits and lifetime. The results of the rolling contact fatigue tests show that contact pressures up to  $800 \text{ MPa}$  were endured within the tested load cycles (up to 2 million) without plastic deformation or pitting damage. The roughness decreases

within approximately 70,000 to 100,000 load cycles to  $Ra = 0.2 \mu\text{m}$ . Higher compressive residual stresses were found to result in higher rolling contact fatigue strength (pitting strength). However, the lubrication state and therefore the sliding condition has a major influence on the number of endured load cycles. Higher slippage of 50 % leads to earlier pitting failure than 3 % slippage.

Results of the funding period II are published in [19] and [20].

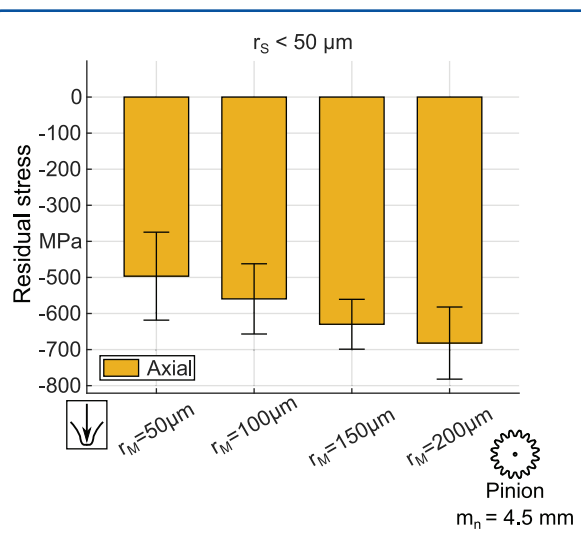


**Figure 17.10** Residual stresses for the different die cutting edge radii  $r_M$  [19].

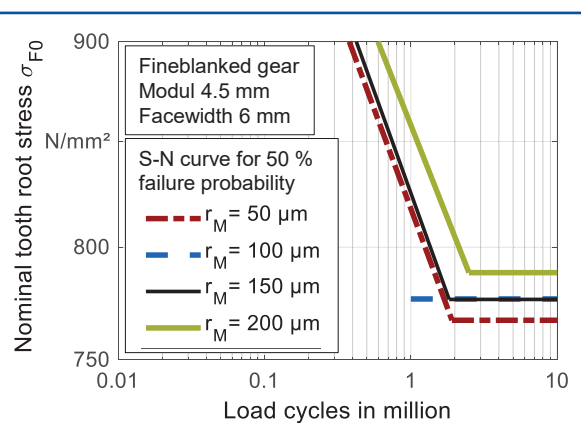


**Figure 17.11** S-N-curves for tooth root breakage of Modul 4.5 mm fineblanked pinion variants with  $r_M = 50 \mu\text{m}$  to  $200 \mu\text{m}$ .

## 17.5 Funding Period III – Application Oriented Pinion/Wheel Pair

The use of base materials with higher strength in combination with process-induced compressive residual stresses has considerable potential in terms of the targeted increase of the load-carrying capacity with regard to the fatigue failure modes pitting and tooth root breakage. This offers the potential to replace cost- and time-intensive heat treatment in the manufacturing of power-transmitting gears by increasing the fatigue strength by locally adapted residual stresses. In funding period III this potential is investigated on a fineblanked pinion/wheel pair made from the previously used reference material and a higher-strength steel. Fundamental relationships were systematically investigated with the models set up and validated by determining the tooth root bending strength in pulsator tests and the flank load-carrying capacity in gear running tests. The residual stress states of the different gear variants were measured both before and after the fatigue tests. This allows tracking of process improvements but also ensures the predictability of the property improvements and the stability of the residual stresses. Thus, these measurements were used to extend the existing residual stress simulation model. By using a higher strength steel material, it was shown that further improvements can be achieved in terms of tooth root bending strength and pitting strength through process-induced residual stresses. Both experimental and numerical investigations were carried out for this purpose. In addition, the prediction of the respective load-carrying capacity for the reference material and the higher strength material was evaluated and improved. By integrating the results into the bidirectional model from funding period II, it was possible to design and manufacture shear blanked gears of different materials and geometries with increased load-carrying capacity by utilizing the positive effect of shear cutting process-induced residual stresses. The focus of the project is the design, layout and optimization of the NNSB processes with regard to an improved residual stress state for higher tooth bending strength and pitting strength,

ensuring the predictability of the property improvements caused by residual stresses, and demonstrating residual stress stability in gear running tests under real operating conditions.

### 17.5.1 Experimental Setup and Test Equipment III

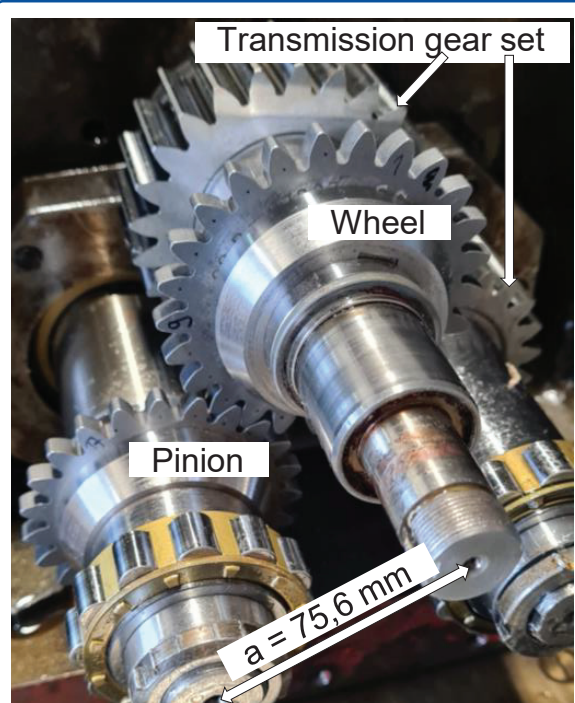


**Figure 17.12** Fineblanked gears in a back-to-back test rig.

Two new sets of active elements were manufactured for the production of the pinion/wheel pair. The basis for this was a selected pinion/wheel geometry with 23 and 25 teeth with a normal module of  $m_n = 3 \text{ mm}$ , which according to [21] corresponds to a degree of difficulty of S<sub>2</sub> for fineblanking. The tip diameters of this pinion/wheel pair were 78.3 mm and 84.5 mm. The geometries of the v-ring were adapted from the pinion ( $m_n = 4.5 \text{ mm}$ ) of funding period II to the increased tip circle diameters. The v-ring on blank holder of the pinion was omitted on the basis of the investigations in funding period I. The v-ring geometry was adapted to the increased tip circle diameters. On the active elements for the wheel, a v-ring was included on the blank holder as well as the die. The punch cutting edges were left in an nearly sharp-edged

condition and rounded only at the tooth tips with  $r_S < 50 \mu\text{m}$ . For the die cutting edges, fillets of  $r_M = 350 \mu\text{m}$  were applied mechanically by brushing. Since pinions and wheels were to be fineblanched from the materials S355MC and S500MC, the cutting tool material SII-2-5-8 (PM) was selected for the punches and dies. For the other active elements, the cold-work tool steel X155CrVMo12-1 was used. The adjustable process forces were set as shown in table 17.2.

**Table 17.2** Process parameters for fineblanking of pinion and wheel

Process parameter	S355MC	S500MC
<b>Pinion</b>		
$u_{rel}$	0.5 %	0.5 %
$r_M$	< 50 $\mu\text{m}$	< 50 $\mu\text{m}$
$r_S$	350 $\mu\text{m}$	350 $\mu\text{m}$
$F_{VR}$	583 kN	742 kN
$F_{CP}$	283 kN	283 kN
$v_B$	50 mm/s	50 mm/s
<b>Wheel</b>		
$u_{rel}$	0.5 %	0.5 %
$r_M$	< 50 $\mu\text{m}$	< 50 $\mu\text{m}$
$r_S$	350 $\mu\text{m}$	350 $\mu\text{m}$
$F_{VR}$	625 kN	796 kN
$F_{CP}$	331 kN	331 kN
$v_B$	50 mm/s	50 mm/s

As in funding period II, the semi-finished products were stress-relief annealed and unit-bored following DIN EN ISO 286-1 [22] prior to fineblanking. In addition to the manufactured samples consisting of pinions and wheels, a stress-relief annealed variant of the fineblanched pinions made of S500MC (named: S500MC GG) was investigated.

In addition to further tooth root bending tests with the pinions in a pulsating test rig, the flank load-carrying capacity was investigated in gear running tests. The pinions and wheels were investigated regarding cutting surface characteristics, hardness,

residual stresses, flank roughness and gear quality.

The standardized flank load-carrying (pitting) tests [17] up to 50 million load cycles were performed in a back-to-back test rig with a center distance of 75.6 mm as shown in figure 17.12. The tests were performed at a rotational speed of 3,000/min with dip lubrication at 60 °C oil temperature. Every 3 million load cycles the gears were visually inspected for the evaluation of flank damages. For all tests a running in procedure for 70000 load cycles is performed at 90 °C oil temperature with a rotational speed of 1,500/min.

### 17.5.2 Results III

The resulting cutting surface characteristics for the pinion made of the materials S355MC and S500MC are shown in figure 17.13 and are very similar to those of the wheels. The cutting surface characteristics at the three measuring points (tooth tip, tooth flank and tooth root) show a dependence on the cutting line geometry. The comparatively high die roll at the exposed points of the cutting line, the tooth tips, reduces the clean cut percentage. However, this is insignificant because the tooth tips are not in the gear contact. At the tooth flank measuring point, significantly lower die rolls were achieved and consequently higher clean cut percentages and contact ratios. Directly in the tooth root rounding very high clean cut percentages of over 99 % of the sheet thickness were achieved. No cracks or fractures were detected at the three different measuring points. However, cracks were present on the wheels at the tip edges of the cutting line close to the die roll. In addition, small isolated fracture areas were detected on the tooth flank near the tooth root area. The largest fracture height, which was found for all the wheels and pinions of both materials examined, was 530  $\mu\text{m}$ . The clean cut angles, especially at the tooth flank measuring point, were very close to the ideal value of 90°. The high burr heights at the tooth tip were striking compared to the other measuring points. One reason for this could be the cutting edge radius of  $r_S < 50 \mu\text{m}$  in the area of the tooth tips at the cutting punch.

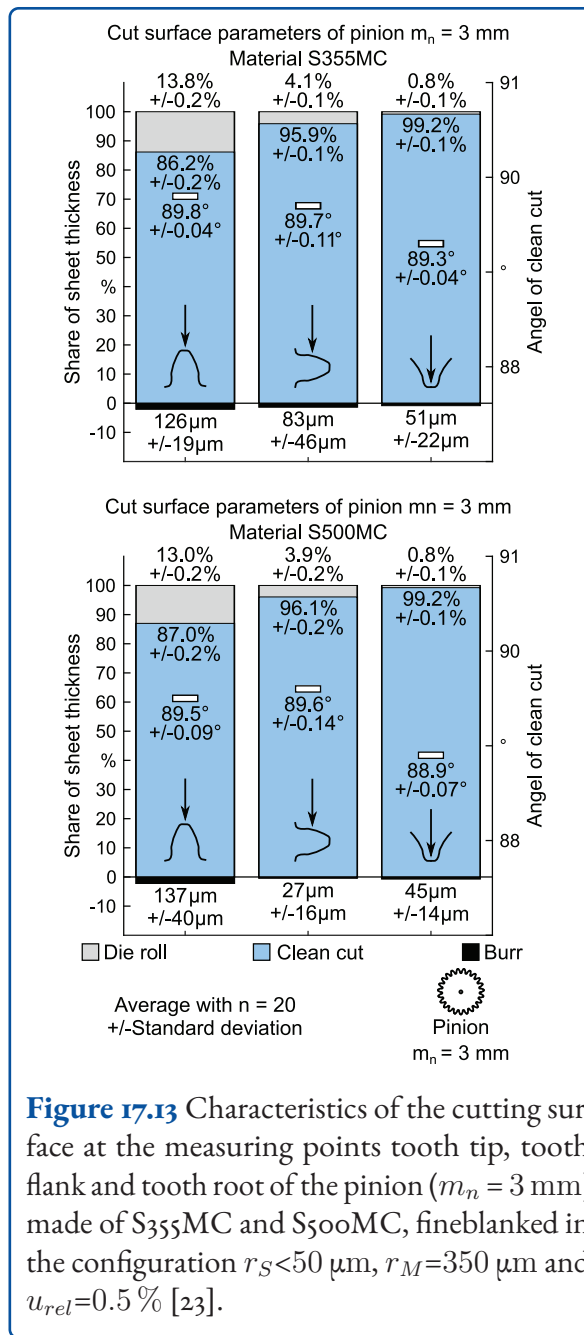


**Figure 17.13** Characteristics of the cutting surface at the measuring points tooth tip, tooth flank and tooth root of the pinion ( $m_n = 3 \text{ mm}$ ) made of S355MC and S500MC, fineblanked in the configuration  $r_S < 50 \mu\text{m}$ ,  $r_M = 350 \mu\text{m}$  and  $u_{rel} = 0.5 \%$  [23].

The radius represents a volume filled when the punches enter and move material for burr formation toward the end of the process [3]. The center hole is enlarged by fineblanking producing the keyway for torque transmission. Various methods were investigated for boring, while using a boring head showing the highest accuracy with regard to centering the hole.

For the pitch variations or the adjacent pitch error a quality of  $Q = 5$  according to DIN ISO 1328

[18] were achieved. The flank trace and profile trace related qualities were usually in the range of  $Q = 5$  to 10. In summary, the quality grade of the fineblanked gears was in the range of milled and case-hardened gears after grinding of the gear.

The flank roughness of the variants before the tests is shown in figure 17.15.

A common roughness distribution of the right and left sides can be seen with values within  $R_a = 0.6 \mu\text{m}$  to  $1.6 \mu\text{m}$ . Noticeable here is the larger roughness of the wheels but especially the larger roughness for the variants made of S500MC. After the running in procedure the flank roughness usually decreases to  $R_a = 0.1 \mu\text{m}$ . The first pretests of a fineblanked gearing in a running test rig showed that the heat development is significantly higher than with the usually used ground gears that have significantly lower surface roughness. A cooling system was installed to maintain a  $60^\circ\text{C}$  oil temperature. Another noticeable characteristic of the fineblanked gears is the significantly lower noise emission of the spur gears. In addition, the first pretests showed that the method for manufacturing of the center hole after the fineblanking of the gears is crucial. First test runs showed plastic deformations at the flanks and considerably higher wear that is caused by an imprecise positioning of the borehole. For further tests only gears with lower runout deviation were used and in addition oil with higher wear resistance with a viscosity index of VI 320 was used for lubrication.

The first test results are shown in figure 17.16. For the gears made of S355MC the failure criterion was reached at 27 million load cycles at a nominal contact stress of  $\sigma_{H0} = 500 \text{ N/mm}^2$ . For the gears made of S500MC the failure criterion was not met for the first two test runs with up to  $\sigma_{H0} = 550 \text{ N/mm}^2$  although these have a significantly higher flank roughness. However, pitting strength is expected to be in this area but further tests are being currently carried out for a more accurate evaluation and the determination of the strength number  $\sigma_{Hlim}$  for the two material variants.

In figure 17.17 the S-N curves for 50 % failure probability regarding tooth root breakage of the

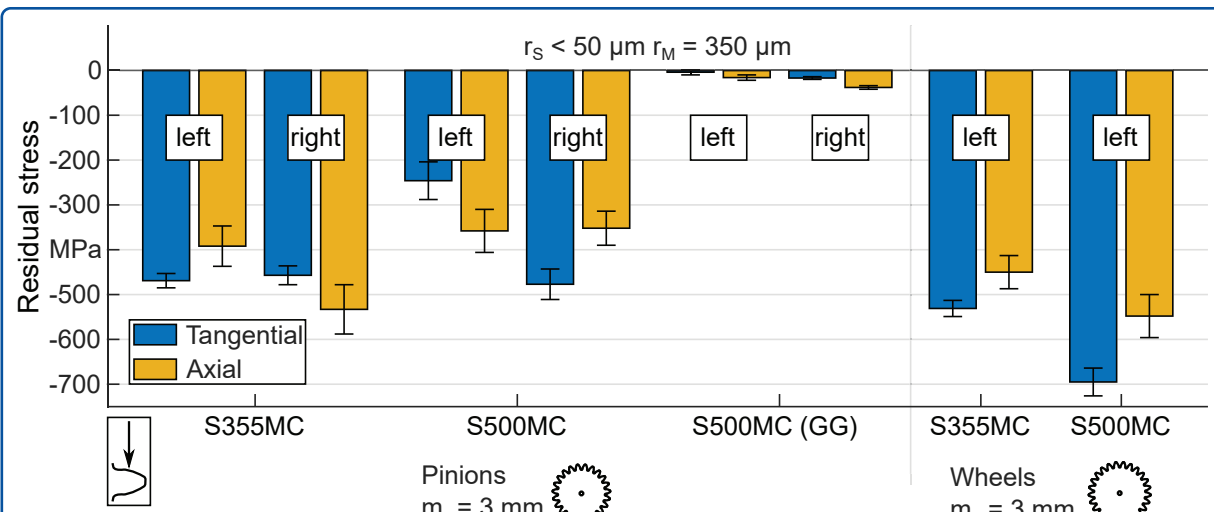


**Figure 17.14** Results of surface residual stress measurements at the right and left tooth flank [23].

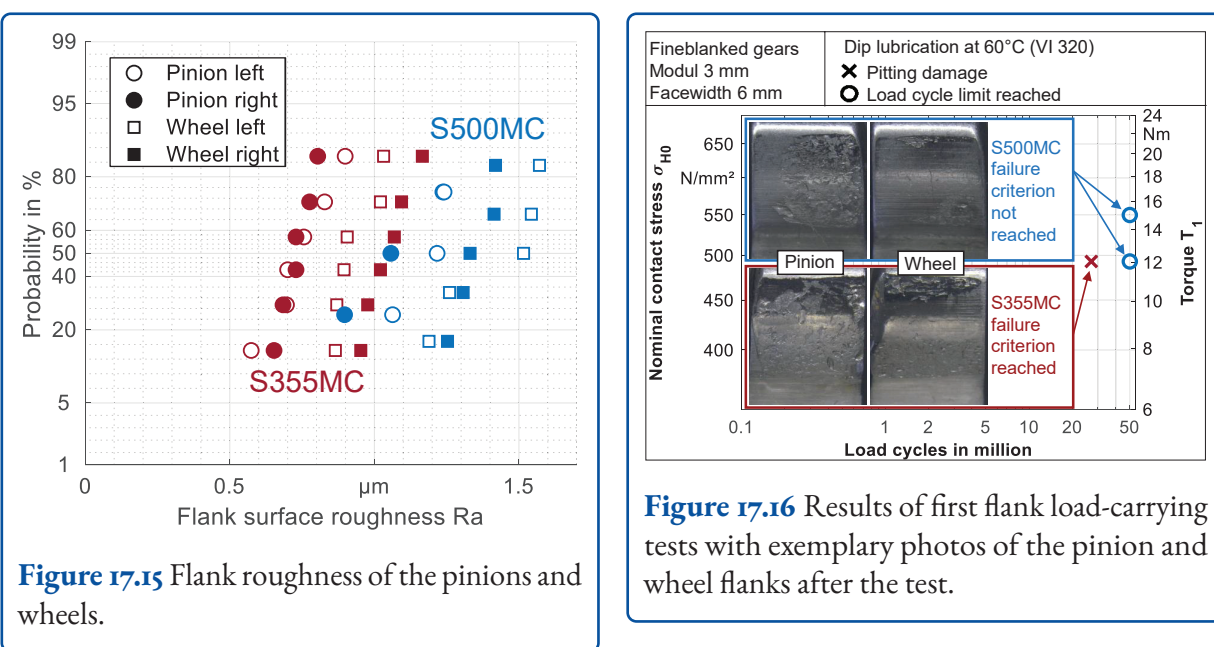


**Figure 17.15** Flank roughness of the pinions and wheels.

fineblanked module 3 mm pinions are shown. A noticeable characteristic here is a material-dependent slope of the S-N curve in the area of the limited lifetime with comparable static strength. It can also be seen that compressive residual stresses shift the failures toward a higher number of load cycles.

The gears of the stress-relieved variant S500MC GG show the lowest endurance strength with a nominal tooth root stress of  $\sigma_{F0} = 792 \text{ N/mm}^2$  whereas the variant of S500MC with process-induced resid-

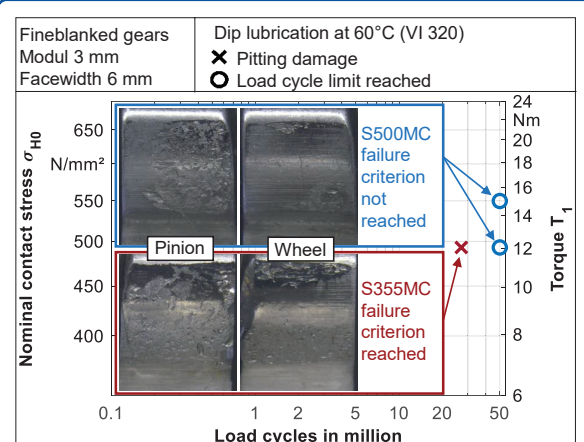


**Figure 17.16** Results of first flank load-carrying tests with exemplary photos of the pinion and wheel flanks after the test.

ual stresses results in  $\sigma_{F0} = 1,030 \text{ N/mm}^2$  despite lower residual stresses (compare figure 17.14) than the S355MC pinions with an endurance strength of  $\sigma_{F0} = 877 \text{ N/mm}^2$ . In figure 17.18 all tested fineblanked gear variants of the three funding periods are entered in the tooth root bending strength diagram of ISO 6336-5 [7]. Due to the increased hardness and higher compressive residual stresses in the tooth root, the tooth root bending strength of these fineblanked gears is multiple times higher than specified in ISO 6336-5 for this material.

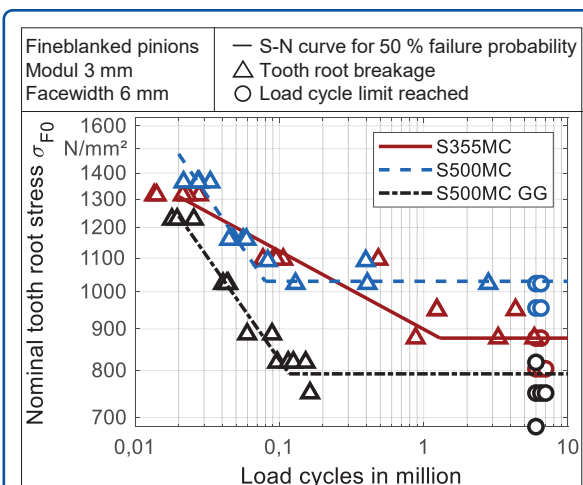


**Figure 17.17** S-N-curves for tooth root breakage of module 3 mm fineblanked gear variants (materials: S355MC and S500MC; GG = stress-relieved).

The test results with the stress-relieved variant S500MC GG also show the influence of the compressive residual stresses on the tooth root bending strength.

When the hardness doubles, the tooth root bending strength also approximately doubles, provided that compressive residual stresses with a correspondingly higher influence on the tooth root bending strength are present. Without residual stresses present, the strength increases by a factor of approximately 1.7 when the hardness is doubled.

## 17.6 Conclusion and Outlook

In this research project, which consists of three funding periods, it was possible to fineblank power-transmitting gears with high process-induced compressive residual stresses. The main results are:

- With NNSB processes cutting surfaces usable as functional surfaces can be manufactured cost and energy efficient.
- All NNSB processes lead to an increased hardness at the cutting surface with comparable hardness value and depth profile.

- Depending on the NNSB process and NNSB parameter selection, different residual stress states on the cutting surface are possible. High compressive residual stresses can be achieved by a suitable selection.
- The residual stresses for fineblanking are comparable on the entire cutting surface independent of the cutting line and are stable within the investigations performed.
- For fineblanking a larger die edge radius leads to higher compressive residual stresses at the cutting surface and higher fatigue strength.
- For higher strength steels higher compressive residual stresses up to  $-700$  MPa and higher tooth root bending strength numbers are achieved with up to  $\sigma_{Flim} = 418$  N/mm<sup>2</sup>.
- The tooth root bending strength numbers for the investigated fineblanked gears are comparable to case carburized gears and are significantly higher than for plastic gears, which are at the same manufacturing cost level.
- In gear running tests the fineblanked gearing shows significantly lower noise emissions compared to case carburized ground spur gears.
- The flank roughness of the fineblanked gears is comparably high and does lead to increased heat and probably lower pitting strength compared to conventionally manufactured gears.

In this research project, the determination of the pitting strength and the investigation of the influence of the residual stresses on the pitting strength is currently ongoing.

In a follow-up research project, the fineblanking process is to be made capable of providing fineblanked gears for use in the industrial environment. To this end, knowledge will be transferred to industrial applications on the basis of the findings obtained in collaboration with industrial partners from the fields of fineblanking technology and drive technology. The focus here is on the requirements of the application, such as the low noise and vibration excitation of long-life gears as well as process reliability combined with very economical production. In the future, these challenges will have to be met by analyzing product and process variables and the resulting control variables. Special atten-

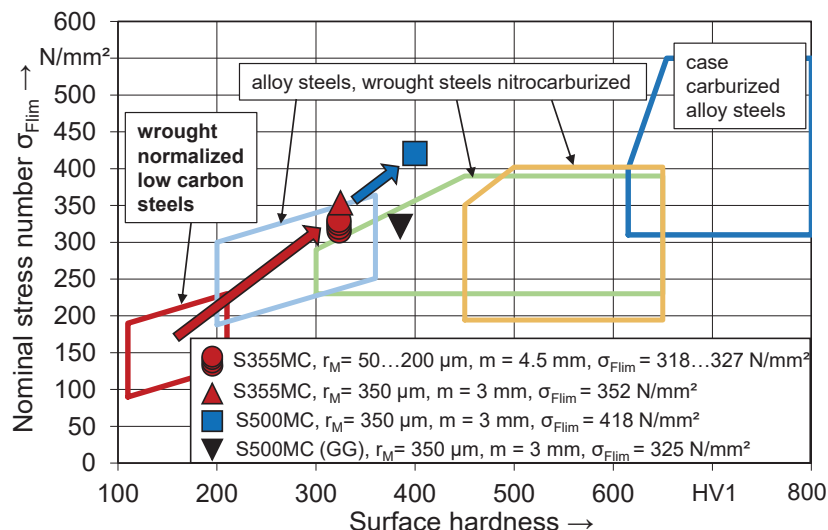


**Figure 17.18** Tooth root bending strength of the fineblanked gears compared to the specifications in ISO 6336-5.

tion must also be paid to the advancing development of materials in order to seize further opportunities for increasing the performance of fineblanked components. It is also important to take advantage of new opportunities that will arise in the future in the area of process simulation with regard to virtual testing and component property prediction. Compared with conventional gear manufacturing, fineblanking of power-transmitting gears offers enormous potential in terms of reduced production times, cost and energy savings, and a reduction in CO<sub>2</sub> emissions.

## Abbreviations

DIN	German institute for standardization
e.g.	exempli gratia
EN	European standard
FEM	Finite elements method
GG	stress relieved variant
ISO	International Organization for Standardization
NNSB	Near-net-shape blanking
PM	Powder metallurgy produced
Q	quality class according to DIN ISO 1328
VI	Viscosity Index

$F_B$	Blanking force
$F_{BH}$	Blank holder force
$F_{CP}$	Counter punch force
$F_{VR}$	V-ring force
$m_n$	normal module
$r_M$	Die cutting edge radius
$r_S$	Punch cutting edge radius
$p_H$	Contact pressure according to Hertz
$R_a$	Roughness (arithmetical mean height)
$s$	Sheet thickness
$u_{rel}$	Relative die clearance
$v_B$	Cutting speed
$\sigma_{F\text{lim}}$	nominal stress number (bending)
$\sigma_{F0}$	nominal tooth root stress
$\sigma_{H\text{lim}}$	allowable stress number (contact)
$\sigma_{H0}$	nominal contact stress

## References

- [1] VDI 2906 Blatt 5. *Schnittflächenqualität beim Schneiden, Brechen und Lösen von Werkstücken aus Metall Feinschneiden*. Berlin: Beuth Verlag, 2013.
- [2] Florian Hörmann. "Einfluss der Prozessparameter auf einstufige Scherschneidverfahren zum Ausschneiden mit endkonturnaher Form". Disser-

- tation. München: Technische Universität München, 2008.
- [3] Peter Demmel et al. "Zerteilen". In: *Handbuch Umformen*. Ed. by Hartmut Hoffmann, Reimund Neugebauer, and Günter Spur. Edition Handbuch der Fertigungstechnik / hrsg. von Günter Spur. München: Hanser, 2012, pp. 679–729. ISBN: 3446427783.
- [4] Jens-Michael Stahl. "Residual stresses induced by shear cutting: Targeted use for manufacturing functional surfaces with an improved fatigue behavior". Dissertation. München: Technische Universität München, 2021.
- [5] ISO 6336-2. *Calculation of load capacity of spur and helical gears: Calculation of Surface Durability (Pitting)*. 2019.
- [6] ISO 6336-3. *Calculation of load capacity of spur and helical gears: Calculation of tooth bending strength*. 2019.
- [7] ISO 6336-5. *Calculation of load capacity of spur and helical gears: Strength and quality of materials*. 2016.
- [8] Christian Guntner, Thomas Tobie, and Karsten Stahl. "Influences of the residual stress condition on the load carrying capacity of case hardened gears". In: *AGMA 2017 Fall Technical Meeting* (2017).
- [9] Gustav Niemann and Heinz Rettig. "Untersuchungen an Blechzahnradern". In: *Mitteilungen der Forschungsgesellschaft Blechverarbeitung e. V.* Nr. 17 (1956).
- [10] DIN EN 10149-1. *Warmgewalzte Flacherzeugnisse aus Stählen mit hoher Streckgrenze zum Kaltumformen – Teil 1: Allgemeine technische Lieferbedingungen*. 2013.
- [11] Jens Stahl et al. "Residual stresses in parts manufactured by near-net-shape-blanking". In: *Production Engineering* 23.3 (2019), p. 217. ISSN: 0944-6524. DOI: 10.1007/s11740-018-0865-5.
- [12] Jens Stahl et al. "The Influence of Residual Stresses Induced by Near-Net-Shape Blanking Processes on the Fatigue Behavior under Bending Loads". In: *IDDRG 2019* (2019). DOI: 10.1088/1757-899X/651/1/012086.
- [13] Daniel Müller et al. "Influence of Shear Cutting Process Parameters on the Residual Stress State and the Fatigue Strength of Gears". In: *Forming the Future* (2021). DOI: 10.1007/978-3-030-75381-8\_195.
- [14] Anian Nürnberger et al. "Comparative study of v-ring indenter configurations in fineblanking in order to derive tool design guidelines". In: *The International Journal of Advanced Manufacturing Technology* 123.11-12 (2022), pp. 4171–4179. ISSN: 0268-3768. DOI: 10.1007/s00170-022-10345-6.
- [15] Fritz Klocke. "Blechtrennung". In: *Fertigungsverfahren 4: Umformen*. Berlin, Heidelberg: Springer Berlin Heidelberg, 2017. DOI: 10.1007/978-3-662-54714-4.
- [16] Rolf-A. Schmidt. *Umformen und Feinschneiden*. 1. Aufl. Carl Hanser Fachbuchverlag, 2006. ISBN: 3446409645. DOI: 10.3139/9783446411050.
- [17] Thomas Tobie and Peter Matt. "FVA Directive 563 I: Standardisation of Load Capacity Tests". In: *FVA Guideline* (2012).
- [18] DIN ISO 1328. *Cylindrical gears - ISO system of flank tolerance classification*. 2018.
- [19] Daniel Müller et al. "Shear Cutting Induced Residual Stresses in Involute Gears and Resulting Tooth Root Bending Strength of a Fineblanked Gear". In: *Archive of Applied Mechanics* (2021). DOI: 10.1007/s00419-021-01915-3.
- [20] Daniel Müller et al. "Einfluss von prozessinduzierten Eigenspannungen auf die Zahndurchschlagsfestigkeit schergeschnittener Zahnräder". In: *Forschung im Ingenieurwesen* (2021). DOI: 10.1007/s10010-021-00511-9.
- [21] Franz Birzer. *Feinschneiden und Umformen: Wirtschaftliche Fertigung von Präzisionsteilen aus Blech*. 3., vollst. überarb. Aufl. Vol. Bd. 134. Die Bibliothek der Technik. Landsberg: Verl. Moderne Industrie, 2014. ISBN: 978-3-86236-068-0.
- [22] DIN EN ISO 286-1. *Geometrical product specifications (GPS) - ISO code system for tolerances on linear sizes - Part 1: Basis of tolerances, deviations and fits*. 2019.

[23] Anian Nürnberger et al. "Advantages in the production of power transmitting gears by fineblanking". In: *The International Journal of Advanced Manufacturing Technology* (2023). DOI: <https://doi.org/10.1007/s00170-023-12160-z>.

## 18 Summary and Outlook

Nürnberg, A.; Gilch, I.; Prauser, S.; Volk, W.

The research within the DFG Priority Program 2013 focused on the utilization of residual stresses in forming processes. Conventionally, residual stresses are avoided in the production of metallic components. Residual stresses are problematic in manufacturing metallic components because – if not explicitly adjusted – they can reduce component service life. However, targeted use of residual stresses can enhance the lifetime of components, reduce warpage or allow new component design.

### 18.1 Summary

The Priority Program 2013 was organized in three phases, which ensured a structured approach (see figure 18.1). In Phase 1 **Validation**, the general research idea of the respective projects was validated. The aim was to induce residual stresses in the components in a reproducible and controllable manner. Measurement methods for analyzing the residual stresses were tested for the applied material and components. Initial simulations for determining the residual stress distributions were set up.

The subsequent Phase 2 **Quantification** evaluated the process and material disturbance variables to adjust the residual stresses. In addition, process and component improvements were validated and the approaches for measuring and numerically determining residual stresses were further improved.

Finally, in Phase 3 **Optimization** took place. The improved properties were quantified, and their stability was considered under service boundary conditions. The process for the targeted induction of residual stresses was designed, structured, and optimized.

In the following, the processes considered are briefly presented, and the component properties

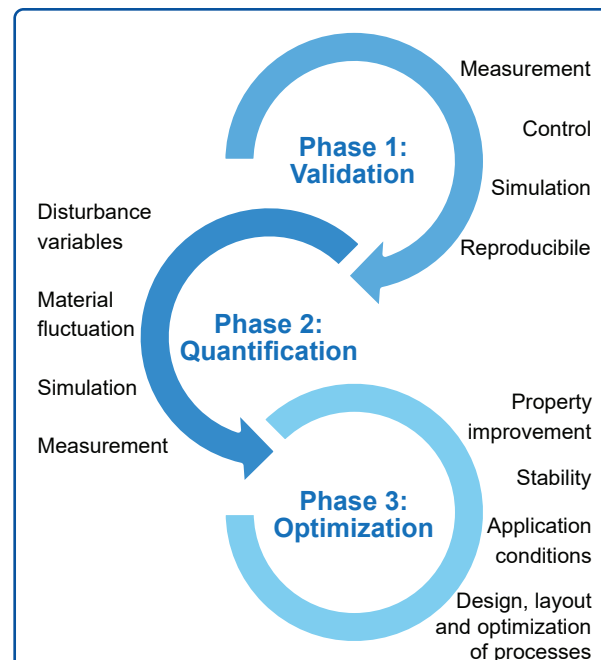
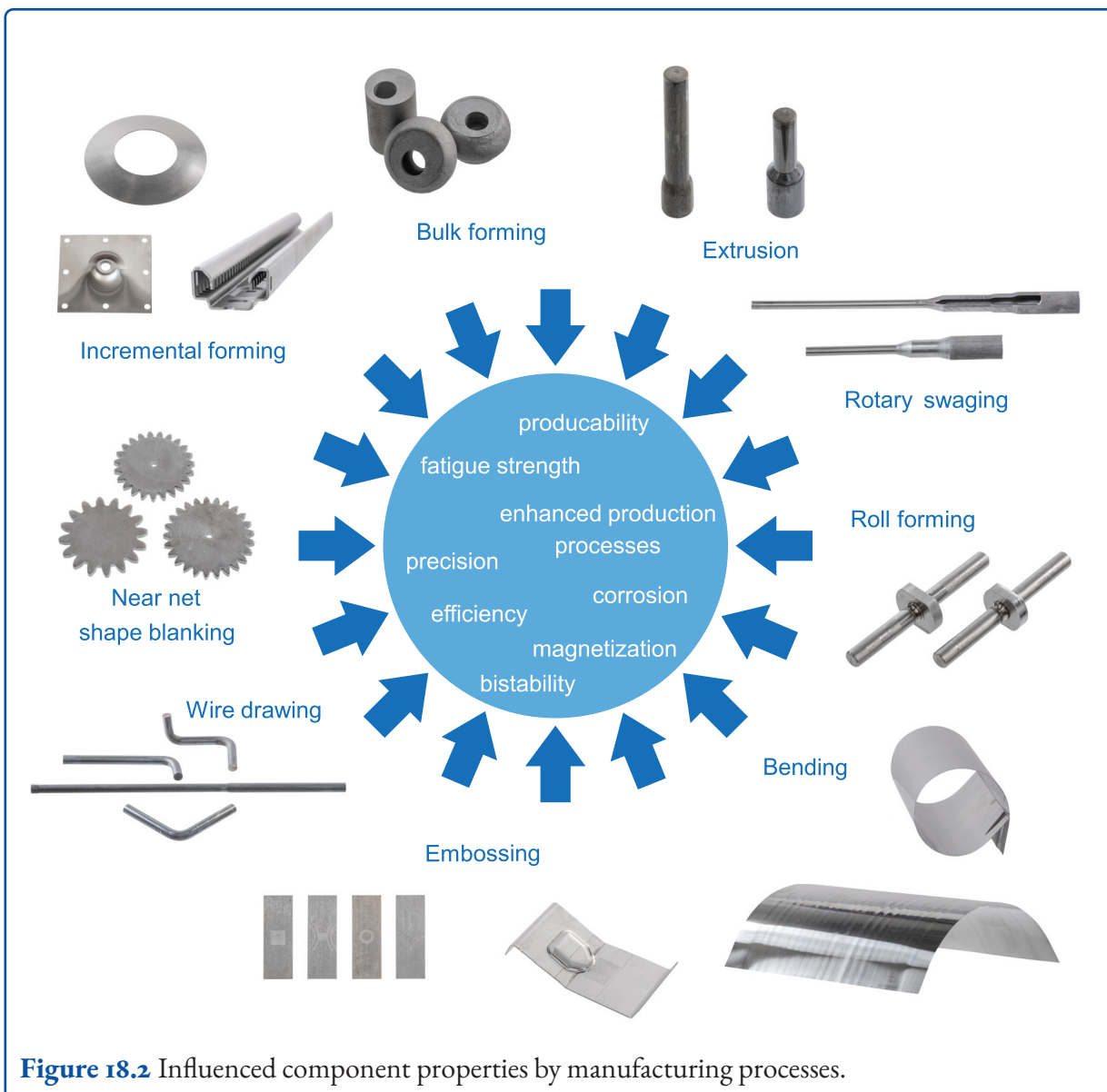


**Figure 18.1** Phases of DFG Priority Program 2013.

improved by residual stresses are listed. Visually, this is summarized together with the fabricated components in figure 18.2.

**Incremental sheet forming** was used to induce compressive residual stresses in the surface layer of disc springs so that service life was significantly increased. This sheet metal forming process was also used to adjust the residual stress state in exemplary specimen geometries so that the design strength and the vibration crack corrosion were improved.

**Embossing** can induce residual stresses in metallic components close to the surface. For example, fatigue strength can be increased, and new lightweight design potentials are created. If residual stresses are induced by embossing in electrical steel, which forms the magnetic core of electrical machines, the magnetic properties of the sheet material are locally degraded. This makes it possible to



achieve targeted magnetic flux control and increase the maximum speed and, thus, the energy density of electric drives.

The bistability of sheet metal is achieved by targeted **rolling** and **incremental bending**. Thus, the volume is greatly reduced when transporting thin-walled tubes.

High tensile residual stresses typically occur on the component surface during **wire drawing**. These are reduced by targeted process control, thus cost-intensive post-processing, such as heat treatment and shot peening, can be avoided.

During **cross-rolling**, the residual stresses of shaft components can also be adjusted. This increases fatigue strength, and at the same time, the connection properties of the shaft and hub is improved.

During **extrusion** and **rotary swaging**, residual stresses are specifically adjusted close to the surface. This reduces the need for downstream processes such as heat treatment, shot peening, and deep rolling, increasing flexural fatigue strength and corrosion resistance and reducing component distortion.

High compressive stresses were induced in the functional surface of fineblanched gears through adapted

**near-net-shape blanking** parameters. This optimized the fatigue strength and the process. In addition, less expensive materials can be used and heat treatment is no longer necessary.

In **bulk forming**, residual stresses can be controlled locally by a targeted cooling process, significantly reducing the probability of cracking under an oscillating load.

In summary, 12 research projects investigated ten different forming processes to improve industrially-relevant components by forming-induced residual stresses.

Four expert groups supported the collaboration on cross-cutting issues. The different production processes were grouped in **Thin-Walled Product Forming** and **Bulk Forming**. The expert group **Simulation and Modeling** compared the different methods to improve the numerical skills. The fourth expert group **Residual Stress Analysis** focussed on the comparison and improvement of the measurement methods used. (Chapter 2–5.)

## 18.2 Outlook

The results obtained in the Priority Program 2013 open up new ways of improving components produced by forming technology to a far-reaching extent. The warpage and manufacturing accuracy of components produced are often accompanied by process-induced residual stresses. The in-depth knowledge gained in the Priority Program makes it possible to produce components with even tighter tolerances or to further minimize the distortion caused by the manufacturing process. Targeted residual stress profiles, which were the subject of intensive research in the Priority Program, bring about significant increases in static component strength and dynamic load capacity in particular. From small structural elements such as screws or springs to bearing rings and gears to highly loaded shafts, the targeted adjustment of component properties has enormous potential with respect to component service life and the load spectrum. Furthermore, component safety can also be increased for

failure-critical components using suitable residual stress profiles. Applying the results to components also breaks new ground regarding weight and material savings. In addition, there is also the opportunity to exploit deliberately induced load-compliant residual stresses to produce components at lower cost. Moreover, forming-induced residual stresses open up new possibilities regarding design freedom, especially for sheet metal components. In addition, the knowledge gained can influence press-fits to produce hybrid components from different materials, which would otherwise be difficult or impossible to achieve. There is also the option of completely rethinking components and the benefits, for example, from the influence of residual stresses in electrical steel.

Increasingly powerful numerical methods will play an important role in the future for the residual stress design of components produced by forming technology to obtain a reliable property prediction efficiently even before the first prototypes are produced. Developing materials that support and improve the induction of residual stresses conducive to component properties would further exploit the unused potential of components produced by forming technology.

Better understood forming-induced residual stresses also promise numerous improvements and savings in manufacturing processes. It may be sufficient to slightly adapt or extend individual processes or process parameters to take advantage of an adapted residual stress design. However, it is also conceivable that individual process steps along a process chain can be eliminated, for example complex downstream processes for residual stress reduction or residual stress induction. Furthermore, it is also possible to completely substitute previous manufacturing processes or achieve savings by combining several manufacturing steps into one. The improvement with minimal effort or the achievement of leaner production processes through controlled management of residual stresses in the component and the associated production processes holds enormous savings potential in production times, material usage, and cost minimization. By reducing energy-intensive component treatments, resources can be conserved

to a considerable extent, and consequently CO<sub>2</sub> emissions can be reduced.

A better understanding of the active use of process-induced residual stresses, as developed in the Priority Program, also helps to make the products and processes more sustainable and is an important step toward green forming technology.

A transfer to industrial production is required to take advantage of the opportunities and potentials (see figure 18.3). The challenges here are transferring the findings to other materials and workpiece types against the background of series production, in some cases with large quantities. Furthermore, it is essential to apply the knowledge acquired in the Priority Program in a targeted manner and link it with expertise from industrial practice to ensure high reproducibility. Attention must also be paid to process integration and the interaction of the novel processes with those already in place. For quality control of component and process monitoring, the extensive investigations and newly developed methods from the Priority Program can also be consulted, adapted, and further developed for individual requirements. The transfer of knowledge to industry and the development of practicable solutions based on the results of the Priority Program will also be accompanied and driven forward by subprojects from the Priority Program in the form of DFG knowledge transfer projects.

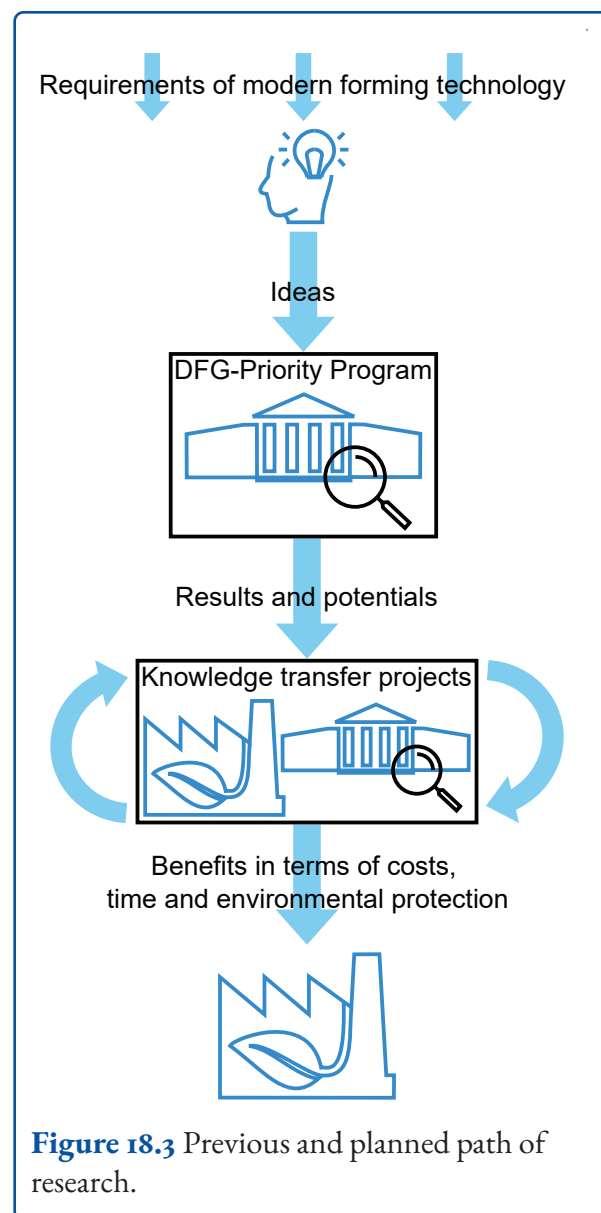


**Figure 18.3** Previous and planned path of research.

## List of Authors

Muhammad Junaid **Afzal**, M. Sc., Chair of Mechanical Design and Manufacturing, Brandenburg University of Technology Cottbus - Senftenberg

Nikolas **Baak**, M. Sc., Department of Materials Test Engineering, TU Dortmund University

Markus **Baumann**, M. Sc., Institut for Machine Tools and Production Processes, University of Techonolgy Chemnitz

Prof. Dr.-Ing. Bernd-Arno **Behrens**, Institute of Forming Technology and Machines, Leibniz Universität Hannover

Tim **Bergelt**, M. Sc., Institute of Materials Science and Engineering, University of Technology Chemnitz

Dr.-Ing. Markus **Bergmann**, Solid Forming Department, IWU Fraunhofer-Institute for Machine Tools and Forming Technology

Lempoi Isedore **Besong**, M. Sc., Chair of Mechanical Design and Manufacturing, Brandenburg University of Technology Cottbus - Senftenberg

Prof. Dr.-Ing. Thomas **Böhlke**, Chair of Continuum Mechanics, Institute of Engineering Mechanics, KIT Karlsruhe Institute of Technology

Dr.-Ing. Dominik **Brands**, Institute of Mechanics, Faculty of Engineering, University Duisburg-Essen

Prof. Dr.-Ing. Alexander **Brosius**, Chair of Forming and Machining Processes, TUD Dresden University of Technology

Dr.-Ing. Johannes **Buhl**, Chair of Mechanical Design and Manufacturing, Brandenburg University of Technology Cottbus - Senftenberg

Dhia **Charni**, M. Sc., Leibniz Institute for Materials Oriented Technologies - IWT

Dr.-Ing. Jérémie **Epp**, Leibniz Institute for Materials Oriented Technologies - IWT

Dr.-Ing. Hannes **Erdle**, Chair of Continuum Mechanics, Institute of Engineering Mechanics, KIT Karlsruhe Institute of Technology

Dr.-Ing. Alessandro **Franceschi**, Institute for Production Engineering and Forming Machines, Technical University Darmstadt

Dr.-Ing. Jens **Gibmeier**, Institute of Applied Materials, KIT Karlsruhe Institute of Technology

Ines **Gilch**, M. Sc., Chair of Metal Forming and Casting, TUM School of Engineering and Design, Technical University of Munich

Prof. Dr.-Ing. Peter **Groche**, Institute for Production Engineering and Forming Machines, Technical University Darmstadt

Dipl.-Ing. Christina **Guilleaume**, Chair of Forming and Machining Processes, TUD Dresden University of Technology

Marlon **Hahn**, M. Sc., Institute of Forming Technology and Lightweight Components, TU Dortmund University

Ramin **Hajavifard**, M. Sc., Department of Materials Test Engineering, TU Dortmund University

Prof. Dr.-Ing. Kay **Hameyer**, Institute of Electrical Machines, RWTH Aachen University

Dr.-Ing. Christoph **Hartmann**, Chair of Metal Forming and Casting, TUM School of Engineering and Design, Technical University of Munich

Pascal **Heinzemann**, M. Sc., Institute for Metal Forming Technology, University of Stuttgart

Dr.-Ing. Sonja **Hellebrand**, Institute of Mechanics, Faculty of Engineering, University Duisburg-Essen

Prof. Dr.-Ing. Gerhard **Hirt**, Institute of Metal Forming, RWTH Aachen University

Dr.-Ing. Holger **Hoche**, Center for Structural Materials, Technical University Darmstadt

Katja **Holzer**, M. Sc., Chair of Metal Forming and Casting, TUM School of Engineering and Design, Technical University of Munich

Fabian **Jäger**, M. Sc., Center for Structural Materials, Technical University Darmstadt

Andreas **Jobst**, M. Sc., Institute of Manufacturing Technology, Friedrich-Alexander-Universität Erlangen-Nürnberg

Dipl.-Ing. Martha **Kalina**, Chair of Computational and Experimental Solid Mechanics, TUD Dresden University of Technology

Prof. Dr.-Ing. Markus **Kästner**, Chair of Computational and Experimental Solid Mechanics, TUD Dresden University of Technology

Christoph **Kock**, M. Sc., Institute of Forming Technology and Machines, Leibniz Universität Hannover

Maximilian **Krause**, M. Sc., Chair of Continuum Mechanics, Institute of Engineering Mechanics, KIT Karlsruhe Institute of Technology

Prof. Dr.-Ing. Verena **Kräusel**, Institut for Machine Tools and Production Processes, University of Techonolgy Chemnitz

Dr.-Ing. Bernd **Kuhfuss**, Center for Materials and Processes - MAPEX, Bremen Institute for Mechanical Engineering, University of Bremen

Dipl.-Ing. David **Kühne**, Chair of Computational and Experimental Solid Mechanics, TUD Dresden University of Technology

Prof. Dr.-Ing. Thomas **Lampke**, Institute of Materials Science and Engineering, University of Technology Chemnitz

Dr.-Ing. Lasse **Langstädtler**, Center for Materials and Processes - MAPEX, Bremen Institute for Mechanical Engineering, University of Bremen

Jose **Lara**, M. Sc., Institute of Applied Mechanics, Friedrich-Alexander-Universität Erlangen-Nürnberg

Junior Prof. Dr.-Ing. Nora **Leuning**, Institute of Electrical Machines, RWTH Aachen University

Prof. Dr.-Ing. Mathias **Liewald**, Institute for Metal Forming Technology, University of Stuttgart

Fabian **Maaß**, M. Sc., Institute of Forming Technology and Lightweight Components, TU Dortmund University

Dr.-Ing. Thomas **Mehner**, Institute of Materials Science and Engineering, University of Technology Chemnitz

Prof. Dr.-Ing. Marion **Merklein**, Institute of Manufacturing Technology, Friedrich-Alexander-Universität Erlangen-Nürnberg

Daniel **Müller**, M. Sc., Institute of Machine Elements, Technical University of Munich

Tobias **Neuwirth**, M. Sc., Research Neutron Source Heinz Maier-Leibnitz, Technical University of Munich

Anian **Nürnberger**, M. Sc., Chair of Metal Forming and Casting, TUM School of Engineering and Design, Technical University of Munich

Prof. Dr.-Ing. Matthias **Oechsner**, Center for Structural Materials, Technical University Darmstadt

Pavlo **Pavliuchenko**, M. Sc., Institute of Metal Forming, RWTH Aachen University

**Maximilian Plötz**, M. Sc., Chair of Metal Forming and Casting, TUM School of Engineering and Design, Technical University of Munich

Dipl.-Chem. Stefanie **Prauser**, Chair of Metal Forming and Casting, TUM School of Engineering and Design, Technical University of Munich

Erwin **Reberger**, M. Sc., Chair of Metal Forming and Casting, TUM School of Engineering and Design, Technical University of Munich

Prof. Dr. Walter **Reimers**, Institute for Materials Science and Technologies, Technical University Berlin

Dr.-Ing. Kim Rouven **Riedmüller**, Institute for Metal Forming Technology, University of Stuttgart

Aron **Ringel**, M. Sc., Institute of Metal Forming, RWTH Aachen University

Benedikt **Schauerte**, M. Sc., Institute of Electrical Machines, RWTH Aachen University

Dipl.-Ing. Christian **Schenck**, Center for Materials and Processes - MAPEX, Bremen Institute for Mechanical Engineering, University of Bremen

Dipl.-Ing. Tom **Schneider**, Chair of Computational and Experimental Solid Mechanics, TUD Dresden University of Technology

Prof. Dr.-Ing. Jörg **Schröder**, Institute of Mechanics, Faculty of Engineering, University Duisburg-Essen

Dr. rer. nat. Michael **Schulz**, Research Neutron Source Heinz Maier-Leibnitz, Technical University of Munich

Simon **Sebold**, M. Sc., Research Neutron Source Heinz Maier-Leibnitz, Technical University of Munich

René **Selbmann**, M. Sc., Solid Forming Department, IWU Fraunhofer-Institute for Machine Tools and Forming Technology

Christian **Siedbürger**, M. Sc., Institute for Production Engineering and Forming Machines, Technical University Darmstadt

Dipl.-Ing. Nicola **Simon**, Institute of Applied Materials, KIT Karlsruhe Institute of Technology

Prof. Dr.-Ing. Karsten **Stahl**, Institute of Machine Elements, Technical University of Munich

Prof. Dr.-Ing. Paul **Steinmann**, Institute of Applied Mechanics, Friedrich-Alexander-Universität Erlangen-Nürnberg

Prof. Dr.-Ing. A. Erman **Tekkaya**, Institute of Forming Technology and Lightweight Components, TU Dortmund University

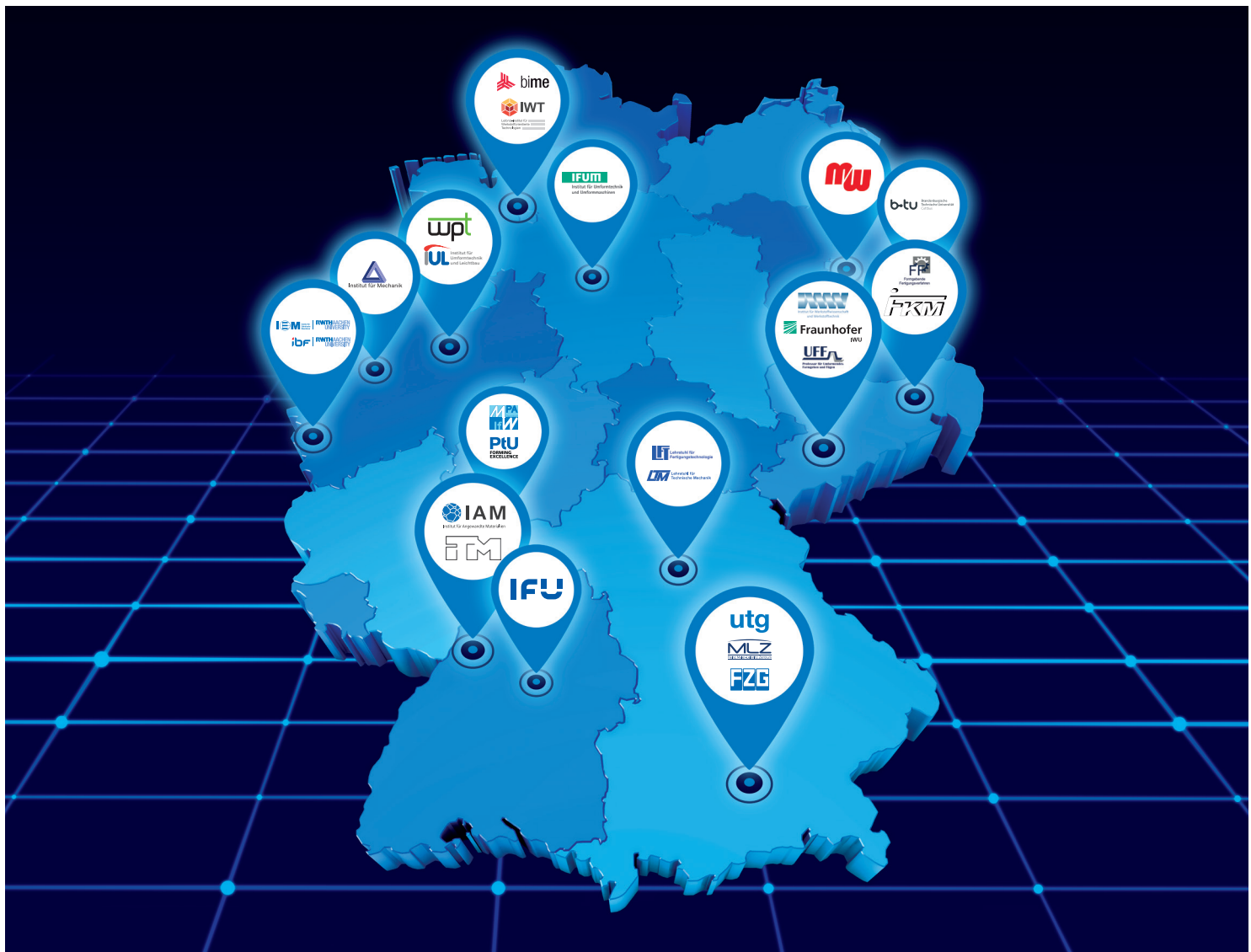
Dr.-Ing. Thomas **Tobie**, Institute of Machine Elements, Technical University of Munich

Prof. Dr.-Ing. Wolfram **Volk**, Chair of Metal Forming and Casting, TUM School of Engineering and Design, Technical University of Munich

Prof. Dr.-Ing. Frank **Walther**, Department of Materials Test Engineering, TU Dortmund University

Hendrik **Wester**, M. Sc., Institute of Forming Technology and Machines, Leibniz Universität Hannover

Dr.-Ing. Lisa **Winter**, Institute of Materials Science and Engineering, University of Technology Chemnitz



Residual stresses are considered critical to quality in conventional manufacturing strategies. This is where the DFG's Priority Programme 2013 comes in, looking instead at the opportunities and possibilities for improving the properties of components by targeted use of residual stresses. In the years 2017 to 2023, research teams from all over Germany were able to prove the stability, controllability and usefulness of residual stresses in flat and solid forming manufacturing processes of metallic components. In addition, the cross-project working groups achieved many insights into the fundamental understanding, simulation and, in particular, industry-oriented measurement of residual stresses.

The extensive results of these six years of research activities are presented in this final report.